# Tuning of novel organic scaffolds for competent detection of bio-relevant, environmentally hazardous ions and chemical weapons

*Thesis submitted for the degree of*

**DOCTOR OF PHILOSOPHY (SCIENCE)**

**June-2025**

**by**

**Mr. Amitav Biswas**

**Index No: 108/21/Chem./27**
**Registration No: SCHEM1110821**


**Department of Chemistry**
**Jadavpur University, Kolkata - 700 032**
**INDIA**

**Dr. T.K. Mondal, Ph. D.**
**Professor**
**Department of Chemistry**
**Inorganic Chemistry Section**

**JADAVPUR UNIVERSITY**
**Kolkata – 700 032, India**
**Telephone: 91-033-2457-2970**
**tapank.mondal@jadavpuruniversity.in**

## CERTIFICATE FROM THE SUPERVISOR(S)

This is to certify that the thesis entitled "**Tuning of novel organic scaffolds for competent detection of bio-relevant, environmentally hazardous ions and chemical weapons**" submitted by **Mr. Amitav Biswas**, M.Sc., who got his name registered on **24.11.2021** for the award of Ph.D. (Science) degree of Jadavpur University, is absolutely based upon his own work under the supervision of **Dr. Tapan Kumar Mondal** and that neither this thesis nor any part of it has been submitted for either any degree / diploma or any other academic award anywhere before.

Tapan K. Mondal 05/06/2025

Signature of the Supervisor(s) date with official seal

Dr. TAPAN KUMAR MONDAL
*Professor*
Department of Chemistry
Jadavpur University
Kolkata-700032

*"What is research but a blind date with knowledge?"*

*~Will Harvey*

*Dedicated to*

*My parents and teachers…*

# ACKNOWLEDGEMENTS

My research journey, which started on 15th October, 2020 has now come to an end, leaving me not only a more proficient researcher but also a more mature individual. Many individuals have had a deep influence on my thought process during this journey, impacting me both directly and indirectly. I would like to take this moment to express my sincere appreciation and gratitude to my supervisor Dr. Tapan Kumar Mondal, Professor, Department of Chemistry, Jadavpur University, Kolkata - 700 032 for allowing me to do research freely in his group. This journey would not have been achievable without his continuous support and inspiring guidance throughout the work. I sincerely appreciate his valuable guidance during my research and his unwavering support in guiding me through the entire thesis.

I would like to express my heartfelt thanks to the faculty members of Department of Chemistry, Jadavpur University, Prof. Kajal Krishna Rajak, Head, Department of Chemistry, Prof. Chittaranjan Sinha, Dean of Science, JU, Prof. Partha Roy, Section-In-Charge, Inorganic Chemistry Section and all other faculty members of Department of Chemistry, Jadavpur University. I extend my sincere gratitude to Dr. Nabin Baran Manik, Head of the physics Department, Jadavpur University, for his invaluable insights that have significantly advanced my research. I extend my heartfelt gratitude to all the teaching and non-teaching staff members of this department and university for their valuable support in numerous ways.

Financial assistance received from Council of Scientific and Industrial Research (CSIR), New Delhi [File no. 09/096(1023)/2020-EMR-I] is gratefully acknowledged.

I also express my appreciation as well as gratefulness to all my present labmates viz., Dr. Saswati Gharami, Mr. Subrata Mandal, Mr. Arpan Halder, Ms. Moumita Ghosh, Mr. Chandrasekhar Mandi, Mr. Wasim Akram, Mr. Toby Biswas, Mr. Sourav Saha, Mrs. Gita Rani Murmu for their constant help and support throughout my research journey. Some of my other former lab colleagues, such as, Dr. Atanu Maji, Dr. Rahul Naskar, Dr. Biswajit Bera, Dr. Akash Das, Dr. Samik Acharyya, Mr. Sandipan Mandal also supported and guided me through the ups and downs during my research journey and a special thanks to Dr. Saswati Gharami for her unconditional support in making my research journey free of obstacles. Last but not the least Dr. Krishnendu Aich Who provided clarity on any doubts that arose during my research process. The journey was made significantly easier and more vibrant with their constant presence and enthusiasm. I will always cherish all the beautiful memories I have made with them and I would like to express my gratitude to each individual for making the lab a warm and cooperative space, enabling me to conduct my research with ease. I extend my sincere gratitude to my collaborators for their insightful input and the generous provision of resources, both of which have played a pivotal role in the development and completion of this thesis.

I express my deepest gratitude to my M.Sc. project supervisor, Prof. Braja Gopal Bag, Vidyasagar University for initializing the spirit of research through me during my masters which ultimately led me to begin this research journey. I am forever grateful to Mr. Atanu Jana, whom I used to learn Inorganic Chemistry during my B.Sc. days Who also encouraged me to embark on the path of research. I am grateful to all my M. Sc. project students, especially to Mr. Arambhik Nath, Mr. Sourav Manna and Mr. Toby Biswas Who not only expanded my knowledge with frequent conversations about their work but also kept the atmosphere lively and enjoyable in their own way. I am filled with gratitude towards my childhood teachers, Mrs. Kuheli Dalui and Mr. Durgadas Ghosh for nurturing my growth, both in academics and beyond, from my school years to the present. I also express my thankfulness to Dr. Buddhadeb Chakraborty, Mr. Agnibha Dutta, Mr. Arnab Rout for their pleasant company during my stay in Jadavpur. I would also like to express my gratitude to Mr. Sasanka Sekhar

Samanta, whose guidance enhanced my understanding of Chemistry during my M.Sc. and whose constant support has been invaluable in all aspects of my life. It would have been a monotonous journey if my closest childhood friends Mr. Samik Hazra, Mr. Subhendu Karmakar, Mr. Atanu Maity, Mr. Bipratim Ghosh, Mr. Manoj Ghosh stand strong with me every single time I needed them.

I am deeply grateful to my wife Mrs. Ahana Biswas for her consistent encouragement and unwavering support, which helped me maintain my motivation in every phase of my research.

Lastly, but most importantly with all the gratitude in my heart I would like to thank my father Sri Debdulal Biswas and my mother Smt. Reba Biswas, Anirban Biswas my younger brother, Smt. Rita Biswas my grandmother for their constant encouragement, backing and firm confidence in me and my capabilities. I will forever try, though unsuccessfully, to love them as fiercely as they love me. My sincere thanks go to all of the people mentioned above for their constant support, mental fortitude, and immense love, which empowered me to remain resilient and complete this journey successfully.

Amitav Biswas
5.6.2025

**(Amitav Biswas)**
Department of Chemistry
Jadavpur University

# CONTENTS


| | | Page Number |
|---|---|---|
| **PREFACE** | | i-iv |
| **Chapter 1** | **A concise and basic prologue to chemosensor and its sensing patterns along with its application** | **1-48** |
| | 1.1 Introduction | 2-7 |
| | 1.2. Supramolecular Chemistry: The origin | 8 |
| | 1.3. Specific molecular interaction | 8-9 |
| | 1.4. Chemosensors and Chemodosimeters: Definitions and Distinctions | 9-11 |
| | 1.5. Classification of sensors | 11-13 |
| | 1.5.1. Optical sensors | 11-12 |
| | 1.5.2. Electrochemical sensors | 13 |
| | 1.6. Non-Covalent Forces Governing Chemosensor-Analyte Binding | 13-18 |
| | 1.6.1. Hydrogen bonding interactions | 14-15 |
| | 1.6.2. Electrostatic interactions | 15 |
| | 1.6.3. Van der Waals forces | 15-16 |
| | 1.6.4. π-π stacking | 16-17 |
| | 1.6.5. Hydrophobic Interactions | 17 |
| | 1.6.6. CH- π interactions | 17-18 |
| | 1.6.7. Close packing in the solid phase | 18 |
| | 1.7. Principles of Chemosensor Design and Molecular Recognition | 18-22 |
| | 1.7.1. Criteria of designing an ideal chemosensor | 18-19 |
| | 1.7.2. Binding of metal cations | 19-20 |
| | 1.7.3. Binding of anions | 20-22 |
| | 1.8. Different mechanisms of Fluorescence-Based Sensing | 23-35 |
| | 1.8.1. ESIPT (Excited State Intramolecular Proton Transfer) mechanism | 23-25 |
| | 1.8.2. Rigidity or chelation enhanced fluorescence (CHEF) effect | 25-26 |
| | 1.8.3. ICT (Intramolecular charge transfer) mechanism | 27-28 |
| | 1.8.4. PET (Photo-induced electron transfer) process | 29-31 |
| | 1.8.5. FRET (Fluorescence resonance energy transfer) process | 31-33 |
| | 1.8.6. Fluorescence quenching | 33-35 |
| | 1.9. Chemosensors: From Molecular Design to Practical Applications | 35-44 |
| | 1.9.1. Drug design | 35-36 |
| | 1.9.2. Optical biosensor | 36 |
| | 1.9.3. Nanoscience | 37 |
| | 1.9.4. Application through Dip-stick experiment | 37-39 |
| | 1.9.5. Application of chemosensors in live cell imaging | 39-43 |

| | | |
|---|---|---|
| | 1.9.6. Application of chemosensors in real-world sample analysis | 43-44 |
| | 1.10. Plan of the thesis | 44-45 |
| | 1.11. References | 45-48 |
| **CHAPTER 2** | **General Instrumentations and analysis techniques** | **49-66** |
| | 2.1. Introduction | 50 |
| | 2.2. Reagents for synthesis | 50 |
| | 2.3. Several physio-chemical characterizations Methods | 51-59 |
| | 2.3.1. $^{1}$H NMR Spectroscopy | 51-53 |
| | 2.3.2. $^{13}$C NMR Spectroscopy | 53-54 |
| | 2.3.3. High resolution mass spectrometry (HRMS) and Elemental analysis | 54 |
| | 2.3.4. Infrared Spectroscopy (IR) | 54-55 |
| | 2.3.5. UV-Vis absorption spectroscopy | 55-56 |
| | 2.3.6. Fluorescence Spectroscopy | 56-57 |
| | 2.3.7. Fluorescence lifetime measurement | 57-58 |
| | 2.3.8. Single crystal X-ray diffraction technique | 58-59 |
| | 2.4. Theoretical calculation | 59 |
| | 2.5. Instrumentation segment of the spectroscopic techniques | 60-64 |
| | 2.5.1. NMR technique | 60 |
| | 2.5.2. HRMS technique | 60-61 |
| | 2.5.3. IR technique | 61-62 |
| | 2.5.4. UV-Vis technique | 62-63 |
| | 2.5.5. Fluorometry | 63-64 |
| | 2.5.6. Fluorescence lifetime technique | 64 |
| | 2.6. Some essential methods to study the chemosensors | 65-66 |
| | 2.7. References | 66 |
| **CHAPTER 3** | **A new "turn-on" molecular switch for idiosyncratic detection of $Al^{3+}$ ion along with its application in live cell imaging** | **67-101** |
| | 3.1. Introduction | 69-70 |
| | 3.2. Prior works | 70 |
| | 3.3. Present work | 70 |
| | 3.4. Results and discussions | 70-85 |
| | 3.4.1. Design and synthesis of the probe HBTC | 70-71 |
| | 3.4.2. 1H NMR and HRMS analysis of HBTC | 71 |
| | 3.4.3. $Al^{3+}$ sensing studies of HBTC using UV-Vis spectroscopy | 71-72 |
| | 3.4.4. $Al^{3+}$ sensing studies of HBTC using emission spectroscopy | 72-74 |
| | 3.4.5. Binding studies of HBTC with $Al^{3+}$ | 74-75 |
| | 3.4.6. Fluorescence lifetime decay studies of HBTC with $Al^{3+}$ | 75-76 |
| | 3.4.7. Reusability study | 76-77 |
| | 3.4.8. Effect of pH | 77-78 |
| | 3.4.9. Time course of sensing | 78 |
| | | 79-81 |

3.4.10. Probable sensing mechanism of HBTC 81-82
3.4.11. Dip-stick experiment: sensing of $Al^{3+}$ using TLC plate 82-84
3.4.12. Bio-imaging study
3.4.13. Computational studies to interpret further structural changes in HBTC and HBTC-$Al^{3+}$ 84-85
3.5. Conclusions 85
3.6. Experimental 85-89
3.6.1. Reagents and methods 85-86
3.6.2. Synthesis of the probe 4-hydroxy-(([1,1'-biphenyl]-3-yl) methylene) thiophene-2-carbohydrazide (HBTC) 86
3.6.3. General Method for UV-Vis and Fluorescence Titration 86-88
3.6.4. Live cell imaging studies 88
3.6.5. Theoretical study 89
3.7. Notes and references 89-91
Appendix 92-101

**Chapter 4** **A biphenyl thiosemicarbazide based chemosensor for selective fluorogenic recognition of $Cd^{2+}$ and as an imaging agent in living cells** **102-143**
4.1. Introduction 104-105
4.2. Prior works 105-106
4.3. Present work 106
4.4. Results and discussions 106-122
4.4.1. Design and synthesis of the receptor HBMC 106
4.4.2. $^1H$ NMR and HRMS analysis of HBMC 107
4.4.3. Binding studies of $Cd^{2+}$ with HBMC using UV-Vis spectroscopy 107-108
4.4.4. Binding studies of $Cd^{2+}$ with HBMC using Fluorescence spectroscopy 108-110
4.4.5. Binding studies of HBMC with $Cd^{2+}$ 110-111
4.4.6. Fluorescence lifetime decay studies of HBMC with $Cd^{2+}$ 111-112
4.4.7. Reusability study 112-113
4.4.8. Effect of pH 113-114
4.4.9. Time course of sensing 114-115
4.4.10. Probable sensing mechanism of $Cd^{2+}$ sensing 115-117
4.4.11. Dip-stick experiment: Sensing of $Cd^{2+}$ using TLC plate 118
4.4.12. Cellular imaging by fluorescence microscopy 119-120
4.4.13. Real water sample analysis 121
4.4.14. Computational studies to interpret further structural changes in HBMC and HBMC-$Cd^{2+}$ 121-122
4.5. Conclusions 122-123
4.6. Experimental 123-127
4.6.1. Reagents and methods 123
4.6.2. Synthesis of probe (E)-2-((4-hydroxy-[1,1'-biphenyl]-3-yl) methylene)-N-methylhydrazine-1- 123-124

carbothioamide (HBMC)
4.6.3. General Method for UV-Vis and Fluorescence Titration 124-126
4.6.4. Live cell imaging studies 126-127
4.6.5. Computational method 127
4.7. Notes and references 127-130
Appendix 131-143

**Chapter 5** **Adaptable coumarin based fluorescent molecular multianalyte sensor for $Zn^{2+}$, $Hg^{2+}$ and $Cu^{2+}$ via different sensing modalities and its bioimaging applications** **144-198**
5.1. Introduction 146-148
5.2. Prior works 148
5.3. Present work 148-149
5.4. Results and discussions 149-171
5.4.1. Synthesis of the sensor (DCMC) 149
5.4.2. Crystal structure of DCMC 150
5.4.3. Supramolecular Interaction and Hirshfeld Surface Analysis of the Sensor DCMC 150-153
5.4.4. Spectroscopic analysis 153-160
5.4.4.1. UV-Vis study of DCMC 153-155
5.4.4.2. Fluorescence study of DCMC 155-157
5.4.4.3. Detection limit (LOD) and binding constant (Ka) 158-159
5.4.4.4. Competitive study 160-161
5.4.4.5. pH effect 161-162
5.4.5. TRPL Study 162-163
5.4.6. Possible sensing mechanism 163-165
5.4.7. Analytical applications 165-167
5.4.8. Application in biological study 167-169
5.4.9. Theoretical computations 169-171
5.5. Conclusions 171-172
5.6. Experimental 172-176
5.6.1. Materials and instrumentations 172-173
5.6.2. Synthesis of probe (E)-2-((7-(diethylamino)-2-oxo-2H-chromen-3-yl) methylene)-N-methylhydrazine-1-carbothioamide (DCMC) 173
5.6.3. UV-Vis and fluorescence method 174
5.6.4. pH solution preparation method 174
5.6.5. X-ray crystallography 174-175
5.6.6. Computational methodology 175
5.6.7. Statistical Analysis 175
5.6.8. Live cell imaging studies 175-176
5.6.9. Determination of fluorescence quantum yield 176
5.7. Notes and references 176-180
Appendix 181-198

**Chapter 6** **A triphenylamine scaffold for fluorogenic sensing of noxious cyanide via ICT mechanism and its** **199-240**

**bioimaging application**
6.1. Introduction 201-202
6.2. Prior works 202
6.3. Present work 203
6.4. Results and discussions 203-219
6.4.1. Design and Synthesis of the sensor (PBIA) 203
6.4.2. Photophysical properties of PBIA 204-212
6.4.2.1. UV-vis spectral studies 204-205
6.4.2.2. Fluorescence spectral study 205-207
6.4.2.3. Binding studies of PBIA with $CN^-$ 207-208
6.4.2.4. Competitive study 208-209
6.4.2.5. Time dependent spectra of PBIA with $CN^-$ 209-210
6.4.2.6. TRPL Study 210-211
6.4.2.7. Effect of pH 211-212
6.4.3. Possible sensing mechanism of PBIA 213-214
6.4.4. Dip-stick experiment: Detection of $CN^-$ using TLC plate 214-215
6.4.5. Real water sample analysis 215-216
6.4.6. Cell Study 216-218
6.4.7. Computational study 218-219
6.5. Conclusions 219-220
6.6. Experimental 220-224
6.6.1. Materials and instrumentations 220
6.6.2. General Method for UV-Vis and Fluorescence Titration 221
6.6.3. pH solution preparation method 221
6.6.4. Synthesis of 4,4'-(phenylazanediyl) dibenzaldehyde 221
6.6.5. Synthesis of 2-cyanomethylbenzimidazole 221
6.6.6. Synthesis of (2E,2'E)-3,3'-((phenylazanediyl)bis(4,1-phenylene)) bis(2-(1H-benzo[d]imidazol-2-yl) acrylonitrile) (PBIA) 221-222
6.6.7. Theoretical study 222-223
6.6.8. Job's plot by absorbance method 223
6.6.9. Determination of fluorescence Quantum Yields (Φ) of PBIA and its complex with CN- 223
6.6.10. Application of PBIA in real water sample analysis 223-224
6.6.11. Live cell imaging studies 224
6.7. Notes and references 224-227
Appendix 228-240

**Chapter 7** **A distinctive and proficient fluorescent switch for ratiometric recognition of the menacing cyanide ion: Biological studies on MDA-MB-231 cells** **241-271**
7.1. Introduction 243-244
7.2. Prior works 244
7.3. Present work 244-245
7.4. Results and discussions 245-258
7.4.1. Synthesis of the probe (BOHB) 245

7.4.2. Sensing studies of the chemodosimeter (BOHB) 246-253
7.4.2.1. UV-vis spectral studies 246-247
7.4.2.2. Fluorescence spectral study 247-248
7.4.2.3. Interaction studies of BOHB with $CN^-$ 248-249
7.4.2.4. Competitive study 249
7.4.2.5. Time dependent spectra of BOHB with CN- 250-251
7.4.2.6. Recyclability of BOHB 251-252
7.4.2.7. Time-resolved photoluminescence study (TRPL) Study 252
7.4.2.8. Effect of pH 253
7.4.3. Possible sensing mechanism of BOHB 253-255
7.4.4. Detection of CN- ion using Dipstick Experiment 255
7.4.5. Real water sample analysis 255-256
7.4.6. Cell Study 256-258
7.5. Conclusions 258
7.6. Experimental 259-262
7.6.1. Materials and methods 259
7.6.2. General Method for UV-Vis and Fluorescence Titration 259
7.6.3. Determination of fluorescence quantum yield: 259-260
7.6.4. Determination of detection limit (LOD) 260
7.6.5. Synthesis of (E)-N'-(3-(benzo[d]oxazol-2-yl)-2-hydroxybenzylidene)-2-hydroxybenzohydrazide (BOHB) 260-261
7.6.6. Live cell imaging studies 261-262
7.7. Notes and references 262-264
Appendix 265-271

**Chapter 8** **An ICT based organic framework for fluorogenic detection of lethal pulmonary agent phosgene** **272-304**
8.1. Introduction 274
8.2. Prior works 275
8.3. Present work 275-276
8.4. Results and discussions 276-288
8.4.1. Synthesis of the probe (BPCI) 276
8.4.2. Spectral characterization and analysis of BPCI & BPCI-PHOS 277
8.4.3. Sensing studies of the probe (BPCI) in solution phase 277-282
8.4.3.1. Phosgene sensing studies of BPCI using UV-Vis spectroscopy 277-278
8.4.3.2. Phosgene sensing studies of BPCI using fluorescence spectroscopy 278-281
8.4.3.3. The binding studies of BPCI with Phosgene 281-282
8.4.3.4. Time dependent fluorescence study of BPCI with phosgene 282
8.4.4. Fluorescence lifetime Study 283
8.4.5. Probable sensing mechanism of BPCI 283-285
8.4.6. Vapour phase detection of Phosgene by BPCI 285-286
8.4.7. Practical application of BPCI loaded test strips in 286-287

gas phase
8.4.8. Computational study 287-288
8.5. Conclusions 288
8.6. Experimental 289-292
8.6.1. Materials and methods 289
8.6.2. Synthesis of 4-hydroxy-[1,1'-biphenyl]-3-carbaldehyde 289
8.6.3. Synthesis of 2-cyanomethylbenzimidazole 289
8.6.4. Synthesis of 3-(1H-benzo[d]imidazol-2-yl)-6-phenyl-2H-chromen-2-imine (BPCI) 290
8.6.5. Synthesis of BPCI-PHOS adduct 290
8.6.6. General Method for UV-Vis and Fluorescence Titration 291
8.6.7. Determination of fluorescence quantum yield 291
8.6.8. Theoretical study 292
8.7. Notes and references 292-294
Appendix 295-304
**LIST OF PUBLICATION** **305-306**

# PREFACE

The design and fabrication of fluorescence chemosensors is a highly interdisciplinary field of research today, owing to their significant importance and wide-ranging applications in chemistry, biology, medicine, environmental science, and beyond. Chemosensors and chemodosimeters are compounds that detect specific analytes by undergoing structural changes that alter properties such as absorption or fluorescence emission. Recent advancements in this field have enabled its application in targeted drug delivery systems and live cell imaging for biological studies.

My thesis work entitled, **"Tuning of novel organic scaffolds for competent detection of bio-relevant, environmentally hazardous ions and chemical weapons"** involves the design and synthesis of a range of fluorescent and non-fluorescent probes, supported by thorough binding studies aimed at the accurate detection of targeted ions and toxic analytes. The newly developed molecules show promise as chemosensors for detecting ions of environmental and biological relevance and chemical weapons. The newly designed chemosensors can be synthesized through a simple, economical, and efficient process. The structures of the synthesized probes were validated using a combination of spectroscopic techniques, such as $^{1}$H NMR, $^{13}$C NMR, 2D NMR, mass spectrometry, IR spectroscopy, and single-crystal X-ray diffraction. The binding interactions of the host-guest system and the resulting complex or adduct formation were comprehensively analyzed using UV-Vis spectroscopy, fluorescence, Job's plot, $^{1}$H/$^{13}$C NMR, and HRMS. The biological relevance of the designed probes was investigated through their application as imaging agents in live-cell studies. The thesis is structured into eight chapters, each addressing the synthesis, structural characterization, and detailed sensing behavior of the newly constructed fluorescent probes. To gain deeper insight into the sensing mechanisms, Density Functional Theory (DFT) calculations were carried out in the Gaussian 09 software suite. Several of the synthesized probes have demonstrated successful applicability in the analysis of real-world samples.

**Chapter 1** provides a brief introduction to the fundamental concepts of chemosensors, including their definitions, classifications, and the underlying principles of various non-covalent

interactions. It also outlines the essential criteria for designing host and guest systems. Additionally, a concise yet comprehensive literature review is presented, highlighting various reported chemosensors based on different molecular recognition mechanisms.

**Chapter 2** outlines the detailed instrumentation techniques employed in the characterization and analysis of chemosensors, including $^{1}H$ and $^{13}C$ NMR, IR spectroscopy, HRMS, UV-Vis absorption, fluorescence spectroscopy, lifetime decay measurements, and single-crystal X-ray crystallography. This chapter also describes essential analytical methods such as quantum yield calculation, detection limit estimation, and association constant determination, which are crucial for the comprehensive evaluation of molecular sensing probes.

**Chapter 3** represents with the fabrication and charecterization of a highly sensitive, reversible, reusable and fluorogenic ‘‘turn-on’’ probe (HBTC) for the sole detection of $Al^{3+}$. On incremental addition of $Al^{3+}$ in a solution of HBTC in ACN: $H_2O$ (4: 1), a sharp ‘‘turn-on’’ emission enhancement is observed. The reusability and real-time application of the probe were also studied. Bioimaging study reveals that HBTC can detect $Al^{3+}$ in human breast cancer cells (MDA-MB-231).

**Chapter 4** presents the fabrication of a biphenyl thiosemicarbazide based chemosensor (HBMC) which showed specific detection of $Cd^{2+}$ in MeOH: $H_2O$ (4:1) solution. Where we observed a chromogenic change from colorless to light yellow colour, as well as it shows a “turn-on” fluorogenic change from non-fluorescent to blooming cyan colour. The reusability study was performed and on-sight detection of cadmium ion by chemosensor (HBMC) was established by Dip-stick experiment. Moreover, In vitro detection of $Cd^{2+}$ in human breast cancer cells (MDA-MB-231) by HBMC discloses its cell permeability and biocompatibility nature.

**Chapter 5** deals with the fabrication of a new fluorescent organic probe DCMC (E)-2-((7-(diethylamino)-2-oxo-2H-chromen-3-yl) methylene)-N-methylhydrazine-1-carbothioamide. The systematic sensing studies of DCMC in DMSO/$H_2O$ (9/1, v/v, pH = 7.2) by fluorescence and absorption method showed selectivity towards $Hg^{2+}$, $Zn^{2+}$ and $Cu^{2+}$ by different sensing modalities. A detailed investigation was performed on the detection mechanism by using Job’s plot, $^{1}H$-NMR, ESI mass analysis and density functional theory (DFT) calculations which established the 2:1 binding stoichiometry for all the three ions. The live cell imaging study on MCF-7 cell line to detect $Zn^{2+}$ and $Hg^{2+}$ also reveals the detection capability of DCMC and its biocompatible nature.

**Chapter 6** introduces a novel triphenylamine benzimidazole based fluorogenic chemosensor (PBIA) which was successfully generated and characterized by varoius spectroscopic techniques. Among various screened anions only cyanide ($CN^-$) showed a distinct fluorogenic property towards PBIA. where we observed that, upon treatment of $CN^-$ to probe solution, the orange fluorescence of ligand showed a blue shift and the orange fluorescence changed to greenish-yellow under UV lamp. Furthermore, the practical efficacy of the probe PBIA was established by dip-stick experiment along with cyanide detection in various natural water resources. Human breast cancer cells MDA-MB 231 makes it susceptible to $CN^-$ sensing in biological system.

**Chapter 7** reports synthesis of a new fluorescent ratiometric switch (BOHB) which showed swift and distinct detection of cyanide ion in aqueous media without any interference of other competitive anions. The blue shift in fluorescence intensity upon the addition of cyanide ion was attributed to the deprotonation mechanism of acidic protons present in BOHB. Also, the detection limit of this new probe was found to be (22.1±0.89) μM. Triple negative breast adenocarcinoma (MDA-MB-231) cells were made susceptible to $CN^-$ sensing in a biological system thereby making BOHB a biomarker tool.

Lastly, **Chapter 8** describes a biphenyl-benzoimidazole based (BPCI) chemodosimeter which displayed a rapid, sensitive and ratiometric detection towards lethal pulmonary agent phosgene. The chemodosimeter (BPCI) showed nucleophilic substitution reaction with phosgene followed by a ring closure to yield the carbamylated final product and showed an explicit ratiometric fluorescence response towards phosgene. This ratiometric switch which we developed, was used as a potential portable kit for detecting phosgene in vapour phase, as well as in solid phase when supported upon TLC plates. Theoretical calculation by DFT/B3LYP/6-31+G(d) method was performed to unveil the electronic properties theoretically and to interpret the probable sensing mechanism.

In summary, this thesis focuses on the synthesis of several novel fluorescent molecules with the potential to detect environmentally and biologically significant ions andchemical weapons, along with their application in live-cell imaging. Andrreal sample analysis. It is gratifying to note that most of these research findings have been published in several reputed international journals.

In keeping with established scientific norms, proper acknowledgement has been made whenever the work is based on the contributions of other researchers. I sincerely acknowledge responsibility for any inadvertent errors or omissions that may remain, despite careful efforts to avoid them.

Amitav Biswas

**(Amitav Biswas)** 5.6.2025

**Department of Chemistry**

**Jadavpur University**

# Chapter 1

# A succinct yet comprehensive prelude to organic chemosensory agents, emphasizing their operative detection models and cross-disciplinary utilizations

# 1.1. Introduction

Metal ions play a fundamental and indispensable role in maintaining a wide range of biological functions in humans, animals, and plants.[1] Some of these ions serve as essential cofactors in participating in crucial biochemical processes such as metabolism,cellular signalling, enzymatic systems, and structural stabilization. However, both the deficiency and excess of metal ions can disrupt physiological balance, potentially leading to various health disorders.Essential metal ions include main group elements such as magnesium (Mg), sodium (Na), potassium (K), and calcium (Ca), as well as transition metals like chromium (Cr), copper (Cu), zinc (Zn), iron (Fe), cobalt (Co), nickel (Ni), cadmium (Cd), molybdenum (Mo),vanadium (V), manganese (Mn), which are essential for biological process.[2] The deficiency of cobalt (Co) or iron (Fe) is associated with anaemia; insufficient levels of zinc (Zn) can result in dermatological issues and growth impairment; chromium (Cr) deficiency can impair glucose tolerance; a lack of copper (Cu) has been linked to cardiovascular and neurological disorders; and calcium (Ca) deficiency often leads to bone demineralization and related skeletal disorders. In addition to biologically essential metals, there exists a group of elements—including arsenic (As), bismuth (Bi), germanium (Ge), mercury (Hg), lead (Pb), nickel (Ni), strontium (Sr), tin (Sn), uranium (U), aluminum (Al), barium (Ba), cadmium (Cd), gold (Au), lithium (Li), platinum (Pt), tellurium (Te), titanium (Ti), antimony (Sb), beryllium (Be), gallium (Ga), indium (In), silver (Ag), thallium (Tl), and vanadium (V)—that are generally regarded as nonessential for biological systems, as they have no well-defined or recognized cellular functions.[3] Conversely, heavy metal elements are widely recognized for their detrimental effects on biological systems. These metals can compromise cellular integrity by damaging the cell membrane and thus disrupting the function of critical organelles such as mitochondria, lysosomes, the endoplasmic reticulum, and the nucleus.[4] Moreover, heavy metal toxicity can lead to the inactivation of vital enzymes, impairing numerous biochemical pathways essential for normal cellular function.The presence of heavy metals has also been shown to alter the conformations of DNA and nuclear proteins, thereby influencing the regulation of the cell cycle and contributing to the onset of carcinogenesis.[5] Among the various toxic elements, mercury (Hg), cadmium (Cd), arsenic (As), lead (Pb), and chromium (Cr) are of particular concern due to their widespread environmental occurrence and severe public health implications.[6] Given that each metal possesses distinct physicochemical characteristics, the mechanisms of toxicity differ considerably and in many cases, remain only

partially understood. As a result of their universaltoxicity and persistent presence in the biosphere, it is critically important to develop effective strategies for the detection, identification, and monitoring of biologically relevant as well as heavy metals. As such efforts are essential for the diagnosis and potential treatment of various metal-induced diseases.

Furthermore, in addition to metal toxicity, emerging threats from hazardous organic compounds have raised new concerns, underscoring the need for comprehensive environmental and biomedical monitoring systems.In addition to metal toxicity, the human population is increasingly threatened by hazardous organic compounds, some of which are synthetically produced for industrial or military purposes, while others originate from natural disasters or environmental degradation. Among these, chemical warfare agents (CWAs) represent one of the most destructive and ethically concerning categories of toxic substances developed by mankind.[7-10] These agents, whether intentionally synthesized or unintentionally formed as byproducts of chemical manufacturing, possess extremely high toxicity and pose severe risks to both human health and ecological systems. Although thousands of chemical compounds exhibit toxic properties, only a selected few are designated as CWAs based on criteria such as toxicity level, rapid onset of action, environmental persistence, and their ability to evade detection by human senses. The use of CWAs as weapons was first witnessed on a large-scale during World War I, when chlorine gas was deployed by the German army in Belgium in 1915.[11] That event marked the beginning of a devastating era, leading to approximately 100,000 deaths and 1.2 million injuries from chemical attacks during the war.[12] Since then, the deployment of CWAs has resulted in repeated tragedies, inflicting mass casualties and long-term environmental and biological damage. Among the various classes of CWAs, organophosphorus nerve agents are particularly lethal and warrant significant attention. Their ease of synthesis, low production cost, and widespread availability make them especially dangerous in the hands of non-state actors or terrorist groups. Even simple organophosphorus compounds, originally designed for agricultural use, have the potential to be repurposed as deadly chemical weapons in warfare or acts of bioterrorism.

In addition to chemical warfare agents, cyanide has also been employed as a chemical weapon, notably in the form of hydrogen cyanide (HCN) during World War I.[13] Due to its extreme toxicity, cyanide is also classified among the fatal chemical warfare agents. Its hazardous nature stems from its potent ability to disrupt vital cellular processes, posing a significant threat to both human health and environmental safety. Despite its toxicity, cyanide continues to play a critical

role in various industrial applications, including electroplating, petrochemical processing, photography, steel manufacturing, gold mining, metallurgy, and the synthesis of resins and synthetic fibres, owing to its versatility in multi-functional chemical reactions.[14] To mitigate its risks, the World Health Organization (WHO) has established a maximum permissible concentration of $1.9 \times 10^{-6}$ mol/L for cyanide in drinking water.[15] Cyanide is also naturally present in certain plants, seeds, roots, and insects, where it is released through the enzymatic hydrolysis of cyanogenic glycosides.[16-18] Biologically, cyanide exerts its toxic effects by binding to the iron centre of cytochrome c oxidase, a key enzyme in the mitochondrial electron transport chain. This binding inhibits ATP production, effectively halting cellular respiration.[19-20] As a result, the energy supply of body to vital organs such as the heart, central nervous system, and respiratory system is severely impaired, often leading to fatal outcomes.[21]

Artificial receptor molecules represent a broad extension of classical coordination chemistry, wherein molecular recognition is no longer confined to transition-metal ions but is also applicable to a diverse array of substrates, including cationic, anionic, and neutral species of organic, inorganic, and biological origin. Among these, the selective detection of trace elements such as copper, zinc, aluminium, cadmium, and mercury hold particular significance due to their essential yet potentially toxic roles in biological systems and environmental matrices. The detection of toxic gases such as phosgene ($COCl_2$) is equally important, especially in contexts involving chemical safety and industrial hazards. Compared to conventional analytical instruments, chemical sensors offer significant advantages, including portability, operational simplicity, facile synthesis, and suitability for in-situ applications due to their compact and lightweight nature. These attributes make them ideal for real-time, on-site measurements, thereby reducing analytical errors that may arise during sample storage or transportation.[22-24]

Chemosensors are specialized molecular systems comprising organic, inorganic, or hybrid complexes engineered to detect specific analytes through a distinct and quantifiable signal alteration. Classically, a chemosensor consists of two primary components: a recognition unit that exhibits selective affinity towards the target analyte, and a signaling moiety that produces an observable response, such as a fluorescence emission or a visible color change. These functional domains may be directly conjugated or connected via a flexible molecular spacer to optimize spatial orientation and performance. The utilization of such systems in analytical applications is broadly referred to as chemosensing, and plays a crucial role in enabling sensitive, selective, and real-time detection in diverse scientific and technological domains.

Functionally, a chemosensor operates similarly to a transducer by converting a non-detectable chemical interaction into a measurable physical signal. The analyte interacts with the recognition site, often resulting in a selective chemical reaction or a specific binding event. This event triggers the signalling unit, which then produces a detectable changecommonly in optical properties such as fluorescence intensity or color or an electrical response such as a shift in potential. This signal is then interpreted by the transducer, correlating signal intensity with the concentration of the analyte.[25]

Chemosensors can be broadly categorized based on their transduction mechanisms into four primary types: optical, electrochemical, mass-sensitive, and thermal (heat-sensitive) sensors. Among these, optical chemosensors have emerged as particularly prominent due to their inherent simplicity, high sensitivity, rapid response times, and wide-ranging applicability in fields such as clinical diagnostics, biomedical imaging, environmental monitoring, and industrial process control.[26-30] These sensors are specifically valuable for detecting contamination sources, tracking the formation and dispersion of hazardous pollutants, and providing timely alerts when toxic substances exceed established safety thresholds.

Optical sensors are effective for identifying sources of contamination, tracking the formation and movement of pollutants, and providing timely alerts when exposure thresholds are exceeded. Nonetheless, optical chemosensors are not devoid of limitations. Some chemical indicators suffer from poor photostability, spectral overlap, suboptimal absorption characteristics, or low molar absorptivity. Additionally, certain systems rely on auxiliary reagents for signal generation, which may complicate their use in practical scenarios. These limitations underscore the continuing need to innovate and design next-generation chemosensors that exhibit enhanced stability, selectivity, and operational consistency across diverse environmental and biological matrices. Addressing these challenges is central to broadening the applicability and reliability of chemosensors in modern analytical and diagnostic fields.

Fluorescence-based indicators have emerged as highly advantageous analytical tools in chemosensor design, particularly owing to their exceptional sensitivity and selectivity.[31-33] This superiority is largely due to the low probability of interfering species exhibiting identical absorption and emission profiles to the target analyte. In addition to the widely applied “turn-on” type fluorescent chemosensors, a considerable number of sensors operate via a “turn-off” mechanism, wherein fluorescence is quenched upon analyte recognition. The quenching phenomenon typically occurs through two mechanisms: static quenching, in which the quencher

interacts with the fluorophore in the ground state, and dynamic or collisional quenching, where the analyte interacts with the excited-state fluorophore, resulting in a substantial decrease in emission intensity and fluorescence lifetime. Chemosensors designed on such principles are capable of producing highly specific responses to guest analytes, often manifested through enhanced fluorescence, emission quenching, or ratiometric shifts in emission maxima. These optical changes are frequently accompanied by distinct color transitions observable under UV light, thereby facilitating rapid, visual detection. The functional chemistry underlying these chemosensors is deeply rooted in coordination chemistry, which is not solely restricted to transition metal cations but is broadly applicable to a diverse range of cationic, anionic, and neutral species spanning inorganic, organic, and biological systems.

The implementation of molecular detection is fundamentally based on the quantitative evaluation of complementarity between the host and guest species, or conversely, their degree of dissimilarity. This recognition process relies heavily on the precise definition and construction of molecular geometries and potential interaction maps. Consequently, the conceptualization and rational design of molecular receptors are of paramount importance in the development of effective chemosensors.[34] The binding or complexation efficiency of a molecular probe with its target analyte is predominantly governed by the number of degrees of freedom and the spatial and electronic compatibilities involved in the binding interaction.[35] Therefore, the synthesis of an ideal chemosensor necessitates careful consideration of several key factors, including selectivity, binding affinity, signal transduction efficiency, and environmental stability. To design and synthesize an ideal molecular probe for chemosensing applications, several critical factors must be considered to ensure effective analyte recognition and signal transduction. These considerations include:

(1) The geometric compatibility between the probe and the analyte is essential. This involves the precise spatial arrangement of convex and concave domains that allow for a comfortable and specific fit, enhancing molecular recognition.

(2) Effective binding depends on the presence and correct positioning of complementary binding sites. These may include electrostatic interactions (e.g., charge-charge, charge-dipole, dipole-dipole), hydrogen bonding (donor-acceptor pairs), and Van der Waals forces. Achieving a complementary distribution of electronic and nuclear densities is crucial for selective interaction.

(3) A larger contact area between the probe and analyte facilitates stronger binding through cumulative weak interactions, improving the overall interaction strength.

(4) Given the relatively weak nature of individual non-covalent interactions compared to covalent bonds, multiple binding interactions are necessary to ensure a stable and selective complex.

(5) High binding affinity and selectivity are critical for a functional probe, ensuring that it interacts predominantly with the intended target under physiological or environmental conditions.

(6) The surrounding medium plays a pivotal role in influencing both the probe and analyte behaviours. Solvent interactions can impact binding efficiency, probe stability, and signal transduction, and must therefore be carefully considered during probe design.

Therefore, for optimal host-guest recognition, both entities should exhibit complementary geometrical features, particularly with respect to their solvophilic or solvophobic domains. Over recent decades, a wide array of receptor architectures has been developed, each tailored to selectively bind specific analytes through non-covalent interactions. Despite the vast progress in sensor design, the field of chemosensor research continues to witness exponential growth, not only in terms of detection sensitivity and selectivity but also in the affordability of probe synthesis, the clarification of binding kinetics and thermodynamics, and the surge in scholarly publications and active research groups globally. Compared to conventional instrument-based analytical techniques, chemical sensors offer significant advantages. They are typically compact, user-friendly, cost-effective, and acquiescent to in-situ fabrication and application. These attributes make them highly suitable for real-time and on-site monitoring of environmentally or biologically relevant species. Moreover, the use of chemical sensors minimizes potential analytical errors that might arise from delays in sample handling, transport, or storage, thereby improving overall data reliability.

The central objective of this thesis is the rational design and synthesis of novel organic molecular probes, engineered to enable facile, cost-effective, and biocompatible chromo-fluorogenic detection of environmentally deleterious ions and compounds. These probes are intended to function efficiently across diverse mediaincluding semi-aqueous environments, solid-state matrices, and the vapor phaseoffering high sensitivity and selectivity through portable and user-friendly sensing platforms.

## 1.2. Supramolecular Chemistry: The origin

Supramolecular chemistry, often described as "chemistry beyond the molecule," provides the conceptual and practical foundation for the design of chemosensors through its emphasis on non-covalent interactions. Originating in the latter half of the 20th century with the groundbreaking work of Pedersen, Cram, and Lehnwho were awarded the Nobel Prize in Chemistry in 1987, where supramolecular chemistry shifted the focus from covalent bond formation to the selective and reversible interactions between discrete molecular entities. This model enables the rational design of molecular receptors that recognize and bind specific analytes through forces such as electrostatic interactions, hydrogen bonding, π-π stacking, van der Waals forces, and metal-ligand coordination. In chemosensing, these interactions reinforce the ability of a receptor to transduce molecular recognition events into measurable signals, often through optical or electrochemical means. The spatial and electronic complementarity between a receptor and its target, along with considerations such as binding affinity and selectivity, are central to sensor performance. As such, supramolecular chemistry has become an indispensable tool in the development of highly sensitive and selective sensors for ions, small molecules, and biomolecules, with wide-ranging applications in environmental monitoring, medical diagnostics, and industrial process control.[36]

## 1.3. Specific molecular interaction

Molecular recognition is a fundamental phenomenon that plays a pivotal role across diverse fields such as chemistry, materials science, biology, and environmental sciences. It refers to the specific, selective interaction between two or more molecules facilitated by various non-covalent forces, electrostatic attractions, hydrogen bonding, hydrophobic interactions, including metalcoordination, π-π stacking, van der Waals forces, halogen bonding, and, in some cases, electromagnetic or resonance effects. These interactions collectively govern the selective binding behaviour between a host and a guest molecule. Solvent effects also significantly influence molecular recognition in solution-phase systems, affecting both binding affinity and selectivity. At the core of this concept lies the intentional design and synthesis of host molecules tailored to identify and bind specific guest species, often of biological or environmental significance.[37] The effectiveness of this host-guest interaction is primarily dictated by the size, shape, functional groups, and spatial arrangement of the binding sites involved.[38-40] This selective binding

underpins a wide range of processes, from synthetic receptor design to biologically inspired sensing and separation technologies.The foundational concept of molecular recognition was first introduced through the development of crown ethers by Charles J. Pedersen, which provided a blueprint for selectively binding metal cations.[41] This innovation was later extended by Jean-Marie Lehn, who explored more complex macrocyclic and bicyclic systems to recognize both ionic and neutral species.[42,43] Donald J. Cram further expanded this work by developing structurally rigid host molecules capable of high selectivity and specificity. These pioneering contributions led to the awarding of the Nobel Prize in Chemistry in 1987 to Pedersen, Lehn, and Cram for their groundbreaking work in establishing the principles of host-guest chemistry and advancing the field of supramolecular chemistry. The concept of host-guest chemistry was initially demonstrated with crown ethers serving as molecular hosts for metal cations.[44-46]

Today, the concept of molecular recognition underlies numerous biological and chemical systems, such as enzyme-substrate interactions, antigen-antibody binding, genetic regulation mechanisms, metal ion transport across membranes, and biomimetic catalysis. Its principles continue to inform the design of advanced functional materials, biosensors, drug delivery systems, and artificial receptors in supramolecular and analytical chemistry.[47]

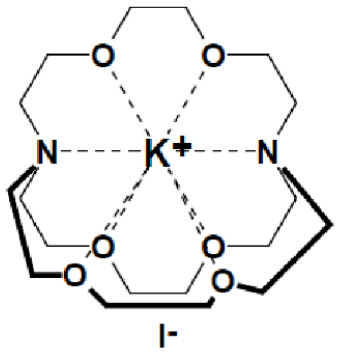


Macrocyclic ether: Pedersen

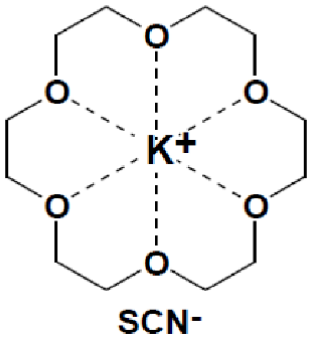


Macrobicyclic ether: Lehn's Model

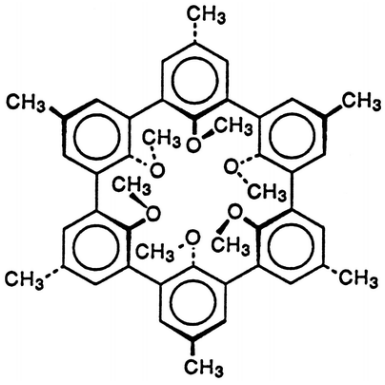


Cram's Model

## 1.4. Chemosensors and Chemodosimeters: Definitions and Distinctions

Chemosensors and chemodosimeters are two distinct yet closely related classes of molecular systems used for the detection and quantification of analytes through chemical recognition processes. Both systems operate on the principle of molecular recognition; however, they differ

fundamentally in their modes of interaction with target species and in the nature of the signals they generate. A chemical sensor is defined as a miniaturized device or material capable of providing real-time information regarding the presence, identity, or concentration of specific chemical speciessuch as compounds or ionswithin complex sample matrices.[48-50] Typically, a chemical sensor comprises a chemically selective sensing layer that interacts with the target analyte through specific chemical or physical processes. This interaction induces a measurable change in a transducible property (e.g., optical, electrochemical, or thermal), allowing for both qualitative and quantitative detection. The selective nature of the sensing layer enables the sensor to respond accurately to a particular analyte, even in the presence of interfering substances, thereby making chemical sensors indispensable tools in environmental monitoring, clinical diagnostics, and industrial process control. In contrast, chemodosimeters operate based on a chemical reaction with the target analyte, leading to an irreversible covalent transformation of the sensor molecule. This transformation results in a permanent structural change that is accompanied by a detectable signal, usually optical. Unlike chemosensors, chemodosimeters are single-use systems but often offer exceptional selectivity and sensitivity for specific analytes, particularly in the detection of biologically and environmentally relevant species such as reactive oxygen species (ROS), metal ions, or toxic gases. Their high degree of specificity arises from the selective reactivity built into their molecular framework.

Fluorescence-based sensing of chemical and biochemical analytes represents a highly active and evolving area of research due to its sensitivity, simplicity, and rapid response capabilities. There is a growing demand for cost-effective, rapid, and reliable testing methods to address a wide array of challenges in chemical, biomedical, and environmental analysis. For optimal performance, fluorescence sensors should exhibit high selectivity toward specific target analytes (guests), enabling not only their detection but also the accurate monitoring of their concentration in complex systems. Such sensors provide real-time quantitative data, which is crucial for applications ranging from medical diagnostics to environmental monitoring. The development of selective and sensitive fluorescence sensors, therefore, holds significant promise for advancing both clinical and environmental technologies. All chemosensors are comprised of a signaling moiety and a recognition unit, which are joined either directly to each other or through some kind of spacer or connector (Fig. 1.1).

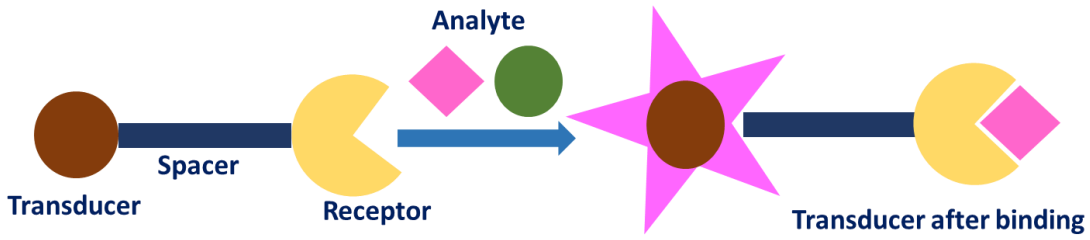


**Figure 1.1:** Schematic representation of Host-Guest Interaction

# 1.5. Classification of sensors

Chemosensors can be classified in various ways, as illustrated in Scheme 1.1. One common method of classification is based on the principle of transduction, which divides sensors into two primary categories: (i) physical sensors, and (ii) chemical sensors. Further subclassification can be made according to the nature of the signal or detection mechanism involved. These subcategories include optical, electrochemical, electrical, mass-sensitive, magnetic, and thermometricsensors, each employing a distinct transduction method to convert the chemical interaction into a measurable output.[51]

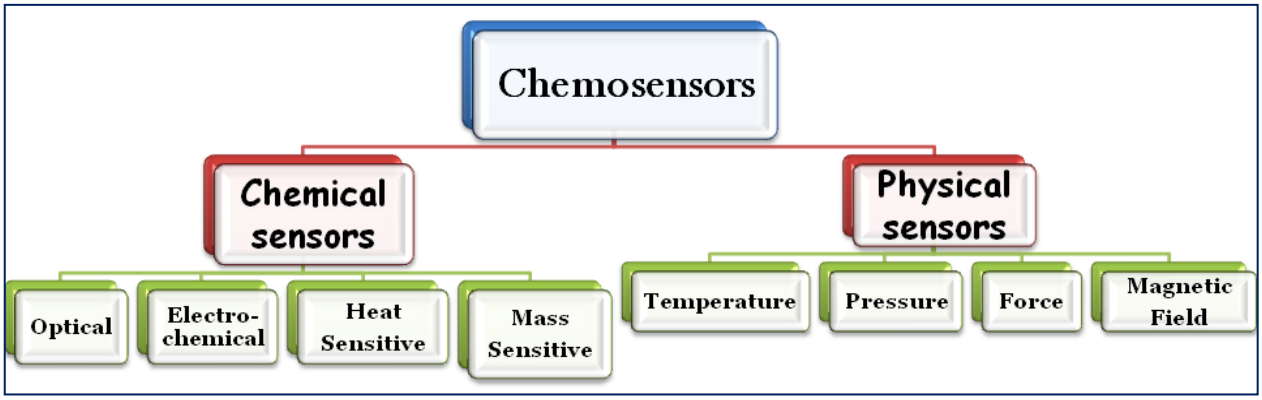


**Scheme 1.1:**General classifications of sensors.

## 1.5.1. Optical sensors

Optical chemosensors generate an optical response upon interaction with a target analyte, often in an irreversible manner. Due to this behavior, they are also commonly referred to as “probes” or “optodes”.[52] These sensors typically comprise four key components, as illustrated in Scheme 1.2:[53,54]

(a) Recognition Element – Responsible for the selective interaction with the analyte, ensuring specific molecular recognition.
(b) Transduction Element – Converts the recognition event into a measurable optical signal, such as changes in absorbance, luminescence, fluorescence polarization, or Raman scattering.
(c) Detection Unit – Captures the resulting optical change and translates it into a readable output, often after signal amplification.
(d) Optical Setup – Incorporates at least one light source to initiate the optical interaction.

The performance and reliability of an optical sensor can be assessed using several key criteria:

1. The sensor should produce an optical signal with a high signal-to-noise ratio, ensuring sensitivity and accuracy.
2. The signal should exhibit a significant and discernible change upon exposure to the target analyte.
3. The sensor materials must demonstrate long-term stability, retaining their sensing capabilities over extended periods.
4. All components involved in the sensor design should be chemically resistant and non-degradable upon contact with the analyte.
5. The indicator dye or fluorophore should remain photostable under prolonged exposure to the light source.
6. The analytical output should be referenced against a secondary signal, such as an alternative wavelength, to improve measurement reliability.
7. The materials used in fabrication should be cost-effective and readily available.
8. The overall sensor should be economical to produce and allow for rapid analysis.
9. Finally, the sensor should be constructed using environmentally benign and non-hazardous materials.

However, fulfilling all of these criteria simultaneously is rarely attainable in practice. Most existing optical sensors face several limitations, such as insufficient long-term stability, poor selectivity in distinguishing the target analyte from structurally similar species, and inadequate detection limits. As a result, the field of optical sensing continues to attract significant research interest, as evidenced by the growing number of publications and reviews dedicated to the development and advancement of novel chemosensors.

### 1.5.2. Electrochemical sensors

Significant research efforts have been dedicated to the advancement of efficient and user-friendly electrochemical sensors. Owing to their rapid response and high sensitivity, these sensors have garnered widespread attention across diverse scientific and industrial fields. As a result, the development of simple, scalable fabrication methods for electrochemical devices capable of monitoring the concentration and activity of a wide range of analytes has become increasingly crucial. In recent years, the emergence of handheld electrochemical devices has demonstrated the feasibility of achieving both precision and sensitivity in compact formats tailored for specific applications. Progress in modern fabrication techniques has played a pivotal role in enhancing the miniaturization and overall performance of these sensors. Consequently, the continued innovation of portable, rapid, cost-effective, and dual-mode detection systems is essential to the future advancement of electro-optical sensor technologies.

## 1.6. Non-Covalent Forces Governing Chemosensor Analyte Binding

The binding event represents a fundamental step in chemosensing, governed by a complex interplay of non-covalent chemical interactions—both attractive and, less desirably, repulsive in nature. The term non-covalent forces encompass a broad spectrum of interactions that play a crucial role in molecular recognition and sensor performance. These forces include hydrogen bonding, electrostatic interactions, π-π stacking, van der Waals forces, and hydrophobic effects, among others. Each of these interactions contributes to the overall stability and specificity of the host-guest complex, and they vary widely in terms of interaction energy. A brief overview of the most relevant non-covalent forces, along with their approximate energetic contributions, is provided below to contextualize their roles in sensor design.

(a) Hydrogen bonding (4-120 kJ/mole)] interactions

(b) Electrostatic interactions

(c) Van der Waals forces (< 5 kJ/mole)

(d) π-π stacking (0-50 kJ/mole) interactions

(e) Hydrophobic Interactions

(f) CH- π interactions

(g) Close packing in the solid phase

## 1.6.1. Hydrogen bonding interactions

A hydrogen bond is defined as an attractive force between a hydrogen atom covalently bonded to an electronegative atom and another nearby electronegative atom. This type of interaction plays a crucial role in molecular recognition processes.[55] Hydrogen bonds can be classified into two types: intermolecular hydrogen bonding, which occurs between different molecules, and intramolecular hydrogen bonding, which occurs within a single molecule. Although weaker than ionic or covalent bonds, hydrogen bonds are significantly stronger than van der Waals forces.The versatility of hydrogen bonding is evident in its widespread applications, both in natural host-guest complexes and in the design of synthetic supramolecular systems. Various donor-acceptor configurations have been extensively explored, leading to the formation of robust and selective host-guest assemblies. Furthermore, hydrogen bonding is fundamental in determining the secondary, tertiary, and quaternary structures of biomacromolecules such as proteins and nucleic acids, as well as in stabilizing the double helical structure of DNA.

Hydrogen bonding has been extensively utilized in the design of receptors for the selective coordination of neutral organic species, such as short-chain alcohols, amides, and various anions. These interactions are widely observed in biological systemsfor example, in the stabilization of the DNA double helixhighlighting their fundamental role in molecular recognition processes. The directional and highly specific nature of hydrogen bonds enables the construction of intricate molecular architectures with well-defined binding sites. Moreover, the donor-acceptor characteristics of the participating species play a crucial role in hydrogen bonding-based recognition. A strong electron pair donor readily serves as a hydrogen bond acceptor, thereby influencing the overall binding affinity. However, the effectiveness of hydrogen bonding can be significantly compromised in solvents that themselves act as good hydrogen bond donors or acceptors.[56] In such cases, competitive solvation of both host and guest molecules can interfere with complex formation, thereby diminishing the strength and selectivity of the binding interaction. J. Hu et al. have developed an intra-molecular NH….O and OH…O hydrogen bonding based chemosensor to recognize cyanide in DMSO/$H_2O$ (2:8, v/v) with excellent selectivity (Fig. 1.2).[57]

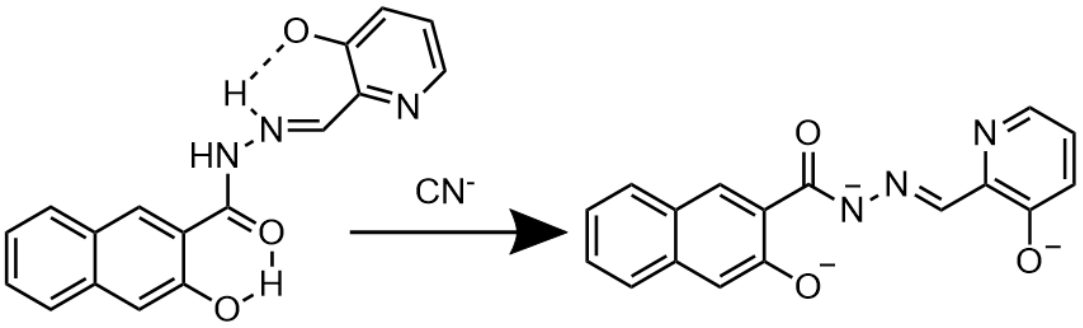


**Figure 1.2:** Example of some H-bonding based chemosensors.(J. Hu et al.)

## 1.6.2. Electrostatic interactions

Selective recognition of specific guest molecules can be effectively achieved through weak, non-covalent interactions involving the sensing probe. Among these, electrostatic interactions play a pivotal role, arising from Coulombic attraction between oppositely charged species. While ion-ion interactions are generally non-directional, ion-dipole interactions require precise alignment of the dipole for optimal binding efficiency. Due to their relatively high interaction strength compared to other non-covalent forces, electrostatic interactions have been extensively utilized in supramolecular chemistry to promote strong and selective binding.

This principle forms the basis for the design of numerous receptors. For instance, cation receptors such as crown ethers, cryptands, and spherands exploit electrostatic attraction to encapsulate metal ions. Similarly, anion receptors, including protonated or alkylated polyammonium macro bicycles, have been developed to selectively bind anionic guests. These host-guest systems rely on carefully tailored electrostatic complementarity to achieve stability and specificity in complex formation.

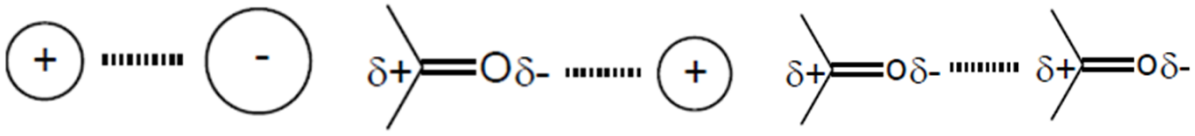


**Figure 1.3:** Electrostatic interactions (a) ion-ion (b) ion-dipole and (c) dipole-dipole.

## 1.6.3. Van der Waals forces

Van der Waals forces arise from transient, fluctuating polarizations between nearby atoms, molecules, or surfaces. These weak, non-covalent interactions play a significant role in the

stabilization of host-guest complexes, particularly in systems involving hydrophobic interactions. Hydrophobic guest molecules are often accommodated within the hydrophobic cavities of host structures through van der Waals forces, resulting in additional enthalpic stabilization of the complex. Although these interactions are considerably weaker than hydrogen bonds in terms of energetic contribution, they are essential for enhancing the overall binding affinity and specificity in many supramolecular assemblies.

## 1.6.4. π-π stacking

In recent years, the term π-π stacking has gained increasing prominence in host-guest chemistry, particularly among organic chemists. Notably, the first synthetic application of π-stacking interactions was proposed by E. J. Corey in 1972, in the context of chiral ketone reduction during the synthesis of prostaglandins.

π-π stacking interactions are a class of non-covalent interactions that occur when two π-conjugated systems come into close proximity and align in a parallel fashion, facilitating intermolecular interactions between their π-orbitals (Fig. 1.4). These interactions can manifest in various geometries, including “face-to-face” (sandwich), “edge-to-face” (T-shaped), and “offset” (parallel-displaced) configurations. Compounds containing aromatic moieties often engage in π–π interactions, significantly influencing crystal packing in solid-state structures, supramolecular recognition processes,[58] and phenomena such as porphyrin aggregation.[59]An illustrative example is provided by Zimmerman's molecular tweezers, where the π-π interactions are believed to adopt a parallel-displaced geometry.[60]Crystal structure analyses reveal complex formation between tweezer units, albeit with minimal π-orbital overlap.[61] Biologically, π-π interactions play a critical role in DNA base stacking, drug-DNA binding, and protein folding processes.[62] Despite their widespread importance, the precise nature of π-π interactions remains a subject of ongoing research. Among the models proposed to explain these interactions, the electron donor-acceptor (EDA) model attributes the attraction to interactions between electron-rich and electron-deficient aromatic systems. Alternatively, the charge transfer (CT) model posits that the formation of a CT complex, characterized by a distinct absorption band in the UV-Vis spectrum, underpins the interaction between a good electron donor and an acceptor.[63]

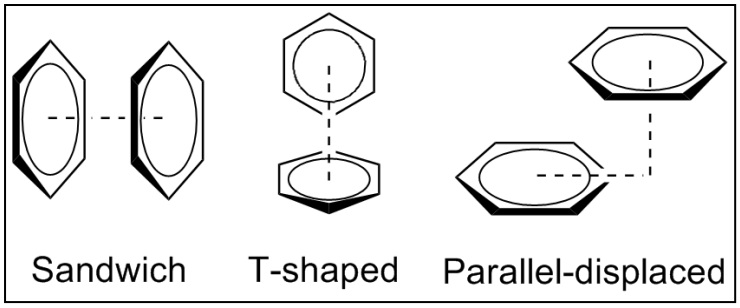


**Figure 1.4:** Different mode of π-staking interactions: (a) face to face (b) edge to face (c) offset (alkene-arene staking).

## 1.6.5. Hydrophobic Interactions

Hydrophobic interactions, also referred to as solvophobic interactions, are characteristic of nonpolar molecules and play a crucial role in driving the self-assembly of these molecules into anhydrous domains within aqueous environments. These interactions offer a valuable mechanism for the construction of DNA-based nanomaterials and other supramolecular architectures with potential applications in biomedicine. The underlying origin of the solvophobic effect lies in an entropic contribution, arising from the disruption of hydrogen bonding networks among water molecules by apolar solutes. Hydrophobic interactions are inherently dynamic and tunable, enabling materials to exhibit enhanced responsiveness to environmental stimuli—a key feature in the development of smart biomaterials. Consequently, receptors possessing hydrophobic interior cavities can be strategically designed to encapsulate organic guest molecules in aqueous media, thereby facilitating selective molecular recognition and functional material development.

## 1.6.6. CH-π interactions

CH-π interactions represent a subtle form of weak hydrogen bonding, occurring between a soft acid, such as a methyl group (–$CH_3$) in an alkyl chain, and a soft base, typically a π-electron-rich system (Fig. 1.5). Despite their relatively low interaction energy—approximately 1 kcal/mol—CH-π interactions play a significant role in molecular recognition, influencing the selectivity of organic reactions, chromatographic behaviour, and the substrate specificity of biologically relevant macromolecules.[64]

Due to their low enthalpic contribution, CH-π interactions are often difficult to distinguish from van der Waals forces, which are non-stereospecific and include both attractive and repulsive

components. Nevertheless, their contribution to supramolecular binding cannot be overlooked, especially when combined with other non-covalent interactions. For instance, A. Singh et al. reported the development of a chemosensor that utilizes both CH-π and π-π interactions between pyrene moieties, highlighting the utility of such weak forces in sensor design.[65]

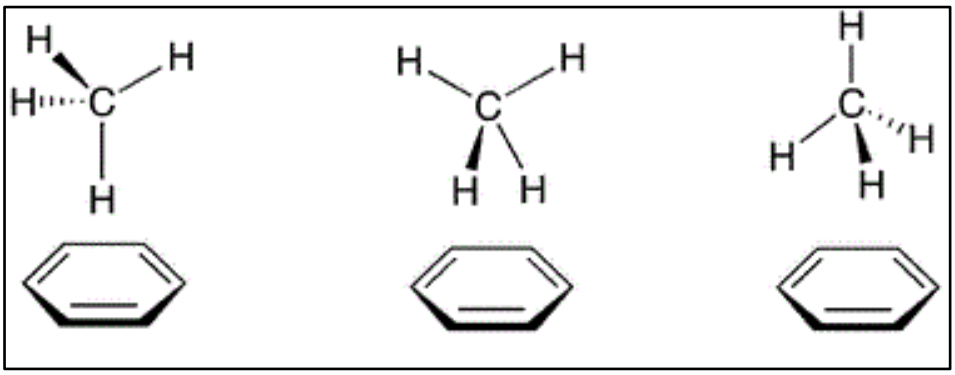

**Figure 1.5:** Modes of CH-π interactions

### 1.6.7. Close packing in the solid phase

The theory of close packing was first introduced by Kitaigorodsky as a means of rationalizing the arrangement of molecules in the solid state to maximize favorable isotropic van der Waals interactions within crystalline structures. In contrast to the ordered nature of crystalline packing, organic compounds in their free state exhibit high entropy, driven by conformational flexibility and dynamic, disordered motion. However, the formation of non-covalent interactions during crystallization acts in opposition to this entropy, promoting molecular organization and reducing the overall free energy of the system. This thermodynamic balance is described by Gibbs' free energy equation:

$\Delta G = \Delta H - T\Delta S$

## 1.7. Principles of Chemosensor Design and Molecular Recognition

### 1.7.1. Criteria of designing an ideal chemosensor

The chemistry of artificial synthetic receptor molecules represents a generalized approach to coordination chemistry, extending beyond traditional interactions with transition metal ions. This domain encompasses a broad range of substrates, including cationic, anionic, and neutral species

of organic, inorganic, and biological origin. The strength of complexation is primarily governed by the number of degrees of freedom involved during a binding event.[66]

In designing an ideal receptor, several key criteria must be considered:

1. Steric compatibility between the receptor and the substrate;
2. The presence of complementary binding sites, arranged to enable optimal electronic and spatial complementarity between host and guest;
3. A large interaction surface area to enhance binding efficiency;
4. Multiple contact points, as non-covalent interactions are inherently weaker than covalent bonds;
5. High stability and selectivity to ensure the robustness and specificity of the receptor;
6. The influence of the medium or solvent, which interacts with both the receptor and the guest and plays a crucial role in the binding process.

Theoretical receptors may be synthesized either through multistep total synthesis or via regio- and stereoselective functionalization of structurally accessible host molecules. For practical applications in molecular sensing, it is often advantageous to design simplified architectures with a limited number of recognition elements. These structural units are typically responsive to, or perturbed by, specific external stimuli. Current research predominantly focuses on endo-receptors, where the binding sites are oriented within a molecular cavity, providing a defined space for guest encapsulation.[67] The design of such host molecules considers all potential recognition elements to ensure efficient and selective binding of guest species.

## 1.7.2. Binding of metal cations

The selectivity of a specific host molecule toward a particular cation is determined by the relative binding affinity of the host for that target ion compared to other competing cations. An effective host exhibits a high binding affinity for a particular guest cation while demonstrating significantly lower affinities for other potential guests. Designing a synthetic host with exceptional selectivity for a single cation is a complex and challenging task, as selectivity is influenced by a multitude of factors. These include the size and geometry of both host and guest, the nature and distribution of electrostatic charges, the polarity and coordinating ability of the solvent, and other subtle structural and environmental considerations.Therefore, the development

of chemosensor that will be extremely specific for a distinct metal cation is a very intricate assignment (Fig.1.6).

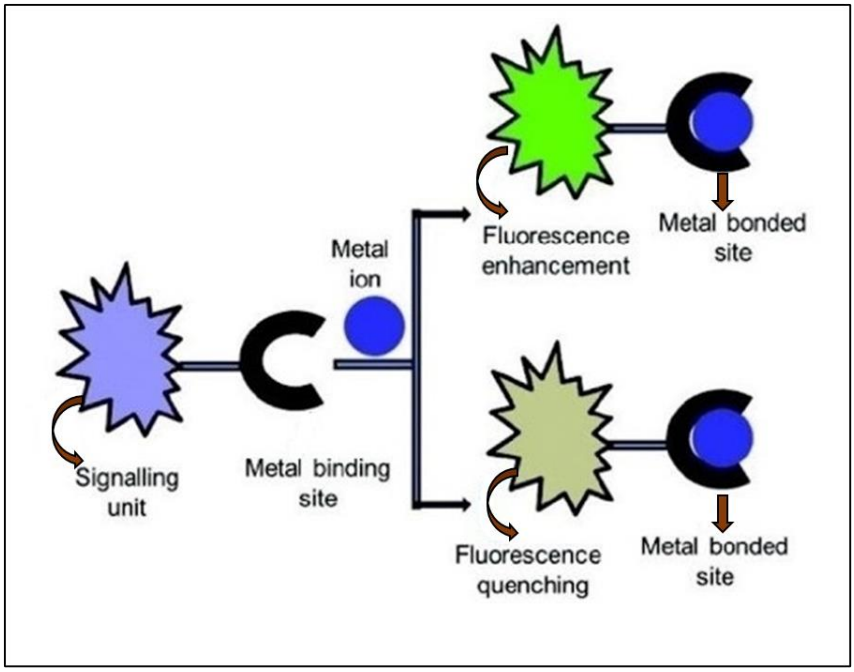


**Figure 1.6:** Modes of metal ion binding interaction and fluorescence response.

## 1.7.3. Binding of anions

A common strategy for the development of anion chemosensors involves the integration of two key components: a binding site for anion recognition and a signaling unit for transducing the binding event into a detectable signal.

### 1.7.3.1. Covalent attachment of signaling subunit and binding site

Many chemical sensors achieve selective interaction with specific anions through covalent bonding, as illustrated schematically in Fig. 1.7.[68] In these systems, the anion covalently binds to the recognition site of the sensor, initiating a response in the signaling unit (reporter). This interaction induces a change in the photophysical properties of the sensor, which may manifest as a visible color change in the case of chromogenic chemosensors, or as a variation in fluorescence emission for fluorogenic chemosensors.

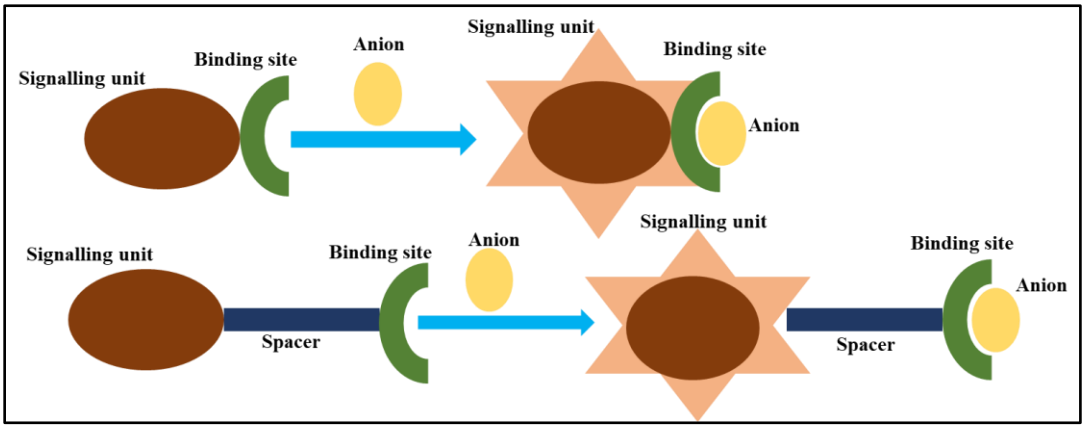


**Figure 1.7:** Anionic chemosensors based on the binding site-signaling subunit approach: (a) binding site is an integral part of the signaling unit (receptor); (b) binding site and signaling subunit connected covalently by a short spacer.

### 1.7.3.2. Displacement approach

In this approach, the chemosensor is coordinatively linked to a signaling subunit to form a molecular ensemble. Upon introduction of a target anion into the solution containing this ensemble, a displacement reaction occurs: the binding site preferentially coordinates the anion, thereby releasing the signaling subunit into the solution. Once free, the signaling subunit regains its non-coordinated spectroscopic characteristics (Fig. 1.8). If the photophysical properties of the signaling subunit in its free state differ from those in the bound ensemble, the binding event can be effectively monitored through spectroscopic techniques. Selectivity in anion sensing can be enhanced by judiciously selecting a binding site-indicator pair with a formation stability constant higher than that between the signaling unit and any potentially interfering anions.[69]

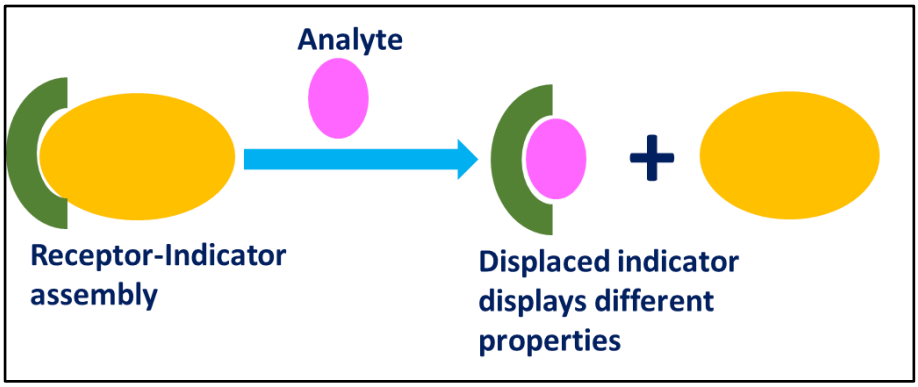


**Figure 1.8:** Anionic chemosensor based on the displacement approach.

### 1.7.3.3. Chemodosimeter approach

Chemodosimeters differ fundamentally from conventional chemosensors where they operate via irreversible chemical reactions that are directly linked to the signal transduction event .[70,71] As a result, chemodosimeters are typically non-reversible and non-reusable.However, they offer high selectivity toward specific anionic or cationic analytes.[72]

Chemodosimeters generally function through one of two mechanisms. In the first, the target anion forms a covalent bond with the chemodosimeter, becoming chemically incorporated into the reaction product. In the second, the anion acts as a catalyst or initiator for a chemical transformation without becoming part of the final product. In either case, the interaction triggers a detectable optical responsesuch as a fluorescence "turn-on" effect or a ratiometric shift in the emission spectrum. These modes of action are graphically illustrated in Fig. 1.9.

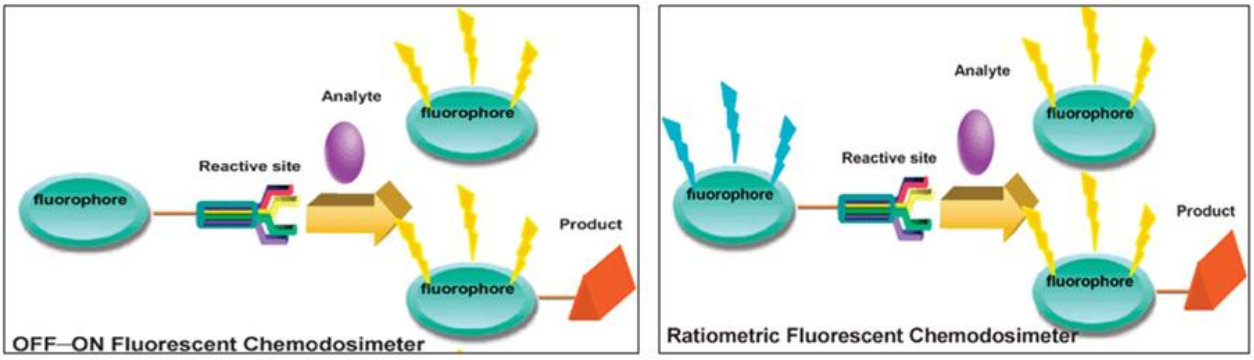


**Figure 1.9:** Types of chemodosimeters.

# 1.8. Different mechanisms of Fluorescence-Based Sensing

Fluorogenic chemosensors represent a class of molecular machines that undergo changes in their luminescent properties upon binding to specific analytes. These systems are typically composed of two functional subunits: a binding site, which selectively interacts with the target analyte, and a signalling unit (fluorophore), which transduces the binding event into a measurable fluorescence response. Among optical signalling mechanisms, fluorescence is particularly advantageous in chemosensor chemistry due to its exceptional sensitivity and ability to detect analytes at extremely low concentrations.Fluorescence spectroscopy is a highly versatile analytical tool capable of monitoring even minute changes in emission in real time, making it

invaluable across diverse research and application domains. Depending on the mode of excitation, luminescent phenomena are categorized into chemiluminescence, radioluminescence, electroluminescence, sonoluminescence, and others. In a fluorescent compound, the absorption of light at a specific wavelength is followed by the rapid emission of light at a longer wavelength, forming the basis for fluorescence detection.[73]

### 1.8.1. ESIPT (Excited State Intramolecular Proton Transfer) mehanism

Excited-State Intramolecular Proton Transfer (ESIPT) chromophores possess a distinctive characteristic—the formation of a keto tautomer upon excitation.[74] In the ground state, these chromophores typically exist in the *cis*-enol form, which is stabilized by intramolecular hydrogen bonding. Upon photoexcitation, the *cis*-enol form is initially promoted to its singlet excited state in accordance with the Franck-Condon principle. This is rapidly followed by an efficient ESIPT process, resulting in the population of the excited singlet state of the *cis*-keto form, which is also stabilized by intramolecular hydrogen bonding.

The ESIPT process occurs on a timescale much faster than that of radiative fluorescence decay. As a result, the fluorescence emission from ESIPT chromophores typically originates from the keto tautomer, with only rare exceptions.[75] The overall mechanism is schematically illustrated in Scheme 1.2. ESIPT-based systems have attracted considerable attention due to their versatile applications in various fields, including molecular probes,[76] luminescent materials[77].

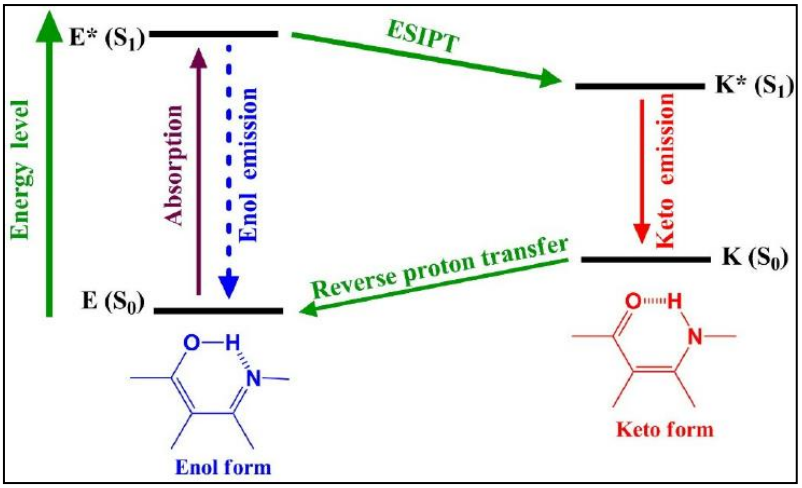


**Scheme 1.2:** Principle photo physics of the ESIPT process.

In 2019, Kaur and co-workers reported a novel naphthalene-based fluorescent chemosensor capable of sequential detection of $Hg^{2+}$ and cysteine via an ESIPT (Excited-State Intramolecular Proton Transfer) sensing mechanism.[78] The presence of a hydroxyl functional group in the naphthalene scaffold facilitates tautomerization, thereby enabling the ESIPT process within the probe. This intramolecular proton transfer is responsible for modulating the fluorescence response, specifically resulting in emission quenching, as illustrated in Fig. 1.10.

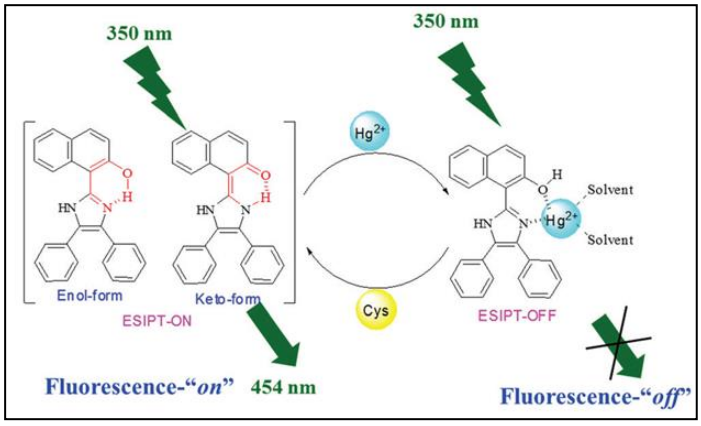


**Figure 1.10:** Naphthalene based ratiometric chemosensors depending on ESIPT process. (Kaur etal.)

Shafiq group published an ESIPT based fluorescence molecular switch in 2023 for sensing $CN^-$ anions selectively via a "turn-on" emission response in Acetonitrile.[79] The schematic diagram has shown the sensing mechanism of the sensor (Fig. 1.11).

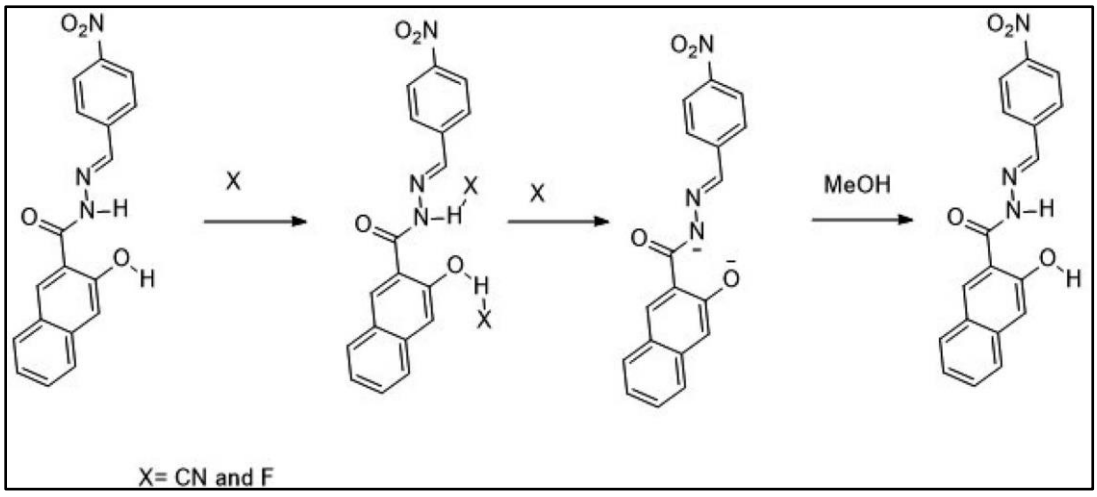


**Figure 1.11:** Chemosensors for the selective detection of cyanide ions showing ESIPT process. (Shafiq et al.)

A novel pyridine-hydrazone-substituted naphthalimide-based probe was developed by the Liu group in 2020 as an efficient and selective colorimetric and fluorescent sensor for cyanide detection in aqueous media.[80] The probe operates via a unique Excited-State Intramolecular Proton Transfer (ESIPT) mechanism, which plays a critical role in its sensing performance. The ESIPT process involved in the sensing mechanism is schematically illustrated in Fig. 1.12.

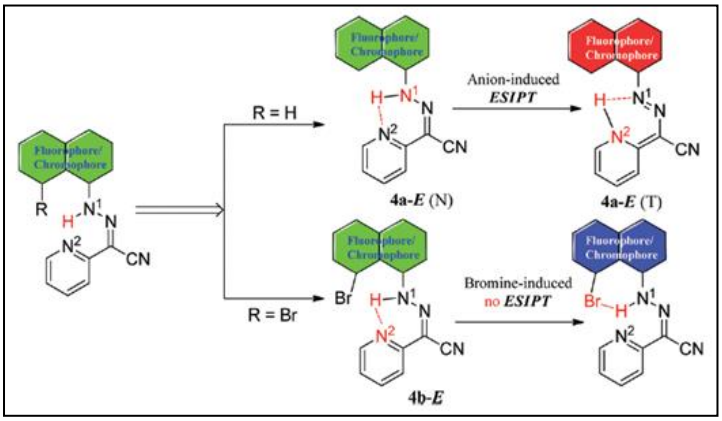


**Figure 1.12:** A new ESIPT strategy for the proposed colorimetric fluorescent cyanide probe. (Liu et al.)

However, in 2022, Jose and co-workers reported an ESIPT-based fluorescent probe for the selective detection of $Cr^{3+}$.[81] As shown in Fig. 1.13, the protection of the hydroxyl group of the probe is involved in the ESIPT process.

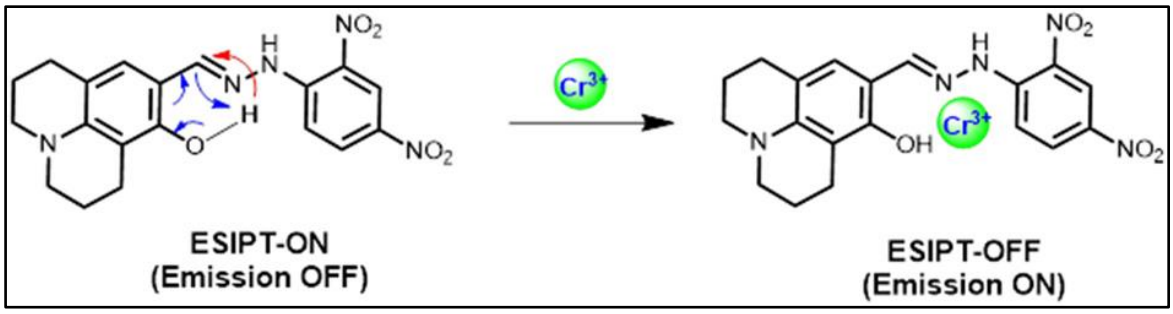


**Figure 1.13:** The ESIPT sensing mechanism of the fluorescent $Cr^{3+}$ recptor. (Jose et al.)

## 1.8.2. Rigidity or chelation enhanced fluorescence (CHEF) effect

Although definitive evidence for the actual existence of the Chelation-Enhanced Fluorescence (CHEF) effect remains limited, this concept has been widely employed to rationalize the fluorescence enhancement observed in chemosensors upon coordination with metal ions. Ion

complexation often leads to increased rigidity in the resulting complex, which in turn suppresses non-radiative decay pathways from the excited state. As a result, the fluorescence intensity is significantly enhanced. Numerous studies have utilized the CHEF effect as a foundational principle to explain the sensing mechanisms of newly developed fluorescent chemosensors.

In some cases, upon complexation with an appropriate metal ion, increases the rigidity of the molecular assemblyby restricting the free rotation of the molecule. As a result, thechelation-enhanced fluorescence (CHEF) effect occurredand leads to a 'turn-on' of fluorescence. AS shown in Fig.1.14[82] by Jiang and co-workers. As for example, in 2022, Sinha et al. published a "turn-on" fluorescent probe for selective detection of $Zn^{2+}$ ion in $CH_3CN/H_2O$ (99:1, v/v) (HEPES buffer, pH 7.5).[83] The probe shows enhancement of intensity at 499 nm of 20 fold The enhancement maybe explained on account of its complexation of $H_2L$ with $Zn^{2+}$ as confirmed from the crystal structure that tends to suppress the non-radiative PET and ESIPT processes and inclusion of Chelation-Enhanced Fluorescence (CHEF).

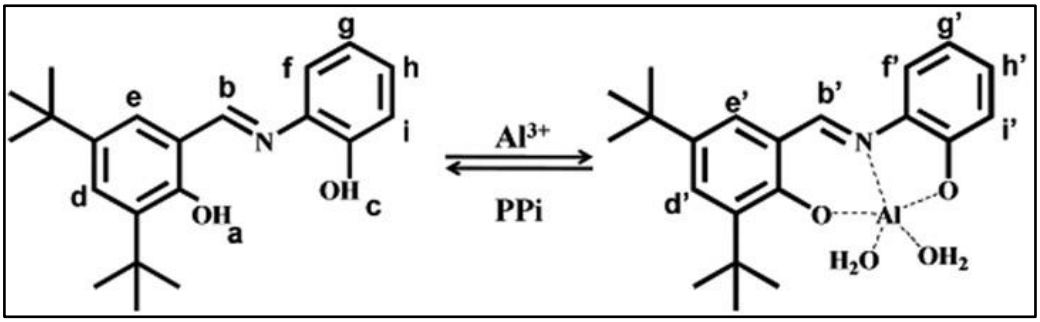


**Figure 1.14:** Schematic representation of sensing mechanism of an $Al^{3+}$ sensor.(Jiang et al.)

Another report on an $Al^{3+}$ sensor by a rhodamine and azobenzene based probe was reported by Mabhai et al. in 2018.[84] The binding of aluminium may be due to the CHEF as well as PET process due to the rigidity of the structure (Fig. 1.15).

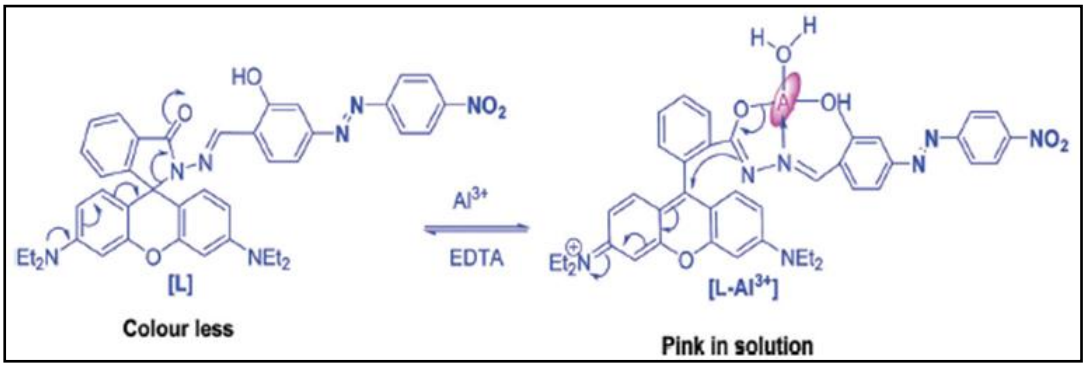


**Figure 1.15:** Probable sensing pattern of the $Al^{3+}$ sensing probe.(Mabhai et al.)

### 1.8.3. ICT (Intramolecular charge transfer) mechanism

The Intramolecular Charge Transfer (ICT) mechanism is commonly observed in chemosensors designed for “naked-eye” detection of analytes. Although colorimetric detection is considered a relatively less advanced technique compared to other spectroscopic methods, it offers significant advantages in terms of simplicity and ease of use. The ability to provide a direct visual response without the need for sophisticated instrumentation makes ICT-based colorimetric sensing particularly appealing for practical applications, especially in field or point-of-care settings.

ICT-based chemosensors typically consist of an electron-donating unit and an electron-accepting moiety connected through a π-conjugated linker (Fig.1.16). In such systems, intramolecular charge transfer occurs from the donor to the acceptor unit. Upon interaction with a target analyte, this electron transfer process is disrupted, resulting in the inhibition of the ICT mechanism. This disruption leads to noticeable shifts in both the absorption and fluorescence emission spectra, enabling analyte detection. Colorimetric ICT chemosensors are particularly attractive due to their operational simplicity. They require minimal calibration and sample preparation and can be effectively used by non-specialists, making them highly suitable for rapid, on-site analysis. Although considered less advanced than other spectroscopic techniques, colorimetric detection offers the significant advantage of providing a direct visual signal, allowing for "naked-eye" detection. This practical ease of use has contributed to the widespread application of ICT-based chemosensors in the field of molecular recognition. To date, numerous ICT-based systems have been reported for the detection of various analytes.[85]

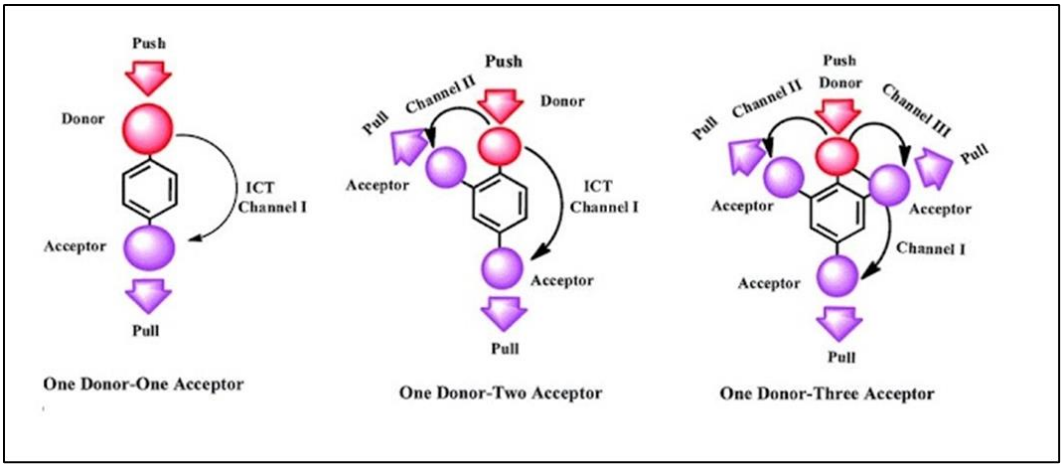


**Figure 1.16:** ICT process in organic probes having electron withdrawing and electron donating moiety.

In 2018, Song et al. reported a ratiometric fluorescent chemosensor for selective and visual detection of phosgene insolutions and as well as in the gas phase.[86] The sensing mechanism is depicted as change in the ICT process to give ratiometric fluorescence response. The fluorescence maxima of Phos-1 (511 nm) and 2 (442 nm) revealed theirdifferent ICT characters: a strong ICT process from the 4,5-diaminemoiety to the imide unit for Phos-1 and a weak such ICT for 2, due to carbamylation of 4,5-diamine weakening its electron-donating ability. (Fig. 1.17).

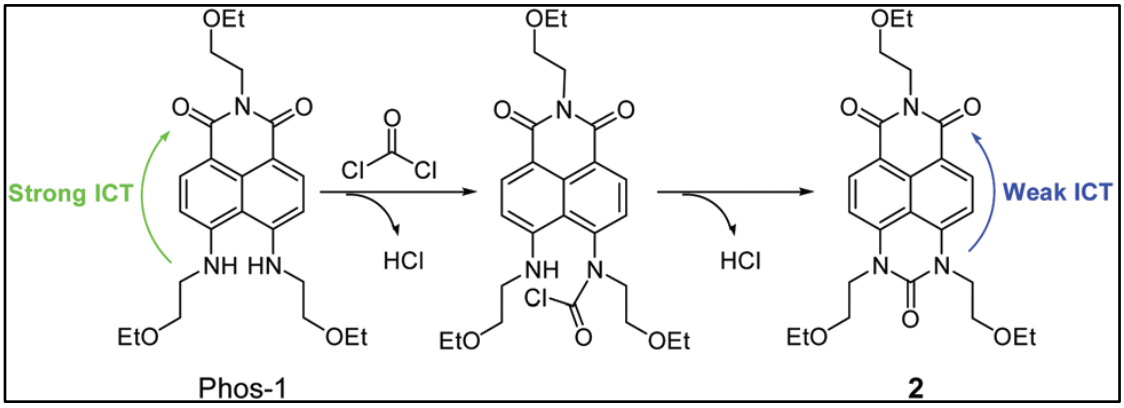


**Figure 1.17:** The design strategy of the use of the ratiometric fluorescent chemosensor, Phos-1, for phosgene. (Song et al.)

In 2019, Song group reported an intramolecular charge transfer based chemosensor for the selective detection of phosgene.[87] The fluorescence maxima of Phos-3 (548 nm) and 3 (486 nm) reveal the difference in their intramolecular charge transfer (ICT): a strong 4-aminedonor for Phos-3 and a weak carbamylated 4-amine donor for 3. (Fig. 1.18).

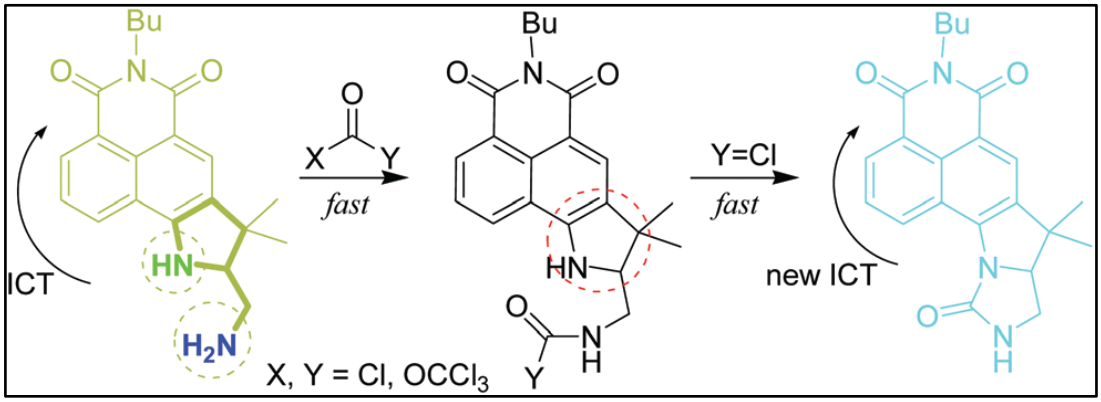


**Figure 1.18:** Design of our fluorescent chemosensor, Phos-3, for phosgene.

## 1.8.4. PET (Photo-induced electron transfer) process

This photo-induced electron transfer (PET) process has been extensively investigated and widely applied in the design of chemosensors for the detection of both cations and anions.[88,89] The thermodynamic foundation of PET was first established for intermolecular systems through the pioneering work of Weller.[90] In general, fluorescence arises when an electron in an excited state—typically in the Lowest Unoccupied Molecular Orbital (LUMO)—returns to the Highest Occupied Molecular Orbital (HOMO), releasing the excess energy as emitted light. However, if an intermediate orbital exists—either from another part of the same molecule or from an interacting molecular species—and this orbital lies energetically between the HOMO and LUMO and is occupied, a PET process can occur. In this scenario, the electron can be transferred from the occupied intermediate orbital to the HOMO of the fluorophore, effectively quenching the fluorescence. A subsequent electron transfer from the LUMO of the fluorophore back to the external orbital restores the system to its stable ground state. This mechanism is schematically illustrated in Scheme 1.3.

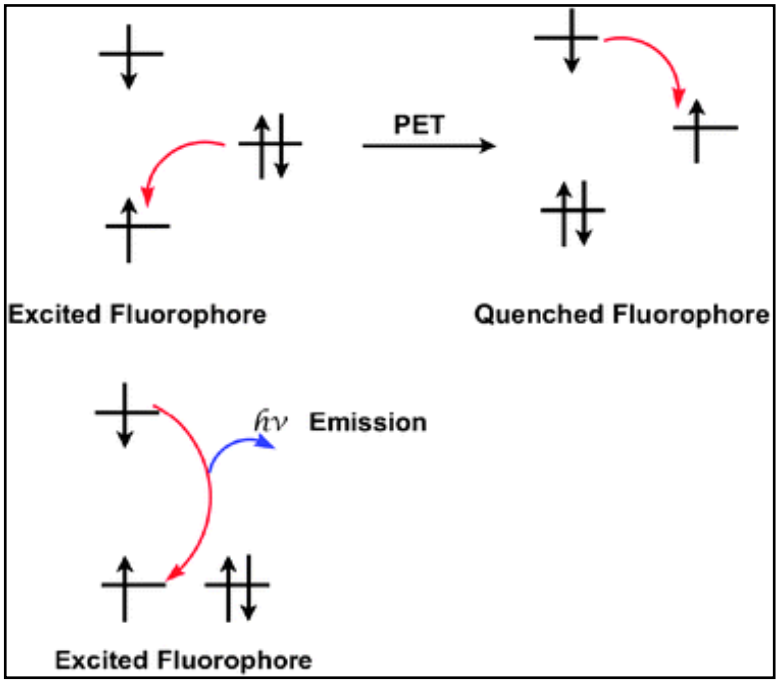


**Scheme 1.3:** Frontier energy diagram illustrating PET and reverse back PET.

In such a sequence, fluorescence quenching occurs because the transition from the excited state to the ground state follows a non-radiative pathway. Macroscopically, this is observed as a reduction in fluorescence intensity or complete suppression of emission. A similar mechanism

can also take place when an unoccupied orbitaloriginating from another part of the molecule or an interacting molecular entity that lies between the HOMO and LUMO of the fluorophore. In this case, a PET event can occur from the excited LUMO to the empty orbital, followed by electron transfer from this orbital to the HOMO of the fluorophore. As with the previous scenario, de-excitation occurs without photon emission, resulting in fluorescence quenching.The design of anion chemosensors often strategically exploits such PET mechanisms, whereby the binding of an ion modulates the PET processeither suppressing or enabling it, thereby causing quenching or enhancement of fluorescence emission. When donor and acceptor units are incorporated within the same molecular framework, they must be appropriately separated by a spacer that facilitates efficient electron transfer while minimizing electronic delocalization. The design of fluorescent chemosensors, therefore, seeks to manipulate PET processes in such a way that the presence of a specific ion selectively alters the emission profile. This principle is well-established, and numerous studies have been dedicated to elucidating the underlying PET mechanisms.[90]

As shown in Fig. 1.19, The lonepair of electrons on –OH functional groups are involved inphotoinduced electron transfer (PET) process which can reducethe emission intensity quite a bit.[91] With increasing amount of $Al^{3+}$ the hydroxyl lone pair ofelectrons got blocked which evidently resulted in suppression ofPET and ESIPT simultaneously.

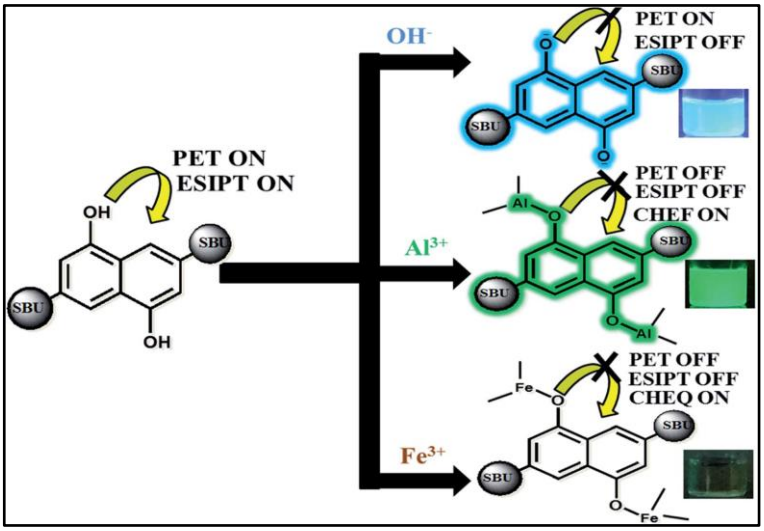


**Figure 1.19:** PET mechanism based fluorescent chemosensor. (Ghosh et al.)

In 2017, Xiao-li Yue and co-workers reported a fluorescence chemosensor for selective detection of $Al^{3+}$, based on a combination of PET (Photoinduced Electron Transfer) and ESIPT (Excited-State Intramolecular Proton Transfer) mechanisms.[92] The sensor comprises a naphthalene fluorophore and a pyridine carboxylic hydrazone moiety linked via a Schiff base (Fig. 1.20). In the uncomplexed state, the imine nitrogen can donate its lone pair of electrons to the partially filled HOMO of the naphthalene acceptor in the excited state, thereby activating the PET process and quenching fluorescence. However, upon complexation with $Al^{3+}$, the lone pair on the imine nitrogen becomes involved in coordination, suppressing the PET pathway. This inhibition of non-radiative decay results in a fluorescence "turn-on" response, enabling selective detection of $Al^{3+}$.

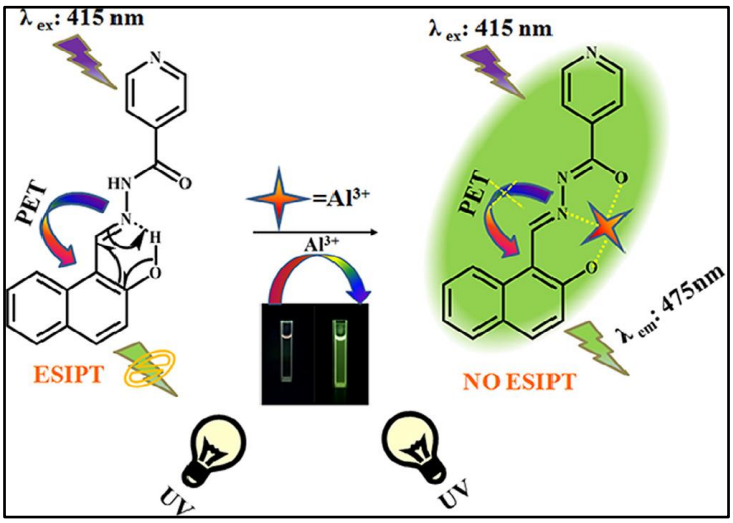


**Figure 1.20:** Sensing scheme for $Al^{3+}$ sensing. (Yue et al.)

## 1.8.5. FRET (Fluorescence resonance energy transfer) process

Fluorescence Resonance Energy Transfer (FRET) is an intermolecular, non-radiative energy transfer process mediated by dipole-dipole interactions, wherein energy is transferred from an excited-state fluorophore (donor) to a neighbouring ground-state fluorophore (acceptor) [93]. The efficiency of this energy transfer is directly related to the degree of spectral overlap between the emission spectrum of the donor and the absorption spectrum of the acceptor. This spectral overlap is quantitatively described by the Förster distance ($R_0$), which is the distance at which energy transfer efficiency is 50%.

The rate of energy transferis given by the Förster equation:

$k_t(r) = (1/\tau_d)(R_0/r)^6$

where r is the distance between the donor and acceptor fluorophores, and $\tau_d$ is the fluorescence lifetime of the donor in the absence of energy transfer. The efficiency of FRET is highly dependent on the donor-acceptor distance, typically effective within a range of 1-10 nm.

The FRET mechanism as follows:

$D^*+A \rightarrow D+A^*$

where an excited donor ($D^*$) transfers energy to the acceptor (A), resulting in the donor returning to the ground state and the acceptor being excited.

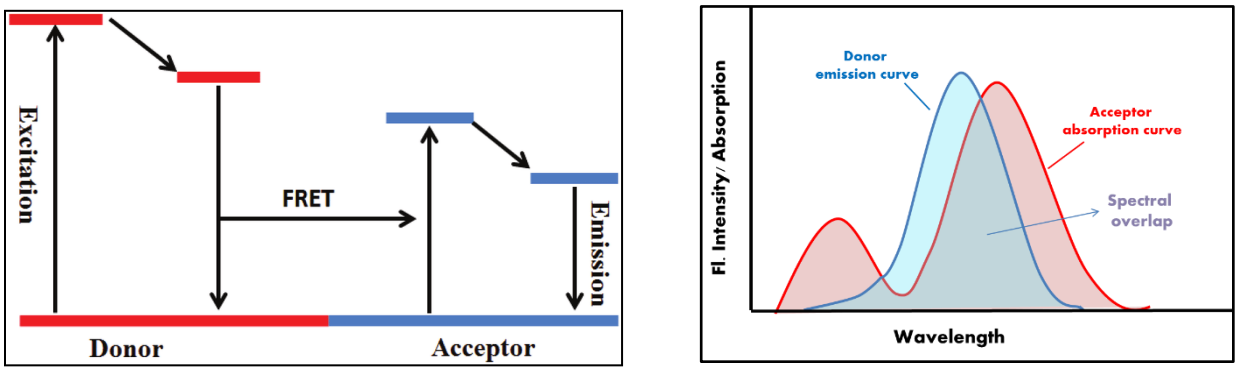


**Scheme 1.4:** General FRET based signaling mechanism.

The extent of spectral overlap between the emission spectrum of a donor and theabsorption spectrum of an acceptor is required to allow for FRET to occur. FRET happens when anenergy transfers from the excited donor to the acceptor which should be in a longer wavelength (D* +A→D + A*), coupled in resonance, accompanied with a loss ofemission from the donor .[94]

In 2014, Chattopadhyay and co-workers introduced a Rhodamine-based chemosensor for selective and ratiometric detection of $Hg^{2+}$ ion [95]and the recognition process can be attributed to the FRET mechanism. The fluorophores used are responsible for efficient FRET fluorescence emission as shown in the following structure of the sensor in Fig. 1.21.

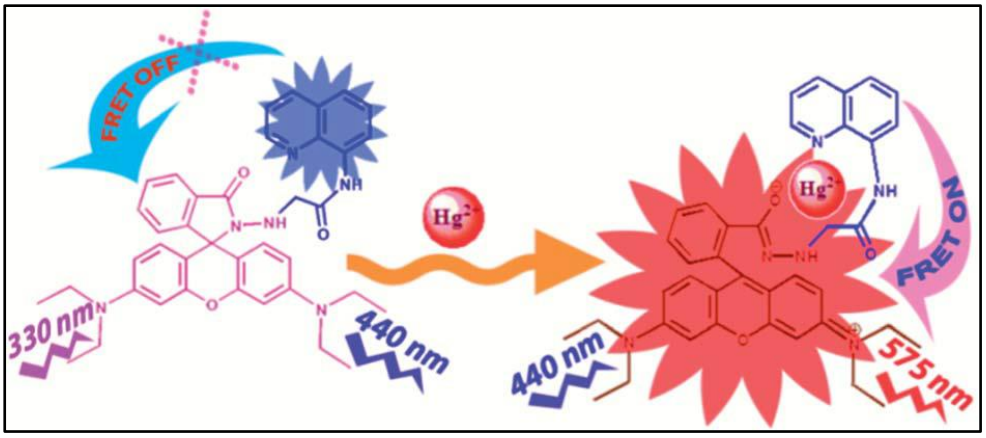


**Figure 1.21:** FRET process in a peptide-based chemosensor. (Chattopadhyay et al.)

In 2016, Das et al. reported a FRET-based fluorescent probe that exhibited a ratiometric emission response toward $Fe^{3+}$ and a colorimetric response toward $Fe^{2+}$.[96] The authors attributed the $Fe^{3+}$ sensing mechanism to a FRET process, which was facilitated by the optimal match between the ionic radius of $Fe^{3+}$ and the spatial dimensions of the probe's binding cavity. The proposed sensing mechanism is illustrated in Fig. 1.22.

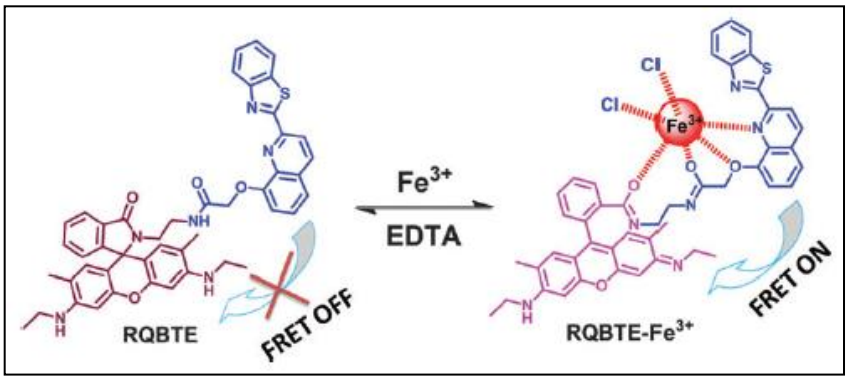


**Figure 1.22:** FRET process in a ratiometricchemosensor.(Das et al.)

## 1.8.6. Fluorescence quenching

Fluorescence quenching refers to any process that leads to a reduction in fluorescence intensity. Such processes can occur during the excited-state lifetime for examples include collisional quenching, charge transfer reactions, and photochemical transformationsor they may arise due to the formation of non-fluorescent complexes in the ground state. Broadly, fluorescence quenching mechanisms can be classified into two main types: (1) collisional or dynamic quenching, which involves interactions between the excited fluorophore and a quencher molecule during the

excited state, and (2) static quenching, which results from the formation of a stable, non-emissive complex between the fluorophore and quencher in the ground state.

### 1.8.6.1. Dynamic quenching

Collisional quenching occurs when an excited-state fluorophore returns to the ground state via a non-radiative pathway as a result of energy transfer upon interaction with another molecule in the solution, known as the quencher. This dynamic interaction leads to a measurable decrease in fluorescence intensity. The reduction in fluorescence intensity due to collisional quenching can be quantitatively described by the Stern-Volmer equation:

$$F/F_0 = 1 + K\,[Q] = 1 + kq\tau_0[Q]$$

where $K$ is the Stern-Volmer rate quenching constant, $kq$ is the bimolecular quenching constant, $\tau_0$ is the unquenched lifetime, and [Q] is the quencher concentration. The constant $K$ mainly represents the sensitivity of the fluorophore to a quencher. A wide variety of molecular species, including oxygen, halogens, and amines, can act as effective fluorescence quenchers. Quenching by heavy atoms is primarily attributed to enhanced spin–orbit coupling, which facilitates intersystem crossing to the triplet state, thereby promoting non-radiative decay pathways. In the case of collisional (dynamic) quenching, not only is the fluorescence intensity reduced, but the excited-state lifetime of the fluorophore is also significantly shortened, providing a useful distinction from static quenching mechanisms.

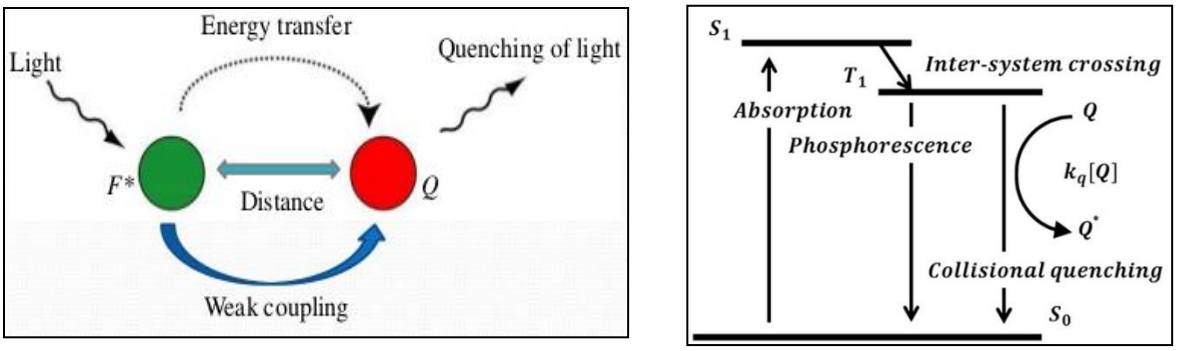


**Scheme 1.5:** Mechanism showing dynamic quenching (left side) and Jablonski diagram showing collision quenching (right side).

### 1.8.6.2. Static quenching

In several instances, a fluorophore can form a stable, non-fluorescent complex with another molecule in the ground state. This phenomenon is referred to as static quenching. Unlike dynamic quenching, static quenching does not involve the excited state of the fluorophore, insteadit results from the formation of a non-emissive ground-state complex. The decrease in fluorescence intensity due to static quenching is described by the following equation:

$F_0/F = 1 + K_a[Q]$, where Ka is the association constant of the complex.

Unlike dynamic quenching, static quenching (as illustrated in Scheme 1.6) does not alter the excited-state lifetime of the fluorophore. This is because only the uncomplexed fluorophores are capable of being excited and emitting fluorescence, thereby retaining their typical excited-state properties. The quencher, in this case, effectively reduces the number of fluorophores available to fluoresce by forming non-emissive ground-state complexes. As a result, the overall fluorescence intensity of the sample is diminished, even though the lifetime of the emitting species remains unchanged.

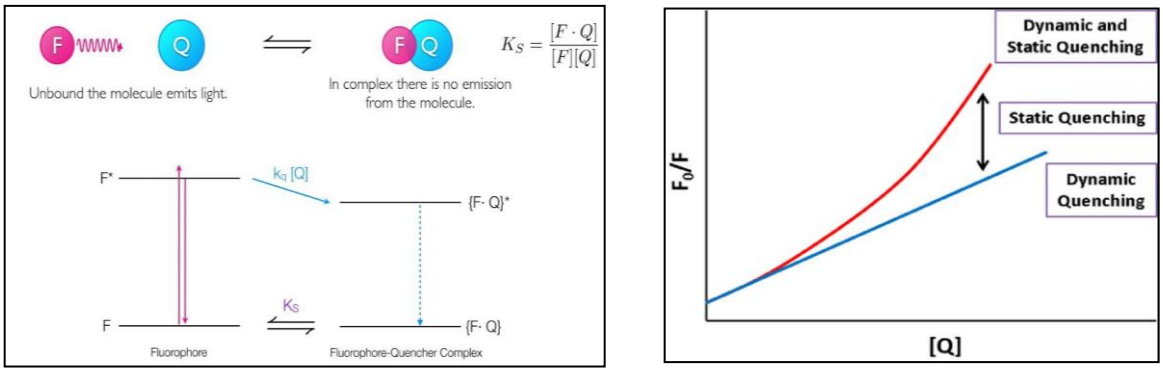


**Scheme 1.6:** Simple mechanism showing dynamic quenching (left side) and schematic of Stern-Volmer plot was shown displaying different forms of fluorescence quenching (right side).

# 1.9. Chemosensors: From Molecular Design to Practical Applications

## 1.9.1. Drug design

The selective recognition of specific molecules in the presence of closely related analogues forms the foundational principle behind numerous biological and chemical processes, including

enzyme catalysis, gene regulation, and chemical reactivity. In modern drug design, the precise binding of small molecules to complex biological targets such as proteins or enzymes is crucial. Drug molecules are engineered to selectively interact with specific receptors or enzymes implicated in a disease pathway, thereby minimizing off-target effects and reducing potential side effects. Notably, many clinically used drugs are administered in racemic forms, although their individual enantiomers often elicit different physiological responses. For instance, *d*-propranolol is approximately 40 times more potent than its *l* counterpart and functions effectively as an antiarrhythmic and antihypertensive agent, while *l*-propranolol exhibits significant efficacy as an anti-anginal agent.[97] Interestingly, β-cyclodextrin demonstrates selective binding toward *d*-propranolol via hydrogen bonding, enabling the enantioselective separation of *d* and *l* isomers—a process known as chiral recognition.[98] Such artificial recognition systems for biologically relevant molecules including peptides, nucleotides, and pharmaceuticals open promising avenues for the development of innovative therapeutic strategies, drug delivery platforms, and chemical sensor designs. These investigations often focus on the selective recognition of the ground-state configurations of target biomolecules.

### 1.9.2. Optical biosensor

An optical biosensor is a device that integrates an immobilized biological component with a transducer, representing a synergistic combination of biotechnology and microelectronics.[99] The application of optical biosensors for the detection of heavy metal ions has been developed based on the interaction mechanisms of biological systems. Various biological elements, including proteins (such as antibodies, enzymes, and metal-binding proteins) and whole cells (both naturally occurring and genetically engineered microorganisms), have been employed to construct sensors for heavy metal ion detection.[100-104] Heavy metal ions typically act as catalysts or inhibitors by chemically reacting with binding groups in proteins and microorganisms within cells. Numerous enzymessuch as urease,[105] cholinesterase,[106,107] and glucose oxidase[108] as well as specific proteins,[109] have been utilized in the development of these biosensors. For instance, Jiang and co-workers developed a biosensor to detect mercury ($Hg^{2+}$) in aqueous samples based on the inhibition of the urease-catalyzed hydrolysis of urea upon exposure to $Hg^{2+}$ ions.[110] In this system, the presence of $Hg^{2+}$ is recognized through changes in pH, ammonia, or carbon dioxide concentrations. The high affinity of $Hg^{2+}$ for thiol and methyl-thiol groups in the enzyme leads to significant inhibition of enzymatic activity.[111]

### 1.9.3. Nanoscience

Supramolecular chemistry plays a crucial role in assembling atoms and molecules into functional materials, serving as a foundational strategy for the development of advanced nanomaterials and nanoscale devices. Owing to its ability to guide molecular organization through non-covalent interactions, supramolecular chemistry forms the basis of many bottom-up approaches in nanotechnology, where large and complex structures are constructed from smaller molecular building blocks.[112] A prominent example of supramolecular systems in nanotechnology is discotic liquid crystals, which can self-assemble into columnar structures driven by π-π stacking interactions. These π-π interactions are fundamental to molecular self-assembly, enabling the controlled formation of nanoscale architectures essential to bottom-up fabrication techniques. Another significant area of interest is the development of synthetic molecular motorsnanoscale devices capable of undergoing controlled rotation in response to an external energy input. The conceptual foundation for such motors was first introduced by Richard Feynman in his seminal 1959 lecture, *There's Plenty of Room at the Bottom*. The key criteria for functional synthetic motors include continuous 360° rotational motion, energy consumption, and unidirectional operation. In addition, emerging research on molecular machines such as nanocars, though currently lacking direct practical applications, holds potential for future technological advancements. These studies are expected to contribute to the development of more efficient catalytic systems and further enrich the field of molecular nanotechnology.[113]

### 1.9.4.Application through Dip-stick experiment

For the visual detection of various compounds and ions, a convenient and efficient portable methodcommonly referred to as the dip-stick techniquewas employed. In this method, the sensing probe serves as a portable test kit, exhibiting its detection capability for specific analyte even in the solid state. To perform the experiment, thin-layer chromatography (TLC) plates or strips of Whatman filter paper were prepared by immersing them in a solution of the sensing probe. After immersion, the plates were allowed to dry in ambient air to ensure complete evaporation of the solvent.Upon exposure to the target analyte, the probe-coated test strips displayed a visible change in color or fluorescence, depending on the nature of the analyte interaction. These changes could be readily observed under ambient light or ultraviolet (UV) illumination, respectively. This approach enables straightforward, on-site qualitative detection. Numerous colorimetric and fluorometric chemosensors have been previously reported and

successfully implemented using this method for the qualitative as well as sometimes quantitative identification of a wide range of analytes.

Recently, in 2021, Tumay et al. reported a CHEF and ESIPT-based probe for turn on detection of Aluminium ion in water:EtOH (1: 4, v/v) (Fig. 1.23). They have established a paper-basedtest strips experiment for qualitative identification of $Al^{3+}$ ion in different concentration.[114]

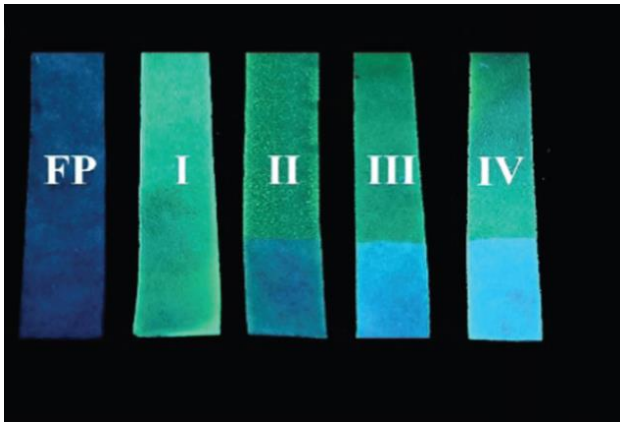


**Figure 1.23:** Pictures of paper-based test kits under UV irradiation ($\lambda_{ex}$ = 365 nm) after treatment with increasing concentrations of $Al^{3+}$. (Tumay et al.)

Again in 2019, Mahapatra et al. synthesized a Betti base chemodosimeter for ultrasensitive and selective sensing of Phosgene gas (Fig. 1.24). They also established a portable solid-state platform for analyte detection. [115]

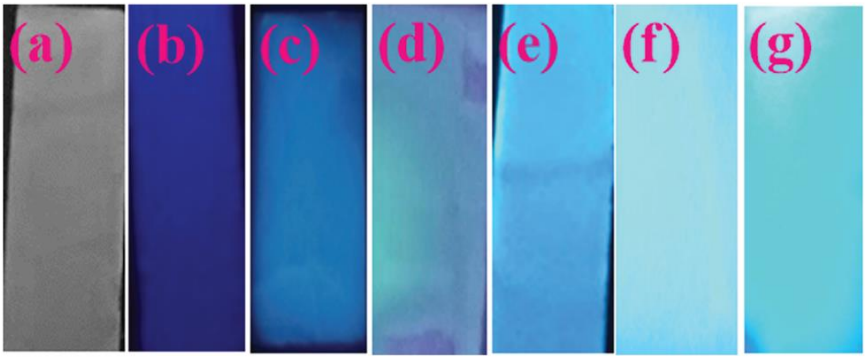


**Figure 1.24:** TLC sticks exposed to a handheld UV lamp todemonstrate fluorescence changes: (a) BB alone, followed by contact with different phosgene concentrations: (b) 5.0 ppm, (c) 10.0 ppm, (d) 20.0 ppm, (e) 40.0 ppm, (f) 60 ppm, and (g) 90 ppm. (Mahapatra et al.)

Mondal et al. reported a carbazole based fluorescent sensor for selective and sole recognition of $CN^-$. Probe-loaded test strips displayed a greenish-yellow color in ambient light and yellowish under UV light. Test strips were dipped into a $CN^-$ solution changed its colour.[116] (Fig.1.25)

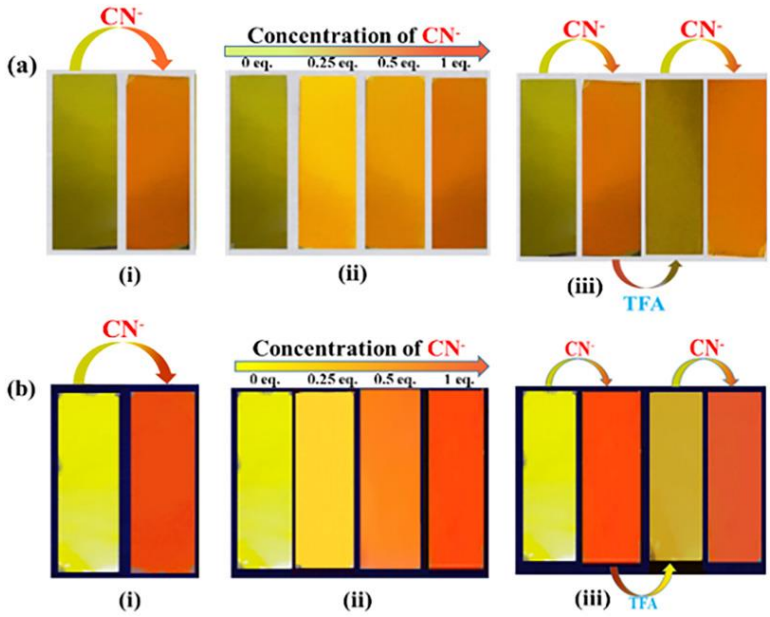


**Figure 1.25:** Pictures of TLC plates after immersion into a DMSO solution (Mondal et al.)

## 1.9.5. Application of chemosensors in live cell imaging

Recently, various newly developed chemosensors have been utilized for *in vitro* cell imaging studies to evaluate their capability for detecting metal ions within intracellular environments. As for example, Goswami *et al*. reported ratiometric fluorescent probe for distinctive detection of $Al^{3+}$[117] and showed detection of intracellular $Al^{3+}$ its application in Peripheral blood mononuclear cells (PBMCs) (Fig. 1.26).

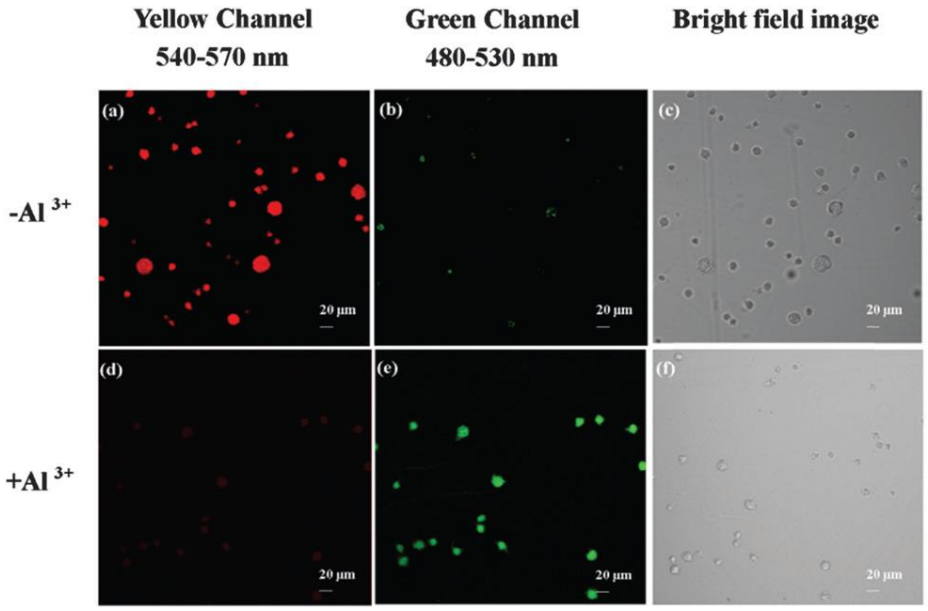


**Figure 1.26:** Confocal fluorescence images (60x) of human PBMCs treated with 10 mM HBTP (a and b), and the same treated with 10 mM $Al^{3+}$ solution (d and e). Images were obtained from (a and d) yellow channel (540-570 nm) and (b and e) green channel (480-530 nm). $\lambda_{ex}$ = 400 nm. Larger cells aremacrophages in PBMC populations. (c and f) Show bright-field images of the cells with probe before and after the addition of $Al^{3+}$, respectively. (Goswami et al.)

Similarly, Li *et al*. reported a "ratiomeric" fluorescent probe for detection of $Cd^{2+}$ recently [118], which is also effective in detection of the metal ion present in the living RAW 264.7 cells. (Fig. 1.27).

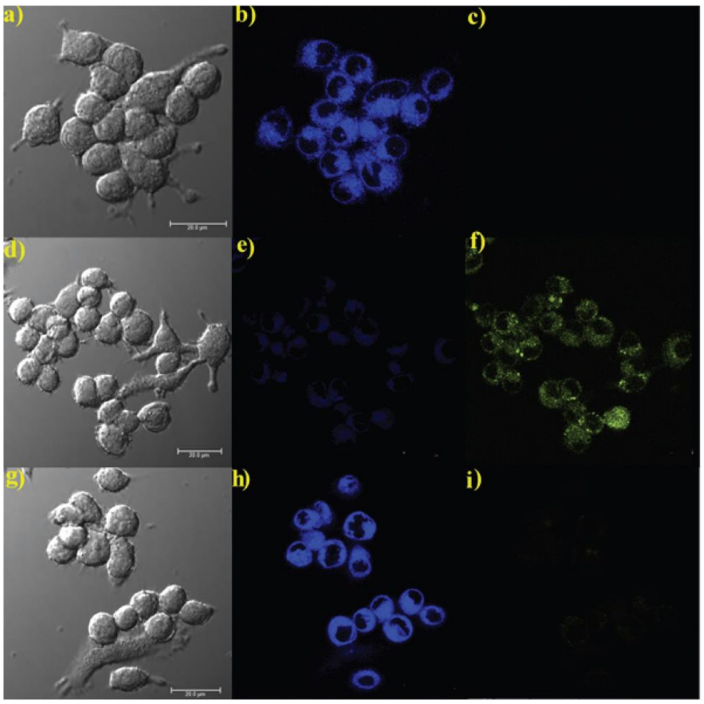


**Figure 1.27:** Confocal fluorescence images of RAW 264.7 cells. (a) Bright field image when treated with L1 (10 μM); (b) blue-channel fluorescence image of (a) detected at 420 nm-460 nm; (c) green-channel fluorescenceimage of (a) detected at 530 nm-570 nm; (d) bright field imagewhen treated with L1 (10 μM) followed by 20 μM $Cd^{2+}$; (e) blue-channelfluorescence image of (d) detected at 420 nm-460 nm; (f) green channel fluorescence image of (d) detected at 530 nm-570 nm; (g)bright images when treated with the L1-Cd(II) complex followed by 20 μM PPi; (h) blue-channel fluorescence image of (g) detected at 420 nm-460 nm; (i) green-channel fluorescence image of (g) detected at 530 nm-570 nm.(Li et al.)

In 2022, Mahapatraand co-workers fabricated an ICT-guided ratiometric naphthalene-benzothiazole-based probe for the detection of cyanide[119] and showed its application in in human breast cancer MDA-MB 231 cells (Fig. 1.28).

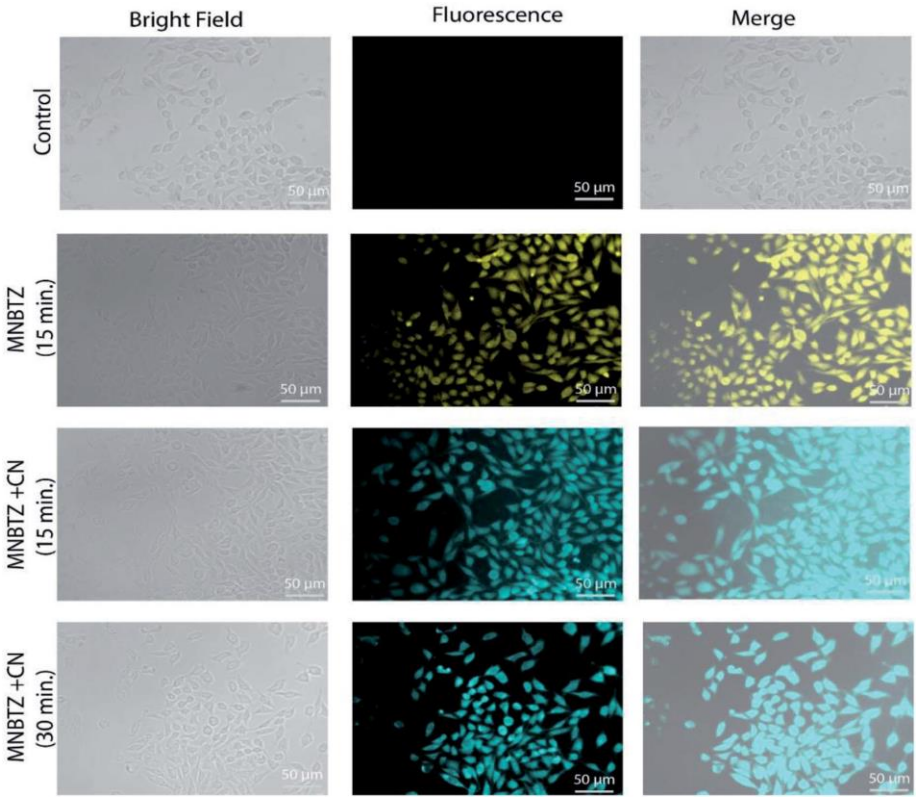


**Figure 1.28:** Fluorescence microscopy images of untreated MDA-MB 231 cells (control), cells treated with the ligand MNBTZ (10 mM), and ligand MNBTZ (10 mM) + cyanide (5 mM) after 15 min and 30 min: bright field, fluorescence and merged (Mahapatra et al.).

Similarly in 2023, Zhang group published a benzimidazole-derived fluorescent chemosensor for turn-off detection of $Cu^{2+}$ and selective ratiometric turn-on detection of $Zn^{2+}$ in aqueous solutions.[120] The application in living cells were perfomed with $Cu^{2+}$ and $Zn^{2+}$ by confocal fluorescence microscopy. Bright green fluorescence was observed in livingcells when incubated only with BBMP then $Cu^{2+}$ caused a quenching of the greenfluorescence whereas brilliant blue fluorescencewas observed in HeLa living cells with further $Zn^{2+}$ incubation (Fig. 1.29).

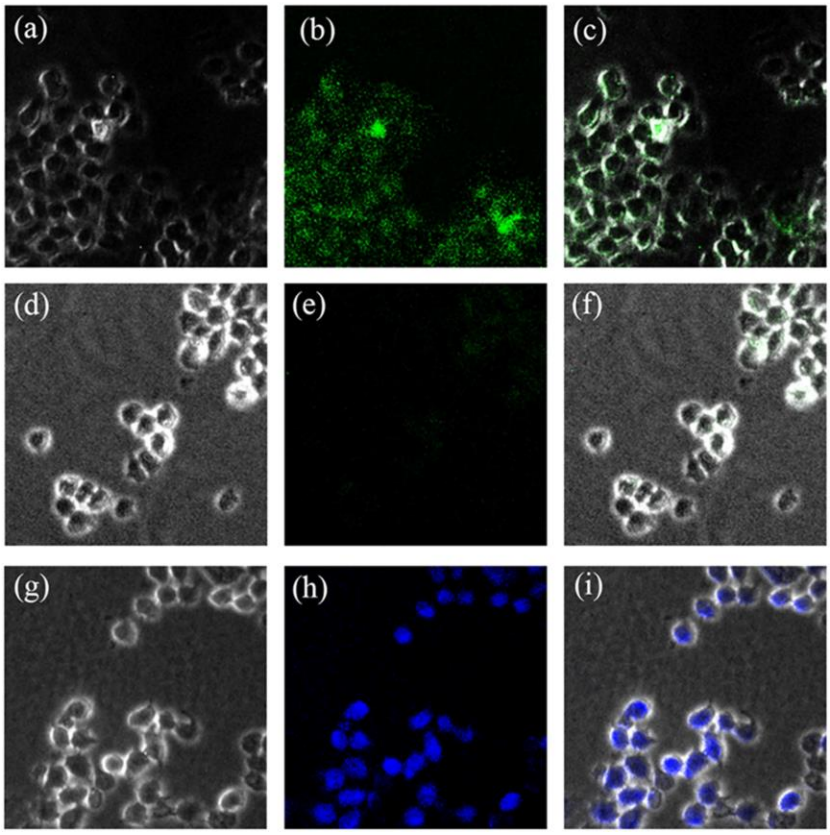


**Figure 1.29:** Bright-field (a, d and g), dark-field (b, e and h), and merged (c, f and i) images of living HeLa cells. The HeLa cells were incubated with BBMP (10 μM) (a-c), BBMP and further with $Cu^{2+}$ (20 μM) (d-f), and BBMP and further with $Zn^{2+}$ (20 μM) (g-i) at 37 °C for 30 min, respectively. (Zhang et al.)

## 1.9.6. Application of chemosensors in real-world sample analysis

The application of chemosensors in real-world sample analysis has become increasingly important due to their high sensitivity with selectivity, and ease of use. Chemosensors have been successfully employed in the detection and quantification of various analytes including environmental samples such as water, soil and biological fluids such as blood, urine and industrial products. Their ability to operate under diverse conditions and deliver rapid, on-site results makes them valuable tools for monitoring environmental pollution, and ensuring product quality in manufacturing processes. Moreover, the development of portable and cost-effective sensing platforms has further enhanced the practicality of chemosensors in field applications. Recent advances also focus on improving the stability, reproducibility, and biocompatibility of these sensors to ensure reliable performance in real-world conditions.WHO (World Health

Organization) has given an enforceable drinking water standard for cadmium of 3 ppb.[121] Also WHO (World Health Organization) stated that the average consumptionof $Al^{3+}$ in the human body through several ways is about 3-10 mg per kg per day and the maximum recommended limit Al-contaminated water is 7.42 mM.[122] Again WHO has set up an acceptable limit of cyanide of 1.9 μM in drinking water due to its toxic nature.[123]

Recently, P. Tharmaraj et al. developed a new Anthracene based chemosensor for recognition of $Cd^{2+}$ ions and also they collected real water samples and applied the sample to detect $Cd^{2+}$ in micro level.[124] Iyer and co-workers in 2021 have reported a sensitive and selective BINOL based ratiometric fluorescence sensor for the detection of cyanide ions. The sensor was applied for $CN^-$ determination in environmental samples.[125]

## 1.10. Plan of the thesis

The primary objective of this thesis is to advance the field of chemosensors for the detection and monitoring of various deleterious and environmentally important ions and chemical warfare agents. Given their profound adverse effects on human health and ecological systems, the recognition and quantification of these species have become imperative and have garnered significant attention from contemporary researchers. Although a variety of conventional analytical methodologies exist, they frequently require sophisticated instrumentation and are often constrained in their applicability for real-time, on-site monitoring. This thesis delineates the application of several optical sensing strategies for the selective recognition of environmentally and biologically hazardous analytes. Specifically, it focuses on the development and characterization of newly synthesized organic compounds capable of detecting toxic species at micromolar (μM) and even nanomolar (nM) concentration levels. The chemosensors discussed herein exhibit rapid and specific binding to target analytes, often accompanied by distinct and observable colorimetric and fluorometric changes, thereby facilitating real-time, naked-eye detection without the need for elaborate equipment.Moreover, several of the reported chemosensors demonstrate reversible binding behavior, highlighting their potential for reuse and sustainable application. Importantly, some of the synthesized probes have been successfully applied in cellular imaging studies, showcasing their biocompatibility and potential for bioanalytical applications. Furthermore, the versatility of these chemosensors extends to the

qualitative analyte identification through the implementation of a simple, cost-effective, and portable "dip-stick" assay and real sample analysis.

## 1.11. References


1. C.Andreini, L.Banci, I. Bertini and A.Rosato, *J. Biol. Inorg. Chem.*, 2008, **13**, 1205.
2. G.M. Barve, M. Mashru, C. Jagtap, B.J. Patgiri and P.K. Prajapati, 2011, *J. Ayurveda Integr. Med.*, **2**, 55.
3. P. B. Tchounwou, C. G. Yedjou, A. K. Patlolla and D. J. Sutton, *Clinical and Environmental Toxicology Exs*., 2012, **101**, 133.
4. G. Genchi, M.S. Sinicropi, G. Lauria, A. Carocci and A. Catalano, *Res. Public Health*., 2020, **17**, 3782.
5. D. Beyersmann and A. Hartwig, *Archives of Toxicology*, 2008, **82**, 493.
6. M. Jaishankar, T. Tseten, N. Anbalagan, B. B. Mathew and K. N. Beeregowda, *Interdiscip. Toxicol.*, 2014, **7**, 60.
7. H. C. Xia, X. H. Xu and Q. H. Song, *ACS Sens.*, 2017, **2**, 178.
8. S. Wang, B. Zhu, B. Wang, P. Fan, Y. Jiu, M. Zhang, L. Jiang and J. T. Hou, *Dyes Pigm.*, 2020, **173**, 107933.
9. Y. Hu, X. Zhou, H. Jung, S. J. Nam, M. H. Kim and J. Yoon, *Anal. Chem.*, 2018, **90**, 3382.
10. X. Liu, Y. Gong, Y. Zheng, W. Xiong, C. Wang, T. Wang, Y. Che and J. Zhao, *Anal. Chem.*, 2018, **90**, 1498.
11. P.F. Walker, *Springer International Publishing*, 2017, 379.
12. Y. L. Duan and Y. S. Zheng, *Talanta*, 2013, **107**, 332.
13. E. Croddy, C. Perez-Armendariz and J. Hart, (2002). *Chemical and biological warfare: a comprehensive survey for the concerned citizen*, New York, USA:: Copernicus Books, **22**, 2002.
14. W. Huang, X. Yu, H. Lin, and H. Lin, A colorimetric sensor for the recognition of biologically important anions, *J. Incl. Phenom. Macrocycl Chem.*, 2011, **69**, 69.
15. M. D. Sobsey and S. Bartram, *Forum Nutr.*, 2003, **56**, 396.
16. D. A. Jones, Phytochem., 1998, **47**, 155.
17. M. Zagrobelny, S. Bak and B. L. Moller, *Phytochem.*, 2008, **69**, 1457.
18. D. G. Barceloux,*Dis.Mon.*, 2009, **55**, 336.
19. G. Jin, R. He, Q. Liu, M. Lin, Y. Dong, K. Li, B. Z. Tang, B. Liu and F. Xu, *Theranostics.*, 2019, **9**, 246.
20. Y. Li, K. Xu, Y. Si, C. Yang, Q. Peng, J. He, Q. Hu and K. Li, *Dyes Pigm.*, 2019, **171**, 107682.
21. U.S. Environmental Protection Agency (EPA), Toxicological Review of Hydrogen Cyanide and Cyanide Salts, 2006.
22. S. F. D'Souza, Microbial biosensors. *Biosensors and Bioelectronics*, 2001, **16**, 337.
23. K. A. Francesconi and D. Kuehnelt, *Analyst*, 2004, **129**, 373.
24. O. S. Wolfbeis, Materials for fluorescence-based optical chemical sensors. Journal of Materials Chemistry, 2006, **15**, 2657.
25. O. S. Wolfbeis, *J. Mater. Chem.*, 2005, **15**, 2657.
26. M. H. Chua, K. W. Shah, H. Zhou and J. Xu, *Molecules.*, 2019, **24**, 2711.
27. T. Ghosh, S. Mitra, S. K. Maity and D. K. Maiti, *Nano Mater.*, 2020, **3**, 3951.
28. K. Santhiya, S. K. Sen and R. Natarajan, *Dyes Pigms.*, 2021, **185**, 108891.

29. Y. Wang, H. Liu, Z. Chen and S. Pu, *Spectrochim. Acta A.*, 2021, **245**, 118928.
30. Y. Liu, A. Qin and B. Z. Tang, *Prog. Polym. Sci.*, 2018, **78**, 92.
31. M. Montalti, L. Prodi and N.J. Zaccheroni, *J. Mater. Chem.*, 2005, **15**, 2810.
32. Z. Liu, W. He and Z. Guo, *Chem. Soc. Rev.*, 2013, **42**, 1568.
33. D. Buccella, J. A. Horowitz and S. J. Lippard, *J. Am. Chem. Soc.*, 2011, **133**, 4101.
34. L. you, D. Zha and E. V. Anslyn, *Chem. Rev.*, 2015,**115**, 7840.
35. J. W.Steed and J. L. Atwood, Supramolecular Chemistry (2nd ed.). Wiley, 2009.
36. J. G. Vos, R. T. Forster and T. E. Keyes, Interfacial supramolecular assemblies, New Jersey, John Wiley, 2003.
37. J. W.Steed and J. L. Atwood,Supramolecular Chemistry (2nd ed.). Wiley, 2009.
38. F. Vogtle, Supramolecular chemistry, An Introduction; Wiley & Sons: Chichester, 1993.
39. P. D. Beer, P. A. Gale and D. K. Smith, Supramolecular Chemistry, Oxford University Press, New York, 1999.
40. S. H. Gellman, *Chem. Rev.*, 1997, **97**, 1231.
41. C. J. Pedersen, *J. Am. Chem. Soc.*, 1967, **89**, 7017.
42. J.M. Lehn, *Acc. Chem. Res.*, 1978, **11**, 49.
43. J.M. Lehn, *Pure Appl. Chem.*, 1979, **50**, 871.
44. D. J. Cram and J.M. Cram, *Science*, 1974, **183**, 803.
45. J.M. Lehn, *Science*, 1985, **227**, 849.
46. D. J. Cram and J. M. Cram, Royal Society of Chemistry, Cambridge, 1994.
47. F. P. Schmidtchen and M. Berger, *Chem. Rev.*, 1997, **97**, 1609.
48. J. Janata, Principles of Chemical Sensors (2nd ed.). Springer, 2009.
49. A. Hierlemann, Sens. Actuators B: Chem., 2008, **121**, 4.
50. D. Buccella, J. A. Horowitz and S. J. Lippard, *J. Am. Chem. Soc.*, 2011, **133**, 4101.
51. Y. Q. Weng, F. Yue and Y. R. Zhong, *Inorg. Chem.*, 2007, **46**, 7749.
52. B. R. Eggins, *Chem. Sens. Biosens.*, John Wiley & Sons, 2002.
53. N. Verma and M. Singh, *BioMetals*, 2005, **18**, 121.
54. E. Hirayama, T. Sugiyama, H. Hisamoto and K. Suzuki, *Anal. Chem.*, 1999, **72**, 465.
55. H. M. Geysen, J. A. Tainer, S. J. Rodda, T. J. Manson, H. Alexander, E. D. Getzoff and R. A. Lerner, *Science*, 1987, **235**, 1184.
56. C. Reichardt and T. Welton, Solvents and Solvent Effects in Organic Chemistry (4th ed.). Wiley-VCH, 2011.
57. H. X. Liu, X. M. Fu, and J. H. Hu, *Inorg. Chem. Commun.*, 2022, **142**, 109662.
58. G. R. Desiraju, Eds. Crystal Design: Structure and Function, Perspectivein Supramolecular Chemistry, Vols. 7, John Wiley & Sons Ltd.: New York, NY, 2003.
59. A. Sygula, F. R. Fronczek, R. Sygula, P. W. Rabideau and M. M. Olmstead, *J. Am. Chem. Soc.*, 2007, **129**, 3842.
60. S. C. Zimmerman, C. M. VanZyl and G. S. Hamilton, *J. Am. Chem. Soc.*,1989, **111**, 1373.
61. S. C. Zimmerman, M. Mrkisch and M. Baloga, *J. Am. Chem. Soc.*, 1989, **111**, 8528.
62. M. G. Khrenova, A. V. Nemukhin, V. G. Tsirelson, Chemical Physics, 2019, **522**, 32.

63. H. M. Colquhoun, J. F. Stoddart, D. J. Williams, J. B. Wolstenholme and R. Zarzycki, *Angew. Chem. Int. Edn. Engl.*, 1981, **20**, 1051.
64. V. Blanco, M. Chas, D. Abella, E. Pia, C. Iglesias, C. Peinador, J. Quintela, *Org. Lett.*, 2008, **10**, 409.
65. A. Singh, P. Raj, J. J. Dubowski and N. Singh, *Cryst. Growth Des.*, 2018, **18**, 4320.
66. F. P. Schmidtchen, *J. Am. Chem. Soc.*, 1986, **108**, 8249.
67. C. J. Pedersen, *Angew. Chem. Int. Ed. Engl.*, 1988, **27**, 1021.
68. R. A. Bissell, A. P. de Silva, H. Q. N. Gunaratne, P. L. M. Lynch, G. E. M. Maguire and K. R. A. S. Sandanayake, *Chem. Soc. Rev.*, 1992, **21**, 187.
69. S. L. Wiskur, H. Ait-Haddou, J. J. Lavigne and E.V. Anslyn, *Acc. Chem. Res.*, 2001, **34**, 963.
70. K. Kaur, R. Saini, A. Kumar, V. Luxami, N. Kaur, P. Singh and S. Kumar, *Coord. Chem. Rev.*, 2012, **256**, 1992.
71. M. Y. Chae and A. W. Czarnik, *J. Am. Chem. Soc.*, 1992, **114**, 9704.
72. A. P. de Silva, T. S. Moody and G. D. Wright, *Analyst*, 2009, **134**, 2385.
73. J. R. Ed. Lakowicz, Principles of Fluorescence Spectroscopy; Plenum Publishers Corporation: New York, 1999.
74. T. Iijima, A. Momotake, Y. Shinohara, T. Sato, Y. Nishimura, T. Arai, *J. Phys. Chem. A.*, 2010, **114,** 1603.
75. S. J. Grabowski, *Chemical reviews*, 2011, **111**, 2597.
76. J. S. Wu, W. M. Liu, J.C. Ge, H.Y. Zhang, P.F. Wang, *Soc. Rev.*, 2011, **40**, 3483.
77. S. Park, J. E. Kwon, S. H. Kim, J. Seo, K. Chung, S. Y. Park, D. J. Jang, B. M. Medina, J. Gierschner and S. Y. Park, *J. Am. Chem. Soc.*, 2009, **131**, 14043.
78. N. Kaur, G. Jindal, Sukhvinder and S. Kumar, *New J. Chem.*, 2019, **43**, 436.
79. R. D. Alharthy, I. Urooj, M. Tasleem, M. Khalid, M. A. Asghar, S. I. Khan, M. Ajmal, N. Ahmed, and Z. Shafiq, *RSC advances*, 2023, **13**, 15208.
80. C. Rao, Z. Wang, Z. Li, L. Chen, C. Fu, T. Zhu, X. Chen, Z. Wang and C. Liu, *Analyst*, 2020, **145**, 1062.
81. S. Gadiyaram, V. D. Ghule, A. Ghosh, and D. A. Jose, *Sens. Diagn.*, 2022, **1**,1224.
82. C. Liang, W. Bu, C.Li, G. Men, M. Deng, Y. Jiangyao, H. Sun and S. Jiang, *Dalton Trans.*, 2015, **44**, 11352.
83. S. Paul, S. Maity, S. Halder, B. Dutta, S. Jana, K. Jana, and C. Sinha, *Dalton Trans.*, 2022, **51**, 3198.
84. S. Mabhai, M. Dolai, S. Dey, A. Dhara, B. Das and A. Jana, *New J. Chem.*, 2018, **42**, 10191.
85. Y. Jiao, B. Zhu, J. Chen and X. Duan, *Theranostics.*, 2015, **5**, 173.
86. S. L.Wang, L. Zhong and Q. H. Song, *Chem. Commun.*, 2017, **53**, 1530.
87. S. L.Wang, C. L. Zhang and Q. H. Song, *J. Mater. Chem. C.*, 2019, **7**, 1510.
88. V. Dujols, F. Ford and A. W. Czarnik, *J. Am. Chem. Soc.*,1997, **119**, 7386.
89. F. Wang, L. Wang, X. Chen, and J. Yoon, *Chem. Soc. Rev.*, 2014, **43**, 4312.
90. A. Weller, *Pure Appl. Chem.*, 1968, **16**, 115.
91. S. Bhowal and A. Ghosh,*RSC advances.*, 2021, **11,** 27787.
92. X. L.Yue, Z. Q. Wang, C. R. Li and Z. Y. Yang, *Tetrahedron Lett.*, 2017, **58**, 4532.
93. S. J.Strickler and R. A. Berg, *J. Chem. Phys.*, 1962, **37**, 814.
94. Y. Jiao, B. Zhu, J. Chen and X. Duan, *Theranostics*, 2015, **5**, 173.
95. B. Sen, M. Mukherjee, S. Pal, K. Dhara, SK. Mandal, A.R.Khuda-Bukhsh, P. Chattopadhyay, *Rsc Advances.*, 2014, 4, 14919.

96. S. Das, K. Aich, S. Goswami, C. K. Quahb and H. -K. Fun, *New J. Chem.*, 2016, **40**, 6414.
97. M. Stępień, B. Donnio and J. L. Sessler, *Angew. Chem. Int. Ed.*, 2007, **46**, 1431.
98. A. G. Wilson, O. G. Brooke, H. J. Lloyd and B. F. Robinson, *Br. Med. J.*,1996,**4**, 399.
99. S. F. D'Souza, *Biosens.Bioelec.*, 2001, **16**, 337.
100. I. Bontidean, J. Ahlqvist, A. Mulchandani, W. Chen, W. Bae, R. K. Mehra, A. Mortari and E. Csöregi, *Biosens. Bioelec.*, 2003, **18**, 547.
101. S. Lee, K. Sode, K. Nakanishi, J.-L. Marty, E. Tamiya and I. Karube, *Biosens.Bioelec.*, 1992, **7**, 273.
102. P. Corbisier, D. V. de Lelie, B. Borremans, A. Provoost, V. de Lorenzo, N. L. Brown, J. R. Lloyd, J. L. Hobman, E. Csöregi, G. Johansson and B. Mattiasson, Anal. Chim. Acta, 1999, **387**, 235.
103. E. M. Bosch, J. R. A. Sanchez, S. F. Rojas and B. C. Ojada, *Sensors*, 2007, **7**, 797.
104. P. Gupta and B. Diwan, *Biotechnol. Rep.*, 2017, **13**, 58.
105. I. Bontidean, C. Berggren, G. Johansson, E. Csoregi, B. Mattiasson, J.R. Lloyd, K. J. Jakeman and N. L. Brown, *Anal. Chem.*,1998, **70**, 4162.
106. N. F. Starodub, N. I. Kanjuk, A. L. Kukla and Y. M. Shirshov, *Anal. Chim. Acta.*, 1999, **385**, 461.
107. A. L. Kukla, N. I. Kanjuk, N. F. Starodub and Y. M. Shirshov, *Sens. Actuators B: Chem.*, 1999, **57**, 213.
108. N. F. Starodub, N. I. Kanjuk, A. L. Kukla and Y. M. Shirshov, *Anal. Chim. Acta.*, 1999, **385**, 461.
109. G. Q. Shi and G. Jiang, *Anal. Sci.*, 2002, **18**, 1215.
110. L. Basabe-Desmonts, D. N. Reinhoudt and M. Crego-Calama, *Chem. Soc. Rev.*, 2007, **36**, 993.
111. E. M. Bosch, J. R. A. Sanchez, S. F. Rojas and B. C. Ojada, *Sensors*, 2007, **7**, 797.
112. K. Sada, M. Takeuchi, N. Fujita, M. Numata and S. Shinkai, *Chem. Soc. Rev.*, 2007, **36**, 415.
113. Y. Shirai, A. J. Osgood, Y. Zhao, K. F. Kelly and J. M. Tour, *Nano Lett.*,2005, **5**, 2330.
114. S. O. Tümay, A. Şenocak, and A. Mermer, *New J. Chem.*, 2021,**45**,18400.
115. A. Gangopadhyay and A. K. Mahapatra, *New J. Chem*., 2019, **43**, 11743.
116. A. Maji, A. Biswas, A. Das, S. Gharami, K. Aich and T. K. Mondal, *New J. Chem*., 2023, **47**, 11557.
117. S. Das, S. Goswami, K. Aich, K. Ghoshal, C. K. Quah, M. Bhattacharyyaand and H. K. Fun, *New J. Chem.*, 2015, **39**, 8582.
118. S. Y. Jiao, K. Li, W. Zhang, Y. H. Liu, Z. Huang and X. Q. Yu, *Dalton Trans.*, 2015, **44**, 1358.
119. S.Banerjee, M. Mandal, S. Halder, A. Karak, D. Banik, K. Jana, A.K. Mahapatra, *Anal. Methods*, 2022, **14**, 3209.
120. W.Y. Zhu, K. Liuand X. Zhang, *Sens. diagn.*, 2023, **2**, 665.
121. World Health Organization,Avenue Appia 20, 1211 Geneva 27, Switzerland.
122. T. Han, X. Feng, B. Tong, J. Shi, L. Chen, J. Zhi and Y. Dong,*Chem. Commun.*, 2012, **48**, 416.
123. T. Zhu, Z. Li, C. Fu, L. Chen, X. Chen, C. Gao, S. Zhang andC. Liu, *Tetrahedron*, 2020, **76**, 131479.
124. J. J.Celestina, P. Tharmaraj and C. D. Sheela, *Opt. Mater.*, 2020, **109**,110176.
125. S.Munusamy, S. Swaminathan, D. Jothi, V.P. Muralidharan, and S.K. Iyer, *RSC Adv.*, 2021, **11**, 15656.

# Chapter 2

# General Instrumentations and analysis techniques

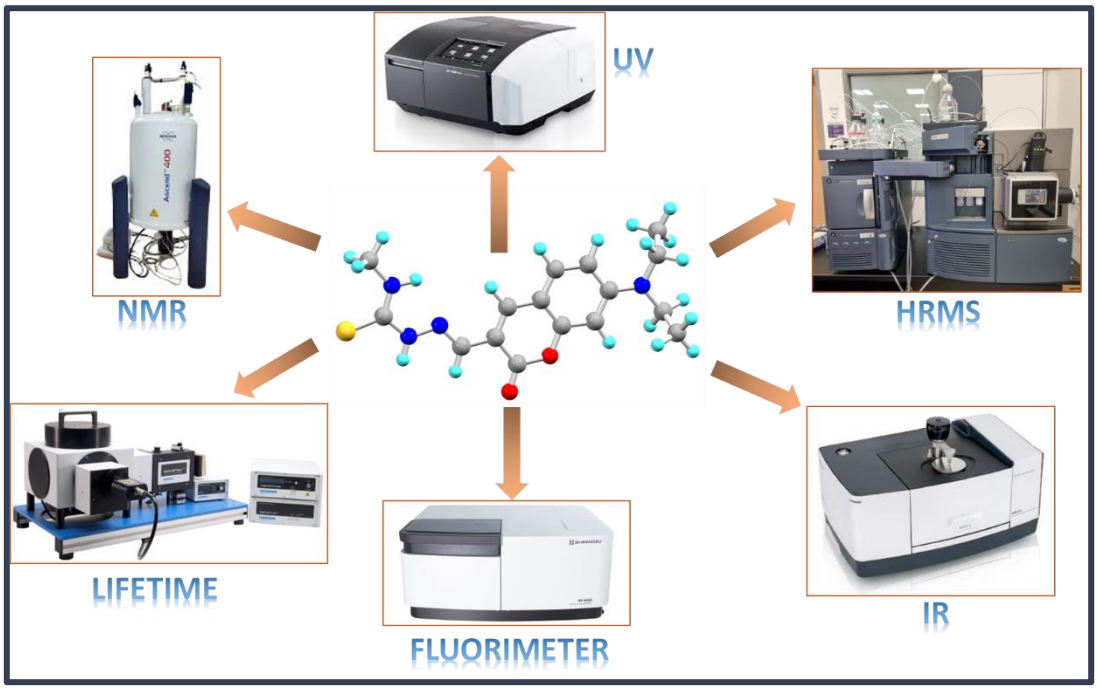

## 2.1. Introduction

The pioneer step in designing a chemosensor includes the planning of a scheme and then the plan is implemented for the synthesis of the targeted molecular chemosensor. This chapter deals with the steps performed after the synthesis of the molecular sensor, which includes the instruments and techniques required for those steps. All the instrumentation techniques are demonstrated in detail, throughout this chapter,which have been used for the characterization and analysis of all fabricated probes as well as all for the adducts formed throughout the thesis work. In this chapter, we have also explained some other useful methods such as calculation of limit of detection, association constant and determination of quantum yield,which were handy in order to study the fabricated sensors more accurately. The characterization of the chemosensorshave been performed thoroughly by elemental analysis, $^{1}$H-NMR, $^{13}$C-NMR, HRMS, IR while other photophysical as well as the spectraltechniques like UV-Vis spectrometry, fluorimetric techniques, lifetime decay study or time resolved photoluminescence study are also executed for studying their optical properties. Additionally, single crystal X-ray studies are carried out to determine the single crystal structure to get the additional structural information.

## 2.2. Reagents for synthesis

All the Solvents that were used for the synthesis and analysis of the sensors throughout my thesis have been purchased from Merck chemicals, India and used without further distillation process.DMSO-$d_6$ and $CDCl_3$ solvents for NMR spectroscopic studies have been bought from Sigma Aldrich and used in its current form. 2-Thiophene carbonic acid hydrazide, 4-phenylphenol, 4-Methyl-3-thiosemicarbazide, ethyl cyanoacetate, triphenyl amine, 2-benzooxazol-2-yl-phenol, 2-hydroxy-benzoic acid, o-phenylenediamine, 5-(Diethylamino)-2-hydroxybenzaldehyde, diethyl malonate, piperidine, acetic acid, Dimethylformamide, Phosphorus oxychloride, triphosgene andtetrabutylammonium cyanide were purchased from Sigma Aldrich chemicals, USA and used without further purification.Anhydrous sodium sulphate, potassium carbonate,calcium chloride, phosphoryl chloride, thionyl chloride, acetyl chloride, tri-n-butyl phosphate, acetic acid, hydrochloric acid, and other metal salts as well as some other toxic molecules used as competitive analytes are purchased from Merck chemicals, Germany. Silica gels and aluminum oxide (basic) are purchased from various commercial sources.

# 2.3. Several physio-chemical characterizations methods

Thorough characterization of the purified chemosensor is of great importance in molecular recognition. Individually all these techniques do not portray complete picture of the entities formed but collectively all the observation gives an imaging of the self-assembled entities. Thedifferent techniques are described thoroughly.

## 2.3.1. $^{1}$H-NMR Spectroscopy

To characterize the structure of a newly fabricated chemosensor, $^{1}$H as well as $^{13}$C NMR spectroscopies are the most useful analytical techniques. Nuclear magnetic resonance involves the interaction between an oscillating magnetic field of electromagnetic radiation and the magnetic energy of the hydrogen nucleus or some other type of nuclei, when these are placed in an external static magnetic field. Among the group of spectroscopic methods, the NMR spectroscopyuses the lowest irradiation energy for excitation. Herethe sample absorbs electromagnetic radiation in radio wave region. The absorption peaks absorbat different frequencies since it depends upon the type of proton or certain nuclei contained in the sample.

The technique is a nondestructive one and gives molar response which allows structure elucidation and quantification simultaneously. Hence this technique provides information about the chemical structure of the desired molecules.In this method the protons in an organic or inorganic molecule are revealed to a powerful field.[1] Under the influence of the external magnetic field the protons start precessing at different frequencies. Now these precessing protons are irradiated with steadily changing frequencies. When these precessing protons are exposed with steadily changing radio frequencies, protons undergo transition from low-energy parallel state to high-energy anti-parallel state. At a certain value of the field strength, the energy needed to spin the protons matches with the energy of the radiation and then absorption occurs with the occurrence of a signal. Thus, the spectrum obtained by this method is called nuclear magnetic resonance spectrum. In the NMR spectrum, applied field strengths for each set of protons is measured and their corresponding absorption peaks are plotted. The total number of signals at different applied field strengths is equal to the different sets of equivalent protons present in the molecule. The positionof each signal in the spectrum range helps us to know the nature of protons whether they are adjacent to someelectron attracting or electron releasing group.

When a molecule is positioned in a magnetic field, the electrons begin to circulate thereby introducing secondary magnetic fields. This rotation of electrons about the proton itself generates a field in such a way that the proton opposes the applied field. Here if the induced field opposes the applied field, then the proton is said to be shielded and the corresponding protons are said to be shifted to upfield region. While if the induced field reinforces the applied field, the proton is said to be deshielded and the protons shifted to the downfield region. Such shifts are known as chemical shifts. For determining chemical shifts of an assortment of protons in a molecule, the signal for tetramethyl silane (TMS) is taken as a reference. Clearly, the NMR signal for a particular proton in a molecule will appear at different field strengths comparedto a signal from TMS. Thus, this difference in the absorption position of the proton with respect to TMS signal is known as chemical shift. It is measured in equivalence frequency and expressed as δ value.

$$\delta = (\nu_{sample} - \nu_{TMS})/\text{operating frequency in per sec.}$$

(unit of numerator in hertz and denominator in megahertz)

The value of δ is expressed in perts per million (ppm). The solvent to be used should be free from protons so that it does not give absorption of its own in NMR spectrum. Conventionally deuterated solvents like $CDCl_3$ and DMSO-$D_6$ are used as deuterium is effectively NMR silent in the operating frequency range of proton NMR.[2]

In an NMR spectrum, various peaks observed represent equivalent sets of protons. The area of each peak gives information about the number of protons in each set present in the studied compound and this area under an NMR signal is directly proportional to the number of protons giving rise to signal. The splitting of a signal is owing to the different surroundings of the absorbing proton with respect to the nearby protons. Importantly the separation between the two adjacent peaks in a multiplet is usually constant and is called the J-coupling constant. The $^1$H-$^1$H and $^1$H-C couplingconstants are expressed in Hz.

NMR spectroscopy is a useful technique for the simpler aggregates by assigning the peaks in the $^1$H-NMR spectrum. For the large complexes, it is very difficult to characterize by NMR spectroscopy, as most of the protonspectrum is uninterpretable.Whereas the Characterization of simple molecular complex is possible from NMR titration. In case of NMR titration, inferences about the stability of the host-guest complex can be calculated by determining the association constant from analysis of the chemical shift values. Analysis of the chemical shift values gives the association constant and infers stability of the complex. There are

different methods to determine the exact stoichiometry of a sensor molecule. When the binding constant is large and exchange is fast, simple titration plot of chemical shift versus the ratio of guest to host suggests the stoichiometry of the complex. When binding constants is of broad range and dynamic exchange between the free host and the complex is fast on the NMR time scale, Job's method is usually adopted for the stoichiometry of the complex, when it is slow on the NMR time scale, the stoichiometry of the complex is apparent.[2]

Each and every $^{1}$H-NMR spectrum of all the synthesized chemosensors and other associated compounds were recorded on a Bruker 300 MHz and 400 MHz FT-NMR spectrometer of ~0.05 M solutions of the compounds in $CDCl_3$ or DMSO-$d_6$ solvent using TMSas an internal standard.

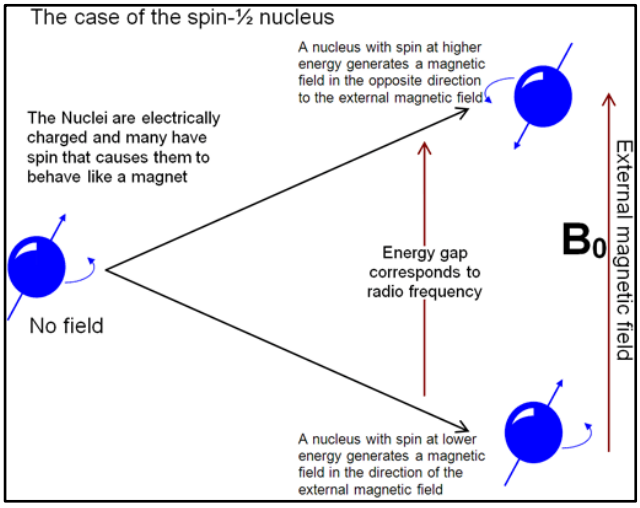


**Fig 2.1:** NMR spin energy levels under external magnetic field ($B_0$).

## 2.3.2. $^{13}$C-NMR Spectroscopy

As it is commonly known $^{13}$C is a comparatively new technique. There are noteworthy differences between the $^{1}$H and $^{13}$C spectra both in the form of recording as well as demonstration. The value of nuclear spin quantum number (I) for $C^{12}$ is equal to zero. Hence due to its non-magnetic nature it does not give rise to any NMR signal. On the other hand, $C^{13}$ has a spin quantum number value equal to ½ and it is NMR active. But its natural abundance is only 1.11%. Every $C^{13}$ resonance is spin coupled, not only to the directly attached proton but also to the protons which are two to four bonds away.Thus, the value of the coupling constants differsin accordance with the $^{13}$C and the proton consequently.

For all the organic molecules, the range of complete $C^{13}$ spectra is 0-200 ppm where TMS is the common internal reference used for $^{13}C$ NMR.

$^{13}C$ NMR spectra were recorded using a Bruker (AC) 300 MHz and 400 MHz FT-NMR spectrometer in $CDCl_3$ or DMSO-$d_6$ solvent using TMS as an internal standard.

### 2.3.3. High resolution mass spectrometry (HRMS) and Elemental analysis

HRMS is one of the most crucial analytical tool to analyze the structure of newly developed probes, in this case, newly fabricated chemosensors as well as chemodosimeters. This spectrometry offers the most accurate method for determining the molecular mass of the compound and its elemental composition. The molecular ion peak generated from HRMS spectra gives information about the molecular weight of the synthesized compound and thus it is comparable with the desired chemosensor. We can also comment about the structural composition of the synthesized molecule by recognizing mass fragments in the spectra.

In this technique, the sample molecules are bombarded with a beam of energetic electrons. Consequently, the molecules get ionized and broken up into numerous fragments. Some of them are positive ions. Each variety of an ion has a particular mass to charge ratio, i.e., m/z ratio. For most of the ions, the charge is one and thus m/z ratio is generally the molecular mass of the ion. The set of ions are scrutinized in such a way that a signal is obtained for each value of m/z. The intensity of each signal corresponds to the relative abundance of the fragment generating the signal. The largest peak in the spectrum is called the base peak and its intensity is taken as 100.

Similarly, elemental analysis is also proved to be a useful technique which indicates to the percentage presence of C, H and N in a compound. So here in this thesis allthe HRMS mass spectral data were recorded on Waters (Xevo G2 Q-TOF) mass spectrometer and elemental analysis was carried out in a 2400 Series-II CHN analyzer, Perkin Elmer, USA.

### 2.3.4. Infrared Spectroscopy (IR)

Infra-red spectrum is another potent method which gives ample amount of information about the structure of the synthesized probe. In ultraviolet spectrum we obtain moderately few peaks, but in IR technique, it offers a spectrum including a huge number of absorption bands from which a lot of information can be gathered about that particular structure. Upon absorption of infra-red radiation,it causes various bands such as stretching and bending with respect to one another. The

most significant infra-red region is observed from 2.5 μ to 15 μ in which molecularvibrations can be detected and measured. The absorption of IR radiations can be articulated eitherin terms of wavelength (λ) or in terms of wave number (ν).

Mainly, IR spectra of compounds are plotted as percentage transmittance against wave number. The correlation between wavelength and wave number is as follows:

Wave number =1/wavelength in cm

Where band intensity is either expressed in terms of absorbance (A) or transmittance (T).

$$A = \log_{10}(1/T)$$

When a molecule absorbs IR radiation,it causes excitation of molecule from a lower to the higher vibrational level. Here each vibrational level is connected with a number of strictly spaced rotational levels. All the bonds present in a molecule are not accomplished of absorbing infra-red energy but only those bonds will absorb in the IR region which are accompanied by a change in dipole moment. In that case such vibrational transitions accompanied by dipole moment change are called IR-active transitions and those compounds will be called IR-active compounds. Hence IR spectroscopy is also known as vibrational-rotational spectroscopy. All the IR datas recorded in this thesis weretaken on a RX-1 PerkinElmer spectrophotometer with samples prepared as KBr pellets.

### 2.3.5. UV-Vis absorption spectroscopy

The change in absorption spectra of the synthesized probes were meticulously studied after addition of specific analyte along with other coexisting analytesinto the solution of those probes. This study is of supreme importance as well as a common method in order to investigate the sensing properties of chemosensors.

The technique is often referred as Electronic spectroscopy sinceit deals with the promotion of electrons from the ground state to the higher energy level. For visible and ultra-violet spectrum, electronic excitations arise in the range between 200-800 nm and leads to the promotion of electrons to the higher energy molecular orbital. Here if the compound is absorbed in the visible range, it will appear colored to the human eyeand any change in the spectrum of such compound will result in the change of color. The wavelength of a particular radiation absorbed can be expressed in the form of frequency or energy.

In the UV-Vis plot or the absorption spectrum, the wavelength (nm)is taken in the x-axis and the absorbance (a.u) is taken in the y-axis as a function of the former. In the UV-Vis spectrum, we

observe a number of absorption bands. There are two well-known laws which explains the absorption changes by the molecules. These are:

(i) Lambert's law and (ii) Beer's law.

By combining these two laws, the Beer-Lambert law can be formulated as:

$$\mathbf{I(\nu) = I_0(\nu)10^{-\varepsilon(\nu)cl}}$$

Where $I_0(\nu)$ and $I(\nu)$ indicates the intensity of incident and transmitted light respectively at the frequency $\nu$, $\boldsymbol{\varepsilon}$ is the molar extinction coefficient at $\nu$ frequency which can be expressed in $L(liters)mol^{-1}cm^{-1}$, c is the concentration of solution in moles $litre^{-1}$ and l is the path length (cm) of the absorbing medium.

To measure the UV-Vis spectrum, a baseline of the solvent in which the probe is dissolved is recorded at first so that the contribution of the solventcan be eliminated from the baseline of the probe itself. This process is known as baseline correction. After baseline correction, the samples of desired concentration were prepared in quartz cuvette and the absorption spectrum measurement was carried out. Perkin Elmer Lambda 750 spectrophotometer was used to record all the electronic spectra reported in this thesis.

## 2.3.6. Fluorescence Spectroscopy

The emission spectral changes of the synthesized chemosensors were also studied along with the absorption spectrum to further gain knowledge about the sensing properties of sensors as well as to understand the sensing pattern of that particular probe.

The fundamentals of photoluminescence or fluorescence processes are explained by studying Jablonski diagram which illustrates a variety of processes that occur between absorption and emission of light. It explains the several molecular processes which occurs after the excitation of the molecule.[3] The Jablonski diagram is shown in Figure 2.2. The symbols $S_0$, $S_1$ and $S_2$ signify the singlet, ground, first and second electronic states respectively. At each of these electronicenergy levels, the fluorophores can exist in a number ofvibrational energy levels, represented as by 0, 1, 2, etc. The electronic transitions occur in about $10^{-15}$ sec thus the displacement of the nucleus is irrelevant. This is illustrated in Frank-Condon principle. At room temperature the excited vibrational levels of the fluorophore are not populated. As a result, absorption and emission take place mostly from molecules withthe lowest vibrational energy. Absorption of light by the fluorophore causes excitation to some highervibrational level of either $S_1$ or $S_2$from $S_0$. After that different kind of transitions takes place. when molecule jumps from

$S_2$ to $S_1$, it is known asinternal conversion. Emission from the $S_1$ to $S_0$ state is termed as fluorescence. Conversion of $S_1$ to $T_1$ is called intersystem crossing. Emission from the triplet ground state to singlet ground state is phrased as phosphorescence.[4] This transition is forbidden and as anoutcome, the rate constants for triplet emission are severalorders of magnitude smaller than those compared to fluorescence.

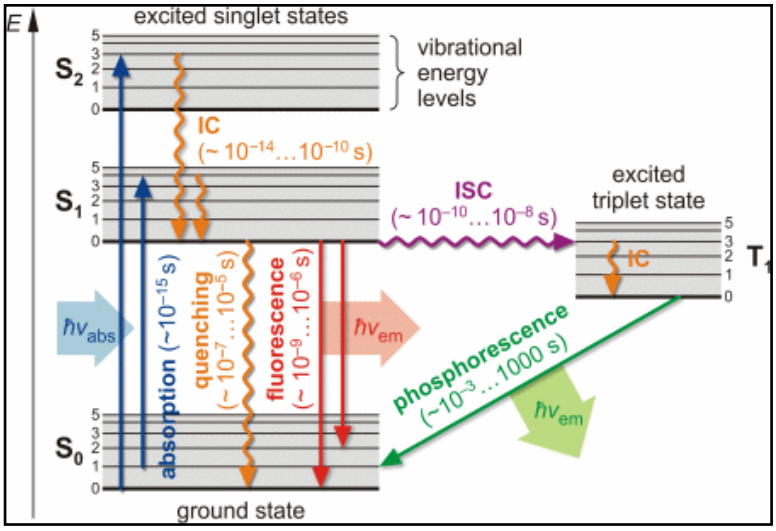


**Figure 2.2:** A schematic of Jablonski diagram showing the excitation and de-excitation processes involved in photoluminescence.

For a typical measurement, the samples of desired concentration of the probes were prepared in quartz cuvette and the emission spectra were recorded without any baseline correction as in photo-luminescence spectra the contribution from the solvent part is negligible. All the fluorescence spectral data were recorded with the aid of Shimadzu RF-6000 fluorescence spectrophotometer at room temperature (298 K), reported in this thesis.

## 2.3.7. Fluorescence lifetime measurement

Fluorescence lifetime of an excited state is the characteristic average time of a molecule that stay in the excited state before undergoing decay. In Fluorescence lifetime of an emission the decay curve plotted against time of a particular emission wavelength, after excitation at a particular wavelength. In general, a fluorescent molecule exhibits a single exponential decay and the relationship between their intensity and time can be expressed as:

$I(t) = I(0) \exp(-kt)$

Where, I(0) and I(t) represents the fluorescence intensity at the original stage (t = 0) and at a given time t, respectively; k is known as rate constant describing the fluorescence decay. Both radiative and non-radiative decays affect the rate constant, k.

A radiative decay rate constant is $k_r$ which is characterized by lifetime $\tau_r$ and a non-radiative decay rate constant is $k_{nr}$, characterized by lifetime $\tau_{nr}$. So, the equation of lifetime formulated as: $k = k_r + k_{nr} = 1/\tau_r + 1/\tau_{nr} = 1/\tau$ and $I(t) = I(0) \exp(-t/\tau)$

One can obtain the overall fluorescence lifetime $\tau$, by fitting a single exponential decay to the experimental fluorescence decay curve.

For a typical measurement, the samples of desired concentration were prepared in quartz cuvette and the emissionspectra were recorded. The lifetime measurement of synthesized probes is a valuable tool to study further about these chemosensors. All the lifetime decay measurement in this thesis work were carried out using a time-correlated single photon counting setup from Horiba Jobin Yvon. Then, the fluorescence decay data were placed on a Hamamatsu MCP photomultiplier (R3809) and analysed using EZ time software. The goodness of fit was evaluated by $\chi^2$ criterion and visual inspection of the residuals of the fitted function to the data. Generally, fluorescence shows lifetime of a few nanoseconds (ns), while spin-forbidden phosphorescence has a lifetime in the order of microsecond (μs) to millisecond (ms).

### 2.3.8. Single crystal X-ray diffraction technique

Single crystal X-ray diffraction is a non-destructive analytical technique which provides detailed information about the internal lattice of crystalline substances, including unit cell dimensions, bond-lengths, bond-angles and details of site-ordering. The technique includes single-crystal structure refinement, where the data generated from the X-ray analysis is interpreted and refined to obtain the crystal structure.

In 1912, Max von Lauediscovered that crystalline substances act as three-dimensional diffraction gratings for X-ray wavelengths similar to the spacing of planes in a crystal lattice. X-ray diffraction has been appeared as a familiarprocedure for the study of crystal structures and atomic spacing. Mainly, X-ray diffraction is based on constructive interference of monochromatic X-rays and a crystalline sample. These X-rays are generated from a cathode ray tube, where it filters to generate monochromatic radiation and directs it towards the sample compound. The interaction of the incident rays with the sample produces constructive interference when the conditions satisfy Bragg's Law ($n\lambda=2d\sin\theta$), where ‘λ’ denotes the

wavelength of electromagnetic radiation, 'θ' is the diffraction angle and 'd' is the lattice spacing in a crystalline sample. This law relates the wavelength of electromagnetic radiation to the diffraction angle and the lattice spacing in a crystalline sample. These diffracted X-rays are then detected, processed and counted. By changing the geometry of the incident rays, the orientation of the centered crystal and the detector, all possible diffraction directions of the lattice should be attained.[5] All diffraction methods are based on generation of X-rays in an X-ray tube. The angle between the incident and diffracted beams is a vital component of all diffraction.

Single crystals were mounted on glass fibers with epoxy cement as described in relevant thesis work. X-ray analysis was done using Apex II CCDC diffractometer with fine-focus sealed tube graphite-monochromated Mo $K_\alpha$ radiation ($\lambda$ = 0.71073 Å) at room temperature. The data collected was processed with SAINT and corrected for absorption using SADABS.[6] The structures were then solved by direct method using the program SHELXTL[7] and was refined by full-matrix least squares technique on F2 using anisotropic displacement parameters for all non-hydrogen atoms. While for all hydrogen atoms they were included in the refinement process as per the riding model. The Mercury 3.0 software was used for the analysis of bond distances and angles.

# 2.4. Theoretical calculation

In order to achieve more important information about a molecular assemble, quantum mechanical calculations have been performed. We have used density functional theory (DFT) for the theoretical calculations of theoptimized electronic structure. Full geometrical optimizations of some probes, chemodosimeters and their corresponding complex or adductswere performed using DFT method at B3LYP, level using 6-31-G(d) as basic set. Additionally, the vibrational frequency calculations on the optimized geometries were carried out to assure that optimized structural geometries represent the local minima and there were only positive eigen values. Based on B3LYP optimized geometries, the vertical electronic excitations were computed using TDDFT (time-dependent density functional theory) method in selected solvent using the conductor like polarizable continuum formalism (CPCM) model. All theoretical calculations were successfully performed with the Gaussian09 program package with the aid of the Gauss View visualization program.

# 2.5. Instrumentation segment of thespectroscopic techniques

## 2.5.1. NMR technique

The work function of Nuclear magnetic resonance spectrophotometer involves the use of a magnet, a radio-frequency, a detector and an amplifier. The detection system is employed to note down the energy that is being transferred from the radio-frequency beam to the nucleus. The sample to be examined is taken in a glass tube which is positioned between the pole faces of a magnet. Then a radio-frequency source is made to fall on the sample. It was accomplished by feeding energy into a coil placedaround the sample tube. A signal is then observed if the nuclei in the sample resonates with the source. Energy is driven through the source via nuclei to the detector coil. The output from the detector can be directed to a cathode ray oscillograph or to a strip of chart recorder after amplification.

The instrumentation technique is shown in Figure 2.3.

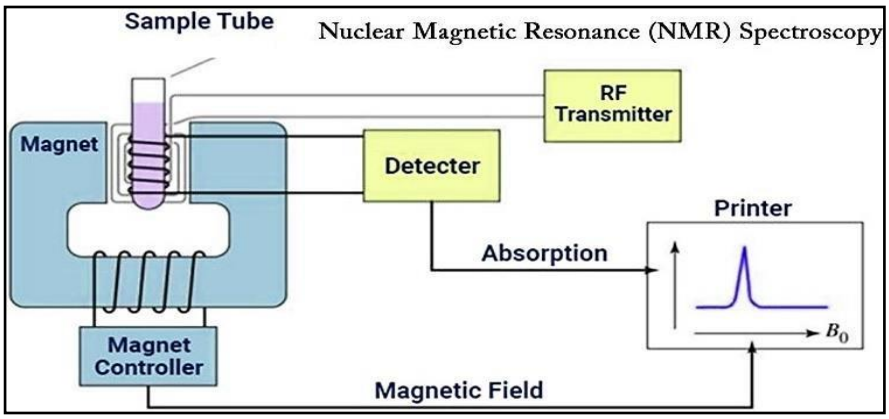


**Figure 2.3:** Schematic diagram of instrumentation of NMR spectroscopy.

## 2.5.2. HRMS technique

The mass instrument consists of three main parts:

**(a) Ion source.** The first and crucial step of achieving a mass spectrum is to ionize the sample compound. The common procedure used for the fabrication of ion in mass spectrometer is by the bombardment of electrons. The source used for bombarding electrons is from an electrically heated tungsten filament. A few milligram of the substance is produced as vapour in the source at an operating pressure of $10^{-6}$ mm. Then the vapour is permitted to pass through a slit into the

ion chamber. Here it is bombarded by a flow of electrons produced by a tungsten filament. Due to bombardment, the molecules generally lose one electron to form a parent ion radical. But if the energy of the bombarding electron is around 70 eV, additional energy is consumed in fragmenting the parent ion. This results in the formation of fragment ions or the daughter ions.

**(b) Mass analyser.** The positively charged ions generated in the ion chamber are then accelerated by pertaining an acceleration potential. Theses ions then go through the mass analyser. Here the fragmented ions are differentiated based on their m/z ratio.

**(c)Ion detector.** Finally, the ions which are separated by the mass analyser, are detected and measured electrically. The ions pass through the collecting slit one after the other and fall on the detector. The instrumentation technique is depicted in Figure 2.4.

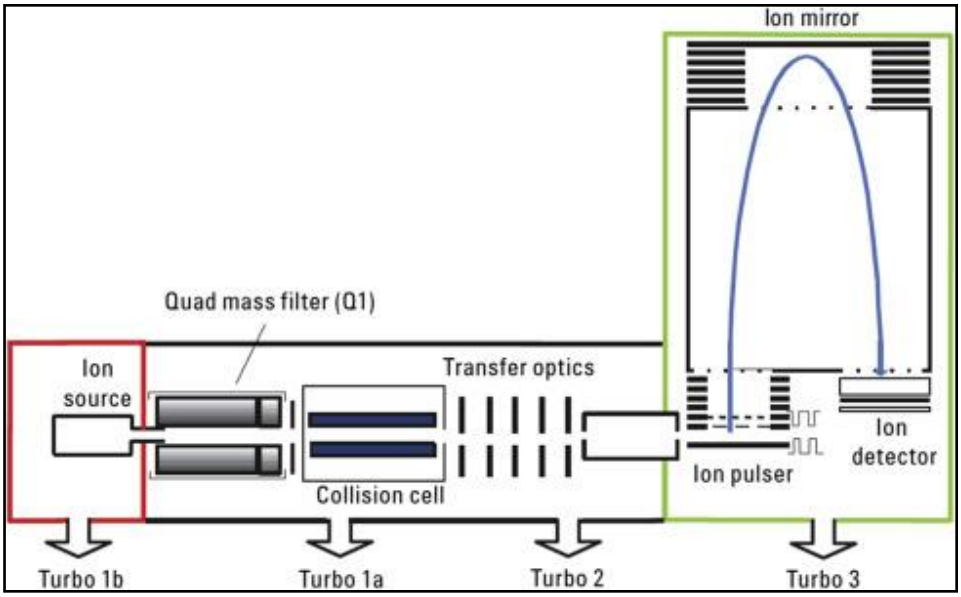


**Figure 2.4:** Schematic diagram of instrumentation of High-resolution mass spectrometry.

## 2.5.3. IR technique

The main source of Infra-red light for scanning the spectrum of an organic compound is Nernst glower.It consists of a rod containing sintered mixture of the oxides of Zirconium, Ytterium and Erbium. The rod is then electrically heated to 1500°C to produce Infra-red radiations.

Silicon carbide rod can alsobe electrically heated to produce Infra-red radiations. Optical prisms or gratings can be used to obtain monochromatic light. Glass or quartz cannot be used for prism

material since they absorb strongly through most of the IR-region. Sodium chloride or certain alkali metal halides are commonly used as cell containers or for prism materials as these are transparent to most of the IR region under consideration. Light from the source is split into two beams, where one of the beams is passed through the sample under examination and is called the sample beam and the other beam is called the reference beam. When the beam passes through the sample, it becomes less intense due to the absorption of certain frequencies. Now there will be a difference in the intensities of the two beams. Intensities of the bands can be recorded as a linear function T (transmittance) against the corresponding wave-number.

The instrumentation technique is illustrated in Figure 2.5.

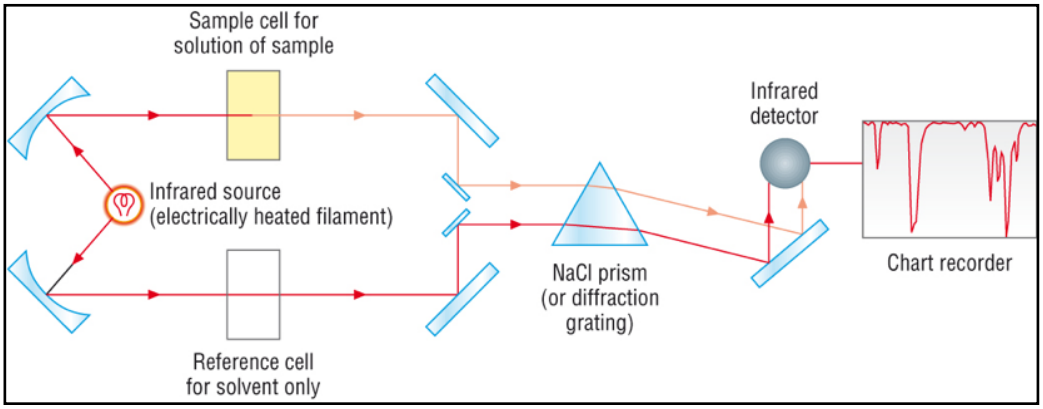


**Figure 2.5:** Schematic of instrumentation of IR spectroscopy.

## 2.5.4. UV-Vis technique

The role of a spectrophotometer is to detect the percentage transmittance of light radiation when light of certain intensity and frequency range is passed through a sample compound. Hence, the instrument compares the intensity of the transmitted light with that of the incident light.

The modern UV-Vis spectrometer consists of various key parts Viz. light source, monochromator, detector, amplifier, and the recording devices. The most suitable sources of light which cover the whole of the UV-Vis region aretungsten Filament lamp and hydrogen-deuterium discharge lamp. Most spectrophotometers are double beam instruments. The primary source of light is divided into two beams of equal intensity by a beam splitter. One of which passes though the sample and the other through the reference. A schematic presentation is given below in Figure 2.6. which shows the detailed instrumentation of an ultra-violet spectrophotometer.

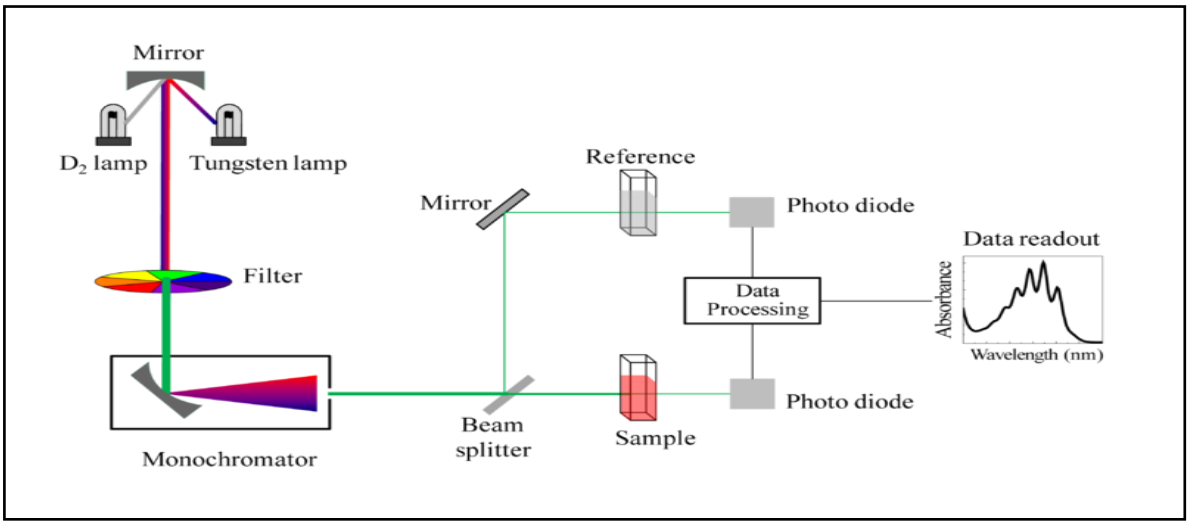


**Figure 2.6:** Schematic presentation of different parameters involved in absorption spectra measurement.

## 2.5.5. Fluorometry

A fluorimeter is a device that measures the intensity and its distribution throughout the wavelength range visible to human eye. After excitation by a certain wavelength of light, generally from UV region of the spectrum, the fluorophore undergoes radiative relaxation and emits visible light which is then detected, quantified, and represented digitally by a detector-computer assembly. Modern fluorometers can detect the emission from a fluorescent molecule in very minute concentrations.

The basic component of a fluorimeter comprises of an excitation source, an excitation monochromator, a cuvette, an emission monochromator, and a detector. Most commercial instruments use the right angle detector approach as it reduces the background noise. In normal instrumentation mode, the sample compound is excited with polarized light and the intensity of the emitted florescence by that compound is measured by a polarizer analyser. A schematic presentation is given below in Figure 2.7 which shows the detailed instrumentation.

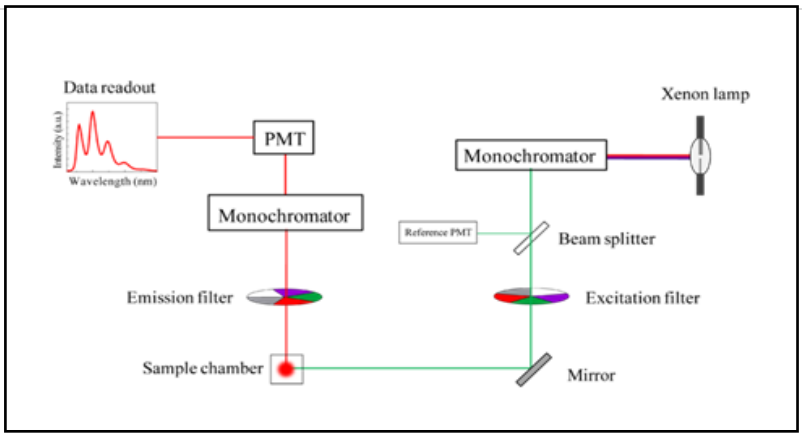


**Figure 2.7:** Schematic diagram of a fluorometer.

## 2.5.6. Fluorescence lifetime technique

The Fluorescence lifetime instruments record the life time of the excited state of a certain fluorophore over the course of many events. The principle of time-correlating single photon counting is a common technique for fluorescence lifetime measurement of a compound. Here it involves the detection of single photons and their arrival times in respect to a reference signal, typically the light source. TCSPC or time-correlating single photon counting is a statistical method requiring a high repetitive light source to accumulate enough photon that events for a required statistical data precision. The instrumentation of a TCSPC is shown in the following schematic diagram (Figure 2.8).

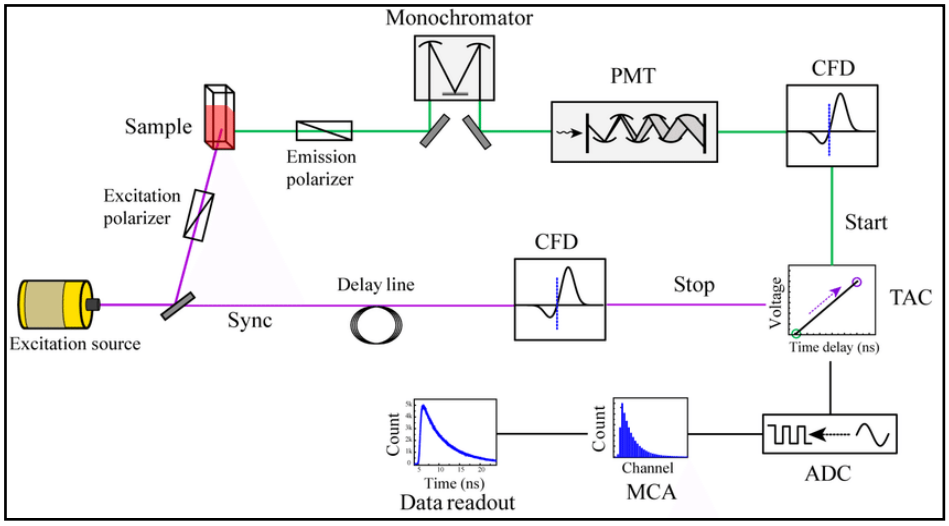


**Figure 2.8:** Schematic diagram of instrumentation of atime-correlated single photon counting

# 2.6. Some essential methods to study the chemosensors

## 2.6.1. Determination of limit of detection of synthesized chemosensors

The limit of detection or LOD value is a very important term in the field of chemosensors and chemodosimeters. The value of limit of detection determines the sensitivity of a chemosensor towards a specific analyte. The lower is the LOD value of a sensor, the greater will be its ability to sense the analyte in very minuscule concentrations. And in case of some toxic analytes, the low detection limit value is very much desirable as it indicates that to detect those toxic harmful analytes, one needs very little amount of those analytes which is environmentally friendly as well as important for human health also.

The limit of detection value was calculated based on the fluorescence titration of the developed probe. To determine the S/N ratio, the emission intensity of the probe itself was measured by 10 times and the standard deviation of blank measurements was determined. So throughout my thesis work the detection limit of the desired probes were determined from the following equation:

$DL = K \times Sb_1/S$

Where K = 2 or 3 (we take 3 in this case); $Sb_1$ is the standard deviation of the blank solution; S is the slope of the calibration curve.

## 2.6.2. Determination of binding constant of synthesized chemosensors

The association constant of a chemosensor is a parameter that actually indicates the stability of the adduct formed when the chemoensor bind with a particularcorresponding analytes. Binding constant ($K_a$) value was calculated from the emission intensity data according to the Benesi-Hildebrand equation where $K_a$ was calculated following the equation stated below.

$$1/(F-F_o) = 1/\{K_a(F_{min}–F_o)\ [M^{n+}]^x\} + 1/[F_{min}-F_o]$$

Here $F_0$, F and $F_{min}$ indicate the emission in absence of, at intermediate and at infinite concentration of metal ion respectively. $K_a$ is the binding constant and $[M_n]$ is the concentration of the analyte (in maximum case, the metal with which the probe binds to). From the plot of 1/

$(F-F_0)$ against $[M^{n+}]$ for sensor, the value of $K_a$ has been determined from the ratio of intercept and slope of Benesi-Hildebrand plot.

### 2.6.3. Fluorescence quantum yield measurement

Photoluminescence quantum yield of luminescent particles are defined as the efficiency of converting absorbing light into emitted light, i.e.,

Q.Y = no. of emitted photons / no. of absorbed photons

Quantum yield is also termed as quantum efficiency (QE) or fluorescence efficiency. Quantum yieldvalue can vary in between 0 to 1 and higher the yield value indicates brighter is the emission. The quantum yield value of a sample is measured by comparing it with a reference dye with known quantum yield, or measuring it an absolute quantum yield. At first the absorbance of both the sample and the reference dye were recorded. After that the emission spectra were recorded using the maximal excitation wavelengths and then the integrated areas of the spectra were calculated further. The quantum yields were then measured by using the following equation:

$$\Phi X = \Phi S \times \left(\frac{I_x}{I_s}\right) \times \left(\frac{A_s}{A_x}\right) \times \left(\frac{n_x}{n_s}\right)^2$$

Where, x & s stands for the unknown and standard solution respectively, φ is the quantum yield, I is the integrated area under the fluorescence spectra, A is the absorbance and n is the refractive index of the solvent.

According to the absorbance peak position the reference dye was selected for each case throughout all the thesis work. All the absorption and fluorescence spectra were recorded using Perkin Elmer Lambda 750 spectrophotometer and Shimadzu RF-6000 fluorescence spectrophotometer respectively.

# 2.7. References


1. B. Diehl, NMR Spectroscopy in Pharmaceutical Analysis, 2008, **Chapter 1**, 1.
2. Marc Loudon, Jim Parise, Organic Chemistry, 7th Ed., 2021, **Chapter 13**, 611.
3. A. Jablonski, *Z. Phys*., 1935, **94**, 38.
4. J. R. Lakowicz, *Plenum Press*, 1983, 496.
5. C. P. Gomez and R. A. Jacobson,John Wiley & Sons, Inc., 2012.
6. Bruker. APEX2, SAINT and SADABS. Bruker AXS Inc., Madison, Winconsin, USA. 2009.
7. Sheldrick G. M. A short history of SHELX. *ActaCryst.* 2008, **A64**, 112.

# Chapter 3

# A new “turn-on” molecular switch for idiosyncratic detection of $Al^{3+}$ ion along with its application in live cell imaging

# A new "turn-on" molecular switch for idiosyncratic detection of $Al^{3+}$ ion along with its application in live cell imaging

## Abstract

A highly sensitive, reversible, reusable and fluorogenic ''turn-on'' probe (HBTC) is fabricated for the sole detection of $Al^{3+}$. On incremental addition of $Al^{3+}$ in a solution of HBTC in ACN:$H_2O$ (4:1), a sharp ''turn-on'' emission enhancement is observed at 480 nm. The reversibility of the probe (HBTC) was displayed on the addition of $F^-$ solution. The detection limit is found to be of the order of 10^-9 (M) which suggests that HBTC can detect $Al^{3+}$ at a very minute level. The mechanism for $Al^{3+}$ detection in ACN:$H_2O$ (4:1) is attributed to forbidding C=N isomerization and ESIPT process simultaneously turning on the chelation-enhanced fluorescence process. The reusability and real-time application of the probe are also studied. Bioimaging study reveals that HBTC can detect $Al^{3+}$ in human breast cancer cells (MDA-MB-231). Electronic structure of the probe is explained by density functional theory.

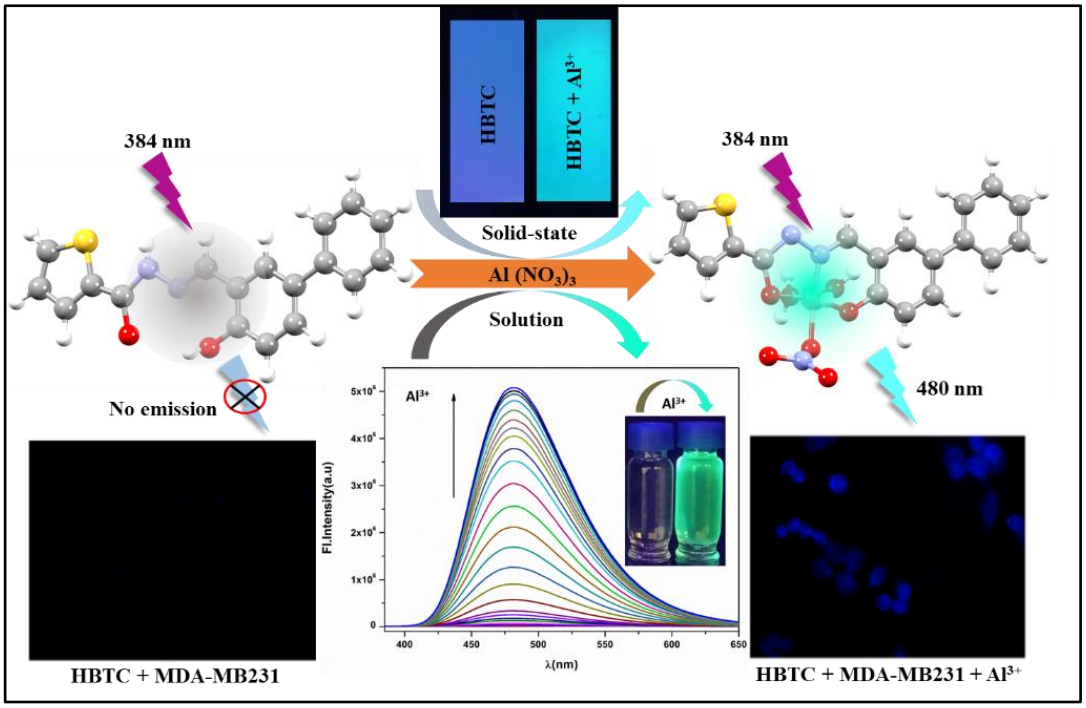

# 3.1. Introduction

Nowadays undue use of ionic pollutants in industry and the farming sector has become a menace to the environment.[1,2] Hence rapid and accurate detection of those ions has become a promising part in the research field in modern times. It is well-known that aluminum is the most abundant metallic element in earth's crust. And it has become an integrated part of daily lifestyle such as in drinking water supplies, utensils, packaging of foods, powder, cosmetic products, processed dairy products, cookware, bleached flour, component of medicine, medicine storage containers and manufacturing of cars.[3-7] The WHO(World Health Organization) stated that the average consumption of $Al^{3+}$ in the human body through several ways is about 3-10 mg per kg per day and the maximum recommended limit Al-contaminated water is 7.42 mM.[8-10] Although it has negative effects on both biological and environment systems, it is extensively used on a daily basis. The central nervous system is deeply affected by overexposure of Al.[11] Abnormal concentration of Al in the human body is related to many neurological disorders including Alzheimer's disease, Parkinson's disease and dementia.[12-14] On the other hand, regular intake of aluminium beyond permissible limits causes bone disease, damage in the gastrointestinal tract, encephalopathy, microcytic hypochromicanaemia, myopathy, bone softening, impaired lung function, fibrosis and chronic renal failure.[15-18] Therefore, it is imperative to develop probes that can detect and track aluminium ions with high sensitivity using minimal resources and under biological conditions. Among different sensing tools for detection of such kinds of environmental hazardous metal, fluorescence-based chemosensors are considered to be efficient for specifically detecting target analytes.[19] Different mechanisms like excited state intra-/intermolecular proton transfer (ESIPT), chelation enhanced fluorescence (CHEF), metal-ligand charge transfer, photoinduced electron/energy transfer, fluorescence resonance energy transfer, intramolecular charge transfer, and –C=N– isomerization are considered to be the reason for chemosensingprocesses.[20,21] A strong oxidizing site is preferred for the CHEF process, through which a radiative process gets turn on.[22] Comparing with different transition metal ions, chemosensors detecting solely $Al^{3+}$ are limited, due to poor coordination power, strong hydration enthalpy and lack of spectroscopic characteristics.[23,24]Being a hard acid, $Al^{3+}$ always prefers to bind hard centers like N and O donor sites. Schiff bases possess excellent coordinating capabilities, showing different biological activities and have potential analytical application.[25,26]Hence, development of probes with such binding sites causing metal-ligand

CHEF is an interesting approach due to a fluorescence ‘‘turn-on’’ mechanism on interaction with a guest.

## 3.2. Prior works

Recently in 2021, Singh et al. reported a silatrane-based Schiff base-functionalized probe which can detect $Al^{3+}$ ions and exhibits a limit of detection (LOD) value of 10^-7 (M) while ahydrazide-based ‘‘turn-on’’ switch was designed by Aydin et al. to recognise $Al^{3+}$ ion only which showed a LOD value of 6.47 nM.[27,28] Das et al. reported a pyridine-pyrazolehydrazide-based fluorescent probe for solely detecting aluminium ion with a detection limit of 4.78 mM, while in 2019, Liu et al. reported a Schiff base fluorescent ‘‘off-on-off’’ switch to detect $Al^{3+}$ with a limit of detection of 10^-8 M.[29,30]

## 3.3. Present work

Herein, we have designed and synthesized a simple biocompatible biphenyl-thiophene-based framework with high yield, which can solely detect $Al^{3+}$ in ACN/$H_2O$ (4/1 v/v, 10 mM HEPES buffer, pH = 7.2). Fluorescence study, ultraviolet-visible (UV-Vis) absorption, time-resolved fluorescence experiments and density functional theory (DFT) calculations were carried out. The biphenyl-thiophene-based probe with its hydroxyl group, imine nitrogen and carbonyl group of carbazide createsa felicitous cavity for $Al^{3+}$ to bind and ‘‘turn on’’ the CHEF process. The formation of the probe is established by $^{1}$H-NMR, $^{13}$C-NMR, HRMS and FT-IR analyses whereas the formation of adduct is proved by TRPL study, $^{1}$H-NMR, HRMS and DFT calculation. On the other hand, practical application like cell imaging was investigated, and paper strip study and reusability study were also performed.

## 3.4. Results and discussions

### 3.4.1. Design and synthesis of the probe HBTC

The probe (HBTC) was synthesized following a very simple route. The formylation of 4-phenylphenol to obtain 4-hydroxy-[1,10-biphenyl]-3-carbaldehyde was performed according to are ported method.[35] The probe HBTC was then synthesized by reflux condensation of the aldehyde and 2-thiophenecarbonicacid hydrazide in ethanol (Scheme 3.1). Formation of the

desired probe was confirmed by $^{1}$H-NMR, $^{13}$C-NMR, mass spectral, IR and elemental analyses (Fig. A3.1-A3.4, Appendix).

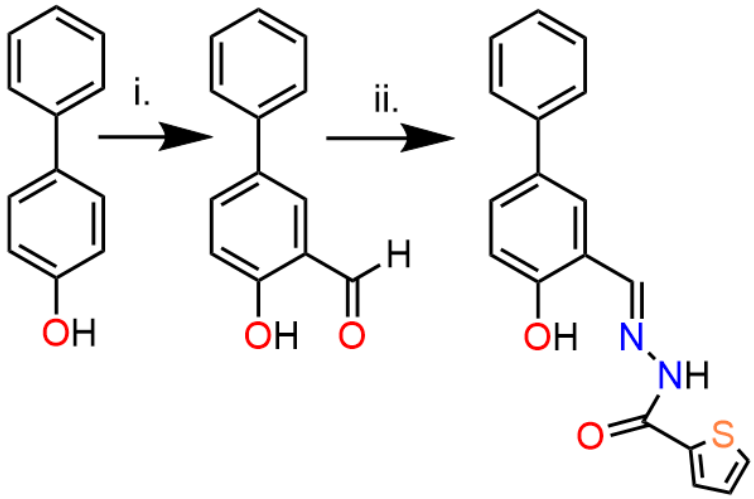


**Scheme 3.1:** Synthesis of the probe (HBTC). Reagents and conditions: (i) TFA, hexamine, 90-100 °C, reflux, 6 h; (ii) 2-thiophenecarbonic acid hydrazide, reflux, 8 h.

### 3.4.2. $^{1}$H NMR and HRMS analysis of HBTC

We studied $^{1}$H NMR titration of the probe (HBTC) upon addition of 1equivalent of $Al^{3+}$ in DMSO-$d_6$ solvent. From the NMR data, it was observed that the -OH peak arises at δ 12.21 ppm and all the aromatic protons are observed in the expected region of 7.02-8.70 ppm. (See appendix). We have also studied the HRMS of HBTC. The HRMS of HBTC shows a peak at m/z 345.0211, probably for $[HBTC + Na]^{+}$.

### 3.4.3. $Al^{3+}$ sensing studies of HBTC using UV-Vis spectroscopy

The UV-Vis spectrum of the HBTC probe exhibits an absorption band at 345 nm in ACN/$H_2O$ (4/1 v/v, 10 mM HEPES buffer, pH = 7.2). On gradual addition of $Al^{3+}$ (40 μM) to the probe solution (20 μM), the absorption band at345 nm disappears along with the formation of a low-energy moderately intense band at 384 nm with an isosbestic point at364 nm (Fig.3.1). UV-Vis spectra of HBTC were also obtained in the presence of other metal ions, i.e., $Ca^{2+}$, $Mg^{2+}$, $Mn^{2+}$, $Fe^{3+}$, $Cr^{3+}$, $Zn^{2+}$, $Co^{2+}$, $Ni^{2+}$, $Cu^{2+}$, $Pb^{2+}$, $Cd^{2+}$ and $Hg^{2+}$, but they do not show any significant changes in the spectral pattern (Fig. 3.1).

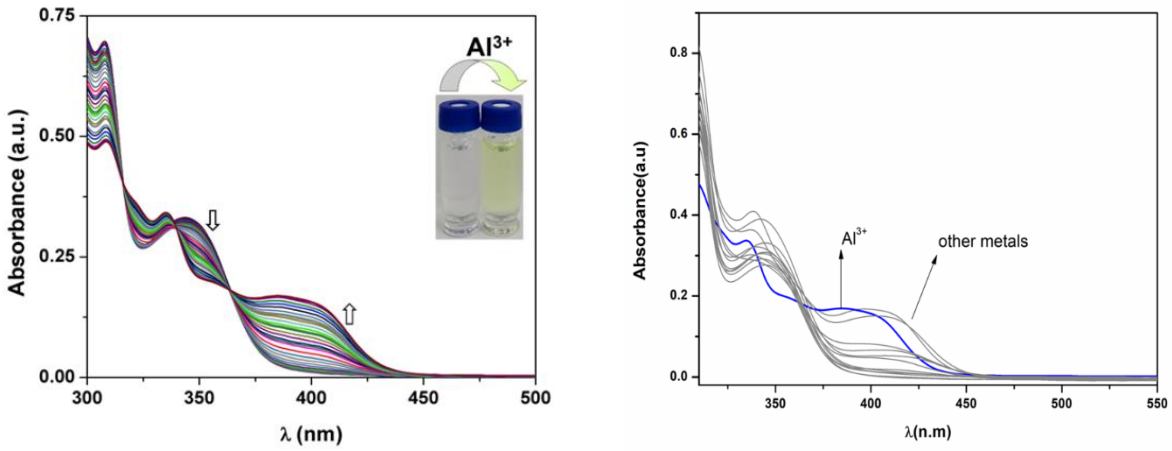


**Figure 3.1:** Change of absorption spectra of HBTC (20 µM) upon gradual addition of $Al^{3+}$ (40 µM). Inset: Photograph shows the visible color change of HBTC before and after addition of $Al^{3+}$ (40 µM) (left side) and 40 µM various metal ions i.e. $Ca^{2+}$, $Mg^{2+}$, $Al^{3+}$, $Mn^{2+}$, $Fe^{3+}$, $Cr^{3+}$, $Co^{2+}$, $Ni^{2+}$, $Cu^{2+}$, $Zn^{2+}$, $Pb^{2+}$, $Cd^{2+}$ and $Hg^{2+}$ in ACN/$H_2O$ (4/1, v/v, pH = 7.2) solution (right side).

### 3.4.4. $Al^{3+}$ sensing studies of HBTC using emission spectroscopy

The emission spectrum of HBTC was recorded in ACN/$H_2O$ solvent (4/1 v/v, 10 mM HEPES buffer, pH = 7.2). The change in emission intensity of HBTC was monitored with the gradual addition of $Al^{3+}$ (40 µM). Free HBTC probe exhibits very low emission intensity at 480 nm upon excitation at 384 nm. On subsequent addition of $Al^{3+}$ solution (40 µM) to HBTC solution (20 µM) in ACN/$H_2O$ solvent (4/1 v/v, 10 mM HEPES buffer, pH = 7.2), the emission intensity is significantly increased at 480 nm with a high emission quantum yield ($\phi$ = 0.196) (Fig. 3.2). The increase of emission intensity is due to the formation of HBTC-$Al^{3+}$ complex, with inhibition (turn-off) of the ESIPT process and ‘‘turn-on’’ of the CHEF effect. Thus, the increase in the emission property corresponds to an ‘‘off-on’’ type molecular switch.

.

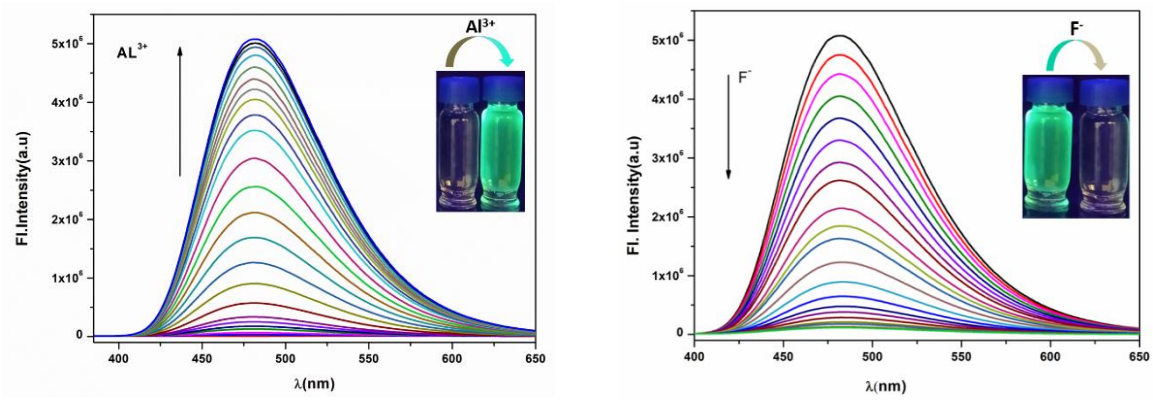


**Figure 3.2:** Change in emission spectra of of HBTC (20 μM) upon gradual addition of $Al^{3+}$ (40 μM) in ACN/$H_2O$ (4/1 v/v, pH = 7.2) solution. Inset: Visual effect of addition of $Al^{3+}$ to HBTC under UV light. $\lambda_{ex}$ = 384 nm (left side) and change in emission spectrum of HBTC-$Al^{3+}$ complex (20 μM) upon gradual addition of $F^-$ (40 μM) in ACN/$H_2O$ (4/1, v/v, pH = 7.2) solution. Inset: The visual effect of addition of $F^-$ to HBTC-$Al^{3+}$ solution under UV light. $\lambda_{ex}$ = 384 nm (right side).

Furthermore, on addition of $F^-$ to HBTC-$Al^{3+}$ solution (20 μM) (mixture of HBTC and $Al^{3+}$ solution in 4:1 ACN/$H_2O$ solvent), we noticed the emission intensity reverts to that of the free probe at 480 nm, suggesting HBTC as a reversible probe. The formation of free receptor and $AlF_3$ compound is thereason for the gradual decrease of emission intensity (Fig. 3.2). Thus, HBTC behaves as a reversible chemosensor towards $Al^{3+}$.

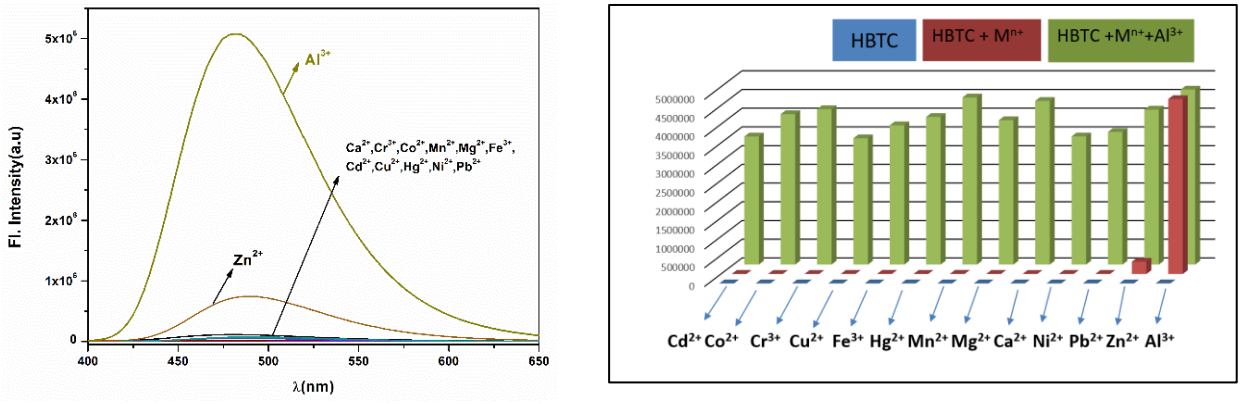


**Figure 3.3:** Change in emission spectrum of HBTC (20 μM) upon addition of different cations (40 μM) in ACN/$H_2O$ (4/1, v/v, pH = 7.2) solution, $\lambda_{ex}$ = 384 nm (left side) and change in emission intensity upon addition of various metals (40 μM) in ACN:$H_2O$ (4:1, v/v) (pH = 7.2).HBTC (blue bars), HBTC-other metals (brown bars), HBTC-$Al^{3+}$ in presence of other metals (green bars).

The sensing experiment was also performed in ACN/$H_2O$ (1/1 v/v) solution (20 μM), but this composition of solvent is not as sensitive as ACN/$H_2O$ (4/1 v/v); hence we have optimized the acetonitrile/water ratio and conducted all spectroscopic studies in ACN/$H_2O$ (4/1 v/v). Furthermore, the emission is almost unaltered in the presence of other metal ions (40 μM) such as $Cr^{3+}$, $Co^{2+}$, $Mn^{2+}$, $Fe^{3+}$, $Mg^{2+}$, $Cd^{2+}$, $Cu^{2+}$, $Hg^{2+}$, $Ni^{2+}$, $Ca^{2+}$ and $Pb^{2+}$ (Fig. 3.3). Only $Zn^{2+}$ ion shows a slight increase in emission intensity among these metal ions.

An efficient chemosensor is a one which can detect its guest selectively and efficiently within very minute level in presence of other interfering guest. Hence competitive study is an important method to examine whether the presence of other metal ions interfere in the detection of the target cation. For this reason, sensing capability for HBTC was studied in presence of other competing metal ions such as $Ca^{2+}$, $Cr^{3+}$, $Co^{2+}$, $Mn^{2+}$, $Fe^{3+}$, $Mg^{2+}$, $Cd^{2+}$, $Cu^{2+}$, $Hg^{2+}$, $Ni^{2+}$, $Zn^{2+}$ and $Pb^{2+}$ to exhibit the distinct sensitivity towards $Al^{3+}$. Thus, the experiment result reveals that competitive metal ions do not interfere significantly towards the sole detection of $Al^{3+}$ except $Zn^{2+}$ (Fig.3.3).

### 3.4.5. Binding studies of HBTC with $Al^{3+}$

Now to understand the stoichiometry of complex formation, Job's plot analysis was carried out which reveals 1: 1 complexation for $Al^{3+}$ ion with the probe HBTC (Fig. A3.5, Appendix), as the maximum occurs at 0.5 mole fraction. From Benesi-Hildebrandplot, the association constant for HBTC with $Al^{3+}$ was calculated by using fluorescence titration data and it was found to be $3\times 10^4$ $M^{-1}$ (Fig. 3.4). For quantitative study, the change in fluorescence intensity of HBTC at 480 nm with the increase of $Al^{3+}$ concentration was plotted and a linear curve observed (Fig. 3.4). Hence HBTC can be used for quantitative detection in the selected concentration range. The LOD of HBTC towards $Al^{3+}$ detection is calculated from the emissionspectral change using the equation LOD = K×SD/S, where SD stands for standard deviation of blank probe solution, S is the slope of a linear calibration curve and K = 2 or 3 (we take 3 in this case). The limit of detection is found to be $(8.74 \pm 0.36) \times 10^{-9}$ (M) for $Al^{3+}$ detection (Fig. 3.4). Hence, it may be concluded that HBTC is able to detect $Al^{3+}$ even at a very minute level. To understand the efficiency of HBTC, the LOD values and testing media used for some reported chemosensors for $Al^{3+}$ are compared in (Table A3.4, Appendix).

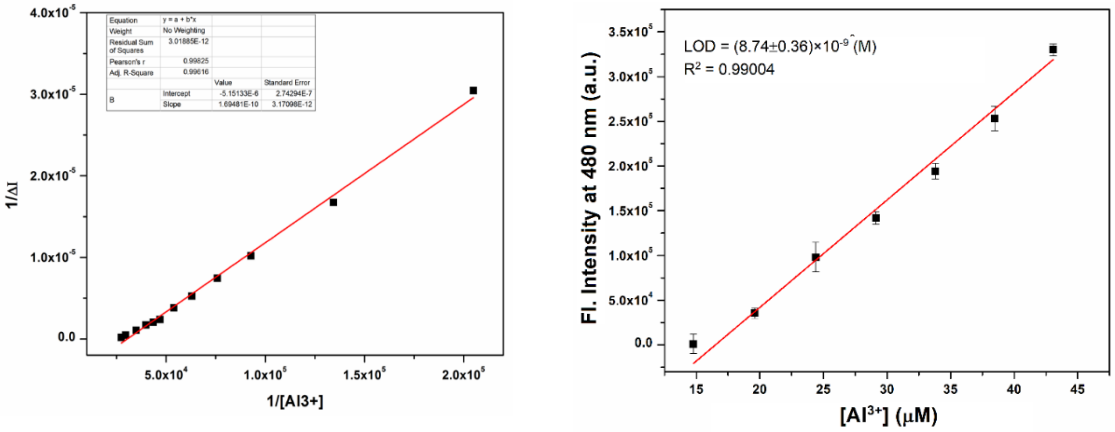


**Figure 3.4:** Benesi-Hildebrand plot from fluorescence titration data of HBTC (20 μM) with $Al^{3+}$(left side) and Linear response curve of HBTC at 480 nm depending on the $Al^{3+}$ concentration (right side).

## 3.4.6. Fluorescence lifetime decay studies of HBTC with $Al^{3+}$

For better understanding of the excited state property of free HBTC and HBTC-$Al^{3+}$ complex, we performed nanosecondtime-resolved fluorescence study. The radiative rate constant ($k_r$) and the non-radiative rate constant ($k_{nr}$) of HBTC, HBTC-$Al^{3+}$ and HBTC-$Al^{3+}$-$F^-$ species were calculated according to the equation $\tau^{-1} = k_r + k_{nr}$, where $k_r = \phi_f/\tau$ (Table A3.1, Appendix). Fluorescence lifetime decay plot is fitted according to bi- andmono-exponential functions for HBTC, HBTC-$Al^{3+}$ and HBTC-$Al^{3+}$-$F^-$ with acceptable $\chi^2$ values (Fig. 3.5). We observed that HBTC has a very low fluorescence lifetime in acetonitrile/$H_2O$ (4:1, v/v) but after complexation with $Al^{3+}$ there is an increase in the lifetime value. For HBTC, $\tau$ = 1.42 ns ($\chi^2$ = 1.08) while for HBTC-$Al^{3+}$ it increases to $\tau$ = 5.14 ns ($\chi^2$ = 1.01). After sequential addition of $F^-$to HBTC-$Al^{3+}$, lifetime decreases to t = 2.31 ns ($\chi^2$ = 0.96) which is nearly the free receptor lifetime value. The increase in radiative constant value and the decrease in non-radiative constant (Table A3.1, Appendix) for the complex could be attributed to rigidity gain, thus resulting in a "turn on" of the CHEF effect and inhibition of the ESIPT effect.[32,33] The HBTC-$Al^{3+}$ complex resulting in the CHEF effect could be attributed to enhancement in lifetime, while after addition of $F^-$ it dissociates to give free probe and $AlF_3$ resulting in a decrease of lifetime to 2.31 ns.

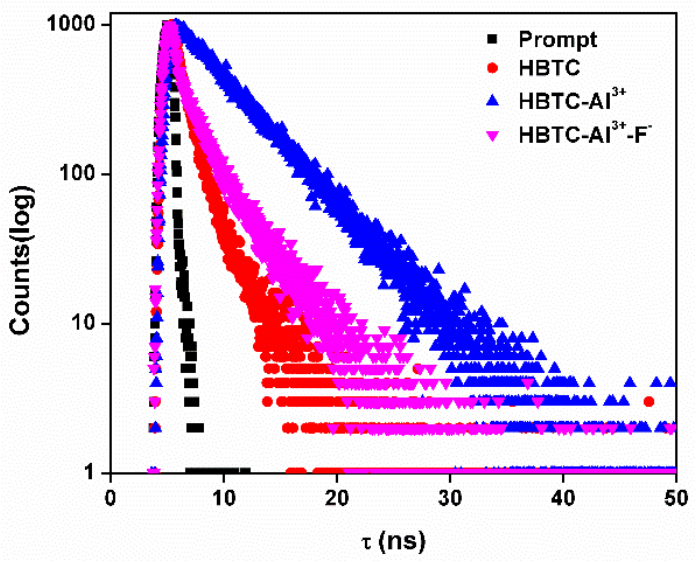


**Figure 3.5:** Time-resolved fluorescence decay of HBTC (●●●), HBTC-$Al^{3+}$ (▲▲▲), HBTC-$Al^{3+}$-$F^-$ (▼▼▼).

## 3.4.7. Reusability study

To increase their application in practice, chemosensors must have two properties: reusability and reversibility. So, in the case of HBTC a reversibility experiment was carried out in ACN/$H_2O$ (4:1, v/v) medium followed by alternate addition of $Al^{3+}$ and $F^-$ ions. We observed that with addition of 40 µM of $Al^{3+}$ to 20 µM HBTC, it gives a turn-on emission; with further addition of $F^-$ ion we observed a decrease in fluorescence intensity for HBTC as it removes $Al^{3+}$ from the solution, leading to free HBTC (Fig. 3.6). On further sequential addition of $Al^{3+}$ and $F^-$, we observed ‘‘turn-on’’ and ‘‘turn-off’’ emission indicating the formation of HBTC-$Al^{3+}$ complex and free HBTC. After every cycle we observed a decrease in fluorescence intensity for HBTC-$Al^{3+}$, which is attributed to the presence of excess $F^-$ in solution interfering in the complex formation. Hence the cycling demonstrates that HBTC can be used for practical determination of $Al^{3+}$ in real samples with high proficiency.[34]

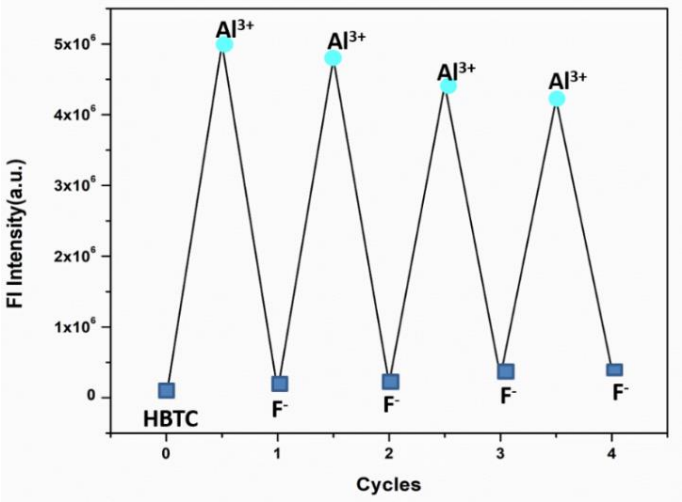


**Figure 3.6:** Reversibility pattern of the fluorescence profile at 480 nm ($\lambda_{ex}$= 384 nm) upon repetitive addition of $Al^{3+}$ and $F^-$.

## 3.4.8. Effect of pH

To explore the pH dependence of HBTC emission, we assessed its sensitivity in the absence and presence of $Al^{3+}$. The experiment is carried out in ACN/$H_2O$ (4:1, v/v) in the pH range 2.0-12.0, where solutions of probe with $Al^{3+}$ were prepared separately. We found that emission intensity for the free receptor solution remains almost unchanged with the variation of pH (Fig. 3.7). For HBTC-$Al^{3+}$ solution it is observed that maximum emission occurs near pH 7.0. On further increase in pH, we noticed a decrease in the emission for HBTC-$Al^{3+}$ due to removal of $Al^{3+}$ as its hydroxide, generating free probe.[31] Thus we can conclude that HBTC can be used for efficient detection of $Al^{3+}$ at physiological pH (7.2).

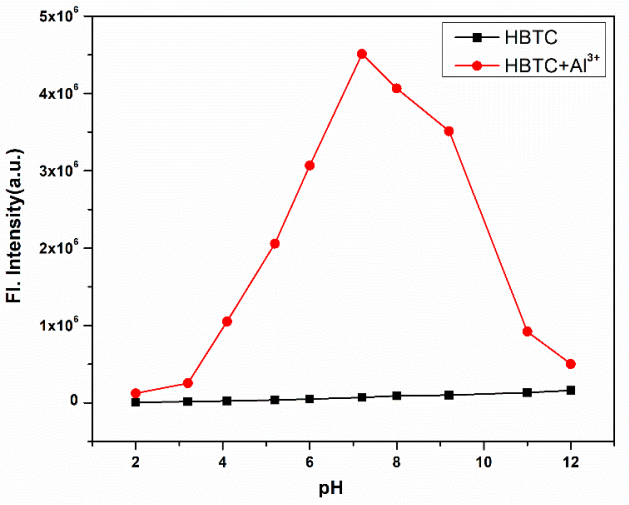


**Figure 3.7:** Fluorescence response of HBTC (-■-■-) and HBTC-$Al^{3+}$ (-●-●-) as a function of pH in ACN/$H_2O$ (4/1, v/v), pH is adjusted by using aqueous solutions of 1 M HCl or 1 M NaOH.

## 3.4.9. Time course of sensing

An instant sensing probe is necessary for real-time application. At different concentrations of $Al^{3+}$ (5 µM, 10 µM, 15 µM) the fluorescence intensity was measured with different time intervals. We observed that the present HBTC probe can detect $Al^{3+}$within 15-20 seconds after addition, but 50% of the reaction is completed within 10 seconds of $Al^{3+}$ addition (Fig. 3.8). After 20 seconds of addition no significant change in fluorescence intensity is observed, which indicates completion of reaction. Thus, HBTC is found to be a reliable probe for the detection of $Al^{3+}$ in a short time frame.

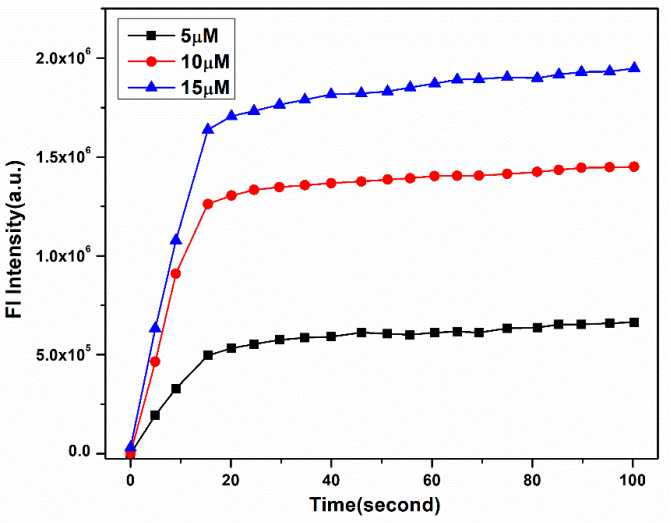


**Figure 3.8:** Fluorescence response of HBTC (20 µM) with different concentrations of $Al^{3+}$ (5-15 µM) at different times in ACN/$H_2O$ (4/1, v/v, pH = 7.2).

### 3.4.10. Probable sensing mechanism of HBTC

ESIPT and/or C=N isomerization are the two important factors responsible for the weak emission property of HBTC (Fig. 3.10). When HBTC coordinates with $Al^{3+}$, the ESIPT process is prohibited and the CHEF effect gets "turned on" which is responsible for the fluorescence enhancement. Also, due to the free rotation in the imine part (C=N) of HBTC, it can take both cis and trans conformations thereby quenching fluorescence intensity in the free form (Fig. 3.10). After binding with $Al^{3+}$ the rotation around the C=N bond gets prohibited; thus, the rigidity in the structure gets enhanced and hence we see an increase in fluorescence emission of HBTC.

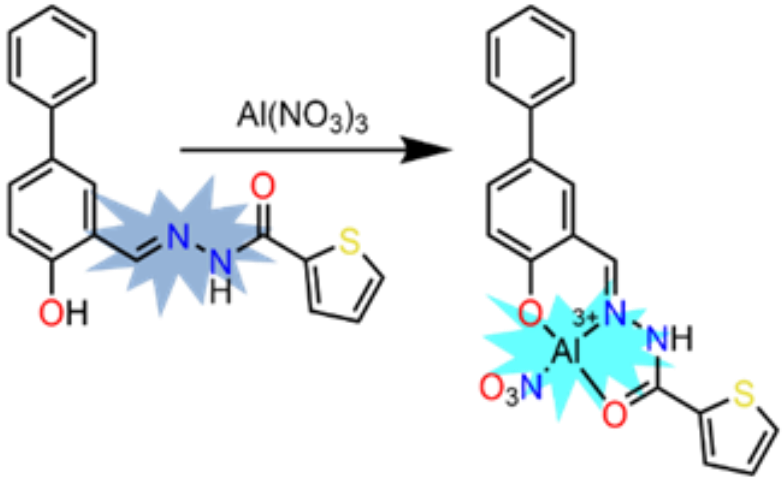


**Figure 3.9:** Probable binding mode of HBTC with $Al^{3+}$.

The phenolic -OH proton present in HBTC is the reason for ESIPT. In the presence of $Al^{3+}$ the -OH proton gets dissociated due to coordination with $Al^{3+}$ and thus the ESIPT process is inhibited.

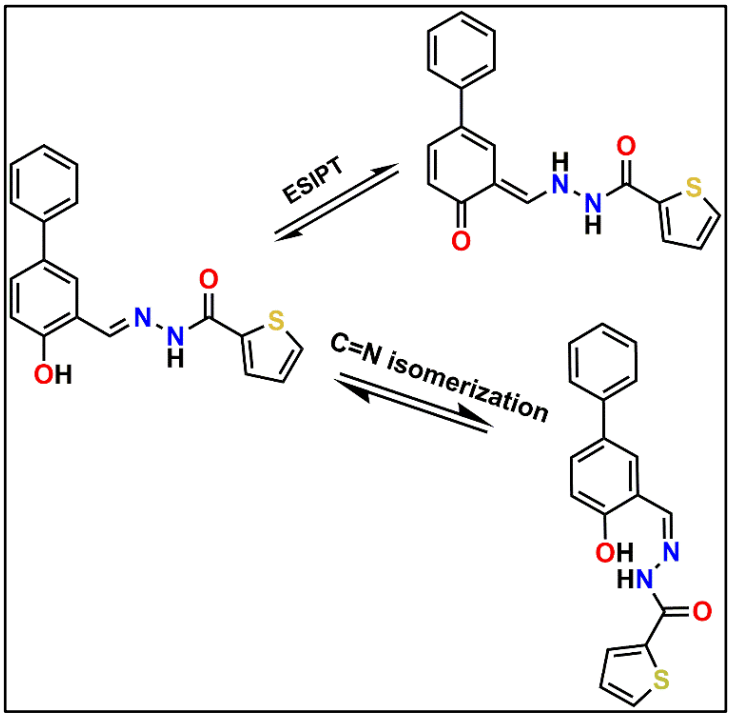


**Figure 3.10:** Tautomers and isomers of HBTC.

The dissociation of -OH proton is further confirmed by the disappearance of -OH proton signal in the $^{1}$H-NMR spectra of HBTC in the presence of $Al^{3+}$ (Fig. 3.11). Furthermore, the binding mechanism of HBTC with $Al^{3+}$ is supported by the Job's plot (Fig. A3.5, Appendix) and HRMS of HBTC-$Al^{3+}$ complex (Fig. A3.7, Appendix).

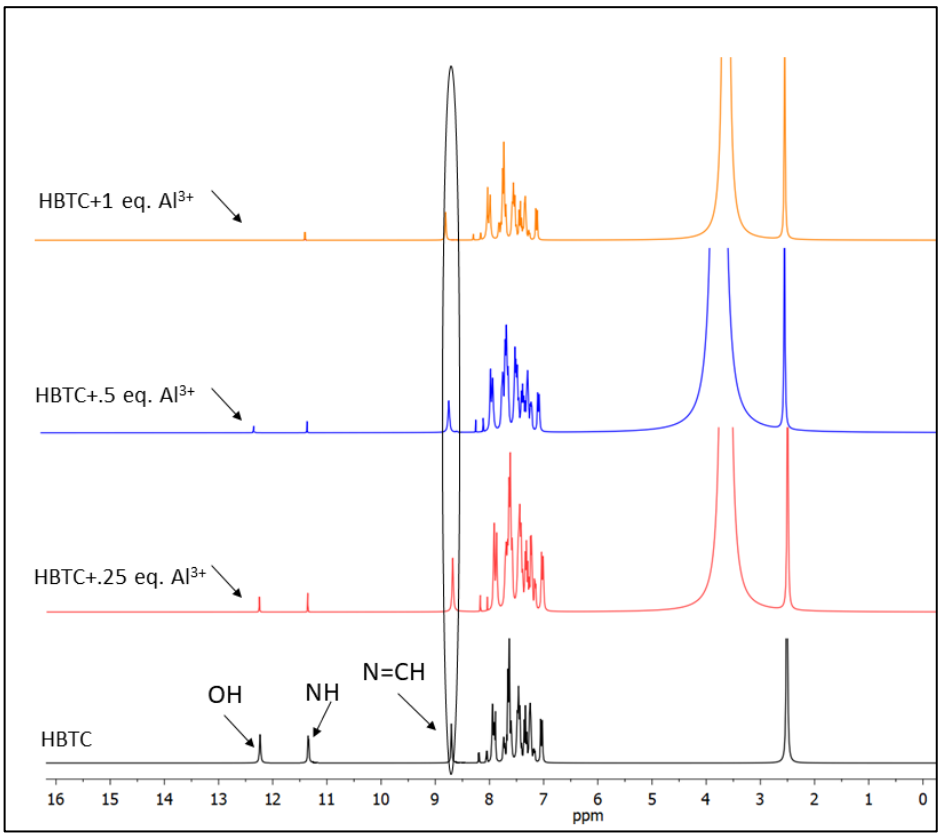


**Figure 3.11:** Changes in $^{1}$H-NMR spectra of HBTC in various concentration of $Al^{3+}$.

## 3.4.11. Dip-stick experiment: sensing of $Al^{3+}$ using TLC plate

Inspired by the distinct detection of $Al^{3+}$ ion by HBTC, we decided to make a practical application tool by using the probe alone to detect the metal cation. In this method we can qualitatively detect the specific analyte without using any kind of sophisticated instrument. The experiment gives qualitative results for the binding of $Al^{3+}$ with HBTC. Thus, to execute this experiment we prepared thin-layer chromatography (TLC) plates dipped in a solution of HBTC in acetonitrile ($2\times10^{-4}$ M) and left for a few minutes to dry. Then the TLC plates were dipped in $Al^{3+}$ ($2\times10^{-3}$ M) solution and again exposed to air to evaporate the solvent. Now we observed the changes in colour of the TLC plates by the naked eye as well as under UV light. A distinct blue fluorescence is observed under UV light in the presence of $Al^{3+}$ (Fig. 3.12). Hence this experiment indicates that, devoid of any instrumental analysis, only using TLC plates and the naked eye, instant detection of $Al^{3+}$ can be done using the HBTC probe.

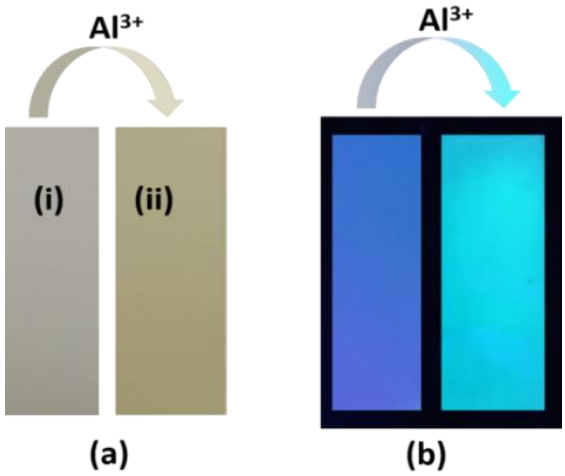


**Figure 3.12:** Photographs of TLC plates after immersion in HBTC-acetonitrile solution (i) and after immersion in HBTC-$Al^{3+}$acetonitrile solution (ii) taken in ambient light (a) and under UV light (b) Excitation wavelength of the UV light is 384 nm.

## 3.4.12. Bio-imaging study

For bio-imaging study, first the cytotoxicity of HBTC, $Al^{3+}$-salt and HBTC-$Al^{3+}$ complex was examined with a breast cancer cell line (MDA-MB231) by the MTT method. Cell viability study of HBTC reveals that in the 1-200 µM concentration range there is a significant number of viable cells (Fig. 3.13, Fig. 3.14), which signifies that HBTC is safe to use in a biological system, although cells have lower survivability in higher concentration.

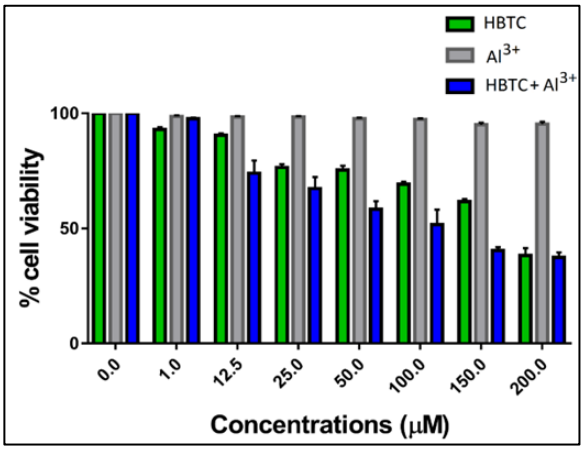


**Figure 3.13:** MTT assay of HBTC and HBTC-$Al^{3+}$ complex on breast cancer cell line (MDA-MB231).

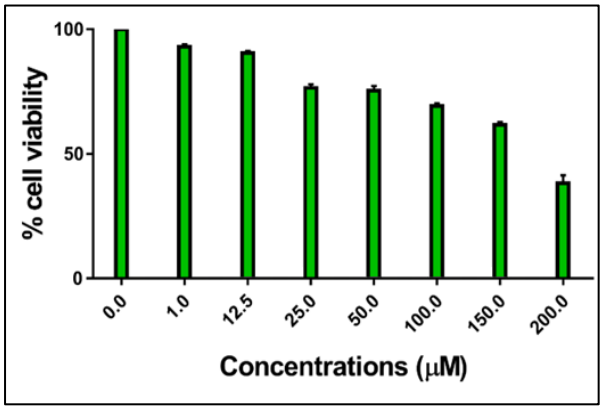


**Figure 3.14:** MTT assay of HBTC on breast cancer cell lines (MDA-MB231).

The $IC_{50}$ value of HBTC is found to be 167.2 μM. (Fig. 3.15); hence the selected dosage for the experiment was chosen to be 15 μM, as the dosage should be less than the $IC_{50}$ value.

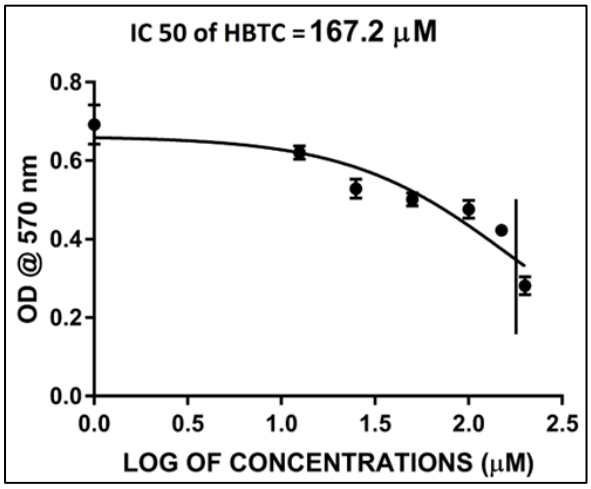


**Figure 3.15:** $IC_{50}$ dose of the receptor HBTC in breast cancer cell lines (MDA-MB231)

Now at the chosen concentration of HBTC (15 μM) for imaging, a fairly high number of viable cells were found. Fluorescence images in the presence of HBTC and HBTC-$Al^{3+}$ complex were taken with MDA-MB231 cells under a fluorescence microscope. Fig. 3.16 clearly indicates that treatment of breast cancer cells with HBTC showed no fluorescence itself, while incubation with $Al^{3+}$ complex shows bright blue fluorescence in the intracellular region of MDA-MB231 cells (Fig. 3.16). Hence it is noteworthy to mention that our HBTC probe can penetrate through cell membranes and can bind with intracellular $Al^{3+}$. We also conclude that, in bright field images, cells do not show any physical or morphological change when incubated with $Al^{3+}$ indicating the non-toxic nature of HBTC at that concentration and those MDA-MB231 cells are viable.

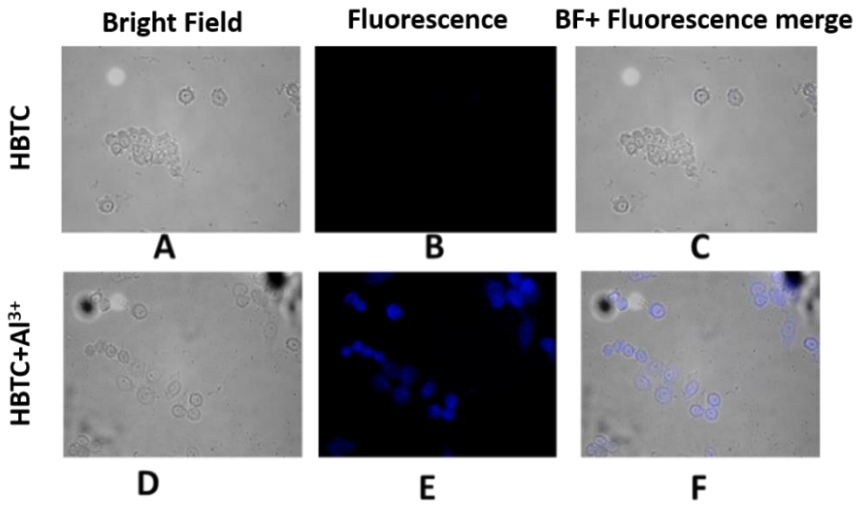


**Figure 3.16:** (A) Bright field image of (MDA-MB231) cells after incubation with 15 μM HBTC, respective fluorescence image (B), merged field (C). (D) Bright field image of (MDA- MB231) cells after incubation with 15 μM of HBTC and 15 μM of $Al^{3+}$ and its respective fluorescence image (E) as well as merge field (F). Incubation period was 12h in each case.

## 3.4.13. Computational studies to interpret further structural changes in HBTC and HBTC-$Al^{3+}$

Theoretical calculation is performed by the DFT/B3LYP method to clarify the sensing mechanism of the probe in the ground state as well as to gain insight into the optimized geometries of the free probe (HBTC) and HBTC-$Al^{3+}$ complex (Fig. 3.17). Contour plots of selected molecular orbitals of HBTC and HBTC-$Al^{3+}$ complex are shown in Fig. A3.8 Appendix, Fig. A3.9 Appendix. The HOMO-LUMO energy gap in HBTC (3.72 eV) is significantly decreased in HBTC-$Al^{3+}$ complex (3.51 eV). The change in HOMO-LUMO energy gap is well reflected in the electronic transitions calculated by the TDDFT/B3LYP method (Table A3.3, Appendix).

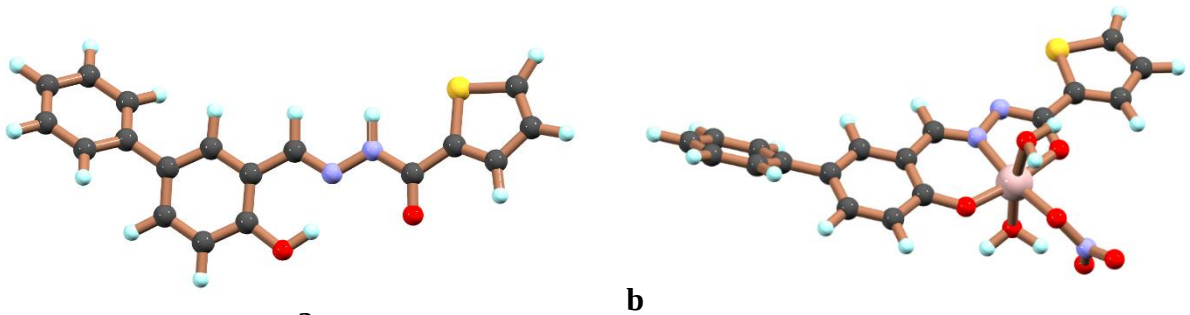

**a** **b**

**Figure 3.17:** Optimized structures of **(a)** HBTC and **(b)** HBTC-$Al^{3+}$calculated by DFT/B3LYP/6-31+G(d) method.

# 3.5. Conclusions

In summary, we have explored the design and synthesis of a biphenyl-thiophene-based moiety, which showed selective detection of $Al^{3+}$ over other cations in ACN/$H_2O$ (4/1, v/v, 10 mM HEPES buffer, pH = 7.2). The simultaneous effect of ESIPT and C=N isomerization induces the non-fluorescent property in free HBTC, while complexation with $Al^{3+}$ inhibits these quenching processes and turning on the CHEF mechanism. The spectroscopic data (UV-Vis, fluorescence, NMR, HRMS etc.) supported the chelation of HBTC with $Al^{3+}$. The detection limit is found to be of the order of $10^{-9}$ M for $Al^{3+}$ in ACN/$H_2O$ medium. Moreover, HBTC is suitable for qualitative analysis by a dip-stick method and has potential biological application in live cell bio-imaging studies.

# 3.6. Experimental

## 3.6.1. Reagents and methods

All the organic, inorganic compounds and solvents used for the experiment were purchased from commercial sources. 2-Thiophene carbonic acid hydrazide and 4-phenylphenol were purchased from Sigma Aldrich and used without further purification. $^1H$ and $^{13}C$ NMR spectra were recorded by Bruker (AC) 300 MHz NMR instrument of ~0.05 M solutions in DMSO-$d_6$ solvent, where TMS was used as internal standard. HRMS mass spectra were recorded on Waters (Xevo G2 Q-TOF) mass spectrometer. For thin layer chromatography (TLC) Merck 60 $F_{254}$ plates was used with 0.25 mm thickness. Perkin Elmer Lambda 750 spectrophotometer was used for UV-Vis studies. Elemental analysis was performed in a 2400 Series-II CHN analyzer, Perkin Elmer, USA. Infrared spectroscopy was recorded using RX-1 Perkin Elmer spectrophotometer where

samples prepared as KBr pellets. Fluorescence property was studied using Shimadzu RF-6000 fluorescence spectrophotometer at room temperature (298 K). Time-resolved spectrofluorometer from IBH, UK was used for lifetime measurement.

## 3.6.2. Synthesis of the probe 4-hydroxy-(([1,1'-biphenyl]-3-yl)methylene) thiophene-2-carbohydrazide (HBTC)

4-hydroxy-[1,1'-biphenyl]-3-carbaldehydewas prepared according to previously reported procedure.[35]At first 4-hydroxy-[1,1'-biphenyl]-3-carbaldehyde (0.2 g, 1 mmol) was dissolved in 10 mL of ethanol in a round bottom flux then 2-thiophenecarbonic acid hydrazide (0.14 g, 1 mmol) was added to it and refluxed for 8 h. A light-yellow precipitate was appeared which was then filtered and washed with ethanol. Then the product was dried and collected. Yield: (0.276 g) 86%.

**Anal. data for $C_{18}H_{14}N_2O_2S$ (HBTC):**

**Elemental analysis**: Anal. Calculated for $C_{18}H_{14}N_2O_2S$, C, 67.06%; H, 4.38%; O, 9.93; N, 8.69%; S,9.94% Found C, 67.15%; H, 4.29%; O, 9.87%; N, 8.74%; S, 9.95%.

**$^1$H NMR data (300 MHz,DMSO-$d_6$)**: δ (ppm): 12.21 (s, 1H), 11.27 (s, 1H), 8.70 (s, 1H), 7.88-7.95(m, 2H), 7.63 (t, J=6Hz,3H), 7.46 (t, J = 9Hz, 3H), 7.33 (t, J =7.5 Hz, 2H), 7.25 (s, 1H), 7.04 (d, J =8.4Hz, 1H).

**$^{13}$C NMR (75 MHz, DMSO-$d_6$):** δ(ppm): 158.08, 157.43, 147.90, 139.99, 139.95, 138.10, 135.18, 132.69, 130.20, 129.76,129.39, 128.71, 127.33, 126.64, 119.65, 117.48.

**HRMS:** MS-ES$^+$ (m/z): $[M+Na]^+$: $C_{18}H_{14}N_2O_2S$ Calculated: 345.070, Found: $[M+Na]^+$; 345.0211.

**IR (cm$^{-1}$, KBr):** υ(C=N) 1642.19, υ(O-H) 3418.85, υ(N-H) 3156.51,υ(C=O) 1766.13.

## 3.6.3. General Method for UV-Vis and Fluorescence Titration

### 3.6.3.1. UV-Vis Study

For UV-vis titrations study, stock solution of the probe (20 μM) was prepared in [(ACN/$H_2O$), 4/1, *v/v*] (at 25°C) solution using 10 mM HEPES buffer. For this study stock solution of the cations were prepared separately in deionized water using HEPES buffer at pH=7.2 in the order of 40 μM. The solutions of metal ions were prepared using their chloride and perchloate salts. Solutions of various concentrations containing the probe and different increasing concentrations of cations were prepared individually to record UV-Vis spectra.

### 3.6.3.2. Fluorescence Method

For fluorescence titrations, the probe stock solution (20 μM) was prepared the same way as that used for UV-Vis titration study and the solutions of the guest cations with their chloride and perchlorate salts were also prepared same as of UVtitration. Solution of fluoride (40 μM) was prepared using ammonium fluoride salt. Different concentration of probe and metal salts were prepared separately for fluorescence study. The emission spectrum was recorded at ($\lambda_{ex}$= 384 nm, excitation slit = 10.0 and emission slit = 10.0).

### 3.6.3.3. Job's Plot by Fluorescence Method

By using fluorescence data jobs plot was calculated. A series of solution of total volume 5 ml was prepared with different concentration of probe and metal ion using HBTC (10 μM) and $Al^{3+}$ (10 μM). The solutions were prepared in ACN-$H_2O$ (4:1, v/v) solvent at pH=7.2 using 10 mM HEPES buffer. Excitation at 384 nm was used for fluoresence emmision. We plotted $\Delta I.X_h$ versas $X_h$ ($\Delta I$ denotes the change in emission intensity at 480 nm during titration and $X_h$ is the mole fraction of host solution in each case).

### 3.6.3.4. Determination of association constant:

Binding constant was calculated according to the Benesi-Hildebrand equation. $K_a$ was calculated following the equation stated below.

$$1/(F-F_o) = 1/\{K_a(F_{max}–F_o)\,[M^{n+}]^x\} + 1/[F_{max}-F_o]$$

Here $F_0$, F and $F_{max}$ indicate the emission in absence of, at intermediate and at infinite concentration of metal ion respectively.

Plot of $1/[F-F_0]$ vs. $1/[Al^{3+}]$ gives a straight line indicating 1:1 complexation between HBTC and $Al^{3+}$ where $K_a$ is found to be $3.04\times10^4\ M^{-1}$ for HBTC.

### 3.6.3.5. Determination of fluorescence quantum yield:

The luminescence quantum yield was determined using coumarin 153 as reference dye. The compounds and the reference dye were excited at the same wavelength, maintaining nearly equal absorbance (~0.1), and the emission spectra were recorded. The area of the emission spectrum was integrated using the software available in the instrument and the quantum yield is calculated according to the following equation:

$$\phi_S/\phi_R = [A_S / A_R] \times [(Abs)_R /(Abs)_S] \times [n_S^2/n_R^2]$$

where, $\phi_S$ and $\phi_R$ are the luminescence quantum yields of the sample and reference, respectively. $A_S$ and $A_R$ are the area under the emission spectra of the sample and the reference respectively, $(Abs)_S$ and $(Abs)_R$ are the respective optical densities of the sample and the reference solution at the wavelength of excitation, and $n_S$ and $n_R$ are the values of refractive index for the respective solvent used for the sample and reference.

We calculated the quantum yields of HBTC and HBTC-$Al^{3+}$ using the abovementioned equation; the values are found 0.001 and 0.196 respectively.

## 3.6.4. Live cell imaging studies

### 3.6.4.1. MTT assay

Triple negative breast cancer cell lines MDA MB-231 were evaluated for cytotoxicity with HBTC and HBTC-$Al^{3+}$ complex. MB-231 cells were seeded in 96 well plate at a density of $5 \times 10^3$ cells per well followed by incubation at 37°C for 24 h at a 5% $CO_2$ atmosphere. The cells were separately treated with increasing doses of HBTC and HBTC-$Al^{3+}$ complex concentrations (0, 1, 12.5, 25, 50, 100, 150, 200) µM, along with control for 24 h. $Al^{3+}$ was treated in aqueous medium while the receptor HBTC was dissolved in DMSO but final concentration of DMSO was maintained below 1%. After 24h, methyl tetrazolium dye (MTT) (5 mg/mL) solution was added to each well (10 µl/well). The plates were incubated under dark condition in $CO_2$ atmosphere at 37°C for 3 h. Then 100 µL DMSO was added to each well to solubilize the formazan crystals and the plates were shaken briefly before quantification at 570 nm with the help of a multi-mode reader (SpectraMax i3x, Molecular devices). $IC_{50}$ value of HBTC was determined by plotting a non-linear regression curve between the log of concentration of HBTC and O.D value at 570 nm. Untreated cells were served as 100% viable.

### 3.6.4.2. Cell bio-imaging

In a six well plate containing 22×22 mm glass cover slips placed at the bottom of the well, the MDA MB 231 cells were seeded and allowed to adherer overnight. 15 µM of the HBTC as well as HBTC-$Al^{3+}$ were added to the respective well containing cells along with a separate control. Then fixation of the cells was done with methanol and washed with 0.5% phosphate buffer saline tween (PBST) twice and then with 1 × PBS thrice. The cover slips were then mounted on a glass slide by glycerol and were observed under a fluorescence microscope (Leica DM4000 B, Germany) at 40x magnification.

### 3.6.5. Theoretical study

Gaussian 09 (G09) program along with Gauss View visualization programs were used for computational study.[36] DFT calculations were carried out at the B3LYP level for the geometry optimization of HBTC and HBTC-$Al^{3+}$ complex.[37, 38] For C, N, O, S and H atoms the 6-31+G(d) basis set was assigned while for Al Lanl2dz basis set with the effective core potential (ECP) was used.[39, 40]The vibrational frequency calculations were performed on the optimized geometries to confirm the local minima and there were only positive eigen values. The Vertical electronic excitations which were based on B3LYP optimized geometries were computed using the time-dependent density functional theory (TDDFT) formalism[41-43] in acetonitrile using the conductor-like polarizable continuum model (CPCM)[44-46].

## 3.7. Notes and references


1. C. Lodeiro, J. L. Capelo, E. Oliveira and C. Nuñez, *Environ. Sci. Pollut. Res.*, 2016, **23**, 24419.
2. M.C. Bubalo, K. Radošević, I. R. Redovniković, J. Halambek and V. G. Srček, *Ecotoxicol. Environ. Saf.*, 2014, **99**, 1.
3. M. A. AI-Ashmawy, *J. Food Sci.*, 2011, **76**, T73.
4. L. C. Becker, I. Boyer, W. F. Bergfeld, D. V. Belsito, R. A. Hill, C. D. Klaassen, D. C. Liebler, Jr. J. G. Marks, R. C. Shank, T. J. Slaga and P. W. Snyder, *Int. J. Toxicol.*, 2016, **35**, 16S.
5. G. Liedl, R. Bielak, J. Ivanova, N. Enzinger, G. Figner, J. Bruckner, H. Pasic, M. Pudar and S. Hampel, *Phys. Procedia*, 2011, **12**, 150.
6. C. Exley, *Environ. Sci.: Processes Impacts***,** 2013, **15**, 1807.
7. T. Stahl, H. Taschan and H. Brunn, *Environ. Sci. Eur.*, 2011, **23**, 1.
8. Z. Krejpcio and R. W. Wojciak, *Pol. J. Environ. Stud.*, 2002, **11**, 251.
9. T. Han, X. Feng, B. Tong, J. Shi, L. Chen, J. Zhi and Y. Dong, *Chem. Comm.*, 2012, **48**, 416.
10. J. Barcelo and C. Poschenrieder, *Environ. Exp. Bot.*, 2002, **48**, 75.
11. C. A. Shaw and L. Tomljenovic, *Immunol. Res*., 2013, **56**, 304.
12. M. Dey and R. K. Singh, Toxicol. Mech. Methods, 2022, **32**,616.
13. R. H. Alasfar and R. J. Isaifan, *Environ. Sci. Pollut. Res.* Int., 2021, ***28***, 44587.
14. G. Dalla Torre, J. I. Mujika, J. I. Lachowicz, M. J. Ramos and X. Lopez, *Dalton Trans.*, ***48***, 6003-.
15. H. H. Malluche, *Nephrol. Dial. Transplant.*, 2002, ***17***, 21.
16. C. E. Elger, O. Knoll, A. C. Ludolph and H. Raidt, *Springer*, 1987, **4**,304.
17. O. A. Taiwo, *J. occup. Environ. Med.*, 2014, ***56***, S71.
18. K. Berend, G. Van Der Voet and W. H. Boer, *Kidney international*, 2001, **59**, 746.
19. D. Wu, A. C. Sedgwick, T. Gunnlaugsson, E. U. Akkaya, J. Yoon and T. D. James, ***Chem. Soc. Rev.,*** 2017, **46**, 7105.

20. (a) S. Goswami, S. Das, K. Aich, B. Pakhira, S. Panja, S. K. Mukherjee and S. Sarkar, *Org. Lett.*, 2013, **15**, 5412; (b) S. Goswami, A. Manna, S. Paul, A. K. Das, K. Aichand, P. K. Nandi, *Chem. Commun.*, 2013, **49**, 2912; (c) Y. Tong, B. Liu, Y. Wu, B. Yang, G. Wen, Y. T. Yang, J. Chai and X. Hu, *Sens. Actuators B Chem*, 2017, **252**, 794.
21. B. Liu, P. F. Wang, J. Chai, X. Q. Hu, T. Gao, J. Bin Chao, T. G. Chen and B. S. Yang, *Spectrochim. Acta, Part A*, 2016, **168**, 98.
22. A. K. Das and S. Goswami, *Sens. Actuators, B*, 2017, **245**, 1062.
23. Z. Yang, D. Wu, K. Dai, S. Cao, Z. Li, H. Huang, Z. Shang, H. Liang, M. Yan and S. Xie, *J. Mol. Struct.*, 2020, **1201**, 127155.
24. V. E. Barlette, L. C. G. Freitas, P. H. Guadagnini and C. A. Bertran, *J. Braz. Chem. Soc.*, 2008, **19**, 101.
25. A. Kajal, S. Bala, S. Kamboj, N. Sharma and V. Saini, *J. Catal*., 2013, **2013**.
26. S. Omidi and A. Kakanejadifard, *RSC Adv.*, 2020, **10**, 30186.
27. D. Aydin, I. B. Gunay, S. N. K. Elmas, T. Savran, F. N. Arslan, G. Sadi and I. Yilmaz, *New J. Chem.*, 2020, ***44,*** 12079.
28. G. Singh, A. Singh, P. Satija, J. Singh and J. Singh, *New J. Chem.*, 2021, ***45***, 7850.
29. B. Das, M. Dolai, A. Ghosh, A. Dhara, A. D. Mahapatra, D. Chattopadhyay, S. Mabhai, A. Jana, S. Dey and A. Misra, *Anal. Methods*, 2021, ***13***, 4266.
30. Z. Liu, S. Li, G. Ge, Y. Li, C. Zhao, H. Zhang and Z. Yang, *RSC Adv.*, 2019, ***9***, 5377.
31. S. Mabhai, M. Dolai, S. K. Dey, S. M. Choudhury, B. Das, S. Dey, A. Jana and D. R. Banerjee, *New J. Chem*., 2022, **46**, 6885.
32. A. Dhara, N. Guchhait, I. Mukherjee, A. Mukherjee and S. C. Bhattacharya, *RSC Adv.*, 2016, **6**, 105930.
33. B. Das, S. Dey, G. P. Maiti, A. Bhattacharjee, A. Dhara and A. Jana, *New J. Chem.*, 2018, **42**, 9424.
34. J. Wang, L. Feng, J. Chao, Y. Wang, and S. Shuang, *Anal. Methods*, 2019, ***11***, 5598.
35. L. Patra, S. Das, S. Gharami, K. Aich and T. K. Mondal, *New J. Chem.*, 2018, ***42***, 19076.
36. Gaussian 09, Revision D.01, M. J. Frisch, G. W. Trucks, H. B. Schlegel, G. E. Scuseria, M. A. Robb, J. R. Cheeseman, G. Scalmani, V. Barone, B. Mennucci, G. A. Petersson, H. Nakatsuji, M. Caricato, X. Li, H. P. Hratchian, A. F. Izmaylov, J. Bloino, G. Zheng, J. L. Sonnenberg, M. Hada, M. Ehara, K. Toyota, R. Fukuda, J. Hasegawa, M. Ishida, T. Nakajima, Y. Honda, O. Kitao, H. Nakai, T. Vreven, J. A. Montgomery, Jr., J. E. Peralta, F. Ogliaro, M. Bearpark, J. J. Heyd, E. Brothers, K. N. Kudin, V. N. Staroverov, R. Kobayashi, J. Normand, K. Raghavachari, A. Rendell, J. C. Burant, S. S. Iyengar, J. Tomasi, M. Cossi, N. Rega, J. M. Millam, M. Klene, J. E. Knox, J. B. Cross, V. Bakken, C. Adamo, J. Jaramillo, R. Gomperts, R. E. Stratmann, O. Yazyev, A. J. Austin, R. Cammi, C. Pomelli, J. W. Ochterski, R. L. Martin, K. Morokuma, V. G. Zakrzewski, G. A. Voth, P. Salvador, J. J. Dannenberg, S. Dapprich, A. D. Daniels, Ö. Farkas, J. B. Foresman, J. V. Ortiz, J. Cioslowski and D. J. Fox, Gaussian, Inc., Wallingford CT, 2009.
37. A. D. Becke, *J. Chem. Phys.*, 1993, **98**, 5648.
38. C. Lee, W. Yang and R. G. Parr, *Phys. Rev. B*, 1988, **37**, 785.
39. W. R. Wadt and P. J. Hay, *J. Chem. Phys.*, 1985, **82**, 284.
40. P. J. Hay and W. R. Wadt, *J. Chem. Phys.*, 1985, **82**, 299.

41. R. Bauernschmitt and R. Ahlrichs, *Chem. Phys. Lett.*, 1996, **256**, 454
42. R. E. Stratmann, G. E. Scuseria and M. J. Frisch, *J. Chem. Phys.*, 1998, **109**, 8218.
43. M. E. Casida, C. Jamorski, K. C. Casida and D. R. Salahub, *J. Chem. Phys.*, 1998, **108**, 4439.
44. M. Cossi and V. Barone, *J. Chem. Phys.*, 2001, **115**, 4708.
45. V. Barone and M. Cossi, *J. Phys. Chem. A*, 1998, **102**, 1995.
46. M. Cossi, N. Rega, G. Scalmani and V. Barone, *J. Comput. Chem.*, 2003, **24**, 669.

# APPENDIX

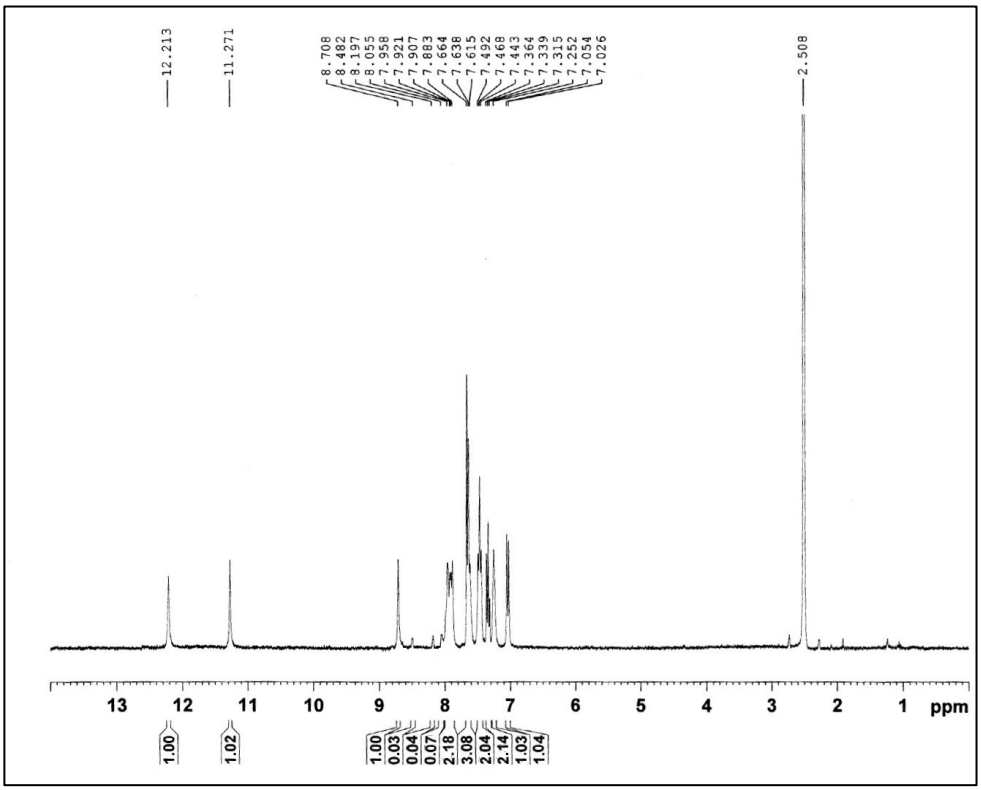


**Fig. A3.1:** $^{1}$H NMR (300 MHz) spectrum of HBTC in DMSO-$d_6$

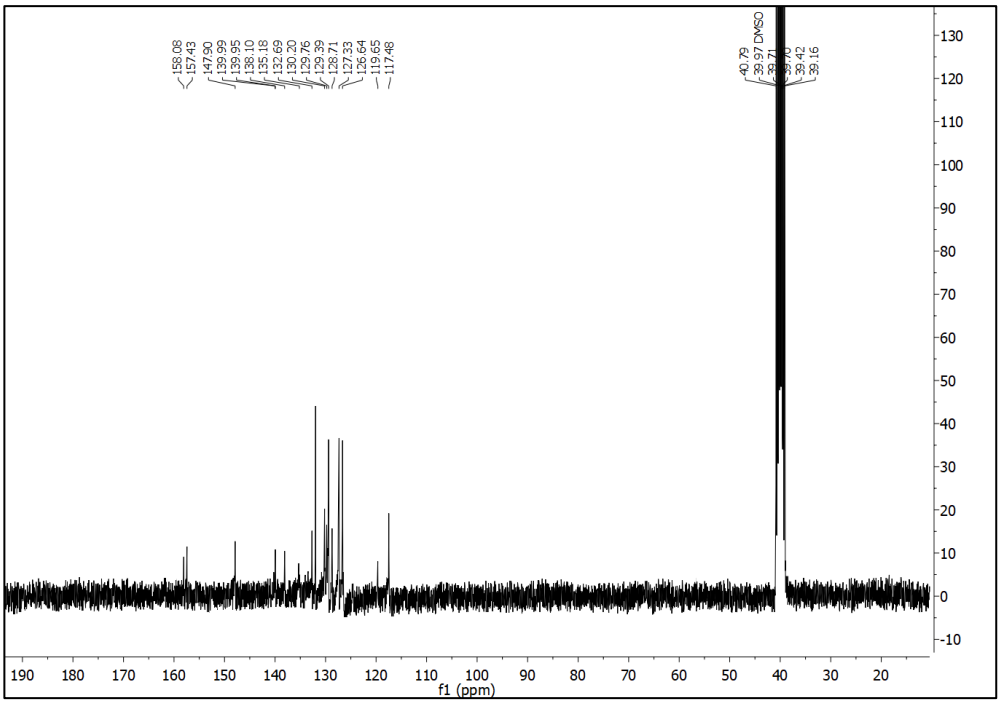


**Fig. A3.2:** $^{13}$C NMR (75 MHz) spectrum of HBTC in DMSO-$d_6$

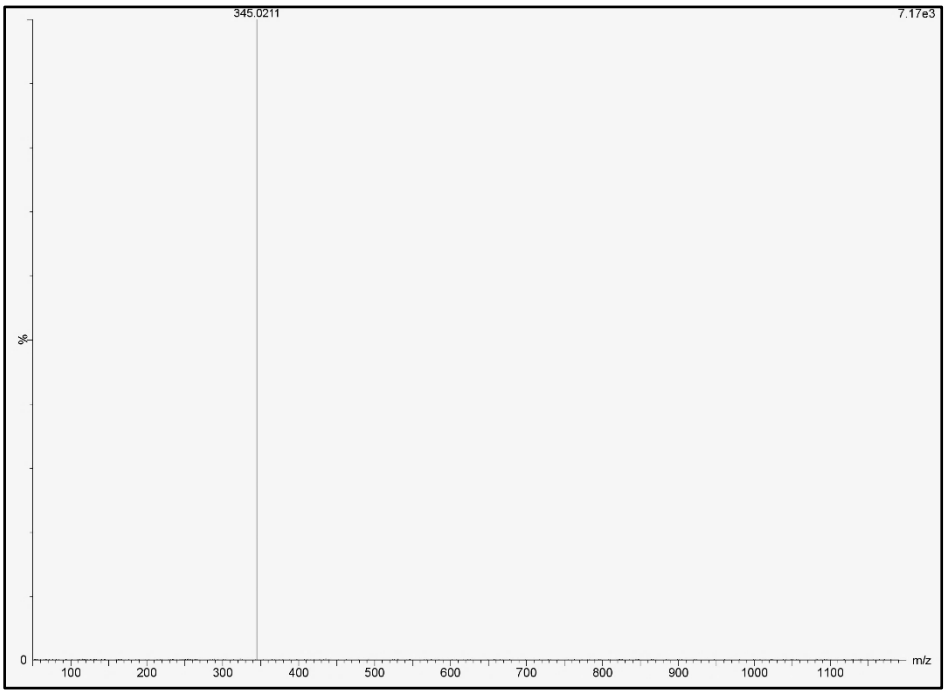


**Fig. A3.3:** HRMS of probe HBTC

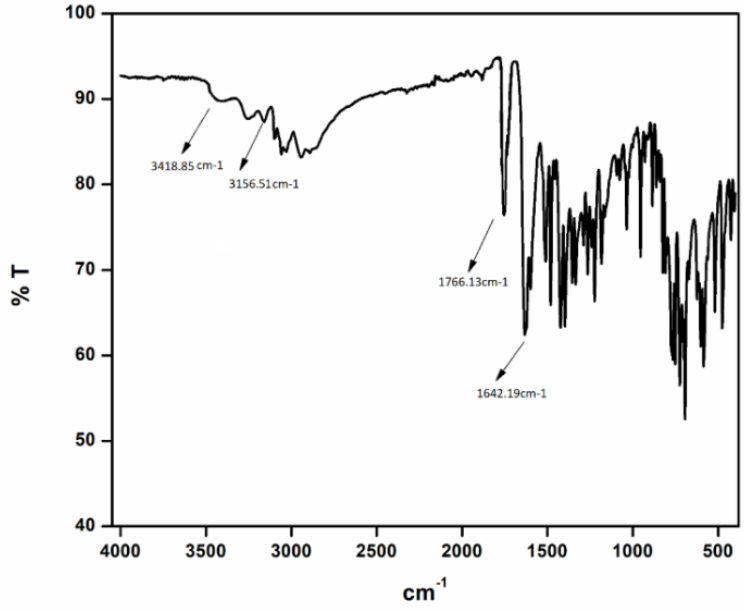


**Fig. A3.4:** IR spectra of the probe HBTC

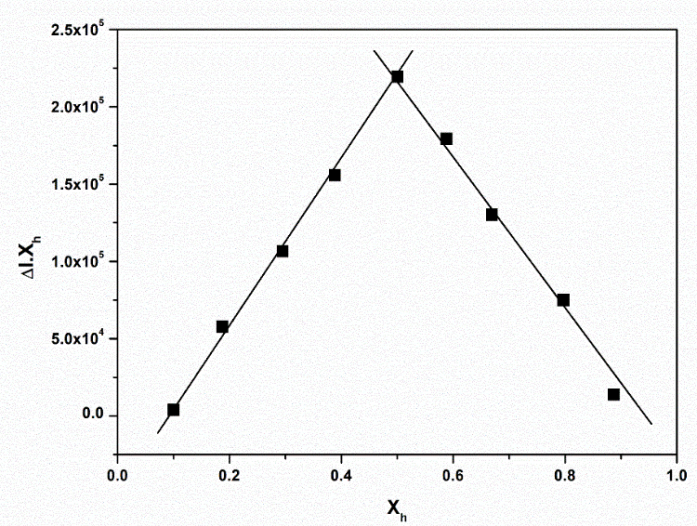


**Fig. A3.5:** Job's plot for HBTC (10 μM) with $Al^{3+}$ in 10 mM HEPES buffer solution (pH = 7.2) ($\lambda_{ex}$ = 384 nm); where $X_h$ is the mole fraction of the host and ΔI indicates the change of emission intensity at 480 nm.

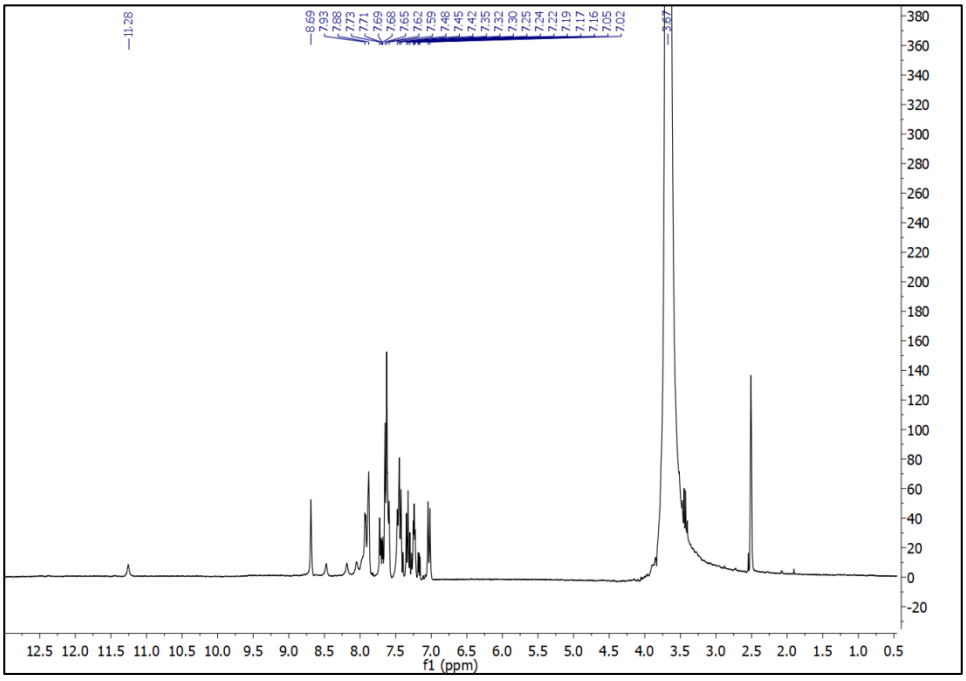


**Fig. A3.6:** $^1H$ NMR spectrum of the HBTC with $Al^{3+}$ in DMSO-$d_6$

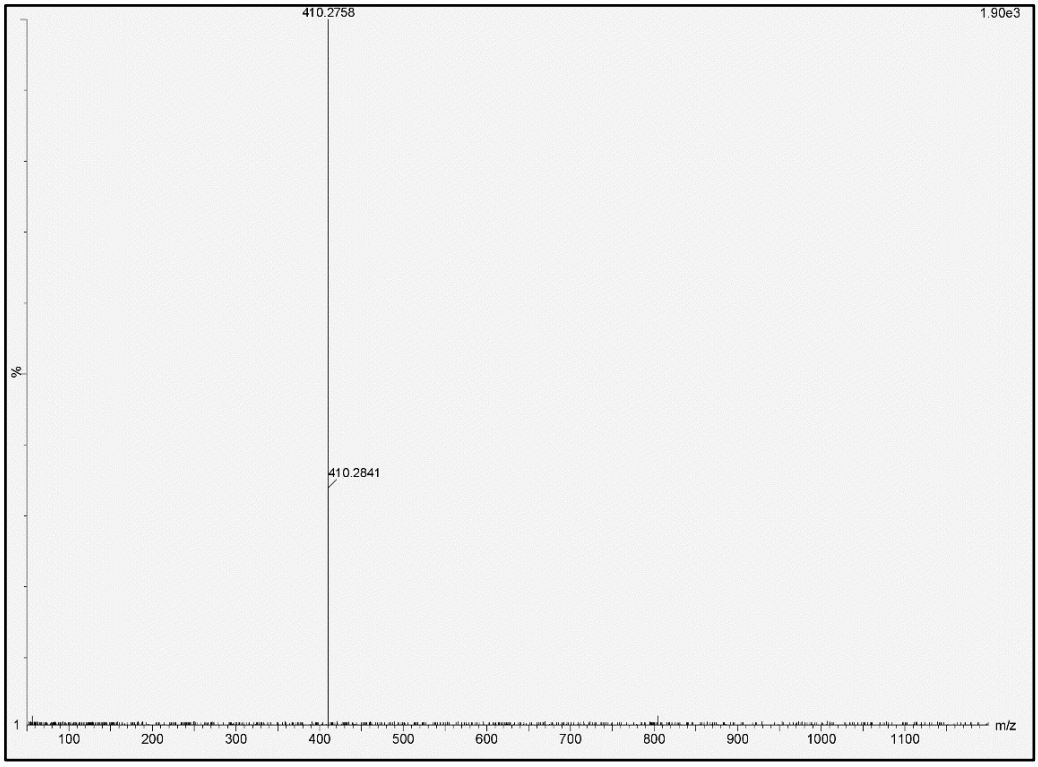


**Fig. A3.7:** HRMS spectrum of HBTC-$Al^{3+}$ complex

**Table A3.1: Fluorescence lifetime data**

| Compounds | Quantum yield *(φ)* | τ (ns) | $k_r$ ($10^8 \times s^{-1}$) | $k_{nr}$ ($10^8 \times s^{-1}$) |
|---|---|---|---|---|
| HBTC | 0.001 | 1.42 | 0.008 | 7.04 |
| HBTC-$Al^{3+}$ | 0.196 | 5.14 | 0.381 | 1.564 |

Radiative rate constant $K_r$ and total non-radiative rate constant $K_{nr}$ have been calculated using the equation $\tau^{-1} = K_r + K_{nr}$ and $K_r = \varphi_f / \tau$

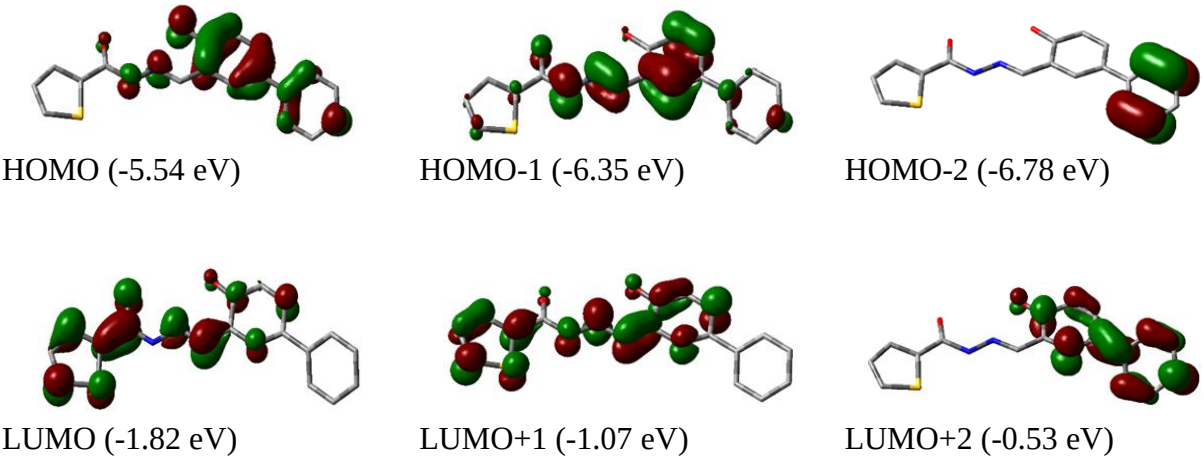


**Fig. A3.8:** Contour plot of some selected molecular orbitals of HBTC

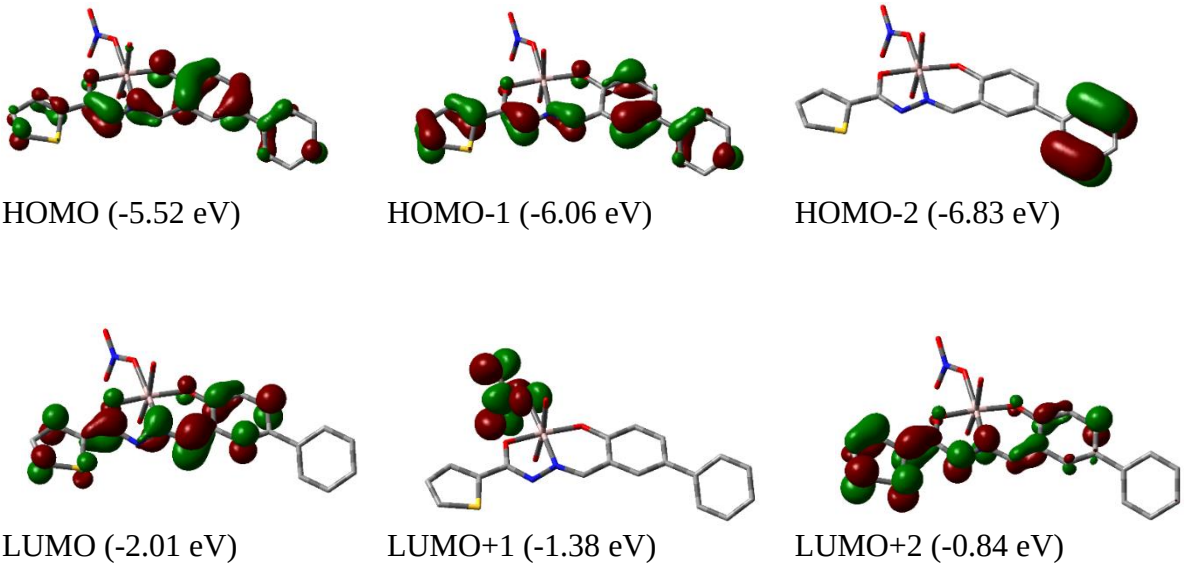


**Fig. A3.9:** Contour plot of some selected molecular orbitals of HBTC-$Al^{3+}$

**Table A3.2:** Energy and compositions of some selected molecular orbitals of HBTC-$Al^{3+}$ complex.

| MO | Energy | % of composition | |
|---|---|---|---|
| | | HBTC | Al |
| LUMO+5 | 0.46 | 99 | 1 |
| LUMO+4 | -0.07 | 100 | 0 |
| LUMO+3 | -0.61 | 100 | 0 |
| LUMO+2 | -0.84 | 100 | 0 |
| LUMO+1 | -1.38 | 98 | 2 |
| LUMO | -2.01 | 100 | 0 |
| HOMO | -5.52 | 99 | 1 |
| HOMO-1 | -6.06 | 100 | 0 |
| HOMO-2 | -6.83 | 100 | 0 |
| HOMO-3 | -6.91 | 100 | 0 |
| HOMO-4 | -6.97 | 100 | 0 |
| HOMO-5 | -7.05 | 100 | 0 |
| HOMO-6 | -7.32 | 98 | 2 |
| HOMO-7 | -7.75 | 99 | 1 |
| HOMO-8 | -7.76 | 100 | 0 |
| HOMO-9 | -8.16 | 97 | 3 |
| HOMO-10 | -8.6 | 100 | 0 |

**Table A3.3.** Vertical electronic excitations of HBTC and HBTC-$Al^{3+}$ calculated by TDDFT/CPCM method

| Compds. | E (eV) | λ (nm) | Osc. Strength (f) | Transition | Character |
|---|---|---|---|---|---|
| HBTC | 4.0500 | 306.13 | 0.6054 | (88%) HOMO-1→LUMO | $\pi \rightarrow \pi^*$ |
| | 3.4153 | 363.03 | 0.3381 | (97%) HOMO→LUMO | $\pi \rightarrow \pi^*$ |
| | 4.5817 | 270.61 | 0.3756 | (80%) HOMO→LUMO+2 | $\pi \rightarrow \pi^*$ |
| | 4.9552 | 250.21 | 0.4244 | (65%) HOMO-1→LUMO+1 | $\pi \rightarrow \pi^*$ |
| | 4.2420 | 292.28 | 0.1656 | (82%) HOMO→LUMO+1 | $\pi \rightarrow \pi^*$ |
| HBTC-$Al^{3+}$ | 3.0712 | 403.70 | 0.5377 | (98%) HOMO→LUMO | L( $\pi$) → L($\pi^*$) |
| | 3.6314 | 341.42 | 0.6558 | (97%) HOMO-1→LUMO | L( $\pi$) → L($\pi^*$) |
| | 4.8482 | 255.73 | 0.2353 | (67%) HOMO-1→LUMO+2 | L( $\pi$) → L($\pi^*$) |
| | 4.4416 | 279.14 | 0.2155 | (58%) HOMO→LUMO+3 | L( $\pi$) → L($\pi^*$) |
| | 5.6347 | 220.04 | 0.1212 | (57%) HOMO-3→LUMO+2 | L( $\pi$) → L($\pi^*$) |

**Table A3.4:** Comparison of solvent systems and limit of detection (LOD) of the receptor (HBTC) with some recently reported fluorescence organic probes for the detection of $Al^{3+}$

| Chemosensors | Solvent system | LOD | References |
|---|---|---|---|
| 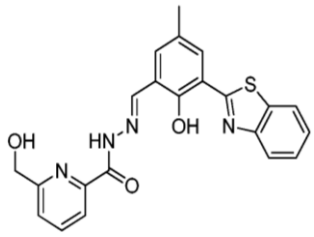 | $CH_3OH/H_2O$ (1/9, v/v, pH = 7.3, 25°C) | $6.72\times10^{-8}$ M | *New J. Chem.*, 2015, **39**, 8582. |
| 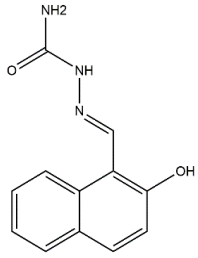 | $EtOH/H_2O$ (1:9, v/v, pH = 5.3) | $6.75\times10^{-8}$ M | *RSC Adv.*, 2020, **10**, 21629. |
| 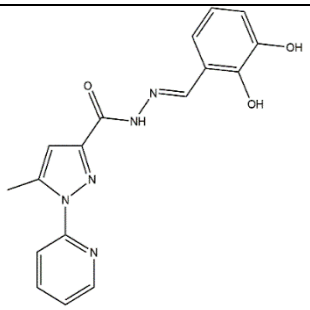 | MeOH-$H_2O$ (9:1, v/v) | 4.78 µM | *Anal. Methods*, 2021, **13**, 4266. |
| 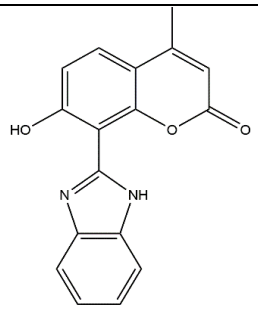 | Acetonitrile-water (2:1, v/v) of pH, 7.2(HEPES buffer) | 0.62 µM | *J. Mol. Struct.*, 2022, **1250**, 131870. |
| 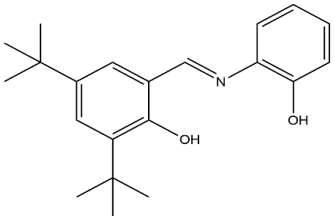 | HEPES buffer (1% EtOH, pH = 7.04). | $2.94\times10^{-8}$ M | *Dalton Trans.*, 2015, **44**, 11352. |

| | | | |
|---|---|---|---|
| 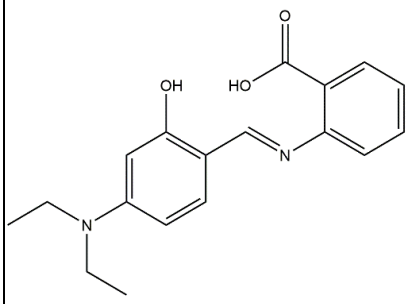 | Water:$CH_3OH$ =1:1 (v/v), pH 7.0 | $2.9\times10^{-7}$ M | *New J. Chem.*, 2016, **40**, 171. |
| 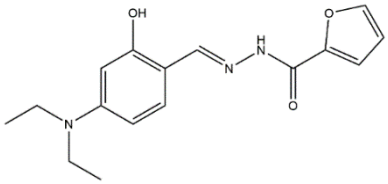 | bis–Tris buffer solution, pH 7.0 | 0.19 mM | *New J. Chem.*, 2017, **41**, 15590. |
| 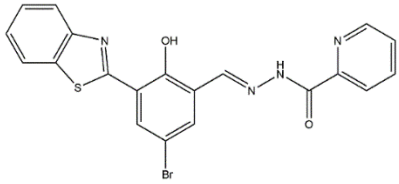 | MeOH/water (v/v,1:1, pH 6.0) | 31.2 nM | *Anal. Methods*, 2019, **11**, 5598. |
| 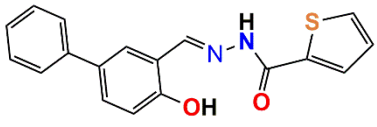 | Aetonitrile/$H_2O$ (4/1,v/v, pH = 7.2) | $(8.74\pm0.36)\times10^{-9}$ M | **Present work** |

# Chapter 4

# A biphenyl thiosemicarbazide based chemosensor for selective fluorogenic recognition of $Cd^{2+}$ and as an imaging agent in living cells

# A biphenyl thiosemicarbazide based chemosensor for selective fluorogenic recognition of $Cd^{2+}$ and as an imaging agent in living cells

## Abstract

A diversified biphenyl thiosemicarbazide based chemosensor (HBMC) has been fabricated and reported towards specific detection of $Cd^{2+}$ in MeOH:$H_2O$ (4:1) solution. Where we observed a chromogenic change from colorless to light yellow colour, as well as it shows a "turn-on" fluorogenic change from non-fluorescent to blooming cyan colour. In fluorometric titration the sharp "turn-on" emission for $Cd^{2+}$ was observed, with ~16-fold increase in fluorescence intensity value at 496 nm by incremental addition of $Cd^{2+}$ ion in MeOH:$H_2O$ (4:1) solution. The reversibility of the chemosensor (HBMC) was confirmed by sequential addition of EDTA solution. Again, the binding stoichiometry of HBMC with $Cd^{2+}$ was found to be 2:1, approved by jobs plot analysis and HRMS spectra of HBMC-$Cd^{2+}$ complex. The mechanism for the $Cd^{2+}$ sensing in MeOH:$H_2O$ (4:1) is based upon inhibition of C=N isomerization and ESIPT process and simultaneously turning on the CHEF (chelation enhanced fluorescence) process. The limit of detection for $Cd^{2+}$ was found to be in the order of $10^{-8}$ (M), which implies that HBMC is an efficient probe to detect $Cd^{2+}$ at microscopic level. The reusability study was performed and on-sight detection of cadmium ion by chemosensor (HBMC) was established by Dip-stick experiment. In vitro detection of $Cd^{2+}$ in human breast cancer cells (MDA-MB-231) by HBMC discloses its cell permeability and biocompatibility nature. Computational study (DFT and TDDFT) with the probe HBMC and HBMC-$Cd^{2+}$ complex were also performed.

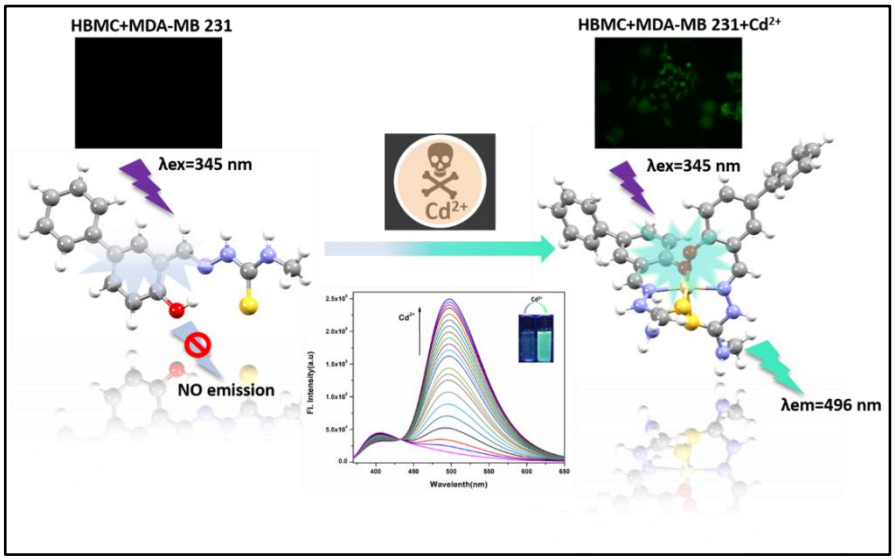

# 4.1. Introduction

With reference to human health and environmental system, discriminative detection of heavy and toxic metal ions is one of the most noteworthy aspects in the field of chemosensors. Among those heavy metal ions $Cd^{2+}$ tops the list in relation to its hazardous nature and detrimental effects.[1] Due to its irreversible damage in the field of batteries, smelting, mining, pigments, metallurgy, fertilizer it has become a hazardous global pollutant.[2-5] Hence due to its outrageous use, it has triggered an inescapable contamination to our soil, water, food, and air.[6-8] Simultaneously living organisms and human health are also being threatened by the excessive use of Cadmium.[9] Mainly through water or air, food and inhalation of cigarette smoke humans are exposed to cadmium.[10] The toxicity level of Cadmium is so soaring that US Environmental Protection Agency (EPA) and Agency for Toxic Substances and Disease Registry has enlisted this toxic heavy metal as the seventh on the Top 20 Hazardous Substances Priority List.[11] While WHO (World Health Organization) has given an enforceable drinking water standard for Cadmium of 3 ppb to prevent kidney related disease.[12] This continuous short and long term exposure of cadmium to human health system causes different disorder resulting lung, breast and prostate cancer.[13-15] Therefore the International Agency for Research on Cancer (IARC) has categorized cadmium compounds as carcinogens of category I.[16] The abnormal concentration of cadmium also causes wound to several organs such as brain ,kidney, bones, gastrointestinal tract and has increased risk of cardiovascular disease.[17-20] Renal, adipose tissue dysfunction and calcium metabolism are also factors that causes by excessive cadmium intake.[21-24] Although the mechanism involved in the uptake of $Cd^{2+}$ by cellular and environmental system and $Cd^{2+}$ carcinogenesis remain obscured.[25-27] Therefore developing reliable technique to detect $Cd^{2+}$ in environmental system is an absolute necessity. However there are several techniques such as atomic absorption/emission spectroscopy (AAS/AES), inductively coupled plasma mass spectrometry (ICP-MS), inductively coupled plasma atomic emission spectroscopy (ICP-AES), anode stripping voltammetric analysis, but these techniques faces huge obstacle due to their tedious process of sample preparation, complicate to operate and time consumption.[28-31] Out of various methodology fluorescence detection is one of the authentic and established.[32-35] Due to its easy operational technique, high selectivity, sensitivity, short period of detection and low cost operation.[36-38] So here we have fabricated a probe which can encounter and monitor Cadmium ion in biological environment with high susceptibility by very cheap economical procedure

utilizing fluorescent technique. There are different mechanisms which works behind chemosensing process such as, excited-state intra/intermolecular proton transfer (ESIPT), chelation-enhanced fluorescence (CHEF), -C=N- isomerisation, intramolecular charge transfer (ICT), metal-ligand charge transfer (MLCT), photoinduced electron/energy transfer (PET) and fluorescence resonance energy transfer (FRET).[39] Again Schiff bases have gain huge interest due to their high coordinating capabilities and have different biological applications.[40,41] The presence of CH=N- in the structure promotes the coordination power to bind heavy metal ion with lone pair of electron.[42,43] Another aspect is excited state intramolecular proton transfer (ESIPT) is unique due to its dual emission mode of keto and enol forms.[44] A characteristic spectral change is observed when heavy metal ion binds with ESIPT centre prohibiting the proton transfer resulting in fluorescence change.[45] Taking these factors in account a biocompatible biphenyl thiosemicarbazide based framework has been designed, synthesized with good yield percentage, which has noteworthy selectivity and prompt detection value towards $Cd^{2+}$ ion against other metal ion. Then spectroscopic measurements like fluorescence, ultraviolet-visible (UV-VIS) absorption were carried out along with density functional theory (DFT) and time resolved fluorescence study which supported the evidence of "turn-on" fluorescence property of our designed probe towards $Cd^{2+}$.

## 4.2. Prior works

Recently in 2022, Zhang et al. reported quinolimide derivative which detects $Cd^{2+}$ in $CH_3CN$/Tris-HCl buffer with limit of detection value of 17.9 nM.[46] Fan et al. synthesized a photochromic diarylethene moiety in 2021 which detects $Cu^{2+}$ through colour change and $Cd^{2+}$ through enhanced fluorescence intensity in $CH_3CN$-$H_2O$ (9:1, v/v).[47] Sooksimuang et al. in 2022 showed a tetrahydro-[5]helicine based fluorescent sensor which detects $Cd^{2+}$ in H2O/dioxane (1/19, v/v).[48] While Dong's group in 2022 reported a pyridine based Schiff base for detection of cadmium ion with a 'turn-on' fluorescence response and a LOD value of 0.12 μM in acetonitrile.[49] A phenazine-imidazole basedratiometric fluorescent probe was designed by Wang et al. to recognise $Cd^{2+}$ ion only in 2022, which showed limit of detection value of $2.10x10^{-8}$(M).[50] Although Schiff bases containing N,O,S donor binding with $Cd^{2+}$ with 2:1 stoichiometry are less known. Rajesh et al. in 2021 published a work consists of quinoline based Schiff base

detecting cadmium in semi aqueous medium with 2:1 stoichiometry and LOD value of 14.8 nM.[51]

# 4.3. Present work

Now in this present work, we have successfully designed and fabricated a simple, cost-effective biphenyl thiosemicarbazide based fluorescent "turn-on" reversible chemosensor which detects $Cd^{2+}$ with a detection limit of (1.59±.054) x $10^{-8}$(M), which is a pretty good value compared to many previous reports. Meanwhile the noteworthy aspects of the chemosensor (HBMC) are that it binds with cadmium ion with 2:1 stoichiometry in company of N, O, S donor site. Intracellular detection of $Cd^{2+}$ by our probe (HBMC) has also been successfully carried out.

# 4.4. Results and discussions

## 4.4.1. Design and synthesis of the receptor HBMC

The two-step synthesis process of our desired probe begins with formylation of 4-phenylphenol to obtain 4-hydroxy-[1,1'-biphenyl]-3-carbaldehyde, which has been done previously in our laboratory. Then the final step involved the reflux condensation of the aldehyde and 4-Methyl-3-thiosemicarbazide in ethanol for about 5 h, which yields the desired probe (Scheme 4.1). Different spectroscopic techniques namely $^{1}$H-NMR, $^{13}$C-NMR, mass spectral, IR and elemental analysis were employed for the characterization of probe HBMC (Fig. A4.1-A4.4, Appendix).

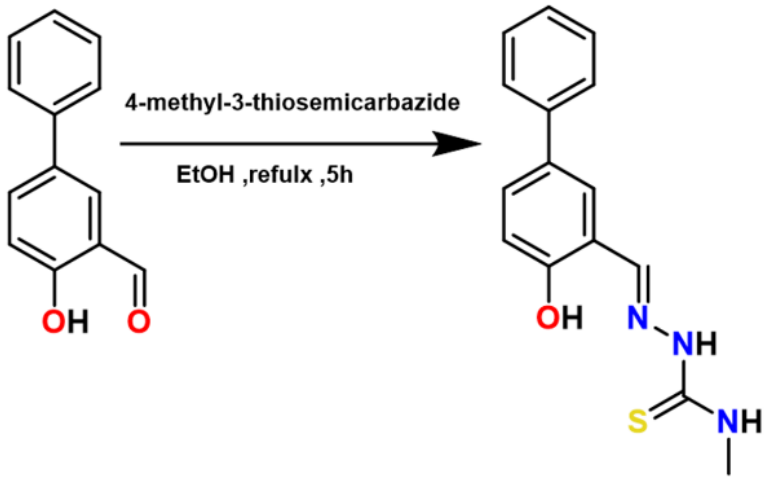


**Scheme 4.1:** Synthesis of the probe (HBMC). Reagents and conditions: 4-Methyl-3-thiosemicarbazide, reflux, 5h.

### 4.4.2. $^1$H-NMR and HRMS analysis of HBMC

We studied $^1$H-NMR titration of the probe (HBMC) upon addition of 1equivalent of $Al^{3+}$ in DMSO-$d_6$ solvent. From the NMR data, it was observed that the -OH peak arises at δ 11.46ppm and all the aromatic protons are observed in the expected region of 6.95-8.43 ppm. (See appendix). We have also studied the HRMS of HBMC. The HRMS of HBMC shows a peak at m/z 286.0868, probably for $[HBMC + H]^+$.

### 4.4.3. Binding studies of $Cd^{2+}$ with HBMC using UV-Vis spectroscopy

The photophysical study of the probe (HBMC) was carried out in MeOH/$H_2O$ (4/1, v/v, 10 mM HEPES buffer, pH = 7.2). The probe itself shows three absorption bands at 340 nm, 306 nm and 265 nm respectively. With gradual addition of $Cd^{2+}$ the probe colour changes from colourless to light yellow. In UV-Vis spectra we observe that a prominent band at ~396 nm appears and the two bands at 306 nm and 265 nm gradually vanishes and merges together to generate a new band near 276 nm (Fig. 4.1). Proportionately we also clearly observe two isosbestic point at 362 nm and 312 nm. The UV-Vis spectrum was also checked in presence of the other metal cations i.e., $Ca^{2+}$, $Mg^{2+}$, $Mn^{2+}$, $Fe^{3+}$, $Al^{3+}$, $Cr^{3+}$, $Zn^{2+}$, $Co^{2+}$, $Ni^{2+}$, $Cu^{2+}$, $Pb^{2+}$, $Mn^{2+}$ and $Hg^{2+}$, but they do not show any noteworthy change in the spectral pattern except $Cu^{2+}$ and $Hg^{2+}$(Fig. 4.1). In case of $Cu^{2+}$ we observe a bathochromic shift and a new band at 285 nm, whereas for $Hg^{2+}$ a band at 365 nm appears and hypsochromic shift in the absorption band is noted. This indicates that HBMC can form complex with these two metal ions.[52]

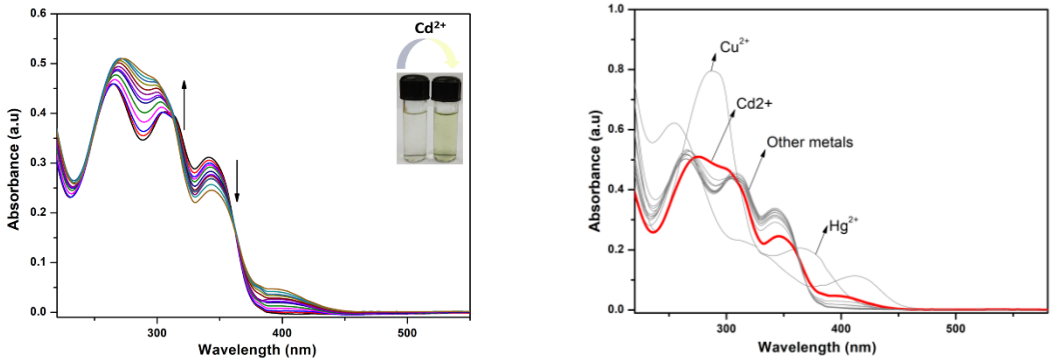


**Figure 4.1:** Change of absorption spectra of HBMC (20 µM) upon addition of $Cd^{2+}$ (40 µM). Inset: Photograph shows the visible colour change of HBMC before and after addition of $Cd^{2+}$ (40 µM) (left

side) and 40 μM various metal ions i.e., $Ca^{2+}$, $Mg^{2+}$, $Al^{3+}$, $Mn^{2+}$, $Fe^{3+}$, $Cr^{3+}$, $Co^{2+}$, $Ni^{2+}$, $Cu^{2+}$, $Zn^{2+}$, $Pb^{2+}$, $Cd^{2+}$ and $Hg^{2+}$ in MeOH/$H_2O$ (4/1, v/v, pH = 7.2) solution (right side).

### 4.4.4. Binding studies of $Cd^{2+}$ with HBMC using Fluorescence spectroscopy

The emission spectra of HBMC and its titration with $Cd^{2+}$ was studied in MeOH/$H_2O$ (4/1, v/v, 10 mM HEPES buffer, pH = 7.2). Upon excitation at 345 nm, we observe a very low fluorescence intensity at 402 nm and a very low quantum yield (ϕ = 0.024) for HBMC. Upon gradual addition of $Cd^{2+}$ to the free probe solution (20 μM) we observe a bathochromic shift in the fluorescence intensity from 402 nm to 496 nm (~94nm). Moreover, we noticed a drastic increase in fluorescence intensity at 496 nm in presence of $Cd^{2+}$, which is attributed to CHEF mechanism as shown in (Fig. 4.2). Consequently, the fluorescence quantum yield (ϕ = 0.508) also increased significantly compare to free probe, which indicates the formation of HBMC-$Cd^{2+}$ complex. Hence it can be noted that HBMC forms a stable chelate complex with $Cd^{2+}$, which in return effectively "turn-off" ESIPT mechanism, at the same time CHEF effect gets "turn on", which results a clear naked eye detection under UV light where we observe it changes from turn off to cyan colour.

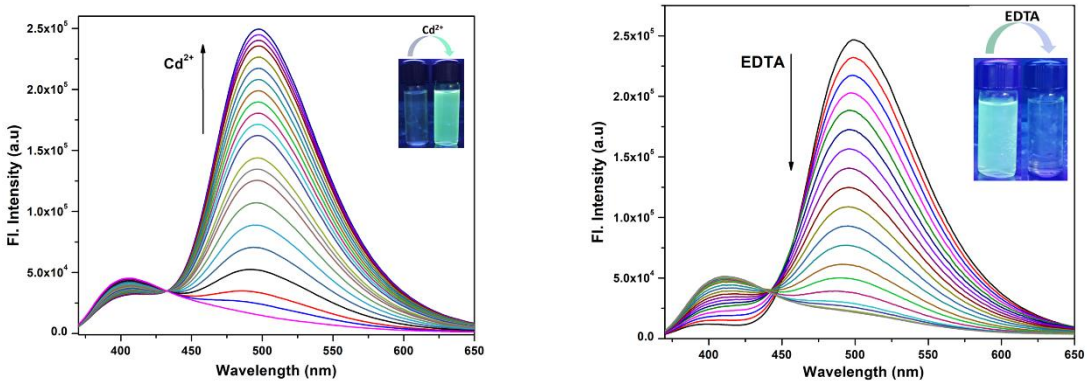


**Figure 4.2:** Change in emission spectrum of HBMC (20 μM) upon addition of $Cd^{2+}$ (40 μM) in MeOH/$H_2O$ (4/1, v/v, pH = 7.2) solution. Inset: The visual effect of addition of $Cd^{2+}$ to HBMC under UV light. $\lambda_{ex}$ = 345 nm (left side) and change in emission spectrum of HBMC-$Cd^{2+}$ complex (20 μM) upon gradual addition of EDTA (40 μM) in MeOH/$H_2O$ (4/1, v/v, pH = 7.2) solution, $\lambda_{ex}$ = 345 nm. Inset: The visual effect of addition of EDTA to HBMC-$Cd^{2+}$ solution under UV light (right side).

Reversibility is an important aspect for a probe to reuse it. Hence to examine reversibility of HBMC-$Cd^{2+}$ complex, a 20 µM solution of it was taken and gradually 40 µM solution of EDTA was added. We noticed that the fluorescence intensity at 496 nm is reverted back and finally we get a free probe like spectra, where there is no emission intensity at 496 nm and a very low intensity at 402 nm (Fig. 4.3) which suggests that HBMC is a reversible probe. EDTA being an excellent chelating ligand with high formation constant, replaces $Cd^{2+}$ from HBMC-$Cd^{2+}$ complex and forms Cd-EDTA complex. As only our free probe HBMC remains in the solution we observe the decrease in the fluorescence intensity. Hence reversibility of HBMC chemosensor is established.

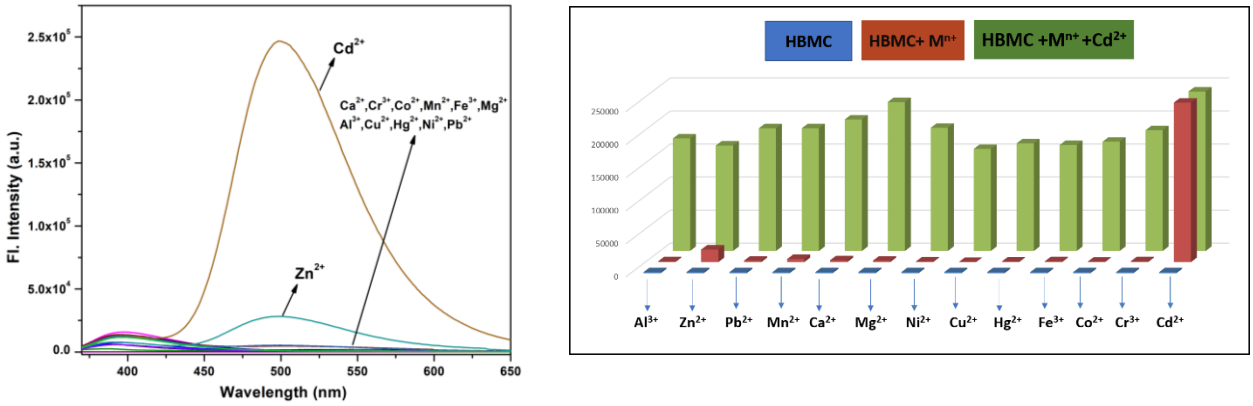


**Figure 4.3:** Change in emission spectrum of HBMC (20 µM) upon addition of different cations (40 µM) in MeOH/$H_2O$ (4/1, v/v, pH = 7.2) solution, $\lambda_{ex}$ = 345 nm (left side) and change in emission intensity upon addition of various metals (40 µM) in MeOH: $H_2O$ (4:1, v/v) (pH = 7.2). HBMC (blue bars), HBMC-other metals (brown bars), HBMC-$Cd^{2+}$ in presence of other metals (green bars). HBMC under UV light. $\lambda_{ex}$ = 345 nm, $\lambda_{em}$ = 496 nm (right side).

The emission property of HBMC was also studied in MeOH/$H_2O$ (1/1, v/v) solution (20 µM) to detect of $Cd^{2+}$, but we found that this composition of solvent is not as much sensitive as in the case for MeOH/$H_2O$ (4/1, v/v), so we have optimized the methanol water ratio and performed all spectroscopic studies in MeOH/$H_2O$ (4/1, v/v).

The selectivity of the chemosensor was also studied towards different metal ions (40 µM) such as $Cr^{3+}$, $Co^{2+}$, $Mn^{2+}$, $Fe^{3+}$, $Mg^{2+}$, $Al^{3+}$, $Zn^{2+}$, $Cu^{2+}$, $Hg^{2+}$, $Ni^{2+}$, $Ca^{2+}$, and $Pb^{2+}$ (Fig. 4.3). They display no change in the emission property except for $Zn^{2+}$ ion, which shows a slight

enhancement in emission intensity among other metal ions (Fig. A4.7, Appendix). This could be attributed to the same chemical properties of $Cd^{2+}$ and $Zn^{2+}$ ion.

Selectivity and sensitivity are two important aspects of a proficient chemosensor. Hence an efficient chemosensor must detect its guest precisely and rapidly in presence of other environmentally and biologically relevant interfering guests. So here comes competitive study, which is a major tool to determine whether the presence of other guest ions interfere or not for specific recognition of the target cation. For this reason, fluorescence property was studied in presence of other competing metal ions such as $Ca^{2+}$, $Cr^{3+}$, $Co^{2+}$, $Mn^{2+}$, $Fe^{3+}$, $Mg^{2+}$, $Cd^{2+}$, $Cu^{2+}$, $Hg^{2+}$, $Ni^{2+}$, $Zn^{2+}$ and $Pb^{2+}$. For this competitive binding experiment same concertation (40 µM) of other metals and $Cd^{2+}$ were used. Thus, it is noteworthy from the experiment that our probe HBMC is specific towards detection of $Cd^{2+}$. Other competitive metal ions do not interfere significantly except $Zn^{2+}$ and $Cu^{2+}$, which shows slight decrease in the fluorescence intensity profile (Fig. 4.3).

## 4.4.5. Binding studies of HBMC with $Cd^{2+}$

Limit of detection study is a handy tool to determine the efficiency of a chemosensor. LOD is calculated from the fluorescence spectral change data and the equation that is applied for the calculation is LOD = K × SD/S, where k=2 or 3 (here 3 is taken), SD denotes standard deviation of blank probe solution and S is slope in linear calibration curve respectively. The limit of detection is found to be very low (1.59±.054) $x10^{-8}$ (M) (Fig. 4.4) for $Cd^{2+}$. Which suggest our synthesized probe HBMC is highly efficient in detecting $Cd^{2+}$ in minuscule level. To disclose the binding stoichiometry of complex formation Job's plot analysis was carried out and emission intensity was measured, while sum of the total volume of HBMC and $Cd^{2+}$ was maintained to 5 ml, where relative change in intensity ($X_h$ x $\Delta I$) vs mole fraction ($X_h$) of probe HBMC was plotted. The relative intensity maximum was found to be near 0.66, which reveals 2:1 complexation for $Cd^{2+}$ ion with the probe HBMC (Fig. A4.5, Appendix). Again Benesi-Hildebrand plot was employed to determine the binding constant for HBMC with $Cd^{2+}$ from fluorescence titration data and it was calculated to be (72.85±2.9)$M^{-1/2}$ respectively (Fig. 4.4). Some of the reported chemosensors for $Cd^{2+}$ with their LOD values and testing media used are compared in (Table A4.5, Appendix).

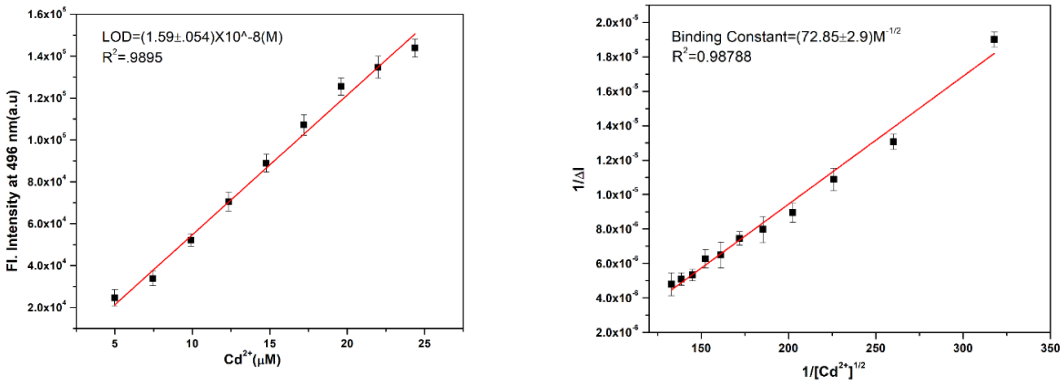


**Figure 4.4:** Linear response curve of HBMC at 496 nm depending on the $Cd^{2+}$ concentration. (left side) and Benesi-Hildebrand plot from fluorescence titration data of receptor (20 μM) with $Cd^{2+}$ (right side).

## 4.4.6. Fluorescence lifetime decay studies of HBMC with $Cd^{2+}$

Nano second time resolved fluorescence study is a handy tool to understand the excited state behaviour of the probe and its complex. Hence, we have taken the free probe and its $Cd^{2+}$ solution in MeOH:$H_2O$ (4;1, v/v) and performed the study. The equations $\tau^{-1} = k_r + k_{nr}$, where kr = $\phi_f/\tau$ (Table A4.1, Appendix) were employed to calculate the radiative rate constant ($k_r$) and the non-radiative rate constant ($k_{nr}$) of HBMC, HBMC-$Cd^{2+}$ Species. The fluorescence lifetime decay diagram is fitted by using bi exponential function for HBMC, HBTC-$Cd^{2+}$ with acceptable $\chi^2$ values (Fig. 4.5). For HBMC species the fluorescence life time was measured in MeOH:$H_2O$ (4:1, v/v) which was found very low, but after complexation with $Cd^{2+}$ we observed a significant increase in the lifetime value. For HBMC we calculated and found $\tau$ = 0.28 ns ($\chi^2$ = 0.97), while for HBMC-$Cd^{2+}$ the value increases to $\tau$ =1.58 ns ($\chi^2$ = 1.03). The increase in the lifetime value for complex is atributed to the increase in the radiative constant value simultaneously decrease in the nonradiative constant value (Table A4.1, Appendix). Hence, HBMC proves its credentials as a good sensor towards $Cd^{2+}$, where it gains its rigidity developing a “turn-on” CHEF effect.

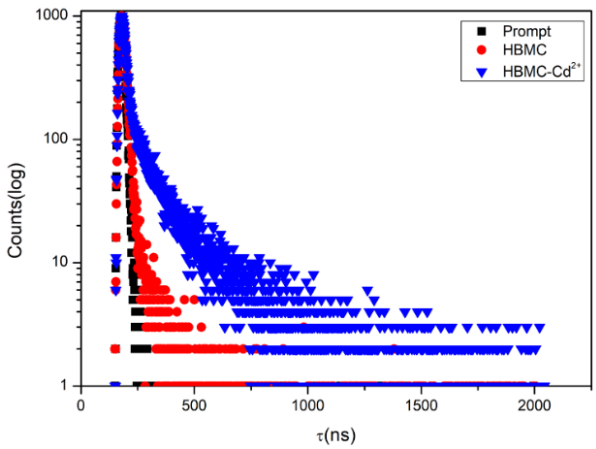


**Figure 4.5:** Time-resolved fluorescence decay of HBMC (●●●), HBMC-$Cd^{2+}$ (▲▲▲) ($\lambda_{ex}$ = 345 nm).

## 4.4.7. Reusability study

For real time application of a probe, it must show reusability, regenerability and reversibility of signal. For the accomplishment of reversibility, EDTA was used. The reversible detection of probe HBMC was proved by carrying out four reversible cycles with alternative addition of $Cd^{2+}$ to HBMC solution, followed by addition of EDTA. The experiment was carried out in MeOH-$H_2O$ system with excitation at 345 nm and fluorescence profile taken at 496 nm. It was observed that, when we add $Cd^{2+}$ solution to HBMC it gives a 'turn on' emission, while with further addition of the potent complexing agent EDTA, we observe a decrease in fluorescence intensity for HBMC at 496 nm, as $Cd^{2+}$ is removed from the solution resulting a free HBMC probe. Again, successive addition of $Cd^{2+}$ and EDTA an 'ON-OFF' switchable change in the fluorescence intensity was resulted due to crossover in equilibrium, assisted by $Cd^{2+}$ induced CHEF process and EDTA promoted decomplexation. Though the response is not 100% efficient every time, still the cycle can be repeated up to four times. The decrease in fluorescence intensity for HBMC-$Cd^{2+}$, attributed to the presence of excess EDTA in solution, which interfere in the complex formation due to its better chelating nature compared to HBMC. Hence the cycle in the (Fig. 4.6) exemplifies that our synthesized probe HBMC can be used for hands-on experimental detection of $Cd^{2+}$ in real sample with regeneration and reuse.

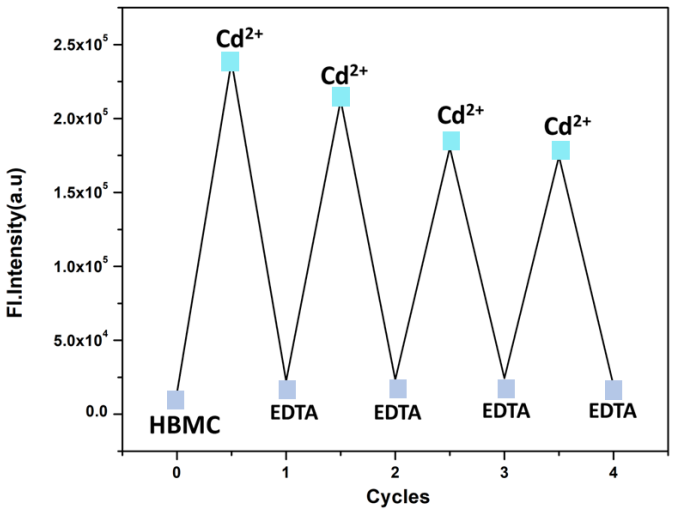


**Figure 4.6:** Reversibility pattern of the fluorescence profile at 496 nm ($\lambda_{ex}$= 345 nm) upon repetitive addition of $Cd^{2+}$ and EDTA.

## 4.4.8. Effect of pH

To investigate the pH dependence of our synthesized probe we have analysed pH sensitivity in absence and in presence of $Cd^{2+}$ion. The experiment was done in MeOH: $H_2O$ (4:1, v/v) solution, where the pH range was kept between (2.0-12.0) and the solution of probe HBMC with $Cd^{2+}$ was prepared separately. For the free receptor we found that fluorescence emission property remains almost unchanged from pH 2-7 after that with increase in pH (>8) we observe a slight increase in fluorescence value, presumably owing to deprotonation of -OH proton. On the other hand, in presence of $Cd^{2+}$ we observe a large increase in emission intensity at 496 nm in the pH range of 2-12. But highest emission occurs approximately near pH 7.0 for HBMC-$Cd^{2+}$ solution. In strong acidic condition pH>5, we observe less fluorescence intensity due to protonation of oxygen and nitrogen binding sites present in probe. Then a decrease in the emission for HBMC-$Cd^{2+}$ was noticed at higher pH (>7) which is attributed to formation of $Cd(OH)_2$ in the solution, simultaneously decreasing the HBMC-$Cd^{2+}$ concentration and generating free probe. Based on this experimental result, we can conclude that our probe can detect $Cd^{2+}$ from pH range 6-9, which indicates that the probe HBMC can be a competent candidate for the substantial detection of $Cd^{2+}$ at physiological pH (7.2) (Fig.4.7).

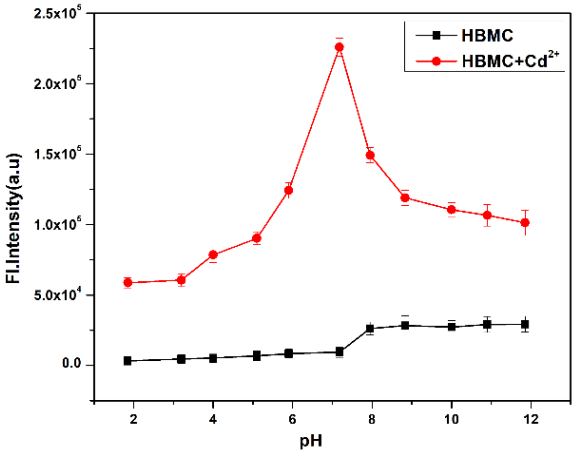


**Figure 4.7:** Fluorescence response of HBMC (-■-■-) and HBMC-$Cd^{2+}$ (-●-●-) as a function of pH in MeOH/$H_2O$ (4/1, v/v), pH is adjusted by using aqueous solutions of 1 (M) HCl or 1 (M) NaOH. $\lambda_{em}$ = 496 nm.

## 4.4.9. Time course of sensing

Time dependent study is a handy tool to check the kinetic stability. Hence fluorescnce spectrum was recorded for 90 senonds to a 20 µM solution of HBMC with different concentration (5 µM, 10 µM, 15 µM) of $Cd^{2+}$. Again, to carry out real time application a rapid sensing probe is necessary. Now from the (Fig. 4.8) we observe that our synthesized probe HBMC detects $Cd^{2+}$ instantly within (less than 5 seconds) and attains stability.

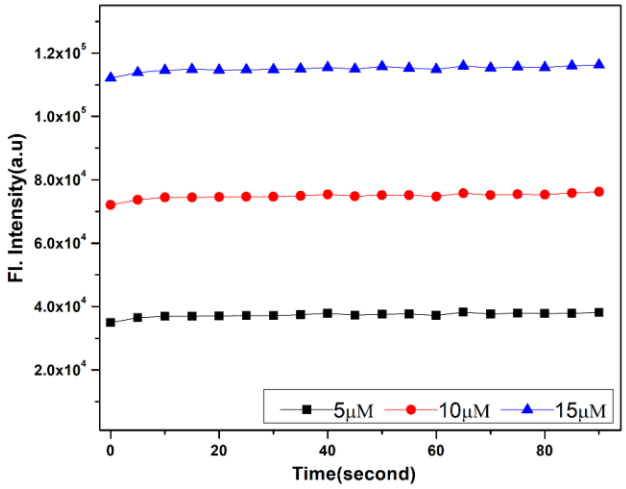


**Figure 4.8:** Time dependentl fuorescence response of HBMC (20 µM) with different concentrations of $Cd^{2+}$ (5-15 µM) in MeOH/$H_2O$ (4/1, v/v, pH = 7.2).

Again, photostability is an important issue relating to the fluorescent based sensors due to their high detecting power and to provide constant analytical signals. Generally, biphenyl-based sensors are known for their photostability due to their pi electron system resulting high quantum yield value.[53] So it is necessary that this type of system must be highly photostable and must show consistent analytical signals. Hence here we have performed the photostability study for HBMC and HBMC-$Cd^{2+}$ for 30 minutes in daylight condition (Fig. 4.9). We observe that fluorescence intensity does not alter much (less than 5%) for HBMC-$Cd^{2+}$ complex. Hence, we can conclude that HBMC shows highly photostable 'turn-on' fluoresce response towards $Cd^{2+}$ making it a reliable probe for prompt detection of $Cd^{2+}$ and for fluorometric analysis in real samples.

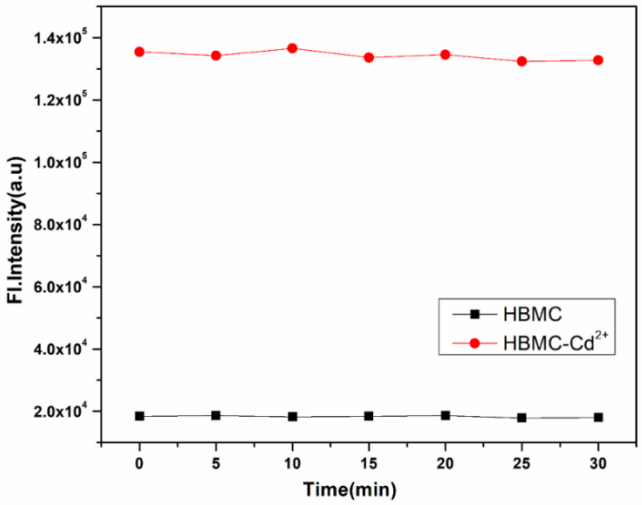


**Figure 4.9:** Photostability study in MeOH: $H_2O$ (4:1, v/v) pH=7.2.

## 4.4.10. Probable sensing mechanism of $Cd^{2+}$ sensing

For a non-fluorescent probe, the mechanisms that works behind its non-emissive nature are excited state intra molecular proton transfer (ESIPT) and C=N isomerization. Thus, in case of HBMC also these are the reasons for its non-fluorescent property (Fig. 4.11). While when it binds with $Cd^{2+}$ then both these mechanisms got restricted and concurrently chelation enhanced fluorescence (CHEF) mechanism gets a "turn-on" signal, which is accountable for the amplification of its fluorescence profile (Fig. 4.10).

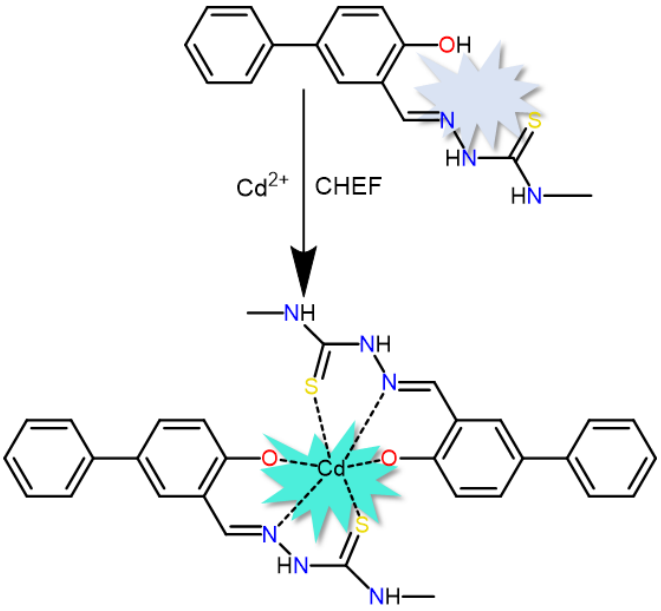


**Figure 4.10:** Probable binding mode of HBMC with $Cd^{2+}$.

Venkatesan et al. reported a zinc sensor in 2019 which showed the similar sensing mechanism reported in our work[54]. Also in 2016, Torawane et al. published a work of "turn-on" $Al^{3+}$ sensor which includes CHEF and C=N isomerization as the sensing mechanism[55].

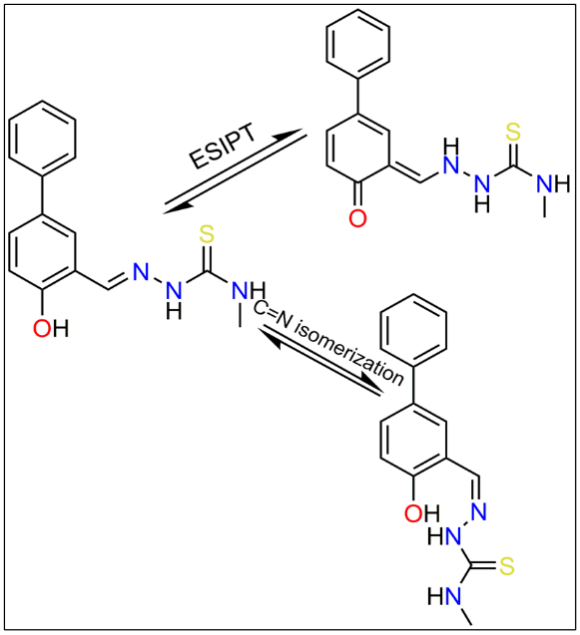


**Figure 4.11:** Probable ESIPT effect and isomerisation effect; cause of very weak emission of Probe HBMC.

Again, the Binding mechanism of the probe and $Cd^{2+}$ was studied by jobs plot to determine the exact stoichiometry of complex formation, where we observed a maximum near 0.66, which suggests a 2:1 complex formation of HBMC and $Cd^{2+}$ (Fig. A4.5, Appendix). The experiment was carried out in MeOH/$H_2O$ (4/1, V/V) with change in emission at 496 nm. The mass spectrum also supports this 2:1 complex formation where we found a peak at 682.9818 (Fig. A4.6, Appendix). Further the coordination mechanism was studied through NMR titration, by addition of $Cd^{2+}$ in HBMC solution in DMSO-$d_6$ medium. The free probe displayed δ -OH peak at 11.46 ppm, -NH peak at 10.08 ppm, the imine CH peak at 8.52 ppm and there are aromatic protons ranging from 8.43 to 6.96 ppm. Upon addition of $Cd^{2+}$ we observe that the -OH peak disappears slowly and the peaks of -NH and N=CH moves towards lower field region i.e., we observe a downfield shift (Fig. 4.12). This clearly implies that the binding sites of probe are oxygen -OH group and nitrogen of N=CH group. The -OH group which results the ESIPT, after binding with $Cd^{2+}$ this ESIPT of HBMC get ceases due to dissociation of proton. Based on this NMR titration, HRMS data and jobs plot analysis we have proposed an interaction model which is shown in Fig. 4.10.

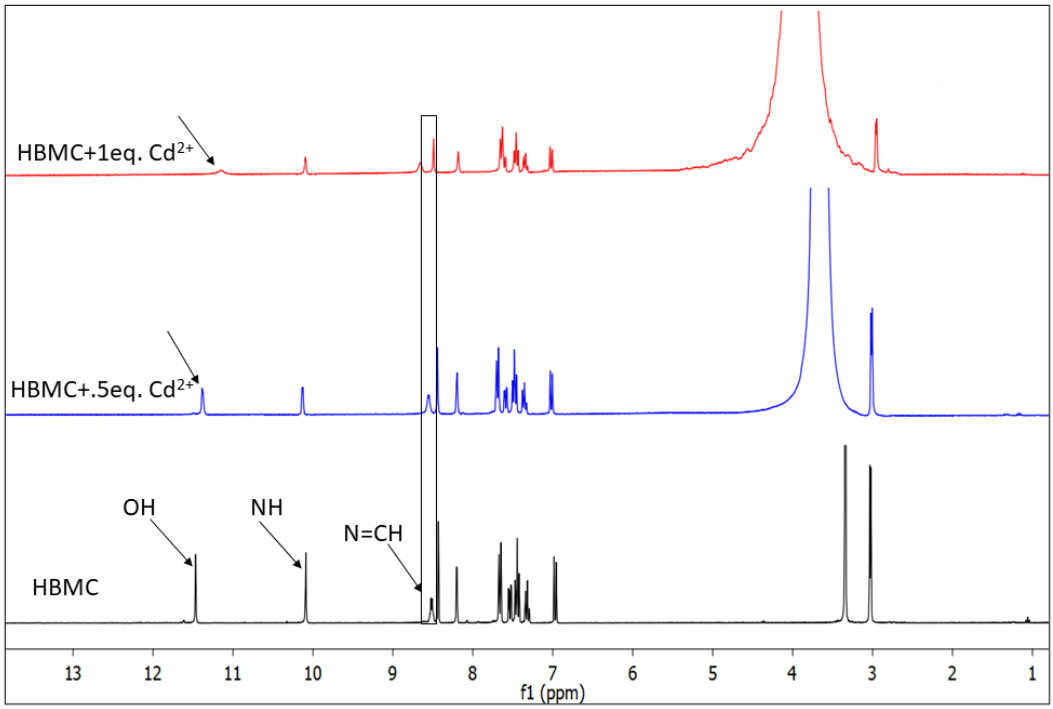


**Figure 4.12:** Changes in $^1H$ NMR spectra of HBMC with various concentration of $Cd^{2+}$.

### 4.4.11. Dip-stick experiment: Sensing of $Cd^{2+}$ using TLC plate

Encouraged by the distinct detection of $Cd^{2+}$ion by HBMC, we decided to make a usable tool, to increase its potential application as a chemosensor. Here we have accomplished a rational analytical technique known as dipstick method. This experiment reveals the sensing ability of probe detecting a particular metal ion in solid state too. Here without support of any kind of instrumentation technique we get a qualitative result about the binding of $Cd^{2+}$ with our probe HBMC. Hence in order to carry out this experiment we prepared thin-layer chromatography (TLC) plates immersed in the solution of HBMC in MeOH ($2\times10^{-4}$ M) and then kept aside for few minutes to evaporate the solvent. Followed by this, the TLC plates were immersed in $Cd^{2+}$ ($2\times10^{-3}$ M) solution and again kept open in the air to evaporate the solvent in order to dry out the plates. Now the experiment reveals the colour change of the TLC plates in ambient light as well as under UV light as shown in Fig.4.13. Under ambient light we observe that the TLC plates changes its colour from colourless to light brown and under UV light it changes from blue to cyan. Hence this dipstick experiment concludes that, without aid any instrumental analysis, barely using TLC plates a convenient test kit can be made, through which naked eye prompt detection of $Cd^{2+}$ can be investigated.

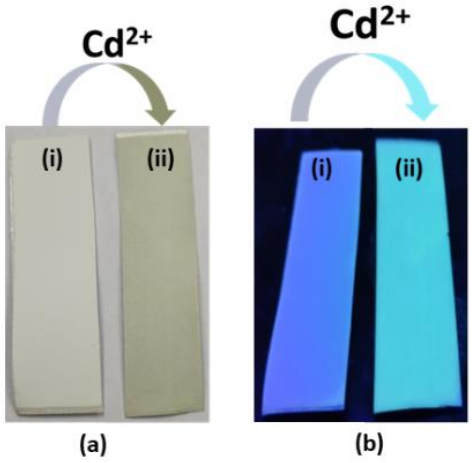


**Figure 4.13:** Photographs of TLC plates after immersion in HBMC-methanol solution (i) and after immersion in HBMC-$Cd^{2+}$ methanol solution (ii) taken in ambient light (a) and under UV light (b) Excitation wavelength of the UV light is 345 nm.

## 4.4.12. Cellular imaging by fluorescence microscopy

The cytotoxicity of HBMC, $Cd^{2+}$-salt, HBMC-$Cd^{2+}$ was examined on human breast cancer cell lines (MDA- MB231) by MTT method for bio imaging study. Cell viability represented in Fig.4.14, indicates that from 1-200 µM concentration of HBMC shows high number of viable cells, which signifies that HBMC is safe to use in a biological system, although cell has lower survivability in higher concentration.

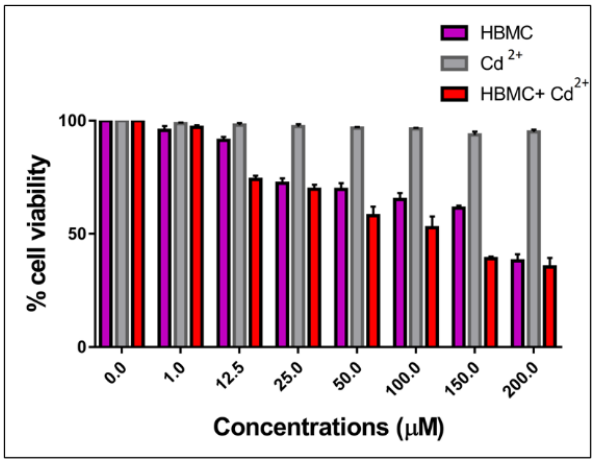


**Figure 4.14:** MTT assay of HBMC and HBMC-$Cd^{2+}$complex on breast cancer cell lines (MDA-MB231).

The $IC_{50}$ value of the probe was found to be 141.3 µM (Fig. 4.15). So, the dosage for the experiment was chosen to be 15 µM, as the amount of dosage should be less than $IC_{50}$ value.

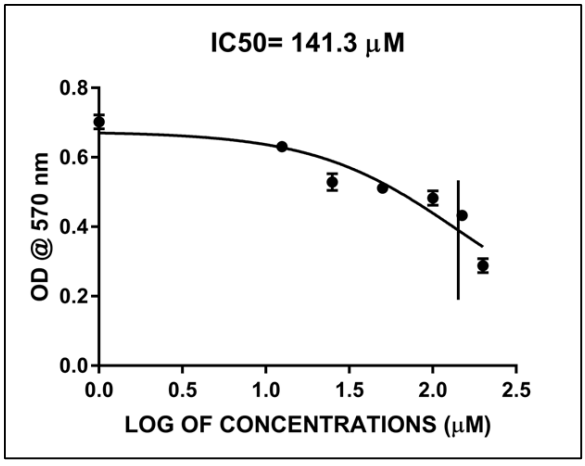


**Figure 4.15:** $IC_{50}$ dose of the receptor HBMC in breast cancer cell lines (MDA-MB231) cells was calculated to be 141.3 µM.

The MTT assay demonstrates that HMBC has a modest influence on cell viability at low doses when tested against human breast cancer (MDA-MB-231) cell lines, but at high concentrations (75 µM), HBMC had no effect on cell viability at all (Fig. 4.16). Because the $IC_{50}$ value of HBMC was discovered to be 141.3 µM, we decided that the dose for the experiment should be 15 µM because the chosen dose should be lower than the $IC_{50}$ value (Fig. 4.15). Now, the fluorescence imaging study revealed that the treatment of breast cancer cells with HBMC itself does not show any fluorescence. However, when the MDA-MB-231 cells were incubated with 15 µM of $Cd^{2+}$ and HBMC, a bright greenish fluorescence was observed in the intracellular region of the cells (Fig. 4.16). Therefore, we can draw a conclusion from the observation by pointing out the fact that the probe HBMC, is able to easily pass through the cell membrane in order to bond with the $Cd^{2+}$ that is found inside the cell. In addition, after incubation with $Cd^{2+}$, no discernible morphological change can be seen in the cells when they are viewed in bright field, indicating that the MDA-MB-231 cells are still capable of surviving and that the dose of HBMC used was not harmful.

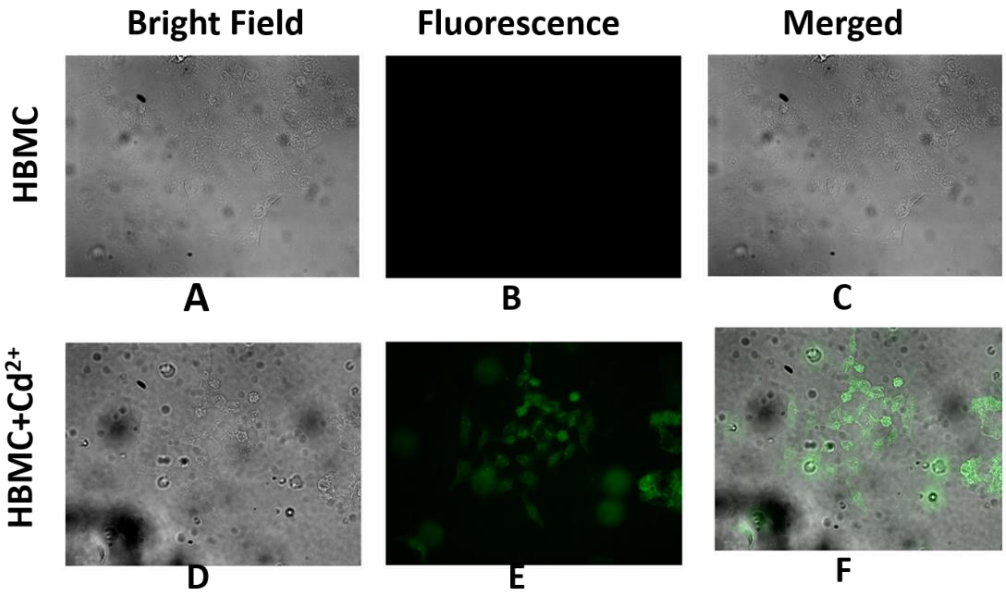


**Figure 4.16:** (A) Bright field image of (MDA- MB231) cells after incubation with 15 µM HBMC, respective fluorescence image (B), merged field (C). (D) Bright field image of (MDA- MB231) cells after incubation with 15 µM of HBMC and 15 µM of $Cd^{2+}$ and its respective fluorescence image (E) as well as merge field (F). Incubation period was 12h in each case.

### 4.4.13. Real water sample analysis

In order to further establish the reliability of our designed chemosensor HBMC, real water sample analysis was carried out. Hence actual water sample was collected from Jadavpur university campus lake water and tap water (from laboratory), which were further analyzed according to previously reported procedure. [56,57] First of all, the water samples collected were filtered by using whatman no.1 filter paper to remove the suspended particles. Then $Cd^{2+}$ was added into the real water samples with different concentration gradient. To obtain the standard curves, $Cd^{2+}$ was dissolved in deionized water to prepare samples with different concentrations. The fluorescence spectra of HBMC (20 µM) with different concentration of $Cd^{2+}$ under excitation of 345 nm was measured. The experimental data is well tabulated in Table 4.1, where the Recover (%) is calculated. It was observed that the recovery % for $cd^{2+}$ lies in the range between 97.25% to 102.25%. Which reveals that HBMC is potent enough for analysing $Cd^{2+}$ in real water systems.

**Table 4.1:** Application in practical samples for the detection of $Cd^{2+}$

| Samples | $Cd^{2+}$ added(µM) | $Cd^{2+}$ determined(µM) | Recovery (%) |
|---|---|---|---|
| Jadavpur university campus lake water | 8 | 7.78 | 97.25 |
| | 10 | 10.09 | 100.9 |
| | 12 | 12.17 | 101.41 |
| Tap water | 8 | 7.86 | 98.25 |
| | 10 | 9.87 | 98.7 |
| | 12 | 12.27 | 102.25 |

### 4.4.14. Computational studies to interpret further structural changes in HBMC and HBMC-$Cd^{2+}$

To get further insight the relationship of structural change of HBMC and its complex with $Cd^{2+}$ we performed density functional theory (DFT) and time-dependent density functional theory

(TDDFT) calculations with the B3LYP/6-31+G(d) method basis set using the Gaussian 09 program. The optimized geometry and the contour plots of different molecular orbitals of HBMC and HBMC-$Cd^{2+}$ complex are presented in Fig. 4.17 and Fig. A4.10, Fig. A4.11, Appendix. Electronic excitations of HBMC and HBMC-$Cd^{2+}$ complex were calculated in methanol medium using TDDFT method. We observe that calculated absorption peak matches well with observed peak. For probe HBMC, the transition from HOMO→LUMO, HOMO-2→LUMO and HOMO-3→LUMO transitions are mainly contributed for the absorption at 354 nm, 307 nm and 281 nm respectively (Table A4.3, Appendix). Whereas for HBMC-$Cd^{2+}$ complex the absorption peak at 400 nm and 286 nm correspond to HOMO-1→LUMO and HOMO-1→LUMO+2/LUMO+3 transitions (Table A4.4, Appendix).

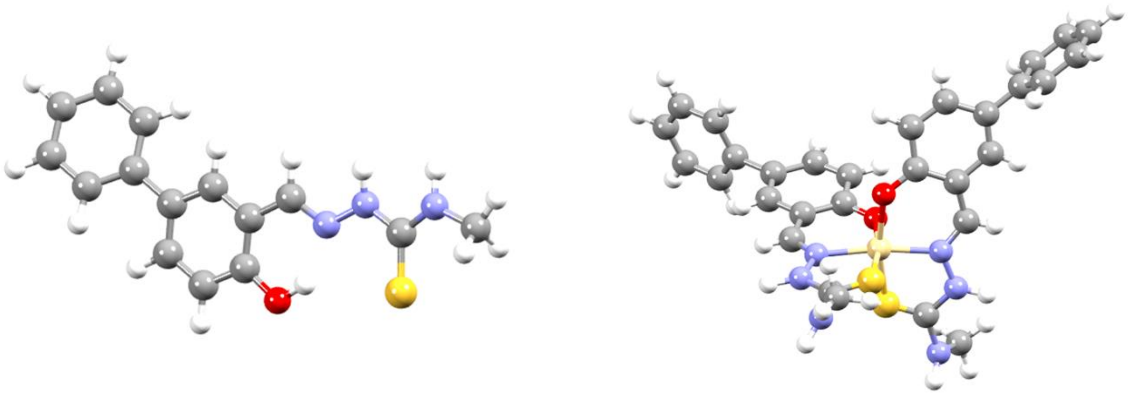

**a** **b**

**Figure 4.17:** Optimized structures of **(a)** HBMC and **(b)** HBMC-$Cd^{2+}$ calculated by DFT/B3LYP/6-31+G(d) method.

# 4.5. Conclusions

In conclusion, we have successfully designed and synthesized a fluorescent probe based on biphenyl thiosemicarbazide based moiety, which is capable to detect $Cd^{2+}$ over other cations in MeOH/$H_2O$ (4/1, v/v, pH = 7.2, 10 mM HEPES buffer). Continuous addition of $Cd^{2+}$ exhibits significant increase in the fluorescence intensity accompanied by red shift in the emmision spectrum. Binding with $Cd^{2+}$ is attributed to, simultenious prohibition of ESIPT effect and C=N isomerization and switching on the CHEF mechanism. Where the absorption, fluorescence, NMR titration and HRMS data assisted the complex formation. In presence of $Cd^{2+}$ the quantum yeild value increases upto 21 fold which is reflected on the acceptable binding constant value.

Again, this ESIPT and CHEF based chemosensor is very selective towards $Cd^{2+}$ over other analytes with very low limit of detection in the order of $10^{-8}$ (M) in MeOH-$H_2O$ medium. The practical application of our synthesized probe is disclosed by dip stick experiment as well as bio imaging study where intracellular detection of poisonous $Cd^{2+}$ in MDA-MB231 cells was performed. Again, the non-toxic nature of HBMC when cultured for 24 h in MDA-MB231 holds an engrossing prospect in analytical and biomedical application. Probable binding mode and energy calculations were further carried out by DFT and TDDFT calculations. Hence these promising characteristics of our probe enlisted above, endow HBMC as a competent candidate for $Cd^{2+}$ sensing.

# 4.6. Experimental

## 4.6.1. Reagents and methods

All the organic, inorganic materials and solvents used for the experiment were purchased from commercial suppliers. 4-Methyl-3-thiosemicarbazide and 4-phenylphenol were purchased from Sigma Aldrich and used without further purification. HRMS mass spectra were recorded on Waters (Xevo G2 Q-TOF) mass spectrometer. $^1H$ and $^{13}C$ NMR spectra were recorded by Bruker (AC) 400 MHz NMR instrument of ~0.05 M solutions in DMSO-$d_6$ solvent and TMS was used as internal standard. Thin layer chromatography (TLC) and dip-stick experiment was carried out on Merck 60 $F_{254}$ plates with 0.25 mm of thickness. UV-Vis spectra were recorded on a Shimadzu UV-1900i spectrophotometer. Fluorescence property was studied using Shimadzu RF-6000 fluorescence spectrophotometer at room temperature (298 K). Luminescence lifetime measurements were carried out by using time-correlated single photon counting set up from Horiba Jobin-Yvon. The fluorescence decay data were placed on a Hamamatsu MCP photomultiplier (R3809) and analyzed using IBH DAS6 software. Infrared spectra were taken on a RX-1 Perkin Elmer spectrophotometer where samples prepared as KBr pellets. Elemental analysis was performed in a 2400 Series-II CHN analyzer, Perkin Elmer, USA.

## 4.6.2. Synthesis of probe (E)-2-((4-hydroxy-[1,1'-biphenyl]-3-yl) methylene)-N-methylhydrazine-1-carbothioamide (HBMC)

At first to the suspension of 4-hydroxy-[1,1'-biphenyl]-3-carbaldehyde (0.200 g, 1 mmol) in 10 ml of ethanol, 4-methyl-3-thiosemicarbazide (0.105 g, 1 mmol) was added with continuous

stirring. Then the reaction mixture was refluxed for 5 h. We observe a light-yellow color precipitate in the reaction medium. Then the reaction mixture was allowed to cool at room temperature. The light-yellow color precipitate obtain was then filtered and washed with ethanol for few times. Lastly, the product was dried in vacuum and collected. Yield: (0.242 g) 85%.

**Anal. data for $C_{15}H_{15}N_3OS$ (HBMC):**

**Elemental analysis**: Anal. Calculated for $C_{15}H_{15}N_3OS$, C, 63.13%; H, 5.30%; N, 14.73%. Found C, 63.44 %; H, 5.22%; N, 13.45 %.

**$^1$H NMR data (300 MHz, DMSO-$d_6$)**: **)**: δ(ppm): 11.46 (s, 1H), 10.08 (s, 1H), 8.52 (s, 1H), 8.43(s, 1H), 8.20 (s, 1H), 7.66 (d, 2H, J=9), 7.53 (d, 1H, J=8.49), 7.44 (t, 2H, J=7.32), 7.31 (t, 1H, J=7.32), 6.96 (d, 1H, J=8.49), 3.03(s, 3H).

**$^{13}$C NMR (75 MHz, DMSO-$d_6$):** δ(ppm): 175.89, 157.44, 147.90, 139.95, 138.08, 132.69, 131.99, 130.17, 129.40, 127.34, 126.64, 119.65, 117.49, 25.27.

**HRMS:** MS-ES$^+$ (m/z): $[M+H]^+$: $C_{15}H_{15}N_3OS$ Calculated: 286.1, Found: $[M+H]^+$; 286.08.

**IR (cm$^{-1}$, KBr):** υ(C=N) 1650, υ(O-H) 3450, υ(N-H) 3152.

## 4.6.3. General Method for UV-Vis and Fluorescence Titration

### 4.6.3.1. UV-Vis Study

For UV-Vis titrations study, we prepared stock solution of the probe (20 μM) [($MeOH/H_2O$), 4/1, *v/v*] (at 25 °C) solution using HEPES buffer. Again, stock solutions of the guest cations were prepared separately in the order of 40 μMin deionized water using HEPES buffer at pH=7.2 (25 °C). The solutions of the respective metal ions were prepared using their perchlorate and chloride salts respectively in deionized water. Solutions of different concentrations containing the probe and various increasing concentrations of cations were prepared separately. These solutions were prepared individually to record UV-Vis spectra.

### 4.6.3.2. Fluorescence Method

For fluorescence titrations, the probe stock solution (20 μM) was same as that used for UV-Vis titration study. The solutions of the guest cations with their chloride and perchlorate salts were prepared in the order of 40 μM. Solution of EDTA (40 μM) was prepared using its disodium salt. Solutions of different concentration of probe and metal salts were prepared separately and spectra were recorded by means of fluorescence method. The emission spectrum was recorded at ($\lambda_{ex}$= 345 nm, excitation slit = 10.0 and emission slit = 10.0).

### 4.6.3.3. Job's Plot by Fluorescence Method

Jobs plot analysis was carried out using fluorescence emission spectrum. A series of solution of various concentration were prepared by using HBMC (10 µM) and $Cd^{2+}$ (10 µM) maintaining a total volume of each solution to 5ml.The solutions were prepared in MeOH-$H_2O$ (4:1, v/v) solvent at pH=7.2 using 10 mM HEPES buffer. Emission spectrum was recorded by using excitation at 345 nm. $\Delta I.X_h$ versas $X_h$ was plotted. ($\Delta I$ denotes the change in emission intensity at 496 nm during titration and $X_h$ is the mole fraction of host solution in each case).

### 4.6.3.4. Determination of association constant

Binding constant was calculated according to the Benesi-Hildebrand equation. $K_a$ was calculated following the equation stated below.

$$1/(F-F_0) = 1/\{K_a(F_{max}–F_0)\,[M^{n+}]^x\} + 1/[F_{max}-F_0]$$

Here $F_0$, F and $F_{max}$ indicate the emission in absence of, at intermediate and at infinite c Plot of $1/[F-F_0]$ vs. $1/[Cd^{2+}]^{1/2}$ gives a straight line indicating 2:1 complexation between HBMC and $Cd^{2+}$ where $K_a$ is found to be (72.85±2.9) $M^{-1/2}$ for HBMC concentration of metal ion respectively.

### 4.6.3.5. Determination of detection limit (LOD) for $Cd^{2+}$

The detection limit was calculated based on the fluorescence titration. To determine the S/N ratio, the emission intensity of HBMC without the ion ($Cd^{2+}$) was measured by 10 times and the standard deviation of blank measurements was determined. The detection limit of HBMC for $Cd^{2+}$ was determined from the following equation: $DL = K \times Sb_1/S$ Where K = 2 or 3 (we take 3 in this case); $Sb_1$ is the standard deviation of the blank solution; S is the slope of the calibration curve. Thus, using the formula, we get the Detection Limit = (1.59±.054) $\times 10^{-8}$ (M) i.e., HBMC can detect $Cd^{2+}$ in this minimum concentration by fluorescence techniques.

### 4.6.3.6. Determination of fluorescence quantum yield

The luminescence quantum yield was determined using coumarin 153 as reference dye. The compounds and the reference dye were excited at the same wavelength, maintaining nearly equal absorbance (~0.1), and the emission spectra were recorded. The area of the emission spectrum was integrated using the software available in the instrument and the quantum yield is calculated according to the following equation:

$$\phi_S/\phi_R = [A_S / A_R] \times [(Abs)_R /(Abs)_S] \times [n_S^2/n_R^2]$$

where, $\phi_S$ and $\phi_R$ are the luminescence quantum yields of the sample and reference, respectively. $A_S$ and $A_R$ are the area under the emission spectra of the sample and the reference respectively, $(Abs)_S$ and $(Abs)_R$ are the respective optical densities of the sample and the reference solution at the wavelength of excitation, and $n_S$ and $n_R$ are the values of refractive index for the respective solvent used for the sample and reference.

We calculated the quantum yields of HBMC and HBMC-$Cd^{2+}$ using the abovementioned equation; the values are found 0.024and 0.508respectively.

## 4.6.4. Live cell imaging studies

### 4.6.4.1. MTT assay

According to the protocol outlined by Hamdi et al., a cell cytotoxicity experiment was carried out on the triple negative breast cancer cell line MDA MB-231 using Cadmium perchlorate ($Cd^{2+}$), HBMC, and HBMC-$Cd^{2+}$ complex. MDA MB-231 cells were seeded at a density of 5 × $10^3$ cells per well in a 96 well plate, then incubated at 37°C for 24 hours in a 5% $CO_2$ atmosphere. Individual doses of free HBMC, $Cd^{2+}$, and HBMC - $Cd^{2+}$ complex (0, 1, 12.5, 25, 50, 100, 150, 200 µM) were given to the cells for 24 hours, along with a control. The probe HBMC was dissolved in DMSO, whereas $Cd^{2+}$ was used by dissolving it in an aqueous medium while keeping the final DMSO concentration below 1%. After 24 hours of treatment, 10 µl of MTT solution (5 mg/ml) was added to each well. The plates were then placed in a $CO_2$ incubator at 37 °C for 3 hours while kept in the dark. In order to dissolve the formazan crystals, 100 µl of DMSO was added to each well, and the plates were agitated quickly before being scanned by a multi-mode reader and quantified at 570 nm (SpectraMax i3x, Molecular devices). The half-maximal inhibitory concentration ($IC_{50}$) of HBMC was calculated by fitting a non-linear regression curve from log HBMC concentration to optical density at 570 nm.

### 4.6.4.2. Cell bio-imaging

MDA-MB-231 cells were seeded and left to adhere overnight on a six well plate containing 22×22 mm glass cover slips positioned at the bottom of each well. In addition to a control, 15 µM of the probe, HBMC, and HBMC-$Cd^{2+}$ complex were added to each well containing cells. The cells were then fixed with methanol and rinsed with 0.5% phosphate buffer saline tween (PBST) twice, followed by 1 × PBS three times. The cover slips were then put on a glass slide

with glycerol and viewed at 40x magnification using a fluorescence microscope (Leica DM4000 B, Germany).

### 4.6.5. Computational method

For computational method Gaussian 09 (G09) program along with Gauss View visualization program was employed.[59] Geometry optimization were carried out at B3LYP level for the probe and its Cd complex.[60,61] All elements except Cd were used the 6-31+G(d) basis set, whereas for Cd, Lanl2dZ basis set with the effective core potential (ECP) of Hay and Wadt was used.[62,63] Again, the vibrational frequency calculations were performed to ensure the optimized geometries represents local minima and there were only positive eigen values. The Vertical electronic excitations which were based on B3LYP optimized geometries were computed using the time-dependent density functional theory (TDDFT) formalism[64-66] in methanol using the conductor-like polarizable continuum model (CPCM).[67-69]

## 4.7. Notes and references


1. P. B. Tchounwou, C. G. Yedjou, A. K. Patlolla and D. J. Sutton, *Molecular Clinical and Environmental Toxicology*, 2012, **101**, 133.
2. F. U. Haider, C. Liqun, J. A. Coulter, S. A. Cheema, J. Wu, R. Zhang, M. Wenjun and M. Farooq, *Ecotoxicol. Environ. Saf.*, 2021, **211**, 111887.
3. G. Genchi, M.S. Sinicropi, G. Lauria, A. Carocci and A. Catalano, *Int. J. Environ. Res. Public Health*, 2020, **17**, 3782.
4. T.L. Roberts, *Procedia Eng.*, 2014, **83**, 52.
5. F. Pinot, S.E. Kreps, M. Bachelet, P. Hainaut, M. Bakonyi and B.S. Polla, *Rev. Environ. Health*, 2000, **15**, 299.
6. A. Kubier, R.T. Wilkin and T. Pichler, *Appl. Geochem.*, 2019, **108**, 104388.
7. M.A. Khan, S. Khan, A. Khan and M. Alam, *Sci. Total Environ.*, 2017, **601**, 1591.
8. W. De Vries, P. F. Romkens and G. Schutze, *Rev. Environ. Contam. Toxicol.*, 2007, **191**, 91.
9. J. Godt, F. Scheidig, C. Grosse-Siestrup, V. Esche, P. Brandenburg, A. Reich and D.A. Groneberg, *J. Occup. Med. Toxicol.*, 2006, **1**, 1.
10. A. Navas-Acien, E. Selvin, A. R. Sharrett, E. Calderon-Aranda, E. Silbergeld and E. Guallar, Circ. J., 2004, **109**, 3196.
11. Agency for Toxic Substances and Disease Registry, 4770 Buford Hwy NE, Atlanta, GA 30341. http://www.atsdr.cdc.gov/cercla/07list.html.

12. (a) United States Environmental Protectioin Agency, http://water.epa.gov/drink; (b) World Health Organization, Avenue Appia 20, 1211 Geneva 27, Switzerland. http://www.who.int/water_sanitation_health/dwq/chemicals/cadmium/en/
13. A. Åkesson, B. Julin and A. Wolk, *Cancer Res.*, 2008, **68**, 6435
14. G. Jiang, L. Xu, S. Song, C. Zhu, Q. Wu, L. Zhang and L. Wu, *Toxicology*, 2008, **244**, 49.
15. V. Violaine, L. Dominique and H. J. Philippe, *J. Toxicol. Environ. Health, Part A*, 2003, **6**, 227.
16. J. Huff, R.M. Lunn, M.P. Waalkes, L. Tomatis and P.F. Infante, *Int. J. Occup. Environ. Health*, 2007, **13**, 202.
17. J. A. McElroy, M. M. Shafer, A. T. Dietz, J. M. Hampton and P. A. Newcomb, *J. Natl. Cancer Inst.*, 2006, **98**, 869.
18. M. Waisberg, P. Joseph, B. Hale and D. Beyersmann, *Toxicology*, 2003, **192**, 95.
19. M. P. Waalkes, *J. Inorg. Biochem.*, 2000, **79**, 241.
20. A. Åkesson, P. Bjellerup, T. Lundh, J. Lidfeldt, C. Nerbrand, G. Samsioe, S. Skerfving and M. Vahter, *Environ. Health Perspect.*, 2006, **114**, 830.
21. S.M. Attia, K Varadharajan, M Shanmugakonar, S.C. Das and H.A. Al-Naemi, *Expos. Health*, 2021, 14, 1.
22. C.D. Klaassen, J. Liu and B. A. Diwan, *Toxicol. Appl. Pharmacol*., 2009, **238**, 215.
23. R. Peng, F. Wang and Y. Sha, *Molecules*, 2007, **12**, 1191.
24. W. Liu, L. Xu, R. Sheng, P. Wang, H. Li and S. Wu, *Org. Lett.*, 2007, **9**, 3829.
25. S. Satarug, J. R. Baker, S. Urbenjapol, M. Haswell-Elkins, P. E. B. Reilly, D. J. Williams and M. R. Moore, *Toxicol. Lett.*, 2003, **137**, 65.
26. M. Waisberg, P. Joseph, B. Hale and D. Beyersmann, *Toxicology*, 2003, **192**, 95.
27. R. K. Zalups and S. Ahmad, *Toxicol. Appl. Pharmacol.*, 2003, **186**, 163.
28. C. Cloquet, J. Corrigan, G. Libourel, T. Sterckeman and E. Perdrix, *Environ. Sci. Technol.*, 2006, **40**, 2525.
29. S. M. Pyle, J. M. Nocerino, S. N. Deming, J. A. Palasota, J. M. Palasota, E. L. Miller, D. C. Hillman, C. A. Kuharic, W. H. Cole, P. M. Fitzpatrick, M. A Watson and K. D. Nichols, *Environ. Sci. Technol.*, 1996, **30**, 204.
30. Q. Y. Ye, Y. Li, Y. Jiang and X. P. Yan, *J. Agric. Food Chem.*, 2003, **51**, 2111.
31. Y. Wang, Y. H. Wang and Z. L. Fang, *Anal. Chem.*, 2005, **77**, 5396.
32. E. M. Nolan and S. J. Lippard, *J. Am. Chem. Soc.*, 2007, **129**, 5910.
33. W. Jiang, Q. Fu, H. Fan, J. Ho and W. Wang, *Angew. Chem., Int. Ed.*, 2007, **46**, 8445.
34. C. Lu, Z. Xu, J. Cui, R. Zhang and X. Qian, *J. Org. Chem.*, 2007, **72**, 3554.
35. J. Wang, X. Qian and J. Cui, *J. Org. Chem.*, 2006, **71**, 4308.
36. K. Komatsu, Y. Urano, H. Kojima and T. Nagano, *J. Am. Chem. Soc.*, 2007, **129**, 13447.
37. C. W. Rogers and M. O. Wolf, *Angew. Chem., Int. Ed.*, 2002, **41**, 1898.
38. J. F. Callan, A. P. de Silva and D. C. Magri, *Tetrahedron*, 2005, **61**, 8551.

39. C. Lu, Z. Xu, J. Cui, R. Zhang and X. Qian, *J. Org. Chem.*, 2007, **72**, 3554.
40. P. Ghanghas, A. Choudhary, D. Kumar and K. Poonia, *Inorg. Chem. Commun.*, 2021, **130**, 108710.
41. C.M. Da Silva, D.L da Silva, L.V. Modolo, R.B. Alves, M.A. de Resende, C.V. Martins, Â de Fátima, *J. Adv. Res.*, 2011, **2**, 1.
42. J. L. Liu, X. Meng, H. D. Duan, T. Xu, Z. Y. Ding, Y. Liu and L. Lucia, *Sens. Actuators B Chem.*, 2016, **227**, 296.
43. K. X. Xu, X. M. Xie, H. J. Kong, P. Li, J. L. Zhang and X. B. Pang, *Sens. Actuators B Chem.*, 2014, **201**, 131.
44. A.C. Sedgwick, L. Wu, H.H. Han, S.D. Bull, X.P. He, T.D. James, J.L. Sessler, B.Z. Tang, H. Tian and J. Yoon, *Chem. Soc. Rev.*, 2018, **47**, 8842.
45. A. Helal, N.T.T. Thao, S.W. Lee and H.S. Kim, *J. InclusionPhenom. Macrocyclic Chem.*, 2010, **66**, 87.
46. L. Li, Y. Zhang, J. Yang, W. Qu and H. Cao, *Tetrahedron*, 2022, **121**, 132917.
47. T. Fan, F. Liu, C. Fan and S. Pu, *Tetrahedron*, 2022, **104**, 132583.
48. A. Petdum, N. Kaewnok, W. Panchan, A. Charoenpanich, J. Sirirak, S. Sahasithiwat, T. Sooksimuang and N. Wanichacheva,*J. Photochem. Photobiol*. *A*, 2022, **423**, 113578.
49. J. Ma, Y. Dong, Z. Yu, Y. Wu and Z. Zhao, *New J. Chem.*, 2022, **46**, 3348.
50. J.H. Wang, Y.M. Liu, J.B. Chao, Y. Wang, H. Wang, S.M. Shuang, *Anal. Methods*, 2022, **14**, 1462.
51. D. Mohanasundaram, R. Bhaskar, G.G. Kumar, J. Rajesh and G. Rajagopal, *Microchem. J.*, 2021, **164**, 106030.
52. J. H. Wang, Y. M. Liu, J. B. Chao, H. Wang, Y. Wang and S. Shuang, *Sens. Actuators B Chem.*, 2020, **303**, 127216.
53. X. Tang, Y. Wang, J. Han, L. Ni, H. Zhang, C. Li, J. Li and Y. Qiu, *Dalton Trans.*, 2018, **47**, 3378.
54. V. Venkatesan, S. A. Kumar and S. K. Sahoo, *Inorg. Chem.Commun.*, 2019, **102**, 171.
55. P. Torawane, K. Tayade, S. Bothra, S. K. Sahoo, N. Singh and A. Borse, *Sens. Actuators, B*, 2016, **222**, 562.
56. X. Wu, J. Chen and J. X. Zhao, *Analyst*, 2013, **138**, 5281.
57. S. Qu, C. Zheng, G. Liao, C. Fan, G. Liu and S. Pu, *RSC Adv.*, 2017, **7**, 9833.
58. A. Biswas,R. Naskar, D. Mitra, A. Das, S. Gharami, N. Murmu and T.K. Mondal, *New J. Chem.*, 2022, **46**, 21968.
59. M. J. Frisch, G. W. Trucks, H. B. Schlegel, G. E. Scuseria, M. A. Robb, J. R. Cheeseman, G. Scalmani, V. Barone, B. Mennucci, G. A. Petersson, H. Nakatsuji, M. Caricato, X. Li, H. P. Hratchian, A. F. Izmaylov, J. Bloino, G. Zheng, J. L. Sonnenberg, M. Hada, M. Ehara, K. Toyota, R. Fukuda, J. Hasegawa, M. Ishida, T. Nakajima, Y. Honda, O. Kitao, H. Nakai, T. Vreven, J. A. Montgomery, Jr., J. E. Peralta, F. Ogliaro, M. Bearpark, J. J. Heyd, E. Brothers, K. N. Kudin, V. N. Staroverov, R. Kobayashi, J. Normand, K. Raghavachari, A. Rendell, J. C. Burant, S. S. Iyengar, J. Tomasi, M. Cossi, N. Rega, J. M. Millam, M. Klene, J. E. Knox, J. B. Cross, V. Bakken, C. Adamo, J. Jaramillo, R. Gomperts, R. E. Stratmann, O. Yazyev, A. J. Austin, R. Cammi, C. Pomelli, J. W. Ochterski, R. L. Martin, K. Morokuma, V. G.

Zakrzewski, G. A. Voth, P. Salvador, J. J. Dannenberg, S. Dapprich, A. D. Daniels, Ö. Farkas, J. B. Foresman, J. V. Ortiz, J. Cioslowski and D. J. Fox, *Gaussian 09, Revision D.01*, Gaussian, Inc., Wallingford CT, 2009.

60. A. D. Becke, *J. Chem. Phys.*, 1993, **98**, 5648.
61. C. Lee, W. Yang and R. G. Parr, *Phys. Rev. B: Condens. Matter Mater. Phys.*, 1988, **37**, 785.
62. W. R. Wadt and P. J. Hay, *J. Chem. Phys.*, 1985, **82**, 284.
63. P. J. Hay and W. R. Wadt, *J. Chem. Phys.*, 1985, **82**, 299.
64. R. Bauernschmitt and R. Ahlrichs, *Chem. Phys. Lett.*, 1996, **256**, 454.
65. R. E. Stratmann, G. E. Scuseria and M. J. Frisch, *J. Chem. Phys.*, 1998, **109**, 8218.
66. M. E. Casida, C. Jamorski, K. C. Casida and D. R. Salahub, *J. Chem. Phys.*, 1998, **108**, 4439.
67. M. Cossi and V. Barone, *J. Chem. Phys.*, 2001, **115**, 4708.
68. V. Barone and M. Cossi, *J. Phys. Chem. A*, 1998, **102**, 1995.
69. M. Cossi, N. Rega, G. Scalmani and V. Barone, *J. Comput. Chem.*, 2003, **24**, 669.

# APPENDIX

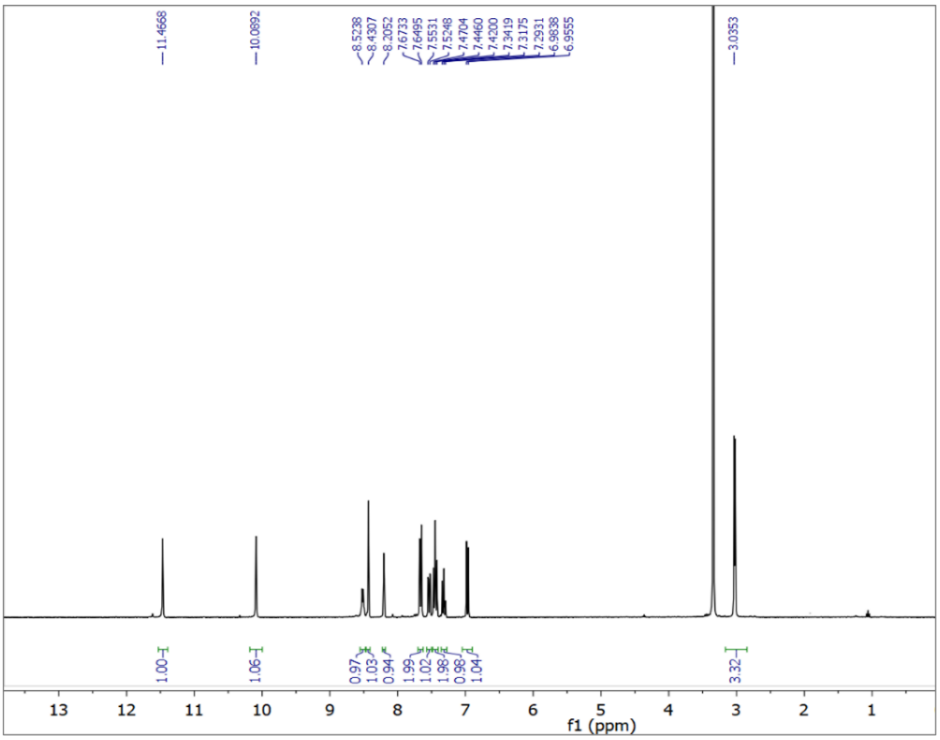


**Fig. A4.1:** $^{1}$H NMR (300 MHz) spectrum of HBMC in DMSO-$d_6$

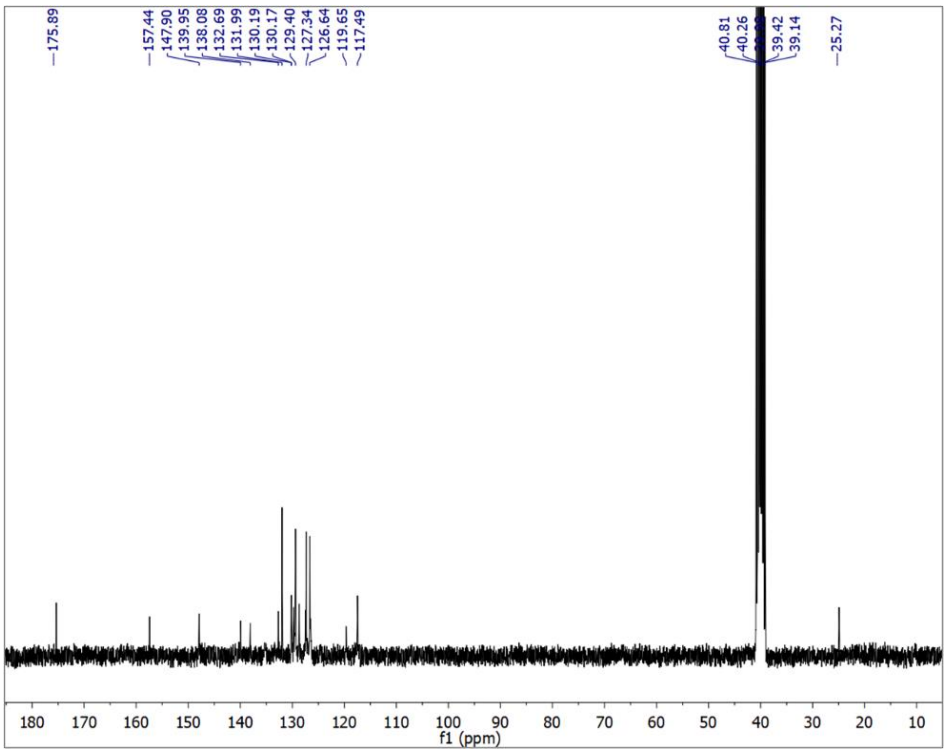


**Fig. A4.2:** $^{13}$C NMR (75 MHz) spectrum of HBMC in DMSO-$d_6$

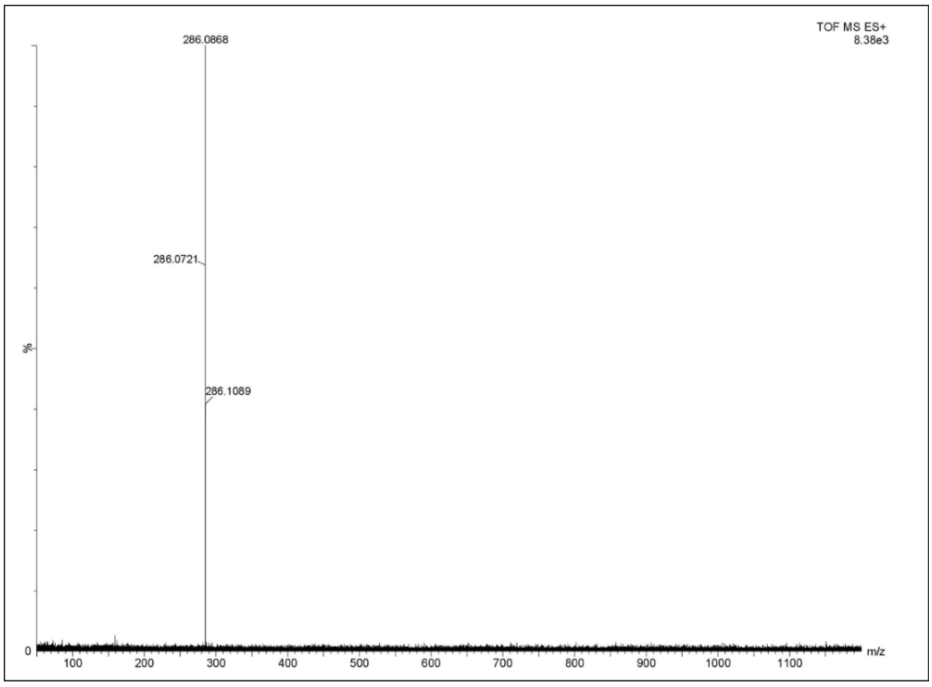


**Fig. A4.3:** HRMS of probe HBMC

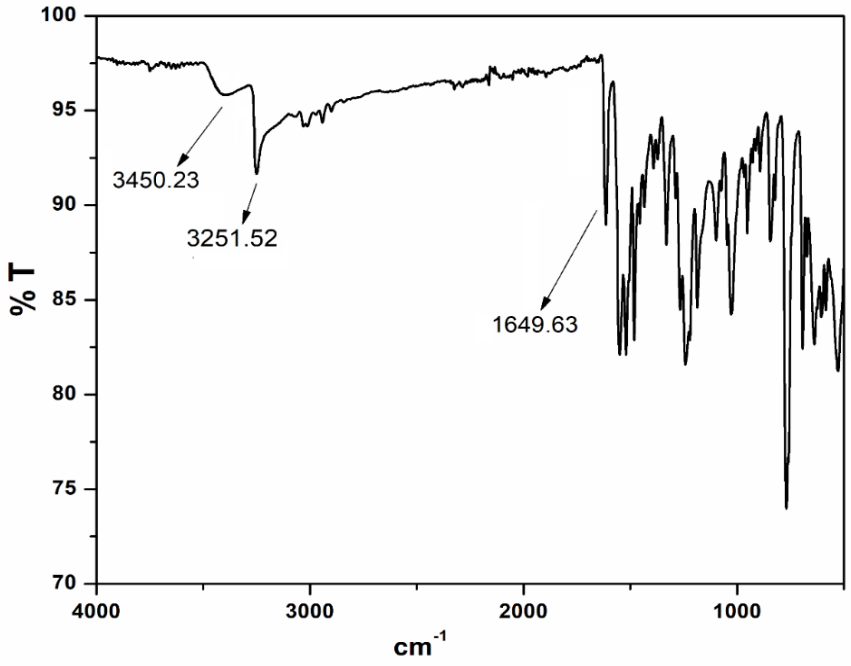


**Fig. A4.4:** IR spectra of the probe HBMC

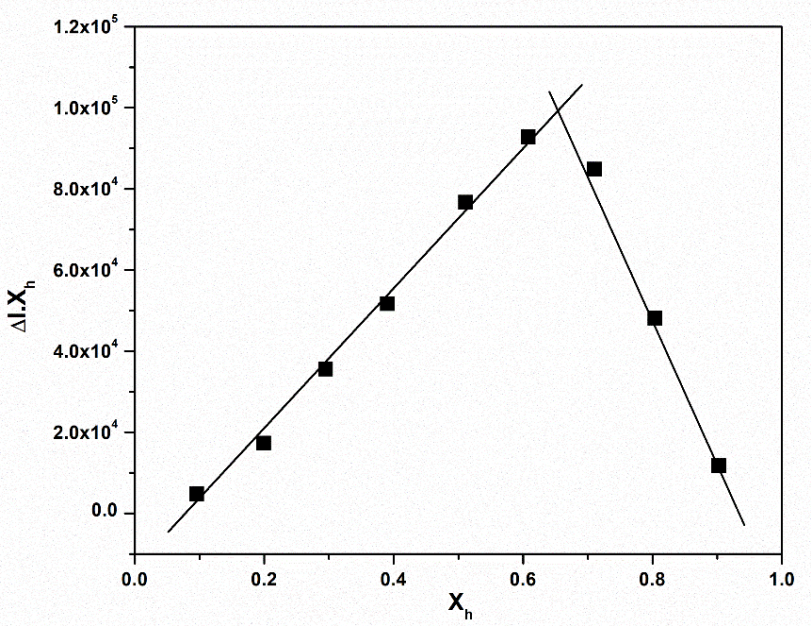


**Fig. A4.5:** Job's plot for HBMC-$Cd^{2+}$ complex formation using fluorescence emission titration experiment ($\lambda_{ex}$ = 345 nm); where $X_h$ is the mole fraction of the host and $\Delta I$ indicates the change of emission at 496 nm.

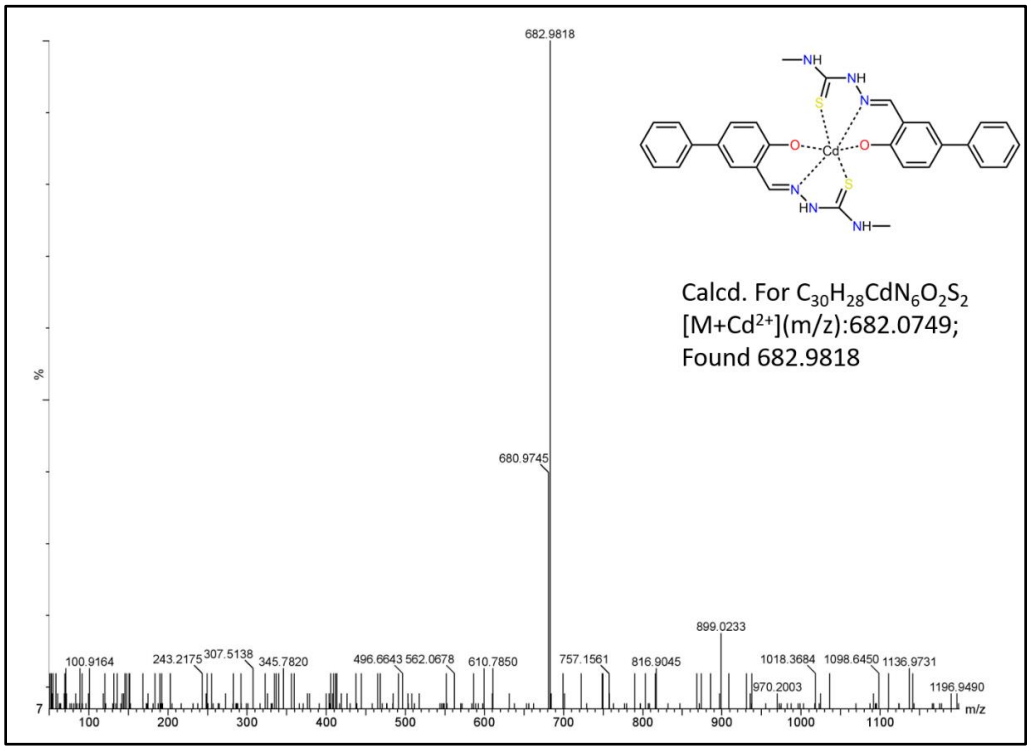


**Fig. A4.6:** HRMS of the HBMC-$Cd^{2+}$.

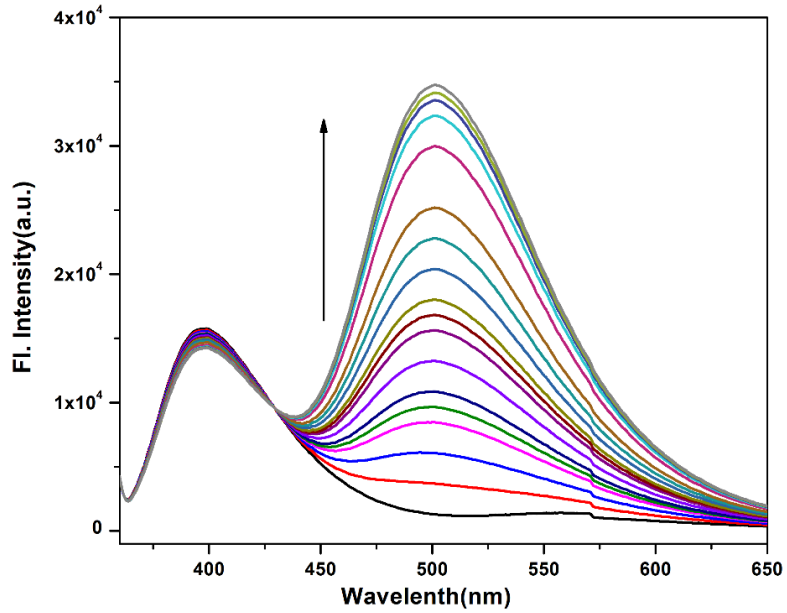


**Fig. A4.7:** Change in emission spectrum of HBMC (20 μM) upon addition of $Zn^{2+}$(40 μM) in MeOH/$H_2O$ (4/1, v/v, pH = 7.2) solution, $\lambda_{ex}$ = 345 nm.

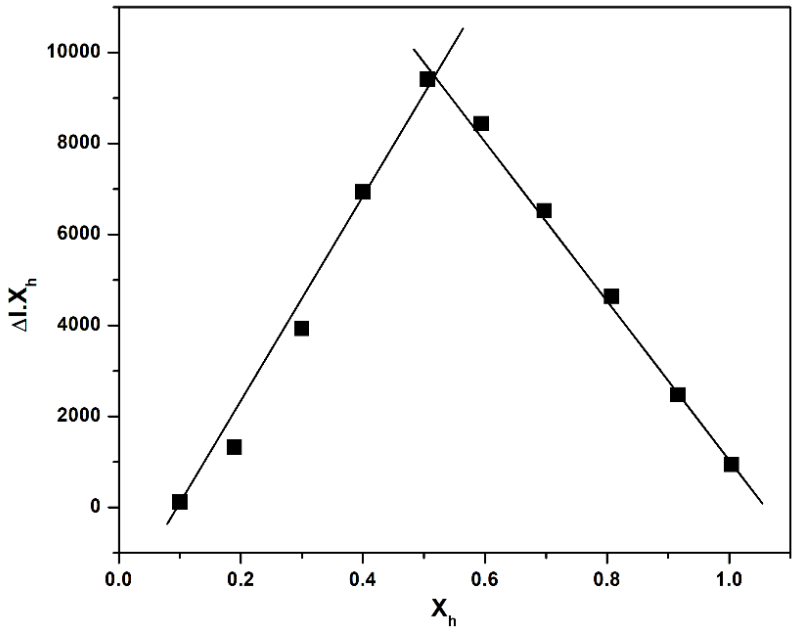


**Fig. A4.8:** Job's plot for HBMC-$Zn^{2+}$ complex formation using fluoroscence emission titration experiment ($\lambda_{ex}$ = 345 nm); where $X_h$ is the mole fraction of the host and ΔI indicates the change of emission at 502 nm.

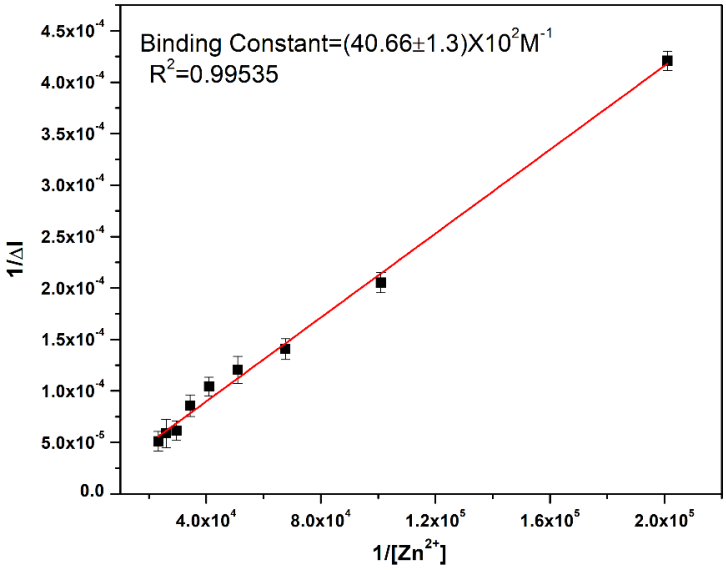


**Fig. A4.9:** Benesi–-Hildebrand plot from fluorescence titration data of receptor (20 µM) with $Zn^{2+}$.

**Table A4.1: Fluorescence lifetime data**

| Compounds | Quantum yield *(φ)* | τ (ns) | $k_r$ ($10^8 \times s^{-1}$) | $k_{nr}$ ($10^8 \times s^{-1}$) |
|---|---|---|---|---|
| HBMC | 0.024 | 1.42 | 0.29 | 0.084 |
| HBMC-$Cd^{2+}$ | 0.508 | 5.14 | 1.58 | 0.321 |

Radiative rate constant $K_r$ and total non-radiative rate constant $K_{nr}$ have been calculated using the equation $\tau^{-1} = K_r + K_{nr}$ and $K_r = \varphi f / \tau$

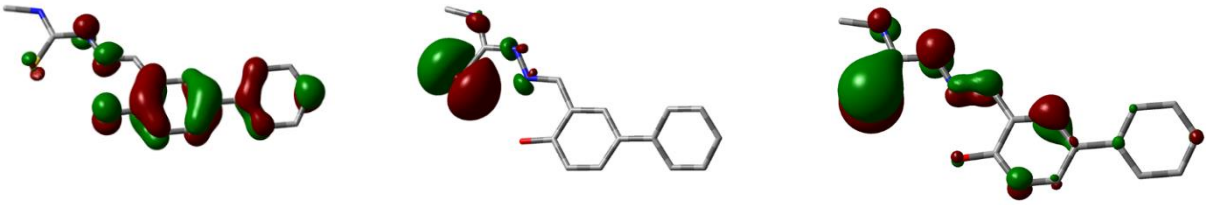

HOMO ((-5.73 eV ) HOMO-1 (-5.93 eV ) HOMO-2 (-6.3 eV )

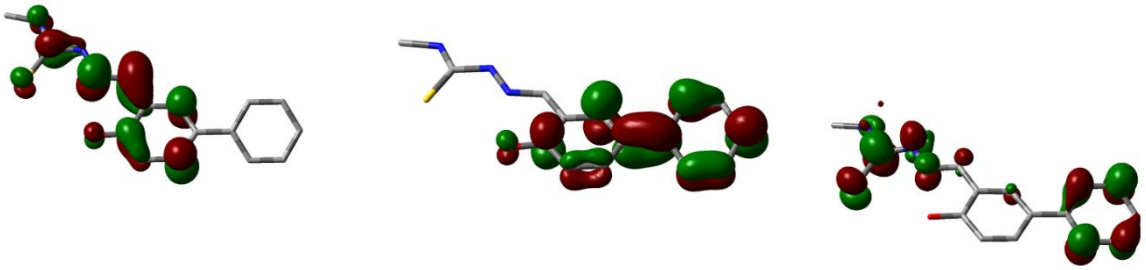

LUMO (-1.82 eV ) LUMO+1 (-1.06 eV ) LUMO+2 (-0.82 eV )

**Fig. A4.10:** Contour plot of some selected molecular orbitals of HBMC.

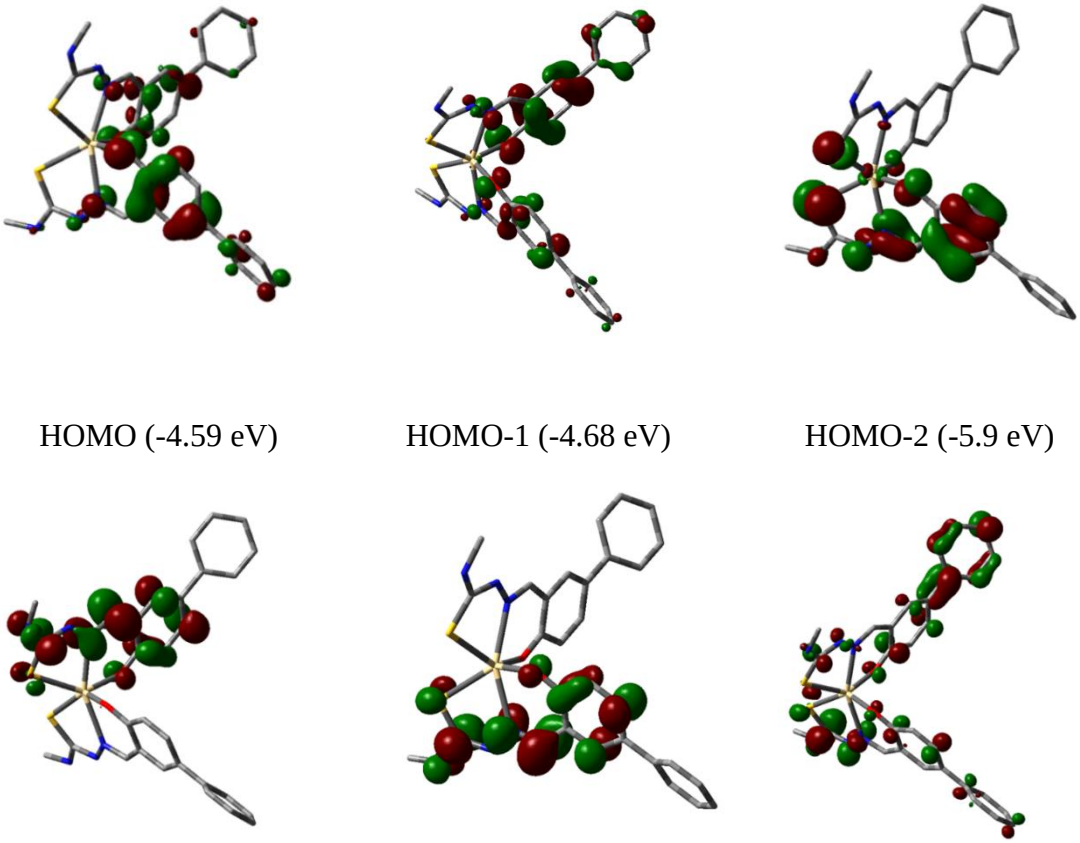


**Fig. A4.11:** Contour plot of some selected molecular orbitals of HBMC-$Cd^{2+}$

**Table A4.2.** Energy and compositions of some selected molecular orbitals of HBMC-$Cd^{2+}$ complex

| MO | Energy | % of composition | |
|---|---|---|---|
| | | HBMC | Cd |
| LUMO+5 | 0.05 | 97 | 3 |
| LUMO+4 | 0.01 | 99 | 1 |
| LUMO+3 | -0.03 | 99 | 1 |
| LUMO+2 | -0.08 | 97 | 3 |
| LUMO+1 | -1.23 | 99 | 1 |
| LUMO | -1.28 | 99 | 1 |
| HOMO | -4.59 | 99 | 1 |
| HOMO-1 | -4.68 | 99 | 1 |
| HOMO-2 | -5.9 | 98 | 2 |
| HOMO-3 | -5.95 | 98 | 2 |
| HOMO-4 | -5.97 | 98 | 2 |
| HOMO-5 | -6.2 | 95 | 5 |
| HOMO-6 | -6.28 | 97 | 3 |
| HOMO-7 | -6.41 | 99 | 1 |
| HOMO-8 | -6.42 | 100 | 0 |
| HOMO-9 | -6.43 | 99 | 1 |
| HOMO-10 | -6.44 | 100 | 0 |

**Table A4.3.** Vertical electronic excitations of HBMC calculated by TDDFT/CPCM method

| Energy (eV) | Wave-length (nm) | Osc. Strength (f) | Transition | Character |
|---|---|---|---|---|
| 3.5046 | 353.7 | 0.2269 | (92%) HOMO→LUMO | Lig(π)→Lig(π*) |
| 4.0384 | 307.0 | 0.4287 | (92%) HOMO-2→LUMO | Lig(π)→Lig(π*) |
| 4.2897 | 289.0 | 0.5960 | (89%) HOMO→LUMO+1 | Lig(π)→Lig(π*) |
| 4.4120 | 281.0 | 0.6366 | (90%) HOMO-3→LUMO | Lig(π)→Lig(π*) |
| 6.1509 | 201.6 | 0.2183 | (40%)HOMO-4→LUMO+2 | Lig(π)→Lig(π*) |

**Table A4.4.** Vertical electronic excitations of HBMC calculated by TDDFT/CPCM method

| Energy (eV) | Wave-length (nm) | Osc. strength (f) | Transition | Character |
|---|---|---|---|---|
| 3.1030 | 399.6 | 0.1659 | (70%) HOMO-1→LUMO | Lig(π)→Lig(π*) |
| 4.1640 | 297.7 | 0.6424 | (72%) HOMO→LUMO+3 | Lig(π)→Lig(π*) |
| 4.2566 | 291.3 | 0.7818 | (71%) HOMO→LUMO+2 | Lig(π)→Lig(π*) |

**Table A4.5:** Comparison of solvent systems and limit of detection (LOD) of the receptor (HBMC) with some recently reported fluorescence organic probes for the detection of $Cd^{2+}$.

| Chemosensors | Solvent system | LOD | References |
|---|---|---|---|
| 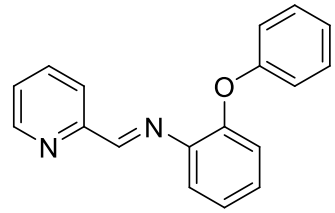 | Acetonitrile | 0.12 µM | *New J. Chem.*, 2022, **46**, 3348. |
| 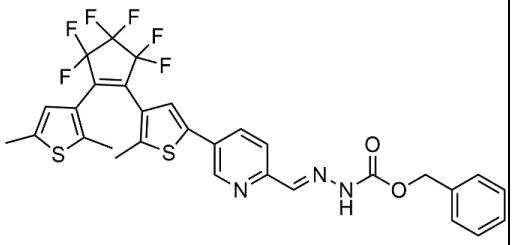 | THF | $1.71\times10^{-7}$ mol $L^{-1}$ | *RSC Adv.*, 2019, **9**, 29141. |
| 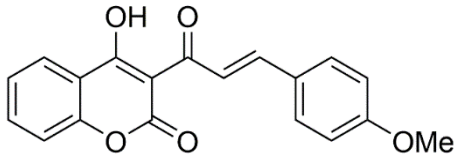 | $CH_3CN:H_2O$, (3:7, v/v), pH 7.0 | $5.84\times10^{-8}$M. | *New J. Chem.*, 2017, **41**, 14746. |
| 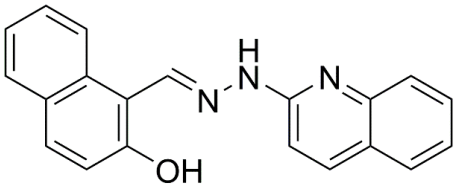 | ACN:$H_2O$ (8:2, v/v) | $1.48 \times 10^{-8}$ M | *Microchemical Journal*, 2021, **164**, 106030. |

| | | | |
|---|---|---|---|
| 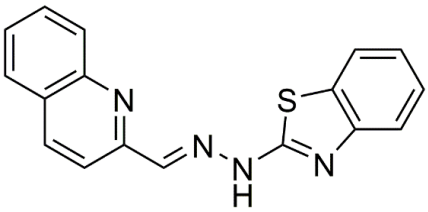 | 4:1 (EtOH/HEPES buffer), pH=7.4 | $1.75x10^{-7}$ M | *RSC Adv.*, 2016, **6**, 112246. |
| 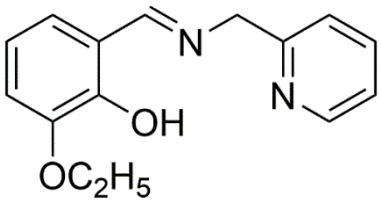 | EtOH | $9.2x10^{-6}$ M | *RSC Adv.*, 2015, **5**, 27682. |
| 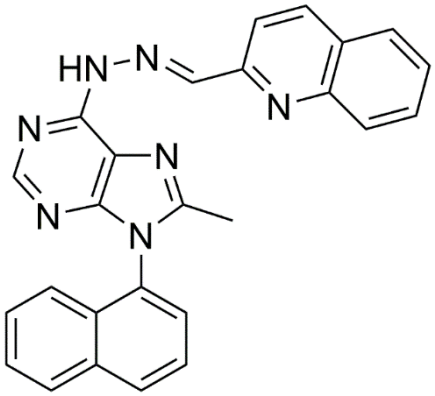 | (9/1, v/v, pH 7.4, HEPES buffer, 0.2 mM) | 41.0 nM | *Tetrahedron*, 2021, **88**, 132123. |
| 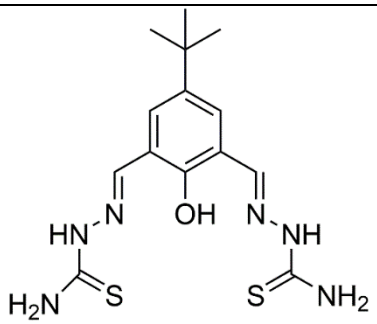 | $H_2O$:DMSO (95:5 v/v) | 3.4 µM | *Spectrochim. Acta Part A*, 2020, **241**, 118610. |

| | | | |
|---|---|---|---|
| 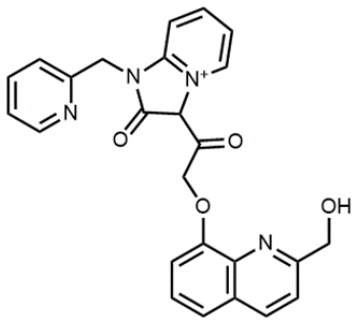 | distilled water | $1.18\times10^{-6}$ M | *Sens. Actuators B*, 2017, **251**, 877. |
| 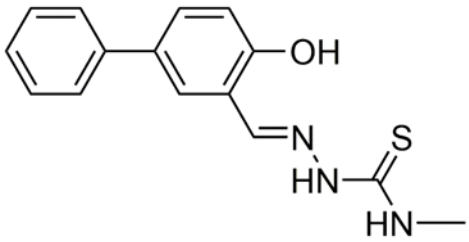 | MeOH/$H_2O$ (4/1, v/v, pH = 7.2) | (1.59±.054) x$10^{-8}$ M | **This work** |

# Chapter 5

# Adaptable coumarin based fluorescent molecular multianalyte sensor for $Zn^{2+}$, $Hg^{2+}$ and $Cu^{2+}$ via different sensing modalities and its bioimaging applications

# Adaptable coumarin based fluorescent molecular multianalyte sensor for $Zn^{2+}$, $Hg^{2+}$ and $Cu^{2+}$ via different sensing modalities and its bioimaging applications

## Abstract

A new organic probe DCMC (E)-2-((7-(diethylamino)-2-oxo-2H-chromen-3-yl) methylene)-N-methylhydrazine-1-carbothioamide was successfully designed and synthesized. Characterization techniques such as single crystal X-ray diffraction, $^{1}$H-NMR, $^{13}$C-NMR, IR, and mass spectroscopy have been used to analyse the chemical structure of the sensor. The systematic sensing studies of DCMC in DMSO/$H_2O$ (9/1, v/v, pH = 7.2) by fluorescence and absorption method shows selectivity towards $Hg^{2+}$, $Zn^{2+}$ and $Cu^{2+}$ by different sensing modalities. DCMC shows distinctive red shift in UV-Vis spectra for $Cu^{2+}$, where we observe a colour change from cyan-yellow to brown colour in ambient light while no similar response was observed for $Hg^{2+}$ and $Zn^{2+}$. Additionally, it shows significant fluorescence quenching towards $Hg^{2+}$ and for $Zn^{2+}$ eminent ratiometric fluorescence response is observed, where the colour changes from cyan to yellow under UV light. All the changes can be observed by naked eye. The detection limit of DCMC towards $Hg^{2+}$ and $Zn^{2+}$ was calculated and established to be order of $10^{-9}$ (M) and for $Cu^{2+}$ it was in the order of $10^{-8}$ (M) respectively. A detailed investigation was performed on the detection mechanism by using Job's plot, $^{1}$H-NMR, ESI mass analysis and density functional theory (DFT) calculations which established the 2:1 binding stoichiometry for all the three ions.The probe also coherently recognised the sensing cations when it was applied to solid state platform of TLC plate and silica gel base with distinguishable colour change making DCMC a portable kit for onsite analysis and detection. Besides, the live cell imaging study on MCF-7 cell line to detect $Zn^{2+}$ and $Hg^{2+}$ also reveals the detection capability of DCMC and its biocompatible nature. Finally, density functional theory and time-dependent density functional theory were implemented which established the experimental outcomes theoretically.

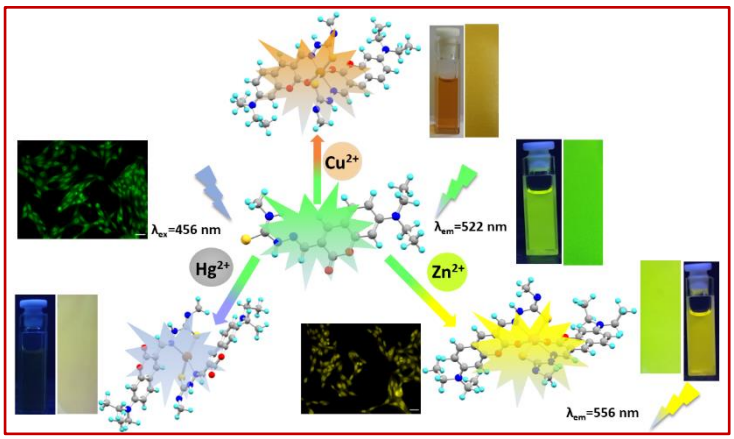

# 5.1. Introduction

Owing to their universal existence, the metal ions represent itself as an active topic of research globally. In our surroundings, metal ions can be found in food, soil, and water.[1] Metal ions are found to participate in numerous biological processes in a human body. Nevertheless, the existence of metal ions at concentrations beyond the allowable limit may result into harmful impacts on the environment as well as on human beings.[2-5] Heavy metal ions are very significant for many industries and for our daily lives as they play an essential task in many areas such as industrial, chemical, biological and environmental. But excessive quantity of heavy metals causes danger to both living organisms and the environment.[6-12] Now among the heavy metals, zinc and mercury play crucial roles. The second-most ubiquitous component in the human body, $Zn^{2+}$, is crucial for a number of biological actions including gene transcription, neural signaling, controlling of enzyme, brain function, apoptosis etc.[13-15] $Zn^{2+}$ is also found in metalloproteins and it affords both the catalytic and structural support.[16-18] Generally, the amount of $Zn^{2+}$ in the living body needs to be observed cautiously as low level of $Zn^{2+}$ can lead to different diseases including hair loss, Alzheimer's disease and Parkinson's disease, diabetes, prostate cancer etc.[19-21] Moreover, $Zn^{2+}$ ions in their free forms are extremely lethal to vertebrate fish, invertebrates and plants. Also, $Zn^{2+}$ may lead to a drop of microbial action in the soil owing to a common pollutant in food waste and agriculture. Therefore, it is very important to detect the zinc ion in both biological and environmental systems.[22] Mercury ion ($Hg^{2+}$) is the steadiest inorganic form of mercury and considered as an extremely toxic and widespread metal pollutant even at very low concentrations.[23,24-27] Due to its bioaccumulation and toxicity, metal mercury is a perilous pollutant albeit it shows significant industrial applications.[28] $Hg^{2+}$ which is present in soil or waste water is absorbed by lower types of aquatic organisms which consequently, converted into methylmercury by those organisms.[29] Methylmercury is a powerful neurotoxin affecting human health via causing cyanosis, nephritic syndrome and minamata disease.[30] Due to the extreme toxic nature of $Hg^{2+}$, it demolishes all sorts of physiological systems including nerves, enzymes, genetics and respiratory systems. As $Hg^{2+}$ is not biodegradable, it can get easily accumulated in organisms through the food chain, thereby resulting into many diseases, such as kidney malfunction, brain damage, and emotional disarray.[31-34] A maximum allowable level of 2 ppb (10 nM) has been set for mercury contamination in food and drinking water by the Environmental Protection Agency (EPA).[35] Furthermore, the advancement of pharmaceutics, cosmetics, battery industry as well as fertilizer industry result into a probable risk of inhaling mercury.[36-39] Therefore, it should be a significant and vital mission to produce quick and competent methods

for the recognition of mercury ions in biological and environmental systems.[40-43] Now, after iron and zinc, copper ion is acknowledged as the third most abundant transition metal ion in the human body and it also possesses a crucial position in human physiology for its distinctive redox active nature.[44,45] However, intake of excessive copper can lead to gastrointestinal disorder, Wilson or Alzheimer's disease etc.[46,47] Diseases of mitochondrial abnormality and neuronal degeneration may be attributed to the deficiency of Cu(II).[48,49] Although, copper ion is extensively used both in industry and agriculture, it has been branded as an environmental contaminant. Additionally, too much copper can cause unnecessary amount of oxygen in eukaryotic cells and prokaryotes thereby resulting into the destruction of cell membranes, proteins and nucleic acids.[50] Hence to recognize Cu (II) ions has significant implications for qualitative and quantitative study from both the biological and environmental viewpoint.

Thus, new advancements in the fabrication of sensing tools that are vastly sensitive and specific to $Cu^{2+}$, $Zn^{2+}$, and $Hg^{2+}$ should be nurtured. Till date, a couple of detecting methods for heavy ions were introduced which includes atomic absorption spectroscopy,[51] inductively coupled plasma mass spectroscopy,[52] inductively coupled plasma atomic absorption emission spectrometry (ICP-AES), surface enhanced raman spectroscopy,[53] electrochemical methods[54-56] and chromatography.[57,58] But as these detection techniques typically demand luxurious equipments, intricate sample pre-treatment, excessive time and high implementation and preservation costs, the new method of identification with easy, straightforward and swift process, low cost and elevated sensitivity is anticipated enthusiastically. Recently, small-molecule fluorescence sensors have been designed and fabricated fast as they can beat the drawbacks of the abovementioned conventional expensive and time-consuming detecting methods.[59,60] The design and synthesis of single molecular probes for the distinct and sensitive detection of multiple analytes simultaneously is rising as a research area of immense fascination,[61-64] in view of the fact that such systems would result into quicker analytical processing and cost reductions. However, most of the reported fluorescent molecules are efficient in selectively identifying only a particular analyte.[65-71] Those multifunctional sensors which are responsible for producing different responses in fluorescence or color to different metal ions will display more prospective in environmental applications. Therefore, extreme research has been carried out on the fabrication of sensitive and distinctive probes for the qualitative and quantitative identification of multi metal ions to fit in with the atomic economy; precisely, researches on the sensors for the specific recognition of three analytes in multiple signals has been a noteworthy development lately.[72-76] Additionally, if a fluorescent sensor for multiple analytes utilizes same solvent system

for identification of different analytes, the sample handling cost would be shortened significantly and also the efficiency of the detection method of this probe would be much more improved compared to that of the conventional sensors. Now, much more attention has been focused in development of those probes which are proficient to sense three kinds of metal ions.[77-81] As the detection units of the developed probes are idiosyncratic in identifying the analyte activities, designing of such probes with multiple analyte detection capacity is a demanding job.

## 5.2. Prior works

Now, in the past few years, the application of organic moieties in chemosensors has been gained much interest,[82-86] exclusively huge numbers of the sensors with high sensitivity and distinctive nature for identifying $Cu^{2+}$,[87-89] $Hg^{2+}$,[90,91] $Zn^{2+}$ [92,93] have been reported. For example, in 2020, Shen group reported a schiff base sensor containing coumarin fluorophores which shows colorimetric and ratiometric responses to Cu(II) and Zn(II) ions respectively along with low detection limits of 141 nM and 72 nM, in aqueous media.[50] Another report was published by Pu et al., regarding a multifunctional aggregation-induced emission (AIE) active fluorescent switch for recognition of $Zn^{2+}$ in THF along with the detection of $Hg^{2+}$ in THF-water with detection limit of $1.24x10^{-6}$ mol $L^{-1}$. And $2.55x10^{-9}$ mol $L^{-1}$ respectively in 2019.[94] In the year of 2018, Xu group introduced a new single molecule based on pyrrole moiety as a multianalyte sensor for $Cu^{2+}$, $Zn^{2+}$ and $Hg^{2+}$ with detection limit of 38.2, 88.3 and 69.4 nM respectively.[95] Another similar type of work was reported in 2019 by Wang et al. in which a probe containing multiple nitrogen heterocycles was designed and fabricated for the distinctive detection of $Cu^{2+}$, $Hg^{2+}$ and $Zn^{2+}$ in same solvent system by different mechanisms with showcasing different LOD values such as 1.12 nM for $Cu^{2+}$, 0.2 µM for $Hg^{2+}$ and 0.94 µM for $Zn^{2+}$.[96] But although a few reports have been found in the literature detecting trace amounts of the abovementioned metal ions based on fluorescence enhancement or quenching, there are plenty of rooms for further improvements in fabricating more suitable and sensitive fluorescent probes for the multiple detection of metal ions. Therefore, there is still abundance for development in designing highly sensitive fluorescent probes with efficient multiple ions sensing functions.

## 5.3. Present work

So herein we have designed and successfully fabricated a coumarin framework based fluorescent sensor (DCMC) which display chromogenic detection of $Cu^{2+}$ and fluorogenic detection of both $Hg^{2+}$ (turn-off) and $Zn^{2+}$ (ratiometric) simultaneously in the same solvent system, which is

DMSO:$H_2O$ (9/1, v/v) via different sensing mechanisms. The noteworthy aspect of our synthesized probe is that the O, N and S centers present in the newly developed probe actually aid in the concurrent detection of the three abovementioned metal ions via 2:1 binding ratio for each without having any sorts of interference from the other competitive ions. The real time analytical applications and intracellular detection of the ions by DCMC further established its prominent features.

# 5.4. Results and discussions

## 5.4.1. Synthesis of the sensor (DCMC)

For the synthesis of DCMC very economic cheap precursor i.e., 5-(Diethylamino)-2-hydroxybenzaldehyde, diethyl malonate and 4-methyl-3-thiosemicarbazide were utilized for the fabrication of our probe DCMC. The synthetic design of DCMC is displayed in Scheme 1 where compounds 'a' and 'b' were synthesized using formerly reported procedure.[97] The final step involved the reflux condensation of the 7-diethylamino-2-oxo-2H-chromene-3-carboxyldehyde and 4-methyl-3-thiosemicarbazide in ethanol for about 2 h, which produces the anticipated probe DCMC. Diverse spectroscopic techniques i.e., $^1$H-NMR, $^{13}$C-NMR, mass spectrometry and FT-IR were used for the characterization of the probe DCMC. (Fig. A5.1-A5.4, Appendix)

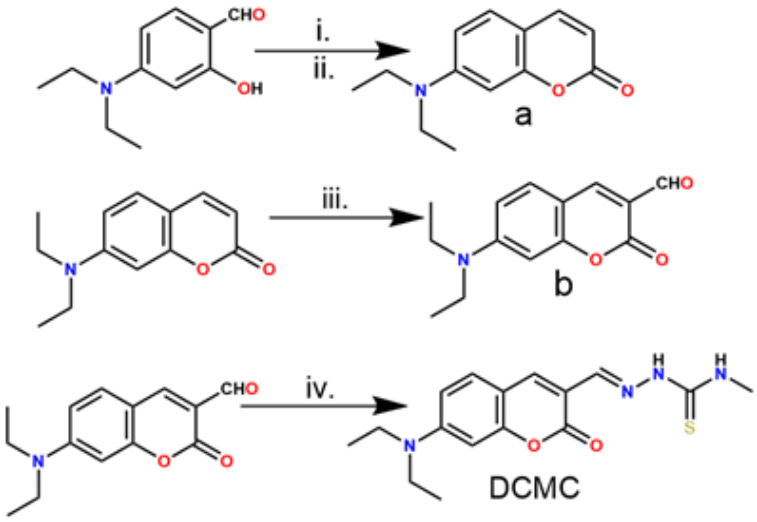


**Scheme 5.1:** Synthesis of the probe (DCMC). Reagents and conditions: (i) Diethylmalonate, piperidine, AcOH, EtOH, reflux (ii) HCl, AcOH, reflux (iii) DMF, $POCl_3$, 60°C, 24 h (iv) 4-methyl-3-thiosemicarbazide, ethanol, reflux, 2 h.

## 5.4.2. Crystal structure of DCMC

Single-crystal X-ray diffraction technique was employed to decide the molecular geometry of our synthesized probe, DCMC. Single crystals of DCMC were developed by slow evaporation method in ethanol solvent. The probe crystallizes in the monoclinic crystal system with a $P2_1/c$ space group as it contains both hard and soft donor atoms like O, N and S atoms. Details concerning data collection, crystal study and structural refinement are recorded in Table A5.1, Appendix. A various range of bonding angles and distances are shown in Table A5.2, Appendix. The ORTEP diagram of DCMC with the atom labelling approach is unveiled in Fig.5.1. In probe, DCMC the N, O and S atoms acts as a chelating agent, where each of the donor atoms lies on identical plane. The torsion angles of O2-C1-C2-C3 (178.85°), N2-N1-C14-C2 (177.73°), N1-N2-C15-S1 (176.99°) are in good agreement with it.

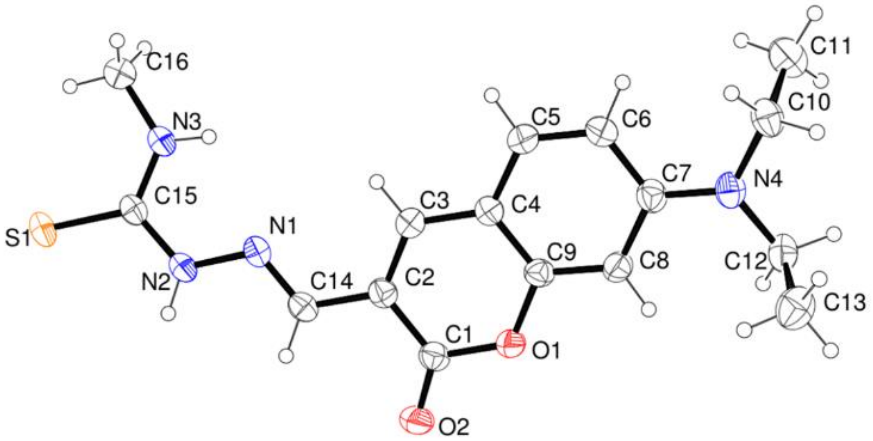


**Figure 5.1.** ORTEP plot of the probe DCMC with 35% ellipsoidal probability.

## 5.4.3. Supramolecular Interaction and Hirshfeld Surface Analysis of the Sensor DCMC

Crystal of DCMC forms 1D supramolecular architecture via π···π interaction and intermolecular H-bonding interaction. The packing diagram of DCMC elucidates how aromatic rings interact with another aromatic ring {shown in green (•••) color} to form 1D supramolecular interaction (Fig. 5.2). The dimer is repeated down through the axis and the π- stack is designed by the face-to-face π···π contact between the surrounding molecules' phenyl ring attached to amino group and coumarin ring with a centroid-centroid distance of 3.7060(9) Å for [Cg(2)···Cg(3) and Cg(3)···Cg(2)] (symmetry: 1−x, 1−y, 1−z). Strong H-bonding interactions are found to be between N2-H2…O2 (acceptor) with distance of 2.18 Å respectively.

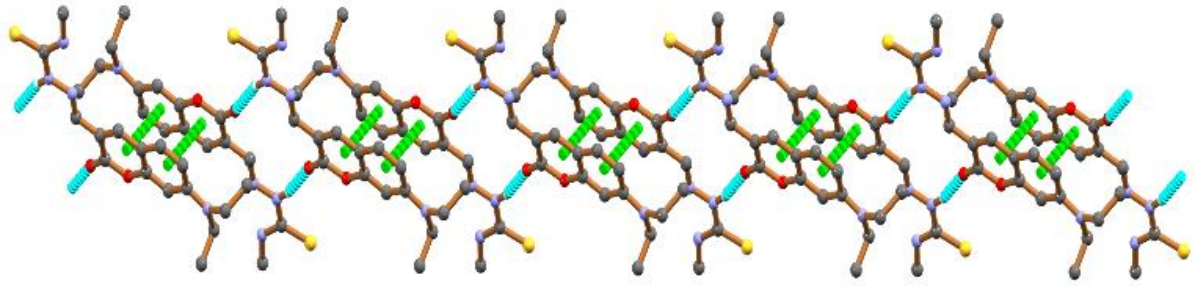

**Figure 5.2:** 1D supramolecular structure formed by H-bonding between N2-H2…O2 (●●●) and π-π interactions between the coumarin unit with the amino group attached phenyl ring of adjacent molecule (●●●).

Hirshfeld surfaces (HSs) is a three-dimensional outlook of the close contacts that are present in a solid crystal which furnishes valued data about the crystal packing[98]. The HS of DCMC projected across $d_{norm}$ (varying from 0.25 to 1.12 Å), shape index (varying from -1.0 to 1.0 Å), curvedness (varying from -4.0to 0.4 Å) and fragment patch are shown in Fig.5.3. The **c**ircular deep red (depressions) noticeable on the $d_{norm}$ surfaces are indicative of hydrogen-bonding contacts and other weak contacts (C-H···π/π···π). Whereas, in the shape index of HS of the compound the adjacent red and blue triangles confirm the presence of π···π interactions.

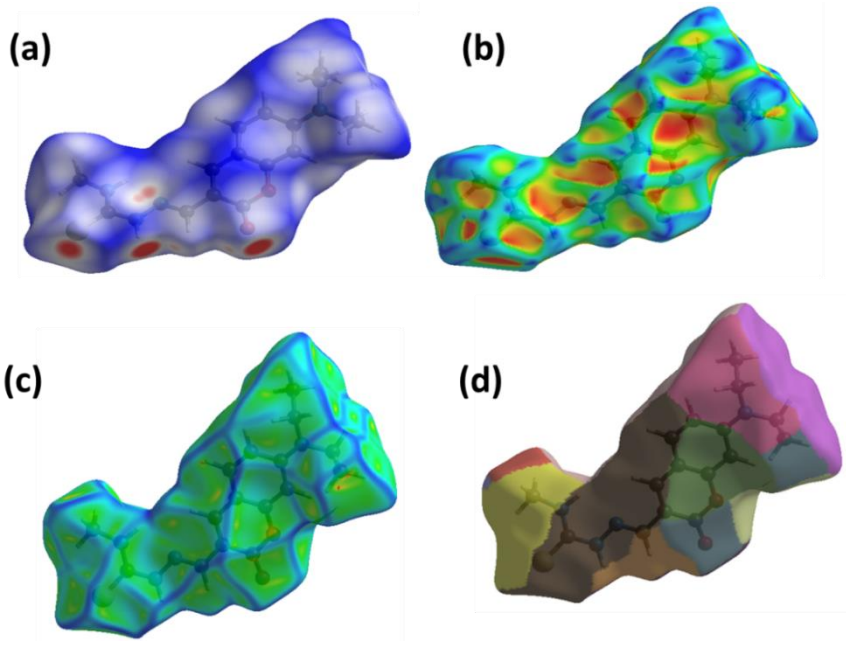


**Figure 5.3:** Hirshfeld surfaces (HSs) of DCMC mapped with (a) dnorm (b) shape index (c) curvedness & (d) fragment patch.

All the available contacts that are present in DCMC are abridged in a 2D fingerprint plot as individual spikes [Fig.5.4 (a)]. By studying the fingerprint plot we can emphasize all the

interactions available present in probe (H…H, C…C, H…C/C…H, H…O/O…H, H…S/S…H, H…N/N…H, etc.) and their respective contribution to the total HS (Pie chart) [Fig. 5.4(b) & Fig. 5.5]. It is clear that majority of contribution is due to interaction of H…H, which is 45.6% as there are higher number of H atoms present in probe DCMC. From the HS study it is clear that H-atom contacts play a crucial role and apart from that there is broad array of H···C/C···H, and H···(O/N/S)/ (O/N/S)···H, C···C interactions present in DCMC, which plays a major role in founding the crystal packing. Electronic feature of the molecular system affects the formation of supramolecular association; thus, these potential interactions present in the molecule plays an important role towards sensing of incoming analytes (here $Zn^{2+}$, $Hg^{2+}$ and $Cu^{2+}$).

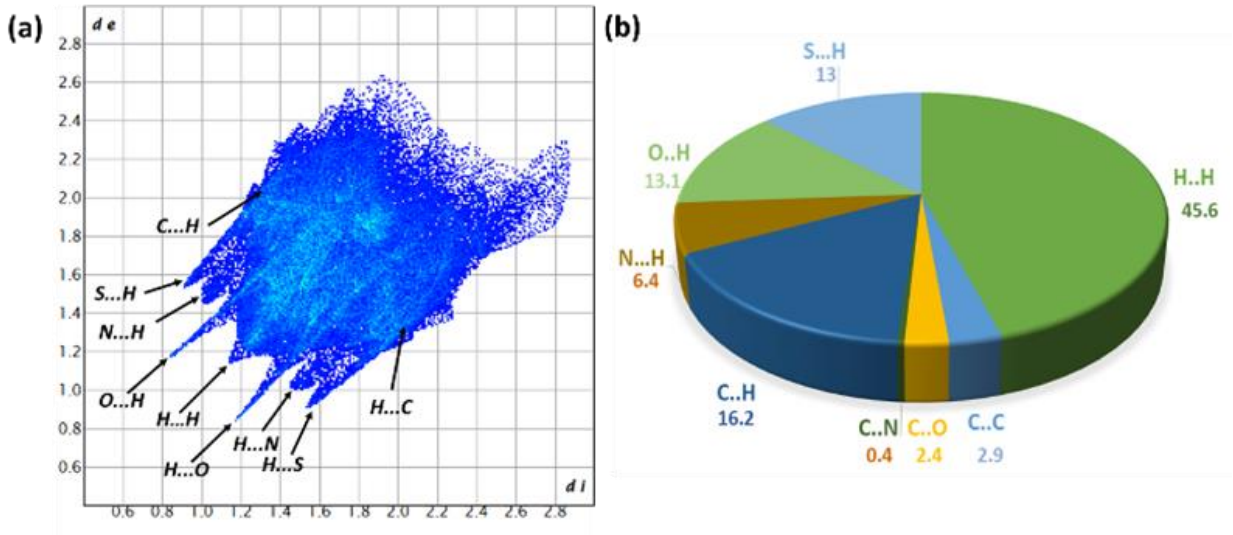


**Figure 5.4:** 2D fingerprint plot (full) of the probe DCMC (a) and relative contributions of different intermolecular interactions to the HS area shown in the pie chart (b).

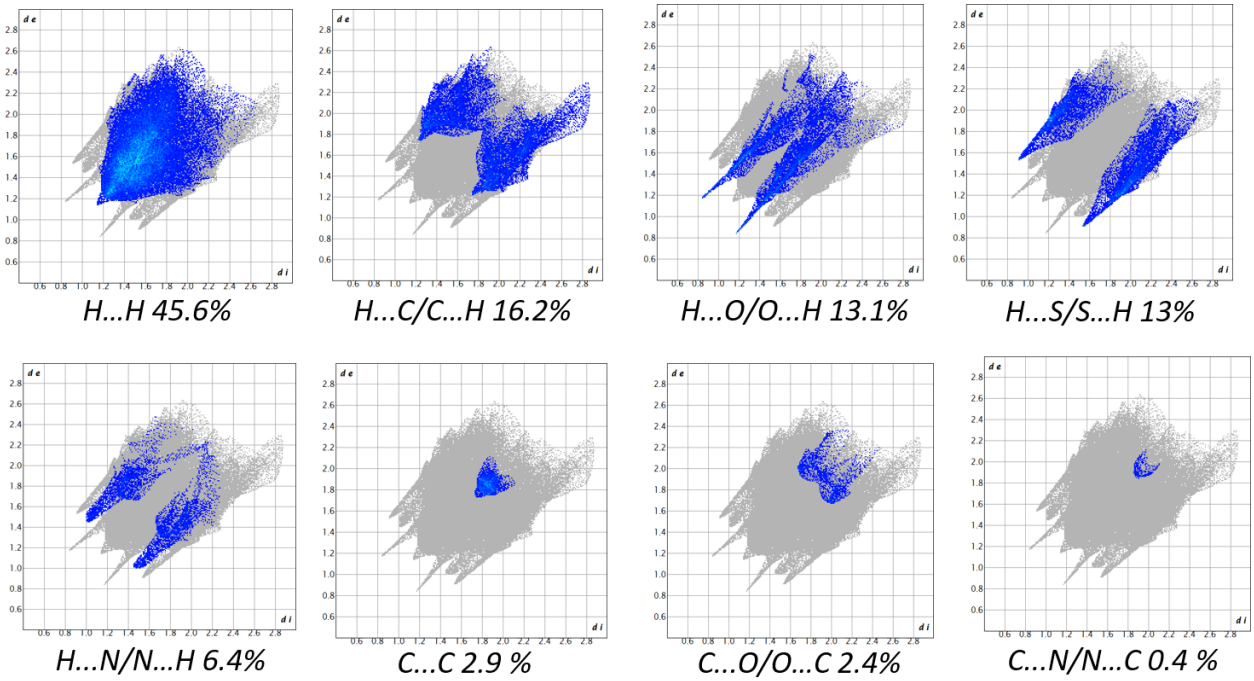


**Figure 5.5:** 2D Fingerprint plot resolved into different contacts contributed to the total Hirshfeld Surface area of DCMC.

## 5.4.4. Spectroscopic analysis

### 5.4.4.1. UV-Vis study of DCMC

The photophysical study of the probe (DCMC) was studied in DMSO/$H_2O$ (9/1, v/v, pH = 7.2). The probe itself shows a strong absorption maxima located at 456 nm mainly due to π-π* transition and shows a neon yellow colour under ambient light. In order to inspect the sensing proficiency of the probe, DCMC towards $Cu^{2+}$, we gradually added $Cu^{2+}$ to the probe solution. A ratiometric change was observed in the UV-Vis spectra where the peak at 456 nm decreases and simultaneously a new absorption signal profile is produced at 490 nm with an isosbestic point at 464 nm (Fig. 5.6). Hence this large red shift of 34 nm in absorption spectra changes the neon yellow colour of probe to light brown colour is mainly attributed to the electron transfer process.

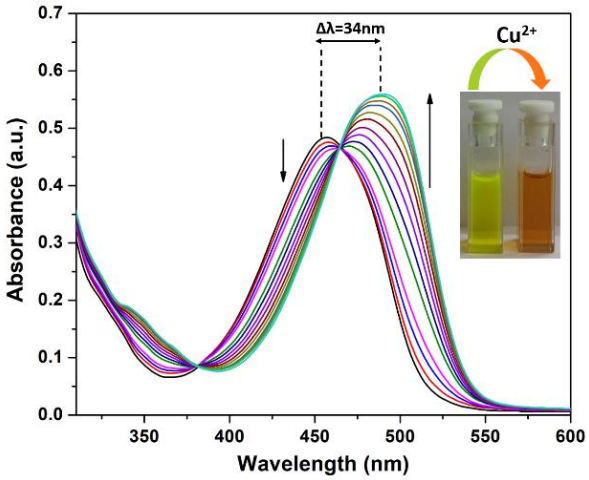


**Figure 5.6:** Change of absorption spectra of DCMC (20 µM) upon addition of $Cu^{2+}$ (40 µM). Inset: The photograph shows the visible colour change of DCMC before and after addition of $Cu^{2+}$.

The UV-Vis absorption titration of DCMC was also executed with $Hg^{2+}$ and $Zn^{2+}$ to explore the interaction. For $Zn^{2+}$, upon gradual addition of $Zn^{2+}$ the absorption maxima shift towards red region with increase in absorption value. The absorption maxima shift from 456 nm to 474 nm (Fig. 5.7). The shift in absorption maxima of about 18 nm indicating the complexation process. For $Hg^{2+}$ titration we observed a change in absorption maxima of 10 nm (Fig. 5.7). Although different wavelength with red shift can be found for $Hg^{2+}$ and $Zn^{2+}$, but the changes are unnoticeable in naked eye. But DCMC is able to detect $Cu^{2+}$ via bare eyes under visible light.

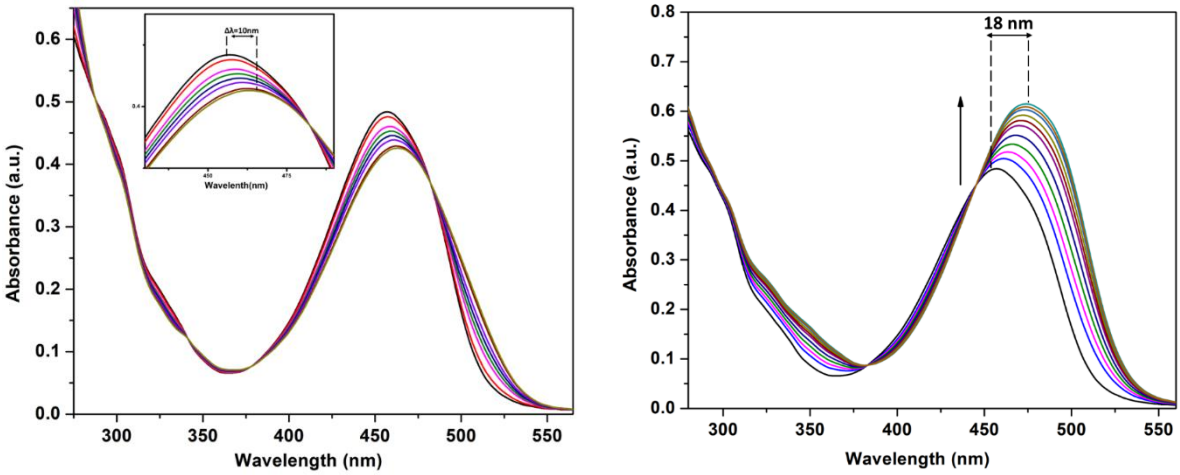


**Figure 5.7:** Change in UV-Vis spectrum of DCMC (20 µM) upon addition of $Hg^{2+}$ (40 µM) in DMSO/$H_2O$ (9/1, v/v, pH=7.2). Inset shows the shift in absorption band (left side) and change in UV-Vis spectrum of DCMC (20 µM) upon addition of $Zn^{2+}$ (50 µM) in DMSO/$H_2O$ (9/1, v/v, pH=7.2) (right side).

The effect in UV-Vis spectrum was also checked for the additional metal cations, i.e., $Ca^{2+}$, $Mg^{2+}$, $Al^{3+}$, $Mn^{2+}$, $Fe^{3+}$, $Al^{3+}$, $Cr^{3+}$, $Co^{2+}$, $Ni^{2+}$, $Pb^{2+}$ and $Mn^{2+}$ but they do not demonstrate any major alterations in the spectral design of DCMC, indicating the fact that DCMC does not interact with the other metal ions (Fig. 5.8).

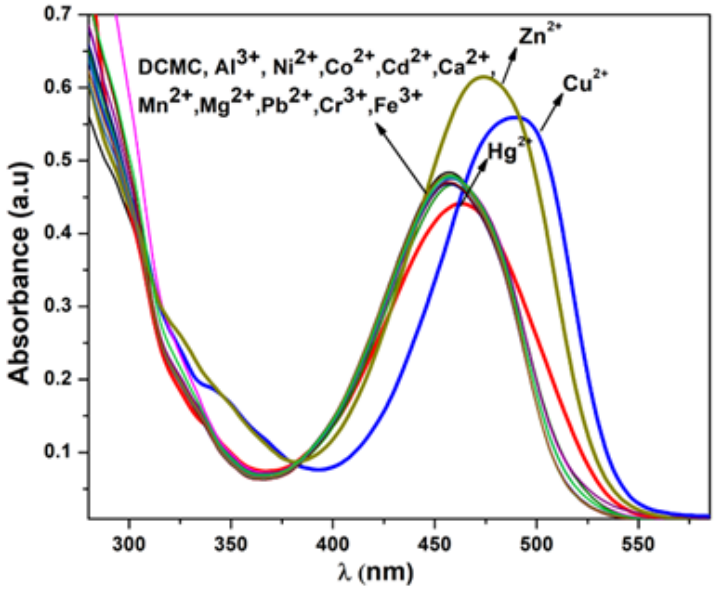


**Figure 5.8:** UV-Vis spectra of (DCMC) (20 μM) upon addition of (40 μM) various metal ions i.e., $Ca^{2+}$, $Mg^{2+}$, $Al^{3+}$, $Mn^{2+}$, $Fe^{3+}$, $Cr^{3+}$, $Co^{2+}$, $Ni^{2+}$, $Cu^{2+}$, $Zn^{2+}$, $Pb^{2+}$, $Cd^{2+}$ and $Hg^{2+}$ in DMSO/$H_2O$ (9/1, v/v, pH = 7.2) solution.

### 5.4.4.2. Fluorescence study of DCMC

The fluorescence response of sensor DCMC towards $Zn^{2+}$ and $Hg^{2+}$, were explored by fluorescence titration experiments in DMSO/$H_2O$ (v/v, 9/1, pH=7.2) at room temperature. The fluorescence intensity of DCMC was monitored with continuing addition of $Zn^{2+}$ solution (50 μM). Upon excitation at 456 nm DCMC exhibits a strong emission band with maxima at 522 nm and shows high quantum yield value (φ = 0.6604) (Table A5.3, Appendix). DCMC shows a strong green colour emission under hand held UV lamp. On subsequent addition of $Zn^{2+}$ solution (50 μM) to DCMC solution (20 μM) in DMSO /$H_2O$ solvent (9/1, v/v, pH=7.2) the emission intensity slowly decreases with red shift and finally the maxima shifted to 556 nm (Fig. 5.9). Also, the quantum yield value changes to (φ = 0.5611) (Table A5.3, Appendix). Subsequently, we also observe that the colour of the solution also changes to yellow (Fig. 5.9). Thus, this ratiometric change in the emission intensity pattern of about 34 nm towards red region confirms the formation of DCMC-$Zn^{2+}$ complexation and generation of new ICT process. In Commission International de L'Eclairage (CIE) Chromaticity coordinates, we also observed noticeable

changes from green to yellow with change in the coordinates from (x = 0.3253, y =0.6118) to (x =0.4391, y =0.5461) (Fig. 5.9). Thus, these changes in the fluorescence pattern with addition of $Zn^{2+}$ is attributed to the filled $d^{10}$ electronic configuration of $Zn^{2+}$ ion which commonly does not include in the energy transfer mechanism for activating the excited state.

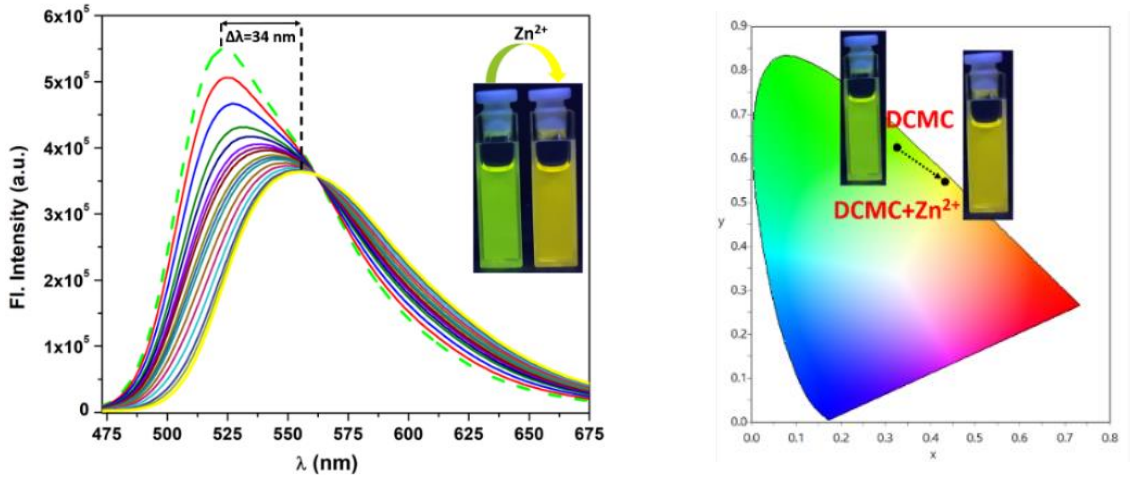


**Figure 5.9:** Change in emission spectrum of DCMC (20 μM) upon gradual addition of $Zn^{2+}$ (50 μM) in DMSO/$H_2O$ (9/1, v/v, pH = 7.2) solution. Inset: The visual effect of addition of $Zn^{2+}$ to DCMC under UV light. ($\lambda_{ex}$ = 456 nm) (left side) and CIE1931 chromaticity diagram of DCMC probe with $Zn^{2+}$ (right side).

We also explored fluorescence response of DCMC towards $Hg^{2+}$ by fluorescence titration experiment. With addition of $Hg^{2+}$ solution the fluorescence intensity simultaneously quenches at 522 nm about 96% with slight red shift. At the same time the bright greenish fluorescence colour also vanishes as shown in Fig.5.10. Hence this spectroscopic observation reveals that a complex is formed between DCMC and $Hg^{2+}$, where due to ligand-metal charge transfer (LMCT) process fluorescent quenching happens.

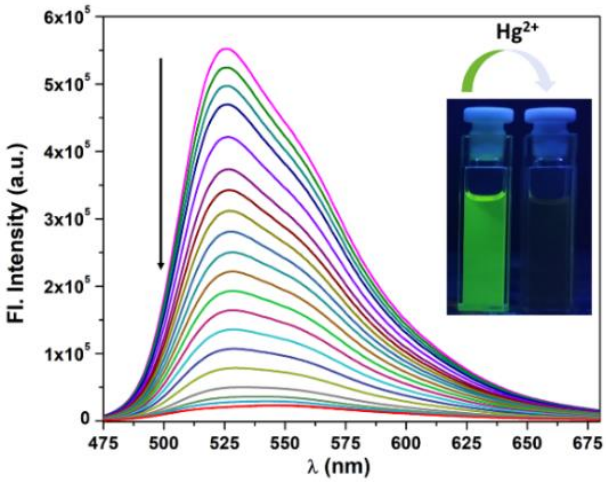


**Figure 5.10:** Change in emission spectrum of DCMC (20 μM) upon gradual addition of $Hg^{2+}$ (40 μM) in DMSO/$H_2O$ (9/1, v/v, pH = 7.2) solution. Inset: The visual effect of addition of $Hg^{2+}$ to DCMC under UV light. $\lambda_{ex}$ = 456 nm.

The emission property of DCMC was also studied in various DMSO/$H_2O$ ratio to detect $Zn^{2+}$ and $Hg^{2+}$ but we observed that other composition of solvents is not as much sensitive as in the case for DMSO/$H_2O$ (9/1, v/v). So, we have optimized the DMSO/$H_2O$ ratio and executed all spectroscopic studies in DMSO/$H_2O$ (9/1, v/v).The selectivity of the chemosensor was also studied towards different metal ions such as $Cr^{3+}$, $Co^{2+}$, $Mn^{2+}$, $Fe^{3+}$, $Mg^{2+}$, $Al^{3+}$, $Cd^{2+}$, $Ni^{2+}$, $Ca^{2+}$ and $Pb^{2+}$. They display no variation in the emission property of DCMC (Fig. 5.11).

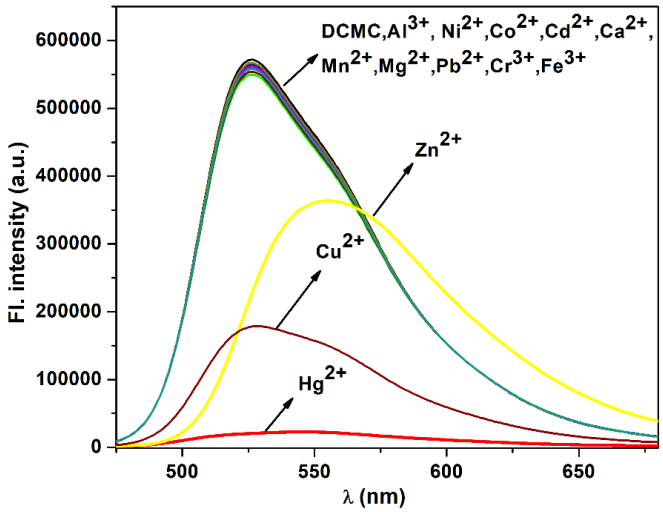


**Fig. 5.11:** Change in emission spectrum of DCMC (20 μM) upon addition of different cations i.e., $Mg^{2+}$, $Al^{3+}$, $Ca^{2+}$, $Mn^{2+}$, $Fe^{3+}$, $Cr^{3+}$, $Co^{2+}$, $Ni^{2+}$, $Cu^{2+}$, $Zn^{2+}$, $Pb^{2+}$, $Cd^{2+}$ and $Hg^{2+}$ (40 μM) in DMSO/$H_2O$ (9/1, v/v, pH=7.2). ($\lambda_{ex}$ =456 nm)

### 5.4.4.3. Detection limit (LOD) and binding constant ($K_a$)

The fabricated probe DCMC can be used for quantitative recognition of the ions in its selected concentration range. LOD was calculated from the fluorescence spectral change data for $Zn^{2+}$ and $Hg^{2+}$ and from absorption spectral change data for $Cu^{2+}$. The equation that is utilized for the calculation is LOD = K × SD/S, where k = 2 or 3 (here 3 is taken) where SD signifies the standard deviation of blank probe solution and S stands for the slope in the linear calibration curve respectively. The detection limit value was calculated and established to be (2.69 ± 0.09) × $10^{-9}$ (M) for $Hg^{2+}$, (5.35 ± 0.18) × $10^{-9}$ (M) for $Zn^{2+}$ and (1.85 ± 0.07) × $10^{-7}$ (M) for $Cu^{2+}$ respectively (Fig. 5.12 &Fig. 5.13 (left side)).

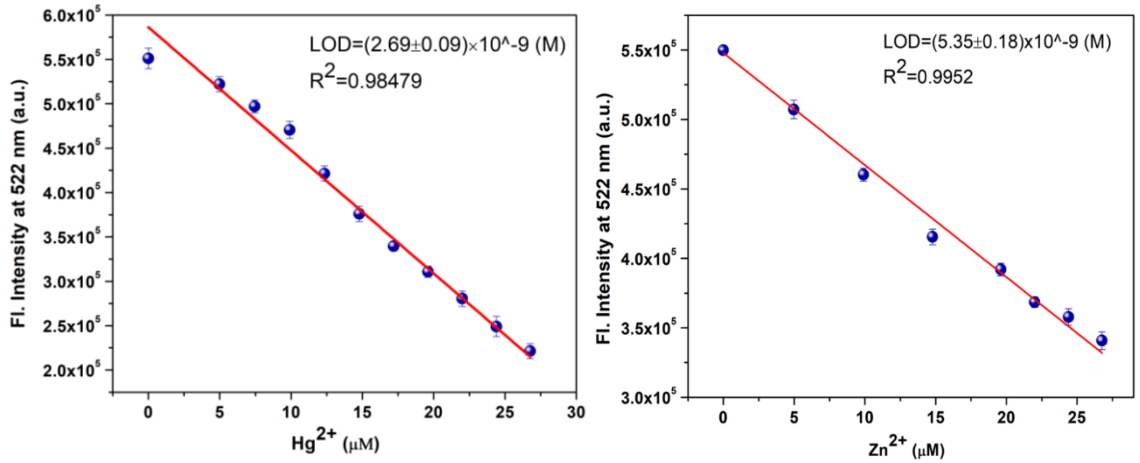


**Figure 5.12:** Linear response curve of DCMC at 522 nm depending on the $Hg^{2+}$ concentration (left side) and Linear response curve of DCMC at 522 nm depending on the $Zn^{2+}$ concentration (right side).

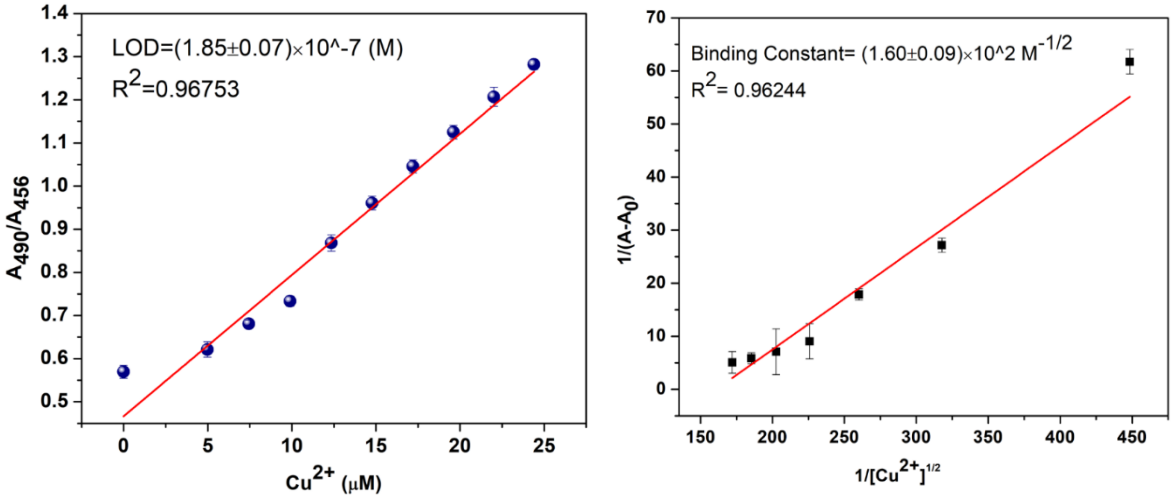


**Figure 5.13:** Linear response curve of DCMC at $A_{490}/A_{456}$ depending on the $Cu^{2+}$ concentration (left side) and Benesi-Hildebrand plot from absorption titration data of probe DCMC (20 μM) with $Cu^{2+}$(right side).

These values suggest that DCMC is efficient to detect the ions in very miniscule level. To reveal the binding stoichiometry of complex formation, Job's plot analysis was executed. Emission intensity and absorption spectra was measured, while the sum of the entire volume of DCMC and the metal ions was maintained to a constant volume. Where change in fluorescence intensity (ΔI) vs. mole fraction ($X_h$) of the probe DCMC was plotted for $Hg^{2+}$ and the intersection point the two straight line was found to be at 0.66, which proposes that a 2:1 complex formation between DCMC and $Hg^{2+}$ (Fig. A5.5, Appendix). Also, for $Cu^{2+}$, the plot between absorption vs mole fraction of $Cu^{2+}$ shows maxima near 0.33, indicating a 2:1 complexation between DCMC and $Cu^{2+}$ (Fig. A5.6, Appendix). Binding constant was calculated according to the Benesi-Hildebrand equation. $K_a$ was calculated following the equation stated below.

$$1/(F-F_0) = 1/\{K_a (F_{max}–F_0) [M^{n+}]^x\} + 1/[F_{max}-F_0]$$

Here $F_0$, F and $F_{max}$ indicate the emission in absence of, at intermediate and at infinite concentration of metal ion respectively.

From absorption titration data the binding constant for $Cu^{2+}$ was calculated to be (1.60 ± 0.9) × $10^2$ $M^{-1/2}$ respectively (Fig. 5.13 (right side)). From fluorescence titration data the binding constant for $Zn^{2+}$ and $Hg^{2+}$ was evaluated to be (1.17 ± 0.05) × $10^2$ $M^{-1/2}$and (1.41 ± 0.06) × $10^2$ $M^{-1/2}$ respectively (Fig. 5.14).

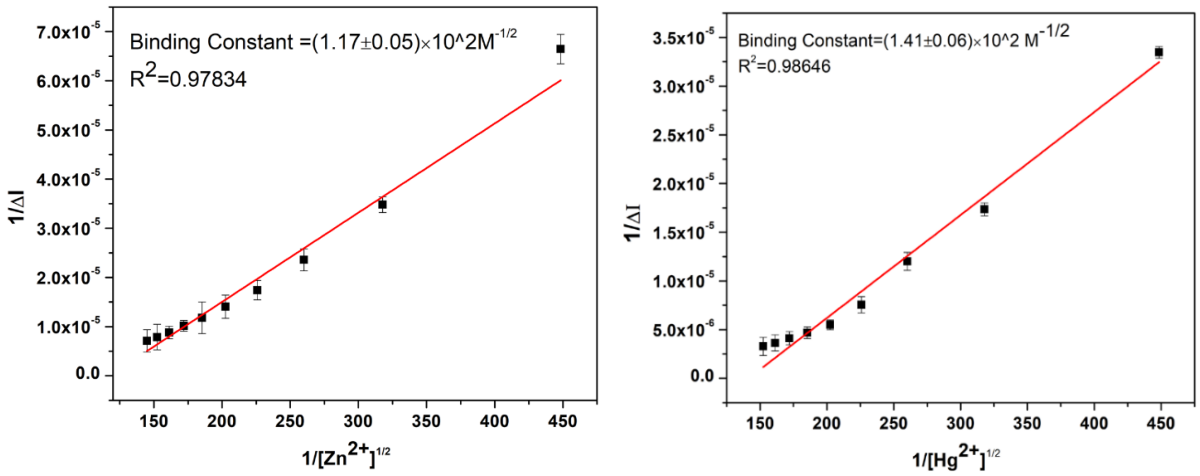


**Figure 5.14:** Benesi-Hildebrand plot from fluorescence titration data of probe DCMC (20 µM) with $Zn^{2+}$ (left side) and Benesi-Hildebrand plot from fluorescence titration data of probe DCMC (20 µM) with $Hg^{2+}$ (right side).

### 5.4.4.4. Competitive study

A proficient chemosensor must be selective towards its guest specifically and swiftly in presence of other environmentally and biologically appropriate metal ions. As reported recently the anti-interference ability of probe DCMC towards $Cu^{2+}$, $Zn^{2+}$ and $Hg^{2+}$ was examined with one target analyte and one interference species. As can be seen from Fig. 5.15., for $Cu^{2+}$ no other metal ions have interference value of absorption at 590 nm.

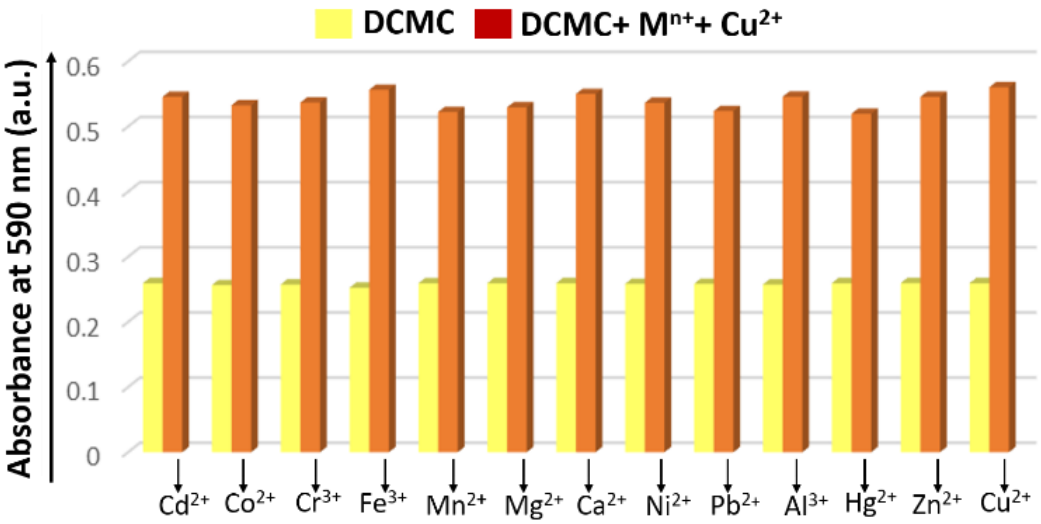


**Figure 5.15:** Change in absorption spectra upon addition of various metals (40 μM) in DMSO/$H_2O$ (9/1, v/v, pH=7.2). DCMC (yellow bars), and DCMC-$Cu^{2+}$ in the presence of other metals (brown bars).

For $Hg^{2+}$ the fluorescence quenching efficacy is above 90% at 522 nm in all cases (Fig. 5.16). For $Zn^{2+}$, also no other cations have no significant effect on 540 nm value. As this competitive experiment was performed by a pair of analytes, hence the deficiency of the method is it is difficult to judge the performance, in presence of coexistence of multiple analytes. Although it is still a challenge to simultaneously detect target analyte and evade interference of other high valent metal ions, still DCMC is able to detect $Cu^{2+}$, $Hg^{2+}$ and $Zn^{2+}$ in presence of other metal ions.

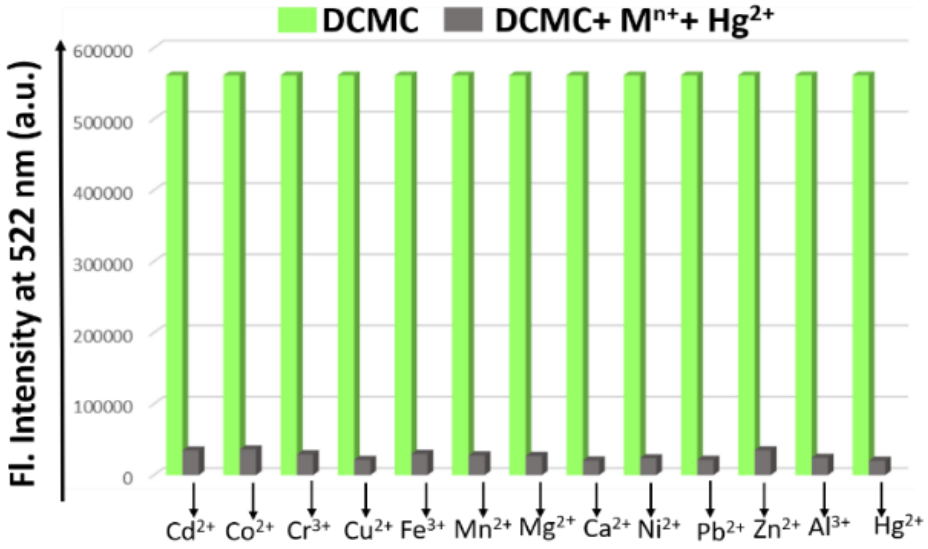


**Figure 5.16:** Change in emission spectra upon addition of various metals (40 μM) in DMSO/$H_2O$ (9/1, v/v, pH=7.2). DCMC (grey bars), and DCMC-$Hg^{2+}$ in the presence of other metals (green bars).

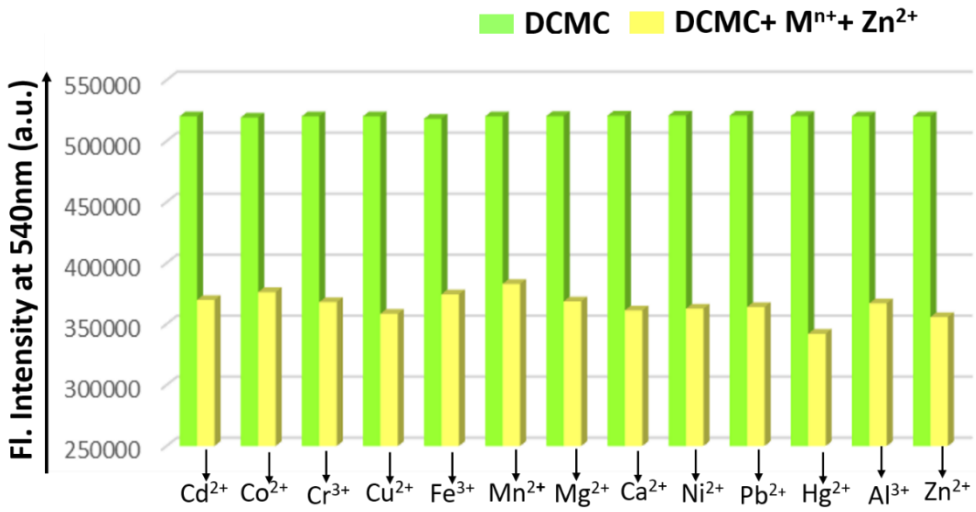


**Figure 5.17:** Change in emission intensity upon addition of various metals (40 μM) in DMSO/$H_2O$ (9/1, v/v, pH=7.2). DCMC (green bars), and DCMC-$Zn^{2+}$ in the presence of other metals (yellow bars).

### 5.4.4.5. pH effect

To investigate the pH dependency of DCMC emission, its sensitivity has been evaluated in presence and absence of $Hg^{2+}$ and $Zn^{2+}$ solution. Hence, we executed the experiment in DMSO/$H_2O$ (9/1, v/v) in the pH range of 2.0-12.0. For DCMC in neutral pH it shows high emission intensity, whereas with increase in acidity we observe that the emission intensity decreases at 522 nm due to protonation of N atom on diethyl amino group attached to coumarin moiety suppressing the ICT process. With increase in basicity also the sudden drop of emission

intensity is noticed due to deprotonation of -NH- fragment inhibiting the ICT process within the molecule. For DCMC-$Hg^{2+}$ species the intensity at 522 nm remains constant from pH range of 4-12 indicating DCMC can detect $Hg^{2+}$ in a wide range of pH value (Fig. 5.18). For DCMC-$Zn^{2+}$ species in the pH range of 7-9 the intensity pattern at 522 nm shows similar to that of DCMC. But with increase in pH above 9 the intensity started to decrease and with decrease in pH below 7 the intensity started to increase at 522 nm. Hence this concludes that DCMC can be used for efficient detection of $Hg^{2+}$ in the physiological pH of 7.2 (Fig. 5.18).

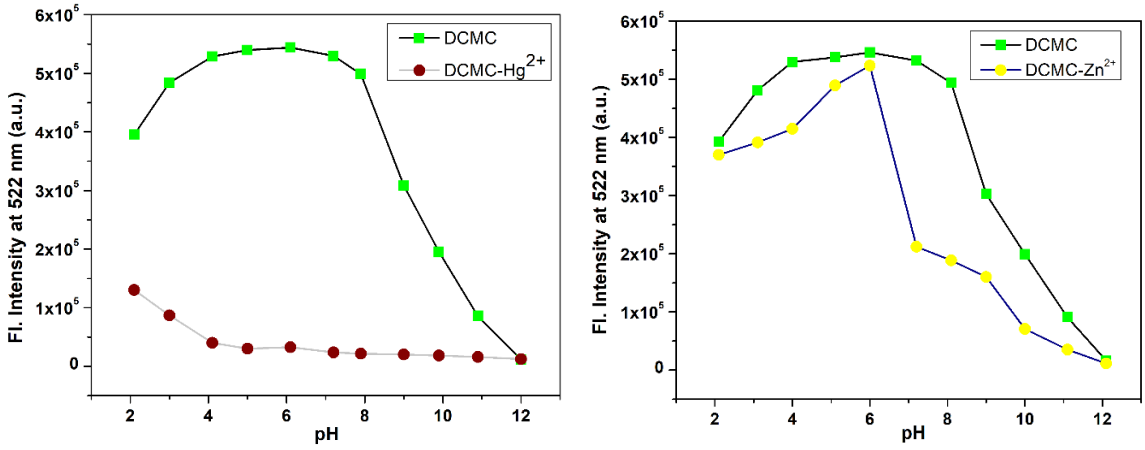


**Figure 5.18**: Fluorescence response of DCMC (-■-■-) and DCMC-$Hg^{2+}$ (-●-●-) as a function of pH in DMSO/$H_2O$ (9/1, v/v) (left side) and Fluorescence response of DCMC (-■-■-) and DCMC-$Zn^{2+}$ (-●-●-) as a function of pH in DMSO /$H_2O$ (9/1, v/v). The pH is adjusted by using aqueous solutions of 1 M HCl or 1 M NaOH. ($\lambda_{ex}$=456 nm) (right side).

## 5.4.5. TRPL Study

To elucidate the excited state behavior of DCMC, its ratiometric fluorescence response towards $Zn^{2+}$ and its quenching approach towards $Hg^{2+}$, we have performed nanosecond time-resolved fluorescence study (TRPL). Herein, the free probe and its $Zn^{2+}$, $Hg^{2+}$ solution in DMSO/$H_2O$ (9: 1, v/v) were taken and the study was performed. For DCMC a mono exponential life time plot was obtained and lifetime(τ) was calculated to be 3.1095 ns ($\chi^2$ = 1.04). While for DCMC-$Zn^{2+}$ species by fitting mono exponential curve with suitable $\chi^2$ value the lifetime(τ) value was calculated and it increases slightly to 3.2119 ns (Fig. 5.19 and Table A5.3, Appendix). The observation assists the fact that DCMC binds effectively with $Zn^{2+}$ making the ligand framework more rigid by prohibiting the rotation around single bond, thus increasing the chance of new ICT process. To get further insight of the quenching process TRPL study was obtained with addition of $Hg^{2+}$ in DCMC where, for DCMC-$Hg^{2+}$ species a mono exponential plot was obtained with

acceptable $\chi^2$ value and the τ remained to be 3.1609 ns ($\chi^2$ = 1.03) (Fig. 5.19). This suggests that the lifetime of DCMC is not affected by $Hg^{2+}$ indicating static quenching phenomenon where the ground state non fluorescent complexation happens between the luminophore and quencher.The radiative rate constant ($k_r$) and the non-radiative rate constant ($k_{nr}$) of DCMC, DCMC-$Zn^{2+}$ and DCMC-$Hg^{2+}$ species were determined by following the equation $\tau^{-1} = k_r + k_{nr}$, where $kr = \varphi_f/\tau$. Radiative rate constant ($K_r$) and total non-radiative rate constant ($K_{nr}$) have been calculated and abridged in Table A5.3, Appendix. This change in the value of τ, $K_r$ and $K_{nr}$ clearly confirmed the complexation of the probe with the metal ions. Hence DCMC proves its credentials as an efficient sensor towards $Zn^{2+}$ and $Hg^{2+}$ by TRPL study.

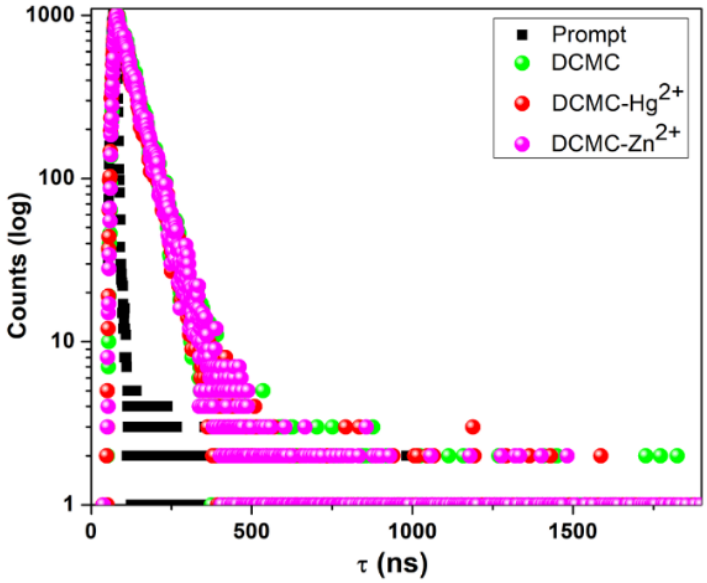


**Figure 5.19:** Time-resolved fluorescence decay of DCMC (●●●), DCMC-$Hg^{2+}$ (●●●) and DCMC-$Zn^{2+}$ (●●●). ($\lambda_{ex}$=456 nm).

## 5.4.6. Possible sensing mechanism

We can observe DCMC is itself a fluorescence probe (shows maxima at 522 nm) due to presence of long resonance starting from N atom (Diethyl amino group) present in coumarin moiety, responsible for charge transfer within the probe. When DCMC binds with $Cu^{2+}$ the photoinduced electron transfer (PET) process appears in the complex, which triggers the quenching process in the sensing system. In order to confirm the binding mode with $Cu^{2+}$, ESI-MS was done for DCMC-$Cu^{2+}$, we observed a prominent peak at (m/z) 725.1052, which could be assigned to the formation of $[2DCMC-2H+Cu^{2+}]^+$ species (Fig. A5.10, Appendix). According to the coordination mode of coumarin oxygen, imine nitrogen and sulphur atom present in DCMC, we proposed the biding mode with $Cu^{2+}$, in Fig. 5.20 and Fig. 5.26 forming an octahedral complex. Also, the jobs plot analysis showed the exact 2:1 stoichiometry of complex formation between

DCMC and $Cu^{2+}$ (Fig. A5.6, Appendix). Further we observed upon addition of $Zn^{2+}$ a ratiometric change in the fluorescence pattern, this could be attributed to the $d^{10}$ electronic configuration of the Zn(II) system, which does not involve in the energy transfer mechanism for activating the excited state. $^{1}$H-NMR titration was carried out in DMSO-$d_6$ upon addition of $Zn^{2+}$, where we observed that the peak of the -NH proton at 8.5016 ppm which is beside -$CH_3$ group vanishes, also the other doublet peak of -$CH_3$ proton is converted to singlet peak of 3.0506 ppm (Fig. A5.8, Appendix). So, this suggests the binding combination of DCMC with its imine nitrogen, coumarin oxygen and the Sulphur atom which results in a significant change of intermolecular charge transfer (ICT) process within DCMC. Thus, we observe a change in fluorescence maxima. In addition, the mixture of DCMC with $Zn^{2+}$ exhibited a complex peak at (m/z) 727.1149, which is attributed to formation of [2 DCMC-2H+$Zn^{2+}$+$H^{+}$]$^{+}$ species, which in a way supported the 2:1 stoichiometry between DCMC and $Zn^{2+}$(Fig. A5.9, Appendix). Similarly, in $^{1}$H NMR of DCMC-$Hg^{2+}$ we observed the -NH peak at 8.5016 ppm diminishes and the neighbouring -$CH_3$ doublet peak is converted to a singlet peak of 2.2479 ppm, signifying that $Hg^{2+}$ ion may be bonded to imine -N atom and sulphur atom of the sensor DCMC forming a Tetrahedral complex (Fig. A5.7, Appendix). Along with NMR titration jobs plot analysis between DCMC and $Hg^{2+}$ also confirmed the 2:1 stoichiometry (Fig. A5.5, Appendix). Further the ESI-MS spectra of DCMC-$Hg^{2+}$ showed a peak at (m/z) 865.1475 confirmed the [2 DCMC-2H+ $Hg^{2+}$+$H^{+}$]$^{+}$ species (Fig. A5.11, Appendix). Thus, the complex formed between DCMC and $Hg^{2+}$ causes fluorescence quenching, which could be attributed to the Ligand to metal charge transfer (LMCT) occurring between DCMC and $Hg^{2+}$(Fig. 5.20). Further to study the binding model and sensing mechanism of DCMC towards $Hg^{2+}$, $Zn^{2+}$ and $Cu^{2+}$ we have simulated the structures of DCMC and its corresponding complexes and optimized them. The frontier molecular orbitals involved for DCMC is shown in (Fig. A5.12, Appendix), where the orbital electron cloud distribution proposed that the ICT mechanism exists in DCMC.

From DFT study, it can be established that highest occupied molecular orbital (HOMO) of sensor DCMC is located throughout DCMC, on coumarin moiety as well as in the thiosemicarbazide part as well (Fig. A5.12, Appendix). On contrast lowest unoccupied molecular orbital (LUMO) of sensor DCMC is mainly distributed on coumarin ring and a little on the thiosemicarbazide part. The HOMO-LUMO energy gap decrease for DCMC-$Cu^{2+}$, which generates the formation of PET process. When $Cu^{2+}$ complex is formed with DCMC the PET process occurs in the complex, leading to fluorescence quenching. From Fig. A5.15, Appendix, it can also be observed that DCMC-$Hg^{2+}$ can be generated due to its lower energy. In case of

DCMC-$Hg^{2+}$ electron cloud redistribution occurs, which induces the LMCT process between DCMC and $Hg^{2+}$. Thus, the fluorescence quenching happens in presence of $Hg^{2+}$. In addition, for DCMC-$Zn^{2+}$ also electron cloud is redistributed and the energy gap also decreases which in a way beneficial to generate a new ICT process within the probe, thus these leads to a fluorescence colour change from cyan green to yellow. Thus, based on above investigation we can conclude that DCMC is able to bind different metal ions by different sensing modalities and the proposed interaction model for all the three sensing cations is shown in Fig 5.20.

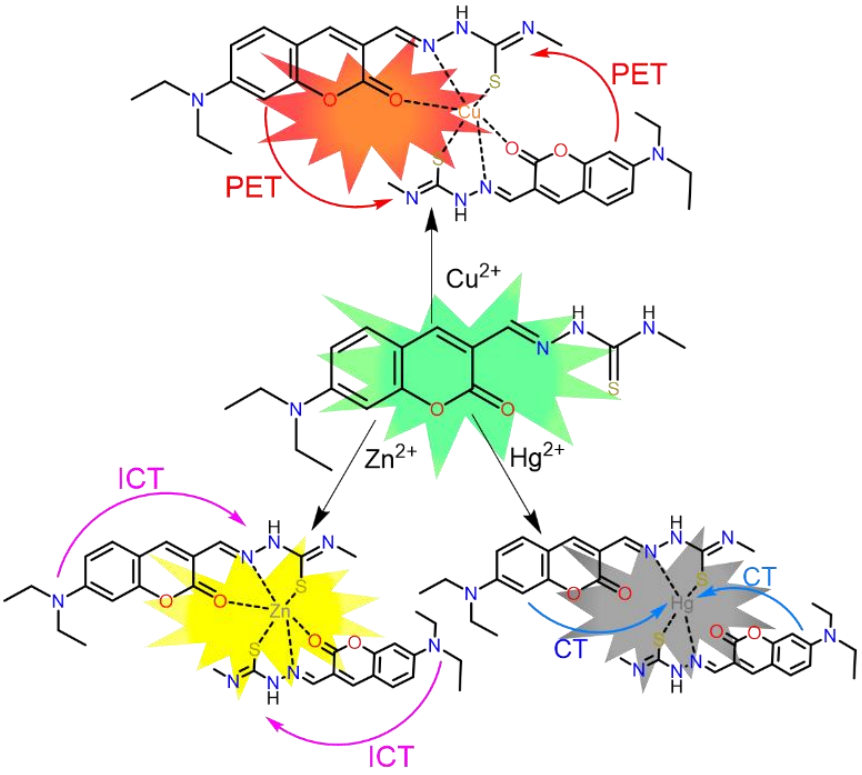


**Figure 5.20:** Proposed sensing mechanism of DCMC towards $Cu^{2+}$, $Zn^{2+}$ and $Hg^{2+}$.

## 5.4.7. Analytical applications

A practical application tool was proposed after getting inspired by the distinct detection of $Cu^{2+}$, $Hg^{2+}$ and $Zn^{2+}$ ion by DCMC through different modes, which is a capable as well as portable method known as dip stick experiment. By this method we can qualitatively sense exact analytes without any classy instrumentation technique. Hence, to carry out this experiment, we arranged few thin-layer chromatography (TLC) plates and dipped them into DCMC-treated DMSO solution ($2x10^{-4}$ M) after that the plates were allowed to dry in air for sometimes. The Probe-loaded TLC plates itself displayed a greenish colour under 365 nm hand held UV light (Fig. 5.21, a). Then one of the probes loaded TLC Plate was dipped in $Zn^{2+}$ ($2\times10^{-3}$ M) solution and again kept in air to vaporize the solvent, now we observed that the green fluorescent under UV

light changed to yellowish green (Fig. 5.21, a).Also, another probe loaded TLC plate was dipped in a $Hg^{2+}$ ($2\times10^{-3}$ M) solution and allowed to dry, which under UV light changed its colour from green to ash grey colour (Fig. 5.21, a). In normal light the probe itself shows golden yellow colour, the TLC plate was dipped in a $Cu^{2+}$ ($2\times10^{-3}$ M) solution and exposed to air to dry out the solvent and the colour changes from golden yellow to light brown colour (Fig. 5.21, b). These colour changes can be simply be distinguished by bare eye when TLC plates were exposed UV light and in ambient light. Hence this experiment describes that, without the aid of any instrumental analysis, only by using TLC plates and through the naked eye, instantaneous recognition of $Zn^{2+}$, $Cu^{2+}$ and $Hg^{2+}$ can be done using the DCMC probe.

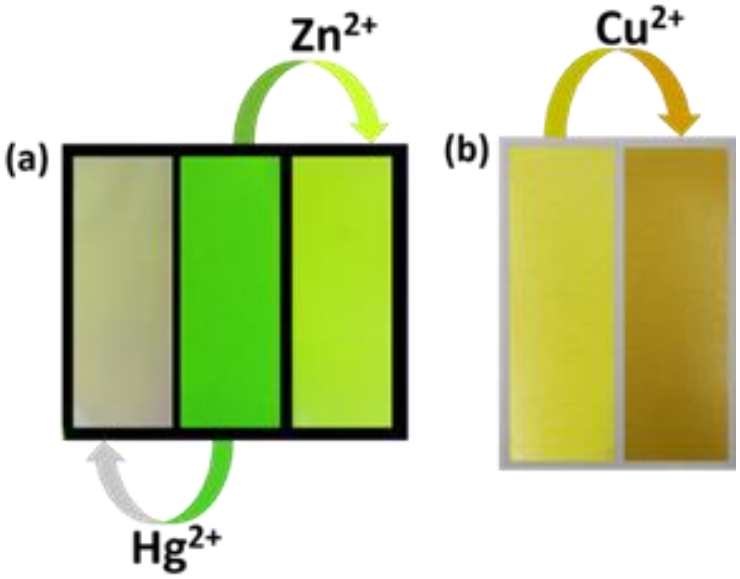


**Figure 5.21:** Pictures of probe-loaded TLC plates after immersion into $Hg^{2+}$ and $Zn^{2+}$ solution under UV chamber (a) and probe loaded TLC plates after immersion in $Cu^{2+}$ solution in ambient light (b). [DCMC] = $2 \times 10^{-4}$ (M), [$Hg^{2+}$] = $2 \times 10^{-3}$ (M), [$Cu^{2+}$] = $2 \times 10^{-3}$ (M), [$Zn^{2+}$] = $2 \times 10^{-3}$ (M). Excitation wavelength of the UV light is 345 nm.

Additionally, we also applied the probe DCMC solution on silica gel base for another solid state supported practical application. The silica loaded sensor was prepared according to the previously reported procedure.[99] The 60-120 mesh size silica gels were loaded with probe ($2\times10^{-4}$ M) solution and it was kept for drying for 1 h in an oven. The silica loaded probe showed lemon-yellow colour in ambient light and greenish colour under hand held UV light. Treatment of $Zn^{2+}$ solution ($2 \times 10^{-3}$ M) transformed the green colour of silica gel to yellow colour under UV light (Fig. 5.23). Also, treatment of $Cu^{2+}$ solution ($2 \times 10^{-3}$ M) to DCMC

rapidly transformed the lemon-yellow colour of DCMC treated silica gel to brown colour under ambient light, indicating real time application in solid state (Fig. 5.22).

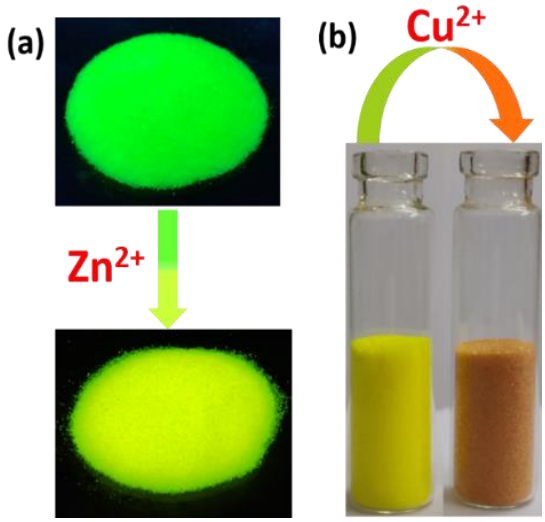


**Figure 5.22:** Colour changes of **DCMC** in the solid state (silica gel base) upon addition of $Zn^{2+}$ ion under UV light (a) and upon addition of $Cu^{2+}$ under ambient light (b). [DCMC] = $2 \times 10^{-4}$ (M), [$Zn^{2+}$] = $2 \times 10^{-3}$ (M), [$Cu^{2+}$] = $2 \times 10^{-3}$ (M).

## 5.4.8. Application in biological study

### 5.4.8.1. Cytotoxicity assay

The cell viability percentages and cytotoxic effect of DCMC at several concentrations on MCF-7 cells were determined by in-vitro cytotoxicity study using the MTT reagent, following our established lab protocol.[100] Briefly, MCF-7 cells were seeded in 96 well plates, at a density of $1 \times 10^4$ cells/well for 24 h. Then, the cells were treated with DCMC at a range of 5-160 μM, and incubated for 24 h (Fig. 5.23). After 24 h, the MTT reagent was added to each well and then incubated for 3-4 h. Lastly, DMSO-Methanol (1:1) was added to each well, and all of the absorbance values were recorded at 570 nm in a microtiter plate-reader (Spectramax i3x). The percentage of cell viabilities at several concentrations were calculated by means of the following formula:

Percentage (%) Cell viability = $[(A_{treated} - A_{blank}) / (A_{untreated} - A_{blank})] \times 100$

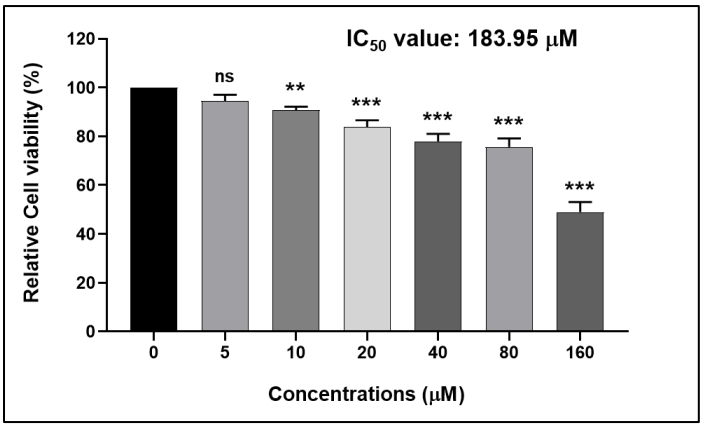


**Figure 5.23:** Bar diagrams represent cell viabilities of DCMC with different concentrations (5-160 µM) against human breast epithelial adenocarcinoma cells (MCF-7). All the experiments were performed independently thrice and the data were calculated as Mean ± SD where *P < 0.05, **P < 0.01, ***P < 0.001.

### 5.4.8.2. Cellular imaging by fluorescence microscopy

To observe the biological efficacy of DCMC, we performed the *in-vitro* cytotoxicity study and cellular imaging study on the breast epithelial adenocarcinoma cell line (MCF-7). The *in-vitro* cytotoxicity study determined that the DCMC shows negligible cytotoxicity ($IC_{50}$ value: 183.95 µM) on MCF-7 cells. Therefore, we have preferred the $IC_{50}$ dosage of DCMC to execute the cellular imaging experiment. Next, to corroborate with the application of the live cell imaging of DCMC, the cells were treated with only DCMC (183.95 µM) for 30 minutes. After 30 minutes, the incubated cells exhibited strong green fluorescence under the fluorescence microscope, which directed to the fact that treating the MCF-7 cells with only DCMC displays a clear green fluorescence. Whereas, in the presence of Hg along with the DCMC, no fluorescence was detected but in the presence of Zn along with the DCMC the green fluorescence, previously showed in the case of only DCMC, gradually changed into strong yellow fluorescence (Fig. 5.24).

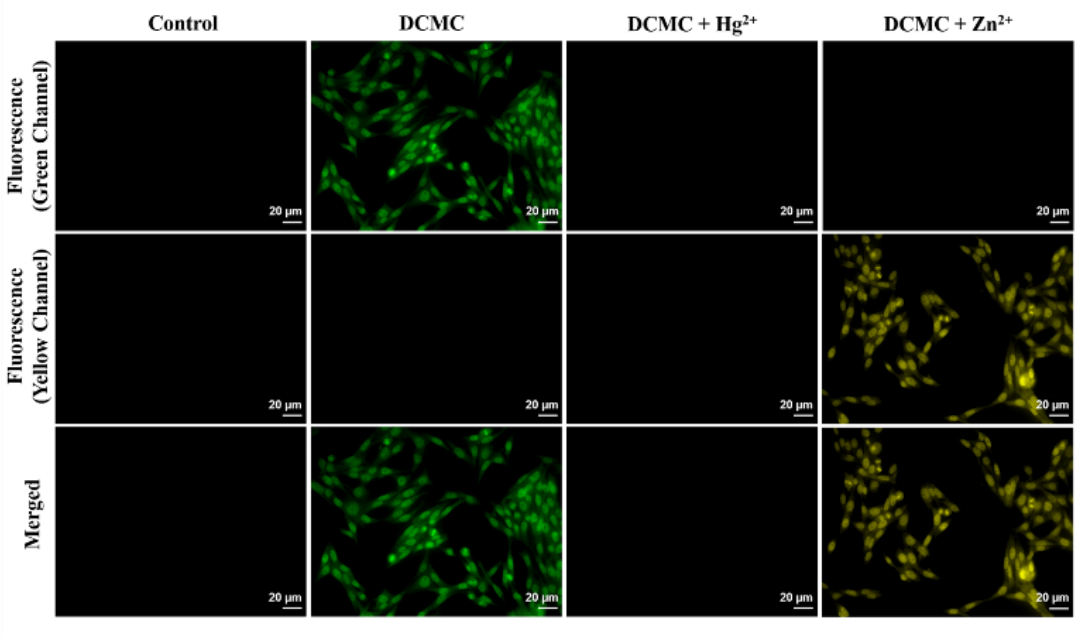


**Figure 5.24:** Fluorescence images of MCF-7 cells after incubation with only DCMC, DCMC along with $Hg^{2+}$, and DCMC along with $Zn^{2+}$ under a fluorescence microscope at 40X magnification. (Scale bar correspondence to 20 µm)

## 5.4.9. Theoretical computations

To elaborate the sensing mechanism and the structural changes of DCMC towards $Hg^{2+}$, $Zn^{2+}$ and $Cu^{2+}$, we conducted density functional theory (DFT) calculations by B3LYP/6-31+G(d) method by means of Gaussian 09 program. The contour plot of some selected molecular orbitals of DCMC and its corresponding complexes are shown in Fig. A5.12- Fig. A5.16, Appendix respectively. Electronic excitations of DCMC, DCMC-$Hg^{2+}$, DCMC-$Zn^{2+}$ and DCMC-$Cu^{2+}$ complexes were calculated in DMSO medium using the TDDFT method by the CPCM method on the optimized geometries. The HOMO-LUMO gap for DCMC was calculated to be 3.03 eV. For DCMC the calculated vertical excitations displayed a lowest energy strong emission (f = 1.2233) band at 453 nm, which resembles to the HOMO-LUMO transition. For DCMC-$Zn^{2+}$, the HOMO-LUMO energy gap decreases to 2.48 eV. Moreover, the decrease in the HOMO-LUMO energy gap for the DCMC-$Zn^{2+}$ complex is well reflected in the red shift of UV-Vis spectra. The decrease in energy gap also assists the generation of new ICT process which ultimately leads to the colour change of DCMC after reacting with $Zn^{2+}$ from cyan-green to yellow under UV light. The energy and their % compositions for DCMC-$Zn^{2+}$ are shown in Table A5.7, Appendix. Again, for DCMC-$Hg^{2+}$, the HOMO-LUMO energy gap was calculated to be 2.91 eV. For DCMC-$Hg^{2+}$ the calculated HOMO-LUMO transition was shifted to 472 nm (f = 2.6252). The

energy and their % compositions for DCMC-$Hg^{2+}$ are comprised in Table A5.8, Appendix. The electron density on the selected contour plots suggested the Ligand to metal charge transfer (LMCT) process between DCMC and $Hg^{2+}$. In case of DCMC-$Cu^{2+}$ for both alpha and beta spin the HOMO-LUMO energy gap decreases to 2.51 eV and 2.10 eV respectively. Considering DCMC-$Cu^{2+}$, it was noted that the charges were evidently distributed, this is in accordance with the fact that DCMC-$Cu^{2+}$ complexes had paramagnetic properties that caused fluorescence quenching by PET process. The energy and their % compositions of DCMC-$Cu^{2+}$ for both alpha and beta forms are shown in Table A.5, Appendix and Table A.6, Appendix. The decrease in energy gap is also well reflected on the red shift in the UV-Vis spectra. Therefore, the decrease of the energy gap between the DCMC-$Zn^{2+}$/$Hg^{2+}$/$Cu^{2+}$ complexes noticeably certify that the complexes were more stable and more rigid compared to DCMC and the coordination with the metal ions produces noteworthy red shift in the absorption spectrum (Fig. 5.25).

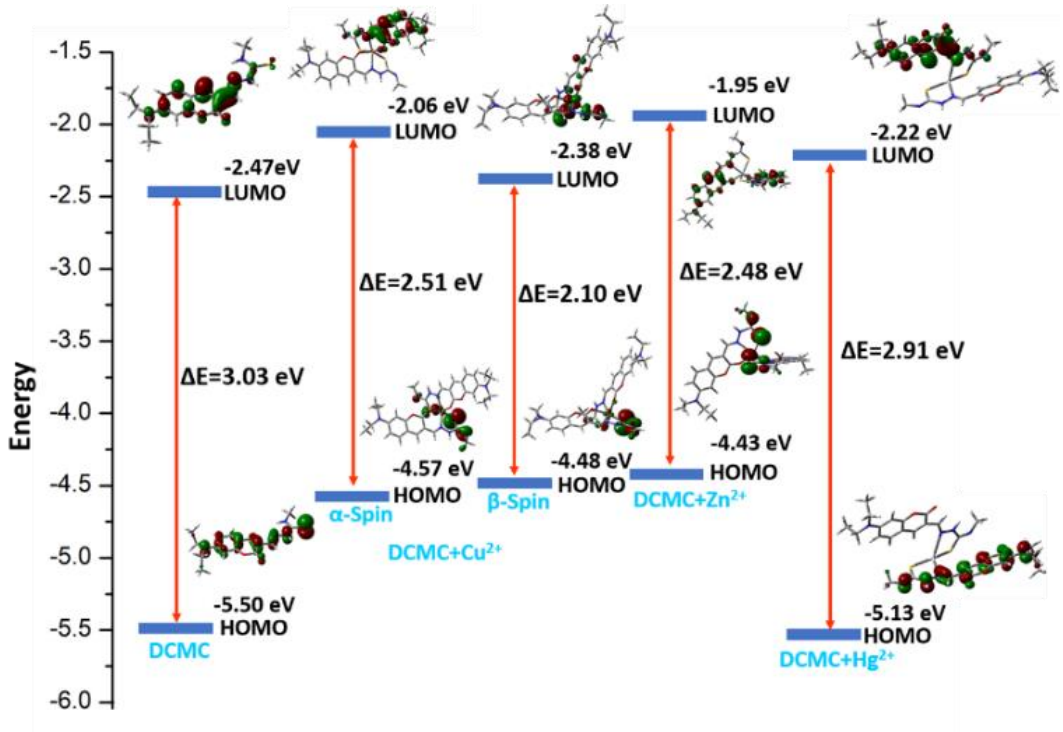


**Figure 5.25:** The HOMO-LUMO energy gap of DCMC, DCMC-$Cu^{2+}$(α and β spin), DCMC-$Zn^{2+}$ and DCMC-$Hg^{2+}$ calculated using the DFT/B3LYP/6-31+G(d) method.

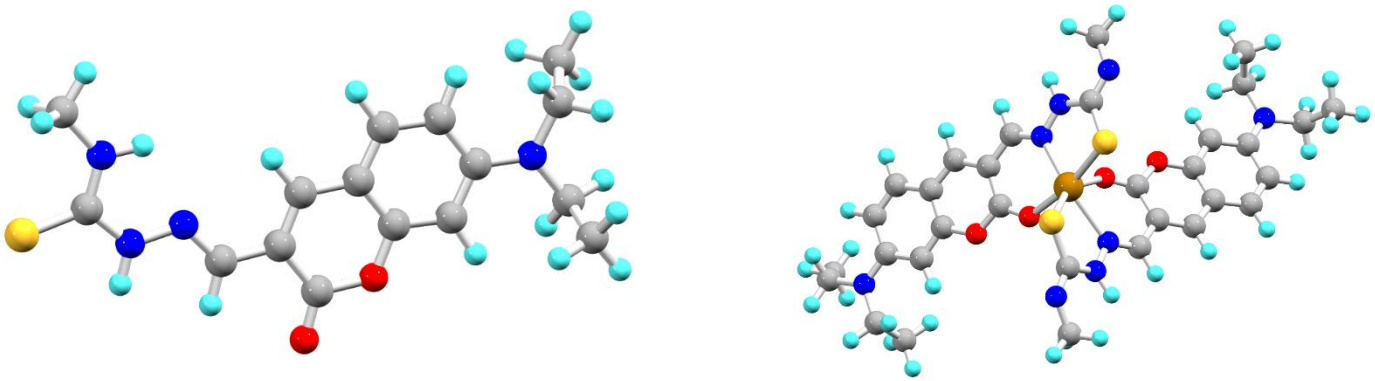

**Figure 5.26:** Optimized structure of DCMC by DFT/B3LYP/6-31+G(d) (left side) and Optimized structure of DCMC-$Cu^{2+}$ complex by DFT/B3LYP/6-31+G(d)/LanL2DZ method (right side).

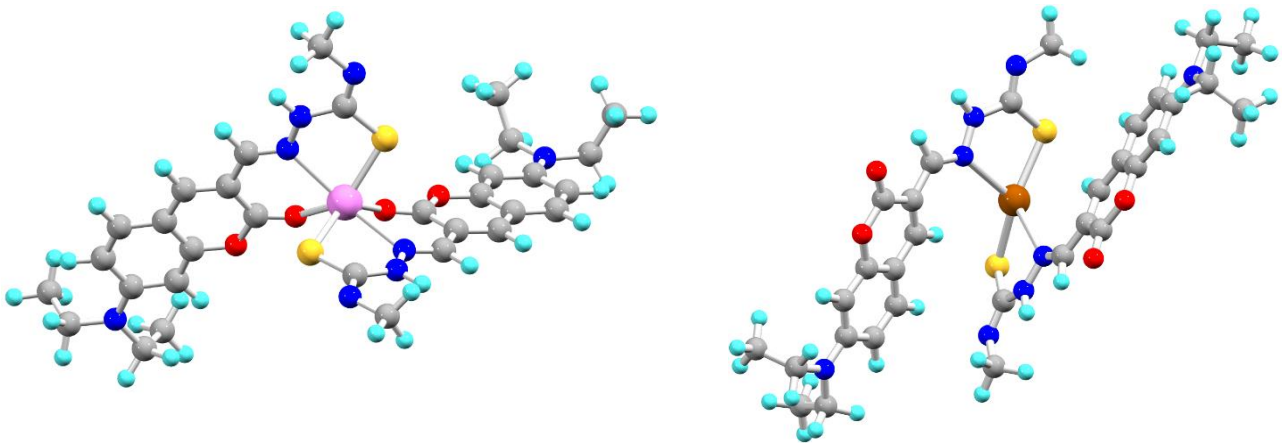

**Figure 5.27:** Optimized structure of DCMC-$Zn^{2+}$ complex by DFT/B3LYP/6-31+G(d)/LanL2DZ method (left side) and Optimized structure of DCMC-$Hg^{2+}$ complex by DFT/B3LYP/6-31+G(d)/LanL2DZ method (right side).

# 5.5. Conclusions

In summary, a novel coumarin based fluorometric sensor (DCMC) has been successfully developed which displayed its sensing performance towards $Hg^{2+}$, $Zn^{2+}$ and $Cu^{2+}$ via different sensing modalities in DMSO/$H_2O$ (v/v, 9/1, pH=7.2). DCMC shows high selectivity and rapid response towards these metal ions and showed decent pH tolerability towards them. The LOD of sensor DCMC for $Hg^{2+}$ and $Zn^{2+}$ are found to be order of $10^{-9}$ (M) and for $Cu^{2+}$ it was in the order of $10^{-8}$ (M). The stoichiometry experiment as well as the mass spectrum of the adducts indicates 2:1 binding ratio between DCMC with the sensing metal ions. The fluorescence

quenching phenomenon occurs by CT mechanism for $Hg^{2+}$ and for $Cu^{2+}$ PET mechanism is responsible for its spectroscopic changes, while in presence of $Zn^{2+}$, the ratiometric fluorescence changes can be observed due to ICT effect. Most essential is the recognition of three metal ions can be observed by naked eye according to their diverse sensing signals. The details of the sensing mechanism are further confirmed by DFT and TDDFT calculations. Furthermore, the probe DCMC can act as a fluorescence based chemosensor for the effectual recognition of $Hg^{2+}$, $Zn^{2+}$ and $Cu^{2+}$ via TLC plate and silica gel solid state platform. Moreover, DCMC was efficaciously applied to live cell imaging study where it exhibits high cell membrane penetration, low cytotoxicity and detects $Zn^{2+}$ and $Hg^{2+}$ in cell system.

# 5.6. Experimental Section

## 5.6.1. Materials and instrumentations

All the organic chemicals, reagents and solvents used in the synthetic procedure of DCMC such as 5-(Diethylamino)-2-hydroxybenzaldehyde, diethyl malonate, 4-methyl-3-thiosemicarbazide, piperidine, acetic acid, Dimethylformamide, Phosphorus oxychloride and ethanol were purchased from Sigma Aldrich and used without further purification. While the other solvents used were available from commercial sources.DMSO and other solvents used for spectroscopic studies were of HPLC grade.For $^{1}H$ and $^{13}C$-NMR spectra a Bruker (AC) 400 MHz instrument was used where DMSO-$d_6$ was used as a solvent using TMS as an internal standard of ~0.05 M concentration.The chemical shifts are reported as δ in units of parts per million (ppm). HRMS mass spectra were confirmed on Waters (Xevo G2 Q-TOF) mass spectrometer. The infrared spectrum of the probe was recorded using an RX-1 PerkinElmer spectrophotometer by preparing a KBr pellet of the sample. We used a Shimadzu UV-1900ispectrophotometer to record the UV-vis spectra at room temperature (298k). The emission property was measured using a Shimadzu RF-6000 fluorescence spectrophotometer at room temperature (298 K). Luminescence lifetime measurements were carried out using a time-correlated single photon counting setup from Horiba Jobin Yvon. Then, the fluorescence decay data were placed on a Hamamatsu MCP photomultiplier (R3809) and analysed using EZ time software. We used a silica gel of mesh 200-300, for the column chromatographic technique where petroleum benzene and ethyl acetate were used as solvents. Suitable single crystals of probe DCMC was mounted on a glass fibre, and diffraction intensities were measured at 293˚C with an automated Bruker SMART APEX CCD diffractometer using graphite monochromatized Mo-Kα radiation (λ = 0.71073 Å). To conceptualize the intermolecular interactions, prevailing in the crystal, Molecular Hirshfeld

surfaces (HS)[101] and the associated 2D-fingerprint[102,103] plots of DCMC were calculated using *CrystalExplorer 17.5*software[104,105]. Geometry optimization using the density functional theory (DFT) method was performed using the GAUSSIAN 09 (B3LYP/LanL2DZ) package. Merck 60 F254 plates of 0.25 mm thickness were used for thin layer chromatography (TLC) and dipstick experiments.

Earle's MEM (#Cat. No: 41500034), Heat inactivated Fetal Bovine Serum (HI-FBS) (#Cat. No: 10438026), Trypsin-EDTA (#Cat. No: 25200072) and Antibiotic-Antimycotic (#Cat. No: 15240062) were purchased from Gibco. MTT reagent [3-(4,5-Dimethylthiazol-2-yl)-2,5-Diphenyltetrazolium Bromide] (#Cat. No: 475989) and 37 % Formaldehyde (#Cat. No: 104003), and DMSO (#Cat. No: 102952) were purchased from Merck. All the materials were subsequently utilized without any further rounds of purification.

## 5.6.2. (E)-2-((7-(diethylamino)-2-oxo-2H-chromen-3-yl) methylene)-N-methylhydrazine-1-carbothioamide (DCMC)

7-(diethylamino)-2-oxo-2H-chromene-3-carbaldehydewas synthesized according to the previously reported procedure.[97] Then 4-methyl-3-thiosemicarbazide (.10 gm,1 mmol) was added into the ethanolic solution of 7-(diethylamino)-2-oxo-2H-chromene-3-carbaldehyde (0.25 gm, 1mmol). A change was observed in the colour of the reaction mixture after few minutes, then the whole mixture was refluxed for 2 h. After completion of the reaction, the reaction mixture was allowed to cool and we observed an orange colour precipitation in the reaction mixture. The precipitation was collected through filtration and washed with ethanol several times. Lastly, the product was dried in a vacuum and collected. Yield: 0.285 g (86%).

**Anal. data for $C_{16}H_{20}N_4O_2S$ (DCMC):**

**$^1$H-NMR (400 MHz, DMSO-$d_6$):** δ(ppm): δ1.14 (t, J = 8 Hz, 3H), 3.03 (d, J = 4 Hz, 3H ), 3.47 ( q, J = 8 Hz, 2H ), 6.58 (s, 1H), 6.78 ( d, J = 8 Hz, 1H ), 7.45 ( d, J = 8 Hz, 1H ), 8.08 ( s, 1H ), 8.50 ( s, 1H ), 8.57( s, 1H ), 11.58 ( s, 1H ).

**$^{13}$C-NMR (100 MHz, DMSO-$d_6$):** δ(ppm): 12.84, 31.21, 44.70, 97.03, 108.59, 110.31, 113.29, 130.62, 136.59, 138.87, 151.58, 156.82, 161.17, 177.87.

**HRMS:** calculated for $C_{16}H_{20}N_4O_2S$ [DCMC + Na]$^+$ (m/z): 355.12; found: 355.0303.

**IR** (KBr): ν(cm$^{-1}$) 3244.79 (-NH stretching), 2978.20 (Ar C-H stretching), 1688.34 (-C=N stretching).

### 5.6.3. UV-Vis and fluorescence method

For UV-Vis titration study, we prepared a stock solution of the probe (20 μM) in [(DMSO/$H_2O$), 9/1, v/v, pH=7.2] solution using HEPES buffer (at 298 K). Deionized water was used to prepare all the solutions of guest cations using their perchlorate and chloride salts respectively. The solution of mercury ion was prepared using its chloride salt at physiological pH. For zinc and copper ion, we used their perchlorate salt respectively. Solutions of different concentrations of the probe and all the cations were prepared separately and then the spectra of these solutions were recorded with the help of UV-Vis method. Similarly, for fluorescence titrations, stock solutions were prepared following the similar procedures and then the spectra were recorded by means of fluorescence method. The excitation wavelength used was 456 nm (where the excitation slit was 5.0, and the emission slit was 5.0). The detection limit was calculated using the fluorescence titration data for $Hg^{2+}$ and $Zn^{2+}$. For $Cu^{2+}$ we used UV titration data to calculate LOD value.

### 5.6.4. pH solution preparation method

For pH dependent study, stock solution of the sensor, DCMC (20 μM) was prepared in DMSO/$H_2O$ (9/1, v/v, pH=7.2) at 298 k. Aqueous solution of 1M HCl and 1M NaOH were used to adjust the pH. For titration of probe solutions, different concentrations of acids and bases were prepared separately while adjusting the pH, and the emission spectra of these solutions were monitored by means of fluorescence technique. Similar experiment was carried out while recording the pH titration of probe (DCMC) in presence of mercury and zinc solution.

### 5.6.5. X-ray crystallography

Suitable single crystals of probe DCMC was mounted on a glass fibre, and diffraction intensities were measured at 293˚C with an automated Bruker SMART APEX CCD diffractometer using graphite monochromatized Mo-Kα radiation (λ = 0.71073 Å). Reflection data were recorded using the ω scan technique and the data were reduced and integrated through SAINT5[106] program and corrected for Lorentz and polarization effects. A multi-scan absorption correction was made with SADABS.[107]All the non-hydrogen atoms were refined anisotropically and the positions of hydrogen atoms were generated using SHELXL and treated as riding model. The crystal structure was solved by direct methods and refined by full-matrix least squares refinements on $F^2$ using SHELXL-2016/6 program[108]which was implemented in WinGX system.[109] The details of crystal analysis, data collection and structure refinement are given in

Table A5.1 and the molecular structure of the crystal is drawn with ORTEP-32 and shown in Fig.5.1.

## 5.6.6. Computational methodology

For the computational methodology the Gaussian 09 (G09) program along with the Gauss-View, Version 5 visualization program was utilized.[110] Density functional theory (DFT) was used to optimize the full geometry of DCMC, DCMC-$Hg^{2+}$, DCMC-$Zn^{2+}$ and DCMC-$Cu^{2+}$ using B3LYP hybrid exchange correlation function.[111]For all elements the 6-31+G(d) basis set was used, whereas for Zn, Hg and cu the Lanl2dZ basis set with the effective core potential (ECP) of Hay and Wadt was used.[112,113]Again, the vibrational frequency calculations were performed to ensure that the optimized geometries represent local minima on the potential energy surface and there were only positive eigenvalues. The vertical electronic transition which was based on B3LYP optimized geometries were calculated using the time-dependent density functional theory (TDDFT) formalism[114-116] using conductor-like polarizable continuum model (CPCM)[117] in DMSO to simulate the solvent.

## 5.6.7. Statistical Analysis

All the statistical analysis was performed using the GraphPad Prism 8.0.2 Software. All the biological experiments were performed three times independently and the data were recorded as Mean ± SD. One-way ANOVA was performed to calculate the significant difference between control and treated groups where the $P< 0.05$ was considered statistically significant. Using Chou-Talalay's method in the CompuSyn Software, the Inhibitory Concentration ($IC_{50}$) values were calculated.[118]

## 5.6.8. Live cell imaging studies

### 5.6.8.1. Cell culture and culture conditions

A human breast epithelial adenocarcinoma cell line (MCF-7) was procured from the National Centre for Cell Science (NCCS), Pune, India. Then, the cells were cultured in Earle's MEM supplemented with 10% HI-FBS, and 1% Antibiotic-Antimycotic. Therefore, cells were kept in a humidified $CO_2$ incubator at 37°C. All the biological experiments were performed after at least three passages.

#### 5.6.8.2. Live cell imaging study

The live cell imaging study was carried out, following our established lab protocol.[119] Briefly MCF-7 cells were seeded on sterile cover glasses placed in a 6-well plate at a density of $2 \times 10^5$ cells/well and incubated for 24 h. Then, the cells were treated with only DCMC, DCMC along with Hg, and DCMC along with Zn. After 30 min of incubation, cells were washed with PBS, fixed with formalin (4%) for 1 h, and subsequently washed with PBS. Finally, the coverslips were mounted on the glass slides, and the cellular morphologies were observed under a fluorescence microscope at 40X magnification (20 μm).

### 5.6.9. Determination of fluorescence quantum yield

The luminescence quantum yield was determined using coumarin 153 as reference dye. The compounds and the reference dye were excited at the same wavelength, maintaining nearly equal absorbance (~0.1), and the emission spectra were recorded. The area of the emission spectrum was integrated using the software available in the instrument and the quantum yield is calculated according to the following equation:

$$\phi_S/\phi_R = [A_S / A_R] \times [(Abs)_R /(Abs)_S] \times [n_S^2/n_R^2]$$

where, $\phi_S$ and $\phi_R$ are the luminescence quantum yields of the sample and reference, respectively. $A_S$ and $A_R$ are the area under the emission spectra of the sample and the reference respectively, $(Abs)_S$ and $(Abs)_R$ are the respective optical densities of the sample and the reference solution at the wavelength of excitation, and $n_S$ and $n_R$ are the values of refractive index for the respective solvent used for the sample and reference.

We calculated the quantum yields of DCMC, DCMC-$Zn^{2+}$ and DCMC-$Hg^{2+}$ using the abovementioned equation; the values are found 0.6604, 0.5611 and 0.0435 respectively.

## 5.7. Notes and references


1. J. K. S. Egorova and V. P. Ananikov, *Organometallics*, 2017, **36**, 4071.
2. J. K. Fawell, E. Ohanian, M. Giddings, P. Toft, Y. Magara and P. Jackson, WHO, Guidelines for Drinking-water Quality, 2004.
3. F. S. Al-fartusie and S. N. Mohssan, *Indian J. Adv. Chem. Sci.*, 2017, **5**, 127.
4. A. L. Berhanu, Gaurav, I. Mohiuddin, A. K. Malik, J. S. Aulakh, V. Kumar and K. H. Kim, *Trends Anal. Chem.*, 2019, **116**, 74.
5. M. Kumar and A. Puri, *Indian J. Occup. Environ. Med.*, 2012, **16**, 40.
6. B. R. Jali, K. Masud and J. B. Baruah, Polyhedron., 2013, **51**, 75.
7. E. M. Nolan and S. J. Lippard, *Acc Chem Res.*, 2009, **42**, 193.

8. J. H. Wang, Y. M. Liu, J. B. Chao, H. Wang, Y. Wang and S. M. Shuang, *Sens. Actuators B: Chem.*, 2020, **303**, 127216.
9. J. H. Hu, J. B. Li, J. Qi and J. J. Chen, *New J. Chem.*, 2015, **39**, 843.
10. H. Shuai, C. Xiang, L. Qian, F. Bin, L. Xiaohui, D. Jipeng, Z. Chang, L. Jiahui and Z. Wenbin, *Dyes Pigm.*, 2021, **187**, 109125.
11. W. M. Singh, B. R. Jali, B. Das and J. B. Baruah, *Inorg. Chim. Acta*, 2011, **372**, 37.
12. K. Krishnaveni, M. Iniya, A. Siva, N. Vidhyalakshmi, S. Sasikumar, U. K. P. Ramesh and S. Murugesan, *J. Mol. Struct.*, 2020, **1217**, 128446.
13. S. W. Zhang, R. Adhikari, M. X. Fang, N. Doth, C. Li, M. Jaishi, J. T. Zhang, A. Tiwari, R. J. Pati, F. T. Luo and H. Y. Liu, *ACS Sens.*, 2016, **12**,1408.
14. G. Jiang, L. Xu, S. Song, C. Zhu, Q. Wu, L. Zhang and L. Wu, *Toxicology*, 2008, **244**, 49.
15. K. Karuppiah, H. Muniyasamy, M. Sepperumal and S. Ayyanar, *Microchem. J.*, 2020, **159**, 105543.
16. S. L. Sensi, P. Paoletti, A. I. Bush and I. Sekier, *Nat. Rev. Neurosci.*, 2009,**10**, 780.
17. A. Q. Truong-Tran, J. Carter, R. Ruffin and P. D. Zalewski, *Immunol. Cell Biol.*, 2001, **79**, 170.
18. S. R. Powell, *J. Nutr.*, 2000, **130**, 1447.
19. A. Takeda and H. Tamano, *Brain Res. Rev.*, 2009, **62**, 33.
20. W. K. Dong, S. F. Akogun, Y. Zhang, Y. X. Sun and X. Y. Dong, *Sens. Actuat. B: Chem.*, 2017, **238**, 723.
21. A. B. D. Santos, M. A. Bezerra, M. E. Rocha, G. E. Barreto and K. A. Kohlmeier, *J. Neural Transm.*, 2019, **126**, 1291.
22. K. Tayade, S. K. Sahoo, B. Bondhopadhyay, V. K. Bhardwaj, N. Singh, A. Basu, R. Bendre and A. Kuwar, *Biosens. Bioelectron.*, 2014, **61**, 429.
23. F. D. Natale, A. Lancia, A. Molino, M. D. Natale, D. Karatza and D. Musmarra, *J. Hazard. Mater.*, 2006, **132**, 220.
24. C. G. Chen, N. Vijay, N. Thirumalaivasan, S. Velmathi and S. P. Wu, *Spectrochim. ActaA: Mol. Biomol. Spectrosc.*, 2019, **219**, 135.
25. Mercury Update: Impact on Fish Advisories; EPA Fact Sheet EPA-823-F-01-011., Environmental Protection Agency, Washington DC., 2001.
26. E. M. Nolan and S. J. Lippard, *J. Am. Chem. Soc.*, 2003, **125**, 14270.
27. J. Sivamani, V. Sadhasivam and A. Siva, *Sens. Actuators B: Chem.*, 2017, **246**, 108.
28. P. W. Davidson, G. J. Myers and B. Weiss, *Pediatrics*, 2004, **113**, 1023.
29. G. Chen, Z. Guo, G. Zeng and L. Tang, *Analyst*, 2015, **140**, 5400.
30. S. Gharami, K. Aich, P. Ghosh, L. Patra, N. Murmu and T. K. Mondal, *Dalton Trans.*, 2020, **49**, 187.
31. C. J. Wu, J. B. Wang, J. J. Shen, C. Bi and H. W. Zhou, *Sens. Actuators B: Chem.*, 2017, **243**, 678.
32. P. Li, D. Z. Zhang, C. X. Jiang, X. Q. Zong and Y. H. Cao, *Biosens. Bioelectron.*, 2017, **98**, 68.
33. J. P. Nandre, S. R. Patil, S. K. Sahoo, C. P. Pradeep, A. Churakov, F. B. Yu, L. X. Chen, C. Redshaw, A. A. Patil and U. D. Patil, *Dalton Trans.*, 2017,**46**, 14201.
34. Q. Lin, K. P. Zhong, J. H. Zhu, L. Ding, J. X. Su, H. Yao, T. B. Wei and Y. M. Zhang, *Macromolecules*, 2017, **50**, 7863.
35. Environmental Protection Agency (EPA), Fed. Regist., 2002, **9**, 1811.

36. J. Hu, X. Yu, X. Zhang, C. Jing, T. Liu, X. Hu, S. Lu, K. Uvdal, H.W. Gao and Z. Hu, *Spectrochim. Acta - Part A Mol. Biomol. Spectrosc.*, 2020, **241**, 118657.
37. S. Xue, P. Wang and K. Chen, *Spectrochim. Acta - Part A Mol. Biomol. Spectrosc.*, 2020, **226**, 117616.
38. N. Singh and D. O. Jang, *J. Hazard. Mater.*, 2009, **168**, 727.
39. A. Manna, D. Sarkar, S. Goswami, C. K. Quah and H. K. Fun, *RSC Adv.*, 2016, **6**, 57417.
40. S. Mandal, A. Banerjee, S. Lohar, A. Chattopadhyay, B. Sarkar, S. K. Mukhopadhyay, A. Sahana and D. Das, *J. Hazard. Mater.*, 2013, **261**, 198.
41. H. Lee, H. -S. Lee, J. H. Reibenspies and R. D. Hancock, *Inorg. Chem.*, 2012, **51**, 10904.
42. Y. C. Lin, T. Wu, Y. W. Lin, *Anal. Methods*, 2018, **10**, 1624.
43. M. Sethupathi, A. Jayamani, G. Muthusankar, P. Sakthivel, K. Sekar, S. Gandhi, N. Sengottuvelan, G. Gopu and C. Selvaraju, *J. Photochem. Photobiol. B, Biol.*, 2020, **207**, 111854.
44. A. Rai, A. K. Singh, K. Tripathi, A. K. Sonkar, B. S. Chauhan and S. Srikrishna, *Sens. Actuators B Chem.*, 2018, **266**, 95.
45. S. Erdemir and O. Kocyigit, *Sens. Actuators B: Chem.*, 2018, **273**, 56.
46. C. S. Atwood, X. Huang, R. D. Moir, R. E. Tanzi and A. I. Bush, *Met Ions Biol Syst.*, 1999, **36**, 309.
47. A. Torres-Vega, B. F. Pliego-Rivero, G. A. Otero-Ojeda, L. M. Gómez-Oliván and P. Vieyra- Reyes, *Nutr. Rev.*, 2012, **70**, 679.
48. A. G. Reaume, J. L. Elliott, E. K. Hoffman, N. W. Kowall, R. J. Ferrante, D. R. Siwek, H. M. Wilcox, D. G. Flood, M. F. Beal, R. H. Brown Jr., R. W. Scott and W. D. Snider, *Nat Genet.*, 1996, **13**, 43.
49. L. Mezzaroba, D. F. Alfieri, A. N. C. Simão and E. M. V. Reiche, *Neurotoxicology.*, 2019, **74**, 230.
50. X. He, Q. Xie, J. Fan, C. Xu, W. Xu, Y. Li, F. Ding, H. Deng, H. Chen and J. Shen, *Dyes Pigm.*, 2020, **177** 108255.
51. J. Chen, P. Chakravarty, G. R. Davidson, D. G. Wren, M. A. Locke, Y. Zhou, G. Jr Brown and J. V. Cizdziel, *Anal. Chim. Acta.*, 2015, **871**, 9.
52. G. M. L. Dico, F. Galvano, G. Dugo, C. Dáscenzi, A. Macaluso, A. Vella, G. Giangrosso, G. Cammilleri and V. Ferrantelli, *Food Chem*., 2018, **245**, 1163.
53. L. Cui, Y. J. Zhang, W. E. Huang, B. F. Zhang, F. L. Martin, J. Y. Li, K. S. Zhang and Y. G. Zhu, *Anal. Chem.*, 2016, **88**, 3164.
54. A. Daňhel, L. Havran, L. Trnková and M. Fojta, *Electroanalysis.*, 2016, **28**, 2785.
55. J. Wang, *Electroanalysis.*, 2005, **17**, 1341.
56. L. Bian, Y. J. Li, J. N. Nie, F. Q. Dong, M. X. Song, L. S. Wang, H. L. Dong, H. L. Li, X. Q. Nie, X. Y. Zhang, X. X. Li and L. Xie, *J. Hazard. Mater.*, 2017, **336**, 174.
57. N. Solovyev, M. Vinceti, P. Grill, J. Mandrioli and B. Michalke, *Anal. Chim. Acta.*, 2017, **973**, 25.
58. R. Sedghi, B. Heidari and M. Behbahani, Synthesis, *J. Hazard. Mater.*, 2015, **285**, 109.
59. N. Wang, C. Xin, Z. Li, G. Zhang, L. Bai and Q. Gong, *Dyes Pigm.*, 2019, **163**, 425.
60. K. Gu, W. Qiu, Z. Guo, C. Yan, S. Zhu and D. Yao, *Chem Sci.*, 2019, **10**, 398.
61. A. Liu, L. Yang, Z. Zhang, Z. Zhang and D. Xu, *Dyes Pigm.*, 2013, **99**, 472.
62. Q. Zeng, P. Cai, Z. Li, J. Qin and B. Z. Tang, *Chem. Commun.*, 2008,**9**, 1094.
63. K. M. Vengaian, C. D. Britto, G. Sivaraman, K. Sekar and S. Singaravadivel, *RSC Adv.*, 2015, **5**, 94903.
64. G. Sivaraman, T. Anand and D. Chellappa, *Anal. Methods*, 2014, **6**, 2343.

65. G. Sivaraman, B. Vidya and D. Chellappa, *RSC Adv.*, 2014, **4**, 30828.
66. O. Sunnapu, N. G. Kotla, B. Maddiboyina, S. Singaravadivel and G. Sivaraman, *RSC Adv.*, 2016, **6**, 656.
67. J. Hatai, S. Pal and S. Bandyopadhyay, *Tetrahedron Lett.*, 2012, **53**, 4357.
68. G. Sivaraman, T. Anand and D. Chellappa, *Analyst.*, 2012, **137**, 5881.
69. T. Anand, G. Sivaraman, P. Anandh, D. Chellappa and S. Govindarajan, *Tetrahedron Lett.*, 2014, **55**, 671.
70. T. Anand, G. Sivaraman and D. Chellappa, *J. Photochem. Photobiol. A.*, 2014, **281**, 47.
71. C. Arivazhagan, R. Borthakur, R. Jagan and S. Ghosh, *Dalton Trans.*, 2016, **45**, 5014.
72. L. H. Cao, F. Shi, W. M. Zhang, S. Q. Zang and T. C. W. Mak, *Chem Eur J.*, 2015, **21**, 15705.
73. H. W. Ma, F. Li, P. Li, H. L. Wang, M. Zhang and G. Zhang, *Adv Funct Mater.*, 2016, **26**, 2025.
74. H. Park, J. W. Kim, S. Y. Hong, G. Lee, D. S. Kim, J. H. Oh, S. W. Jin, Y. R. Jeong, S. Y. Oh, J. Y. Yun and J. S. Ha, *Adv Funct Mater.*, 2018, **28**, 1707013.
75. G. X. Yin, T. T. Niu, Y. B. Gan, T. Yu, P. Yin and H. M. Chen, *Angew Chem Int Ed.*, 2018, **57**, 4991.
76. A. Jimenez-Sanchez, E. K. Lei and S. O. Kelley, *Angew Chem Int Ed.*, 2018, **57**, 8891.
77. Y. Wang, P. D. Mao, W. N. Wu, X. J. Mao, Y. C. Fan and X. L. Zhao, *Sens Actuators B Chem.*, 2018, **255**, 3085.
78. W. Su, S. Z. Yuan and E. J. Wang, *J Fluoresc.*, 2017, **27**, 1871.
79. N. Behera and V. Manivannan, *J Photochem Photobiol A.*, 2018, **353**, 77.
80. M. Faraz, A. Abbasi, F. K. Naqvi, N. Khare, R. Prasa and I. Barman, *Sens. Actuators B: Chem.*, 2018, **269**, 195.
81. Y. Y. Zhang, X. Z. Chen, X. Y. Liu, M. Wang, J. J. Liu and G. Gao, *Sens. Actuators B Chem.*, 2018, **273**, 1077.
82. X. J. Meng, S. L. Li, W. B. Ma, J. L. Wang, Z. Y. Hu and D. L. Cao, *Dyes Pigm.*, 2018, **137**, 194.
83. Y. Y. Li, W. Y. He, Q. C. Peng, L. Y. Hou, J. He and K. Li, *Food Chem.*, 2019, **287**, 55.
84. Y. Tachapermpon, S. Chaneam, A. Charoenpanich, J. Sirirak and N. Wanichacheva, *Sens Actuators B Chem.*,2017, **241**, 868.
85. Y. C. Wu, S. H. Luo, L. Cao, K. Jiang, L. Y. Wang and J. C. Xie, *Anal. Chim Acta*, 2017, **976**, 74.
86. Y. C. Wu, J. P. Huo, L. Cao, S. Ding, L. Y. Wang and D. R. Cao, *Sens. Actuators B: Chem.*, 2016, **237**, 865.
87. M. G. Choi, Y. J. Lee, I. J. Chang, H. Ryu, S. Yoon and S. K. Chang, *Sens. Actuators B: Chem.*, 2018, **268**, 22.
88. Y. S. Yang, S. S. Ma, Y. P. Zhang, J.X. Ru, X. Y. Liu and H. C. Guo, *Spectrochim Acta Part A*, 2018, **199**, 202.
89. A. Rai, A. K. Singh, K. Tripathi, A. K. Sonkar, B. S. Chauhan and S. Srikrishna, *Sens. Actuators B Chem.*, 2018, **266**, 95.
90. H. Zhang, C. Nie, J. H. Wang, R. F. Guan and D. X. Cao, *Talanta*, 2019, **195**, 713.
91. A. Malek, K. Bera, S. Biswas, G. Perumal, A. K. Das and M. Doble, *Anal. Chem.*, 2019, **91**, 3533.
92. S. C. Sun, Q. H. Shu, P. C. Lin, Y. Y. Li, S. H. Jin and X. Chen, *RSC Adv.*, 2016, **6**, 93826.
93. K. Boonkitpatarakul, A. Smata, K. Kongnukool, S. Srisurichan, K. Chaino and M. Sukwattanasinitt, *J Lumin.*, 2018, **198**, 59.
94. A. Tang, Y. Yin, Z. Chen, C. Fan, G. Liu and S. Pu, *Tetrahedron.*, 2019, **75**, 130489.
95. Y. Wang, P. D. Mao, W. N. Wua, X. J. Mao, Y. C. Fan, X. L. Zhao, Z. Q. Xu and Z. H. Xu, *Sens. Actuators B: Chem.*, 2018, **255**, 3085.

96. C. M. Panga, S. H. Luo, K. Jianga, B. W. Wang, S. H. Chen, N. Wang and Z. Y. Wang, *Dyes Pigm.*, 2019, **170**, 107651.
97. O. García-Beltrán, B.K. Cassels, N. Mena, M.T. Nuñez, O. Yañez and J.A. Caballero, *Tetrahedron Letters.*, 2014, **55**, 873.
98. P. K. Bhaumik, R. M. Gomila, A. Frontera, S. Benmansour, C. J. Gómez-García and S. Chattopadhyay, *New J. Chem.*, 2022, **46**, 11286.
99. R. Bhaskar and S. Sarveswari, *Inorg. Chem. Commun.*, 2019, **102**, 83.
100. S. Guha, D. Talukdar, G. K. Mandal, R. Mukherjee, S. Ghosh, R. Naskar, P. Saha, N. Murmu and G. Das,*J. Ethnopharmacol.*, 2024, **332**, 118389.
101. M. A Spackman, D. Jayatilaka, *Cryst. Eng. Comm.*, 2009, **11**, 19.
102. A. L.Rohl, M. Moret, W. Kaminsky, K. Claborn, J. J. McKinnon and B. Kahr, *Cryst. Growth Des.*, 2008, **8** 4517.
103. M. A. Spackman and J. McKinnon, *Cryst. Eng. Comm.*, 2002, **4**, 378.
104. C. F.Mackenzie, P. R. Spackman, D. Jayatilaka and M. A. Spackman, *IUCrJ.*, 2017, **4**, 575.
105. P. R. Spackman, M. J. Turner, J. J. McKinnon, S. K. Wolff, D. J. Grimwood, D. Jayatilaka and M. A. Spackman, *J. Appl. Crystallogr.*, 2021, **54**, 1006.
106. S. Bruker, Bruker A. Inc., Madison, Wisconsin, USA, 2004.
107. L. Krause, R. Herbst-Irmer, G. M. Sheldrick and D. Stalke, *J. Appl. Crystallogr.*, 2015, **48**, 3.
108. G. M. Sheldrick, *Acta Crystallogr. A.*, 2008, **64**, 112.
109. L. Farrugia, *J. Appl. Crystallogr.*, 2012, **45**, 849.
110. M. J. Frisch, G. W. Trucks, H. B. Schlegel, G. E. Scuseria, M. A. Robb, J. R. Cheeseman, G. Scalmani, V. Barone, B. Mennucci, G. A. Petersson, H. Nakatsuji, M. Caricato, X. Li, H. P. Hratchian, A. F. Izmaylov, J. Bloino, G. Zheng, J. L. Sonnenberg, M. Hada, M. Ehara, K. Toyota, R. Fukuda, J. Hasegawa, M. Ishida, T. Nakajima, Y. Honda, O. Kitao, H. Nakai, T. Vreven, J. A. Montgomery, Jr., J. E. Peralta, F. Ogliaro, M. Bearpark, J. J. Heyd, E. Brothers, K. N. Kudin, V. N. Staroverov, R. Kobayashi, J. Normand, K.Raghavachari, A. Rendell, J. C. Burant, S. S. Iyengar,J. Tomasi, M. Cossi, N. Rega, J. M. Millam, M. Klene, J. E. Knox, J. B. Cross, V. Bakken, C. Adamo, J. Jaramillo, R. Gomperts, R. E. Stratmann, O. Yazyev, A. J. Austin, R. Cammi, C. Pomelli, J. W. Ochterski, R. L. Martin, K. Morokuma, V. G. Zakrzewski, G. A. Voth, P. Salvador, J. J. Dannenberg, S. Dapprich, A. D. Daniels, O¨. Farkas,J. B. Foresman, J. V. Ortiz, J. Cioslowski and D. J. Fox,Gaussian 09, Gaussian, Inc., Wallingford CT, 2009.
111. A. D. Becke, *J. Chem. Phys.*, 1993, **98**, 5648.
112. W. R. Wadt and P. J. Hay, *J. Chem. Phys.*, 1985, **82**, 284.
113. P. J. Hay and W. R. Wadt, J. Chem. Phys., 1985, **82**, 299.
114. R. Bauernschmitt and R. Ahlrichs, *Chem. Phys. Lett.*, 1996, **256**, 454.
115. R. E. Stratmann, G. E. Scuseria and M. J. Frisch, *J. Chem. Phys.*, 1998, **109**, 8218.
116. M. E. Casida, C. Jamorski, K. C. Casida and D. R. Salahub, *J. Chem. Phys.*, 1998, **108**, 4439.
117. M. Cossi and V. Barone, *J. Chem. Phys.*, 2001, **115**, 4708.
118. T. C. Chou, *Cancer Res.*, 2010, **70**, 440.
119. A. Biswas, S. Gharami, A. Maji, S. Guha, G. Das, R. Naskar and T. K. Mondal, *Anal. Methods*, 2024, **16**, 8010.

# APPENDIX

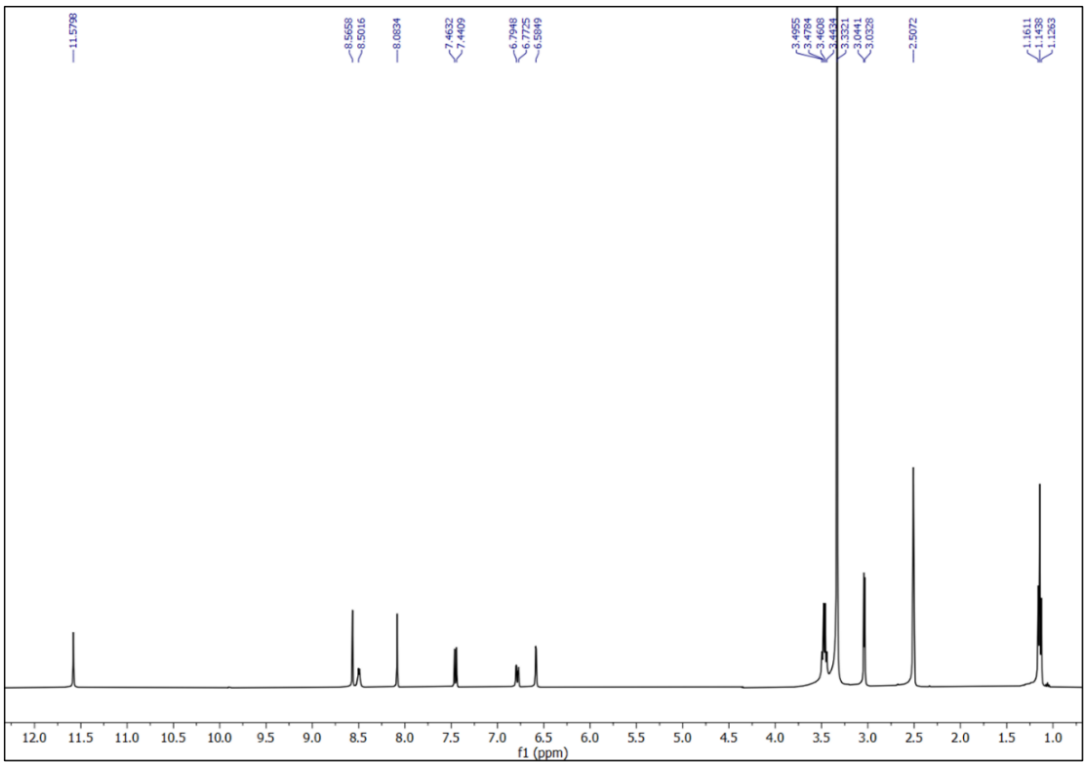


**Fig. A5.1:** $^{1}$H NMR (400 MHz) spectrum of DCMC in DMSO-$d_6$

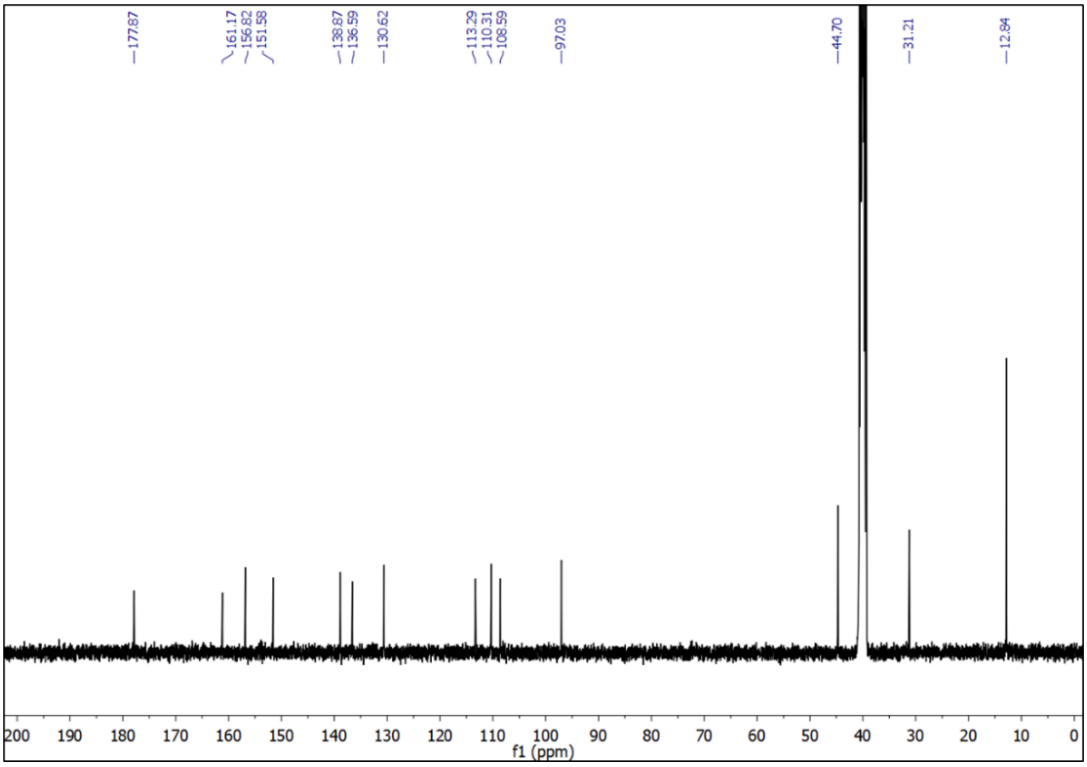


**Fig. A5.2:**$^{13}$C NMR (100MHz) spectrum of DCMC in DMSO-$d_6$

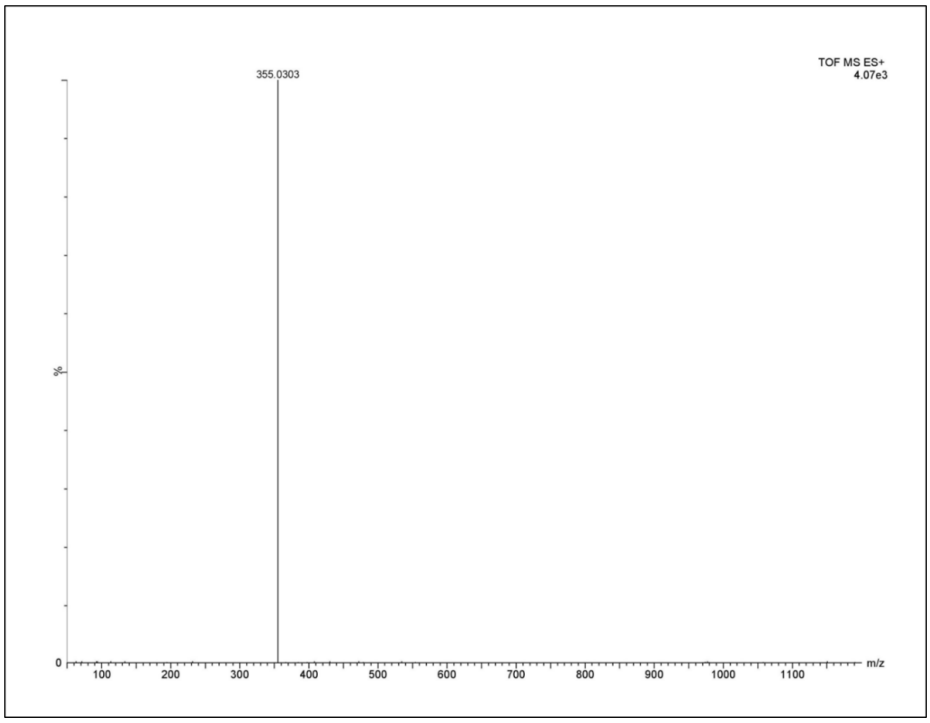


**Fig. A5.3:** Mass spectrum (HRMS) of DCMC

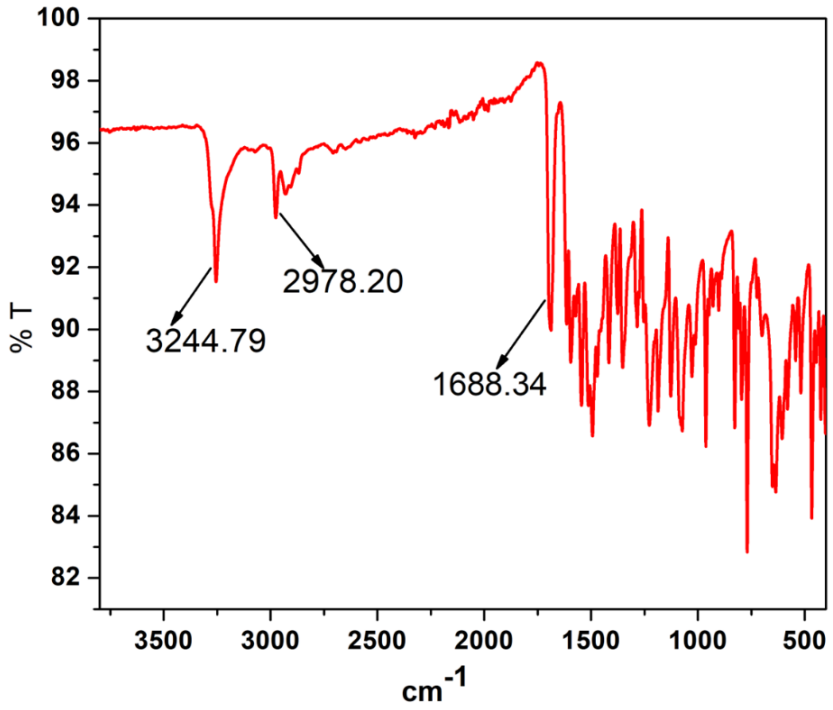


**Fig. A5.4:** IR spectra of the probe HBTC

**Fig. A5.1:** Summarized crystallographic data and refinement parameters for the probe DCMC

| | |
|---|---|
| Formula | $C_{16}H_{20}N_4O_2S$ |
| Formula Weight | 332.42 |
| Crystal System | *monoclinic* |
| Space group | P $2_1/c$ |
| a, b, c [Å] | 9.5546(5), 15.7449(3), 11.5528(2) |
| α | 90 |
| β | 103.6660(10) |
| γ | 90 |
| V [ $Å^3$] | 1688.76 |
| Z | 4 |
| D(calc) [$g/cm^3$] | 1.307 |
| μ (Mo Ka) [$mm^{-1}$] | 0.207 |
| F(000) | 704 |
| Absorption Correction | multi-scan |
| Temperature (K) | 293(2) |
| Radiation [Å] | 0.71073 |
| θ(Min-Max) [°] | 3.161- 25.998 |
| Dataset (h; k; l) | -11 to 11, -19 to 19, -14 to 14 |
| Total reflection ($N_{total}$), Unique Data ($N_{ref}$) | 3273/2718 |
| $R^a$, $wR_2^b$ | 0.0379, 0.1028 |
| Goodness of fit(S) | 1.039 |
| CCDC No. | 2416618 |

[a] $R = \sum(|F_o| - |F_c|)| / \sum|F_o|$

[b] $wR_2 = [\sum [w (F_o 2 - Fc^2)^2] / \sum [w (Fo^2)^2] ]^{1/2}$,

[c] GOF (S) = $\{\sum [w (F_o 2 - F_c^2)^2] / (n - p)\}1/2$, where n = number of measured data and p = number of parameters.

**Table A5.2:** Selected X-ray and calculated bond distances and angles of the probe (DCMC)

| Bonds(Å) | X-ray | Calc. |
|---|---|---|
| S1-C15 | 1.6744(15) | 1.6805 |
| O1-C1 | 1.3784(18) | 1.3922 |
| O1-C9 | 1.3803(17) | 1.3667 |
| O2-C1 | 1.2131(18) | 1.2135 |
| N1-C14 | 1.2738(19) | 1.2914 |
| N1-N2 | 1.3725(16) | 1.3567 |
| N2-C15 | 1.3613(19) | 1.3789 |
| N3-C15 | 1.3220(19) | 1.3469 |
| N3-C16 | 1.450(2) | 1.4534 |
| Angles (°) | X-ray | Calc. |
| C1-O1-C9 | 122.39(12) | 123.35 |
| C14-N1-N2 | 117.82(12) | 117.32 |
| C15-N2-N1 | 119.39(12) | 122.29 |
| C15-N3-C16 | 124.95(14) | 123.74 |
| C7-N4-C12 | 121.8(7) | 121.79 |
| C7-N4-C10 | 121.9(6) | 122.15 |
| C12-N4-C10 | 116.3(6) | 116.05 |
| O2-C1-O1 | 116.22(14) | 117.14 |
| O2-C1-C2 | 125.88(14) | 126.04 |
| O1-C1-C2 | 117.90(12) | 116.81 |

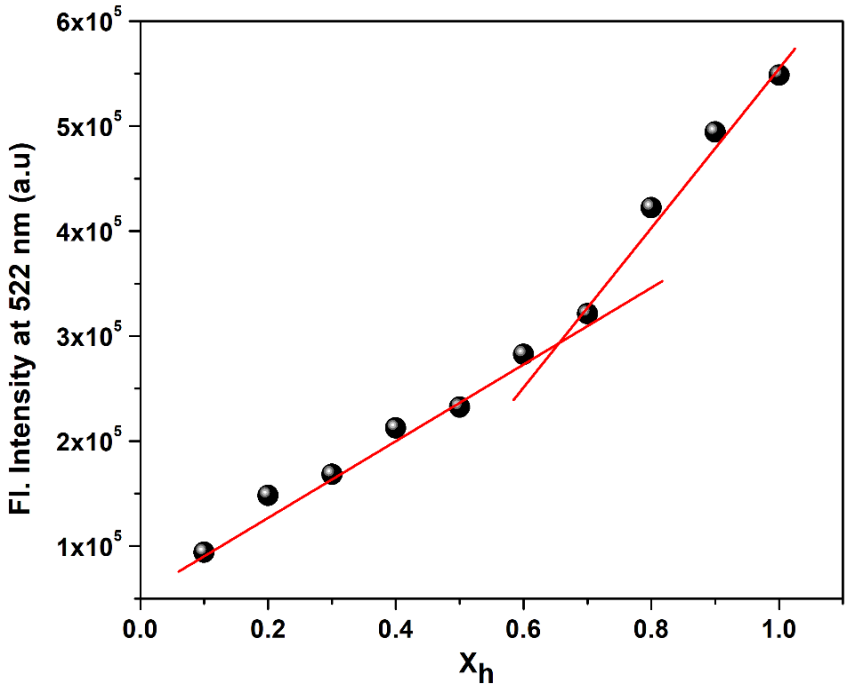


**Fig. A5.5:** Job's plot diagram of DCMC for $Hg^{2+}$.

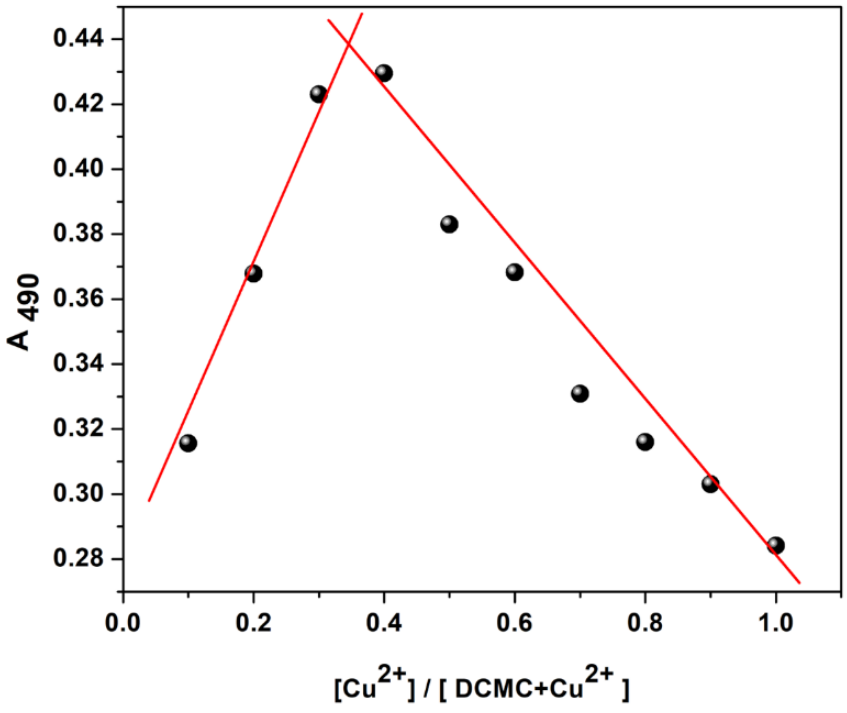


**Fig. A5.6:** Job's plot diagram of DCMC for $Cu^{2+}$.

**Table A5.3:** Fluorescence lifetime data

| DMSO (solvent) | Quantum yield *(φ)* | τ (ns) | $k_r$ ($10^9 \times s^{-1}$) | $k_{nr}$ ($10^9 \times s^{-1}$) |
|---|---|---|---|---|
| DCMC | 0.6604 | 3.1095 | 0.2123 | 0.1092 |
| DCMC-$Hg^{2+}$ | 0.0435 | 3.1609 | 0.0137 | 0.3026 |
| DCMC-$Zn^{2+}$ | 0.5611 | 3.2119 | 0.1746 | 0.1367 |

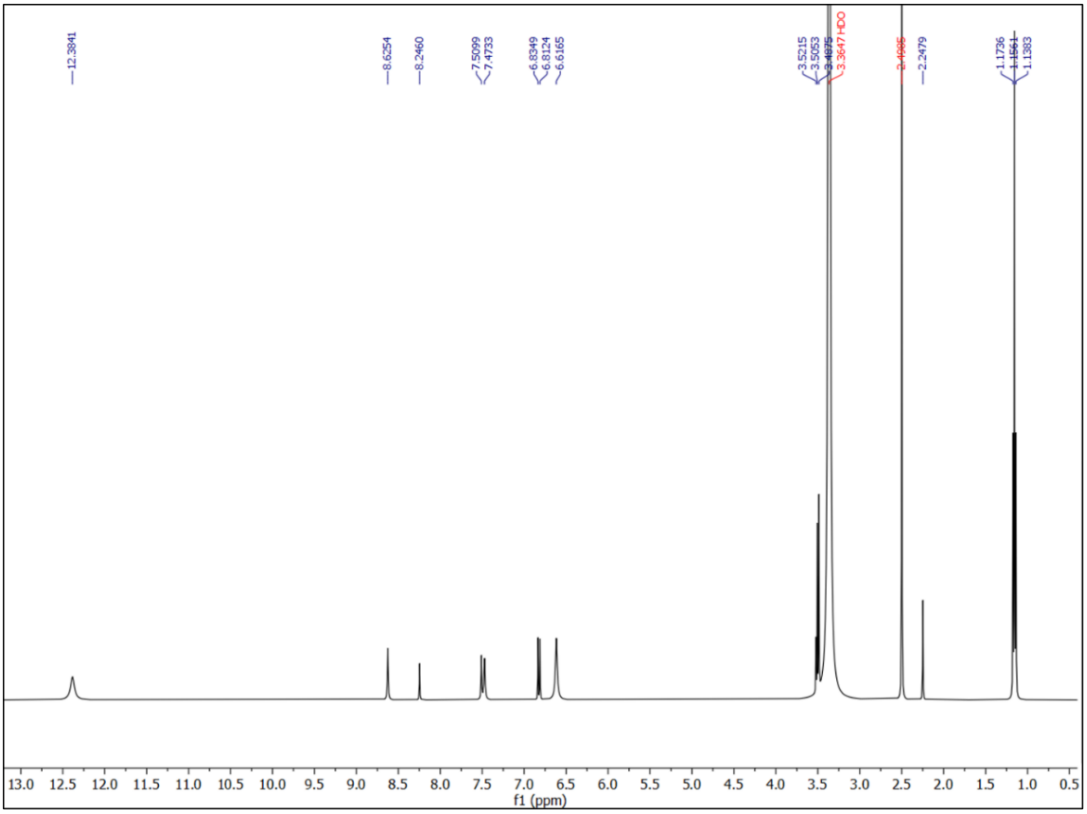


**Fig. A5.7:** $^1H$ NMR (400 MHz) spectrum of the DCMC with $Hg^{2+}$ in DMSO-$d_6$

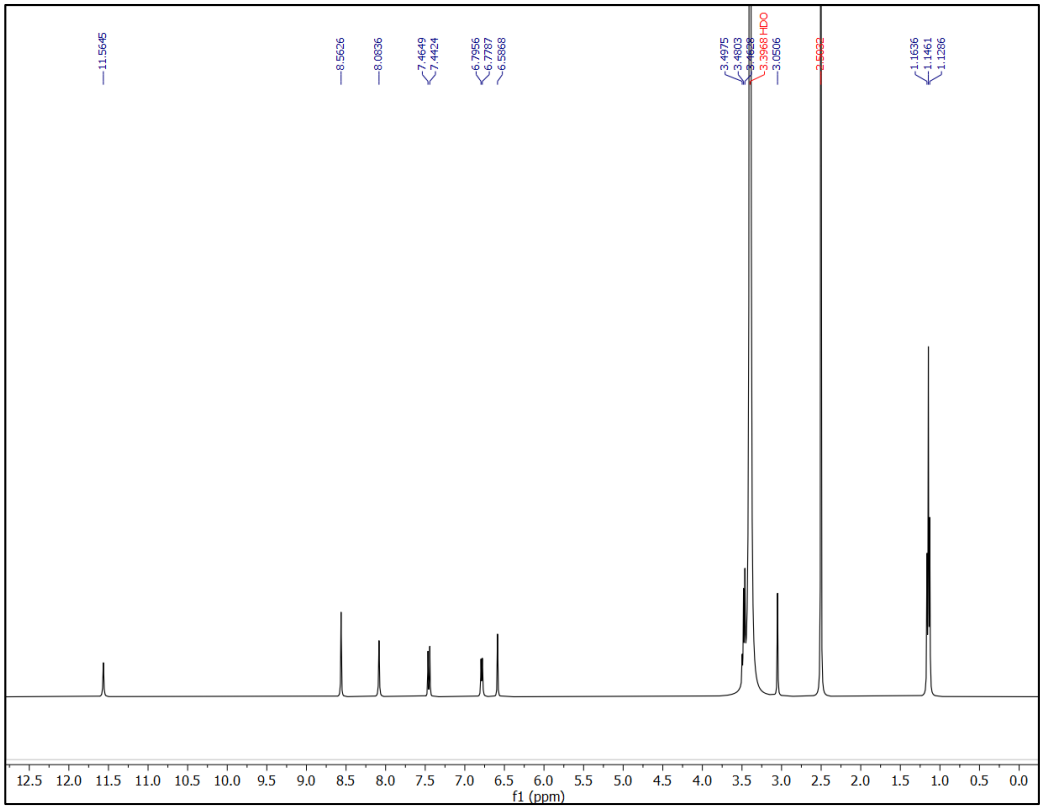


**Fig. A5.8:** $^{1}$H NMR (400 MHz) spectrum of the DCMC with $Zn^{2+}$ in DMSO-$d_6$.

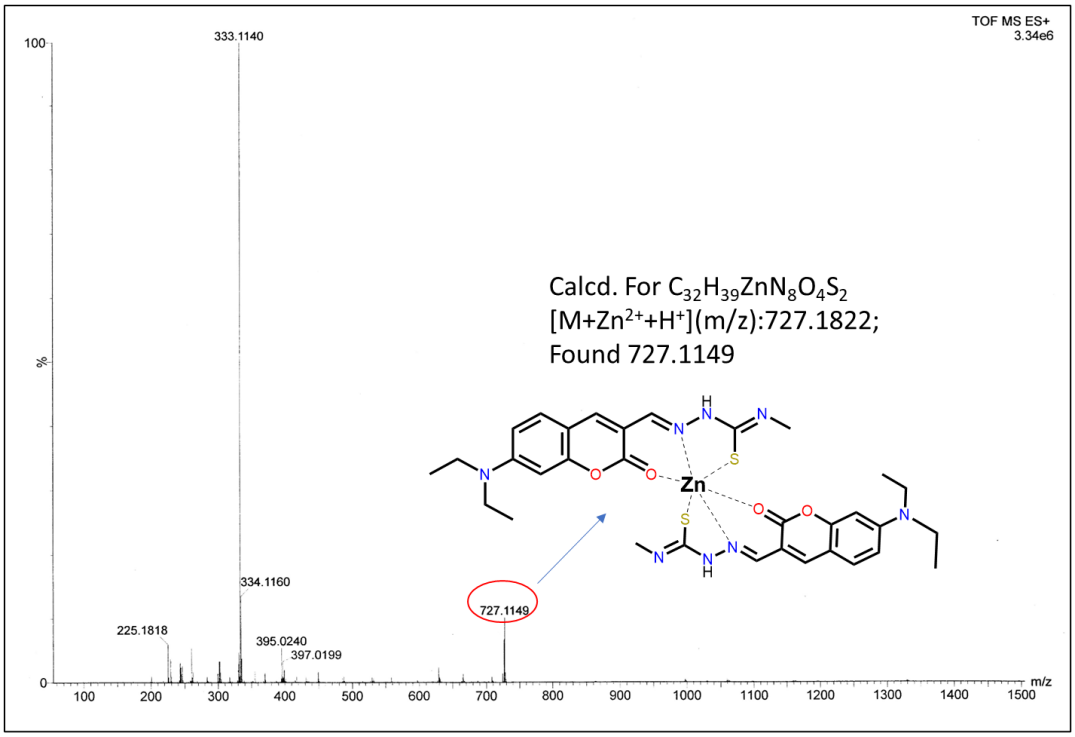


**Fig. A5.9:** Mass spectrum (HRMS) of DCMC-$Zn^{2+}$

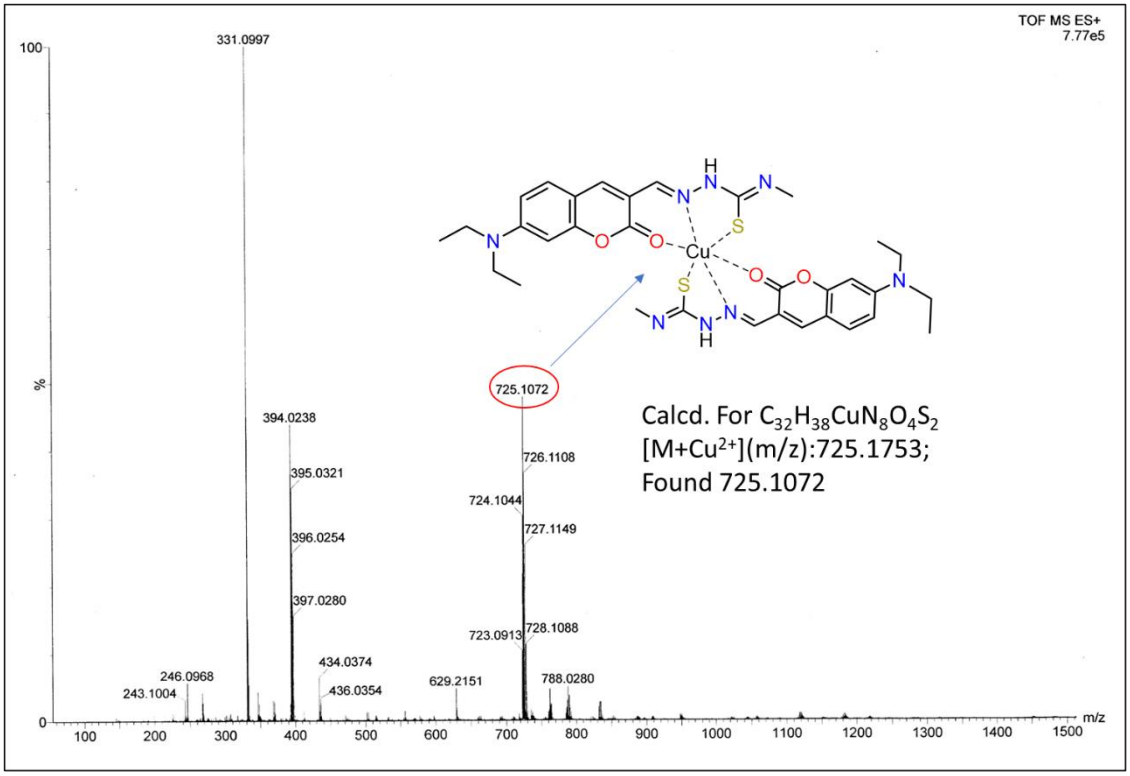


**Fig.A5.10:** Mass spectrum (HRMS) of DCMC-$Cu^{2+}$

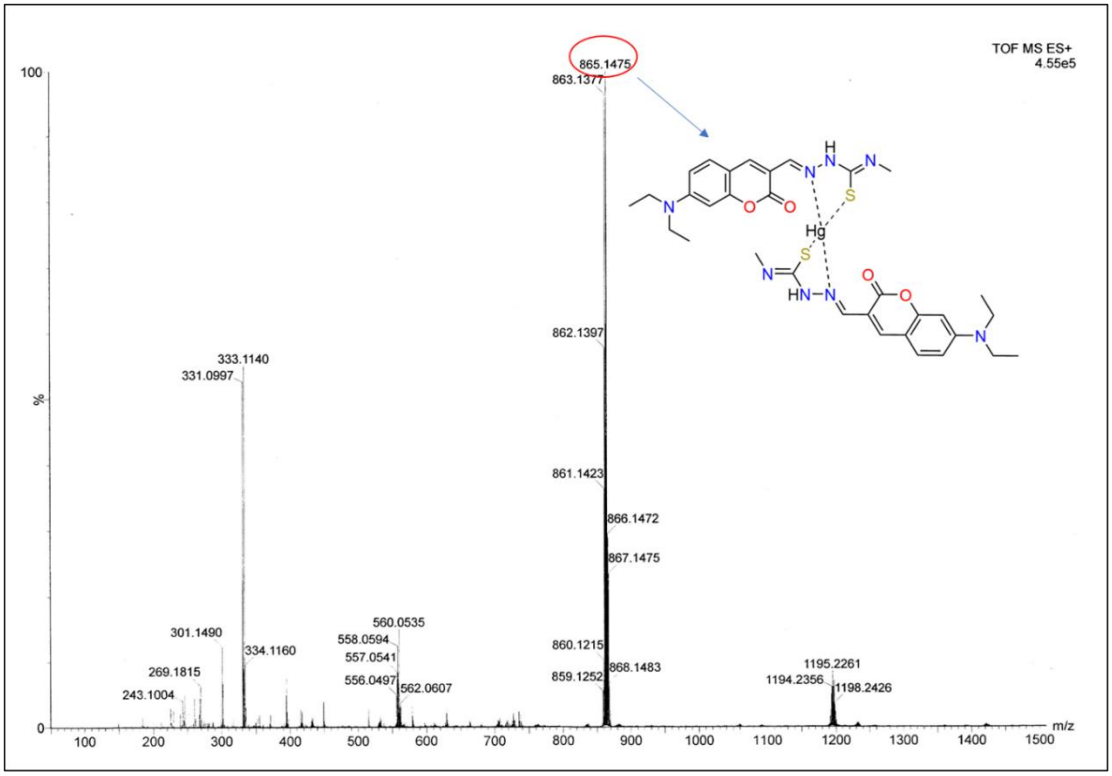


**Fig. A5.11:** Mass spectrum (HRMS) of DCMC-$Hg^{2+}$

**Table A5.4:** Vertical electronic excitations of DCMC, DCMC-$Zn^{2+}$, DCMC-$Cu^{2+}$, DCMC-$Hg^{2+}$ calculated by TDDFT/CPCM method.

| Compound | Energy (eV) | Wave-length (nm) | Osc. Strength (f) | Transition | Character |
|---|---|---|---|---|---|
| DCMC | 2.7341 | 453.47 | 1.2233 | (98%) HOMO→LUMO | Lig(π)→Lig($\pi^*$) |
| | 3.9841 | 311.19 | 0.2259 | (62%) HOMO→LUMO+1 | Lig(π)→Lig($\pi^*$) |
| DCMC-$Zn^{2+}$ | 2.8382 | 436.85 | 1.2538 | (75%) HOMO-1→LUMO | Lig(π)→Lig($\pi^*$) |
| | 2.8986 | 427.74 | 0.8580 | (53%) HOMO-1→LUMO+1 | Lig(π)→Lig($\pi^*$) |
| DCMC-$Cu^{2+}$ | 2.5857 | 479.50 | 0.0257 | (89%) HOMO-9→LUMO(β) | Lig(π)→Lig($\pi^*$) |
| | 2.8638 | 432.94 | 0.9455 | (55%) HOMO-1→LUMO+1(β) | Lig(π)→Lig($\pi^*$) |
| | 2.9356 | 422.35 | 0.4916 | (68%) HOMO→LUMO+2(β) | Lig(π)→Lig($\pi^*$) |
| DCMC-$Hg^{2+}$ | 2.6252 | 472.29 | 0.0086 | (99%) HOMO→LUMO | Lig(π)→Lig($\pi^*$) |
| | 2.7686 | 445.70 | 0.1137 | (55%) HOMO-1→LUMO | Lig(π)→Lig($\pi^*$) |
| | 2.8239 | 439.05 | 1.9465 | (46%) HOMO→LUMO+1 | Lig(π)→Lig($\pi^*$) |

**Table A5.5:** Energy and compositions of some selected molecular orbitals of DCMC-$Cu^{2+}$ complex (alpha).

| | **Energy** | **% of composition** | |
|---|---|---|---|
| | | **HBMC** | **Cu** |
| LUMO+5 | 0.05 | 99 | 1 |
| LUMO+4 | -0.21 | 100 | 0 |
| LUMO+3 | -0.40 | 99 | 1 |
| LUMO+2 | -0.70 | 99 | 1 |
| LUMO+1 | -1.78 | 100 | 0 |
| LUMO | -2.06 | 100 | 0 |
| HOMO | -4.57 | 97 | 3 |
| HOMO-1 | -4.70 | 91 | 9 |
| HOMO-2 | -4.76 | 91 | 9 |
| HOMO-3 | -5.10 | 98 | 2 |
| HOMO-4 | -5.10 | 96 | 4 |
| HOMO-5 | -5.67 | 89 | 11 |
| HOMO-6 | -5.89 | 94 | 6 |
| HOMO-7 | -5.99 | 98 | 2 |
| HOMO-8 | -6.10 | 87 | 13 |
| HOMO-9 | -6.22 | 99 | 1 |
| HOMO-10 | -6.64 | 93 | 7 |

**Table A5.6:** Energy and compositions of some selected molecular orbitals of DCMC-$Cu^{2+}$ complex (beta).

| MO | Energy | % of composition | |
|---|---|---|---|
| | | DCMC | Cu |
| LUMO+5 | -0.21 | 100 | 0 |
| LUMO+4 | -0.40 | 99 | 1 |
| LUMO+3 | -0.69 | 99 | 1 |
| LUMO+2 | -1.77 | 99 | 1 |
| LUMO+1 | -2.02 | 95 | 5 |
| LUMO | -2.38 | 65 | 35 |
| HOMO | -4.48 | 94 | 6 |
| HOMO-1 | -4.62 | 94 | 6 |
| HOMO-2 | -5.05 | 98 | 2 |
| HOMO-3 | -5.20 | 83 | 17 |
| HOMO-4 | -5.34 | 91 | 9 |
| HOMO-5 | -5.74 | 96 | 4 |
| HOMO-6 | -5.87 | 96 | 4 |
| HOMO-7 | -6.01 | 96 | 4 |
| HOMO-8 | -6.19 | 96 | 4 |
| HOMO-9 | -6.41 | 60 | 40 |
| HOMO-10 | -6.61 | 77 | 23 |

**Table A5.7:** Energy and compositions of some selected molecular orbitals of DCMC-$Zn^{2+}$ complex**.**

| MO | Energy | % of composition | |
|---|---|---|---|
| | | DCMC | Zn |
| LUMO+5 | -0.11 | 100 | 0 |
| LUMO+4 | -0.13 | 100 | 0 |
| LUMO+3 | -0.60 | 100 | 0 |
| LUMO+2 | -0.63 | 99 | 1 |
| LUMO+1 | -1.95 | 100 | 0 |
| LUMO | -1.95 | 100 | 0 |
| HOMO | -4.43 | 99 | 1 |
| HOMO-1 | -4.59 | 97 | 3 |
| HOMO-2 | -5.03 | 97 | 3 |
| HOMO-3 | -5.08 | 99 | 1 |
| HOMO-4 | -5.24 | 93 | 7 |
| HOMO-5 | -5.54 | 96 | 4 |
| HOMO-6 | -5.71 | 99 | 1 |
| HOMO-7 | -5.93 | 93 | 7 |
| HOMO-8 | -6.08 | 100 | 0 |
| HOMO-9 | -6.12 | 99 | 1 |
| HOMO-10 | -6.87 | 100 | 0 |

**Table A5.8:** Energy and compositions of some selected molecular orbitals of DCMC-$Hg^{2+}$ complex.

| MO | Energy | % of composition | |
|---|---|---|---|
| | | DCMC | Hg |
| LUMO+5 | -0.09 | 97 | 3 |
| LUMO+4 | -0.39 | 97 | 3 |
| LUMO+3 | -0.56 | 97 | 3 |
| LUMO+2 | -1.44 | 40 | 60 |
| LUMO+1 | -1.95 | 98 | 2 |
| LUMO | -2.22 | 98 | 2 |
| HOMO | -5.13 | 100 | 0 |
| HOMO-1 | -5.34 | 100 | 0 |
| HOMO-2 | -5.93 | 98 | 2 |
| HOMO-3 | -5.94 | 99 | 1 |
| HOMO-4 | -6.32 | 97 | 3 |
| HOMO-5 | -6.44 | 98 | 2 |
| HOMO-6 | -6.58 | 99 | 1 |
| HOMO-7 | -6.60 | 99 | 1 |
| HOMO-8 | -6.66 | 98 | 2 |
| HOMO-9 | -6.79 | 100 | 0 |
| HOMO-10 | -7.08 | 95 | 5 |

| | | |
|---|---|---|
| 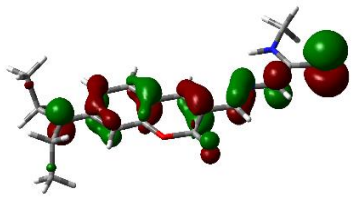 | 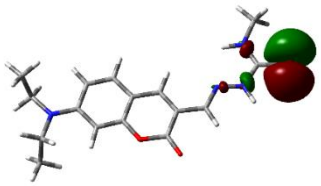 | 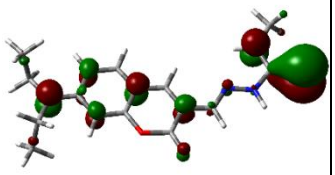 |
| HOMO (-5.50 eV) | HOMO-1 (-5.75 eV) | HOMO-2 (-6.09 eV) |
| 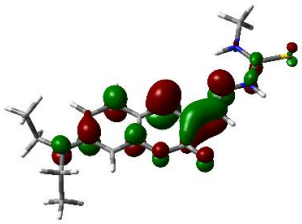 | 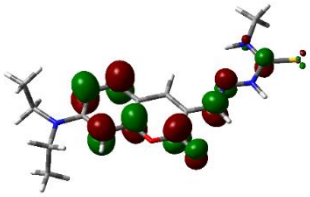 | 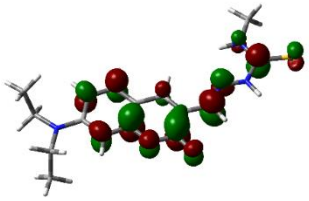 |
| LUMO (-2.47 eV) | LUMO+1 (-0.97 eV) | LUMO+2 (-0.57 eV) |

**Fig. A5.12:** Contour plot of some selected molecular orbitals of DCMC**.**

| | | |
|---|---|---|
| 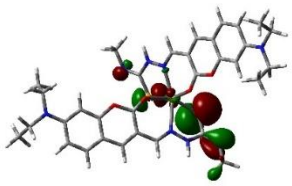 | 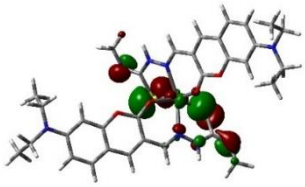 | 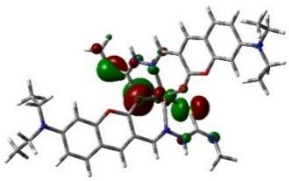 |
| HOMO (-4.57 eV) | HOMO-1 (-4.70 eV) | HOMO-2 (-4.76 eV) |
| 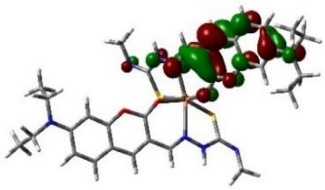 | 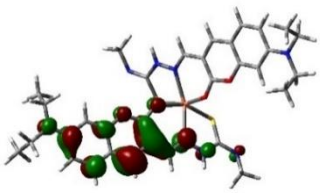 | 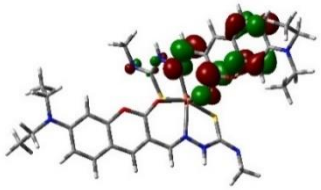 |
| LUMO (-2.06 eV) | LUMO+1 (-1.78 eV) | LUMO+2 (-0.70 eV) |

**Fig. A5.13:** Contour plot of some selected molecular orbitals of DCMC-$Cu^{2+}$ (basis set: LanL2DZ) (α-spins) ++

| | | |
|---|---|---|
| 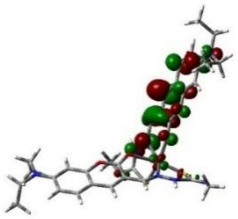 | 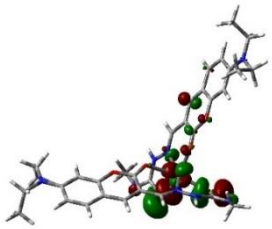 | 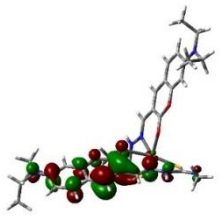 |
| HOMO (-4.48 eV) | HOMO-1 (-4.62 eV) | HOMO-2 (-5.05 eV) |
| 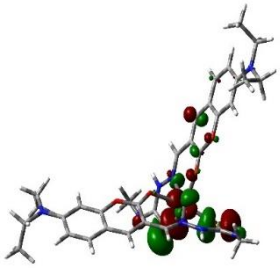 | 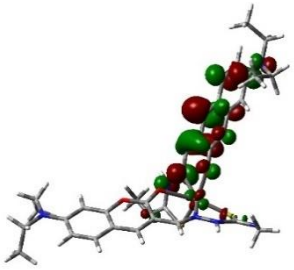 | 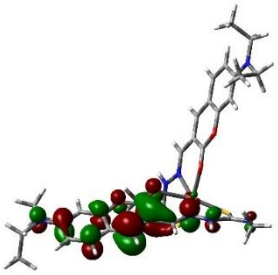 |
| LUMO (-2.38 eV) | LUMO+1 (-2.02 eV) | LUMO+2 (-1.77 eV) |

**Fig. A5.14:** Contour plot of some selected molecular orbitals of DCMC-$Cu^{2+}$ (basis set: LanL2DZ) (β-spins) ++

| | | |
|---|---|---|
| 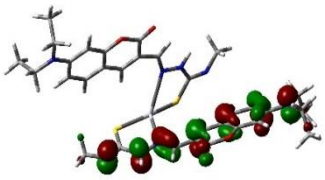 | 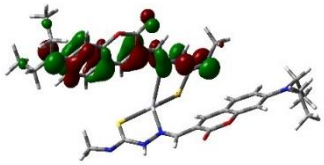 | 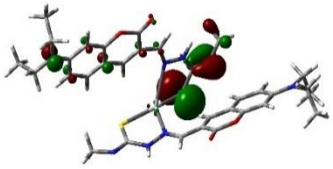 |
| HOMO (-5.13 eV) | HOMO-1 (-5.34 eV) | HOMO-2 (-5.93 eV) |
| 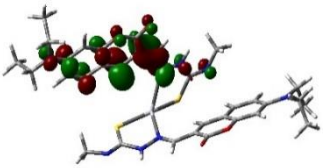 | 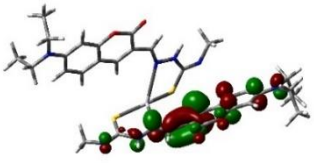 | 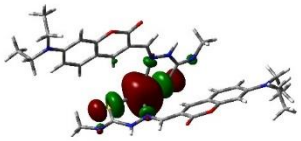 |
| LUMO (-2.22 eV) | LUMO+1 (-2.01 eV) | LUMO+2 (-1.44 eV) |

**Fig. A5.15:** Contour plot of some selected molecular orbitals of DCMC-$Hg^{2+}$.

| | | |
|---|---|---|
| 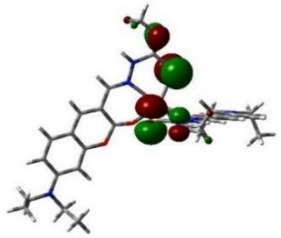 | 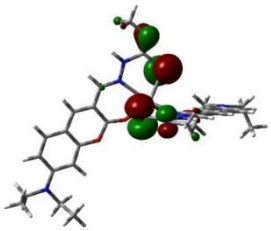 | 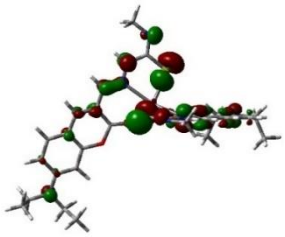 |
| HOMO (-4.43 eV) | HOMO-1 (-4.59 eV) | HOMO-2 (-5.03 eV) |
| 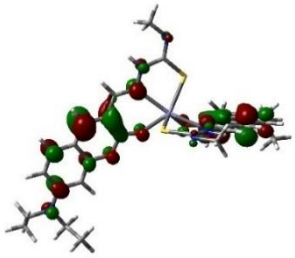 | 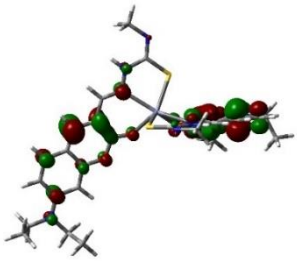 | 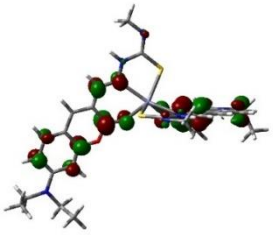 |
| LUMO (-1.95 eV) | LUMO+1 (-1.95 eV) | LUMO+2 (-0.63 eV) |

**Fig. A5.16:** Contour plot of some selected molecular orbitals of DCMC-$Zn^{2+}$**.**

**Table A5.9:** Comparison of solvent systems and limit of detection (LOD) of the receptor (DCMC) with some recently reported fluorescence organic probes for the detection of $Cu^{2+}$, $Hg^{2+}$ and $Zn^{2+}$.

| Chemosensors | Solvent system | Type | LOD | References |
|---|---|---|---|---|
| 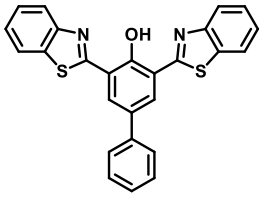 | 1:1 ratio of DMSO and $CHCl_3$ | $Zn^{2+}$ (Ratiometric) | 0.25 ppm | *ACS omega*, 2021, **6**, 24473. |
| | | $Cu^{2+}$ (Colorimetric) | 0.34 ppm | |
| | | $Ni^{2+}$ (Colorimetric) | 0.30 ppm | |
| 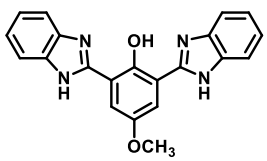 | Aqueous Tris-HCl solution (10 mM, pH 7.4, 70% THF | $Cu^{2+}$ (Turn-off) | 0.16 μM | *Sens. Diagn.*, 2023, **2**, 665. |
| | | $Zn^{2+}$ (Ratiometric turn-on) | 0.1 μM | |

| | | | | |
|---|---|---|---|---|
| 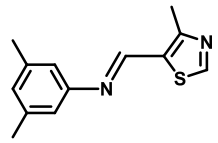 | THF:$H_2O$ (9:1) | $Hg^{2+}$ (Colorimetric) | 0.64 × $10^{-6}$ (M) (UV-Vis), 0.1126 × $10^{-9}$ (M) (FL) | *ACS Omega*, 2022, **7**, 24638. |
| 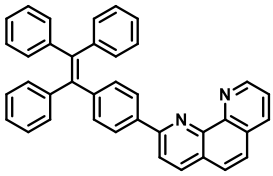 | THF-water mixture, $f_w$ = 90%) | $Hg^{2+}$ (Turn off) | 2.55×$10^{-9}$ mol $L^{-1}$ | *Tetrahedron*, 2019, **75**, 130489. |
| | | $Zn^{2+}$ (Turn on) | 1.24×$10^{-6}$ mol $L^{-1}$ | |
| 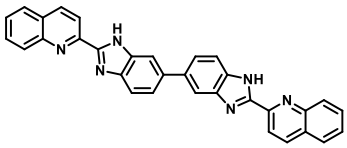 | DMSO/$H_2O$ (10 μM, v/v, 9/1) | $Zn^{2+}$ (Ratiometric) | 0.94 μM | *Dyes Pigm.*, 2019, **170**, 107651. |
| | | $Cu^{2+}$ (Colorimetric) | 1.12 nM | |
| | | $Hg^{2+}$ (Turn-off) | 0.2 μM | |
| 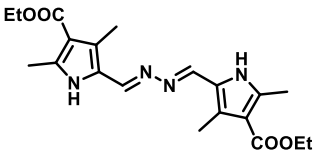 | EtOH/$H_2O$ (1:1, v:v) | $Zn^{2+}$ (Turn on) | 88.3 nM | *Sens. Actuators B: Chem.*, 2018, **255**, 3085. |
| | | $Cu^{2+}$(Colorimetric) | 38.2 nM | |
| | | $Hg^{2+}$ (Turn on) | 69.4 nM | |
| 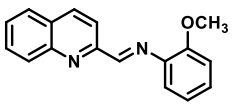 | DMSO/water mixture (1/99 v/v) | $Zn^{2+}$ (Turn on) | 0.011 μM | *Dalton Trans.*, 2017, **46**, 6769. |
| | | $Hg^{2+}$ (Turn on) | 0.040 μM | |
| 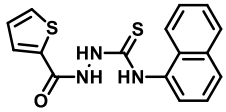 | Bis-tris buffer and aqueous DMSO | $Zn^{2+}$ (Turn on) | 3.17 μM | *J. Photochem. Photobiol. A*, 2022, **428**, 113882. |
| | | $Hg^{2+}$ (Turn on) | 4.92 μM | |
| 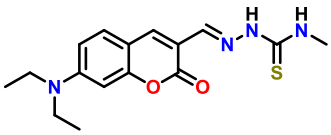 | DMSO/$H_2O$ (9/1, v/v, pH = 7.2) | $Zn^{2+}$ (Ratiometric) | (5.35±0.08) x$10^{-9}$(M) | **This work** |
| | | $Cu^{2+}$ (Colorimetric) | (1.85±0.07) x$10^{-7}$(M) | |
| | | $Hg^{2+}$ (Turn off) | (2.69±0.09) x$10^{-9}$(M) | |

# Chapter 6

# A triphenylamine scaffold for fluorogenic sensing of noxious cyanide via ICT mechanism and its bioimaging application

# A triphenylamine scaffold for fluorogenic sensing of noxious cyanide via ICT mechanism and its bioimaging application


## Abstract

A novel triphenylamine benzimidazole based fluorogenic chemosensor named (2E,2'E)-3,3'-((phenylazanediyl)bis(4,1-phenylene)) bis(2-(1H-benzo[d]imidazol-2-yl) acrylonitrile) (PBIA) has been successfully generated and characterized by various spectroscopic techniques. Among various screened anions only cyanide ($CN^-$) showed a distinct fluorogenic property towards PBIA. Hence, Optical properties of PBIA were investigated in the presence of cyanide ($CN^-$) by means of UV-Vis spectrophotometry and fluorescence spectroscopy in DMSO, where we observed that, upon treatment of $CN^-$ to probe solution, the orange fluorescence of ligand showed a blue shift and the orange fluorescence changed to greenish-yellow under UV lamp. The hypsochromic shift in fluorescence maxima upon addition of cyanide was attributed to nucleophilic addition of cyanide to PBIA inhibiting the electron flow within the molecule and disrupting the ICT process. The interaction involved behind the sensing of cyanide was investigated by $^1$H-NMR titration, mass spectroscopic study and DFT calculations which supported the mechanism. The limit of detection (LOD) was calculated and found to be in order of $10^{-8}$ (M). PBIA showed immediate response in the spectral pattern (< 20s) towards its target cyanide ion and also the effectiveness of the chemosensor was examined in the presence of competing anions. Furthermore, the practical efficacy of the probe PBIA was established by dip-stick experiment along with cyanide detection in various natural water resources. Human breast cancer cells MDA-MB 231 makes it susceptible to $CN^-$ sensing in biological system.


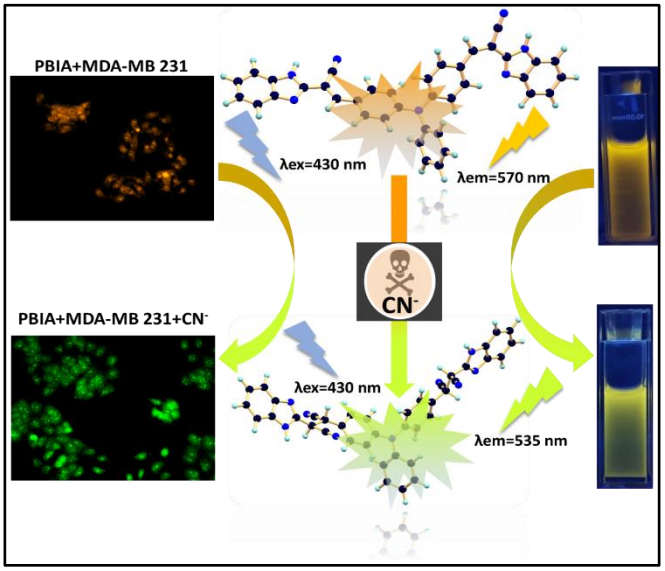

# 6.1. Introduction

We all know that the anions play an imperative roll in different disciplines such as biological systems, environmental chemical processes as well as different technological, clinical and medical processes. [1-4] Among various anions, cyanide is listed as one of the noxious and lethal chemical substance known to us. On the other side, cyanide also has different industrial applications i.e.; making plastics, papers and herbicides.[5,6] Cyanide is also endlessly used in synthesis of resin and synthetic fibres, electroplating, refining, leather making, chelators in water treatment and in metallurgy.[7-10] Again, cyanide salt is majorly used in gold extraction from its ore, where, the gold elemental substance after complexation with cyanide reduces its oxidation potential; as a result, the substance gets easily oxidized by oxygen to form soluble aurate and dissolve under alkali condition which makes gold easily separated from slag.[11] Despite its enormous applications in various fields, cyanide is still very detrimental to humans even at the minimum dosage of 0.05 mg/Kg.[12] Also, WHO has set up acceptable range of cyanide to 1.9 µM in drinking water due to its toxic nature.[13] Cyanide can be absorbed in human body through skin, lungs and gastrointestinal tract which leads to acute effect in human body. Cyanide complex with ferric iron in metalloenzymes leads to histotoxic hypoxia (low oxygen level) by inhibition of cytochrome c oxidase**,** where cyanide gets attached to the active sites of cytochrome oxidase (at cytochrome a3) resulting in the disconnection of mitochondrial oxidative phosphorylation which further leads toobstruction of cellular respiration.[14-16] Excessive exposure to cyanide leads to poisoning of respiratory system, paralysis of central nervous system, haemoglobin poisoning, convulsion, vomiting with loss of consciousness that eventually lead to death.[17] Therefore, huge interest has been sparked to design and develop new fluorescent chemosensor to detect cyanide and monitor it in environmental samples.

There are several well established analytical techniques for qualitative and quantitative detection of cyanide which includes atomic absorption spectroscopy (AAS), inductively coupled plasma-mass spectroscopy (ICPMS), inductively coupled plasma emission spectrometry (ICPES), voltammetry, cyanide selective electrodes, polarography, chromatography (HPLC) and so on.[18-22] But these techniques have several pitfalls as they require hectic sample preparation, trained operators, sophisticated equipment, portabilityand cost issue.[23] These methods are time consuming also . On the other hand, fluorescent chemodosimetric approach to detect its guest

analyte have gained huge interest due to simple synthetic procedure, reusability, and rapid detection through naked eye.[24]

Generally, the strategy behind the design of cyanide sensors is based upon hydrogen bonding, deprotonation, nanotechnology, supramolecular self-assembly, metal cyanide displacement and nucleophilic addition techniques. [25-31] However, the first few approaches lack selectivity due to interference of protic solvent and competing ions; whereas, the ion displacement technique requires stabilized metal-ligand complex. On the other hand, nucleophilic addition reaction based chemosensor known as chemodosimeter, possesses benefits such as, high selectivity, sensitivity, and rapid response time. Reaction based chemosensors mainly involve various functional group such as C = C, C = N and C = O, which are selectively attacked by cyanide ion that creates a strong irreversible chemical bond known as chemodosimeter.[32-34] The photophysical properties of these organic chemodosimeter get disturbed when the nucleophilic addition takes place and the electronic properties of these sensors get transformed. Thus, the change in fluorescence signal results due to nucleophilic addition of analytes. Mainly the probes detecting cyanide involves various mechanisms such as, hydrogen bonding interaction, intra-molecular charge transfer (ICT), twisted intra-molecular charge transfer (TICT), fluorescence resonance energy transfer (FRET), excited state intra-molecular proton transfer (ESIPT), photo-induced electron transfer (PET). [35-41] Among these mechanisms ICT plays a pivotal role in cyanide detection as the push-pull effect between donor acceptor gets disturbed due to the addition of cyanide, which results into the change in ICT process within the organic framework.

## 6.2. Prior works

Till date, several donor-π-acceptor (D-π-A) type sensors have been developed to detect trace amount of $CN^-$ ion, which is based upon intramolecular charge transfer (ICT), where, due to the presence of various subunits such as C=C and C=N, the ICT process gets inhibited as a result of the nucleophilic addition that causes the spectral change.[34,42-50] There are also various reported sensors based upon 1,1-dicyanovinyl group for cyanide sensing.[51-55] A number of chemical motifs are previously reported which involves indolium, benzyl derivatives, acridinium salts, aldehyde and trifluoroacetyl group where cyanide caused change in conjugation and in spectroscopic property.[56-62]

## 6.3. Present work

Hence taking into account the novel reactivity of cyanide ion, we have successfully synthesized a highly fluorescent chemodosimeter (PBIA) that has a backbone of an acceptor-π-donor-π-acceptor (A-π-D-π-A) units. The benzimidazole-2-acetonitrile group present on both sides act as an acceptor group, whereas, triphenylamine moiety plays the role of electron donating subunit. The chemodosimeter serves as a fluorescent sensor for detection of cyanide with high selectivity and sensitivity in DMSO. As cyanide acts as a good nucleophile, it attacks the electrophilic centre of probe resulting into a distinguishable change in colour under UV light from orange to greenish-yellow. We have also successfully applied the chemodosimeter for the detection of cyanide in real water samples. TLC plate experiment has also been executed for qualitative experiment. Biocompatibility study was visualized in MDA-MB 231 cell lines.

## 6.4. Results and discussions

### 6.4.1. Design and Synthesis of the sensor (PBIA)

Very economically cheap precursors, i.e., triphenyl amine, o-phenylene diamine, ethyl cyanoacetate were used for the synthesis of PBIA. The synthetic design for PBIA is shown in scheme 1, where compound '1' and '2' were prepared using previously reported procedure. [63,64] Then 4,4'-(phenylazanediyl) dibenzaldehyde was reacted with 2-(1H-benzo[d]imidazol-2-yl) acetonitrile in absolute ethanol solvent under reflux condition in presence of piperidine, which yielded our desired probe PBIA. Additionally, the sensor PBIA was thoroughly characterized by elemental analysis, $^{1}$H NMR, $^{13}$C NMR, IR and HRMS spectroscopic method, the data are given in (Fig.A6.1-A6.6, Appendix).

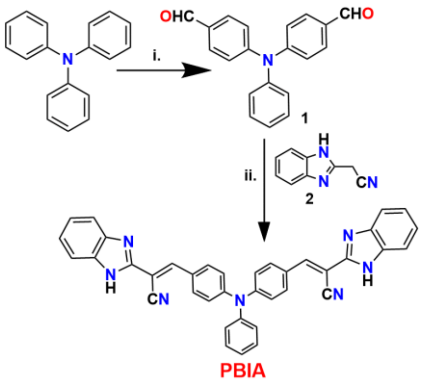


**Scheme 6.1:** Synthetic route of the probe (PBIA) (i) DMF, $POCl_3$, 0ºC,2 h; (ii) EtOH, Piperidine, reflux, 3h.

## 6.4.2. Photophysical properties of PBIA

### 6.4.2.1. UV-Vis spectral studies

We observed the photophysical study of probe PBIA in 100 % DMSO medium. In UV-Vis absorption study we noted that the probe PBIA itself shows a low energy absorption band at 455 nm along with a shoulder peak at 400nm and a high energy small peak at 340 nm respectively. These energy bands correspond to ICT character of PBIA which generates from its structural observation. PBIA contains a triphenyl- amine group, which is strong electron donor in nature and a phenylacrylonitrile benzimidazole conjugated skeleton moiety which is electron acceptor in nature, hence this charge separated structure represents a typical A-π-D-π-A framework.

While gradual addition of $CN^-$, we observed that the absorption peak at 455 nm tends to decreases with blue shift. Thus, new absorption peak appears at 425 nm. Simultaneously we noted that the shoulder peak at 400 nm and the high energy band at 340 nm disappears, with generation of two very small peaks at 294 nm and 310 nm respectively, whereas, two distinct isosbestic points were observed at 320 nm and 282 nm (Fig. 6.1). These shifting of bands to high energy clearly indicates the nucleophilic addition of cyanide to the electron deficient part of PBIA, which results into the distortion in the ICT process and disrupts the electron conjugation between benzimidazole and triphenylamine counterpart.

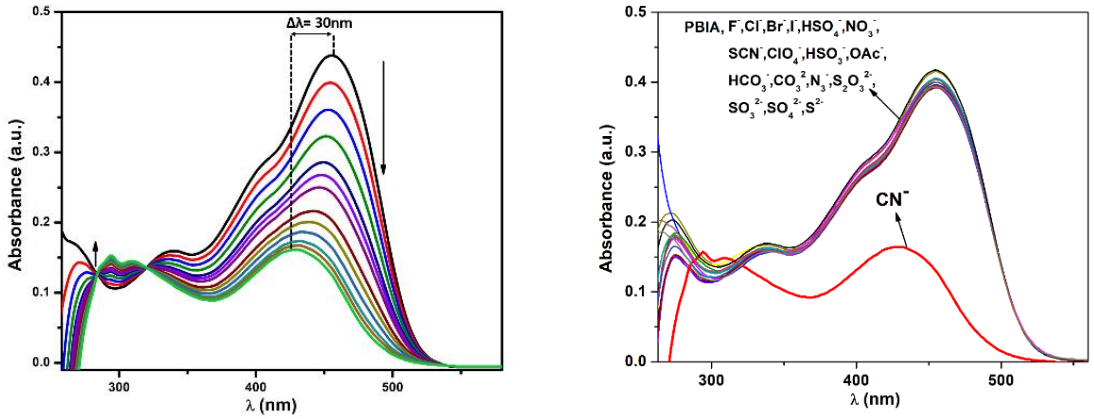


**Figure 6.1:** Change in UV-Vis spectrum of PBIA (20 μM) upon gradual addition of $CN^-$(40 μM) in DMSO. (left side) and UV-Vis change of PBIA (20 μM) upon addition of different anions, i.e., $F^-$, $Cl^-$, $Br^-$, $I^-$, $HSO_4^-$, $NO_3^-$, $SCN^-$, $ClO_4^-$, $HSO_3^-$, $OAc^-$, $HCO_3^-$, $CO_3^{2-}$, $N_3^-$, $S_2O_3^{2-}$, $SO_3^{2-}$, $SO_4^{2-}$, $S^{2-}$ and $CN^-$ (40 μM) in DMSO. (right side).

Furthermore, to establish the selectivity of our probe PBIA we also have performed the UV-Vis studies in presence of other relevant anions; $F^-$, $Cl^-$, $Br^-$, $I^-$, $HSO_4^-$, $NO_3^-$, $SCN^-$, $ClO_4^-$, $HSO_3^-$ ,$OAc^-$, $HCO_3^-$, $CO_3^{2-}$, $N_3^-$, $S^{2-}$, $S_2O_3^{2-}$, $SO_3^{2-}$ and $SO_4^{2-}$ in DMSO at room temperature, although, addition of these other anions does not show any significant changes to ligand absorption spectra (Fig. 6.1).

### 6.4.2.2. Fluorescence spectral study

The probe PBIA itself shows bright orange coloured fluorescence, which occurs due to strong ICT process within the probe. When excited at 430 nm it shows strong emission band with emission maxima at 570 nm and fluorescence quantum yield was calculated to be 0.148. Then fluorescence spectra of PBIA was recorded in DMSO with gradual addition of $CN^-$ (40 µM). We observed that the fluorescence maxima began to decrease with blue shift, finally we observe a new band at 535 nm with an isoemissive point at 520 nm (Fig 6.2). Hence, we observed a clear blue shift of 35 nm, which clearly accounted for the disruption of ICT process with decrease in fluorescence intensity. Subsequently, we also observed the change in the fluorescence colour from orange to greenish-yellow under UV light.

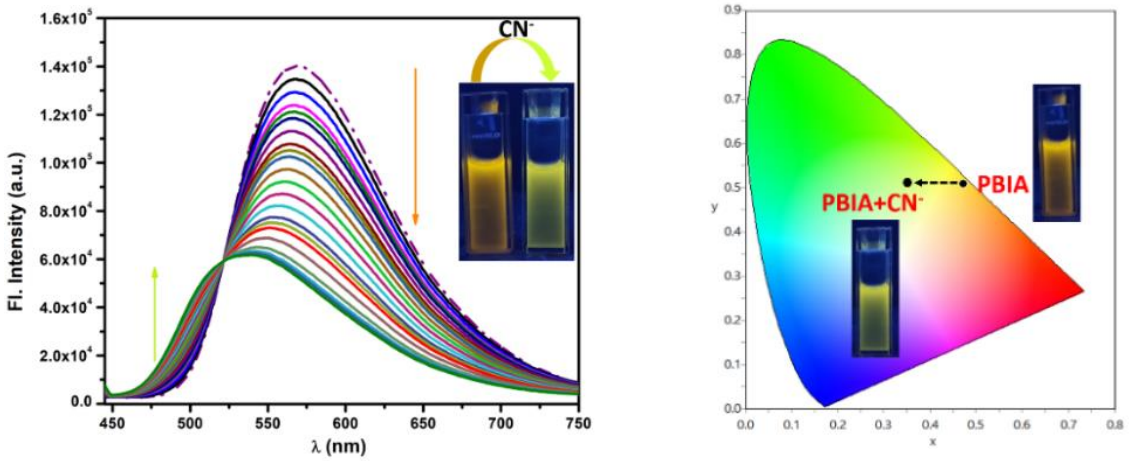


**Figure 6.2:** Change in emission spectra of PBIA (20 µM) upon gradual addition of $CN^-$ (40 µM) in DMSO. Inset: shows the change in colour under UV light (λex = 430 nm)(left side) and The CIE1931 Chromaticity diagram of probe PBIA with cyanide (right side).

The blue shifting of emission band with simultaneous decrease of the emission intensity is attributed to the distortion in ICT process, which is resulted due to nucleophilic addition of cyanide to PBIA forming PBIA-CN adduct. The quantum yield value also changes up to 0.074.

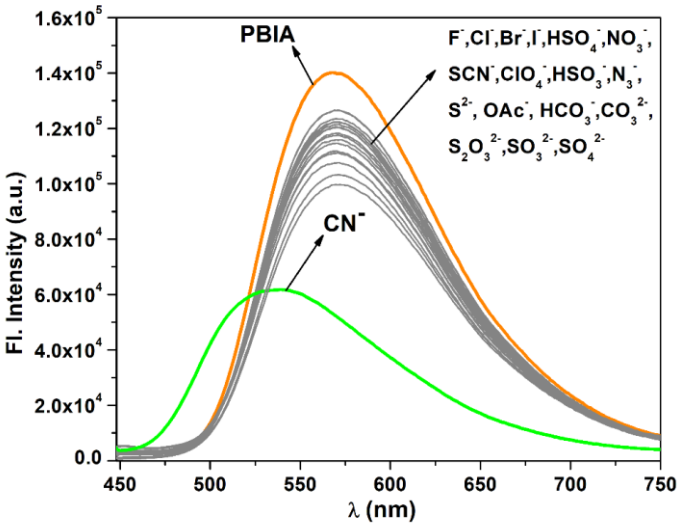


**Figure 6.3:** Fluorescence change of PBIA (20 µM) upon addition of different anions, i.e. $F^-$, $Cl^-$, $Br^-$, $I^-$, $HSO_4^-$, $NO_3^-$, $SCN^-$, $ClO_4^-$, $HSO_3^-$, $OAc^-$, $HCO_3^-$, $CO_3^{2-}$, $N_3^-$, $S_2O_3^{2-}$, $SO_3^{2-}$, $SO_4^{2-}$, $S^{2-}$ and $CN^-$ (40 µM) in DMSO.

To further validate the sensing experiment, we have checked the effect of water on the fluorescence intensity of PBIA. From fluorescence spectral studies it was observed that, the probe showed maximum fluorescence intensity in DMSO medium, with increase in fraction of water, the fluorescence intensity of PBIA decreases with simultaneous red shift (Fig. 6.4). Hence, we have optimized the solvent system to be DMSO only and conducted all spectroscopic studies.

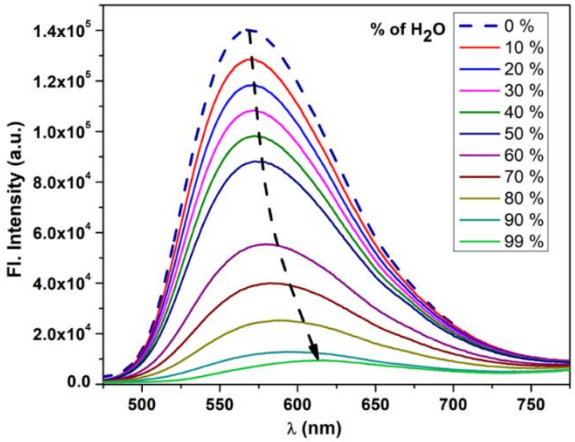


**Figure 6.4:** Emission spectra of PBIA (20 µM) in DMSO with different water fractions ($f_w$) ($\lambda_{ex}$= 430 nm).

In the Commission International de L'Eclairage (CIE) chromaticity coordinates (Fig. 6.2) we have also observed noticeable changes from orange to greenish yellow with a coordinate variation from (X=0.4736, y=0.5073) to (X=0.3689, y=0.5160). The fluorescence response was also studied in the presence of other similar relevant anions; $F^-$, $Cl^-$, $Br^-$, $I^-$, $HSO_4^-$, $NO_3^-$, $SCN^-$, $ClO_4^-$, $HSO_3^-$, $OAc^-$, $HCO_3^-$, $CO_3^{2-}$, $N_3^-$, $S^{2-}$, $S_2O_3^{2-}$, $SO_3^{2-}$and $SO_4^{2-}$ in DMSO to unveil if they show any significant sensing property towards PBIA or not. We remarked that other than slight decrease in the emission intensity of PBIA, these competitive anions do not show any distinguishable change to the fluorescence pattern of PBIA (Fig. 6.3).

### 6.4.2.3. Binding studies of PBIA with $CN^-$

Further, for quantitative measurement of $CN^-$ we plotted the change in the emission intensity at 570 nm with concentration and we observed an almost linear plot. The limit of detection (LOD) of PBIA towards cyanide ion was calculated and found to be $(6.56\pm0.26) \times 10^{-8}$ (M), which was established from the fluorescence titration data upon addition of $CN^-$ to PBIA using the equation, LOD = K×($Sb_1$/S). We had taken k=3, $Sb_1$ is the standard deviation and S stands for the slope of the linear response curve respectively (Fig. 6.5).

The fluorescence quenching is explained by the Stern-Volmer equation

$$F_0/F = 1 + K_{sv}[Q] \ldots\ldots\ldots (1)$$

where $F_0$ and F are the fluorescence intensities in the absence and presence of $CN^-$, respectively. $K_{sv}$ is the Stern– Volmer quenching constant and [Q] is the concentration of the [$CN^-$]. The $K_{sv}$ value is obtained with a slope from the plot of $F_0/F$ versus [Q] and found to be $1.16\times10^3$ $M^{-1}$ respectively. The quenching constant value suggested a good interaction between the probe PBIA and $CN^-$. We have also calculated the quenching constant between PBIA and $CN^-$ using Stern-Volmer plot and it is found to be $1.16 \times 10^3$ $M^{-1}$ (Fig. 6.5).

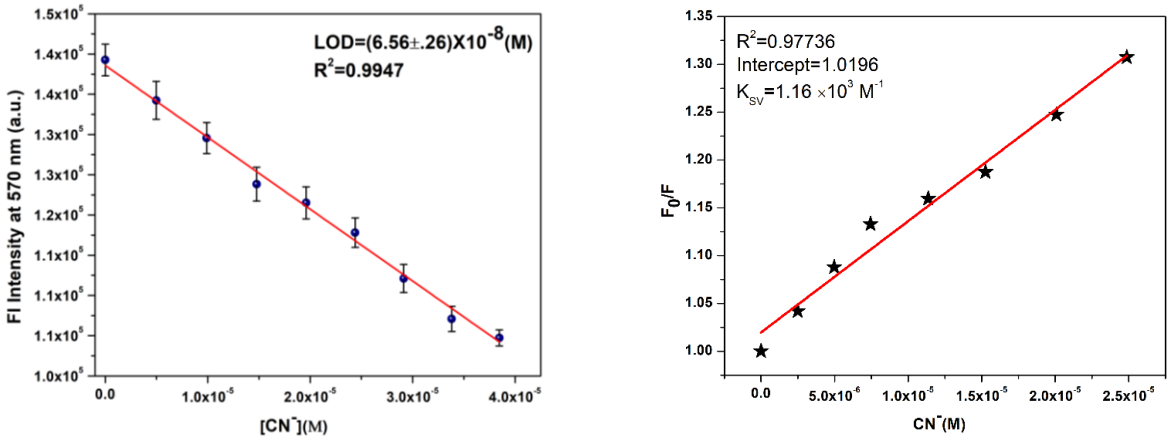


**Figure 6.5:** Linear response curve of PBIA at 570 nm depending on the $CN^-$concentration. (left side) andStern-Volmer plot for $CN^-$ (right side).

## 6.4.2.4. Competitive study

An efficient chemosensor must show selectivity and sensitivity towards its guest analyte. Hence, competitive experiment was performed to study the efficiency of PBIA in the presence of different biologically and environmentally relevant guest anions. $CN^-$ was added to the solution of PBIA, containing other anions such as $F^-$, $Cl^-$, $Br^-$, $I^-$, $HSO_4^-$, $NO_3^-$, $SCN^-$, $ClO_4^-$, $HSO_3^-$, $OAc^-$, $HCO_3^-$, $CO_3^{2-}$, $N_3^-$, $S^{2-}$, $S_2O_3^{2-}$, $SO_3^{2-}$ and $SO_4^{2-}$. Upon excitation at 430 nm PBIA selectively detected $CN^-$ with emission intensity centred around 535 nm in presence of the aforementioned anions. As can be observed from the bar graph represented in Fig. 6.6, the other anions do not alter the intensity pattern of PBIA with fluorescence maxima at 570 nm. The only change was observed when $CN^-$ was added, the fluorescence maxima shifted to 535 nm. Thus, we have represented the bar graph at fluorescence maxima 570 nm. This competitive study clearly demonstrates the binding ability of PBIA towards $CN^-$ and anti-interference ability of PBIA towards other anions, which results due to the strong nucleophilic character of $CN^-$, forming a strong adduct of PBIA-$CN^-$, even if there are other anions present. This proves the high anti-interference ability of our synthesized probe with effective signalling aptitude towards $CN^-$.

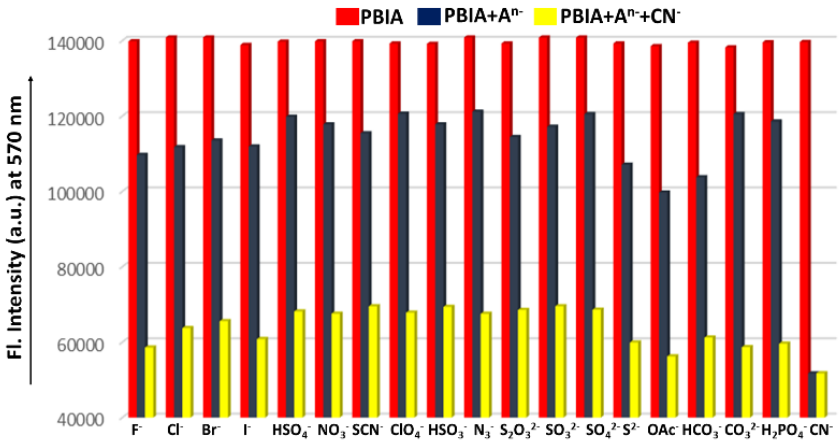


**Figure 6.6:** Competitive experiments of PBIA (20 μM) for $CN^-$ (40 μM) in presence of common anions (40 μM).

## 6.4.2.5. Time dependent spectra of PBIA with $CN^-$

Again, as an efficient sensor must detect its guest anion within short span of time, kinetics study was performed to assess the reaction time of the probe towards $CN^-$. The fluorescence response time scale was taken in the range of 0-60 seconds. The experiment revealed that the fluorescence intensity of the probe at 570 nm remains almost constant, whereas, in case of PBIA-CN the intensity at 570 nm decreases, as fluorescence maxima decreases with blue shift while the reaction progresses. The minimum of the curve reached within 20 s and we observed a plateau indicating the closure of the reaction (Fig. 6.7). This short span of detection time made it clear that our probe is a potential candidate for rapid detection of $CN^-$.

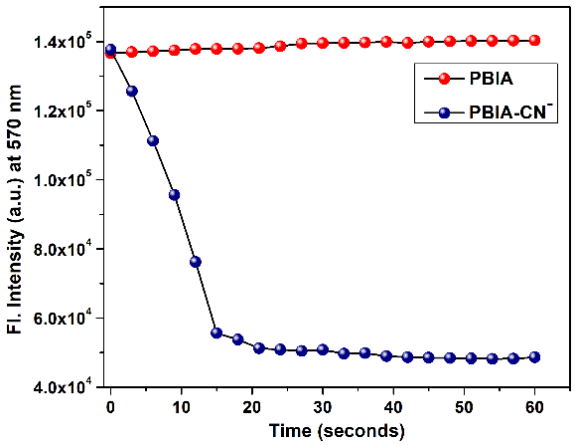


**Figure 6.7:** The time-dependent fluorescence spectrum of PBIA towards $CN^-$ in DMSO.

We have performed time dependent absorption spectra where we have observed that the curve reaches the minima within 24 seconds, then a plateau has been observed indicating the completion of reaction (Fig. 6.8).

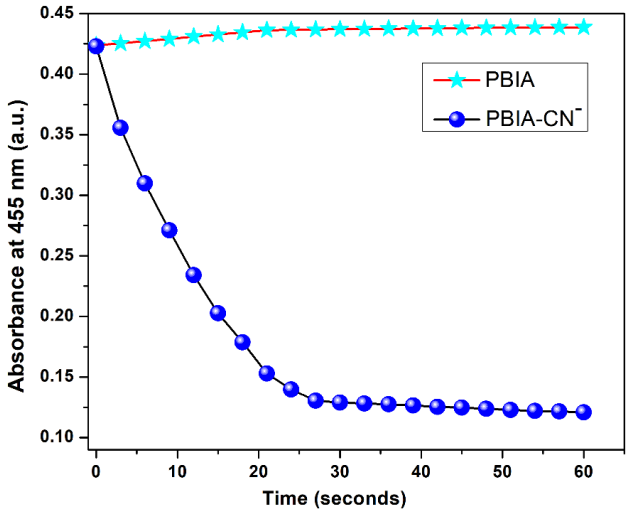


**Figure 6.8:** The time-dependent absorption spectrum of PBIA towards $CN^-$ in DMSO.

## 6.4.2.6. TRPL Study

To get better insight on excited state behaviour, Nano second time resolved fluorescence study (TRPL) is a convenient tool. Hence, we have taken probe (PBIA) and adduct (PBIA-CN) in DMSO and performed the study. The fluorescence lifetime decay plots were fitted using mono exponential function of PBIA and bi exponential function of PBIA-$CN^-$ adduct with acceptable $\chi^2$ values (Fig. 6.9). For PBIA, it was calculated that $\tau$=0.50 ns ($\chi^2$ = 1.07) and forPBIA-CN adduct, the value increased up to, $\tau$=1.92 ns ($\chi^2$=1.01). The increase in lifetime value also supports the mechanism of sensing, where in case of PBIA, due to stronger ICT the energy gap is low, resulting in lower lifetime value. On the other side, for PBIA-$CN^-$ adduct the energy gap is high owing to weak ICT triggering in higher lifetime value. The equation $\tau^{-1}= K_r+K_{nr}$ and $K_r= \varphi_f/\tau$ was also implemented to calculate the radiative rate constant $K_r$ and the total non-radiative rate constant $K_{nr}$ values (Table A6.1, Appendix). The change in the values of $\tau$, $K_r$ and $K_{nr}$ reflects the formation of $CN^-$ adduct which shows a higher lifetime compared to free probe PBIA itself. Hence, fluorescence lifetime measurement experiment reflects that PBIA can be used as a lifetime-based sensor for cyanide ion.

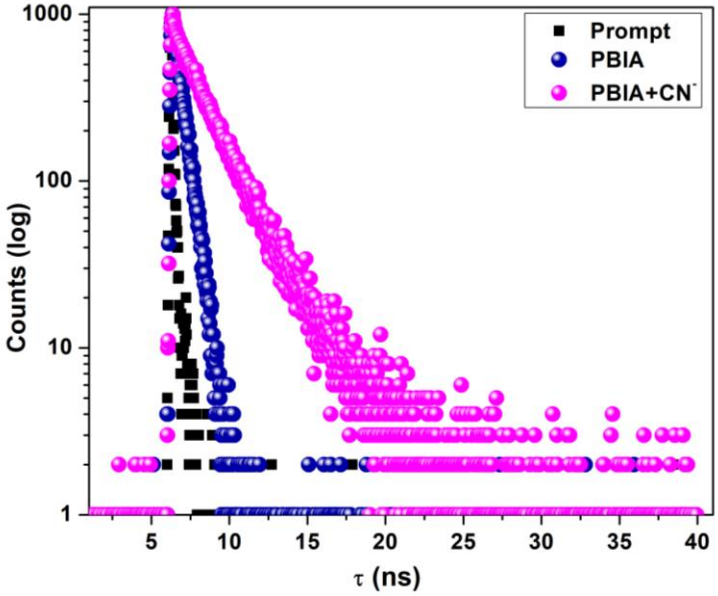


**Figure 6.9:** Time-resolved fluorescence decay of PBIA (●●●), PBIA-CN adduct (●●●) and prompt (■■■) in DMSO ($\lambda_{ex}$ =430nm).

## 6.4.2.7. Effect of pH

$CN^-$ plays an important role in industrial procedures as well as in biological processes. Hence, to investigate the dependency of our probe PBIA towards pH, we recorded the emission spectra of PBIA and PBIA-$CN^-$ in DMSO solution with pH values ranging from 2.0 to 12.0. It was noted that for free probe PBIA with decrease in pH (pH<7) the emission intensity decreases at 570 nm. This is presumably due to protonation of nitrogen atom disrupting the electron transfer process, whereas, we observed the fluorescence intensity at 570 nm decreases, with blue shift also in basic condition, which might result from deprotonation of imidazole protons. For PBIA-$CN^-$ also under strong acidic condition (pH<5), the fluorescence intensity quenches at 535 nm simultaneously decreasing the intensity at value at 570 nm. The fluorescence intensity at 535 nm does not alter so much for higher pH values as it shows blue shift. Hence the intensity remains low at 570 nm also as shown in (Fig. 6.10). It is clear from the plot that the intensity is prominent and shows maxima values only near pH 7. This noteworthy emission maxima near pH 7, indicates that, PBIA is most effective in sensing $CN^-$ near neutral pH (7.2) medium.

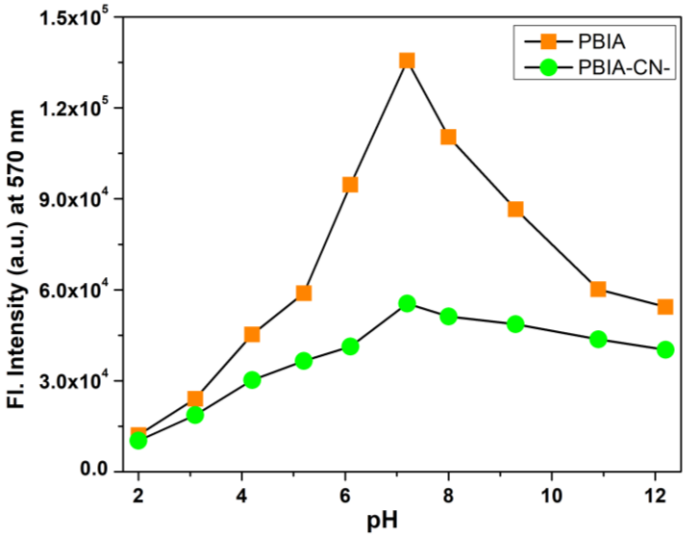


**Figure 6.10:** pH study of PBIA for $CN^-$ (from Fluorescence spectra).

Effect of pH was also examined for absorption spectroscopy in case of PBIA and PBIA-$CN^-$. For PBIA, we observed that the absorption spectra with lowering of pH value shows red shift with decrease in absorption value at 455 nm. Whereas for higher pH, the spectra appear with slight blue shift with increase in absorption value at 455 nm. The values were plotted against pH range of 2 to12. Also, for PBIA-$CN^-$ in acidic condition, we observed that the absorption peak at 425 nm displays red shift with decrease in absorption value at 425nm, whereas, in basic condition the absorption value shows slight increment (Fig. 6.11).

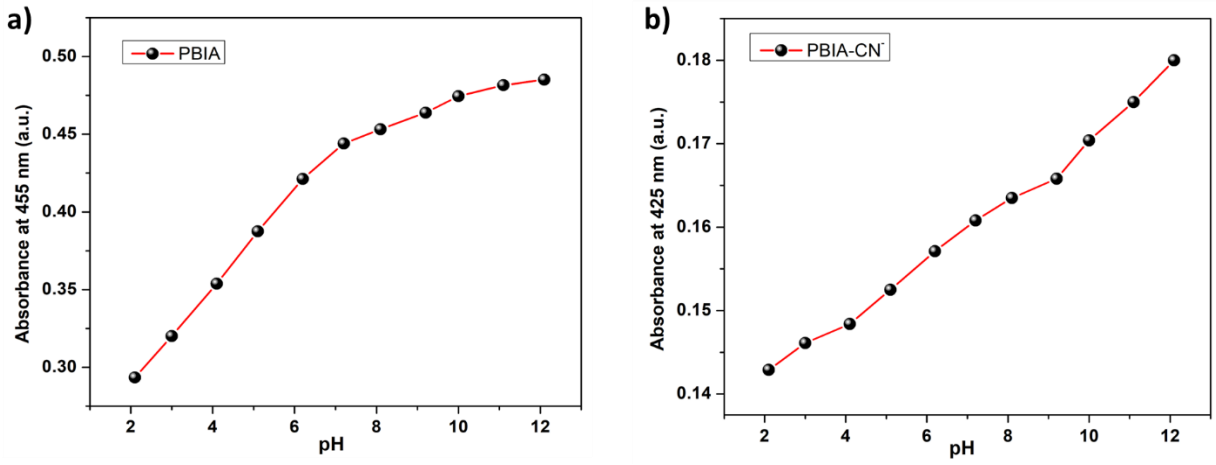


**Figure 6.11:** pH study of PBIA (a) and for PBIA-$CN^-$ (b) (from absorption spectra).

## 6.4.3. Possible sensing mechanism of PBIA

The possible sensing mechanism of the probe PBIA towards $CN^-$ was investigated by $^1$H-NMR spectroscopy. In $^1$H-NMR spectrum of free PBIA, we noted that the -NH proton resonates at 12.97 ppm and the resonance signal of aromatic protons appears to be in the range between 8.00-7.21 ppm, while the vinylic proton corresponds to a peak at 8.26 ppm (Fig. A6.1, Fig. A6.3-A6.4 , Appendix). In case of PBIA-CN adduct, we observed that -NH peak remains as it is with slight upfield shift to 12.54 ppm. Additionally, in case of the aromatic protons it was noted that, they were also shifted to upfield region ranging 7.76-6.18 ppm, which was due to development of negative charge in PBIA-CN adduct (Fig. A6.8, Appendix). Also, the broadening of the aromatic region was observed which could be attributed to interaction occurred via pi stacking between the aromatic rings of PBIA and the large cationic group tetra butyl ammonium [65]. This clearly indicates that conjugation between triphenyl amine group and benzimidazole unit breaks-down, whereas the vinylic proton which was resonating at 8.26 ppm, disappeared in PBIA-CN adduct. The new signal appeared in up field region at 4.40 ppm, that indicated the formation PBIA-CN adduct (Fig. 6.12).

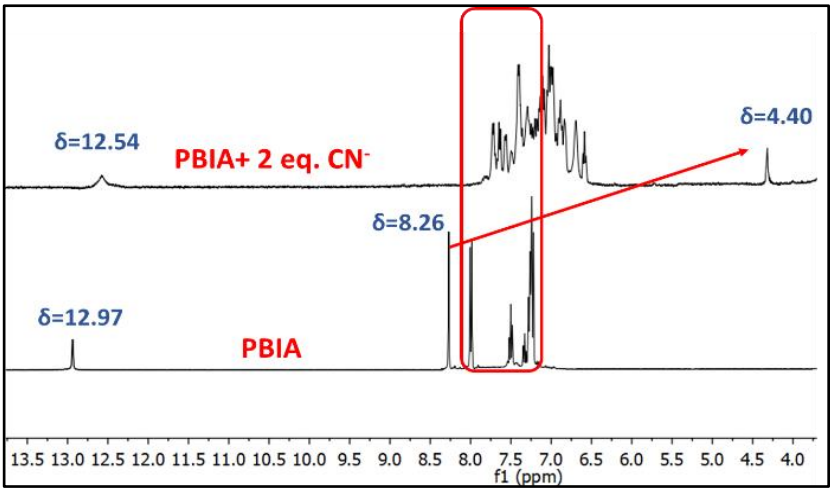


**Figure 6.12:** $^1$H-NMR spectrum of PBIA and PBIA+$CN^-$ (2 equivalent) in DMSO-$d_6$.

The formation of PBIA-$CN^-$ species is also supported by HRMS spectroscopy. In the mass spectrum peak at 634.25 (m/z) confirms the formation of (PBIA+2$CN^-$) adduct respectively (Fig. A6.9, Appendix). The jobs plot by absorbance method also supported the binding ratio of 1:2 between PBIA and $CN^-$ (Fig. A6.7, Appendix). Thus, these results disclose the nucleophilic addition of cyanide at the cyano vinyl position (β position of C=C bond), which leads to the

conversation of $sp^2$ hybridized carbon to $sp^3$ hybridization (Fig. 6.13). We have also compared with some recently reported chemosenors detecting $CN^-$ in terms of their solvent system, LOD values and detection type in Table A6.3, Appendix.

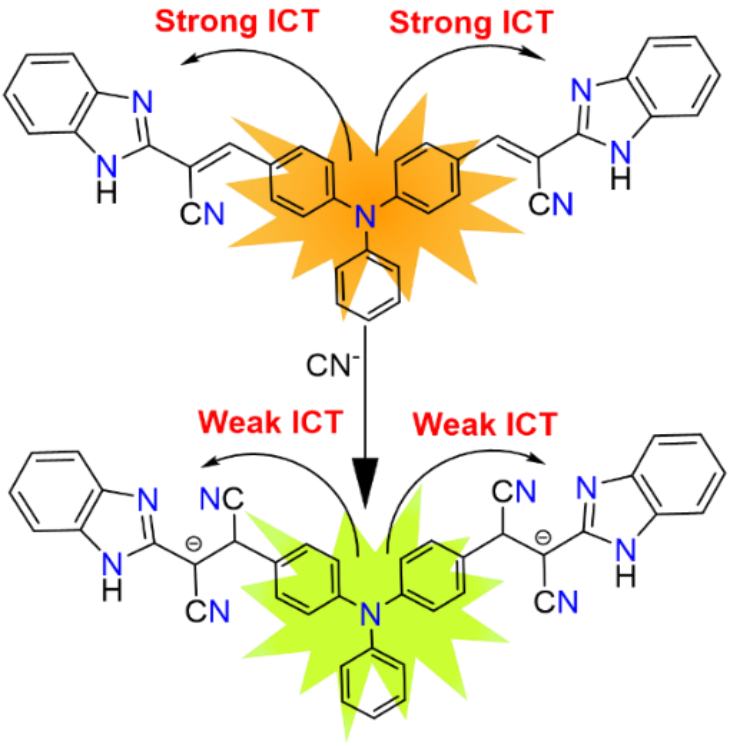


**Figure 6.13:** Probable sensing mechanism of PBIA with $CN^-$.

## 6.4.4. Dip-stick experiment: Detection of $CN^-$ using TLC plate

To detect toxic analytes successfully, a portable solid platform sensing tool is a convenient one. Hence, we have used this rational analytical technique known as dip-stick experiment to increase the potential application of our probe. In order to carry out this experiment, at first thin-layer chromatography (TLC) plates were submerged in the solution of PBIA in DMSO ($2 \times 10^{-4}$ M) and then they were kept aside for a few minutes so that the solvent gets evaporated. Subsequently, the TLC plate was immersed into the aqueous solution ($2 \times 10^{-3}$ M) of cyanide and kept open for the solvent to evaporate so that the plate dries out. Under hand held UV light, we observed that the TLC plate coated with PBIA showed brownish colour, whereas, when it was immersed in $CN^-$ solution its colour changed to greenish-yellow (Fig. 6.14). So, PBIA shows difference in colour in coated TLC platform upon interaction with $CN^-$, which we can distinguish instinctively. Hence, we can conclude that, without any sophisticated instrumental analysis by

barely using transportable solid-state platform, prompt qualitative naked eye detection of cyanide is possible.

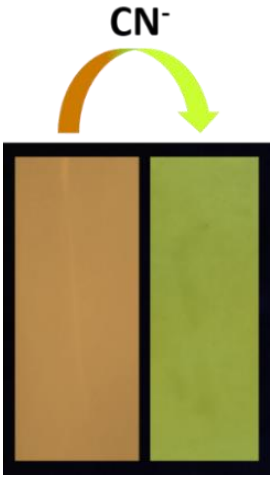


**Figure 6.14:** Pictures of TLC plates after immersion in DMSO solution of PBIA and PBIA-$CN^-$ under hand held UV chamber. [PBIA] = $2 \times 10^{-4}$ M, [$CN^-$] = $2 \times 10^{-3}$ M. Excitation wavelength of the UV light is 346 nm.

## 6.4.5. Real water sample analysis

Nowadays, Water bodies have become polluted as cyanide from different industrial and commercial sources are dumped into water -bodies endangering aquatic life. Thus, development of analytical method for quantitative detection of $CN^-$ in wastewater is of great importance. To corroborate the practicality of our approach, the detection of $CN^-$ was performed in real samples. Drinking water, University campus lake water and tap water (from laboratory) were collected and analysed according to the previously reported procedure. [66-70] The collected water samples were filtered by using Whatman no. 1 filter paper to remove the suspended particles. Now, the standard addition technique was used to calculate the $CN^-$ concentration in water samples, which involved addition of different increasing concentration (10, 20, and 30 µM) of $CN^-$ to the above-mentioned water samples (Fig.A6.12-14, Appendix). The standard curves were obtained by dissolving $CN^-$ in deionized water. Now from the experimental data of Table 6.1., the recovery % was calculated, which states that, it lies within the range from 96.1% to 99.06 %. Hence, this experimental data demonstrates the reliability of the sensor PBIA to detect $CN^-$ in different varieties of environmental water samples.

**Table 6.1:** Recovery % experiment for $CN^-$ detection in various natural water samples.

| Source | $CN^-$ added (µM) | $CN^-$ recovery (µM) | Recovery (%) |
|---|---|---|---|
| Drinking water | 10 | 9.79 | 97.9 |
| | 20 | 19.69 | 98.45 |
| | 30 | 29.56 | 98.53 |
| Tap water | 10 | 9.61 | 96.1 |
| | 20 | 19.29 | 96.45 |
| | 30 | 29.23 | 97.43 |
| Jadavpur University campus lake water | 10 | 9.86 | 98.6 |
| | 20 | 19.75 | 98.75 |
| | 30 | 29.72 | 99.06 |

## 6.4.6. Cell Study

### 6.4.6.1. Cytotoxicity assay

The cytotoxicity of PBIA was evaluated on MDA- MB231 human breast cancer cell line using MTT method. Cells were seeded on a 96 well plate and kept in an incubator for 24 h. for attachment of the cells. The MTT assay demonstrates that PBIA imparts a negligible effect on cell viability at low doses but at higher doses, the viability of the cells was compromised.Cells were treated with the probe PBIA ranging from 20 µM to 640 µM for 24 hrs (Fig.6.15).Cell viability represented in Fig. 6.15 indicates that from 1 to 200 µM concentration PBIA shows a high number of viable cells, which signifies that PBIA is safe to use in a biological system, although the cells have lower survivability in higher concentration. The $IC_{50}$ was found to be 179.727 µM and hence for subsequent experiments, the treatment dose was selected at 10 µM as the amount of dosage should be less than $IC_{50}$ value.

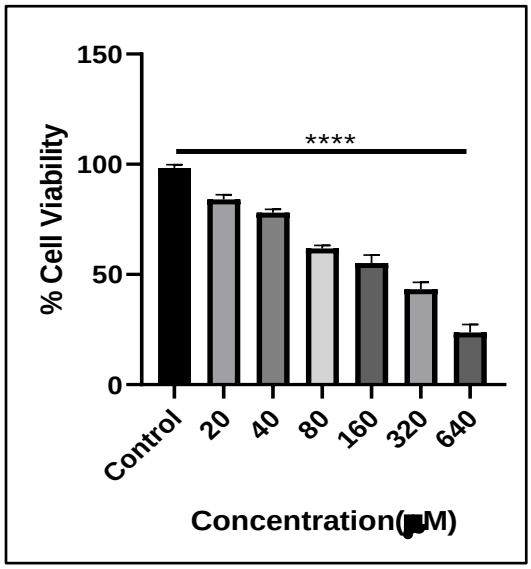


**Figure 6.15:** Cell survivability of MDA-MB 231 cells exposed to different PBIA concentration. Data are representative of at least three independent experiments and bar graph shows mean ± SD, ****$p < 0.0001$

## 6.4.6.2. Cellular imaging by fluorescence microscopy

The MDA-MB 231 cells were incubated with the probe PBIA in one group and in another group, the cells were incubated with cyanide along with the chemosensor PBIA. However, no morphological changes in the cells were noted with the treatment. An orange fluorescence was observed in the cells treated with the probe PBIA. Hence, we can conclude from the Fig. 6.16 that, the probe PBIA can pass the cell membrane. Upon a brief exposure of the cells to cyanide, the cells were found to exhibit a green fluorescence whose intensity increases with time as demarcated in Fig. 6.16. Bright field images were also shown to indicate the morphological changes with the treatment of the chemosensor PBIA along with cyanide.

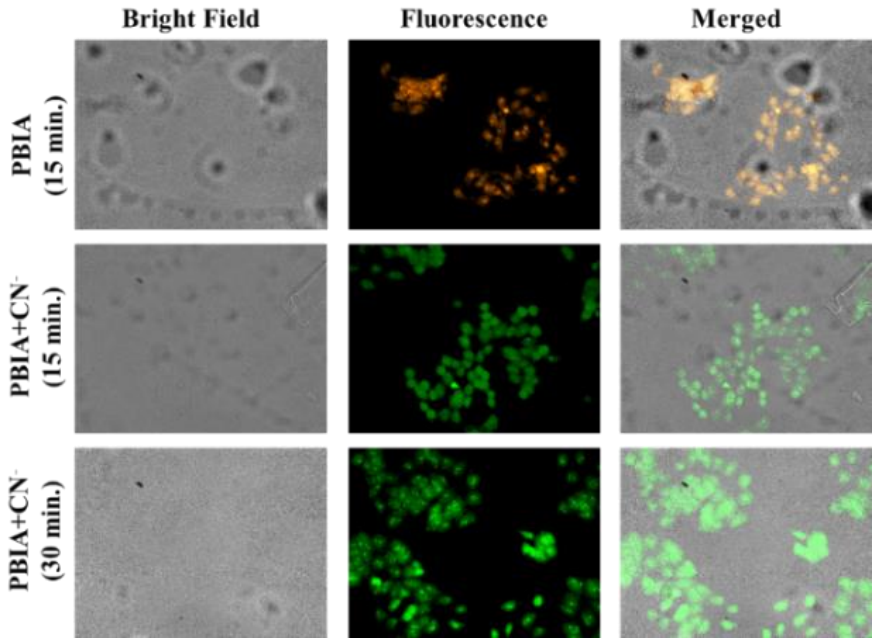


**Figure 6.16:** Fluorescence microscopy images of MDA-MB 231 cells treated with the ligand PBIA and PBIA+CN after 15 min and 30 min under bright, fluorescence and merged field. (Orange channel: 570-610 nm; Green channel: 525-555 nm).

## 6.4.7. Computational study

To get a comprehensive view of the reaction mechanism involved between the probe PBIA with $CN^-$, we performed theoretical calculations. Geometry optimization of PBIA and PBIA-CN were carried out by DFT/B3LYP/6-31+G(d) method using the Gaussian 09 program. Fig. 6.17 (a) and (b) respectively represents the optimized structures of PBIA and PBIA-CN. Also, the contour plots of some selected molecular orbitals of PBIA and PBIA-CN adduct are displayed in Fig. A6.10-11, Appendix.

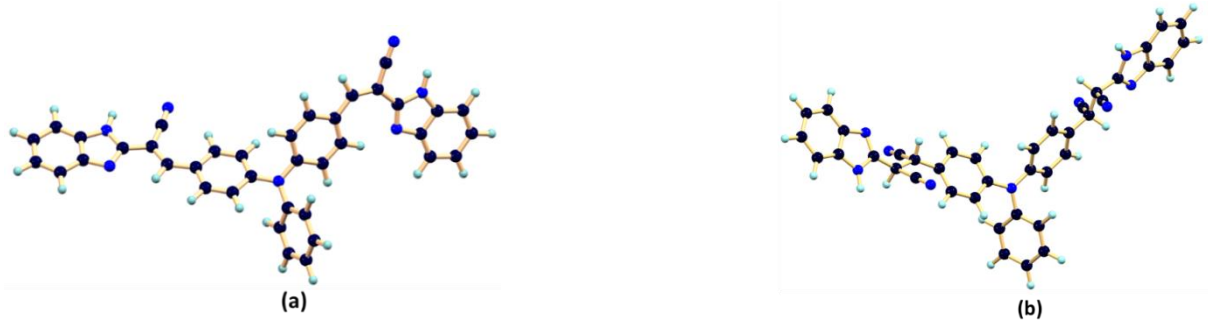


**Figure 6.17:** Optimized structure of (a) PBIA and (b) PBIA-CN calculated by DFT/B3LYP/6-31+G(d) method.

Further from the HOMO of free PBIA it is evident that, the electron cloud is distributed through the entire molecule, which results from the π- Conjugation and the ICT transition. For PBIA-CN adduct, we observed that the HOMO electron cloud is distributed mainly on triphenyl moiety, which was due to the nucleophilic addition of $CN^-$ disrupting π-electron conjugation. Due to the noteworthy difference in π- conjugation, the structures of PBIA and PBIA-CN are different. This is the evident for the different ICT processes responsible for different energy transition in both cases. Additionally, the energy gap between HOMO and LUMO for free PBIA was calculated and found to be 3.22 eV, whereas, for PBIA-CN adduct the HOMO-LUMO energy gap considerably increased to 4.38 eV (Fig. 6.18). This is expected as the cyanide addition breaks the π-conjugation increasing the energy gap weakening the electronic transition and fluorescence property. Also, the increase of HOMO-LUMO energy gap for PBIA-CN adduct reflected on blue shift in UV-vis spectra. To get insight on electronic transitions, the time dependent density functional theory (TDDFT) was performed by CPCM method on the optimized geometries and the results are summarized in Table A6.2. The calculated transitions agreed well with the blue shift in UV-vis spectra which was observed upon addition of $CN^-$ to PBIA.

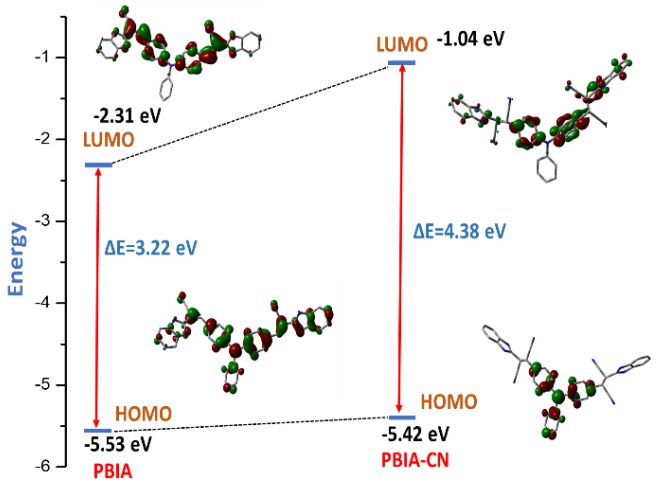


**Figure 6.18:** Calculated frontier molecular orbitals for PBIA and PBIA-CN with their orbital energies using the B3LYP/6-31+G(d) basis set.

# 6.5. Conclusions

To summarize, we have explored the design and synthesis of a novel triphenylamine benzimidazole based sensor PBIA, which showed selective response towards cyanide ion in DMSO medium. The detection of cyanide in the highly conjugated system of PBIA is based

upon the nucleophilic addition of cyanide which brings out the change in the mode of ICT mechanism with hypsochromic shift in both absorption and fluorescence spectroscopy. Theoretical calculations also support the mechanism. The spectral change depicts excellent selectivity towards cyanide ion along with rapid interaction time (within 20 s). Limit of detection was found in the order of $10^{-8}$ (M). Also, the real time application of the chemosensor was successfully utilized by detection of cyanide in real water samples and TLC plate experiment. Additionally, the live cell imaging experiment demonstrates the capability of sensing intracellular cyanide.

# 6.6. Experimental

## 6.6.1. Materials and instrumentations

All the reagents and organic chemicals used in the synthesis of PBIA including o-phenylenediamine, ethyl cyanoacetate and triphenyl amine were purchased from Sigma Aldrich and used without further purification, while the other solvents used were available in the commercial sources. DMSO and other solvents used for spectroscopic studies were of HPLC grade. For $^{1}H$ and $^{13}C$ NMR spectra a Bruker (AC) 400 MHz instrument was used. DMSO-$d_6$ was used as solvent using TMS as an internal standard of ~ 0.05 M concentration. The chemical shifts were reported in δ units of parts per million (ppm). HRMS mass spectra were recorded on Waters (Xevo G2 Q-TOF) mass spectrometer. For elemental analysis a 2400 Series-II CHN analyzer, Perkin Elmer, USA was used. The infrared spectrum of the probe was recorded using the RX-1 PerkinElmer spectrophotometer by preparing the KBr pellet of the sample. We used a Shimadzu UV-1900i spectrophotometer to measure UV-vis spectra. The emission property was measured using Shimadzu RF-6000 fluorescence spectrophotometer at room temperature (298K). Luminescence lifetime measurements were carried out using time-correlated single photon counting set up from Horiba Jobin-Yvon. Then, the fluorescence decay data were placed on a Hamamatsu MCP photomultiplier (R3809) and analysed using the EZ time software. Merck 60 F254 plates of 0.25 mm thickness were used for thin layer chromatography (TLC) and dipstick experiments. For column chromatographic technique we used silica gel of mess 200-300, where petroleum benzene and ethyl acetate were used as solvents.

### 6.6.2. General Method for UV-Vis and Fluorescence Titration

For UV-vis study, stock solution of the probe PBIA (20 μM) was prepared in DMSO. Deionized water was used to make all the solutions of guest anions using their sodium salts (40μM) and for the solution of cyanide ion, tetra butyl ammonium cyanide salt was used. Spectra were recorded using solutions containing probe PBIA and increasing concentration of guest anions. All the solutions were prepared separately. Similarly, for fluorescence titrations also stock solutions were prepared using similar procedures and then the spectra were recorded by means of fluorescence method. The excitation wavelength used was 435 nm (where the excitation slit was 10.0 and the emission slit was 10.0). The detection limit was calculated using the fluorescence titration data.

### 6.6.3. pH solution preparation method

For pH study, we also prepared stock solution of the probe, PBIA (10 μM) in DMSO (at 25°C). The pH of the solution was adjusted by using aqueous solution of 1M HCl and 1M NaOH. For the titration of probe Solutions, different concentration of acids and bases were prepared separately while adjusting pH and the spectra of these solutions were recorded through fluorescence technique. Similarly, we also executed titration of probe (PBIA) in the presence of $CN^-$ while recording the pH.

### 6.6.4. Synthesis of 4,4'-(phenylazanediyl) dibenzaldehyde (1)

This was prepared using the previously reported procedure.[63]

### 6.6.5. Synthesis of 2-cyanomethylbenzimidazole (2)

This was previously synthesized by our group.[64]

### 6.6.6. Synthesis of (2E,2'E)-3,3'-((phenylazanediyl)bis(4,1-phenylene)) bis(2-(1H-benzo[d]imidazol-2-yl) acrylonitrile) (PBIA)

At first 4,4'-(phenylazanediyl) dibenzaldehyde (0.30gm,1mmol) was taken in a round bottom flask and dissolved in ethanolic solution. Then to the ethanolic solution, 2-cyanomethylbenzimidazole (0.31 gm,2 mmol) was added and the whole mixture was refluxed with a catalytic amount of piperidine under inert atmosphere. After 3 hours, we observed a deep

brown colour precipitate within the reaction mixture. Then the reaction mixture was allowed to cool at room temperature. The brown precipitation was collected through filtration, washed with EtOH and dried. Then column chromatography was performed to further purify the product. Yield was calculated to be, 0.452 g, 78%.

**$^{1}$H NMR (400 MHz, DMSO-$d_6$):** δ(ppm) 12.97 (s, 2H), 8.26 (s, 2H), 7.99 (d, 4H, J=8.76 Hz), 7.50 (t, 2H, J=7.8Hz), 7.32 (t, 1H, J=7.6 Hz), 7.28-7.21 (m, 14H).

**$^{13}$C NMR (100MHz, DMSO-$d_6$):** δ(ppm) 149.5, 148.4, 145.6, 144.8, 131.9, 130.8, 127.6, 127.5, 127.3, 126.6, 123.9, 123.2, 122.2, 117.1, 99.9.

**Anal. Calc. for $C_{38}H_{25}N_7$ (PBIA):** Calc. (%) C 78.74, H 4.35, N 16.91. Found (%), C 78.58, H 4.46, N 16.96.

**IR (cm$^{-1}$, KBr):** υ(C=N) 1581.32, υ(C≡N) 2239.03, υ(C-H) 3048.10, υ(N-H) 3244.28.

**HRMS:** calculated for $C_{38}H_{25}N_7$ $[M+H]^+$, (m/z) = 580.2249; found = 580.1038.

**2D NMR study:**

To validate the structural analysis further, we have done $^{1}$H-$^{1}$H 2D COSY NMR. Based on $^{1}$H-$^{1}$H 2D COSY correlation it was observed that the proton peak at 8.26 ppm correlates with the proton peak at 7.99 ppm, which proved that the vinylic proton (a) is correlating with the equivalent phenylic protons (b). Other correlations are also mentioned in the 2D homoneucleur correlation technique, which belongs to other phenylic aromatic proton interactions. (Fig. A6.3, appendix).

Again, to further confirm the peak position of vinylic proton, we have performed $^{1}$H-$^{13}$C 2D HSQC NMR. We observed that, among the four highly deshielded carbon atoms (position 1, 7, 10, 17), only the carbon atom (7) at 144.8 ppm correlates with the vinylic proton, signal at 8.26 ppm (Fig. A6.4, Appendix). Other correlations in $^{1}$H-$^{13}$C 2D HSQC NMR are associated with the carbon and protons of phenylic rings. So, this 2D heteroneucleur correlation technique HSQC also resonates with the fact that 8.26 ppm peak belongs to vinylic proton.

## 6.6.7. Theoretical study

Gaussian 09 program packagewere used for theoretical interpretation.[71] The geometry for PBIA and PBIA-CN were optimized using Density functional theory (DFT) at the B3LYP level for the compounds[72,73] where 6-31+G(d) was assigned as basis set.[74] The vibrational frequency calculations were performed to assure that the optimized geometries stand for the local minima with only positive eigen values. Vertical electronic excitations which were based on B3LYP

optimized geometries were computed using the time-dependent density functional theory (TDDFT) formalism in DMSO using conductor-like polarizable continuum model (CPCM).[75-80]

## 6.6.8. Job's plot by absorbance method

For Job's plot experiment, a series of solutions containing probe PBIA and $CN^-$ were prepared in such a manner that the sum of the total anion and PBIA volume remained constant in DMSO medium. Then Job's plots was drawn by plotting $A_{455}$ versus $X_{CN^-}$ ($A_{455}$ = absorption spectrum at 455 nm for $CN^-$ ion respectively and $X_{CN^-}$ is the mole fraction of the $CN^-$ solution).

## 6.6.9. Determination of fluorescence Quantum Yields (Φ) of PBIA and its complex with $CN^-$

The luminescence quantum yield was determined using coumarin-153 as reference dye. The compounds and the reference dye were excited at the similar wavelength and the emission spectra were then studied. The area of the emission spectrum was integrated and the quantum yield is determind according to the following equation:

$$\phi_S/\phi_R = [A_S / A_R] \times [(Abs)_R / (Abs)_S] \times [n_S^2/n_R^2]$$

Here, $\phi_S$ and $\phi_R$ are the luminescence quantum yields of the sample and reference dye, respectively. $A_S$ and $A_R$ are the area under the emission spectra of the sample and the reference respectively, $(Abs)_S$ and $(Abs)_R$ are the respective optical densities of the sample and the reference solution at the wavelength of excitation, and $n_S$ and $n_R$stand for the values of refractive index for the respective solvent used for the sample and reference. The quantum yields of PBIA and PBIA-CN are determined using the above-mentioned equation and the values are found to be 0.148 and 0.074 respectively.

## 6.6.10. Application of PBIA in real water sample analysis

The good selectivity and sensitivity towards cyanide makes our probe appropriate for real water sample analysis. Hence, to validate the reliability of PBIA to detect cyanide in real water samples, we collected water from Jadavpur University campus lake, tap and drinking water supplied to us. At first water samples were filtered through Whatman no. 1 filter paper to remove the suspended particles. Then blank experiment was conducted to check if there were any dissolved $CN^-$ ions in water samples, but the results were negative as there were no change in probes colour under UV light.

Here our purpose was not to ascertain amount of $CN^-$ in water, but to utilize the real water samples instead of deionized water to make $CN^-$ solutions and conduct titration studies. Hence, cyanide salt was spiked in the stated water samples separately to prepare known concentration of cyanide solutions. Then fluorescence spectral studies were carried out using PBIA with addition of cyanide ion for quantitative measurement of $CN^-$ ion in real water samples (Fig. A6.12-14, Appendix). We observed almost similar spectroscopic response with our previous controlled titration experiment (Fig 6.2). Then standard calibration curves were constructed for determination of $CN^-$ ion, which exhibited good linear relationship between the fluorescence of cyanide treated PBIA solution with cyanide concentration. The percentage of recovery were measured which was above 96% (Table 6.1).

### 6.6.11. Live cell imaging studies

### 6.6.11.1. Cell culture and treatment

A human breast cancer cell line (MDA-MB-231) was obtained from National Centre for Cell Science, Pune, India, and maintained in DMEM High glucose (Gibco, Life Technologies) supplemented with 10% Fetal Bovine Serum (FBS) (Gibco, Life Technologies, USA) and 1% Penicillin Streptomycin. All cell lines were stored at 37 °C in a humidified $C0_2$ incubator. The cells were given at least two passages before commencing the experiments

### 6.6.11.2. Live cell imaging study

MDA MB 231 cells were seeded and left to adhere overnight on a six well plate containing acid washed 22×22 mm glass cover slips positioned at the bottom of each well. In addition to a control, 10 µM of the chemosensor PBIA along with 15 µM of cyanide were added to each well containing cells. The cells were then fixed with methanol and rinsed with 0.5% phosphate buffer saline tween (PBST) twice, followed by 1 × PBS three times. The cover slips were then put on a glass slide with glycerol and viewed at 40x magnification using a fluorescence microscope (Olympus).

## 6.7. Notes and references

1. R. Sakai, T. Satoh and T. Kakuchi, *Polym. Rev.*, 2017, **57**, 159.
2. Y. Liu, Y. Hu, S. Lee, D. Lee and J. Yoon, *Bull. Korean Chem. Soc.*, 2016, **37**, 1661.
3. P. Molina, F. Zapata and A. Caballero, *Chem. Rev.*, 2017, **117**, 9907.

4. S. H. Park, N. Kwon, J. H. Lee, J. Yoon and I. Shin, *Chem. Soc. Rev.*, 2020, **49**, 143.
5. A. Alvillo-Rivera, S. Garrido-Hoyos, G. Buitron, P. Thangarasu-SarasvathI and G. Rosano-Ortega, *J. Mater. Res. Technol.*, 2021, **12**, 1418.
6. K. Grossmann, *Pest Manag. Sci.*, 2010, **66** ,113.
7. G. C. Miller and C. A. Pritsos, Cyanide Social, Industrial and Economic Aspects, in Proceedings of the TMS Annual Meeting, 2001, 73.
8. D. W. Boening and C. M. Chew, *Water, Air, Soil Pollut.*, 1999, **109**, 67.
9. Z.C. Xu, X.Q. Chen, H.N. Kim and J. Yoon, *Chem. Soc. Rev.*, 2010,**39**, 127.
10. J. Ma and P.K. Dasgupta, *Anal. Chim. Acta*, 2010, **673**, 117.
11. T. Z. Sadyrbaeva, *Sep. Purif. Technol.*, 2012, **86**, 262.
12. C. Harper and S. Goldhaber, Toxicological Profile for Cyanide, Department of Health and Human Services Agency for Toxic Substances and Disease Registry, Atlanta, 1997.
13. Guidelines for Drinking-Water Quality, World Health Organization, Geneva, 1996.
14. L. Nelson, *J. Emerg. Nurs.*, 2006, **32**, S8.
15. J. Y. Noh, I. H. Hwang, H. Kim, E. J. Song, K. B. Kim and C. Kim, *Bull. Korean Chem. Soc*., 2013, **34**, 1985.
16. B. Vennesland, E. E. Comm, C. J. Knownles, J. Westly and F. Wissing, Cyanide in Biology, Academic Press, London, 1981.
17. C. Baird and M. Cann, Environmental Chemistry, Freeman, New York, 2005.
18. S. Mardanya, S. Karmakar, M. Bar and S. Baitalik, *Dalton Trans.*, 2015, **44**, 21053.
19. Z. Q. Hu, X. M. Wang, Y. C. Feng, L. Ding, M. Li and C. S. Lin, *Chem. Commun.*, 2011, **47**, 1622.
20. A. Balamurugan and H. Lee, *Macromolecules*, 2015, **48**, 3934.
21. J. B. Chae, H. J. Jang and C. Kim, *Photochem. Photobiol. Sci.*, 2017, **16**, 1812.
22. H. J. Jang, H. M. Ahn, M. S. Kim and C. Kim, *Tetrahedron*, 2017, **73**, 6624.
23. I. G. Casella and M. Gatta, *Electroanalysis*, 2001, **13**, 549.
24. A. Kumar, E. Jeong, N. Youngwoo and P.S. Chae, *Methods*, 2024, **222**, 57-80.
25. C. Yin, F. Huo, M. Xu, C. L. Barnes and T. E. Glass, *Sens. Actuators B: Chem.*, 2017, **252**, 592.
26. W. J. Qu, H.H. Yang, J. P. Hu, P. Qin, X. X. Zhao, Q. Lin, H. Yao, Y. M. Zhang and T. B. Wei, *Dyes Pigm.*, 2021, **186**, 108949.
27. T. B. Wei, J. D. Ding, J. F. Chen, B. B. Han, X. M. Jiang, H. Yao, Y. M. Zhang and Q. Lin, *New J. Chem.*, 2018, **42**, 1271.
28. P. R. Lakshmi, P. S. Kumar and K. P. Elango, *Spectrochim. Acta-A: Mol. Biomol. Spectrosc.*, 2020, **229**, 117974.
29. B. Aydıner, Ö. S¸ ahin, D. Çakmaz, G. Kaplan, K. Kaya, Ü. Ö. Özdemir, N. Seferoğlu and Z. Seferoğlu, *New J. Chem.*, 2020, **44**, 19155.
30. N. Assadollahnejad, M. Kargar, H. R. Darabi, N. Abouali, S. Jamshidi, A. Sharifi, K. Aghapoor and H. Sayahi, *New J. Chem.*, 2019, **43**, 13001.
31. S. Paul, K. Debsharma, S. Dey, S. Halder, K. Jana and C. Sinha, *Mater. Adv.*, 2023, **4**, 3874.

32. J. L. Sessler and D. G. Cho, *Org. Lett.*, 2008, **10**, 73.
33. Y. Kim, H. Zhao and F. P. Gabbaï, *Angew.Chem., Int.Ed*., 2009, **48**, 4957.
34. A. Maji, A.Biswas,A. Das, S. Gharami, K. Aich and T. K. Mondal, *New. J. Chem.*, 2023, **47**, 11557.
35. K. Xiong, F. Huo, C. Yin, Y. Yang, J. Chao, Y. Zhang and M. Xu, *Sens. Actuators B: Chem.*, 2015, **220**, 822.
36. S. Goswami, S. Paul and A. Manna, *Tetrahedron Lett.*, 2014, **55**, 3946.
37. S. H. Park, N. Kwon, J. H. Lee, J. Yoon, I. Shin, *Chem. Soc. Rev.*, 2020, **49**, 143.
38. X. Lv, J. Liu, Y. Liu, Y. Zhao, M. Chen, P. Wang and W. Guo, *Org. Biomol. Chem.* 2011, **9**, 4954.
39. N. Gimeno, X. Li, J. R. Durrant and R. Vilar, *Chem. Eur. J*., 2008, **14**, 3006.
40. A. C. Sedgwick, L. Wu, H. H. Han, S. D. Bull, X. P. He, T. D. James, J. L. Sessler, B. Z. Tang, H. Tian and J. Yoon, *Chem.Soc. Rev.*, 2018, **47**, 8842.
41. W. J. Qu, W. T. Li, H. L. Zhang, T. B. Wei, Q. Lin, H. Yao and Y. M. Zhang, *Sens. Actuators B: Chem.*, 2017, **241**, 430.
42. T. D. Ashton, K. A. Jolliffe and F. M. Pfeffer, *Chem. Soc. Rev.*, 2015, **44**, 4547.
43. A. Liu, R. Ji and S. L. Shen, *New J. Chem.*, 2017, **41**, 10096.
44. Y. Ge, P. Wei and T. Wang, *Sens. Actuators B Chem.*, 2018, **254**, 314.
45. X. Chen, L. Wang, X. Yang and L. Tang, *Sens. Actuators B Chem.*, 2017, **241**, 1043.
46. W. C. Lin and J. W. Hu, *Anal. Chim. Acta*, 2015, **893**, 91.
47. R. Manivannan and Y. A. Son, *Dyes and Pigments*, 2023, **210**, 110941.
48. D. Jothi, S. Munusamy, S. Enbanathan and S.K. Iyer, *RSC advances*, 2022, **12**, 8570.
49. S. D. Padghan, L. C. Wang, W. C. Lin, J. W. Hu, W. C. Liu and K. Y. Chen, *ACS omega*, 2021, **6**, 5287.
50. S. D. Padghan, C. Y. Wang, W. C. Liu, S. S. Sun, K. M. Liu and K. Y. Chen, *Dyes and Pigments*, 2020, **183**, 108724.
51. D. Tamilarasan, R. Suhasini, V. Thiagarajan and R. Balamurugan, *Eur. J. Org. Chem.*, 2020, **2020**, 993.
52. L. Hou, F. Li, J. Guo, X. Zhang, X. Kong, X.T. Cui, C. Dong, Y. Wang and S. Shuang, *J. Mater. Chem. B.*, 2019, **7**, 4620.
53. A. Ozdemir and S. Erdemir, *J. Photochem. Photobiol. A Chem.* ,2020, **390**, 112328.
54. A. Tigreros, J. C. Castillo and J. Portilla, *Talanta*, 2020, **215**, 120905.
55. T. S. Reddy and M. S. Choi, *J. Photochem. Photobiol. A Chem.*, 2018, **351,** 108.
56. Y. Zhang, D. Yu and G. Feng, *RSC Adv.*, 2014, **4**, 14752.
57. Y. Shiraishi, M. Nakamura, K. Yamamoto and T. Hirai, Rapid selective, and sensitive fluorometric detection of cyanide anions in aqueous media by cyanine dyes with indolium-coumarin linkages, *Chem. Commun.*, 2014, **78** , 11583.
58. A. Dvivedi, P. Rajakannu and M. Ravikanth, *Dalton Trans.*, 2015, **44**, 4054.
59. M. K. Bera, C. Chakraborty, P. K. Singh, C. Sahu, K. Sen, S. Maji, A. K. Das and S. Malik, *J. Mater. Chem. B*, 2014, **2**, 4733.
60. S. Pramanik, V. Bhalla and M. Kumar, *ACS Appl. Mater.* I*nterfaces*, 2014, **6**, 5930.
61. Y. Sun, G. Wang and W. Guo, *Tetrahedron Lett.*, 2009, **65**, 3480.

62. Y. Kim, H. Zhao and F. P. Gabbaï, *Angew. Chem. Int. Ed.*, 2009, **48**, 4957.
63. Z. Yu, Z. Zheng, M. Yang, L. Wang, Y. Tian, J. Wu, H. Zhou, H. Xu and Z. Wu, *J. Mater. Chem. C*, 2013, **1**, 7026.
64. A. Biswas, A. Maji, S. Gharami and T. K. Mondal, *New J. Chem.*, 2023, **47**, 14154.
65. R. Quevedo, *J. Mol. Struct.*, 2020, **1207**, 127777.
66. S. Cheng, A. Li, X. Pan, H. Wang, C. Zhang, J. Li and X. Qi, *Anal. Bioanal. Chem.*, 2021, **413**, 4441.
67. X. Pan, S. Cheng, C. Zhang and X. Qi, *Anal. Bioanal. Chem.*, 2020, **412**, 6959.
68. R. Bhaskar and S. Sarveswari, *Inorg. Chem. Commun.*, 2019, **102**, 83.
69. X. Wu, J. Chen and J. X. Zhao, *Analyst*, 2013, **138**, 5281.
70. S. Qu, C. Zheng, G. Liao, C. Fan, G. Liu and S. Pu, *RSC Adv.*, 2017, **7**, 9833.
71. M. J. Frisch, G. W. Trucks, H. B. Schlegel, G. E. Scuseria, M. A. Robb, J. R. Cheeseman, G. Scalmani, V. Barone, B. Mennucci, G. A. Petersson, H. Nakatsuji, M. Caricato, X. Li, H. P. Hratchian, A. F. Izmaylov, J. Bloino, G. Zheng, J. L. Sonnenberg, M. Hada, M. Ehara, K. Toyota, R. Fukuda, J. Hasegawa, M. Ishida, T. Nakajima, Y. Honda, O. Kitao, H. Nakai, T. Vreven, J. A. Montgomery, Jr., J. E. Peralta, F. Ogliaro, M. Bearpark, J. J. Heyd, E. Brothers, K. N. Kudin, V. N. Staroverov, R. Kobayashi, J. Normand, K.Raghavachari, A. Rendell, J. C. Burant, S. S. Iyengar, J. Tomasi, M. Cossi, N. Rega, J. M. Millam, M. Klene, J. E. Knox, J. B. Cross, V. Bakken, C. Adamo, J. Jaramillo, R. Gomperts, R. E. Stratmann, O. Yazyev, A. J. Austin, R. Cammi, C. Pomelli, J. W. Ochterski, R. L. Martin, K. Morokuma, V. G. Zakrzewski, G. A. Voth, P. Salvador, J. J. Dannenberg, S. Dapprich, A. D. Daniels, O¨. Farkas, J. B. Foresman, J. V. Ortiz, J. Cioslowski and D. J. Fox, *Gaussian 09, Revision D.01*, Gaussian, Inc., Wallingford CT, 2009.
72. A. D. Becke, *J. Chem. Phys.*, 1993, **98**, 5648.
73. C. Lee, W. Yang and R. G. Parr, *Phys. Rev. B: Condens. Matter Mater. Phys.*, 1988, **37**, 785.
74. F. Furche and R. Ahlrichs, *J. Chem. Phys.*, 2002, **117**, 7433.
75. R. Bauernschmitt and R. Ahlrichs, *Chem. Phys. Lett.*, 1996, **256**, 454.
76. R. E. Stratmann, G. E. Scuseria and M. J. Frisch, *J. Chem. Phys.*, 1998, **109**, 8218.
77. M. E. Casida, C. Jamorski, K. C. Casida and D. R. Salahub, *J. Chem. Phys.*, 1998, **108**, 4439.
78. M. Cossi and V. Barone, *J. Chem. Phys.*, 2001, **115**, 4708.
79. V. Barone and M. Cossi, *J. Phys. Chem. A*, 1998, **102**, 1995.
80. M. Cossi, N. Rega, G. Scalmani and V. Barone, *J. Comput. Chem.*, 2003, **24**, 669.

# APPENDIX

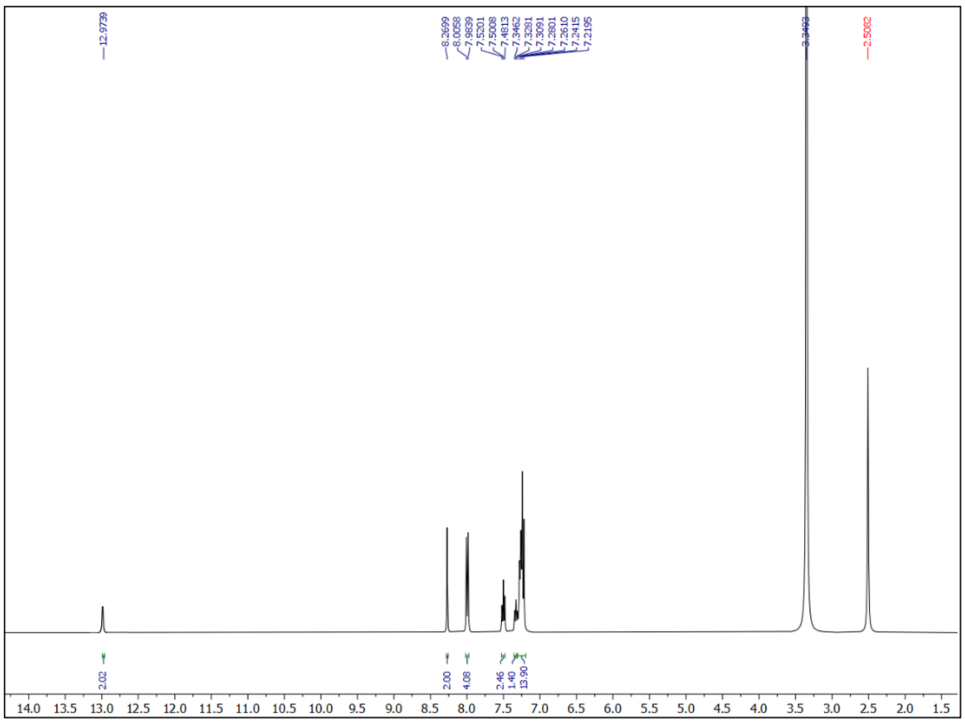


**Fig. A6.1:** $^{1}$H NMR (400 MHz) spectrum of the probe (PBIA) in DMSO-$d_6$

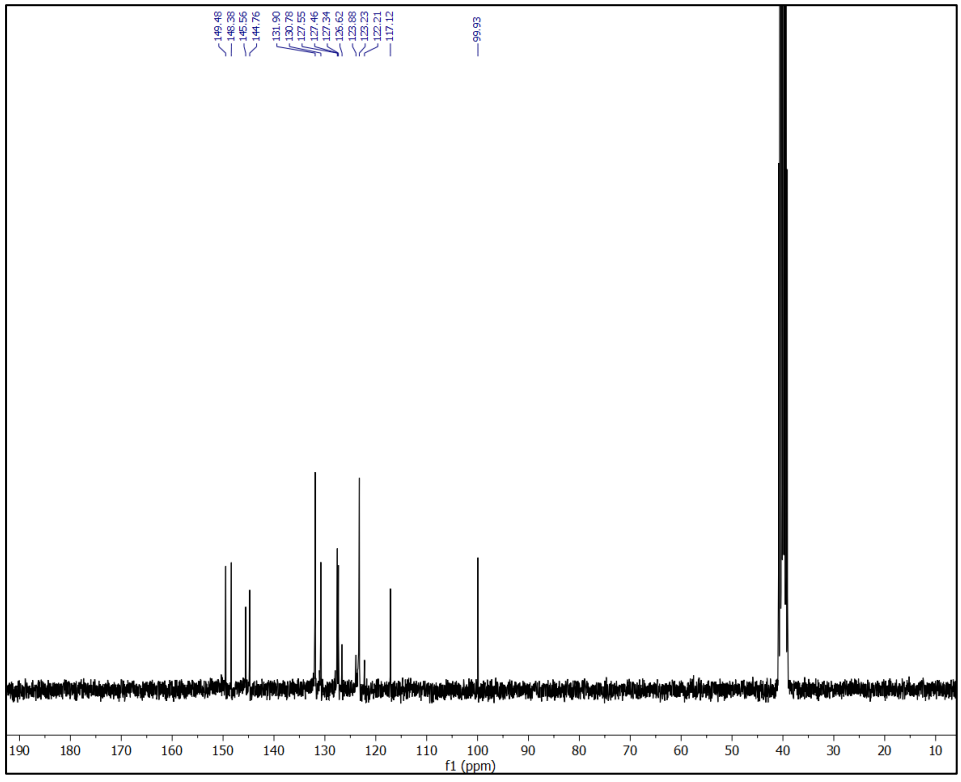


**Fig. A6.2:**$^{13}$C NMR (100 MHz) spectrum of the probe (PBIA) in DMSO-$d_6$

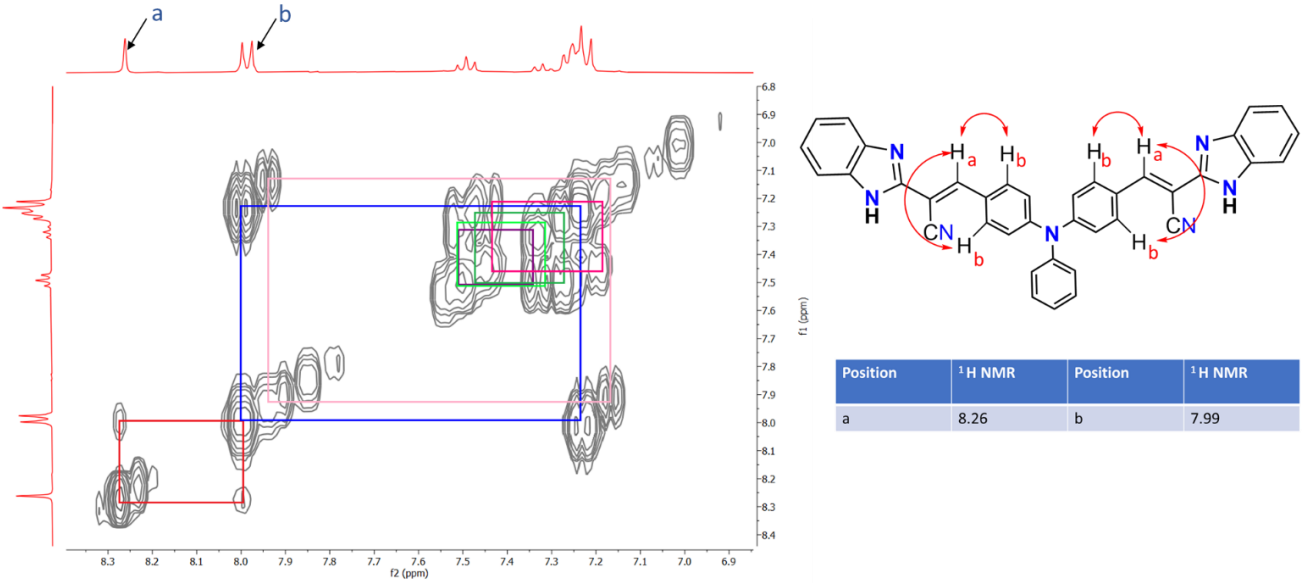


| Position | $^{1}$H NMR | Position | $^{1}$H NMR |
|---|---|---|---|
| a | 8.26 | b | 7.99 |

**Fig. A6.3:** $^{1}$H-$^{1}$H-2D COSY NMR spectrum of ligand (PBIA) in DMSO -$d_6$

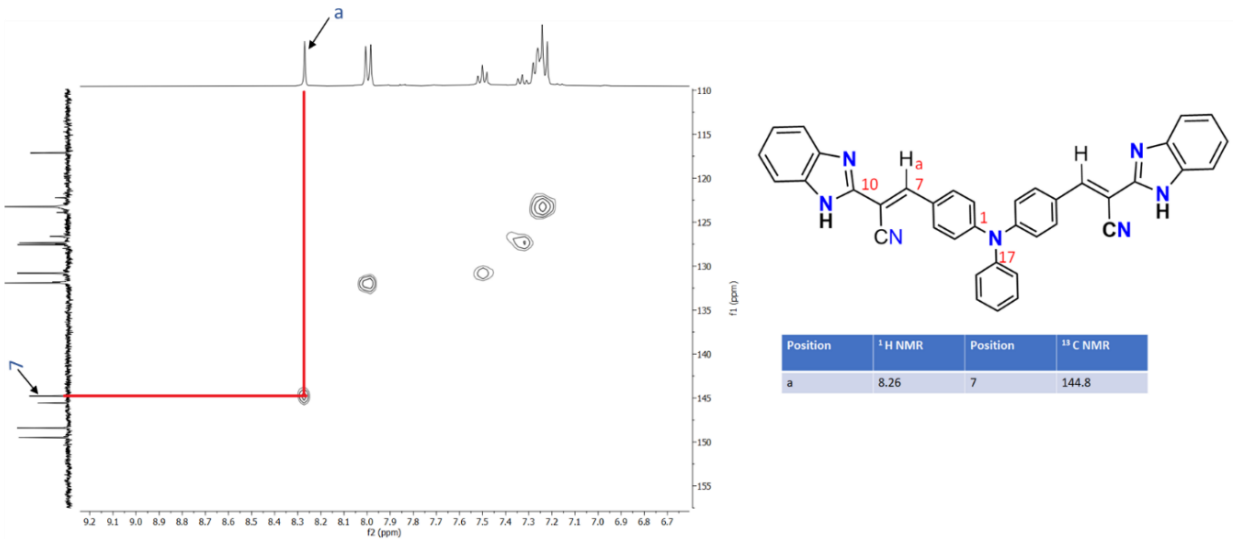


| Position | $^{1}$H NMR | Position | $^{13}$C NMR |
|---|---|---|---|
| a | 8.26 | 7 | 144.8 |

**Fig. A6.4:** $^{1}$H-$^{13}$C-2D HSQC NMR spectrum of ligand (PBIA) in DMSO-$d_6$

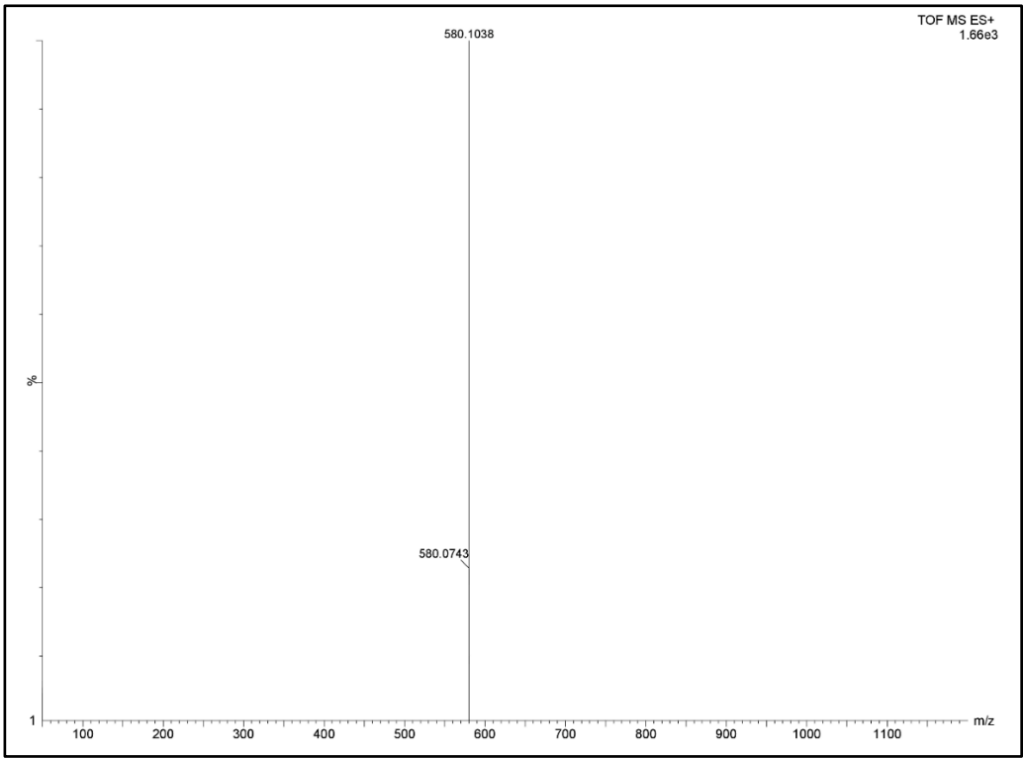


**Fig. A6.5:** HRMS of the probe (PBIA).

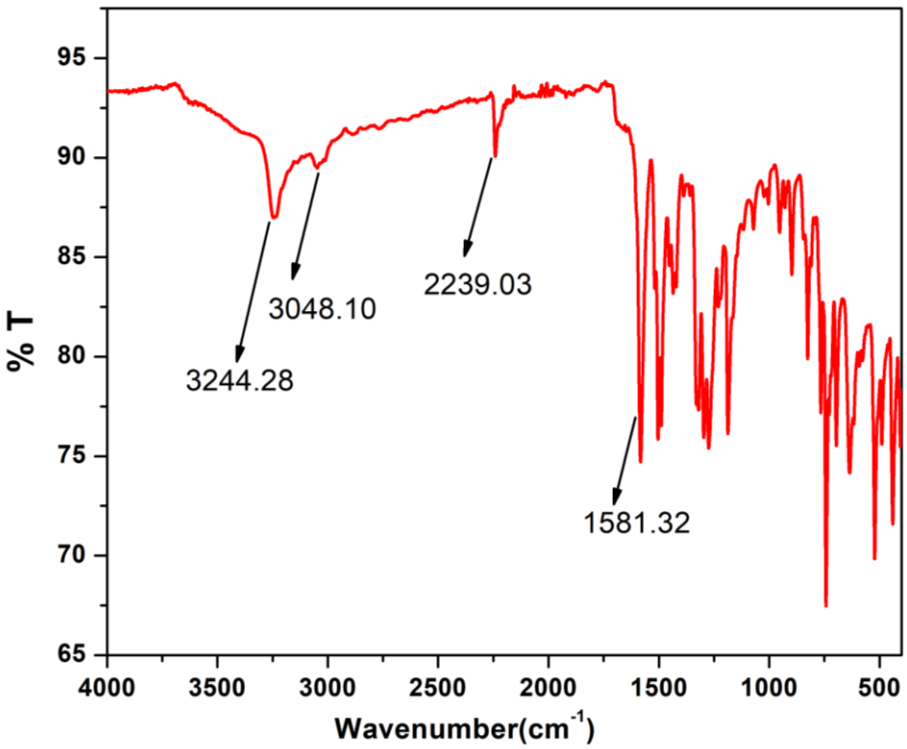


**Fig. A6.6:** IR Spectrum of PBIA.

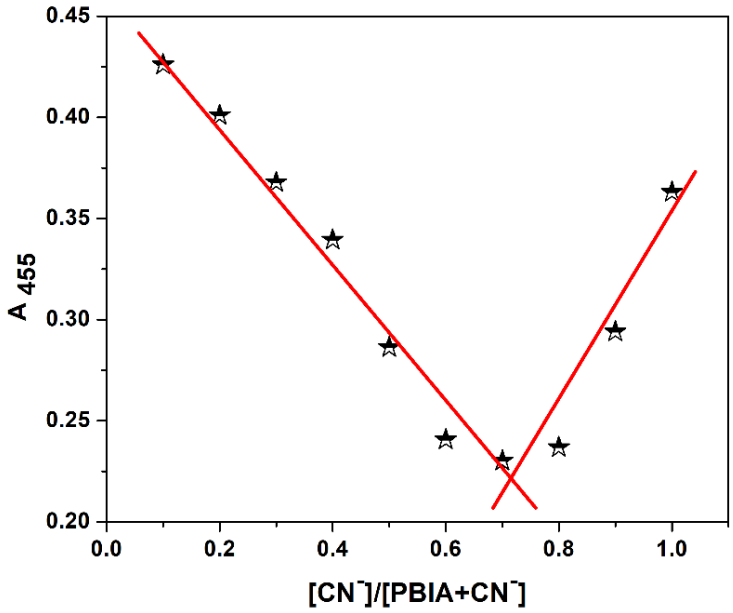


**Fig. A6.7:** Job's plot diagram of PBIAfor $CN^-$.

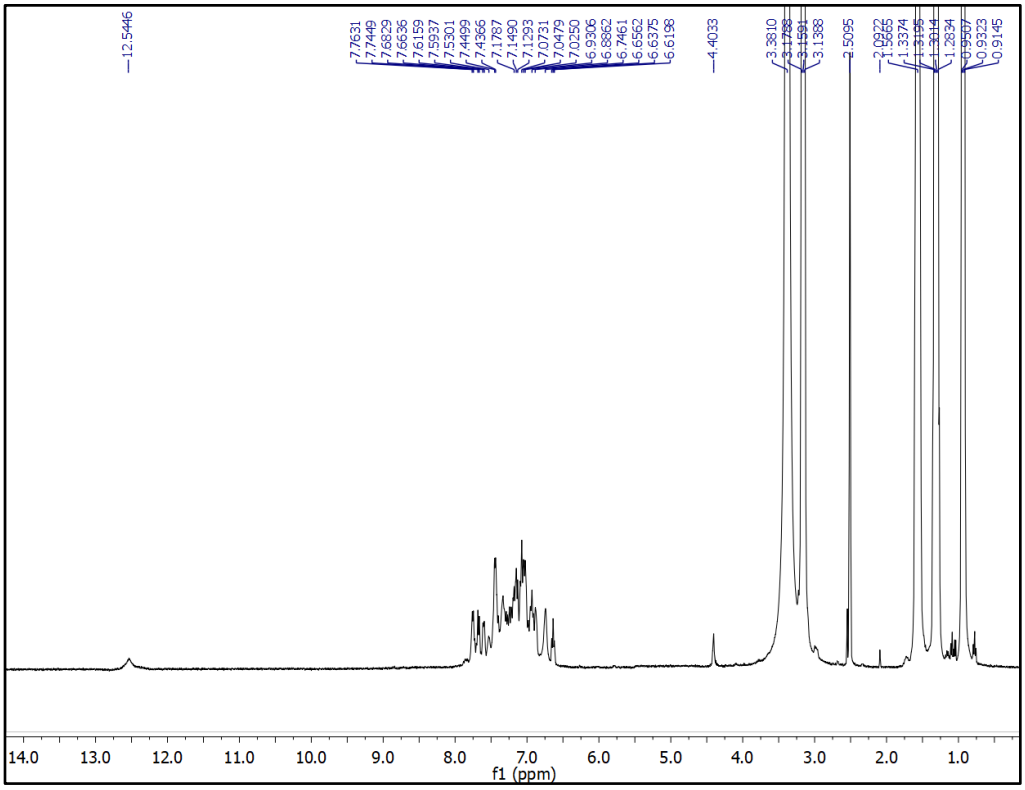


**Fig. A6.8:** $^1$H NMR (400 MHz) spectra of the PBIA-CN adduct in DMSO-$d_6$.

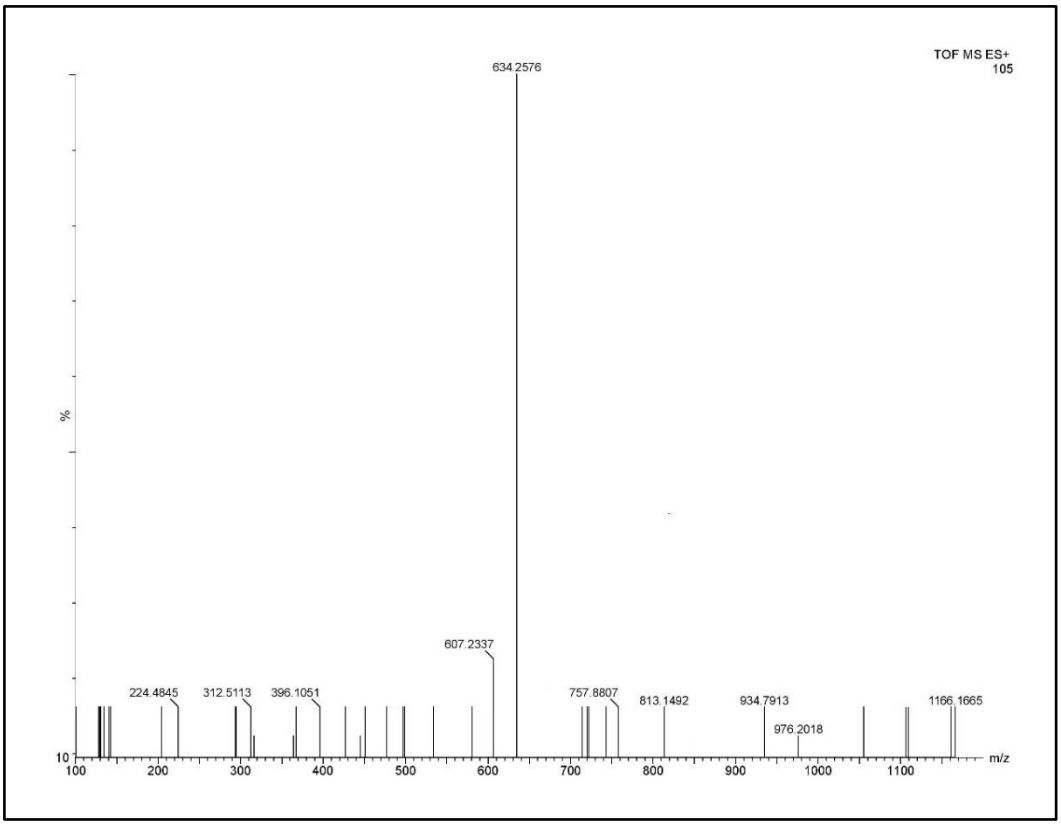


**Fig. A6.9:** HRMS of the PBIA-CN adduct.

**Table A6.1:** Fluorescence lifetime data

| DMSO(Solvent) | Quantum yield(φ) | τ(ns) | $K_r(10^8 \times S^{-1})$ | $K_{nr}(10^8 \times S^{-1})$ |
|---|---|---|---|---|
| **PBIA** | 0.148 | 0.50 | 2.95 | 17.02 |
| **PBIA-CN$^-$** | 0.074 | 1.99 | 0.37 | 4.63 |

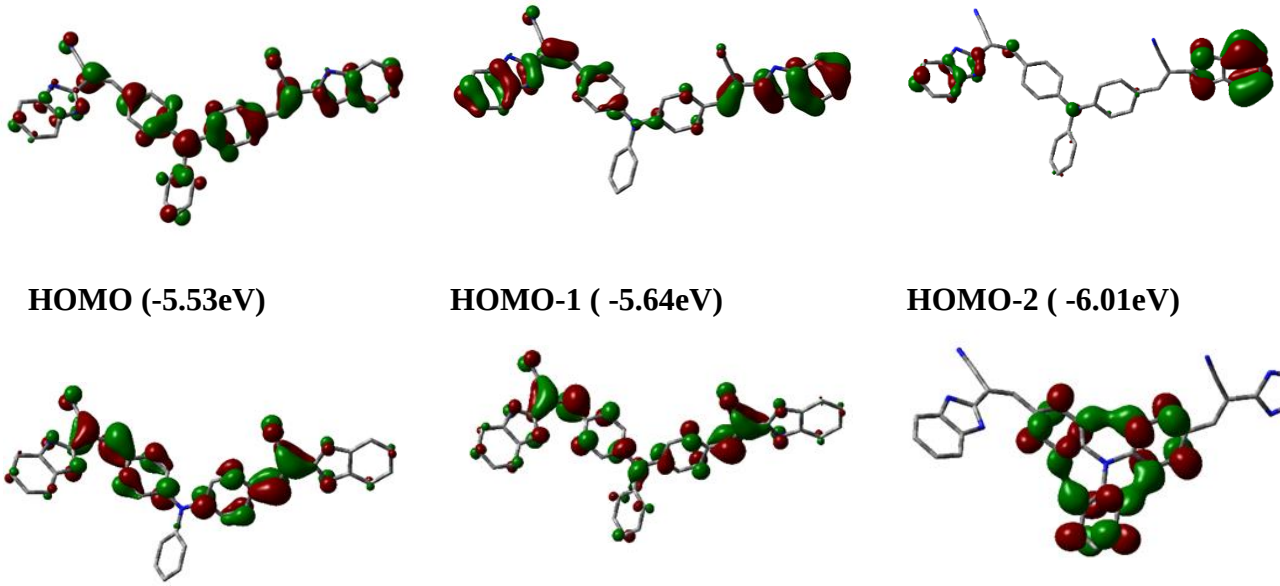

**HOMO (-5.53eV)** **HOMO-1 ( -5.64eV)** **HOMO-2 ( -6.01eV)**

**LUMO (-2.31eV)** **LUMO+1 (-1.99 eV)** **LUMO+2 (-1.64 eV)**

**Fig. A6.10:** Contour plots of some selected molecular orbitals of PBIA

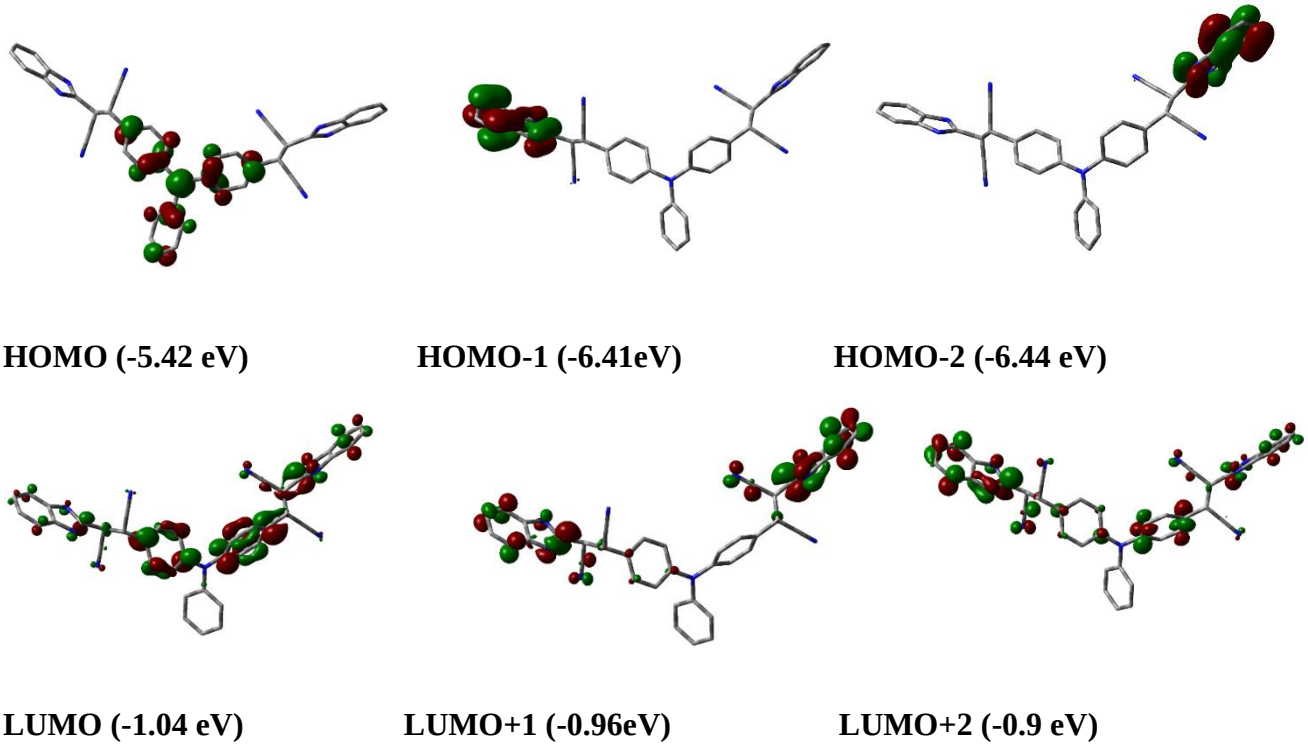

**HOMO (-5.42 eV)** **HOMO-1 (-6.41eV)** **HOMO-2 (-6.44 eV)**

**LUMO (-1.04 eV)** **LUMO+1 (-0.96eV)** **LUMO+2 (-0.9 eV)**

**Fig. A6.11:** Contour plots of some selected molecular orbitals of PBIA-$CN^-$

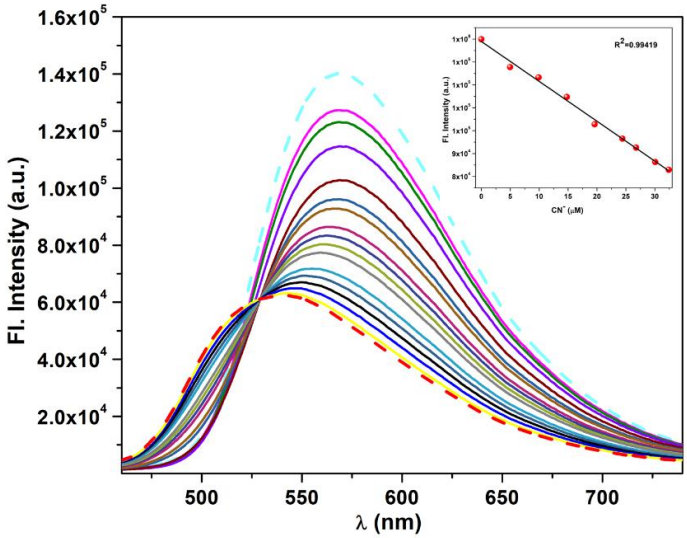


**Fig. A6.12:** Fluorescence spectral titration of the probe solution PBIA (20 μM) with the addition of $CN^-$ in drinking water. Inset:linear fitting plot of fluorescence of probe solution PBIA at 570 nm.

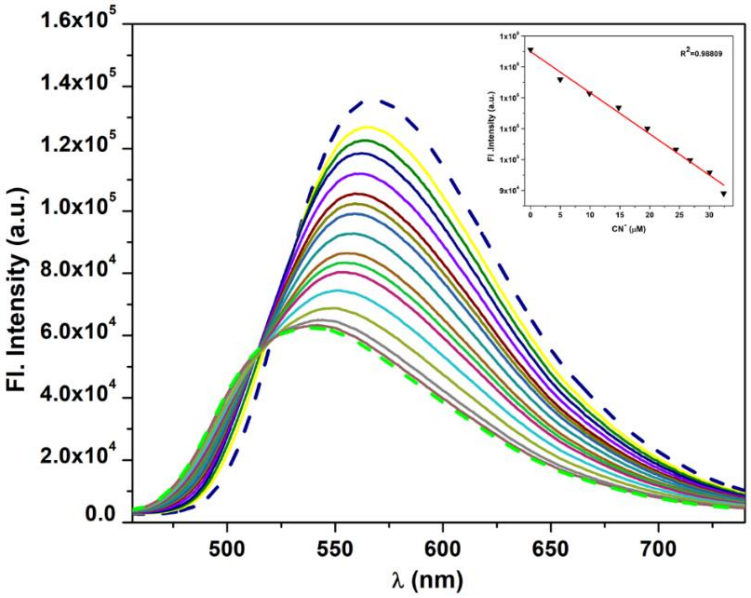


**Fig. A6.13:** Fluorescence spectral titration of the probe solution PBIA (20 μM) with the addition of $CN^-$ in tap water. Inset: linear fitting plot of fluorescence of probe solution PBIA at 570 nm.

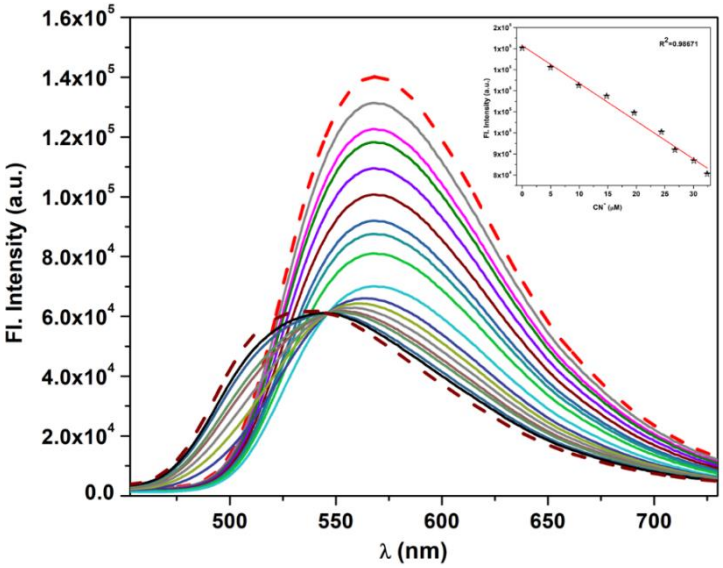


**Fig. A6.14:** Fluorescence spectral titration of the probe solution PBIA (20 μM) with the addition of $CN^-$ in lake water. Inset: linear fitting plot of fluorescence of probe solution PBIA at 570 nm.

**Table A6.2:** Vertical electronic transitions of PBIA and PBIA-$CN^-$ calculated by TDDFT/CPCM method

| Compd. | λ (nm) | E (eV) | Osc. Strength (f) | Key excitations |
|---|---|---|---|---|
| **PBIA** | 526.10 | 2.3567 | 1.6875 | (99 %)HOMO→LUMO |
| | 439.11 | 2.8235 | 0.2083 | (97 %)HOMO→LUMO+1 |
| | 395.92 | 3.1315 | 0.1137 | (96 %)HOMO-1→LUMO |
| | 357.60 | 3.4671 | 0.2311 | (89 %)HOMO-1→LUMO+1 |
| | 355.80 | 3.4846 | 0.1809 | (72%)HOMO-4→LUMO |
| | 289.05 | 4.2893 | 0.1095 | (76 %)HOMO→LUMO+3 |
| **PBIA-$CN^-$** | 343.60 | 3.6083 | 0.6200 | (91%)HOMO → LUMO |
| | 327.03 | 3.7913 | 0.1126 | (69%)HOMO→LUMO+1 |
| | 314.21 | 3.9459 | 0.1191 | (41%)HOMO→ LUMO+3 |
| | 303.82 | 4.0808 | 0.1315 | (52%)HOMO → LUMO+2 |
| | 301.94 | 4.1063 | 0.1047 | (42%)HOMO → LUMO+4 |

**Table A6.3:** Sensor PBIA towards $CN^-$ compared to others previously reported receptors

| Probe | Type | Solvent System | Detection limit | Reference |
|---|---|---|---|---|
| 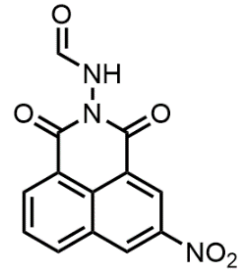 | $CN^-/Fe^{3+}$ and $H_2S$ Turn-on and UV-absorption | 5% aqueous DMSO | 17.5 nM, 8.69 mM and 8.1 mM | *RSC Adv.*, 2020, **10**, 8751. |
| 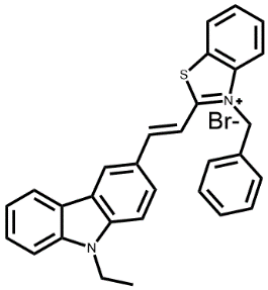 | $CN^-$, Ratiometric | DMSO/$H_2O$ (3: 2, v/v, pH = 7.4) | $3.39\times10^{-7}$ | *J. Mater. Chem. B*, 2019,**7**, 4620. |
| 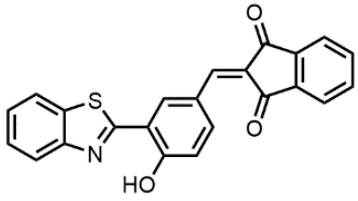 | $CN^-$, Ratiometric | DMSO/$H_2O$ (7:3**)** | $1.4\times10^{-7}$ M | *RSC Adv.*, 2022, **12**, 8570. |
| 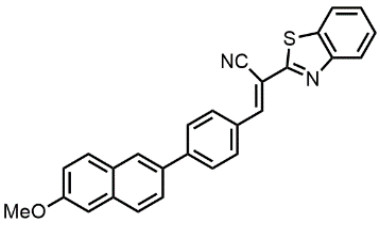 | $CN^-$, Ratiometric | DMSO/$H_2O$ (10 mM HEPES buffer, 1: 1 v/v, pH 7.4 | 2.1(±0.002 2) $\times10^{-8}$ M | *Anal. Methods*, 2022, **14**, 3209. |
| 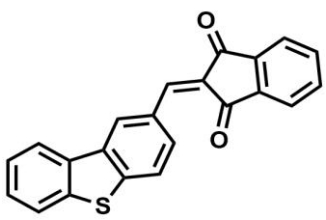 | $CN^-$, Turn-off | DMSO/$H_2O$ (1:99, v/v) | $2.26\times10^{-7}$M | *J. Photochem. Photo biol., A*, 2021, **405**, 112993. |

| | | | | |
|---|---|---|---|---|
| 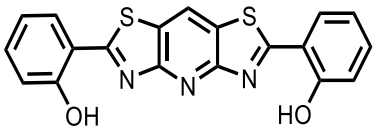 | Ratiometric, $CN^-$ | MeOH: $H_2O$ (9 : 1). | 75 nM | *New J. Chem.*, 2019, **43**, 13001. |
| 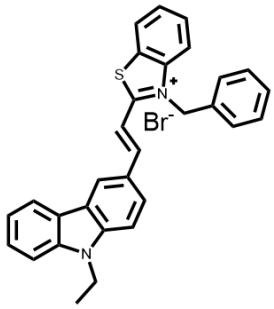 | Ratiometric, $CN^-$ | DMSO/$H_2O$ (3: 2, v/v, pH = 7.4). | 3.39 ×$10^{-7}$ M | *J. Mater. Chem. B*, 2019, **7**, 4620. |
| 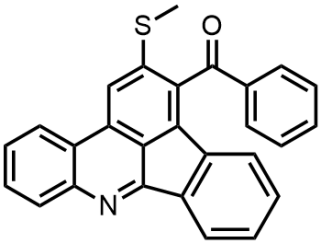 | Ratiometric, $CN^-$ | ACN/$H_2O$ (9 : 1) | 2.95×$10^{-8}$ M | *Sens. Diagn.*, 2023, **2**, 337. |
| 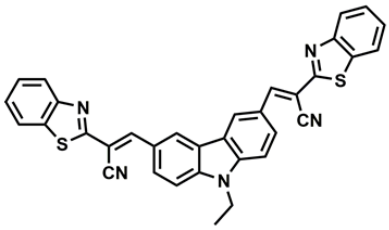 | $CN^-$, Turn-on | DMSO-$H_2O$ (4/1, v/v) | 3.75 nM | *J. Lumin.*, 2018, **201**, 419. |
| 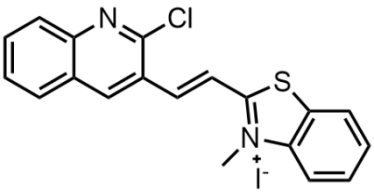 | $CN^-$, Turn-on | HEPES buffer/DMF (70 : 30 v/v) | — | *Anal. Methods*, 2018, **10**, 2368. |

| | | | | |
|---|---|---|---|---|
| 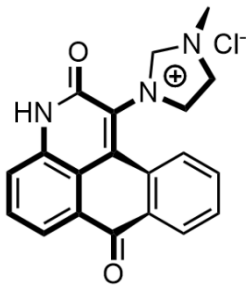 | $CN^-$, Ratiometric | 100% $H_2O$ | 0.13 pM | *Analytica Chimica Acta*, 2023, **1267**, 341376. |
| 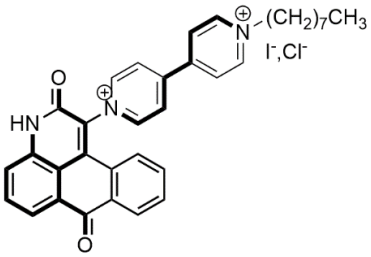 | $CN^-$, Turn-on | HEPES (pH 7.4): EtOH (1:1) | 1 nM | *Sensors and Actuators B: Chemical*, 2020, **304**, 127396. |
| 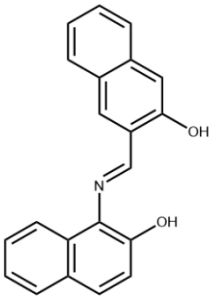 | $CN^-$, Turn-off | DMF/$H_2O$ (1:1, v/v) | 0.21 μM | *Journal of Photochemistry and Photobiology A: Chemistry*,2022, **424 ,** 113651. |
| 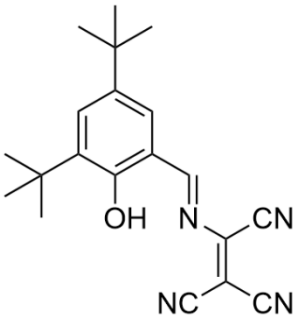 | $CN^-$, Turn-on | $H_2O$:DMSO (1:1 v/v) | 1.3 μM | *Methods*, 2023, **215**, 1. |

| | | | | |
|---|---|---|---|---|
| 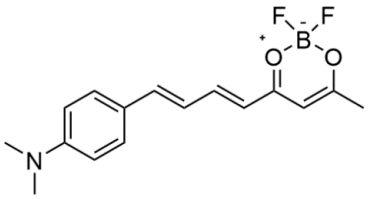 | $CN^-$, Turn-on | $H_2O$/THF (8/2, v/v) | 2.23 μM | *Spectrochimica Acta Part A: Molecular and Biomolecular Spectroscopy*, 2022, **271**, 120882. |
| 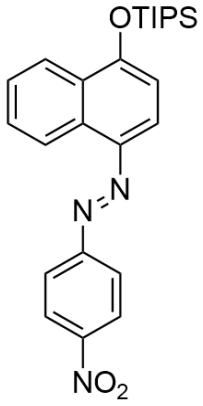 | $CN^-$, Colorometric | ACN/ $H_2O$ | $2.73\times10^{-6}$ mol $L^{-1}$ | *Spectrochimica Acta Part A: Molecular and Biomolecular Spectroscopy*, 2021, **260**, 119950. |
| 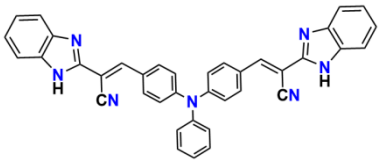 | Ratiometric, $CN^-$ | DMSO | $(6.56\pm0.26)\times10^{-8}$ (M) | **This work** |

# Chapter 7

# A distinctive and proficient fluorescent switch for ratiometric recognition of the menacing cyanide ion: Biological studies on MDA-MB-231 cells

# A distinctive and proficient fluorescent switch for ratiometric recognition of the menacing cyanide ion: Biological studies on MDA-MB-231 cells

## Abstract

A new fluorescent ratiometric switch (BOHB) has been developed for swift and distinct detection of cyanide ion in aqueous media without any interference of other competitive anions. Upon gradual addition of cyanide ion into the probe solution, a prominent fluorescence color change from yellow to cyan was noticed under UV chamber. The fluorescence changes thus observed was ratiometric and the detection limit of this new probe is found to be (22.1±0.89) μM suggesting the efficiency of BOHB for the detection of cyanide ion is brilliant even in minute level. The blue shift in fluorescence intensity upon the addition of cyanide ion was attributed to the deprotonation mechanism of acidic protons present in BOHB. This phenomenon was further explored by 1H-NMR study which supported the mechanism. Further the stability study was performed over a period of 5 days, to establish the stability of BOHB prominently. The probe is also highly capable of recognizing CN- within a very short time-span (almost 15 seconds) thereby being noted as a brilliant fluorescent switch for the swift recognition of CN-. Furthermore, BOHB has been employed for a real water sample analysis to display its practical application. Besides, easy-to-prepare dipstick experiment provides a simple, reusable and recyclable protocol for the qualitative identification of $CN^-$ suitably. Lastly, triple negative breast adenocarcinoma (MDA-MB-231) cells were made susceptible to $CN^-$ sensing in a biological system thereby making BOHB a biomarker tool.

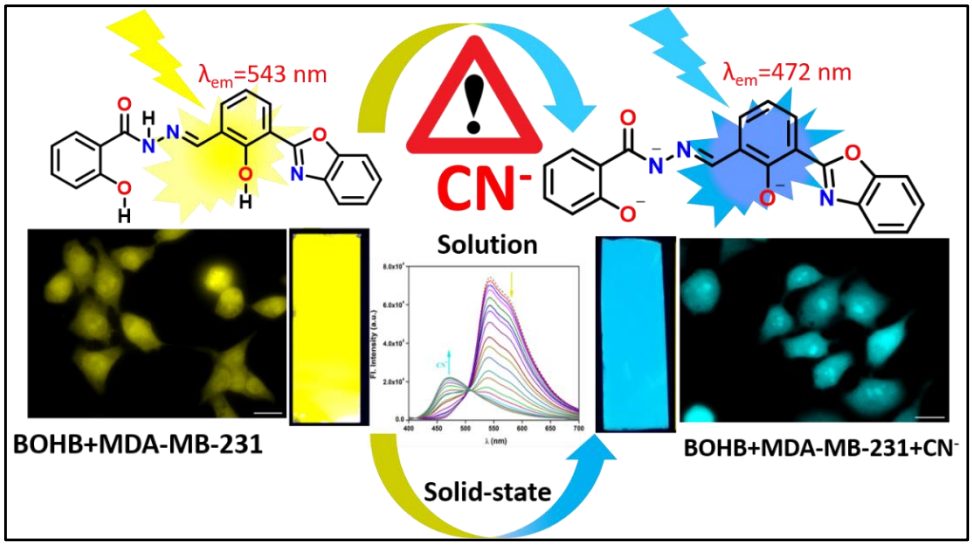

# 7.1. Introduction

Many ions possess an assortment of significant purposes in chemical and biological processes.[1-5] Among them, several anions are naturally occurring, having noteworthy roles in vital fields comprising chemistry, life science, catalysis, medicine, as well as the environment.[6-8] Thus for some time, recognition of anions has been converted to be a genre of budding concern in the area of environmental and biological sciences. Relentless efforts have been made in order to comprehend the essential principles of interaction between a host and a guest anion over the previous years.[9-13] Now although some of the anions like phosphate, sulphate and carboxylate are essential for biological function, the exposure towards cyanide is exceptionally lethal to living organisms. There are numerous types of anions which are thought to be exceptionally deadly but cyanide ($CN^-$) ion, specifically, has been of consistent curiosity universally due to its effectiveness and global existence in several methods such as fabricating plastic and fiber products, metallurgy, tanning, fishing, herbicide and fertilizer manufacture, the petrochemical production, in extraction of silver or gold etc.[14-17] Cyanide is acknowledged as one of the really lethal and fast acting poisons.[18,19] In spite of its vast applications in many fields, $CN^-$ is still dangerous to humans even at a dose of only 0.5 mg per kilogram.[20] Considerable environmental hazards would take place in case of any unintended release of cyanide ions. Toxic HCN can be created by the hydrolysis of cyanogenic glycosides in plants such as bitter almonds, sprouting potatoes, bitter cassava along with apple, cherry, and peach seeds besides industrial dumping.[17,21] The lethal nature of cyanide is chiefly due to its affinity to attach with the heme iron in cytochrome c oxidase,[22] which afterwards affects the oxygen supply to cells and also hinders the role of enzymes in human body which eventually resulted into cytotoxic hypoxia and cellular asphyxiation.[23,24] Additionally, anaerobic metabolism roused by cyanide induces buildup of lactate in the blood which is acknowledged as lactate acidosis. Now the united effects of hypoxia and lactate acidosis generates trouble into the central nervous system thereby instigating serious respiratory seize and death.[25] Now according to World Health Organization (WHO), the maximum suitable concentration level of cyanide is 1.9 mM in drinking water.[26] As minor quantity as 0.5-3.5 mg cyanide per kg of body mass are lethal to humans.[27-29] Cyanide has also been utilized as a chemical warfare reagent[30] and it also can act as a potent inhibitor for some metalloenzymes and non-metalloenzymes.[31] Unrestricted exposures to $CN^-$ can cause paralysis of the central nervous system, poisoning of the respiratory enzymes and also hemoglobin poisoning thereby resulting into difficulty in breathing and the cells in our body start to perish from

hypoxia due to low oxygen levels.[32-35] Therefore, although cyanide ion shows countless health hazards, due to its extensive application in many fields (electroplating, metallurgy and mining), it cannot be avoided. Hence the development of a more sensitive, selective, reliable and accurate analytical method for identifying lethal cyanide ions is still seriously desirable.

In this regard, fabrication of fluorescent dosimeter for the recognition of cyanide ion will be a superior option.[36-43] Among the fluorescent probes, ratiometric probes possess an exclusive benefit and are more reliable as they measure the relative emission intensities at two different wavelengths.[44-48] The utilization of ratiometric fluorescent probes is considered to be the most effective tools for sensitive $CN^-$ recognition among the numerous analytical techniques owing to their extraordinary sensitivity, direct visualization, short response time and primarily, real-time bioimaging.[49,50] Thus the demand to fabricate highly selective probes to identify cyanide ions in environment easily has never stopped. Many conventional detection methods, based on potentiometric, electrochemical, voltammetric, titrimetric and several other techniques have been manufactured for the quantitative analysis of cyanide ion.[51,52] But owing to their time-consuming nature along with their instrumental dependency, these techniques are of inadequate use. The fluorometric response of the specific recognition tool would be deemed to be one of the most appropriate methods owing to their simple-to-synthesize character, high sensitivity, tunability, easy portability, real-time monitoring and cost-effective property.[53-58]

## 7.2. Prior works

Some fluorescent as well as colorimetric probes, planned precisely for cyanide ions, have been reported in literature based on nucleophilic addition,[59] deprotonation mechanism,[59-62] but still there are requirements for distinct fluorescent ratiometric cyanide recognition tools which can also act as a biomarker tool in cell imaging studies. Generally, the mechanism methods for cyanide detection are abridged as nucleophilic addition on the carbonyl units,[63,64] hydrogen bonding concepts,[50,65,66] electron-deficient alkenes,[67-69] cyanide complexation[70,71] and many more. But each of them possesses some drawbacks such as reduced solubility in aqueous media, elongated response time or relatively low detection limit.[72-74]

## 7.3. Present work

So, a chromogenic sensor for the detection of cyanide is highly desirable which will be presented with operational simplicity, low cost, low detection limit and rapid recognition. So, with the aim

to advance the research of molecular recognition with a new suitable cyanide specific probe, herein we report a fluorescent ratiometric probe (BOHB) which selectively and sensitively detects $CN^-$ ion in presence of other anions in MeOH/$H_2O$ (1/1, v/v) solvent in physiological pH. This particular probe is very easy to synthesize and it also have a solvent media which can be regarded as one of the most practical and convenient solvent system. The fluorescence spectra detection limit of the probe for cyanide is found to be in the nano-molar range thereby showcasing an excellent detection limit than some other reported probes in the past few years (Table A7.2, Appendix) and it also demonstrates swift response time in aqueous solution. This newly designed probe (BOHB) shows a sharp blue shift of 72 nm upon incremental addition of aqueous cyanide solution into it thereby proving to be an appropriate analysis kit for the sole detection of $CN^-$ ion.

# 7.4. Results and discussions

## 7.4.1. Synthesis of the probe (BOHB)

The simple synthetic route of **BOHB** is shown in Scheme 1. 3-(benzo[d]oxazol-2-yl)-2-hydroxybenzaldehyde (1) and 2-hydroxybenzohydrazide (2) were prepared as described in the reported literature procedure.[75,76] Then compound 1 and compound 2 were refluxed for almost 9 hours which ultimately yields the desired probe (BOHB). The structure of BOHB was confirmed by $^1$H NMR, $^{13}$C NMR, IR and HRMS spectroscopy (Fig. A7.1-A7.4, Appendix).

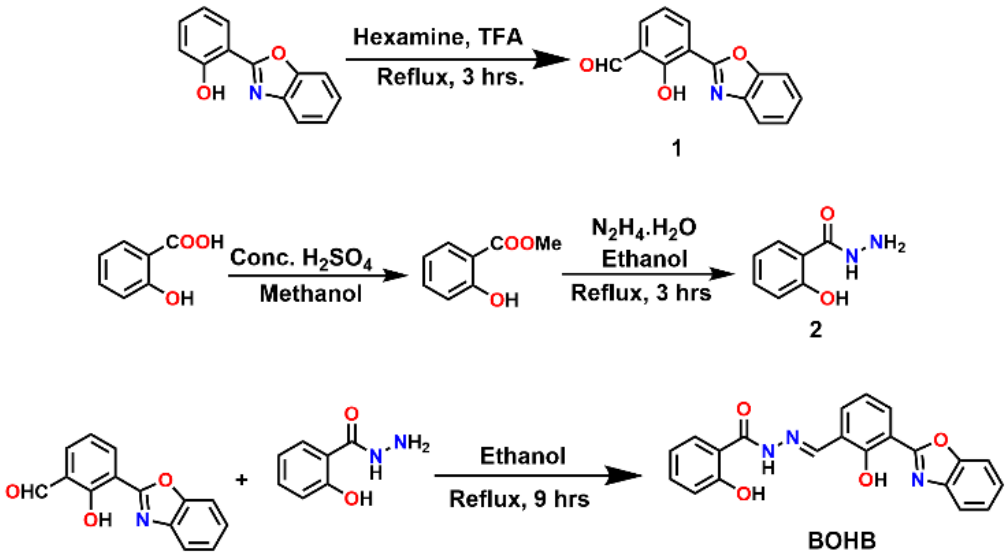


**Scheme 7.1:** Synthesis of the probe (BOHB).

## 7.4.2. Sensing studies of the chemodosimeter (BOHB)

### 7.4.2.1. UV-Vis spectral studies

The absorption spectral studies for the probe (BOHB) shows a moderate absorbance band at 303 nm with a small hump at 326 nm along with a moderately strong shoulder peak at 392 nm in MeOH/$H_2O$ (1/1, v/v) solution using 10 mM HEPES buffered solution at pH=7.2. Gradual addition of aqueous solution of $CN^-$ into the solution of BOHB results into the decrease of absorbance of the band at 392 nm and 326 nm and a new band at 365 nm appeared (Fig. 7.1) supporting the interaction of $CN^-$ to the probe. Three distinct isosbestic points are found at 308 nm, 353 nm and 375 nm respectively.

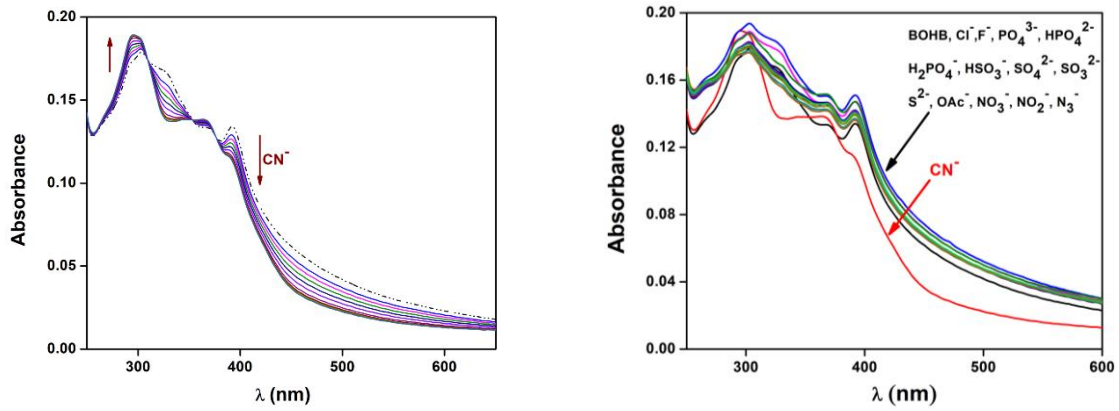


**Figure 7.1:** Absorption spectra of BOHB (10 µM) upon gradual addition of $CN^-$ (0-20 µM) in MeOH/$H_2O$ (1/1, v/v) using HEPES buffered solution at pH=7.2. (left side) and Absorption spectra of BOHB (10 µM) upon addition of various other anions (20 µM) in MeOH/$H_2O$ (1/1, v/v) using HEPES buffered solution at pH=7.2. (right side).

To establish the fact that BOHB selectivity binds with $CN^-$ ion, UV-Vis studies were also carried out in presence of other competitive anions. As a result, no other anions showed any noticeable change on the absorption spectral pattern of BOHB (Fig. 7.1 & Fig.7.2).

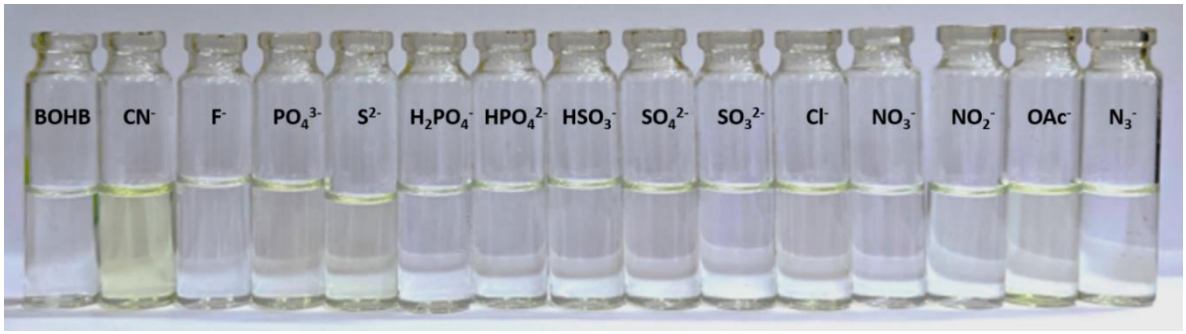


**Figure 7.2:** Color variations upon addition of different anions such as $CN^-$, $Cl^-$, $F^-$, $PO_4^{3-}$, $H_2PO_4^-$, $HPO_4^{2-}$, $HSO_3^-$, $SO_4^{2-}$, $SO_3^{2-}$, $S^{2-}$, $OAc^-$, $NO_3^-$, $NO_2^-$ and $N_3^-$ into the probe solution in MeOH/$H_2O$ (1/1, v/v) in naked eye.

## 7.4.2.2. Fluorescence spectral study

The emission spectra of BOHB (10 µM) itself exhibits a very strong emission band at 543 nm ($\lambda_{ex}$ = 368 nm) in MeOH/$H_2O$ (1/1, v/v) solution ($\varphi$ = 0.245). Upon gradual addition of $CN^-$ into the solution of BOHB, the peak at 543 nm gradually decreases whereas a new peak at 472 nm appears with a blue shift of 71 nm. The shift actually accounts for the ratiometric emission response of BOHB with a distinct isoemissive point at 505 nm (Fig. 7.3). Consequently, this ratiometric fluorescence change results in the prominent emission colour change from yellow to cyan under UV light (Fig. 7.3, Inset).

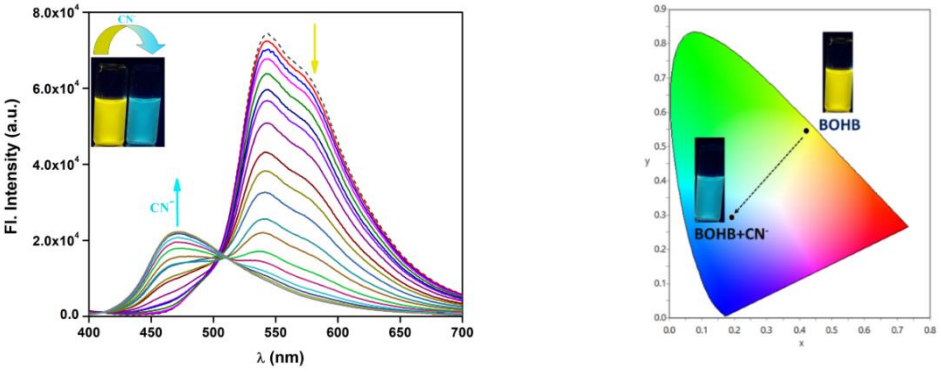


**Figure 7.3:** Emission spectra of BOHB (10 µM) upon the incremental addition of $CN^-$ (0 to 22 µM) in MeOH/$H_2O$ (1/1, v/v) solution. Inset: visible emission color change of BOHB in the absence and presence of 20 µM of $CN^-$ under UV light. (left side) and CIE1931 chromaticity diagram of probe BOHB with $CN^-$ (right side).

In Commission International de L'Eclairage (CIE) chromaticity coordinates (Fig. 7.3), we also witnessed evident changes from yellow to cyan with a variation in coordinates from (x = 0.4215, y = 0.5451) to (x = 0.2000, y = 0.2946).

The sensing abilities of the probe (BOHB) was also studied in presence of other anions like $Cl^-$, $F^-$, $PO_4^{3-}$, $H_2PO_4^-$, $HPO_4^{2-}$, $HSO_3^-$, $SO_4^{2-}$, $SO_3^{2-}$, $S^{2-}$, $OAc^-$, $NO_3^-$, $NO_2^-$ and $N_3^-$ which shows no significant changes in the emission response towards BOHB at all (Fig. 7.4). The selectivity of BOHB towards $CN^-$ can be explained by the activity of its -OH groups, thereby allowing the probe with the capability to differentiate the subtle difference in the affinity of $CN^-$ towards the acidic protons compared to the aforementioned anions. So, from these studies, it can be established that BOHB can act as an imminent ratiometric switch for the selective and sensitive detection of $CN^-$ in MeOH/$H_2O$ (1/1, v/v) solution.

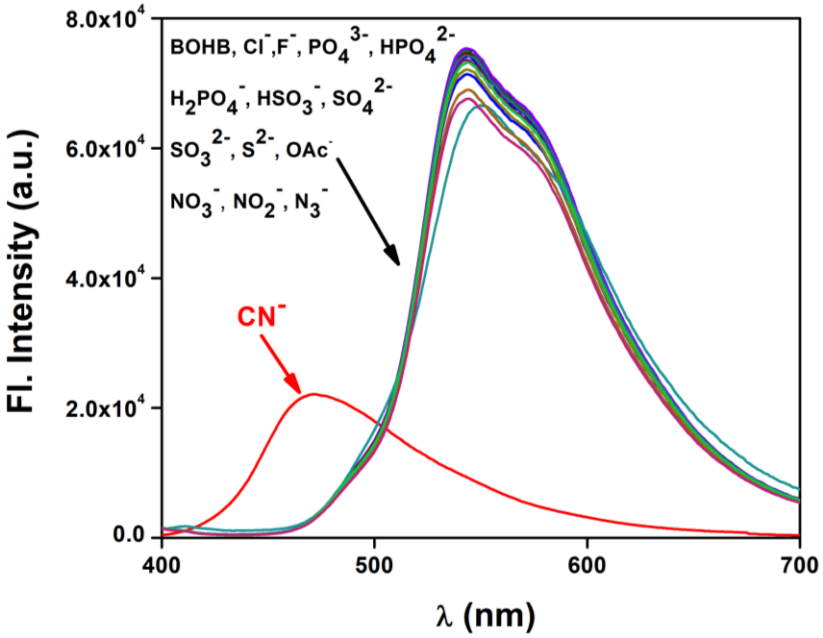


**Figure 7.4:** Change of emission spectra of BOHB (10 μM) after addition of other anions (20 μM) in MeOH/$H_2O$ (1/1, v/v) using HEPES buffered solution at pH=7.2. $\lambda_{ex}$ = 368 nm.

## 7.4.2.3. Interaction studies of BOHB with $CN^-$

The emission intensity of the probe (BOHB) at 472 nm increases linearly within the range of 0 to 18.5 μM with the incremental addition of $CN^-$ and is in accordance with the linear relationship with a good $R^2$ value of 0.985. (Fig. 7.5). Now to calculate the detection limit of BOHB for $CN^-$ from the fluorescence spectral change obtained from the emission titration experiment, the following equation is used: DL = K × $Sb_1$/S, where K = 3, $Sb_1$ is the standard deviation of the blank solution and S is the slope of the calibration curve. Then the detection limit of BOHB for

$CN^-$ was found to be (22.1±0.89) μM (Fig. 7.5). From the mole ratio plot of BOHB, it is clear that after addition of almost 40 μM of $CN^-$, no significant changes in emission intensity at 472 nm is noticed thereby indicating the fact that the saturation has taken place (Fig. 7.5).

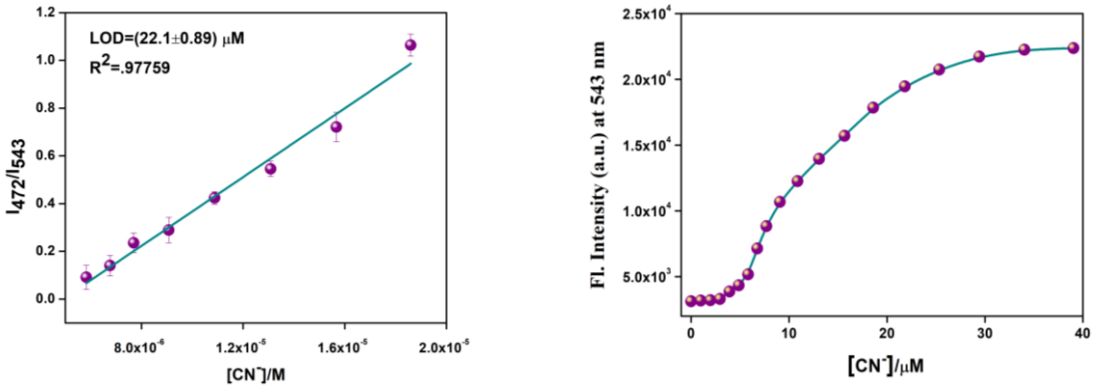


**Figure 7.5:** The linear response curve of emission intensity at $I_{472}/I_{543}$ of BOHB depending on $CN^-$ concentration. (left side) and Plot of emission intensity at 543 nm of BOHB (10 μM) depending upon the $CN^-$ concentration. (right side).

## 7.4.2.4. Competitive study

An interference experiment was then carried out by measuring the emission intensity of BOHB (10 μM) in presence of other anions (20 μM) so as to study the precise selectivity of the ratiometric probe (BOHB). It became evident from the experiment that the ratiometric emission change of BOHB was clearly specific towards $CN^-$ ion (Fig. 7.6) and not at all influenced by the presence of other anions.

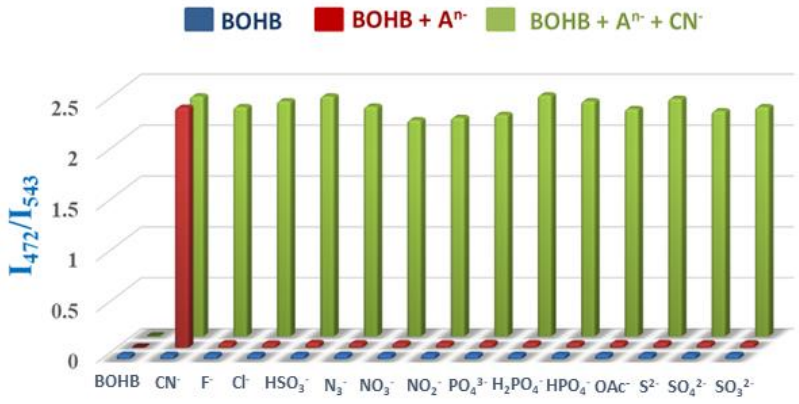


**Figure 7.6:** Bar diagram illustration of the emission intensity of BOHB upon addition of different other anions (20 μM) in MeOH: $H_2O$ (1:1, v/v) (HEPES buffer, pH=7.2) (red bars) and $CN^-$ (20 μM) in presence of other anions (green bars).

### 7.4.2.5. Time dependent spectra of BOHB with $CN^-$

The reaction time has been established to be a very noteworthy aspect in order to elucidate the rapid fluorescence responses of the entire chemodosimetric probes. So, as a competent probe must recognize its guest analyte within short duration of time, the time-dependant emission response study of BOHB towards $CN^-$ is executed to measure the reaction time of the probe. The fluorescence response profile of BOHB (10 μM) was inspected over a 0-2 min time period with addition of 2 equivalents of $CN^-$ into it (Fig. 7.7).

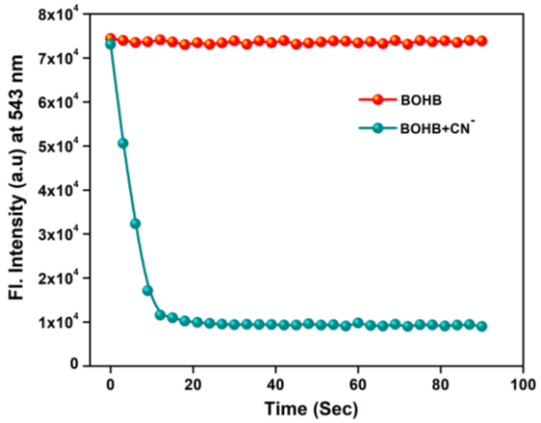


**Figure 7.7:** Time dependent emission spectra of BOHB (10 μM) after addition of $CN^-$ (20 μM), noted within 0-90 sec time interval in MeOH: $H_2O$ (1:1, v/v).

It was noted from the recorded fluorescence spectra that the fluorescence intensity of BOHB remains almost same at 543 nm whereas the emission intensity of BOHB decreases at the same wavelength as the emission maxima showed a decrease with blue shift with the progress of the reaction. The emission intensity reached its saturation after almost 15 seconds and a plateau was noticed thereby implying the end of the reaction. Thus, it can be settled that this new probe, BOHB is highly proficient in identifying $CN^-$ within a very short time-span (almost 15 seconds) thereby making itself a very capable fluorescent switch for the rapid identification of $CN^-$.Further the stability study was executed over a period of 5 days, to explore the stability of the probe, BOHB and its detection efficacy towards $CN^-$ (Fig. 7.8),indicates our probe was highly stable over 5 days period, detecting $CN^-$ with above 96% efficiency.

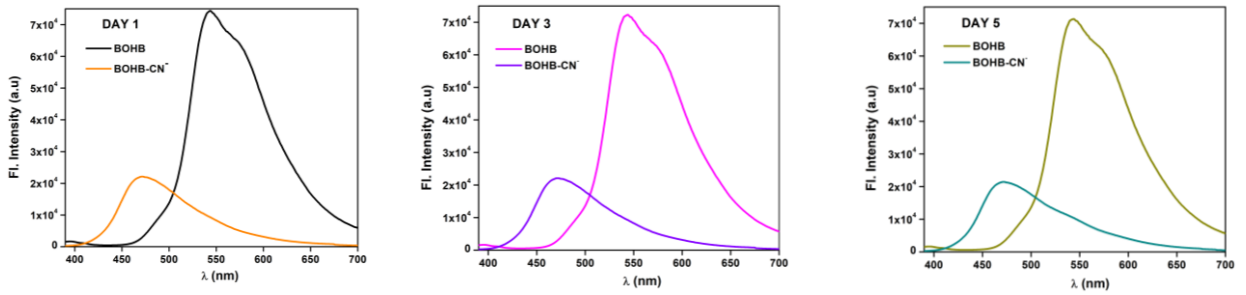


**Figure 7.8:** Fluorescence response of BOHB and BOHB-$CN^-$ over different days.

## 7.4.2.6. Recyclability of BOHB

Recyclability is an essential application in the genre of applications for fluorescence chemosensors. We cautiously observed and recorded the reusability of $CN^-$ detection properties via alternative addition of TFA into the probe solution containing $CN^-$ (Fig. 7.9). Consequently, the fluorescence of the probe (BOHB) changes from yellow to green a number of times upon alternate addition of $CN^-$ ion with little loss of fluorescence efficiency. This observation can be elucidated by the deprotonation mechanism of BOHB upon addition of $CN^-$ and TFA respectively. The increase in the emission intensity of BOHB after $CN^-$ addition occurs due to the hydrogen bonding followed by consequent deprotonation of acidic protons. Conversely, the decrease in the emission intensity after addition of TFA in BOHB-$CN^-$ solution can be attributed to the fact that the hydrogen bonding gets interrupted thereby leading to the inhibition of the deprotonation of acidic protons and the consequent protonation of deprotonated BOHB. Hence the cycling demonstrates that BOHB can be used for practical determination of $CN^-$ in real samples with high proficiency. Hence BOHB can be considered as recyclable and reusable $CN^-$ detection probe as well as ratiometric fluorescence switch.

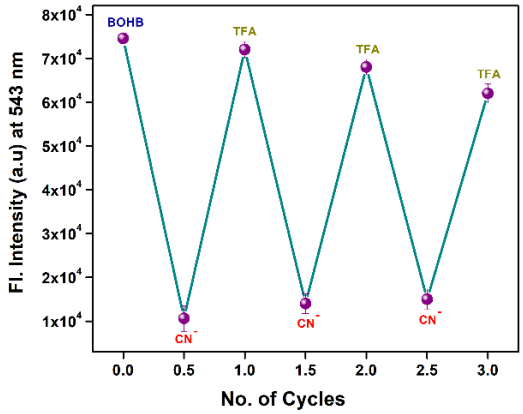


**Figure 7.9:** The fluorescence ratiometric repetitive cycle upon each sequential addition of $CN^-$ and TFA at 543 nm ($\lambda_{ex}$ = 368 nm) in MeOH: $H_2O$ (1:1, v/v) solution.

## 7.4.2.7. Time-resolved photoluminescence study (TRPL) Study

Time resolved fluorescence study (TRPL) is a fitting means to obtain clear understanding on excited state behaviour of the probe before and after addition of $CN^-$. So, we have executed the TRPL study on BOHB and BOHB-$CN^-$ in methanol and observed the decay profile. The lifetime decay plots were fitted via mono exponential function of both BOHB and BOHB-$CN^-$ with suitable $\chi 2$ values (Fig. 7.10). For BOHB, the lifetime was found to be 2.33 ns ($\chi^2$ = 1.12) while for BOHB-$CN^-$, the value was noticed to be 0.92 ns ($\chi^2$=0.91). The radiative rate constant $K_r$ and the total non-radiative rate constant $K_{nr}$ values were calculated using the equations, $\tau^{-1} = K_r + K_{nr}$ and $K_r = \varphi_f/\tau$ and abridged in Table A7.1, Appendix. The change in the values of $\tau$, $K_r$ and $K_{nr}$ reveals the formation of BOHB-$CN^-$ adduct which demonstrates a reduced lifetime compared to the ratiometric switch BOHB itself.

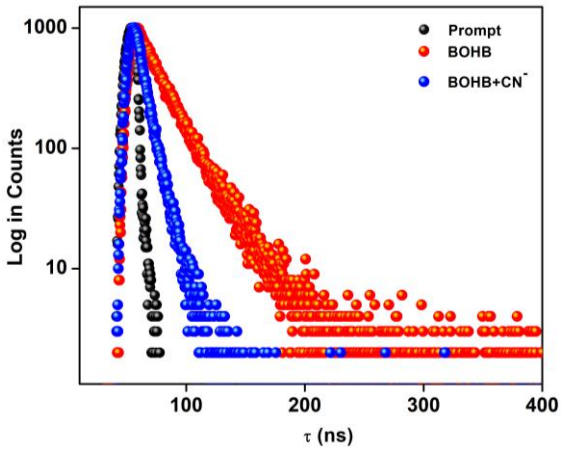


**Figure 7.10:** Time resolved fluorescence decay profile of BOHB and BOHB-$CN^-$ in MeOH: $H_2O$ (1:1, v/v) solution.

### 7.4.2.8. Effect of pH

The effect of pH on the emission intensity of the probe (BOHB) in absence and presence of $CN^-$ is studied and represented it by fluorescence intensity ratio ($I_{472}/I_{573}$) (Fig. 7.11). Thus the pH titration experiment executed stated the fact that in case of BOHB, the ratio of emission intensity remains almost same with increasing pH except showing a sharp increase in basic region owing to the presence of two -OH groups in it whereas on addition of $CN^-$ into the BOHB solution, ratio of fluorescence intensity of the probe increases in the pH range of 7.05-8.49 but starting from the pH 9.38, the ratio of emission intensity decreases thereby indicating that BOHB can detect $CN^-$ selectively in neutral pH range with significant efficacy although not in the very basic region.

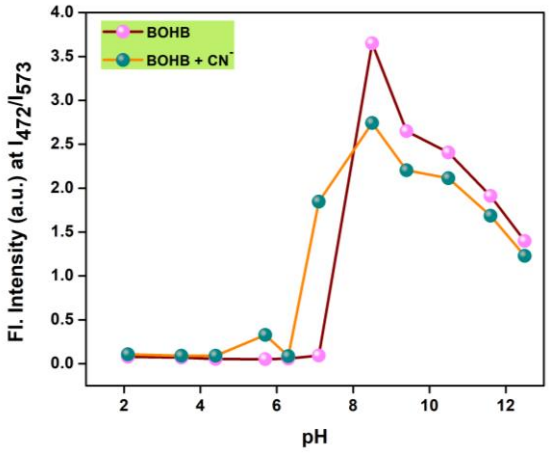


**Figure 7.11:** pH study of BOHB for $CN^-$ (from Fluorescence spectra).

## 7.4.3. Possible sensing mechanism of BOHB

A probable sensing mechanism of this new ratiometric switch (BOHB) with $CN^-$ is discussed and shown in scheme 7.2. The BOHB-$CN^-$ product was isolated and characterized through $^1$H-NMR spectroscopy in order to support the proposed sensing mechanism (Fig. 7.12). $^1$H-NMR titration was executed in DMSO-$d_6$ upon addition of cyanide in order to study the nature of binding mode of BOHB with $CN^-$.

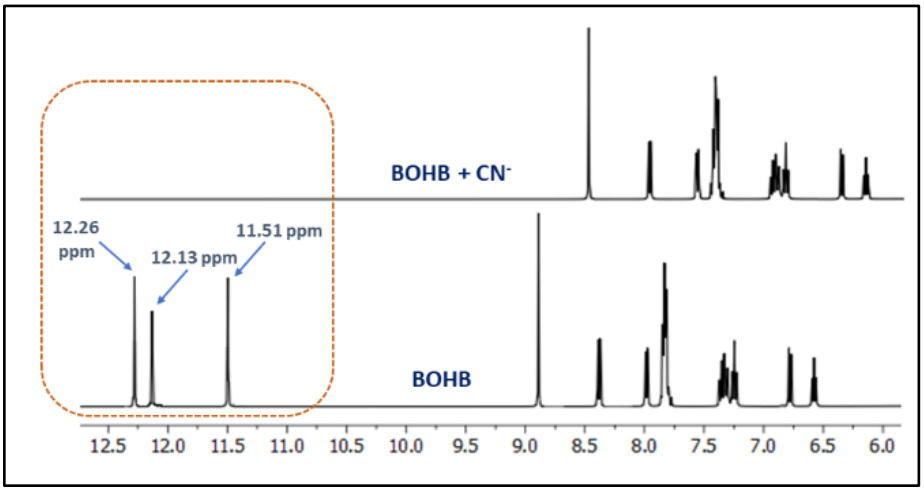


**Figure 7.12:** $^{1}$H-NMR titration of BOHB upon addition of $CN^-$.

As shown in Fig. 7.12, in case of BOHB-$CN^-$, the signal corresponding to –NH peak in the structure of the probe (BOHB) at 11.51 ppm, disappeared along with the other two signals at 12.13 and 12.26 ppm belonging to two –OH peaks were also found to be vanished, suggesting the formation of three H-bonding followed by deprotonation of imidazole –NH protons as well as two phenolic –OH protons. The resonance signal of all aryl protons which appeared around 6.56-8.89 ppm, shifted to upfield region at 6.13-8.46 ppm after the addition of $CN^-$ because of the formation of negative charges on the imidazole and phenol moieties thereby firmly establishing the formation of the BOHB-$CN^-$ adduct.

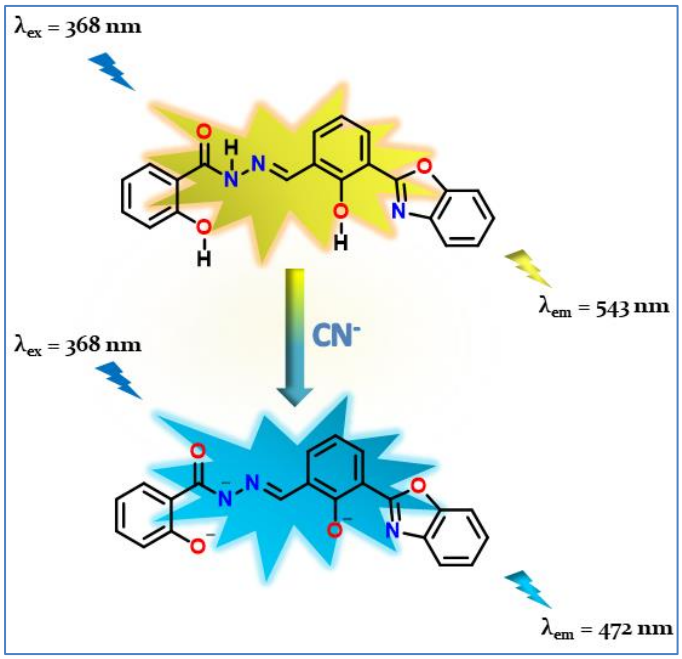


**Scheme 7.2:** Probable sensing mechanism of BOHB with $CN^-$.

A comparison assessment of the probe (BOHB) with few formerly reported $CN^-$ sensing probes is presented in Table A7.2, Appendix.

## 7.4.4. Detection of $CN^-$ ion using Dipstick Experiment

In order to explore the practical use and also for the visual identification of this anew fluorescent switch, the economical and effective dip-stick method has been verified to be a simple but very significant experiment. To carry out the experiment, few thin-layer chromatography (TLC) plates were prepared and then they are dipped into the solution of BOHB ($2 \times 10^{-4}$ M) in methanol and then the plates were kept for some time to dry. Then the TLC plates were dipped into $CN^-$ solution and then again dried in air. A distinct colour change was noticed after executing the experiment by naked eye. The colour of the TLC plates indicates the change of the colour of the test strips from yellow to cyan under UV light (Fig. 7.13). On the other hand, it is very fascinating to notice that the TLC plates used for $CN^-$ recognition can be reused by immersing into a TFA solution. This simple, reusable, recyclable and user-friendly experiment established that BOHB is greatly effective as a sensing kit to identify $CN^-$ ions qualitatively.

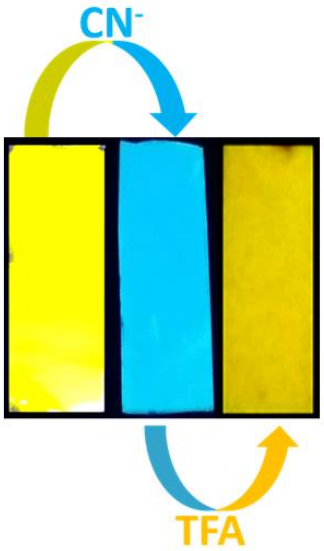


**Figure 7.13:** Photographs of TLC plates after immersion in the BOHB-methanol solution and after each sequential immersion into $CN^-$ and TFA solution under hand-held UV light. [BOHB] = $2 \times 10^{-4}$ M, [$CN^-$] = $2 \times 10^{-3}$ M.

## 7.4.5. Real water sample analysis

Real water sample analysis was executed to further explore the practical applicability of our designed probe BOHB. We used natural water resources (tap and lake) for sensing $CN^-$ by means of fluorescence method, according to the previously reported procedure.[77,78] Firstly, the

water samples were filtered by using whatmann filter paper to eliminate the suspended particles. Then different concentration of $CN^-$ was added into these real water samples. The fluorescence spectra of BOHB (20 µM) with different concentration of $CN^-$ was measured ($\lambda_{ex}$ = 368 nm). The experimental data is well tabulated in Table 7.1, where the Recover (%) is determined. It was observed that the recovery % for $CN^-$ lies above 95% thereby revealing that BOHB is effective enough for analysing $CN^-$ in real water systems.

**Table 7.1:** Recovery % experiment for $CN^-$ detection in various natural water samples

| Samples | $CN^-$ added (µM) | $CN^-$ determined (µM) | Recovery (%) |
|---|---|---|---|
| Drinking water | 5 | 4.79 | 95.8 |
| | 10 | 9.61 | 96.1 |
| Tap water | 5 | 4.86 | 97.2 |
| | 10 | 9.81 | 98.1 |

## 7.4.6. Cell Study

Further, to get an insight into the biological efficacy of this ratiometric probe (BOHB), we have carried out cytotoxicity study and cellular imaging on triple negative breast adenocarcinoma cells (MDA-MB-231). As we all know from different studies, Triple-Negative Breast Cancer (TNBC) is the most lethal, aggressive, and invasive breast cancer subtype.[79] TNBC has a low prognosis and high relapse rate.[80] Thus, early detection of TNBC is essential for researchers and clinicians.[81] So, in this study, we prefer to choose the MDA-MB-231 TNBC cell line where MDA-MB-231 cells were made susceptible to $CN^-$ sensing in a biological system, making BOHB a biomarker tool. The *in-vitro* cytotoxicity study established the fact that BOHB exhibits a very negligible cytotoxicity ($IC_{50}$ value: 178.12 µM) on MDA-MB-231 cells (Fig. 7.14). Therefore, we have preferred Sub $IC_{50}$ and $IC_{50}$ dosages i.e. 89.06 µM and 178.12 µM of BOHB to perform the cellular imaging experiment. Now to explore the live cell imaging applicability of BOHB in human triple-negative breast adenocarcinoma cells (MDA-MB-231), the cells were incubated with only BOHB (178.12 µM) for 30 minutes. After 30 minutes, the incubated cells

exhibit strong yellow fluorescence under a fluorescence microscope, which led to the fact that the treatment of only BOHB on MDA-MB-231 cells displays a clear yellow fluorescence. Whereas, in the presence of 15 µM of $CN^-$ along with the BOHB (Sub $IC_{50}$ and $IC_{50}$ dosages i.e. 89.06 µM and 178.12 µM), the yellow fluorescence, previously showed in case of only BOHB, gradually changed into strong cyan fluorescence inside the human triple-negative breast adenocarcinoma cells (Fig. 7.15). Thus, we can summarize from the results that the probe, BOHB is cell membrane penetrable fluorescent probe which can be used as an intracellular biomarker tool to identify intracellular $CN^-$ in the human triple-negative breast adenocarcinoma cells.

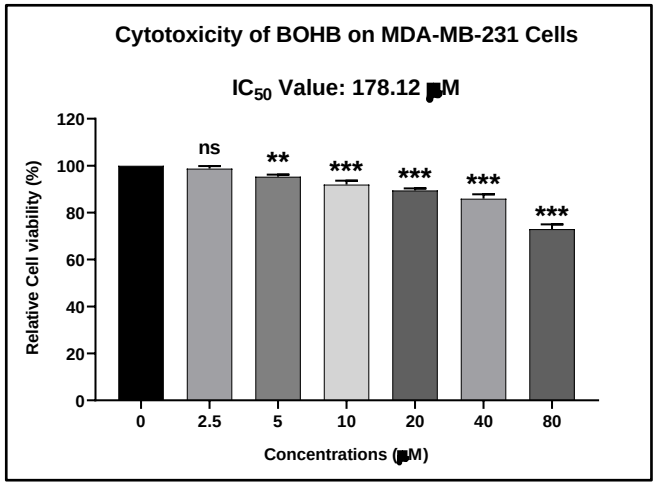


**Figure 7.14:** ***Cytotoxicity study.*** Bar diagrams represent *in-vitro* cell viability percentages of BOHB with different concentrations (0-80 µM) against human triple-negative breast adenocarcinoma cells (MDA-MB-231). All the experiments were performed independently thrice and the data were calculated as Mean ± SD where *P < 0.05, **P < 0.01, ***P < 0.001.

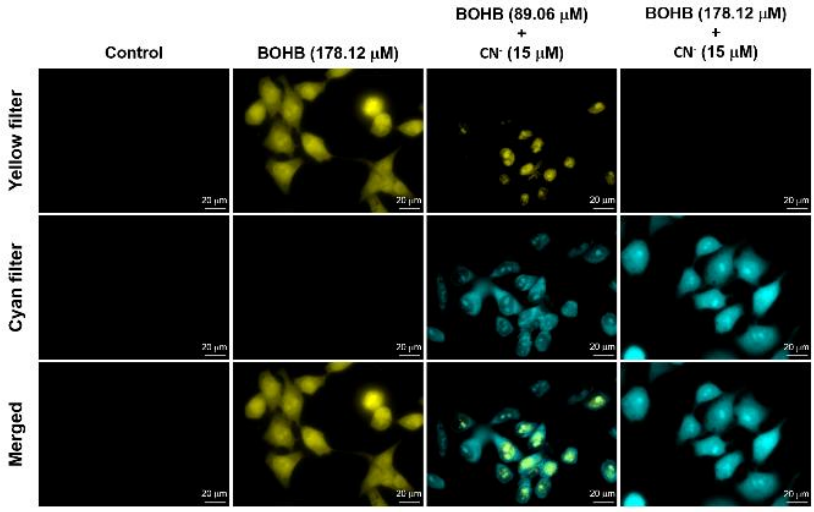


**Figure 7.15:** Live cell imaging study. Fluorescence images of MDA-MB-231 cells after incubation with only BOHB and BOHB-$CN^-$ at 40X magnification under fluorescence microscope. Scale bar correspondence to 20 μm.

# 7.5. Conclusions

So herein a new fluorescent ratiometric chemodosimeter (BOHB) was fabricated for the selective and distinctive sensing response of $CN^-$ ion in aqueous media even in presence of several other anions. The chemodosimeter developed showed an outstanding ratiometric emission change with a blue shift of about 72 nm upon gradual addition of $CN^-$ with a cyan colored emission response under UV-chamber. A low detection limit value was noticed for the newly synthesized probe (BOHB) towards $CN^-$ which is (22.1±0.89) μM in neutral pH. The spectral change portrays brilliant selectivity towards $CN^-$ along with a rapid interaction time (within 15 seconds). Besides, stability study clearly states the fact that BOHB was highly stable over 5 days period thereby sensing $CN^-$ with above 96% efficiency. Additionally, the well-known dipstick experiment helps us to detect $CN^-$ quantitatively without any sophisticated equipment in solid state. These interpretations show that recyclable and reusable BOHB can act as a capable probe for rapid, selective and instant recognition of $CN^-$ in presence of other competing anions. Furthermore, from real water sample analysis, it is proved that BOHB is effective enough for analysing $CN^-$ in real water systems. Moreover, the live cell imaging experiment using triple negative breast adenocarcinoma (MDA-MB-231) cells validates the competency and practical use of the probe for identifying intracellular cyanide.

# 7.6. Experimental

## 7.6.1. Materials and methods

2-benzooxazol-2-yl-phenol and 2-hydroxy-benzoic acid were purchased from Sigma-Aldrich. All other organic chemicals and inorganic salts were available from commercial suppliers and used as it is without any further purification, unless otherwise acknowledged. Elemental analysis was carried out in a 2400 Series-II CHN analyzer, PerkinElmer, USA. NMR spectra of all the products or intermediates were recorded using a Bruker Avance DPX 300/400 MHz spectrometer. DMSO-$d_6$ was used as the NMR solvent and chemical shifts were recorded in δ units in ppm using tetramethylsilane (TMS) as an internal standard. The HRMS mass spectra were recorded on Waters (Xevo G2 Q-TOF) mass spectrometer. UV-vis studies were performed on a Perkin Elmer Lambda 750 spectrophotometer whereas the fluorescence property was measured using Shimadzu RF-6000 fluorescence spectrophotometer at room temperature (298 K). The lifetimes were measured using a time-correlated single photon counting setup from Horiba Jobin Yvon. Then, the fluorescence decay data were placed on a Hamamatsu MCP photomultiplier (R3809) and analysed using EZ time software.

## 7.6.2. General Method for UV-Vis and Fluorescence Titration

For UV-Vis titration, the stock solution of BOHB (10 μM) was prepared in [($MeOH/H_2O$), 1/1, *v/v*] solution at 25°C using HEPES buffered solution.The solutions of all the guest anions were prepared in deionized water using the sodium salts in the order of $1 \times 10^{-5}$ M. The solution of cyanide ion ($1 \times 10^{-5}$ M) was made ready using a tetrabutylammonium cyanide salt at the physiological pH. Solutions of a variety of concentrations of the probe and all other anions were prepared discretely. The spectra of these solutions were recorded with the aid of UV-Vis method.For fluorescence titrations, the stock solution of the probe (10 μM) used was the similar to that used for UV-Vis titration. The solutions of all the anions were prepared in the same solvent as used in case of UV and they were all in the order of $10^{-5}$ M. The host solution and the solution of all the anions were prepared individually in different concentrations. The spectra of these solutions were recorded using fluorescence method.

## 7.6.3. Determination of fluorescence quantum yield:

For measurement of the quantum yields of BOHB and its reaction product with (BOHB-$CN^-$), we recorded the absorbance of the compounds in DMSO solution. The emission spectra were

recorded using the maximal excitation wavelengths and the integrated areas of the emission-corrected spectra were measured. The quantum yields were then calculated by comparison with quinine sulfate ($\varphi_s$ = 0.54 in 0.5M $H_2SO_4$) as reference using the following equation:

$$\Phi_x = \Phi_s \times \left(\frac{Ix}{Is}\right) \times \left(\frac{As}{Ax}\right) \times \left(\frac{nx}{ns}\right)^2$$

Where, x & s indicate the unknown and standard solution respectively, Φ is the quantum yield, I is the integrated area under the fluorescence spectra, A is the absorbance and n is the refractive index of the solvent. We calculated the quantum yields of BOHB and BOHB-$CN^-$ using the above equation and the values are 0.245 and 0.098 respectively.

## 7.6.4. Determination of detection limit (LOD)

The limit of detection was determined based on the fluorescence titration. To determine the S/N ratio, the emission intensity of BOHB without $CN^-$ was measured by 10 times and the standard deviation of blank measurements was determined. The detection limit (DL) of BOHB for $CN^-$ was determined from the following equation: DL = K × $Sb_1$/S, Where K = 2 or 3 (we take 3 in this case); $Sb_1$ is the standard deviation of the blank solution; S is the slope of the calibration curve. We get the value of $Sb_1$ as 0.531. Thus, using the formula, we get the Detection Limit = (22.1±0.89) μM i.e., BOHB can detect $CN^-$ in this minimum concentration by fluorescence techniques.

## 7.6.5. Synthesis of (E)-N'-(3-(benzo[d]oxazol-2-yl)-2-hydroxybenzylidene)-2-hydroxybenzohydrazide (BOHB)

2-hydroxybenzohydrazide (**2**) (0.03 g, 0.21 mmol) was added to the ethanolic solution of 3-(benzo[d]oxazol-2-yl)-2-hydroxybenzaldehyde (**1**) (0.05 g, 0.21 mmol) and the mixture was refluxed for about 9 hours. After completion of the reaction, an off-white precipitate was found and filtered using suction and washed with ethanol to obtain the desired product. The yield was, 0.068 g, 88%.

**$^1$H NMR (400 MHz, DMSO-$d_6$):** δ 6.58 (t, J = 7.8 Hz, 1H), 6.77 (d, J = 8.4 Hz, 1H), 7.22 (t, J = 7.7 Hz, 1H), 7.30 (m, 2H), 7.82 (m, 4H), 7.97 (d, J = 7.7 Hz, 1H), 8.37 (d, J = 7.7 Hz, 1H), 8.89 (s, 1H), 11.51 (s, 1H), 12.13 (s, 1H), 12.26 (s, 1H).

**$^{13}$C NMR (100MHz, DMSO-$d_6$):** δ 111.1, 117.2, 117.8, 118.9, 119.3, 120.0, 125.3, 125.9, 126.2, 128.5, 129.9, 132.7, 133.7, 139.4, 144.8, 147.5, 148.9, 149.6, 158.9, 159.4, 161.7.

**Anal. Calc. for $C_{21}H_{15}N_3O_4$ (BOHB):** Calc. (%), C 67.56, H 4.05, N 11.25. Found (%), C 67.13, H 4.01, N 11.12.

**IR data (KBr, $cm^{-1}$):** 3066 υ(-OH broad stretch), 3243 υ(-NH stretch), 1630 υ(-C=O stretch), 1520 υ(-C=N stretch).

**HRMS:** calculated for $C_{21}H_{15}N_3O_4$ $[M + H]^+$ (m/z) = 374.1141; found = 374.1131.

## 7.6.6. Live cell imaging studies

### 7.6.6.1. Cell culture and treatment

A human triple-negative breast adenocarcinoma cell line (MDA-MB-231) was obtained from National Centre for Cell Science, Pune, India and maintained in DMEM High Glucose (Gibco, Life Technologies, USA) supplemented with 10% Heat inactivated Fetal Bovine Serum (HI-FBS) (V/V) (Gibco, Life Technologies, USA) and 1% Antibiotic-Antimycotic (Gibco, Life Technologies, USA). The MDA-MB-231 cells were cultured in a humidified $CO_2$ incubator at 37°C. All the biological experiments were conducted after at least three passages.

### 7.6.6.2. Cytotoxicity study

The cytotoxic effect and cell viability percentages of BOHB at various concentrations on MDA-MB-231 cells, were estimated by cytotoxicity study using MTT reagent, based on our previously established lab protocol.[82] Briefly, $1 \times 10^4$ cells/well were plated in 96 well plates for 24 h. Then, the cells were treated with BOHB at a range of 0-80 μM and kept for 24 h. Afterwards, MTT reagent was added and incubated for 3-4 h. Finally, DMSO-Methanol (1:1) was added and all the absorbance values were taken at 570 nm in a microtiter plate-reader (Spectramax i3x). The percentage of cell viabilities at various concentrations were determined using the following formula:

Percentage (%) Cell viability = $[(A_{treated} - A_{blank}) / (A_{untreated} - A_{blank})] \times 100$

### 7.6.6.3. Live cell imaging study

The live cell imaging study was conducted based on our previously established lab protocol.[83]Briefly, MDA-MB-231 cells were plated at a density of $2 \times 10^5$ cells/well on sterile cover glasses placed in a 6 well plate and incubated for 24 h. Then, the cells were treated with only BOHB and two different dosages of BOHB along with 15 μM Cyanide. After 30 min of incubation, cells were subsequently washed with PBS and fixed with formalin (4%) for 1 h and again washed with PBS. Finally, the coverslips were mounted on the glass slides in glycerol and

the cellular morphologies were viewed at 40X magnification using a fluorescence microscope (Olympus).

# 7.7. Notes and references


1. R. V. Rathod, S. Bera and D. Mondal, *Spectrochim. Acta, Part. A*, 2020, **238**, 118419.
2. Sala, H. Brisset, A. Margaillan, J.-U. Mullot and C. Branger, *TrAC, Trends Anal. Chem.*, 2022, **148**, 116536.
3. M. Qiao, L. Ding and F. Lv, *Coord. Chem. Rev.*, 2021, **432**, 213696.
4. H. Gomaa, S. El-Safty, M. A. Shenashen, S. Kawada, H. Yamaguchi, M. Abdelmottaleb and M. F. Cheira, *ACS Sustainable Chem. Eng.*, 2018, **6**, 13813.
5. M. El-Sewify, M. A. Shenashen, A. Shahat, M. M. Selim, M. M. H. Khalil and S. A. El-Safty, *Microchem. J.*, 2018, **139**, 24.
6. S. Liu, D. Yang, Y. Liu, H. Pan, H. Chen, X. Qu and H. Li, *Sens. Actuators, B, Chem.*, 2019, **299**, 126937.
7. P. A. Gale, J. T. Davis and R. Quesada, *Chem. Soc. Rev.*, 2017, **46**, 2497.
8. J. T. Davis, P. A. Gale and R. Quesada, *Chem. Soc. Rev.*, 2020, **49**, 6056.
9. Q. Lin, F. Zheng, T.-T. Lu, J. Liu, H. Li, T.-B. Wei, H. Yao and Y.-M. Zhang, *Sens. Actuators, BChem.*, 2017, **251**, 250.
10. R. Arumugaperumal, V. Srinivasadesikan, M. V. R. Raju, M.-C. Lin, T. Shukla, R. Singh and H.-C. Lin, *ACS Appl. Mater. Interfaces*, 2015, **7**, 26491.
11. P. A. Gale, N. Busschaert, C. J. E. Haynes, L. E. Karagiannidis and I. L. Kirby, *Chem. Soc. Rev.*, 2013, **43**, 205.
12. N. Busschaert, C. Caltagirone, W. Van Rossom and P. A. Gale, *Chem. Rev.*, 2015, **115**, 8038.
13. D. M. Gillen, C. S. Hawes and T. Gunnlaugsson, *J. Org. Chem.*, 2018, **83**, 10398.
14. X. Y. Wen, L. Yan, Z. F. Fan, *J. Photochem. Photobiol. A Chem.*, 2021, **405**, 112969.
15. Z. M. Dong, H. Ren, J. N. Wang, Y. Wang, *Microchem. J.*, 2020, **155**, 104676.
16. T. S. Wang, L. Shen, H. X. Wang, H. N. Zhang, *J. Mol. Struct.*, 2021, **1231**, 129671.
17. D. Jothi, S. Munusamy, S. M. kumar, S. Enbanathan and S. K. Iyer, *RSC Adv.*, 2022, **12**, 8570.
18. M. A. Cherian and I. J. Richmond, *J. Clin. Pathol.*, 2000, **53**, 794.
19. M. Laforge, H. Gourlain, D. Fompeydie, F. Buneaux, S. W. Borron and M. J. Galliot-Guilley, *J. Toxicol., Clin. Toxicol.*, 1999, **37**, 337.
20. L. Xue, R. Wang, S. Qi, H. Xu, X. Wang, L. Wu, Q. Yang, J. Du and Y. Li, *Talanta*, 2021, **225**, 122100.
21. K. L. Deng, L. Wang, Q. Xai, R. Y. Liu, J. Q. Qu, *Sens. Actuators B Chem.*, 2019, **296,** 126645.
22. S. I. Baskin, T. G. Brewer, F. Sidell, E. T. Takafuji and D. R. Frenz, Medicinal Aspects of Chemical and Biological Warfare, TMM, Washington, DC, 1997, ch. 10, 271.
23. S. I. Baskin, J. B. Kelly, B. I. Maliner, G. A. Rockwood, C. K. Zoltani and D. T. Shirley, Medicinal Aspects of Chemical Warfare, TMM, Washington, DC, 2008, ch. 11, 331.
24. E. Cooper and G. C. Brown, *J. Bioenerg. Biomembr.*, 2008, **40**, 533.
25. R. Takano, *J. Exp. Med.*, 1916, **24**, 207.
26. Shan, C. Mousty and S. Cosnier, *Anal. Chem.*, 2004, **76**, 178.

27. K. W. Kulig, Cyanide Toxicity, U.S. Department of Health and Human Services, Atlanta, GA, 1991.
28. J. Z. Jiang, X. Y. Wang, W. J. Zhou, H. C. Gao and J. G. Wu, *Phys. Chem. Chem. Phys.*, 2002, **4**, 4489.
29. L. Xue, R. Wang, S. Qi, H. Xu, X. Wang, L. Wu, Q. Yang, J. Du and Y. Li, *Talanta*, 2021, **225**, 122100
30. J. D. Johnson, T. L. Meisenheimer and G. E. Isom, *Toxicol. Appl. Pharmacol.*, 1986, **84**, 464.
31. Baird and M. Cann, Environmental chemistry, Freeman, New York, 2005.
32. L. Nelson, *J. Emerg. Nurs.*, 2006, **32**, 8.
33. J. Y. Noh, I. H. Hwang, H. Kim, E. J. Song, K. B. Kim and C. Kim, *Bull.* Korean Chem. Soc., 2013, **34**, 1985.
34. B. Vennesland, E. E. Comm, C. J. Knownles, J. Westly and F. Wissing, Cyanide in Biology, Academic Press, London, 1981.
35. C. Baird and M. Cann, Environmental Chemistry, Freeman, New York, 2005.
36. W.-J. Qu, W.-T. Li, H.-L. Zhang, T.-B. Wei, Q. Lin, H. Yao and Y.-M. Zhang, *J. Heterocycl. Chem.*, 2018, **55**, 879.
37. M. H. Chua, H. Zhou, T. T. Lin, J. Wu and J. Xu, *J. Mater. Chem. C*, 2017, **5**, 12194.
38. B. Aydıner, Ö. Şahin, D. Çakmaz, G. Kaplan, K. Kaya, Ü. Ö. Özdemir, N. Seferoğlu and Z. Seferoğlu, *New J. Chem.*, 2020, **44**, 19155.
39. S. Li, F. Huo, K. Ma, Y. Zhang and C. Yin, *New J. Chem.*, 2021, **45**, 1216.
40. S. Malkondu, S. Erdemir and S. Karakurt, *Dyes Pigm.*, 2020, **174**, 108019.
41. A. Popczyk, Y. Cheret, A. El-Ghayoury, B. Sahraoui and J. Mysliwiec, *Dyes Pigm.*, 2020, **177**, 108300.
42. G. Sun, W. Chen, Y. Liu, X. Jin, Z. Zhang and J. Su, *Dyes Pigm.*, 2020, **176**, 108224.
43. Y. Liu, J. s. Du, S. l. Qi, L. b. Zhu, Q. b. Yang, H. Xu and Y. x. Li, *Luminescence.*, 2021, **36**, 336.
44. L. Long, X. Yuan, S. Cao, Y. Han, W. Liu, Q. Chen, Z. Han and K. Wang, *ACS Omega*, 2019, **4**, 10784.
45. P. S. Kumar, P. R. Lakshmi and K. P. Elango, *New J. Chem.*, 2019, **43**, 675.
46. L. Hou, F. Li, J. Guo, X. Zhang, X. Kong, X. T. Cui, C. Dong, Y. Wang and S. Shuang, *J. Mater. Chem. B*, 2019, **7**, 4620.
47. J. Kang, F. Huo, Y. Zhang, J. Chao, T. E. Glass and C. Yin, *Spectrochim. Acta, Part A*, 2019, **209**, 95.
48. Y. Hao, K. H. Nguyen, Y. Zhang, G. Zhang, S. Fan, F. Li, C. Guo, Y. Lu, X. Song, P. Qu, Y.-N. Liu and M. Xu, *Talanta*, 2018, **176**, 234.
49. S. Munusamy, S. Swaminathan, D. Jothi, V. P. Muralidharan and S. K. Iyer, *RSC Adv.*, 2021, **11**, 15656.
50. A.Maji, K. Aich, A. Biswas, S. Gharami, B. Bera and T. K. Mondal, *Analyst*, 2024, **149**, 1557.
51. J. Lebeda and S. S. Deshpande, *Anal. Biochem.*, 1990, **187**, 302.
52. J. Ma and P. K. Dagupta, *Anal. Chim. Acta*, 2010, **673**, 117.
53. N. Y. Kang, H. H. Ha, S. W. Yun, Y. H. Yu and Y. T. Chang, *Chem. Soc. Rev.*, 2011, **40**, 3613.
54. A. Arunjegan, P. Rajaji, S. Sivanesan and P. Panneerselvam, *RSC Adv.*, 2021, **11**, 12361.
55. R. Pavadai, A. Amalraj, S. Subramanian and P. Perumal, *ACS Appl. Mater. Interfaces*, 2021, **13**, 27.
56. A. Amalraj, R. Pavadai and P. Perumal, *ACS Omega*, 2021, **6**, 30580.
57. Amalraj, M. Narayanan and P. Perumal, *Analyst*, 2022, **147**, 3234.
58. Amalraj and P. Perumal, *New J. Chem.*, 2022, **46**, 12952.
59. S. Mondal, S. S. Ali, S. Manna, K. Maiti, Md. R. Uddin, S. Mandal, D. Mandal and A. K. Mahapatra, *New. J. Chem.*, 2017, **41**, 12581.

60. Long, J. -H. Hu, P. -W. Ni, Z. -Y. Yin and Q. -Q. Fu, *New. J. Chem.*, 2018, **42**, 17056.
61. M. H. Chua, H. Zhou, T. T. Lin, J. Wu and J. Xu, *J. Mater. Chem. C*, 2017, **5**, 12194.
62. Thanayupong, K. Suttisintong, M. Sukwattanasinittd and N. Niamnont, *New. J. Chem.*, 2017, **41**, 4058.
63. Y. Yue, F. Huo, C. Yin, J. Chao and Y. Zhang, *Sens. Actuators, BChem.*, 2015, **212**, 451.
64. J. Hu, J. Li, J. Qi and Y. Sun, *New J. Chem.*, 2015, **39**, 4041.
65. K. D. Prasad, N. Venkataramaiah and T. N. Guru Row, *Cryst. Growth Des.*, 2014, **14**, 2118
66. H.-X. Liu, X.-M. Fu, J.-H. Hu, *Inorg. Chem. Commun.*, 2022, **142**, 109662.
67. W. C. Lin, S. K. Fang, J. W. Hu, H. Y. Tsai and K. Y. Chen, *Anal. Chem.*, 2014, **86**, 4648.
68. L. Wang, L. Zhu and D. Cao, *New J. Chem.*, 2015, **39**, 7211.
69. A. Maji, A. Biswas, A. Das, S. Gharami, K. Aich and T. K. Mondal, *New J. Chem.*, 2023, **47**, 11557.
70. X. Lou, L. Qiang, J. Qin and Z. Li, *ACS Appl. Mater. Interfaces*, 2009, **1**, 2529.
71. Y.-Y. Guo, X.-L. Tang, F.-P. Hou, J. Wu, W. Dou, W.-W. Qin, J.-X. Ru, G.-L. Zhang, W.-S. Liu and X.-J. Yao, *Sens. Actuators, BChem.*, 2013, **181**, 202.
72. Q. Lin, Y. -P. Fu, P. Chen, T. -B. Wei and Y. -M. Zhang, *Tetrahedron Lett.*, 2013, **54**, 5031.
73. P. Zhang, B. Shi, X. You, Y. Zhang, Q. Lin, H. Yao and T. Wei, *Tetrahedron*, 2014, **70**, 1889.
74. Jothi, S. Munusamy, S. M. kumar, S. Enbanathan and S. K. Iyer, *RSC Adv.*, 2022, **12**, 8570.
75. S. Goswami, A. Manna, S. Paul, A. K. Das, K. Aich and P. K. Nandi, *Chem. Commun.*, 2013, **49**, 2912.
76. J. -P. Costes, C. Duhayon and L. Vendier, *Inorg. Chem.*, 2014, **53**, 2181.
77. X. Wu, J. Chen and J. X. Zhao, *Analyst*, 2013, **138**, 5281.
78. S. Qu, C. Zheng, G. Liao, C. Fan, G. Liu and S. Pu, *RSC Adv.*, 2017, **7**, 9833.
79. W. D. Foulkes, I. E. Smith and J. S. Reis-Filho, *N. Engl. J. Med.*, 2010, **363**, 1938.
80. T. Ovcaricek, S. G. Frkovic, E. Matos, B. Mozina and S. Borstnar, *Radiol. Oncol.*, 2011, **45**, 46.
81. F. Podo, L. M. C. Buydens, H. Degani, R. Hilhorst, E. Klipp, I. S. Gribbestad, S. Van Huffel, H. W. M. van Laarhoven, J. Luts, D. Monleon, G. J. Postma, N. Schneiderhan-Marra, F. Santoro, H. Wouters, H. G. Russnes, T. Sorlie, E. Tagliabue, A.-L. Borresen-Dale and F. Consortium, *Mol. Oncol*., 2010, **4**, 209.
82. S. Guha, D. Talukdar, G. K. Mandal, R. Mukherjee, S. Ghosh, R. Naskar, P. Saha, N. Murmu, G. Das, *J. Ethnopharmacol.*, 2024, **332**, 118389.
83. P. Mukherjee, S. Guha, G. Das, A. Samui, S. K. Sahu, *J. Photochem. Photobiol., A*, 2023, **443**, 114907.

# APPENDIX

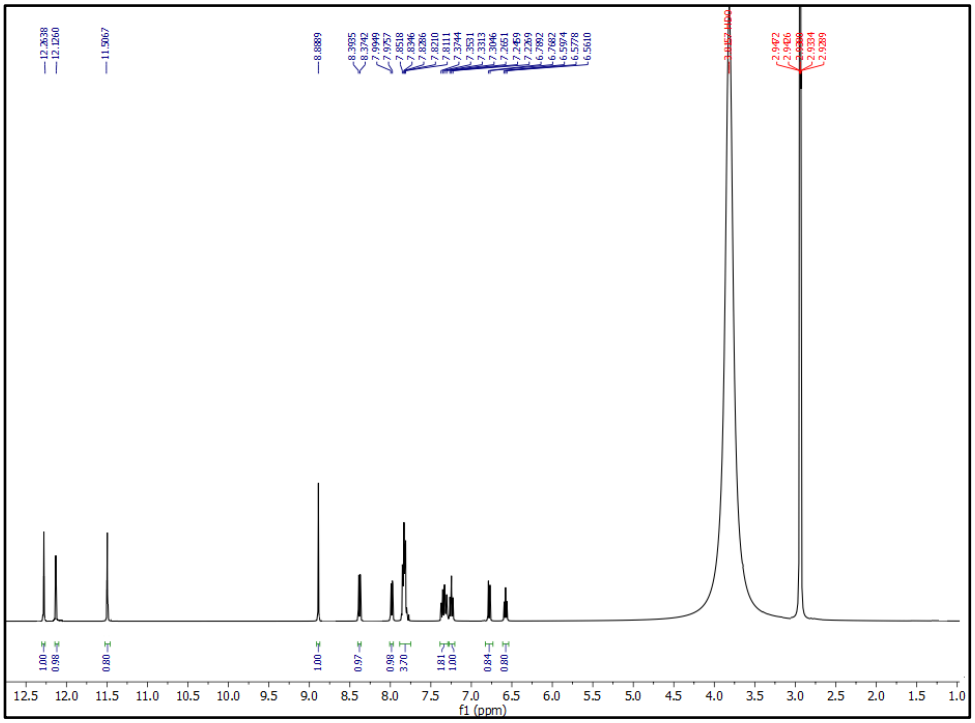


**Fig. A7.1:** $^{1}$H NMR (400 MHz) spectrum of the probe (BOHB) in DMSO-$d_6$

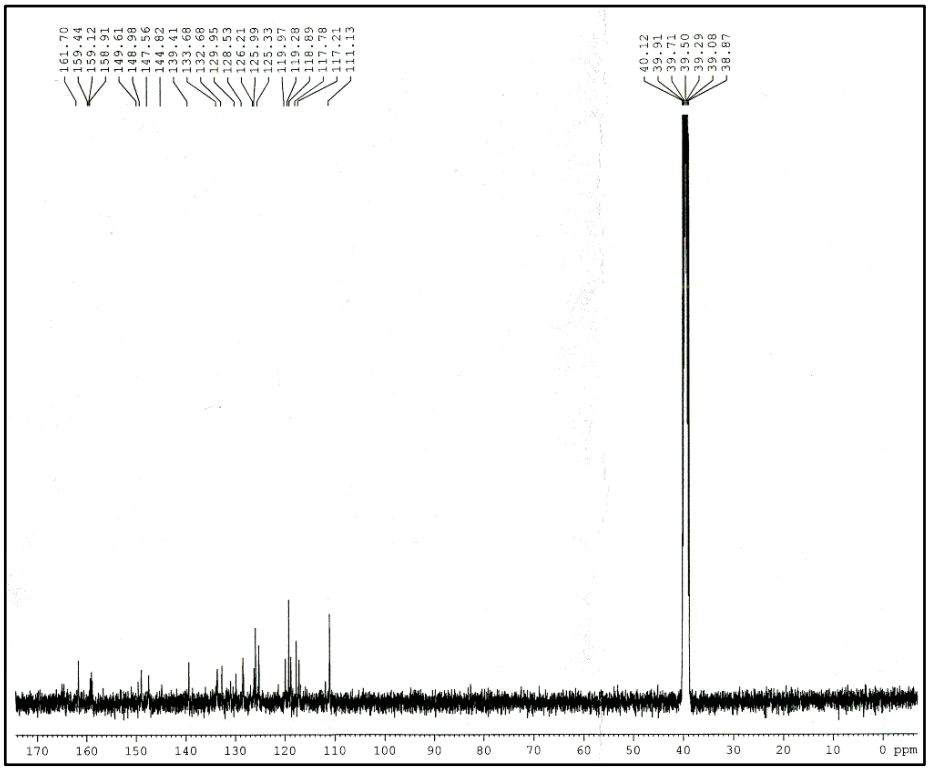


**Fig. A7.2:** $^{13}$C NMR (100 MHz) spectrum of the probe (BOHB) in DMSO-$d_6$

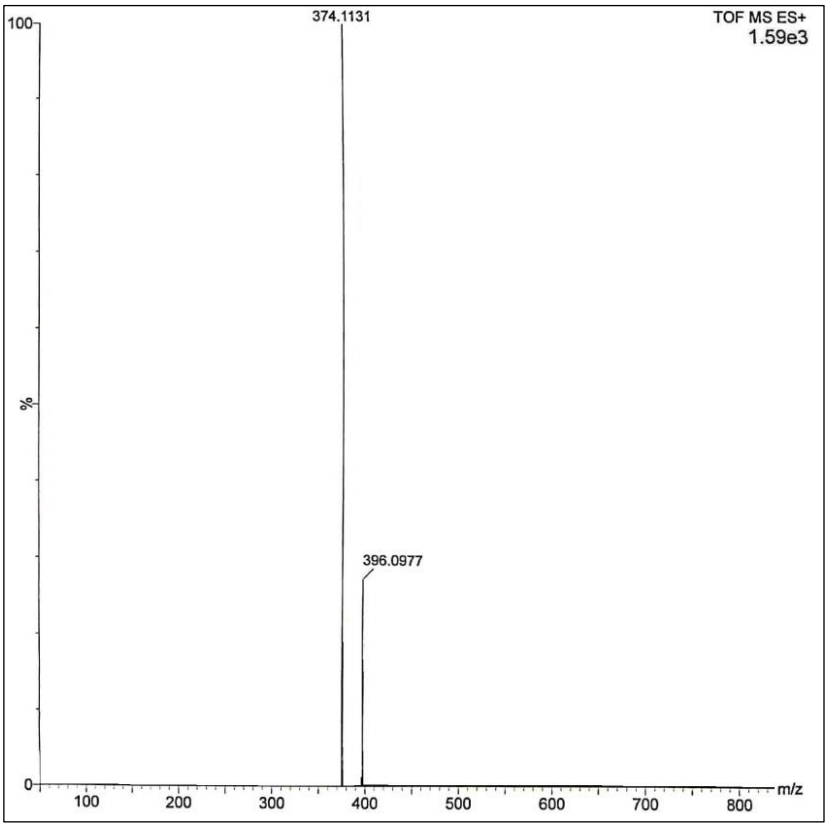


**Fig. A7.3:** HRMS of the probe (BOHB).

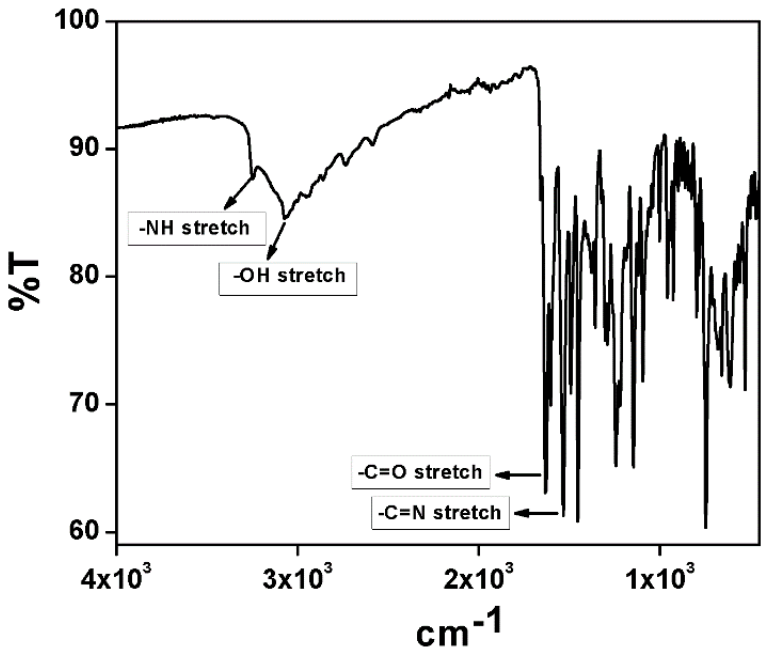


**Fig. A7.4:** IR plot of the probe (BOHB).

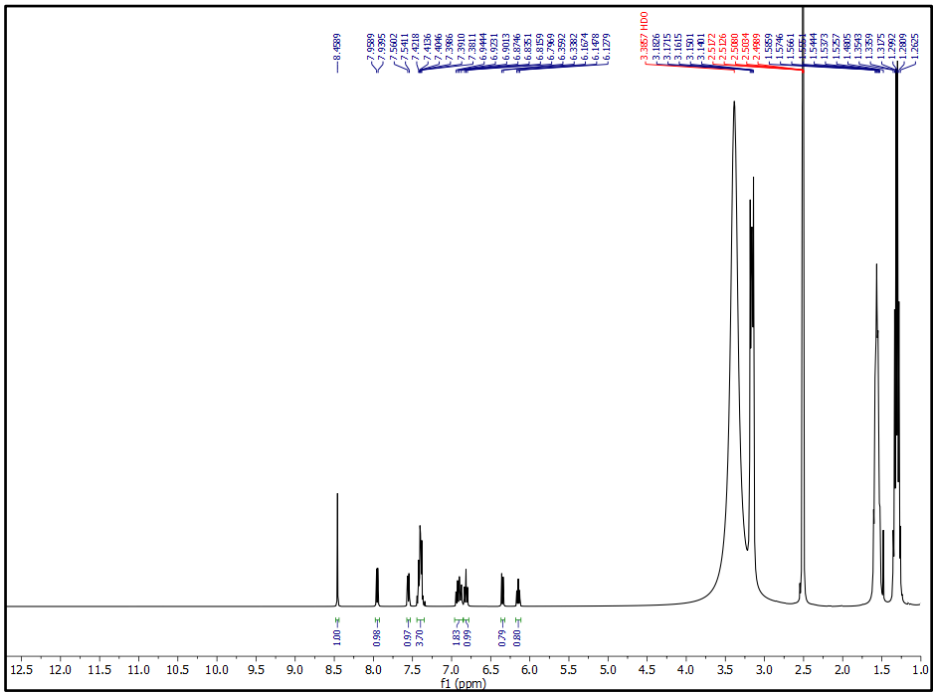


**Fig. A7.5:** $^{1}$H NMR (400 MHz) spectra of the PBIA-CN adduct in DMSO-$d_6$.

**Table A7.1:** Lifetime decay profile of BOHB and BOHB-$CN^-$

| Methanol (Solvent) | Quantum Yield | τ (ns) | $K_r$ ($10^8$ x $S^{-1}$) | $K_{nr}$($10^8$x $S^{-1}$) |
|---|---|---|---|---|
| BOHB | 0.245 | 2.33 | 1.051 | 3.241 |
| BOHB-$CN^-$ | 0.098 | 0.92 | 1.065 | 0.021 |

**Table A7.2:** The comparison of the present probe (BOHB) with some previous probes for $CN^-$

| Probe | Type of response | Response Time (min or sec) | Solvent System | Detection limit | Reference |
|---|---|---|---|---|---|
| 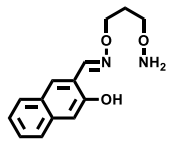 | colorimetric and fluorescent ratiometric turn-on | < 3 seconds | DMSO/$H_2O$, 9/1 | 2.16 ×$10^{-7}$ M | *New J. Chem.*, 2020, **44**, 21038. |
| 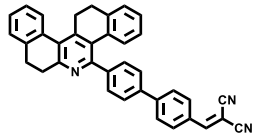 | Fluorescence turn-off | Within 20 seconds | Acetonitrile | 3.93 ×$10^{-8}$ M | *RSC Adv.*, 2020, **10**, 11791. |
| 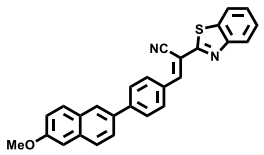 | Ratiometric fluorescence change | Within 2 minutes | DMSO/$H_2O$, 1/1 | 2.1(±0.0022) × $10^{-8}$ M | *Anal. Methods*, 2022, **14**, 3209. |
| 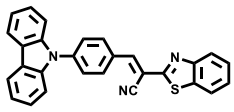 | Ratiometric fluorescence change | Within 22 seconds | DMSO/$H_2O$, 40/60 | (7.68 ± 0.29) × $10^{-8}$ M | *New J. Chem.*, 2023, **47**, 11557. |
| 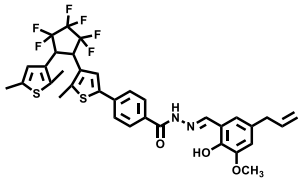 | Fluorescence turn-on | - | Acetonitrile | 1 ×$10^{-7}$ M | *New J. Chem.*, 2022, **46**, 2411. |
| 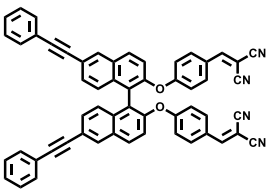 | Ratiometric fluorescence (blue shift) | Within 1 second | $CH_3CN$/HEPES in water, 7/3 | 1.89×$10^{-7}$ M | *RSC Adv.*, 2021, **11**, 15656. |
| 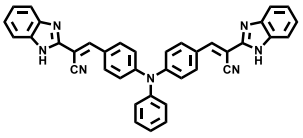 | Ratiometric fluorescence change | Within 20 seconds | DMSO | (6.56 ± 0.26) ×$10^{-8}$ M | *Sens. Diagn.*, 2024, **3**, 1201. |

| | | | | | |
|---|---|---|---|---|---|
| 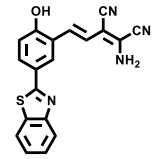 | Fluorescence turn-on | - | DMSO/$H_2O$, 7/3 | $1.4\times10^{-7}$ M | *Dyes Pigm.*, 2020, **174**, 108019. |
| 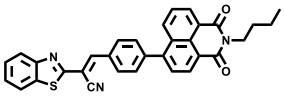 | Fluorescence turn-on | - | THF | $3.4\times10^{-8}$ M | *Spectrochim Acta A.*, 2021, **252**, 119535. |
| 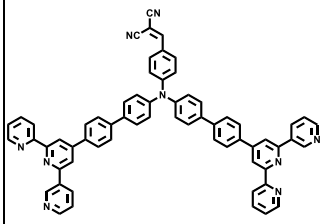 | Fluorescence quenching | - | $H_2O$/THF, 9:1 | $3.8\times10^{-6}$ M | *Dyes Pigm.*, 2020, **173**, 107969. |
| 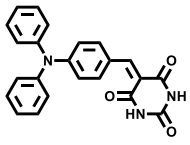 | Fluorescence quenching | - | DMSO/$H_2O$, 1/99 | $2.95\times10^{-8}$ M | *Dyes Pigm.*, 2021, **193**, 109534. |
| 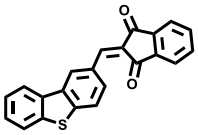 | Fluorometric turn-off | 15 seconds | DMSO/$H_2O$, 1/99 | $2.26\times10^{-7}$ M | *J. Photochem. Photobiol. A. Chem.*, 2021, **405**, 112993. |
| 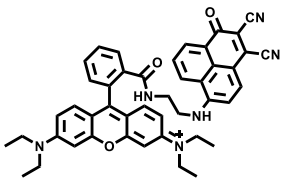 | Fluorometric (turn-off) | - | MeOH/$H_2O$, 4/1 | $1.3\times10^{-7}$ M | *ChemistrySelect*, 2020, **5**, 13429. |
| 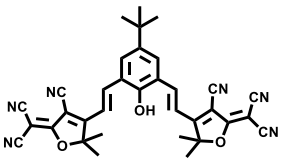 | Fluorometric (turn-on) | - | DMSO | $7.0\times10^{-8}$ M | *Spectrochim Acta A.*, 2023, **302**, 123054. |

| | | | | | |
|---|---|---|---|---|---|
| 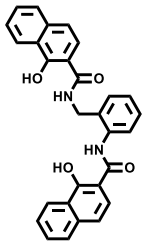 | Fluorometric (turn-on) | Within 8 minutes | DMSO/$H_2O$, 8/2 | $2.65\times10^{-7}$ M | *J. Photochem. Photobiol. A. Chem.*, 2023, **440**, 114661. |
| 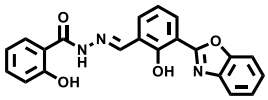 | Fluorometric (ratiometric) | Almost 15 seconds | MeOH/$H_2O$, 1/1 | (22.1±0.89) μM | **Present Work** |

# Chapter 8

# An ICT based organic framework for fluorogenic detection of lethal pulmonary agent phosgene

# An ICT based organic framework for fluorogenic detection of lethal pulmonary agent phosgene

## Abstract

Fluorescent chemosensors detecting a widely used but highly toxic chemical warfare agent (CWA) such as phosgene is of great importance due to their high sensitivity along with low cost and simple method of preparation. In this paper, a biphenyl-benzoimidazole based (BPCI) chemodosimeter was developed which displays a rapid, sensitive and ratiometric detection towards lethal pulmonary agent phosgene. Upon addition of phosgene to BPCI solution in THF, we observed a fluoroscence color change from blue to cyan-green. The chemodosimeter (BPCI) undergoes nucleophilic substitution reaction with phosgene followed by a ring closure to yield the carbamylated final product and shows an explicit ratiometric fluorescence response towards phosgene. The carbamylation was accelerated due to formation of six membered ring which restricts the C-C bond rotation. The probe (BPCI) selctively detected phosgene over other toxic relevant analytes. Now the detection limit (LOD) of BPCI towards phosgene was established to be in the order of $10^{-7}$ M in solution phase which implied that BPCI can detect phosgene in very minuscule level. This ratiometric switch which we developed, can be used as a potential portable kit for detecting phosgene in vapour phase, as well as in solid phase when supported upon TLC plates. Theoretical calculation by DFT/B3LYP/6-31+G(d) method was performed to unveil the electronic properties theoretically and to interpret the probable sensing mechanism.

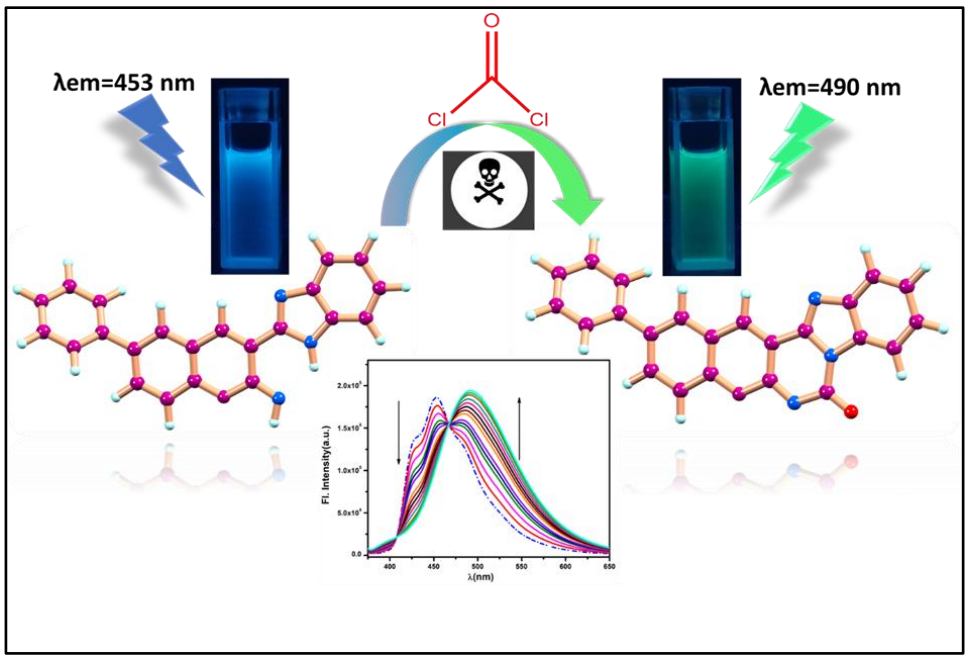

# 8.1. Introduction

In the history of human existence, the weapons which were made for mass destruction (WMD), among them chemical warfare agents are known to be most ferocious created by mankind.[1] These Chemical warfare agents (CWAs) can be categorized as nerve agents, blistering agents, pulmonary agents, blood agents, tear gases, psychomimetic agents, incapacitating agents, toxins etc.[2] Among these CWAs, phosgene is included in the list of pulmonary agents as the most threatening to the humanity.[3] Due to its catastrophic nature phosgene ($COCl_2$) was employed as a chemical warfare agent (CWC) in the World War I and World War II and the poisonous gas bombs made from it, caused mammoth causalities to the humankind.[4-6] Even with a low exposure limit of this colourless phosgene gas up to 0.1 ppm, it can cause serious irritation to eyes, skin, nose, lungs and respiratory system.[7] Outrageous exposure of about 90 ppm of phosgene for 30 minutes can cause dangerous repercussions, such as it induces pulmonary edema, pulmonary emphysema and finally leads to death.[8-12] The production of nerve agents such as sarin, soman, tabun are strictly controlled and prohibited by international laws.[13] But in contrast, due to dynamic nature of phosgene such as cost effectiveness, high reactivity and easy availability, it has wide application in several industries.[14] For instance, it is used as a precursor for the industrial production of chemicals, isocyanate based polymer material, pharmaceuticals, aniline dyes and different type of pesticides such as chloroformates, sulfonylureas.[15-18] Hence due to its in hand accessibility it can be potentially exploited by terrorists as chemical weapons. As well as unexpected industrial leakages can also cause havoc destruction to the mankind. Thus, it is indispensable to construct reliable, cost effective, selective, and sensitive approaches for detecting phosgene, the alerting threat to humanity.

There are various old age techniques for detection of phosgene such as gas chromatography method, HPLC technique, electrochemical methods, Raman techniques.[19-26] However these techniques are criticized due to complexity in sample preparation, poor portability, expensive precious instrumentation, sophisticated procedures. In contrast, fluorescent-based detection of phosgene has gained a progressive interest. This could be attributed to several advantages such as simple preparation procedure, quick response time, suitable in field detection, high selectivity with sensitivity and simple operation techniques.[27-28]

## 8.2. Prior works

Over the past few years, there are several fluorescent probes that have been reported for detection of phosgene utilizing different fluorophores such as coumarins,[29-30] benzothiadiazole,[31] rhodamines,[32-33] napthalimides,[34-37] anthracene carboxyimides,[38-39] BODIPYs[40-43] and others.[44-45] Usually, the molecular design involves the phosgene mediated reaction which involves the electron donating amine or hydroxyl group present in these sensors. Reacting with phosgene, they generally form cyclic compounds generating carbamate or urea groups. These transformation generally includes different mechanisms such as suppression of fluorescence quenching processes, photoinduced electron transfer (PET),[41,43] generation of intramolecular charge transfer (ICT)[31,46] or prohibition of excited state intramolecular proton transfer (ESIPT).[29,34-35] There are also reports of phosgene detection which includes opening of hetero-cross-linking of two amino containing spiro deoxy (lactam) to generate a fluorescent rhodamine,[47] phosgene can also induce hetero-cross-linking of two amino containing fluorophores to achieve fluorescence resonance electron transfer (FRET)[48] and conversion of cinnamic acids into fluorescent coumarins.[49]Also previously Yoon and coworkers developed four sensors with novel design strategy such as they have covalently linked o-phenylenediamine to a fluorophore to develop a nonfluorescent sensor due to intramolecular electron transfer which after sensing phosgene, generates a fluorescent product to block the electron transfer process.[50-51] Despite of the successful application of these elegant sensors, most of them are based on fluorescence turn-on mode.[52-58] Also selectivity of the above sensors was not investigated to discriminate between phosgene and a nerve-gas mimic DCP except for the sensor PY-OPD.[59] However there are relatively inadequate number of reports on ratiometric detection of phosgene.[29,34,39,46,60,61]

## 8.3. Present work

Herein, we have designed and introduced a highly sensitive fluorogenic chemosensor named BPCI after its precursor biphenyl and benzimidazole derivative. Due to presence of two nucleophilic NH moiety in the probe, it readily reacts with electrophilic phosgene to generate a cyclic carbamate moiety BPCI-PHOS adduct. It is observed that BPCI-PHOS adduct have different intramolecular charge transfer (ICT) characteristics compared to BPCI. Thus, it results in a ratiometric fluorescence response towards phosgene. Notably, BPCI is found to exhibit high

selectivity and sensitivity towards phosgene over other nerve agent mimic and other relevant analytes. Portable filter paper test strips as well as TLC sticks have also been prepared which conveniently gives fluorescence response towards phosgene in gas phase and via solid platform. Thus, all these tests have empowered our synthesized probe BPCI, as a fast reliable probe for onsite detection of phosgene, which opens its broad application prospects.

# 8.4. Results and discussions

## 8.4.1. Synthesis of the probe (BPCI)

Very economically cheap precursor i.e., 4 phenyl phenol, o-phenylene diamine and ethyl cyanoacetate were used for the synthesis of our probe BPCI. The synthetic design of **BPCI** was shown in (Scheme 8.1) where compound 'a' and 'b' were prepared using our previously reported procedure.[62-63] Then 4-hydroxy-[1,1'-biphenyl]-3-carbaldehyde(a) was reacted with 2-(1H-benzo[d]imidazol-2-yl) acetonitrile (b) in presence of piperidine in ethanol medium which yielded our desired probe (BPCI). Further the probe BPCI was thoroughly characterized by elemental analysis, $^{1}$H NMR, $^{13}$C NMR, IR and HRMS spectroscopic method which are given in electronic supplementary information (Fig. A8.1-A8.4, Appendix).

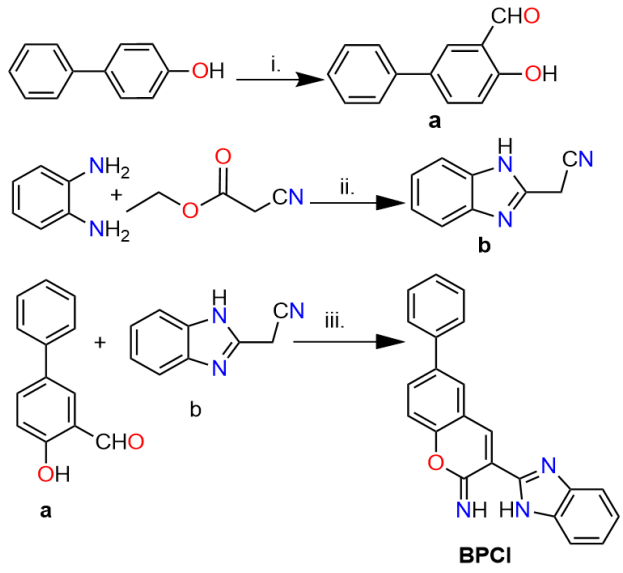


**Scheme 8.1:** Synthesis of the probe (BPCI). Reagents and conditions: (i) TFA, hexamine, 90-100$^{0}$C, reflux, 6 h; (ii) $I_2$, 180-200$^{0}$C, 2 h; (iii) piperidine, EtOH, reflux.

## 8.4.2. Spectral characterization and analysis of BPCI & BPCI-PHOS

$^{1}$H-NMR spectrum of BPCI is recorded in DMSO-$d_6$ which shows singlet peaks at 12.78 and 9.18 corresponded to the imidazole and imine proton present in BPCI,the aromatic ring protons appeared as expected in the region δ 7.15-8.37 ppm, whereas in case of BPCI-PHOS those two singlet peaks disappeared, which suggested the involvement of these two nitrogen centres in the ring formation. While in $^{13}$C NMR also for BPCI-PHOS, we observed an additional peak at 191.88 which corresponded to the carbonyl carbon atom. HRMS ofthe probe (BPCI) shows a peak at m/z 338.0914, while for BPCI-PHOS, a new peak at m/z 364.2578 is observed, which may be due to the formation of $[BPCI\text{-}PHOS+H]^{+}$.

## 8.4.3. Sensing studies of the probe (BPCI) in solution phase

The sensing properties of the probe BPCI was analysed in THF solution. The sensing property of the probe was examined in presence of diethylchlorophosphate (DCP), diethylcyanophosphate (DCNP), acetic acid ($CH_3COOH$), triethyl phosphate (TEP), tributyl phosphate (TBP), $POCl_3$, $SOCl_2$, $CH_3COCl$, p-toluenesulfonic acid (PTSA) and phosgene in THF solution. The changes after interaction of BPCI with phosgene in UV-Vis and fluorescence spectra were shown in (Fig8.1, Fig8.2). Our ICT induced biphenyl benzoimidazole based organic framework showed excellent ratiometric change in fluorescence spectrum with phosgene. This spellbinding approach of our chemosdosimeter (BPCI) with highly distinct ratiometric fluorescence response solely towards phosgene was prominent in liquid and vapour phase as well as via solid platform.

### 8.4.3.1. Phosgene sensing studies of BPCI using UV-Vis spectroscopy

The absorption spectral studies of our probe BPCI were carried out in THF solution. The probe itself showed absorption bands at 387 nm with two shoulder peaks at 370 nm and 408 nm respectively. While upon gradual addition of phosgene solution into the BPCI solution the two peaks at 408 nm and 370 nm were disappeared. Although the absorbance maxima of the peak at 387 nm decreased, it could be observed although very slightly. Simultaneously, we observed two new bands, a broad band at 435 nm and 354 nm with formation of a shoulder peak at 338 nm whereas two distinct isosbestic points at 418 nm and 360 nm were observed respectively.

(Fig.8.1) To establish the selectivity of BPCI solely towards phosgene, UV-Vis studies were executed in presence of other relevant and available analytes such as DCP, DCNP, TEP, TBP, AcOH, $POCl_3$, $SOCl_2$, $CH_3COCl$, and p-TSA respectively. Except $POCl_3$, $SOCl_2$ and $CH_3COCl$, other analytes did not show any significant changes in UV-Vis spectral pattern (Fig. 8.1). The interaction of $POCl_3$, $SOCl_2$, $CH_3COCl$ with probe could be attributed to protonation of the nitrogen atom present in BPCI, which resulted in the change in UV-Vis spectral pattern.

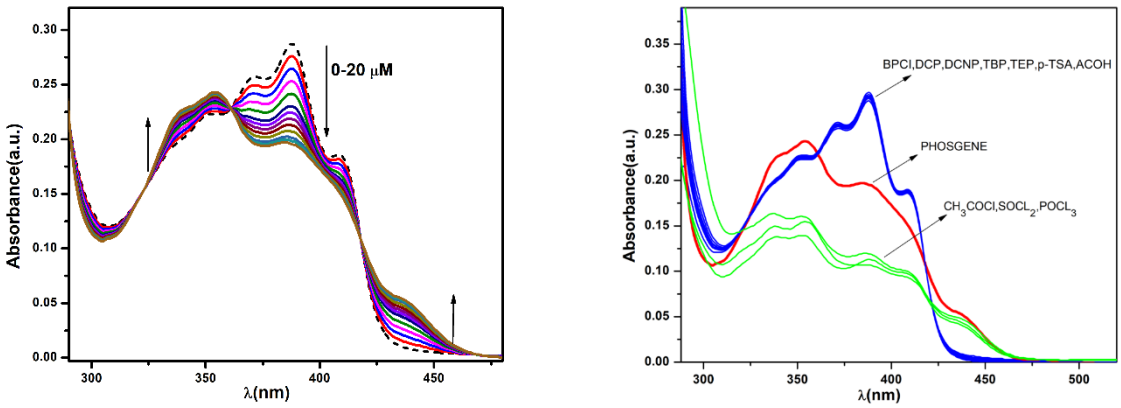


**Figure 8.1:** Absorption spectra of BPCI (10 μM) upon gradual addition of phosgene (20 μM) in THF solution (left side) and change in absorption spectrum of BPCI (10 μM) upon addition of different guest analytes (20 μM) in THF solution (right side).

### 8.4.3.2. Phosgene sensing studies of BPCI using fluorescence spectroscopy

The fluorescence spectra of BPCI (10 μM) was recorded in THF solution with gradual addition of phosgene solution. We observed, upon excitation at 360 nm the probe itself showed a strong emission band at 453 nm and the emission quantum yield was found to be 0.182. But upon gradual addition of phosgene to BPCI solution (20 μM), we observed the peak at 453 nm was gradually decreased along with its small humps, with simultaneous shifting of the peak towards longer wavelength.

After a certain time, we noticed the peak at longer wavelength shifted to 490 nm and gradually intensified with a distinctive isoemissive point at 467 nm. Hence, we observed a sharp red shift of 37 nm which clearly accounted for a sharp ratiometric emission change with slight enhancement of the fluorescence intensity. Subsequently, the change in the emission resulted in the emission colour change from blue to cyan-greenish under UV light (Fig. 8.2).

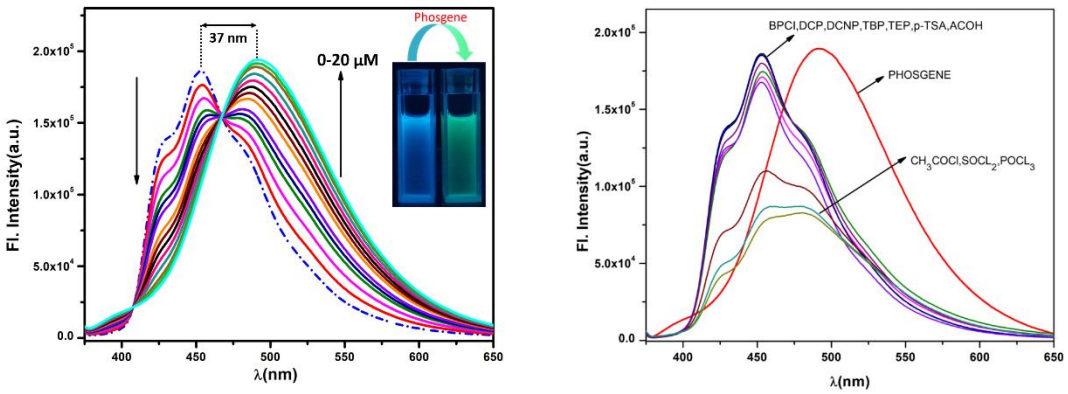


**Figure 8.2:** Emission spectra of BPCI (10 µM) upon the gradual addition of phosgene (20 µM) in THF solution. Inset: visible emission colour change of BPCI in the absence and presence of phosgene under UV light ($\lambda_{ex}$ = 360nm) (left side) and change in emission spectra of BPCI (10 µM) in presence of different guest analytes (20 µM) in THF solution (right side).

The Commission International de L'Eclairage (CIE) chromaticity coordinates (Fig. 8.3) also exhibited noteworthy changes from blue to cyan-green with a coordinate variation from (0.1602, 0.1505) to (0.2103, 0.3610). The emission quantum yield value also increased upto 0.291. The change in the fluorescence intensity could be attributed to nucleophilic substitution by BPCI to give the carbamylated product (Scheme 8.2). Hence BPCI could be converted to its carbamylated product after encountering with phosgene, where we noticed a ratiometric fluorometric response.

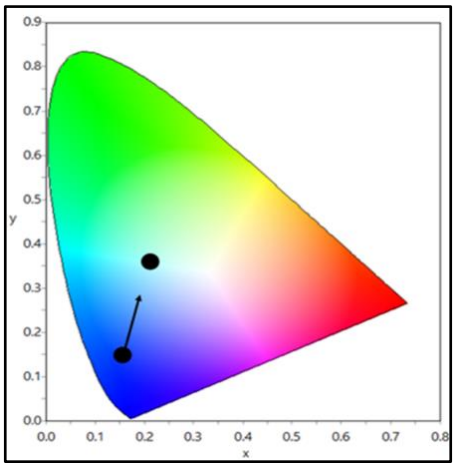


**Figure 8.3:** The CIE1931 Chromaticity diagram of probe BPCI with analyte phosgene.

The fluorescence aptitude of the chemodosimeter, BPCI was also studied in presence of the other similar toxic guest analytes like $CH_3COOH$, DCP, DCNP, TEP, TBP, P-TSA, $POCl_3$, $SOCl_2$, $CH_3COCl$ to disclose whether they had any significant sensing response towards BPCI or not. It was observed that DCP, DCNP, TEP, TBP, P-TSA, $CH_3COOH$ did not show any significant changes in the spectral pattern. While for $POCl_3$, $SOCl_2$ and $CH_3COCl$ the probe responded slightly, this might be due to the protonation of BPCI (Fig. 8.2). However, for phosgene the spectral pattern was completely different than these other analytes. Therefore, it can be concluded that phosgene interacted with BPCI in a different way to give this different fluorescence response.

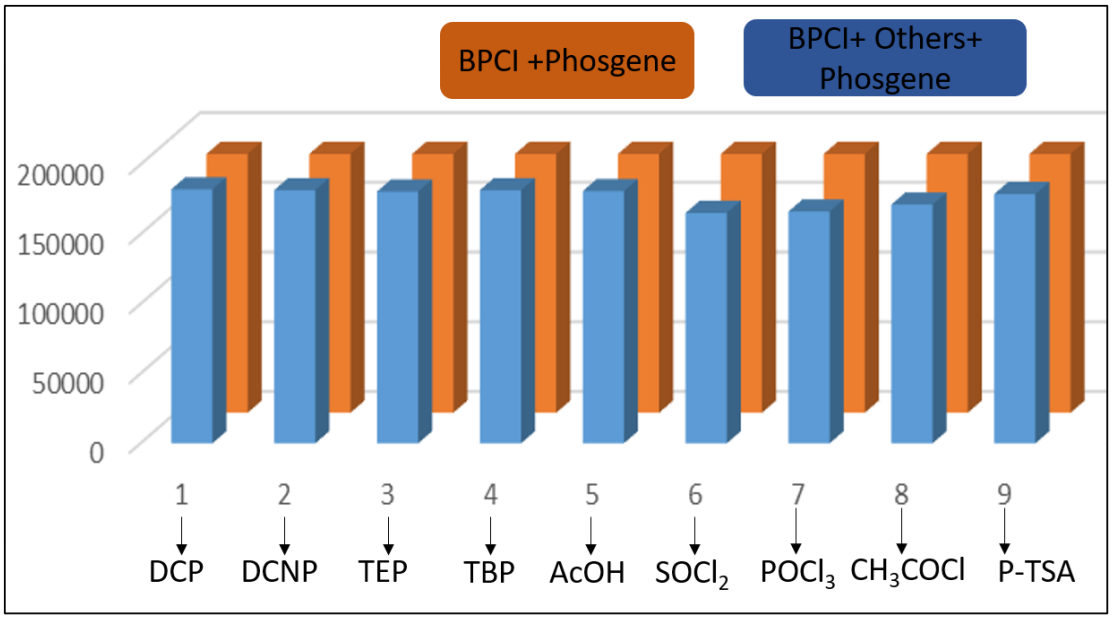


**Figure 8.4:** A comparative study of emission intensity (at 490 nm) after the addition of different analytes in the solution of BPCI in the presence of phosgene.

Therefore, to acknowledge the responsiveness of BPCI towards phosgene, fluorescence response of BPCI-PHOS solution was measured in presence of $CH_3COOH$, DCNP, TEP, TBP, DCP, $POCl_3$, $CH_3COCl$, $SOCl_2$, and PTSA (Fig. 8.4, Fig. 8.5). It was observed that these analytes do not alter the fluorescence intensity significantly, thus BPCI can detect phosgene in presence of other analytes with high efficiency. Therefore, BPCI could be established as a potential ratiometric sensor for the exclusive detection of phosgene in THF solution. Here this noteworthy ratiometric emission change of BPCI was accountable to the intermolecular charge transfer (ICT) mechanism.

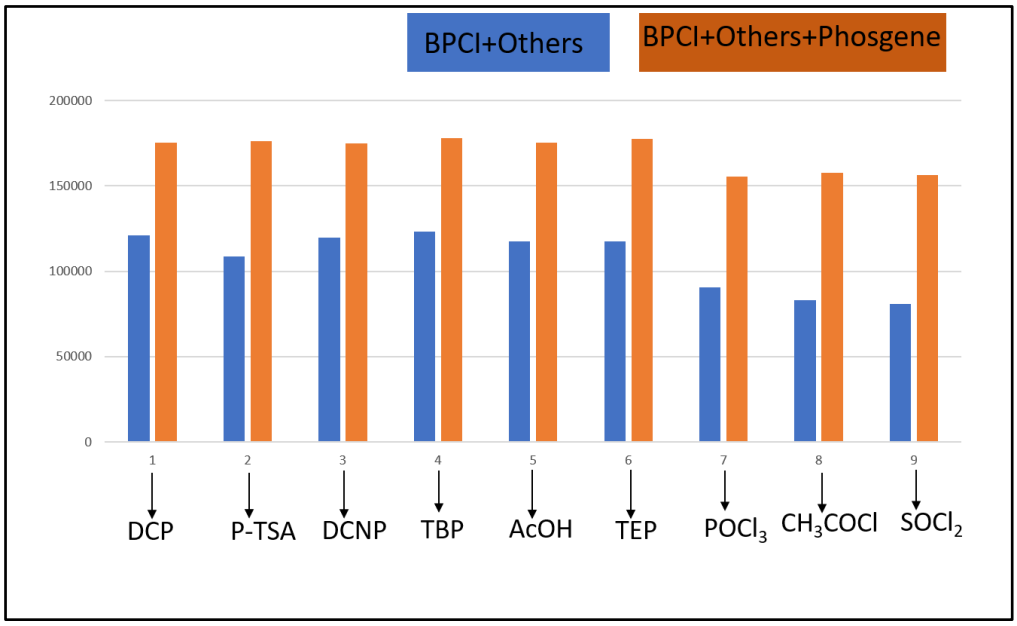


**Figure 8.5:** A comparative study of emission intensity (at 490 nm) after the addition of phosgene in the solution of BPCI in the presence of different analytes.

### 8.4.3.3. The binding studies of BPCI with Phosgene

For quantitative measurement of phosgene, a ratio of the change in fluorescence intensity ($F_{490}/F_{453}$) with concentration was plotted. It was observed that with concentration change the emission intensity ($F_{490}/F_{453}$) changes almost linearly. We know that one of the salient feature of a potent chemosensor is that its limit of detection must be low towards its target analyte. We calculated limit of detection (LOD) using the equation $LOD = K \times Sb_1/S$, where $K = 3$, $Sb_1$ is the standard deviation of the blank solution and S stands for slope of the linear calibration curve respectively. Using the fluorescence titration experiment, where with addition of phosgene the linear relationship was obtained with a good $R^2$ value of 0. 9905. Therefore, LOD was calculated and found to be $(4.25 \pm 0.19) \times 10^{-7}$ (M) (Fig. 8.6). Hence our probe could be used for on spot detection of phosgene.

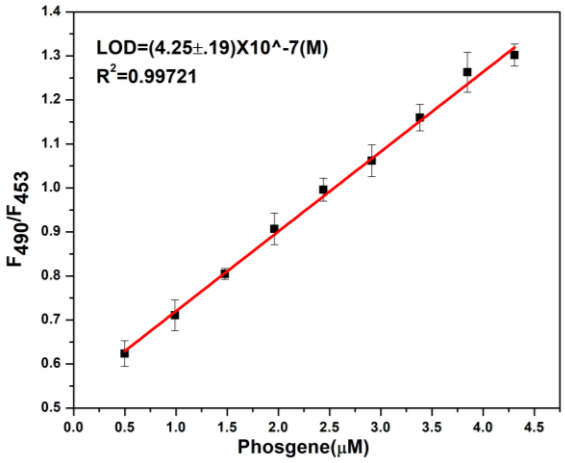


**Figure 8.6:** The linear response curve of emission intensity ratio ($F_{490}/F_{453}$) of BPCI as a function of phosgene concentration ($\lambda_{ex}$= 360nm).

### 8.4.3.4. Time dependent fluorescence study of BPCI with phosgene

Again, another aspect of a proficient chemodosimetric probe is that it should detect its guest analyte within short span of time. Hence, the time-dependant emission response of the probe, BPCI was performed towards phosgene to assess the response time. The fluorescence response was performed over 0-8 min time period with addition of phosgene into it (Fig. 8.7). We noticed that the fluorescence intensity at 490 nm began to enhance almost from 100 seconds and then the saturation in the curve reached almost around 230 seconds. Hence the plateau noticed after 230 seconds indicated the closure of the reaction. Thus, it could be concluded that our synthesized probe, BPCI was highly competent in detecting phosgene within 4 minutes, which is comparable one or even lower compared to some previously reported probes (Table A8.3, Appendix).

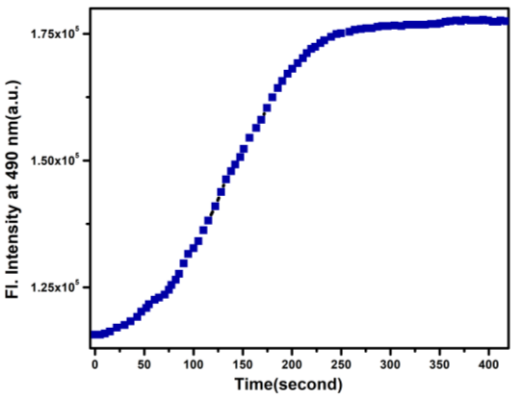


**Figure 8.7:** Time dependent emission spectra of BPCI (10 μM) after addition of phosgene (20 μM), noted within 0-8 min time interval in THF solution.

## 8.4.4. Fluorescence lifetime Study

To evaluate the excited state stability, we carried out nano second time resolved fluorescence study. We measured the fluorescence lifetime of BPCI and its adduct BPCI-PHOS. The lifetime decay profile of BPCI was found to be mono-exponential and lifetime was calculated 0.9463 ns. While for BPCI-PHOS adduct also by fitting the mono-exponential decay curve with acceptable $\chi 2$ value, lifetime was evaluated to be 1.4451 ns. The decay profile of BPCI and BPCI-PHOS were shown in (Fig. 8.8). The radiative rate constant ($k_r$) and the non-radiative rate constant ($k_{nr}$) of BPCI, BPCI-PHOS were calculated according to the equation $\tau^{-1} = k_r + k_{nr}$ where $k_r = \phi_f/\tau$, after due evaluation of quantum yield values for both the species (Table A8.1, Appendix). Hence the increase in lifetime and radiative rate constant values whereas simultaneous decrease in non-radiative rate constant values could be attributed to the rigidity gain by the structure i.e., by the formation of carbamylated product assisted by two nitrogen centre present in BPCI after reaction with phosgene.

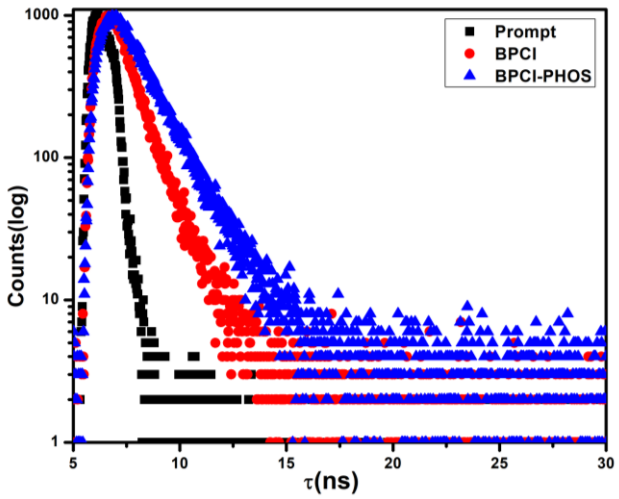


**Figure 8.8:** Time-resolved fluorescence decay of BPCI (●●●), BPCI-PHOS adduct (▲▲▲) and prompt (■■■) in THF ($\lambda_{ex}$ =360 nm).

## 8.4.5. Probable sensing mechanism of BPCI

The binding mode of this chemodosimeter (BPCI) with Phosgene was shown in the pictorial representation in scheme 2, where it was illustrated that the nucleophilic attack from N-atom of the benzimidazole group and imine nitrogen towards phosgene generated a cyclic carbamylated structure. This substituted adduct, BPCI-PHOS which acted as a rigid fluorophore, was

accountable for all the spectral changes of BPCI on addition of Phosgene. The probe itself was a fluorescent one (fluorescent maxima 453 nm) due to presence of electron rich centres such as imine nitrogen and benzimidazole moiety, which was responsible for ICT (Internal charge transfer). Thus, the chemodosimeter displayed bluish fluorescence when held under UV light. When exposed to phosgene the fluorescence maxima changed to 490 nm, thereby resulting in a colour change from bluish to cyan-green under UV light. This could be attributed to generation of a different ICT process with slight increase in intensity from the carbamylated amine donor site. Here, the different ICT mechanisms which was present in BPCI and BPCI-PHOS resulting in blue to cyan-green colour change could be attributed to the magnitude of electron push pull effect

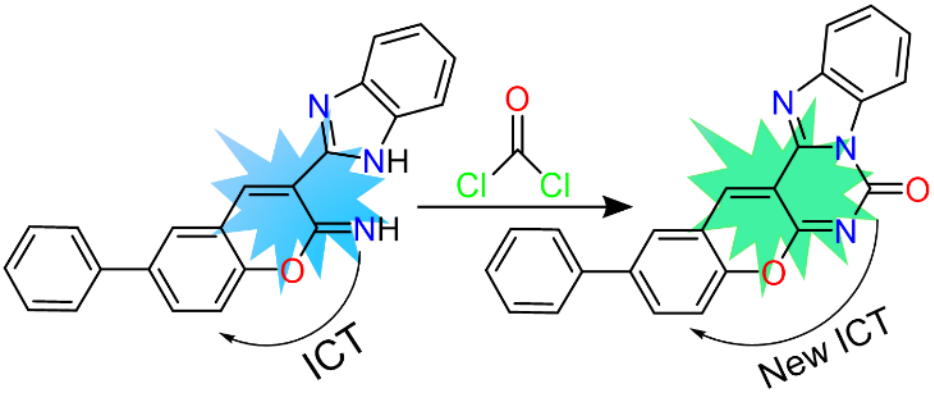


**Scheme 8.2:** Probable sensing mechanism of BPCI with phosgene.

This proposed sensing mechanism was further established by analysing $^{1}H$ NMR, $^{13}C$ NMR spectroscopic analysis. As shown in (Fig. A8.1, Appendix) the singlet peaks at 12.78 and 9.18 corresponded to the imidazole and imine proton present in BPCI, whereas in case of BPCI-PHOS those peaks disappeared (Fig. A8.5, Appendix), which suggested the involvement of these two nitrogen centres in the ring formation. While in $^{13}C$ NMR also for BPCI-PHOS, we observed an additional peak at 191.88 which corresponded to the carbonyl carbon atom. (Fig. A8.6, Appendix) To further support the formation of BPCI-PHOS adduct, HRMS was also executed. The HRMS of BPCI-PHOS showed a new molecular ion peak located at 364.2578 (m/z) which agreed well with molecular peak of the predicted adduct BPCI-PHOS $[M+H]^{+}$ (calcd. 364.1086 for $C_{23}H_{14}N_3O_2$) (Fig. A8.7, Appendix). Further the sensing mechanism towards phosgene was confirmed by the DFT calculations. The frontier molecular orbital involved were shown in (Fig. Fig. A8.8-Fig. A8.9, Appendix), where the orbital electron cloud distribution suggested that ICT

mechanism existed in both BPCI and BPCI-PHOS. Same could be shown for BPCI. The electron density (Fig. A8.8, Appendix) on the lowest unoccupied molecular orbital (LUMO) mainly distributed to the imine nitrogen and the ring attached to it. But in case of BPCI-PHOS, the electron density for LUMO was concentrated in newly formed carbamylated ring. The energy of LUMO also got reduced from -2.42 eV to -3.2 eV and also the distribution of electron cloud of HOMO changed accordingly. By further calculating the HOMO-LUMO energy gap for BPCI-PHOS, it was found to be $\Delta E = 3.09$, which was much smaller compared to BPCI ($\Delta E = 3.39$). This decrease in the energy gap suggested that it was feasible for BPCI to react with phosgene to give the stable BPCI-PHOS adduct and the small HOMO-LUMO energy gap increased the achievability of strong fluorescence.

### 8.4.6. Vapour phase detection of Phosgene by BPCI

As phosgene is one of the toxic chemical warfare agent, it is highly desirable for a probe to detect phosgene gas swiftly and prominently. Here our synthesized probe BPCI can be used to construct a prominent test kit, which can be used for onsite, real time and selective detection of phosgene vapour. The paper test strips embedded with probe BPCI were prepared. Then we analysed the sensing in presence of phosgene and other interfering analytes. Phosgene gas was generated by mixing triphosgene with TEA in the sealed glass vowel itself. We observed that, the test strip containing free probe which displayed a light blue colour under UV light. However, when exposed to phosgene vapour the test paper changed its colour steadily to cyan colour. In contrast, exposure to other chemical vapour did not yield any noticeable change in the emission colour (Fig. 8.9). Hence, the steady response of BPCI towards phosgene, proved its potential in order to use it as an efficient portable kit. The detection of phosgene in solid platform and liquid state showed its own notable changes, but its identification in vapour phase was a consequent addition to its demanding application.

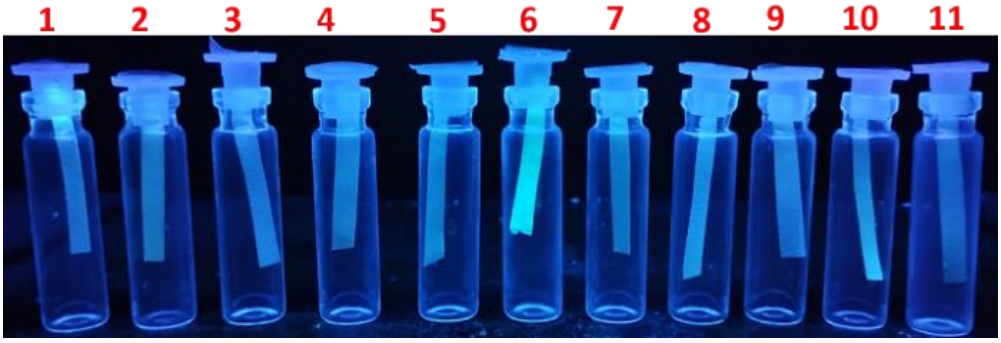


**Figure 8.9:** Photograph showing the fluorescence of BPCI using test papers after exposure for five minutes to phosgene and vapour of various other relevant analytes. The analytes tested are (1) BPCI, (2) DCP, (3) DCNP, (4) TEP, (5) TBP, (6) Phosgene, (7) ACOH, (8) $POCl_3$, (9) $CH_3COCl$, (10) $SOCl_2$ and (11) PTSA. Photos are taken in a UV-chamber ($\lambda_{ex}$ = 346 nm).

## 8.4.7. Practical application of BPCI loaded test strips in gas phase

To further establish BPCI as a potent chemosensor towards phosgene, we manufactured BPCI-loaded TLC plates as a portable tool. Here without using any sophisticated instrument we can detect phosgene with simple, trouble free and convenient method with the help of this feasible solid-state platform. The TLC plates were dipped in the solution of BPCI in THF and left to dry the solvent. As shown in (Fig. 8.10) the TLC plates loaded with BPCI only, showed blue fluorescence under hand held ultraviolet light ($\lambda_{ex}$ = 346 nm). However, when exposed to subsequent increasing concentration (5-40 ppm) of phosgene, the fluorescent colour changed from blue to cyan green. According to Matheson gas Data book,[64]concentration of phosgene gas of 20 ppm can cause lung injuries within 2 minutes and exposure to concentration of 25 ppm for 30 minutes is very dangerous. Also 90 ppm of phosgene concentration is fatal in 30 min or less. Hence from the Fig. 8.10 given below we can analyse that our synthesized chemodosimeter prominently changed its colour even at low concentration of phosgene (15 ppm) which was below the life-threatening concentration of phosgene. At higher concentration (40 ppm) the colour changed completely to cyan-green. Thus, the test strips with BPCI loaded could detect phosgene at the concentrations below health risks. Hence this above encouraging results conveyed that our synthesized probe can detect phosgene distinguishably through visual monitoring.

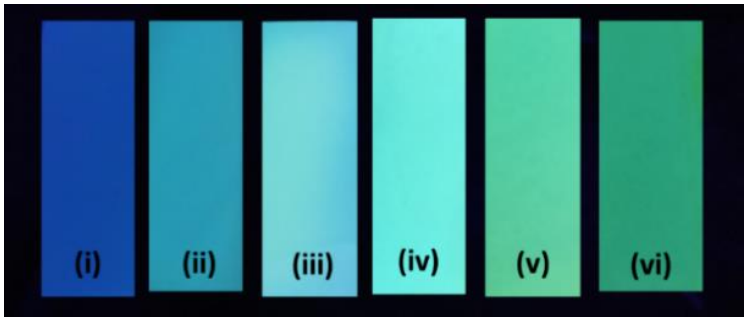


**Figure 8.10:** TLC sticks coated with BPCI (100.0 mM) alone (i) followed by exposure to (ii) 5 ppm, (iii) 10 ppm, (iv) 15 ppm, (v) 25 ppm, (vi) 40 ppm of phosgene when exposed to hand held UV lamp. ($\lambda_{ex}$ = 346 nm).

## 8.4.8. Computational study

To elucidate the sensing mechanism and to get insight of the structural changes of BPCI after reaction with phosgene, density functional theory (DFT) calculations were performed by B3LYP/6-31+G(d) method using Gaussian 09 program. The selected higher energy occupied molecular orbitals (HOMOs) and lower energy unoccupied molecular orbital (LUMOs) of BPCI and BPCI-PHOS were shown in Fig. A8.8 and Fig. A8.9, Appendix respectively. The HOMO-LUMO energy gap of BPCI was calculated to be 3.39 eV which was significantly reduced in BPCI-PHOS adduct to 3.09 eV (Fig. 8.11). The optimized structures of BPCI and BPCI-PHOS were shown in Fig. 8.12.

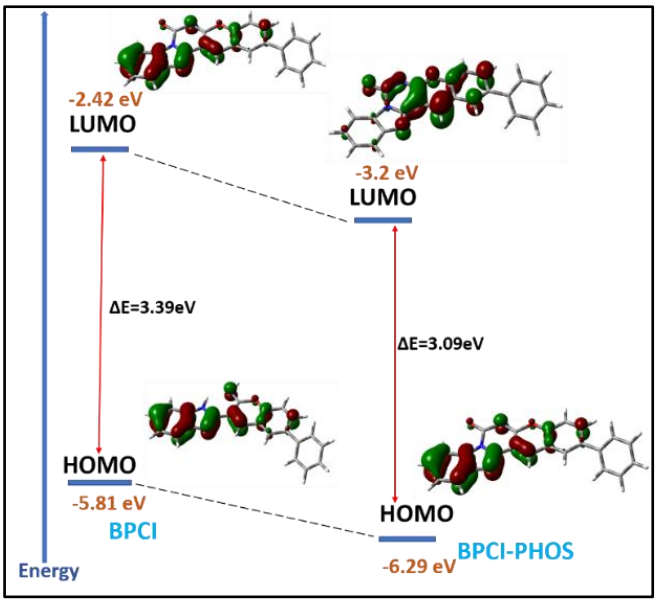


**Figure 8.11:** Calculated frontier molecular orbitals for BPCI and BPCI-PHOS with their orbital energies using the B3LYP/6-31+G(d) basis set.

In the time dependent density functional theory (TDDFT) calculation, solvent correction was included by CPCM model and THF was selected as solvent. The calculated vertical excitations of BPCI displayed a strong transition at 400 nm ($f$ = 0.7762) which was due to HOMO→LUMO transition and for BPCI-PHOS, HOMO→LUMO transition was shifted to 440 nm ($f$ = 0.6757) respectively (Table A8.2, Appendix). Moreover, the calculated absorption peaks of BPCI and BPCI-PHOS have well agreed with the experimental observation.

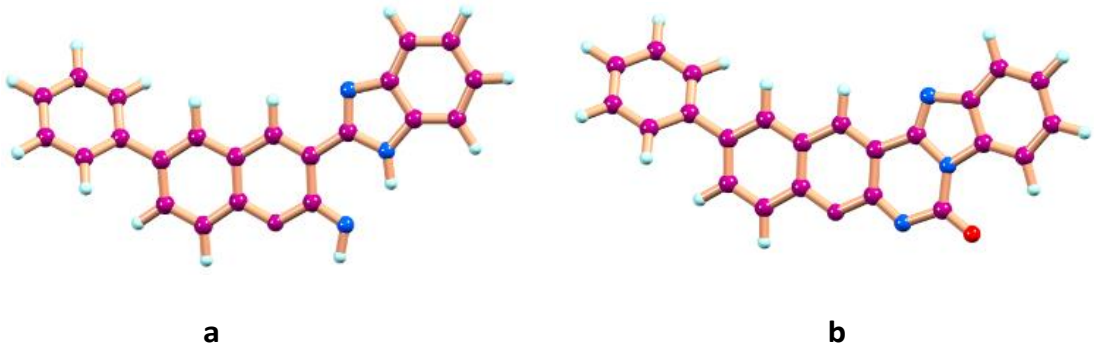


**Figure 8.12:** Optimized structure of (a) BPCI and (b) BPCI-PHOS calculated by DFT/B3LYP/6-31+G(d) method.

# 8.5. Conclusions

In summary, we have rationally designed and synthesized a new fluorescent ratiometric probe (BPCI) through cost- effective pathway for the efficient detection of phosgene, a lethal pulmonary-agent. The sensitivity of the probe is performed in presence of other relevant analytes which unveils that BPCI is competent enough to detect phosgene in presence of these other analytes. Also, other salient features of chemodosimeter BPCI are that it responds in presence of phosgene within four minutes and also has low LOD value of $10^{-7}$ M order. Gas phase response towards phosgene is also noted for our chemodosimeter. BPCI loaded test strips show response towards phosgene at very low concentration of 15 ppm which is below threshold level that can cause prolonged danger to health and life. The sensing mechanism is interpreted based upon the ICT process for both BPCI and BPCI-PHOS adduct. Density functional theory (DFT) calculations are performed that illustrates the electronic structure, which also supports the sensing mechanism of the probe. Overall, our synthesized probe makes a helpful insight for a portable approach to detect phosgene wherever relevant.

# 8.6. Experimental

## 8.6.1. Materials and methods

All the essential reagents used in the synthetic procedure of BPCI, including o-phenylenediamine, 4-Phenyl phenol and ethyl cyanoacetate were purchased from Sigma-Aldrich and the solvents were available from commercial sources. THF and all the other solvents used for spectrometric analyses were of HPLC grade. DMSO-$d_6$ was used as solvent to perform $^{1}H$ and $^{13}C$ NMR with a Bruker (AC) 400 MHz NMR instrument using ~0.05 (M) solutions and chemical shifts were recorded in δ units in ppm using tetramethylsilane (TMS) as an internal standard.

An infrared spectrum of the probe was recorded from RX-1 Perkin Elmer spectrophotometer by preparing KBr pellet of the sample. A 2400 Series-II CHN analyzer, Perkin Elmer, USA was used for Elemental analysis.HRMS mass spectra were recorded on Waters (Xevo G2 Q-TOF) mass spectrometer. UV-Vis spectra were measured on a Shimadzu UV-1900i spectrophotometer. We observed the luminescence properties using Shimadzu RF-6000 fluorescence spectro fluorophotometer at room temperature (298 K). Luminescence lifetime measurements were carried out by using time-correlated single photon counting set up from Horiba Jobin-Yvon. Then the fluorescence decay data were placed on a Hamamatsu MCP photomultiplier (R3809) and analysed using EZ time software. Thin layer chromatography (TLC) and dip stick experiment were done using Merck 60 $F_{254}$ plates of 0.25 mm thickness. The reaction products were further purified by column chromatographic technique using silica gel of mess 200–300, where petroleum benzene and ethyl acetate were used as solvents.

## 8.6.2. Synthesis of 4-hydroxy-[1,1'-biphenyl]-3-carbaldehyde(a)

This was prepared according to a previously reported procedure.[62]

## 8.6.3. Synthesis of 2-cyanomethylbenzimidazole (b)

This was previously synthesized by our group.[63]

### 8.6.4. Synthesis of 3-(1H-benzo[d]imidazol-2-yl)-6-phenyl-2H-chromen-2-imine (BPCI)

4-Hydroxy-[1,10-biphenyl]-3-carbaldehyde (0.2g,1 mmol) was taken in round-bottomed flask and dissolved in 10 mL EtOH solution. Then, 2-cyanomethylbenzimidazole (b) (0.16 g, 1 mmol) was added to the solution. The whole mixture was refluxed while a catalytic amount of piperidine was added to the mixture. The system was refluxed for 4 hours. We observed a light brown colour precipitate within the reaction mixture. The precipitate was then filtered, washed with EtOH and dried. The crude product was further purified by column chromatography. Yield was calculated to be 0.249 g, 74%.

**Anal. Calc. for $C_{22}H_{15}N_3O$ (BPCI):** Calc. (%) C 78.32, H 4.48, N 12.46. Found (%), C 79.09, H 4.03, N 12.01.

**IR ($cm^{-1}$, KBr):** υ(C=N) 1682.10, υ(C-H) 3063.40, υ(N-H) 3168.82.

**$^1$H NMR (400 MHz, DMSO-$d_6$):** δ 12.78 (s, 1H), 9.18 (s, 1H), 8.37 (s, 1H), 8.09 (s, 1H), 8.03 (d, J = 8.5 Hz, 1H), 7.83 (d, J = 8.5 Hz, 1H), 7.78-7.22 (m, 8H), 7.15 (d, J = 7.96, 1H).

**$^{13}$C NMR (100 MHz, DMSO-$d_6$):** δ 157.3, 152.9, 148.2, 144.7, 144.3, 140.0, 139.2, 134.7, 133.1, 132.2, 129.5, 128.0, 127.0, 123.2, 120.3, 119.6, 117.2, 116.7, 111.7.

**HRMS:** calculated for $C_{22}H_{16}N_3O$ $[M + H]^+$ (m/z) = 338.1293; found = 338.0914.

### 8.6.5. Synthesis of BPCI-PHOS adduct

Briefly, 3-(1H-benzo[d]imidazol-2-yl)-6-phenyl-2H-chromen-2-imine (BPCI) (34 mg, 0.10 mmol) was dissolved in 10 mL of THF which was taken in a round bottle flask and stirred. After complete dissolution, solid triphosgene (45 mg, 0.15 mmol) and TEA (0.02mL, 0.15 mmol) was added and the mixture was stirred for 1 hour at room temperature. After completion of the reaction, a light-yellow precipitate was formed which was then filtered, washed with dry THF, dried and collected. Yield was calculated to be 28 mg, 78%. Then spectroscopic techniques were employed for further characterization of the crude product.

**$^1$H NMR (400 MHz, DMSO-$d_6$):** δ 8.65 (s, 1H), 8.17 (s, 1H), 7.90 (d, J = 9.2 Hz, 1H), 7.86-7.58 (m, 7H), 7.54 (t, J = 7.28, 1H), 7.44 (t, J = 7.4, 1H), 7.15 (t, J = 8.56 Hz, 1H).

**$^{13}$C NMR (100 MHz, DMSO-$d_6$):** δ 191.9, 160.8, 158.2, 153.6, 147.2, 144.0, 139.3, 138.4, 138.0, 132.4, 131.9, 129.7, 127.3, 122.9, 122.3, 118.8, 118.5, 117.8, 115.0, 114.9, 112.5.

**HRMS:** calculated for $C_{23}H_{14}N_3O_2$ $[M+H]^+$ (m/z) = 364.1086; found = 364.2578.

## 8.6.6. General Method for UV-Vis and Fluorescence Titration

### 8.6.6.1. UV-Vis Method

For UV-Vis titration, a host (BPCI) stock solution was prepared of 100 μM in THF solvent of HPLC grade. The stock solutions of all the guest analytes were also prepared in the order of 1 mM in THF. Due to highly toxic nature of phosgene, it was not used directly. Instead triphosgene/TEA (triethylamine) were used assuming that 1 eq. of triphosgene is converted to 3 eq. of phosgene.[41] Stock solution of Triphosgene (1mM) was also prepared in THF. In all test concentration of probe (BPCI) was maintained to 10 μM. Solutions of a variety of concentrations of the probe and different increasing concentrations of all other analytes were prepared separately to record UV-Vis spectra.

### 8.6.6.2. Fluorescence method

For fluorescence titrations also the stock solution of the probe (100 μM) used was the same as that used for UV-Vis titration. The solutions of all the relevant analytes were prepared in THF in the order of 1mM. Different concentration of the probe and the different analytes were prepared from the stock solution. The excitation wavelength used was 360 nm (Where excitation slit=10.0 and emission slit=10.0). The spectra of these solutions were recorded by means of fluorescence method.

## 8.6.7.Determination of fluorescence quantum yield:

For measurement of the quantum yields of BPCI and its reaction product with Phosgene (BPCI-PHOS), we recorded the absorbance of the compounds in THF solution. The emission spectra were recorded using the maximal excitation wavelengths and the integrated areas of the emission-corrected spectra were measured. The quantum yields were then calculated by comparison with coumarin 153 ($\varphi_s$ = 0.544) as reference using the following equation:

$$\Phi_x = \Phi_s \times \left(\frac{Ix}{Is}\right) \times \left(\frac{As}{Ax}\right) \times \left(\frac{nx}{ns}\right)^2$$

Where, x & s indicate the unknown and standard solution respectively, Φ is the quantum yield, I is the integrated area under the fluorescence spectra, A is the absorbance and n is the refractive index of the solvent. We calculated the quantum yields of BPCI and BPCI-PHOS using the above equation and the values are 0.182 and 0.291 respectively.

### 8.6.8. Theoretical study

For theoretical calculation we utilized Gaussian 09 (G09) program package.[65] The geometry for BPCI and BPCI-PHOS adduct were optimized by using the density functional theory (DFT) method at the B3LYP level for the compounds. Where 6-31+G(d) was assigned as basis set.[66-67] The vibrational frequency calculations were performed on the optimized geometry to ensure that the optimized geometries represent the local minima having only positive eigen values. Vertical electronic excitations, which was based on B3LYP optimized geometries were computed using the time-dependent density functional theory (TDDFT) formalism[68-70] in THF solvent using conductor-like polarizable continuum model (CPCM).[71-73]

## 8.7. Notes and references


1. K. Ganesan, S. K. Raza and R. Vijayaraghavan,*J. Pharm. Bioallied Sci.*, 2010, **2**, 166.
2. F. R. Sidell and J. Borak, *Ann. Emerg. Med.*, 1992, **21**, 865.
3. L. Chen, D. Wu and J. Yoon, *ACS Sens.*, 2018, **3**, 27.
4. A. M. Prentiss, *Chemicals in War*, McGraw-Hill, New York, 1st edn, 1937, pp. 216.
5. C. B. Bast and D. F. Glass-Mattie, *Hand book of toxicology of chemical warfare agents*, Academic Press, Boston, 2nd edn, 2015, pp. 327.
6. L. Szinicz, *Toxicology*, 2005, **214**, 167.
7. U.S. National Institute for Occupational Safety and Health, NIOSH Pocket Guide to Chemical Hazards, Publication 97-140, NIOSH, Washington, DC, 2005.
8. E. D. Robin, C. E. Cross and R. Zelis, *N. Engl. J. Med.*, 1973, **288**, 292.
9. N. C. Staub, *Physiol. Rev.*, 1974, **54**, 678.
10. W. W. Holmes, B. M. Keyser, D. C. Paradiso, R. Ray, D. K. Andres, B. J. Benton, C. C. Rothwell, H. M. Hoard-Fruchey, J. F. Dillman, A. M. Sciuto and D. R. Anderson, *Toxicol. Lett.*, 2016, **244**, 8.
11. A. M. Sciuto, *Arch. Toxicol.*, 1998, **72**, 283.
12. A. M. Sciuto, R. R. Stotts and H. H. Hurt, *J. Appl. Toxicol.*, 1996, **16**, 381.
13. K. Cheng, N. Yang, Q. Y. Li, X. W. Gao and X. J. Wang, *ACS Omega*, 2019, **4**, 22557.
14. H. Babad and A. G. Zeiler, *Chem. Rev.*, 1973, **73**, 75.
15. Y. Hu, X. Zhou, H. Jung, S. J. Nam, M. H. Kim and J. Yoon, *Anal. Chem.*, 2018, **90**, 3382.
16. S. C. Gad, *Encyclopedia of Toxicology*, Academic Press, Oxford, 3rd edn, 2014, pp. 904.
17. A. Watson, D. Opresko, R. A. Young, V. Hauschild, J. King and K. Bakshi, *Handbook of Toxicology of Chemical Warfare Agents*, Academic Press, Boston, 2nd edn, 2015, pp. 87.
18. *Environmental Health Criteria 193: Phosgene*, World Health Organization, Geneva, 1997.
19. J. P. Hendershott, *Am. Ind. Hyg. Assoc. J.*, 1986, **47**, 742.
20. Y. Juillet, C. Dubois, F. Bintein, J. Dissard and A. Bossee, *Anal. Bioanal. Chem.*, 2014, **406**, 5137.

21. R. J. Rando, H. G. Poovey and S. N. Chang, *J. Liq. Chromatogr.*, 1993, **16**, 3291.
22. S. Virji, R. Kojima, J. D. Fowler, J. G. Villanueva, R. B. Kaner and B. H. Weiller, *Nano Res.*, 2009, **2**, 135.
23. M. Davydova, A. Kromka, P. Exnar, M. Stuchlik, K. Hruska, M. Vanecek and M. Kalbac, *Phys. Status Solidi A*, 2009, **206**, 2070.
24. M. Davydova, M. Stuchlik, B. Rezek, K. Larsson and A. Kromka, *Sens. Actuators, B*, 2013, **188**, 675.
25. R. L. Aggarwal, L. W. Farrar, S. Di Cecca and T. H. Jeys, *AIP Adv.*, 2016, **6**, 025310.
26. Y. Juillet, C. Dubois, F. Bintein, J. Dissard and A. Bossee, *Anal. Bioanal. Chem.*, 2014, **406**, 5137.
27. L. Chen, D. Wu and J. Yoon, *ACS Sens.*, 2018, **3**, 27.
28. H. N. Kim, Z. Guo, W. Zhu, J. Yoon and H. Tian, *Chem. Soc.Rev.*, 2011, **40**, 79.
29. W. Feng, S. Gong, E. Zhou, X. Yin and G. Feng, *Anal. Chim. Acta*, 2018, **1029**, 97.
30. H. C. Xia, X. H. Xu and Q. H. Song, *ACS Sens.*, 2017, **2**, 178.
31. W. Q. Zhang, K. Cheng, X. Yang, Q. Y. Li, H. Zhang, Z. Ma,H. Lu, H. Wu and X. J. Wang, *Org.Chem. Front.*, 2017, **4**(9), 1719.
32. M. Du, B. Huo, J. Liu, M. Li, A. Shen, X. Bai, Y. Lai, L. Fang and Y. Yang, *J. Mater. Chem. C*, 2018, **6**, 10472.
33. Y. Hu, X. Zhou, H. Jung, S. J. Nam, M. H. Kim and J. Yoon, *Anal. Chem.*, 2018, **90**, 3382.
34. S. L. Wang, L. Hong and Q. H. Song, *Chem. Commun.*, 2017, **53**(9), 1530.
35. S. L. Wang, C. L. Zhang and Q. H. Song, *J. Mater. Chem. C*, 2019, **7**, 1510.
36. S.L. Wang, L. Zhong and Q.-H. Song, *Chem.- Eur. J.*, 2018, **24**, 5652.
37. K. Maiti, D. Ghosh, R. Maiti, V. Vyas, P. Datta, D. Mandal and D. K. Maiti, *J. Mater. Chem. A*, 2019, **7**, 1756.
38. L. T. Zeng, H. Y. Zeng, L. R. Jiang, S. Wang and J. T. Hou, *J. Anal. Chem.*, 2019, **91**, 12070.
39. Q. Hu, C. Duan, J. Wu, D. Su, L. Zeng and R. Sheng, *Anal. Chem.*, 2018, **90**, 8686.
40. M. Sayar, E. Karakus, T. Güner, B. Yildiz, U. H. Yildiz and M. Emrullahoglu, *Chem.–Eur. J.*, 2018, **24**, 3136.
41. T. I. Kim, B. Hwang, J. Bouffard and Y. Kim, *Anal. Chem.*, 2017, **89**, 12837.
42. H. C. Xia, X. H. Xu and Q. H. Song, *Anal. Chem.*, 2017, **89**, 4192.
43. T. I. Kim, D. Kim, J. Bouffard and Y. Kim, *Sens. Actuators B*, 2019, **283**, 458.
44. H. Xie, Y. Wu, F. Zeng, J. Chen and S. Wu, *Chem. Commun.*, 2017, **53**, 9813.
45. L. Bai, W. Feng and G. Feng, *Dyes Pigm.*, 2019, **163**, 483.
46. Y. Zhang, A. Peng, X. Jie, Y. Lv, X. Wang and Z. Tian, *ACS Appl. Mater. Interfaces*, 2017, **9**, 13920.
47. X. Wu, Z. Wu, Y. Yang and S. Han, *Chem. Commun.*, 2012, **48**, 1895.
48. H. Zhang and D. M. Rudkevich, *Chem. Commun.*, 2007, **12**, 1238.
49. P. Kundu and K. C. Hwang, *Anal. Chem.*, 2012, **84**, 4594.
50. X. Zhou, Y. Zeng, L. Chen, X. Wu and J. Yoon, *Angew. Chem., Int. Ed.*, 2016, **55**, 4729.
51. Y. Hu, L. Chen, H. Jung, Y. Zeng, S. Lee, K. M. K. Swamy, X. Zhou, M. H. Kim and J. Yoon, *ACS Appl. Mater. Interfaces*, 2016, **8**, 22246.
52. H. C. Xia, X. H. Xu and Q. H. Song, *ACS Sens.*, 2017, **2**, 178.
53. Zhou X. Zhou, Y. Zeng, L. Chen, X. Wu and J. Yoon, *Angew. Chem., Int. Ed.*, 2016, **55**, 4729.
54. F. Zeng, G. Bao, B. Zhou and Y. Han, *New J. Chem.*, 2021, **45**, 5631.

55. X. Wu, Z. Wu, Y. Yang and S. Han., *Chem. Commun.*, 2012, **48**, 1895.
56. T. I. Kim, B. Hwang, J. Bouffard and Y. Kim, *Anal. Chem.*, 2017, **89**, 12837.
57. W. Q. Zhang, K. Cheng, X. Yang, Q. Y. Li, H. Zhang, Z. Ma, H. Lu, H. Wu and X. J. Wang, *Org. Chem. Front.*, 2017, **4**, 1719.
58. B. Zhu, R. Sheng, T. Chen, J. Rodrigues, Q. H. Song, X. Hu and L. Zeng, *Coord. Chem. Rev.*, 2022, **463**, 214527.
59. X. Zhou, Y. Zeng, L. Chen, X. Wu and J. Yoon, *Angew. Chem., Int. Ed.*, 2016, **55**, 4729.
60. K. Maiti, D. Ghosh, R. Maiti, V. Vyas, P. Datta, D. Mandal and D. K. Maiti, *J. Mater. Chem. A*, 2019, **7**, 1756.
61. L. Zeng, T. Chen, B. Zhu, S. Koo, Y. Tang, W. Lin, T. D. James and J. S. Kim, *Chem. Sci.*, 2022, **13**, 4523.
62. A. Biswas, R. Naskar, D. Mitra, A. Das A, S. Gharami ,N. Murmu and T. K. Mondal, *New J. Chem*, 2022; **46**(45), 21968.
63. L. Patra, K. Aich, S. Gharami and T. K. Mondal, *Sens. Actuators, B*, 2021, **326**, 128837.
64. W. Braker and A. L. Mossman, Matheson gas data book, Matheson, South Yarra, VIC, Australia, 6th edn, 1980, p. 596.
65. M. J. Frisch, G. W. Trucks, H. B. Schlegel, G. E. Scuseria, M. A. Robb, J. R. Cheeseman, G. Scalmani, V. Barone, B. Mennucci, G. A. Petersson, H. Nakatsuji, M. Caricato, X. Li, H. P. Hratchian, A. F. Izmaylov, J. Bloino, G. Zheng, J. L. Sonnenberg, M. Hada, M. Ehara, K. Toyota, R. Fukuda, J. Hasegawa, M. Ishida, T. Nakajima, Y. Honda, O. Kitao, H. Nakai, T. Vreven, J. A. Montgomery, Jr., J. E. Peralta, F. Ogliaro, M. Bearpark, J. J. Heyd, E. Brothers, K. N. Kudin, V. N. Staroverov, R. Kobayashi, J. Normand, K.Raghavachari, A. Rendell, J. C. Burant, S. S. Iyengar,J. Tomasi, M. Cossi, N. Rega, J. M. Millam, M. Klene, J. E. Knox, J. B. Cross, V. Bakken, C. Adamo, J. Jaramillo, R. Gomperts, R. E. Stratmann, O. Yazyev, A. J. Austin, R. Cammi, C. Pomelli, J. W. Ochterski, R. L. Martin, K. Morokuma, V. G. Zakrzewski, G. A. Voth, P. Salvador, J. J. Dannenberg, S. Dapprich, A. D. Daniels, O¨. Farkas,J. B. Foresman, J. V. Ortiz, J. Cioslowski and D. J. Fox,*Gaussian 09, Revision D.01*, Gaussian, Inc., Wallingford CT, 2009.
66. A. D. Becke, *J. Chem. Phys.*, 1993, **98**, 5648.
67. C. Lee, W. Yang and R. G. Parr, *Phys. Rev. B: Condens. Matter Mater. Phys.*, 1988, **37**, 785.
68. R. Bauernschmitt and R. Ahlrichs, *Chem. Phys. Lett.*, 1996, **256**, 454.
69. R. E. Stratmann, G. E. Scuseria and M. J. Frisch, *J. Chem.Phys.*, 1998, **109**, 8218.
70. M. E. Casida, C. Jamorski, K. C. Casida and D. R. Salahub, *J. Chem. Phys.*, 1998, **108**, 4439.
71. M. Cossi and V. Barone, *J. Chem. Phys.*, 2001, **115**, 4708.
72. V. Barone and M. Cossi, *J. Phys. Chem. A*, 1998, **102**, 1995.
73. M. Cossi, N. Rega, G. Scalmani and V. Barone, *J. Comput. Chem.*, 2003, **24**, 669.

# APPENDIX

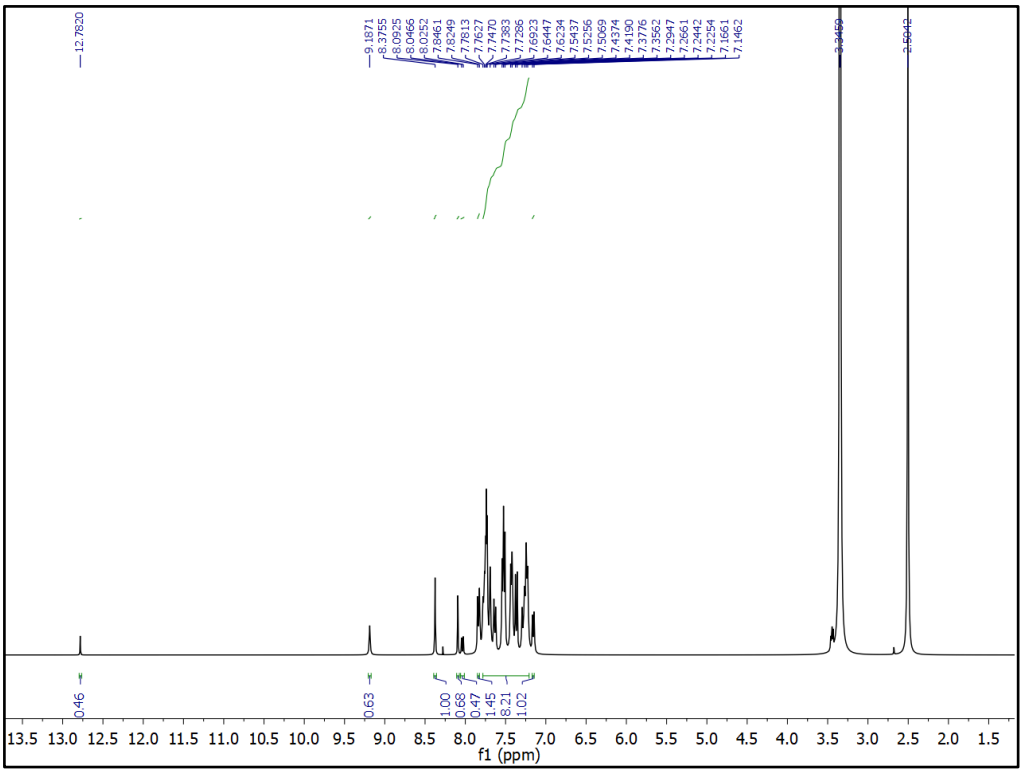


**Fig. A8.1:** $^{1}$H NMR (400 MHz) spectrum of the probe (BPCI) in DMSO-$d_6$.

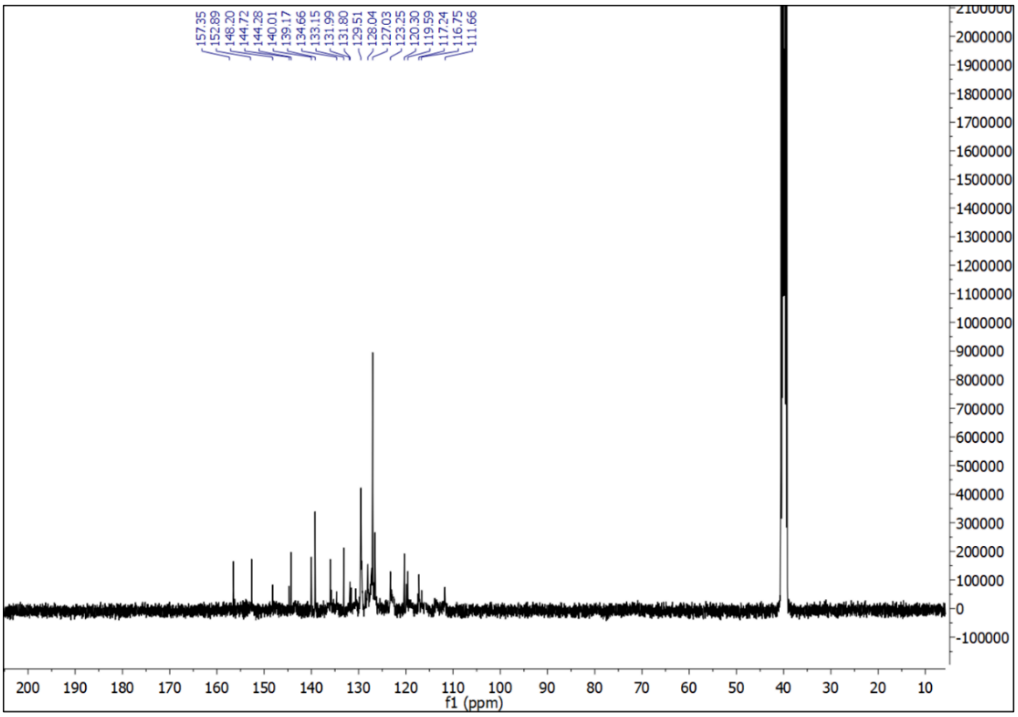


**Fig. A8.2:** $^{13}$C NMR (100 MHz) spectrum of the probe (BPCI) in DMSO-$d_6$.

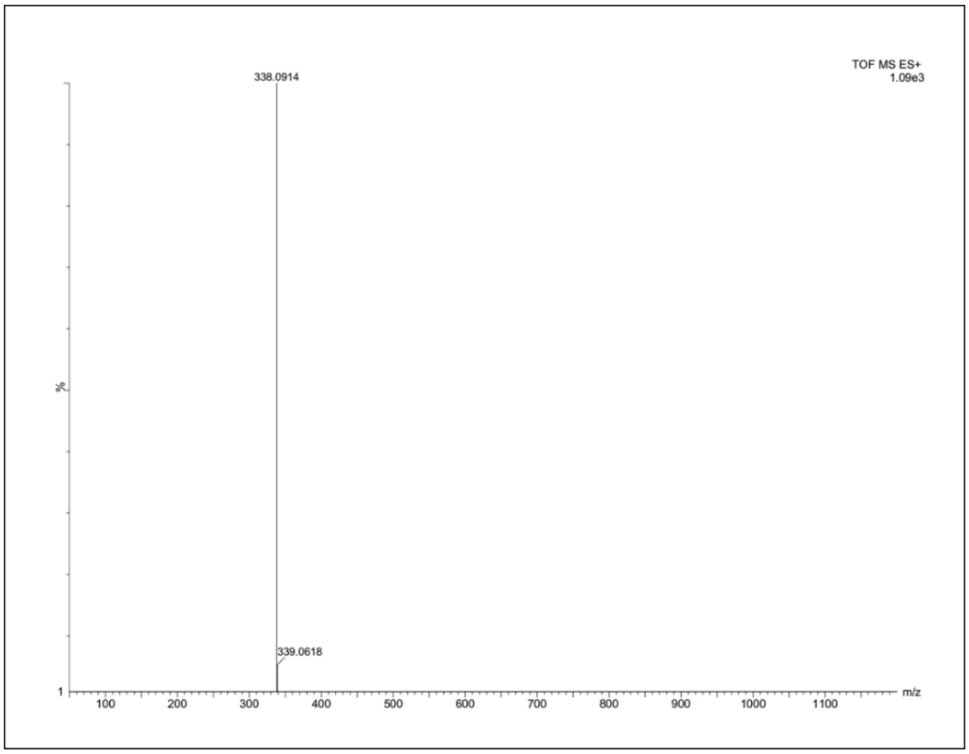


**Fig. A8.3:** HRMS of the probe (BPCI).

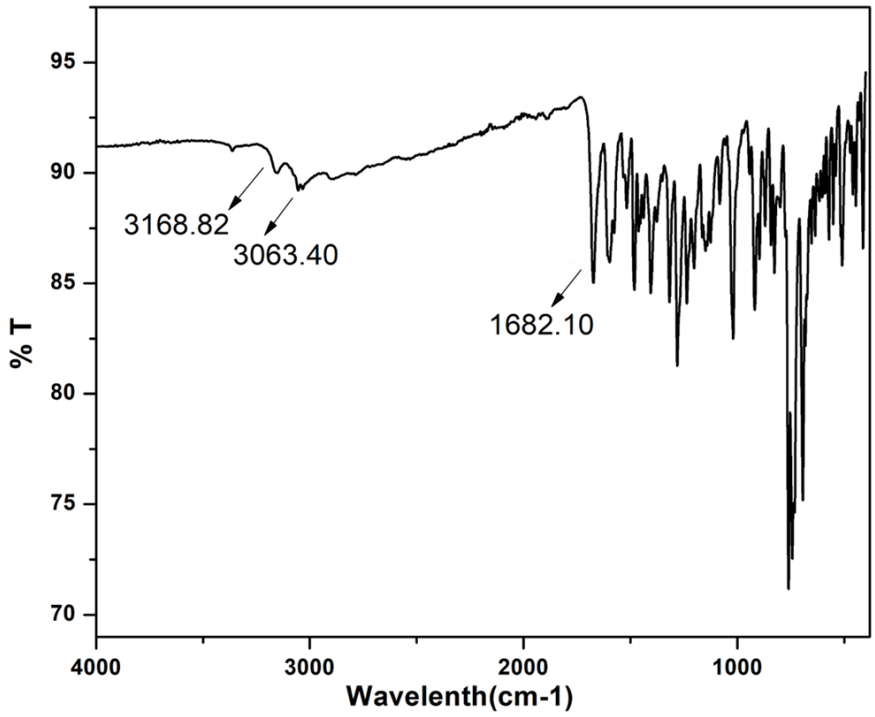


**Fig. A8.4:** IR spectra of the probe BPCI (KBr disk).

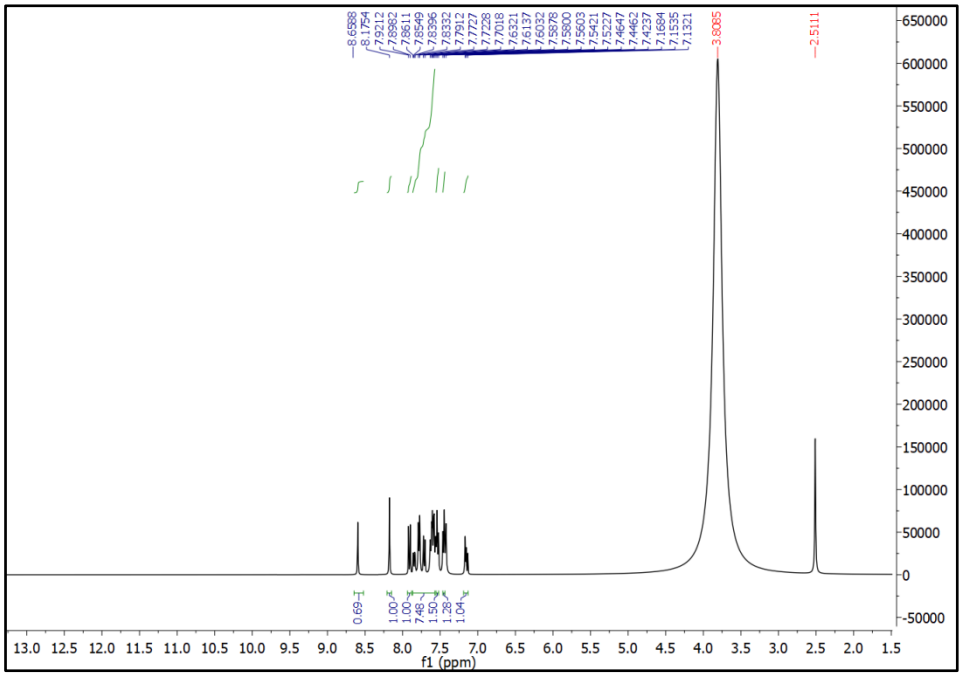


**Fig.A8.5:** $^{1}$H NMR (400 MHz) spectrum of the BPCI-PHOS in DMSO-$d_6$

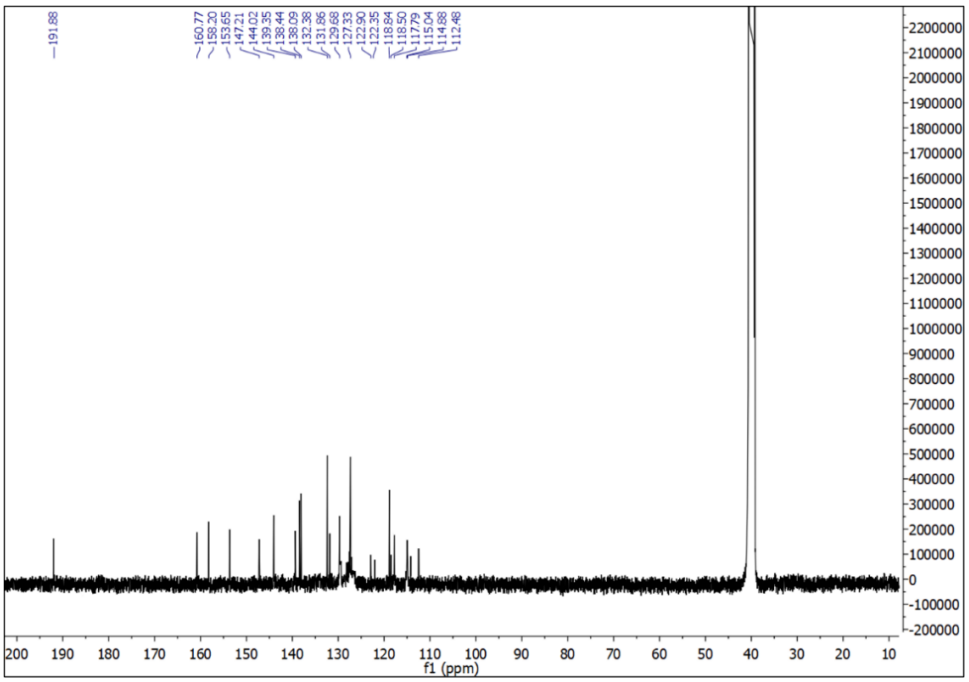


**Fig.A8.6:** $^{13}$C NMR (100 MHz) spectrum of the BPCI-PHOS in DMSO-$d_6$

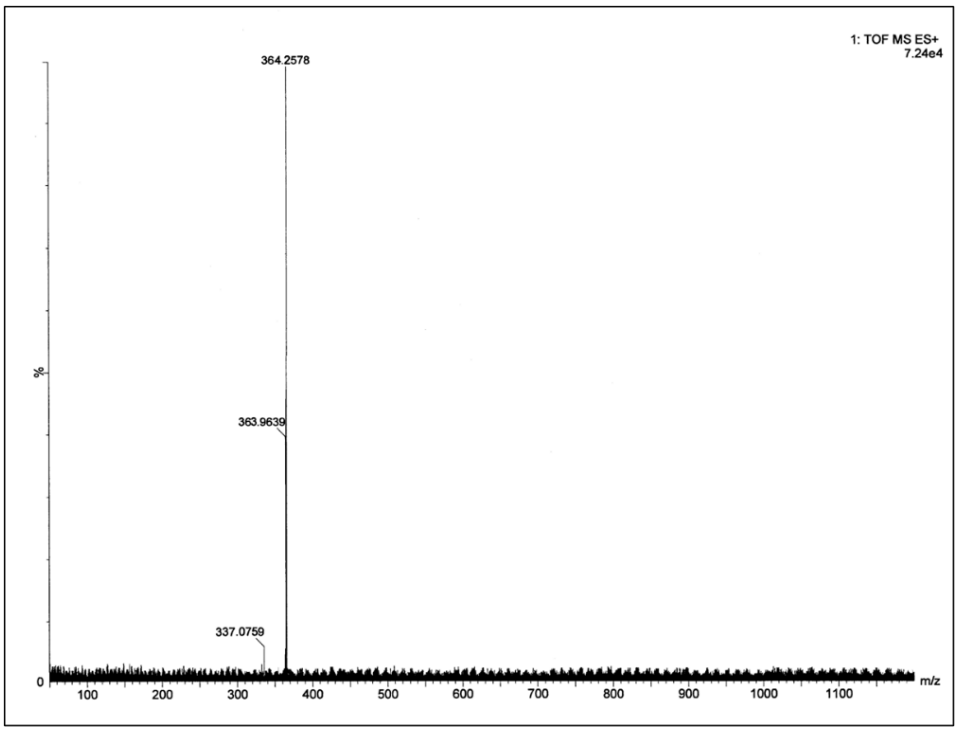


**Fig.A8.7:** HRMS of BPCI-PHOS.

**Table A8.1: Fluorescence lifetime data**

| THF (solvent) | Quantum yield (φ) | τ (ns) | $k_r$ ($10^8$×s-1) | $k_{nr}$ ($10^8$×s-1) |
|---|---|---|---|---|
| BPCI | 0.182 | 0.946 | 1.92 | 8.58 |
| BPCI-PHOS | 0.291 | 1.445 | 2.01 | 4.91 |

Radiative rate constant $K_r$ and total non-radiative rate constant $K_{nr}$ have been calculated using the equation $\tau^{-1} = K_r + K_{nr}$ and $K_r = \varphi_f / \tau$

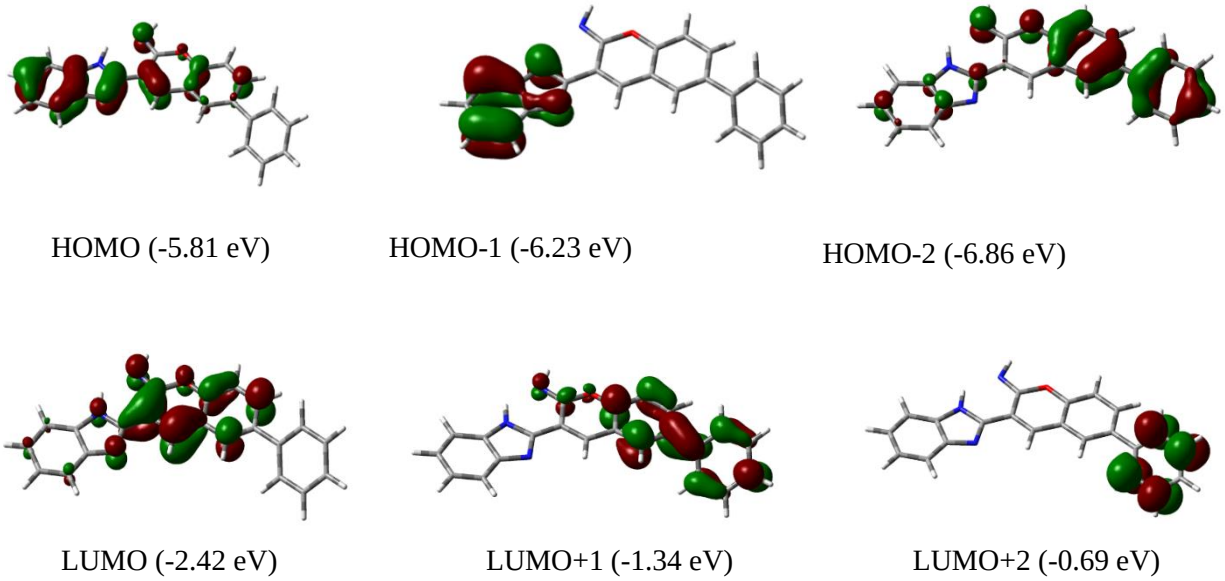


**Fig. A8.8:** Contour plots of some selected molecular orbitals of BPCI

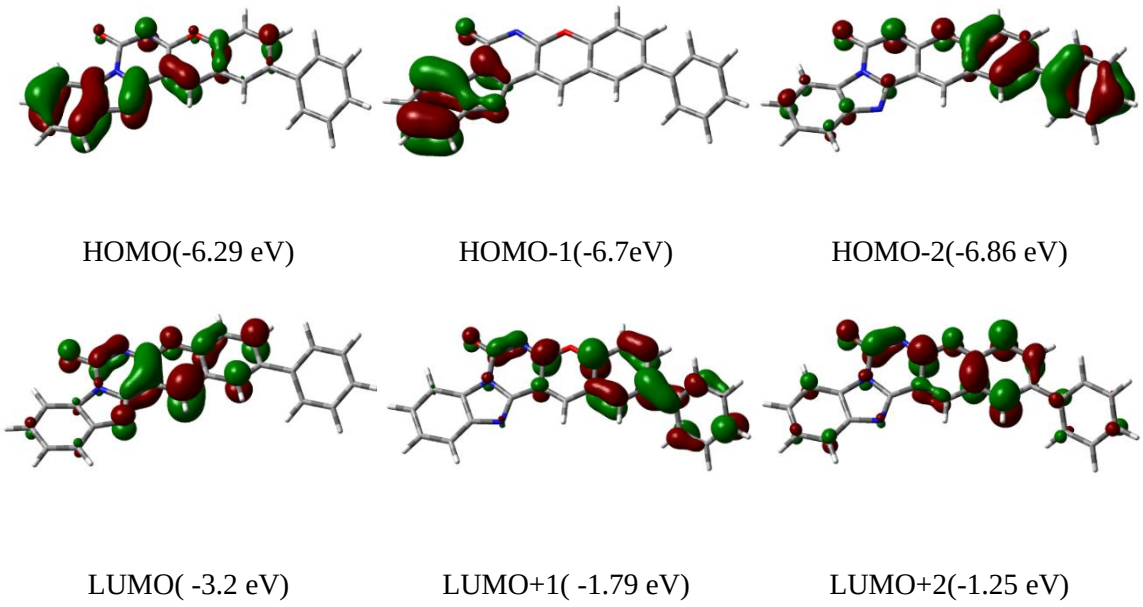


**Fig. A8.9:** Contour plots of some selected molecular orbitals of BPCI-PHOS.

**Table A8.2.** Vertical electronic transition of BPCI and BPCI-PHOS calculated by TDDFT/CPCM method

| Compd. | Wavelength (nm) | Energy (eV) | Osc. Strength (f) | Key transitions | Character |
|---|---|---|---|---|---|
| BPCI | 399.7 | 3.1014 | 0.7762 | (98%) HOMO→LUMO | $\pi\rightarrow\pi^*$ |
| | 351.7 | 3.5249 | 0.1367 | (61%) HOMO-1→LUMO | $\pi\rightarrow\pi^*$ |
| | 354..3 | 3.4990 | 0.0102 | (59%) HOMO-2→LUMO | $\pi\rightarrow\pi^*$ |
| | 296.4 | 4.6850 | 0.0274 | (58%) HOMO→LUMO+1 | $\pi\rightarrow\pi^*$ |
| BPCI-PHOS | 439.9 | 2.8179 | 0.6757 | (98%) HOMO→LUMO | $\pi\rightarrow\pi^*$ |
| | 406.2 | 3.0521 | 0.0135 | (94%) HOMO-1→LUMO | $\pi\rightarrow\pi^*$ |
| | 388.9 | 3.1879 | 0.0431 | (94%) HOMO-2→LUMO | $\pi\rightarrow\pi^*$ |
| | 296.5 | 3.1813 | 0.1388 | (75%) HOMO→LUMO+1 | $\pi\rightarrow\pi^*$ |

**Table A8.3:** The comparison of the present probe (BPCI) with some previous probes for detection of phosgene

| Receptor | Type of response | Test kit | Detection limit | Detection in gaseous phase | Reference |
|---|---|---|---|---|---|
| 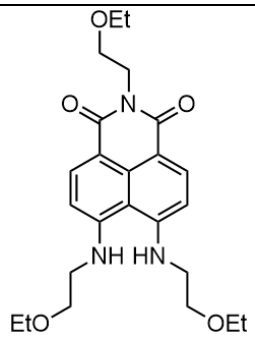 | Fluorometric (ratiometric) | Yes (Test-strip method) | 1.3 nM | Yes | *Chem. Commun.*, 2017, **53**, 1530. |
| 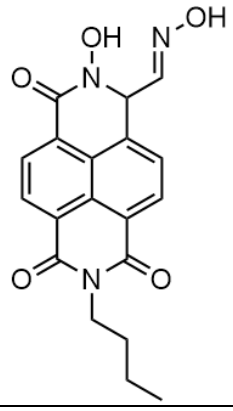 | Colorimetric, fluorometric (ratiometric) | Yes (Test-strip method) | 0.09 nM | Yes | *J. Mater. Chem. A.*, 2019, **7**, 1756. |
| 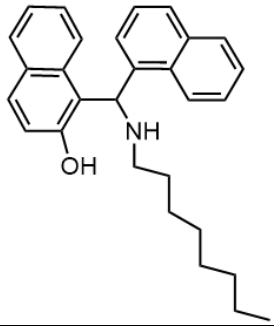 | Fluorometric (turn-on) | Yes (Dip-stick method) | 0.40 µM | No | *New J. Chem.*, 2019, **43**, 11743. |

| | | | | | |
|---|---|---|---|---|---|
| 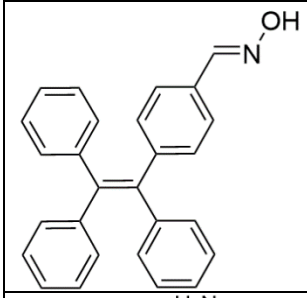 | Fluorometric (Turn-on) | Yes (Test strip method) | 9.3 nM | No | *Chem. Commun.*, 2022, **58**, 5296. |
| 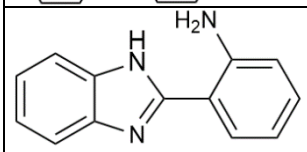 | Fluorometric (ratiometric) | Yes (Dip-stick method) | 1.27nM | Yes | *Talanta*, 2021, **221**, 121477. |
| 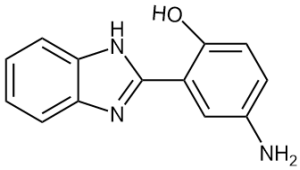 | Fluorogenic (ratiometric) | Yes (Test-strip method) | 5.3 nM | Yes | *RSC Adv.*, 2021, **11**, 10836. |
| 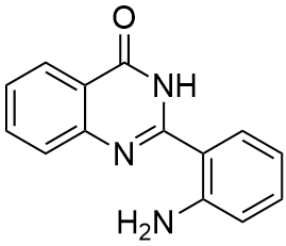 | Fluorometric (Turn-on) | Yes (Test-strip method) | 0.16 ppm | Yes | *New J. Chem.*, 2021, **45**, 5631. |
| 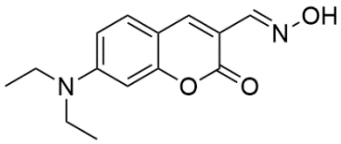 | Colorimetric, fluorometric (ratiometric) | Yes (Dip-stick method) | 0.12 µM | Yes | *New J. Chem.*, 2020, **44**, 5784. |
| 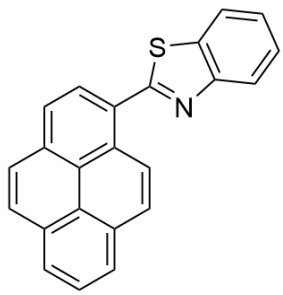 | Colorimetric, fluorometric (ratiometric) | Yes (Dip-stick method) | 1.54 nM | Yes | *New J. Chem.*, 2019, **43**, 14991. |

| | | | | | |
|---|---|---|---|---|---|
| 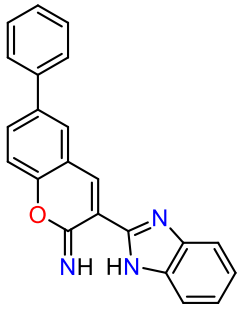 | Fluorometric (ratiometric) | Yes (Dip-stick method, Test-strip method) | (4.25±0.19) x $10^{-7}$ (M) | Yes | **Present Work** |

# List of publications

## Thesis works:

1. A new ‘‘turn-on’’ molecular switch for idiosyncratic detection of $Al^{3+}$ ion along with its application in live cell imaging, **Amitav Biswas**, Rahul Naskar, Debarpan Mitra, Akash Das, Saswati Gharami, Nabendu Murmu and Tapan Kumar Mondal, ***New Journal of Chemistry***, 46, 21968-21975, 2022.
2. A biphenyl thiosemicarbazide based fluorogenic chemosensor for selective recognition of $Cd^{2+}$: application in cell bioimaging, **Amitav Biswas**, Debarpan Mitra, Rahul Naskar, Atanu Maji, Akash Das, Nabendu Murmu and Tapan Kumar Mondal, ***Analytical Methods***, 15, 2745-2754, 2023.
3. An ICT-based organic framework for the fluorogenic detection of lethal pulmonary agent phosgene, **Amitav Biswas**, Atanu Maji, Saswati Gharami and Tapan Kumar Mondal, ***New Journal of Chemistry***, 47, 17154-17162, 2023.
4. A triphenylamine scaffold for fluorogenic sensing of noxious cyanide via the ICT mechanism and its bioimaging application, **Amitav Biswas**, Rimi Mukherjee, Atanu Maji, Rahul Naskar, Krishnendu Aich, Nabendu Murmu and Tapan Kumar Mondal, ***Sensors & Diagnostics,*** 3, 1201-1211, 2024.
5. A distinctive and proficient fluorescent switch for ratiometric recognition of the menacing cyanide ion: biological studies on MDA-MB-231 cells, **Amitav Biswas**, Saswati Gharami, Atanu Maji, Subhabrata Guha, Gaurav Das, Rahul Naskar and Tapan Kumar Mondal, ***Analytical Methods,*** 16, 8010-8018, 2024.

## Other works:

1. A novel carbazole-benzothiazole-based chemodosimeter for the chromogenic and fluorogenic recognition of $CN^-$, Atanu Maji, **Amitav Biswas**, Akash Das, Saswati Gharami, Krishnendu Aich and Tapan Kumar Mondal, ***New Journal of Chemistry***, 47, 11557-11564, 2023.
2. A chemodosimetric Approach for the visual detection of nerve agent simulant Diethyl chlorophosphate (DCP) in liquid and vapour phase, Atanu Maji, **Amitav Biswas**, Biswajit Bera and Tapan Kumar Mondal, ***Analytical Methods***, 15, 6417-6424, 2023.

3. Efficient solid and solution state emissive resuable solvatochromic fluorophore for colorimetric and fluorometric detection of CN-. Atanu Maji, Krishnendu Aich, **Amitav Biswas**, Saswati Gharami, Biswajit Bera and Tapan K. Mondal, ***Analyst***, 149, 1557-1570, 2024.
4. Adaptable Biomolecule-Interactive Dual Colorimetric Chemosensor for $Cu^{2+}$ and $Pd^{2+}$: Insight from Crystal Structure, Photophysical Investigations, Real-Time Sampling, and Molecular Logic Circuits, Subrata Mandal, Akash Das, **Amitav Biswas**, Arpan Halder, Dibyendu Mondal, and Tapan Kumar Mondal, ***Crystal Growth & Design***, 24, 1051-1067, 2024.
5. Modulation of the binding sites for an adaptable DNA interactive probe: efficient chromo-fluorogenic recognition of $Al^{3+}$ and live cell bioimaging, Atanu Maji, Debarpan Mitra, **Amitav Biswas**, Moumita Ghosh, Rahul Naskar, Saswati Gharami Nabendu Murmu and Tapan Kumar Mondal, ***Sensors & Diagnostics,*** 3, 1866-1876, 2024.

NJC

ROYAL SOCIETY OF CHEMISTRY

PAPER

View Article Online
View Journal



Cite this: DOI: 10.1039/d2nj03481f

# A new "turn-on" molecular switch for idiosyncratic detection of $Al^{3+}$ ion along with its application in live cell imaging†

Amitav Biswas,[a] Rahul Naskar,[a] Debarpan Mitra,[b] Akash Das,[a] Saswati Gharami,[a] Nabendu Murmu[b] and Tapan Kumar Mondal *[a]

Received 14th July 2022,
Accepted 21st October 2022

DOI: 10.1039/d2nj03481f

rsc.li/njc

A highly sensitive, reversible, reusable and fluorogenic "turn-on" probe (HBTC) is fabricated for the sole detection of $Al^{3+}$. On incremental addition of $Al^{3+}$ in a solution of HBTC in ACN : $H_2O$ (4 : 1), a sharp "turn-on" emission enhancement is observed at 480 nm. The reversibility of the probe (HBTC) was displayed on the addition of $F^-$ solution. The detection limit is found to be of the order of $10^{-9}$ M which suggests that HBTC can detect $Al^{3+}$ at a very minute level. The mechanism for $Al^{3+}$ detection in ACN : $H_2O$ (4 : 1) is attributed to forbidding C=N isomerization and ESIPT process simultaneously turning on the chelation-enhanced fluorescence process. The reusability and real-time application of the probe are also studied. Bioimaging study reveals that HBTC can detect $Al^{3+}$ in human breast cancer cells (MDA-MB-231). Electronic structure of the probe is explained by density functional theory.



## Introduction

Nowadays undue use of ionic pollutants in industry and the farming sector has become a menace to the environment.[1,2] Hence rapid and accurate detection of those ions has become a promising part in the research field in modern times. It is well known that aluminium is the most abundant metallic element in earth's crust. And it has become an integrated part of daily lifestyle such as in drinking water supplies, utensils, packaging of foods, powder, cosmetic products, processed dairy products, cookware, bleached flour, component of medicine, medicine storage containers and manufacturing of cars.[3–7] The WHO (World Health Organization) stated that the average consumption of $Al^{3+}$ in the human body through several ways is about 3–10 mg per kg per day and the maximum recommended limit Al-contaminated water is 7.42 μM.[8–10] Although it has negative effects on both biological and environment systems, it is extensively used on a daily basis. The central nervous system is deeply affected by overexposure of Al.[11] Abnormal concentration of Al in the human body is related to many neurological disorders including Alzheimer's disease, Parkinson's disease and dementia.[12–14] On the other hand, regular intake of Al beyond permissible limits causes bone disease, damage in the gastrointestinal tract, encephalopathy, microcytic hypochromic anaemia, myopathy, bone softening, impaired lung function, fibrosis and chronic renal failure.[15–18] Therefore, it is imperative to develop probes that can detect and track aluminium ions with high sensitivity using minimal resources and under biological conditions. Among different sensing tools for detection of such kinds of environmental hazardous metal, fluorescence-based chemosensors are considered to be efficient for specifically detecting target analytes.[19] Different mechanisms like excited-state intra-/intermolecular proton transfer (ESIPT), chelation-enhanced fluorescence (CHEF), metal–ligand charge transfer, photoinduced electron/energy transfer, fluorescence resonance energy transfer, intramolecular charge transfer, and –C=N– isomerisation are considered to be the reason for chemosensing processes.[20,21] A strong oxidising site is preferred for the CHEF process, through which a radiative process gets turn on.[22] Comparing with different transition metal ions, chemosensors detecting solely $Al^{3+}$ are limited, due to poor coordination power, strong hydration enthalpy and lack of spectroscopic characteristics.[23,24] Being a hard acid, $Al^{3+}$ always prefers to bind hard centres like N and O donor sites. Schiff bases possess excellent coordinating capabilities, showing different biological activities and have potential analytical application.[25,26] Hence, development of probes with such binding sites causing metal–ligand CHEF is an interesting approach due to a fluorescence "turn-on" mechanism on interaction with a guest.

Recently in 2021, Singh *et al.* reported a silatrane-based Schiff base-functionalized probe which can detect $Al^{3+}$ ions

[a] Department of Chemistry, Jadavpur University, Kolkata, 700032, India. E-mail: tapank.mondal@jadavpuruniversity.in
[b] Department of Signal Transduction and Biogenic Amines (STBA), Chittaranjan National Cancer Institute, Kolkata, 700026, India

† Electronic supplementary information (ESI) available. See DOI: https://doi.org/10.1039/d2nj03481f

Analytical Methods

ROYAL SOCIETY OF CHEMISTRY

PAPER

View Article Online
View Journal | View Issue



Cite this: *Anal. Methods*, 2023, **15**, 2745

# A biphenyl thiosemicarbazide based fluorogenic chemosensor for selective recognition of $Cd^{2+}$: application in cell bioimaging†

Amitav Biswas,[a] Debarpan Mitra,[b] Rahul Naskar,[a] Atanu Maji,[a] Akash Das,[a] Nabendu Murmu[b] and Tapan Kumar Mondal *[a]

A diversified biphenyl thiosemicarbazide based chemosensor (HBMC) has been fabricated and reported for the specific detection of $Cd^{2+}$ in a MeOH : $H_2O$ (4 : 1) solution. We observed a chromogenic change from colorless to light yellow colour, and it showed a "turn-on" fluorogenic change from non fluorescent to blooming cyan colour. In fluorometric titration a sharp "turn-on" emission for $Cd^{2+}$ was observed with a ~16 fold increase in fluorescence intensity value at 496 nm by incremental addition of $Cd^{2+}$ ions in the MeOH : $H_2O$ (4 : 1) solution. The reversibility of the chemosensor (HBMC) was confirmed by a sequential addition of the EDTA solution. Again the binding stoichiometry of HBMC with $Cd^{2+}$ was found to be 2 : 1, as confirmed by Job's plot analysis and HRMS spectra of the HBMC–$Cd^{2+}$ complex. The mechanism for $Cd^{2+}$ sensing in MeOH : $H_2O$ (4 : 1) is based upon the inhibition of C=N isomerization and ESIPT process and simultaneously turning on the CHEF (chelation enhanced fluorescence) process. The limit of detection for $Cd^{2+}$ was found to be in the order of $10^{-8}$ (M), which implies that HBMC is an efficient probe to detect $Cd^{2+}$ at the microscopic level. A reusability study was performed and on-sight detection of cadmium ions by the chemosensor (HBMC) was established by dip-stick experiment. *In vitro* detection of $Cd^{2+}$ in human breast cancer cells (MDA-MB-231) by HBMC discloses its cell permeability and biocompatible nature. Computational studies (DFT and TDDFT) with the probe HBMC and HBMC–$Cd^{2+}$ complex were also performed.

Received 16th March 2023
Accepted 10th May 2023

DOI: 10.1039/d3ay00403a

rsc.li/methods



## Introduction

With reference to human health and the environmental system, discriminative detection of heavy and toxic metal ions is one of the most noteworthy aspects in the field of chemosensors. Among those heavy metal ions $Cd^{2+}$ tops the list in relation to its hazardous nature and detrimental effects.[1] Due to the irreversible damage caused by its use in the fields of batteries, smelting, mining, pigments, metallurgy, and fertilizers it has become a hazardous global pollutant.[2–5] Hence due to its outrageous use, it has triggered an inescapable contamination of our soil, water, food, and air.[6–8] Simultaneously living organisms and human health are also being threatened by the excessive use of cadmium.[9] Mainly through water or air, food and inhalation of cigarette smoke, humans are exposed to cadmium.[10] The toxicity level of cadmium is so soaring that the US Environmental Protection Agency (EPA) and Agency for Toxic Substances and Disease Registry have listed this toxic heavy metal as the seventh on the Top 20 Hazardous Substances Priority List,[11] while the WHO (World Health Organization) has given an enforceable drinking water standard for cadmium of 3 ppb to prevent kidney related diseases.[12] This continuous short and long term cadmium exposure of humans causes different disorders, resulting in lung, breast and prostate cancer.[13–15] Therefore the International Agency for Research on Cancer (IARC) has categorized cadmium compounds as carcinogens of category I.[16] The abnormal concentration of cadmium also causes damage to several organs such as the brain, kidneys, bones, and gastrointestinal tract and has increased the risk of cardiovascular disease.[17–20] Renal and adipose tissue dysfunctions and calcium metabolism are also factors caused by excessive cadmium intake.[21–24] However, the mechanism involved in the uptake of $Cd^{2+}$ by cellular and environmental systems and $Cd^{2+}$ carcinogenesis remains obscured.[25–27] Therefore developing a reliable technique to detect $Cd^{2+}$ in environmental systems is an absolute necessity. However there are several techniques such as atomic absorption/emission spectroscopy (AAS/AES), inductively coupled plasma mass spectrometry (ICP-MS), inductively coupled plasma atomic emission spectroscopy (ICP-AES), and anodic stripping voltammetric analysis, but these techniques

[a]*Department: Chemistry, Jadavpur University, Kolkata-700032, India. E-mail: tapank.mondal@jadavpuruniversity.in*

[b]*Department of Signal Transduction and Biogenic Amines (STBA), Chittaranjan National Cancer Institute, Kolkata-700026, India*

† Electronic supplementary information (ESI) available. See DOI: https://doi.org/10.1039/d3ay00403a

NJC

ROYAL SOCIETY OF CHEMISTRY

PAPER

View Article Online
View Journal | View Issue



Cite this: *New J. Chem.*, 2023, **47**, 17154

# An ICT-based organic framework for the fluorogenic detection of lethal pulmonary agent phosgene†

Amitav Biswas, Atanu Maji, Saswati Gharami and Tapan Kumar Mondal *

Received 3rd June 2023,
Accepted 12th August 2023

DOI: 10.1039/d3nj02580b

rsc.li/njc

Fluorescent chemosensor detecting a widely used but highly toxic chemical warfare agent (CWA) such as phosgene is of great importance due to its high sensitivity along with low cost and simple method of preparation. In this study a biphenyl-benzoimidazole based (**BPCI**) chemodosimeter, which displayed a rapid, sensitive and ratiometric detection of the lethal pulmonary agent phosgene, has been developed. Upon the addition of phosgene to the **BPCI** solution in THF, we observed a fluorescence color change from blue to cyan-green. The chemodosimeter (**BPCI**) undergoes nucleophilic substitution reaction with phosgene followed by ring closure to yield the carbamylated final product and shows an explicit ratiometric fluorescence response towards phosgene. The carbamylation was accelerated due to the formation of a six-member ring, which restricts the C–C bond rotation. The probe (**BPCI**) selectively detected phosgene over other toxic relevant analytes. The detection limit (LOD) of **BPCI** for phosgene was established to be in the order of $10^{-7}$ M in the solution phase, which implied that **BPCI** can detect phosgene at a very minuscule level. This ratiometric switch, which we developed, can be used as a potential portable kit for detecting phosgene in the vapour phase, as well as in the solid phase when supported upon TLC plates. Theoretical calculations using the DFT/B3LYP/6-31+G(d) method were performed to unveil the electronic properties theoretically and to interpret the probable sensing mechanism.



## Introduction

In the history of human existence, certain weapons were made for mass destruction (WMD); among them chemical warfare agents are known to be the most ferocious ones created by mankind.[1] These chemical warfare agents (CWAs) can be categorized as nerve agents, blistering agents, pulmonary agents, blood agents, tear gases, psychomimetic agents, incapacitating agents, toxins, *etc.*[2] Among these CWAs, phosgene is included in the list of pulmonary agents as the most threatening to humanity.[3] Due to its catastrophic nature phosgene ($COCl_2$) was employed as a chemical warfare agent (CWC) in World War I and World War II and poisonous gas bombs made from it, caused mammoth causalities to humankind.[4–6] Even with a low exposure limit of this colourless phosgene gas up to 0.1 ppm, it can cause serious irritation to the eyes, skin, nose, lungs, and respiratory system.[7] Outrageous exposure to about 90 ppm of phosgene for 30 minutes can cause dangerous repercussions, such as inducing pulmonary edema, pulmonary emphysema, and finally death.[8–12] The production of nerve agents such as sarin, soman, and tabun is strictly controlled and prohibited by international laws.[13] However, in contrast, due to the dynamic nature of phosgene such as cost effectiveness, high reactivity, and easy availability, it has wide applications in several industries.[14] For instance, it is used as a precursor for the industrial production of chemicals, isocyanate-based polymer materials, pharmaceuticals, aniline dyes, and different types of pesticides such as chloroformates and sulfonylureas.[15–18] Hence due to its in-hand accessibility, it can be potentially exploited by terrorists as chemical weapons. As well as unexpected industrial leakages can also cause havoc and destruction to mankind. Thus, it is indispensable to construct a reliable, cost-effective, selective, and sensitive approach for detecting phosgene, the alerting threat to humanity.

There are various traditional techniques for the detection of phosgene, such as the gas chromatography method, HPLC technique, electrochemical methods, and Raman techniques.[19–26] However these techniques have problems due to the complexity of sample preparation, poor portability, expensive precious instrumentation, and sophisticated procedures. In contrast, fluorescent-based detection of phosgene has gained progressive interest. This could be attributed to several advantages such as a simple preparation procedure, quick response time, suitable field detection, high selectivity with sensitivity, and simple operation

*Department of Chemistry, Jadavpur University, Kolkata-700 032, India.*
*E-mail: tapank.mondal@jadavpuruniversity.in*

† Electronic supplementary information (ESI) available. See DOI: https://doi.org/10.1039/d3nj02580b

 

Sensors & Diagnostics

PAPER

View Article Online
View Journal | View Issue



Cite this: *Sens. Diagn.*, 2024, **3**, 1201

# A triphenylamine scaffold for fluorogenic sensing of noxious cyanide *via* the ICT mechanism and its bioimaging application†

Amitav Biswas,[a] Rimi Mukherjee,[b] Atanu Maji,[a] Rahul Naskar,[a] Krishnendu Aich,[a] Nabendu Murmu[b] and Tapan K. Mondal *[a]

A novel triphenylamine benzimidazole based fluorogenic chemosensor named (2*E*,2′*E*)-3,3′-((phenylazanediyl)bis(4,1-phenylene))bis(2-(1*H*-benzo[*d*]imidazol-2-yl)acrylonitrile) (PBIA) has been successfully generated and characterized by varoius spectroscopic techniques. Among various screened anions, only cyanide ($CN^-$) showed a distinct fluorogenic property towards PBIA. Hence, the optical properties of PBIA were investigated in the presence of cyanide ($CN^-$) by means of UV-vis spectrophotometry and fluorescence spectroscopy in DMSO, where we observed that, upon treatment with $CN^-$ to the probe solution, the orange fluorescence of the ligand showed a blue shift and the orange fluorescence changed to greenish-yellow under an UV lamp. The hypsochromic shift in fluorescence maxima upon the addition of cyanide was attributed to nucleophilic addition of cyanide to PBIA inhibiting the electron flow within the molecule and disrupting the ICT process. The interaction behind the sensing of cyanide was investigated by $^1$H-NMR titration, a mass spectroscopic study and DFT calculations, which supported the mechanism. The limit of detection (LOD) was calculated and found to be in the order of $10^{-8}$ (M). PBIA showed an immediate response in the spectral pattern (<20 s) towards its target cyanide ion, and the effectiveness of the chemosensor was also examined in the presence of competing anions. Furthermore, the practical efficacy of the PBIA was established by a dipstick experiment along with cyanide detection in various natural water resources. Human breast cancer cells MDA-MB 231 were made susceptible to $CN^-$ sensing in a biological system.

Received 17th January 2024,
Accepted 21st May 2024

DOI: 10.1039/d4sd00018h

rsc.li/sensors



## Introduction

We all know that anions play an imperative role in different disciplines, such as biological systems and environmental chemical processes, as well as different technological, clinical and medical processes.[1–4] Among various anions, cyanide is listed as one of the most noxious and lethal chemical substances known to us. Conversely, cyanide has different industrial applications, *i.e.*, in making plastics, papers and herbicides.[5,6] Cyanide is also endlessly used in the synthesis of resins and synthetic fibres, electroplating, refining, leather making, as a chelator in water treatment and metallurgy.[7–10] Again, cyanide salt is majorly used in the extraction of gold from its ore, where the gold elemental substance after complexation with cyanide has reduced oxidation potential; as a result, the substance gets easily oxidized by oxygen to form soluble aurate and dissolves under alkaline conditions, which makes gold easily separable from slag.[11] Despite its enormous applications in various fields, cyanide is still very detrimental to humans even at the minimum dosage of 0.05 mg $kg^{-1}$.[12] Moreover, WHO has set up an acceptable limit of cyanide of 1.9 μM in drinking water due to its toxic nature.[13] Cyanide can be absorbed in the human body through the skin, lungs and gastrointestinal tract, which leads to acute effects in the human body. Cyanide complex with ferric iron in metalloenzymes leads to histotoxic hypoxia (low oxygen level) by inhibition of cytochrome *c* oxidase, where cyanide gets attached to the active sites of cytochrome oxidase (at cytochrome a3) resulting in the disconnection of mitochondrial oxidative phosphorylation, which further leads to obstruction of cellular respiration.[14–16] Excessive exposure to cyanide leads to poisoning of the respiratory system, paralysis of the central nervous system, haemoglobin poisoning, convulsion, and vomiting with loss of consciousness that eventually lead to death.[17] Therefore, huge

[a] *Department of Chemistry, Jadavpur University, Kolkata-700032, India. E-mail: tapank.mondal@jadavpuruniversity.in*
[b] *Department of Signal Transduction and Biogenic Amines (STBA), Chittaranjan National Cancer Institute, Kolkata-700026, India*

† Electronic supplementary information (ESI) available. See DOI: https://doi.org/10.1039/d4sd00018h

Analytical Methods

ROYAL SOCIETY OF CHEMISTRY

PAPER

View Article Online
View Journal | View Issue



Cite this: *Anal. Methods*, 2024, **16**, 8010

# A distinctive and proficient fluorescent switch for ratiometric recognition of the menacing cyanide ion: biological studies on MDA-MB-231 cells†

Amitav Biswas,[a] Saswati Gharami,[*a] Atanu Maji,[a] Subhabrata Guha,[b] Gaurav Das,[b] Rahul Naskar[a] and Tapan Kumar Mondal[*a]

A new fluorescent ratiometric switch (BOHB) was developed for swift and selective detection of cyanide ions in aqueous media without any interference from other competitive anions. Upon gradual addition of cyanide ions into the probe solution, a prominent fluorescence color change from yellow to cyan was observed under a UV chamber. The fluorescence changes thus observed were ratiometric, and the detection limit of this new probe was found to be (22.1 ± 0.89) μM, suggesting that the efficiency of BOHB for the detection of cyanide ions is brilliant even at a minute level. The blue shift in fluorescence intensity upon the addition of cyanide ions was attributed to the deprotonation mechanism of acidic protons present in BOHB. This phenomenon was further explored using $^1$H-NMR study, which supported the mechanism. Further, stability study was performed over a period of 5 days to prominently establish the stability of BOHB. The probe is also highly capable of recognizing $CN^-$ within a very short time-span (almost 15 seconds), thereby making it a brilliant fluorescent switch for the swift recognition of $CN^-$. Furthermore, BOHB was employed for real water sample analysis to display its practical application. Besides, the easy-to-prepare dipstick experiment provides a simple, reusable and recyclable protocol for the suitable qualitative identification of $CN^-$. Lastly, triple negative breast adenocarcinoma (MDA-MB-231) cells were made susceptible to $CN^-$ sensing in a biological system, thereby making BOHB a biomarker tool.

Received 10th September 2024
Accepted 8th October 2024

DOI: 10.1039/d4ay01676a

rsc.li/methods



## Introduction

Many ions possess an assortment of significant purposes in chemical and biological processes.[1–5] Among them, several anions are naturally occurring, having noteworthy roles in vital fields such as chemistry, life sciences, catalysis, medicine, and environmental science.[6–8] Thus, the recognition of anions is of budding concern in the area of environmental and biological sciences. Relentless efforts have been made in order to comprehend the essential principles of interaction between a host and guest anion over the past years.[9–13] Although some anions such as phosphate, sulphate and carboxylate are essential for biological function, exposure to cyanide is exceptionally lethal to living organisms. There are numerous types of anions that are considered exceptionally deadly, but cyanide ($CN^-$) ions specifically have been of consistent curiosity universally owing to their effectiveness and global existence in several methods such as fabricating plastic and fiber products, metallurgy, tanning, fishing, herbicide and fertilizer manufacture, petrochemical production, and extraction of silver or gold.[14–17] Cyanide is acknowledged as an extremely lethal and fast acting poisons.[18,19] In spite of its vast applications in many fields, $CN^-$ is still dangerous to humans even at a dose of only 0.5 mg per kilogram.[20] Considerable environmental hazards would take place in the case of any unintended release of cyanide ions. Toxic HCN can be created *via* the hydrolysis of cyanogenic glycosides in plants such as bitter almonds, sprouting potatoes, bitter cassava as well as apple, cherry, and peach seeds, besides industrial dumping.[17,21] The lethal nature of cyanide is chiefly due to its affinity for the heme iron in cytochrome c oxidase,[22] which afterwards affects oxygen supply to cells and hinders the role of enzymes in the human body, eventually resulting in cytotoxic hypoxia and cellular asphyxiation.[23,24] Additionally, anaerobic metabolism induced by cyanide leads to the buildup of lactate in the blood, which is defined as lactate acidosis. The combined effects of hypoxia and lactate acidosis cause trouble in the central nervous system, thereby instigating serious respiratory seizure and death.[25] According to the World Health Organization (WHO), the maximum permissible concentration level of cyanide is 1.9 mM in drinking water.[26] As minor a quantity as 0.5–3.5 mg cyanide

[a]*Department of Chemistry, Jadavpur University, Kolkata-700 032, India. E-mail: tapank.mondal@jadavpuruniversity.in; saswatiju91@gmail.com*

[b]*Department of Signal Transduction and Biogenis Amines (STBA), Chittaranjan National Cancer Institute, Kolkata-700026, India*

† Electronic supplementary information (ESI) available. See DOI: https://doi.org/10.1039/d4ay01676a

NJC

ROYAL SOCIETY OF CHEMISTRY

PAPER

View Article Online
View Journal | View Issue



Cite this: *New J. Chem.*, 2023, **47**, 11557

# A novel carbazole-benzothiazole-based chemodosimeter for the chromogenic and fluorogenic recognition of $CN^-$†

Atanu Maji, Amitav Biswas, Akash Das, Saswati Gharami, Krishnendu Aich and Tapan K. Mondal *

A novel colorimetric and fluorescent sensing probe, (*E*)-3-(4-(9H-carbazol-9-yl)phenyl)-2-(benzo[*d*]thiazol-2-yl)acrylonitrile (CBTA), was synthesized and characterized by spectroscopic techniques. CBTA displayed "turn off" fluorescence in the presence of cyanide with a higher selectivity than that of others anions such as $Br^-$, $Cl^-$, $I^-$, $NO_3^-$, $SO_4^{2-}$, $SCN^-$, $CO_3^{2-}$, $N_3^-$, $OH^-$, $HCO_3^-$, $H_2PO_4^-$, $HPO_4^{2-}$, $F^-$, $ACO^-$, and $PO_4^{3-}$ in a DMSO : $H_2O$ medium (40 : 60, v/v, HEPES buffer, pH = 7.2). The "turn off" fluorescence response mechanism can be attributed to the intra-molecular charge transfer (ICT) process, which is blocked by the nucleophilic attack of cyanide ions at the cyano vinyl group of the probe. The LOD was found to be $3.57 \times 10^{-8}$ M. The interaction involved behind the sensing of cyanide was investigated by Job's plot analysis, $^1$H-NMR, and mass spectroscopic studies. DFT and TDDFT were also employed to verify the experimental outcomes. Moreover, the test strip experiment provides a wide application prospect of the receptor for detecting poisonous cyanide in the environment and biological system.

Received 11th March 2023,
Accepted 17th May 2023

DOI: 10.1039/d3nj01157g

rsc.li/njc



## Introduction

The development of a new molecular probe for the detection of anions is of great interest because of their vital roles in a wide range of medicines, catalysis, life science, and environment.[1] Additionally, food safety issues and water pollution by poisonous anions have drawn attention with the development of science and technology nowadays.[2–6] Cyanide is one of the most well-known toxic anions, even at a lower concentration, which can be lethal to human beings, animals, and environment. Cyanide is currently extensively used in many industrial processes such as electroplating, petrochemicals, photography, steel production, gold mining, metallurgy, and the synthesis of resign and fibre due to its critical role in multi-functional reactions.[7] World Health Organization (WHO) stipulates that the permissible acceptable concentration of cyanide in drinking water is $1.9 \times 10^{-6}$ mol $L^{-1}$.[8] By the way, cyanide is present in some insects, fruits, seeds, and roots where it is released through the hydrolysis process of cyanogenic glycosides.[9–14] Cyanide binds to the iron ion in cytochrome *c* oxidase, blocks the electron transport in metabolism, and inhibits the production of ATP in cells, making the biological system inefficient to provide sufficient energy to the heart, central nervous system and other vital organs ultimately.[15,16] Considering the above-mentioned fact, the development of simple, efficient and rapid detection tools with high selectivity and sensitivity towards cyanide is an ongoing hot topic to prevent the harmful effect in the human body from contaminated food and environment.

To date, fluorescent molecular probes capable of detecting $CN^-$ have been reported based on fluorescence resonance energy transfer (FRET),[17–19] intra-molecular charge transfer (ICT),[20,21] twisted intra-molecular charge transfer (TICT),[22] excited state intra-molecular proton transfer (ESIPT),[23,24] and photo-induced electron transfer (PET).[25,26] Recently, several groups have reported detection methods by utilizing the nucleophilic addition reaction of cyanide directly involved in the development of covalent bond formation and showed anti-interference ability and high selectivity.[27–38] Compared with the traditional sophisticated analytical tools such as spectrophotometry, voltammetry, chromatography, and potentiometric methods, optical molecular probes based on colorimetric and fluorometric responses towards $CN^-$ are of great preference in virtue of their convenience, simplicity, tenability, low cost, high selectivity and rapid response.[39] Particularly, a naked-eye optical sensor is very much impressive. Since the Tang *et al.* discovery of the AIE phenomenon in 2001, several research groups have been published a growing number of AIE active

*Department of Chemistry, Jadavpur University, Kolkata-700032, India.*
*E-mail: tapank.mondal@jadavpuruniversity.in*

† Electronic supplementary information (ESI) available: NMR and MS of all new compounds, limit of detection determination, quantum yield calculation. See DOI: https://doi.org/10.1039/d3nj01157g

Analytical Methods

ROYAL SOCIETY OF CHEMISTRY

PAPER

View Article Online
View Journal | View Issue



Cite this: *Anal. Methods*, 2023, **15**, 6417

# A chemodosimetric approach for the visual detection of nerve agent simulant diethyl chlorophosphate (DCP) in liquid and vapour phase†

Atanu Maji, Amitav Biswas, Biswajit Bera and Tapan Kumar Mondal *

Received 27th July 2023
Accepted 31st October 2023

DOI: 10.1039/d3ay01296d

rsc.li/methods

In this work, a novel fluorescent ratiometric switch, 8-((6-(1*H*-benzo[*d*]imidazol-2-yl)pyridin-2-yl)methoxy) quinoline (**BIPQ**), has been introduced for sensing an organophosphorus (OP) chemical vapor threat, diethyl chlorophosphate (**DCP**), the low-toxic mimic of the real nerve agent sarin (**GB**). **BIPQ** is efficient at detecting **DCP** in both solution and gaseous phase and has potential practical application with high sensitivity and selectivity. The probe shows significant ratiometric emission in the presence of **DCP** along with a distinct color change from blue to cyan under UV light. The sensing mechanism of the chemodosimeter is based on the generation of a new adduct, **BIPQ**–**DCP**, through a nucleophilic substitution reaction with **DCP** followed by a ring-closure process to form the final product. The detection limit of **BIPQ** for **DCP** was determined to be in the order of $10^{-8}$ (M) in the liquid state. DFT and TDDFT computational techniques were carried out in order to interpret the electronic properties theoretically.



## Introduction

Nowadays organophosphorus compounds are used in preparing many pesticides and herbicides in modern agriculture. Organophosphorus compounds are conceived as one of the most exceptionally hazardous nerve agents and are extremely harmful to the nervous system of every living being if inhaled or ingested through any kind of contamination of food or drink.[1–4] Some known nerve agents including tabun (**GA**), soman (**GD**) and sarin (**GB**) are extremely dangerous organophosphates (Scheme 1), which bear excellent leaving groups owing to which they are known as essential phosphonylating and phosphorylating agents.[5–9] These poisonous chemicals along with their advantages of cheapness, simplicity in manufacture and destructive effects on civilians encourage terrorism. The phosphate group present in these chemicals binds irreversibly with the hydroxyl group present in acetylcholinesterase (AChE), blocks the hydrolysis of acetylcholine neurotransmitters and restrains the decomposition of acetylcholine.[10–13] The excessive storage of acetylcholine causes neuromuscular paralysis, neurological imbalance in the cholinergic synapse, resistance to muscle relaxation, and organ failure, leading to sudden death.[14–20] So they have became a massive threat to all mankind. As most of these compounds are odorless, colorless and tasteless, making them very difficult to detect,[21] it is very urgent to develop a very sensitive, reliable and rapid method for easy and quick detection of these substances in both solution and vapour phase. Our present work is based on the recognition of highly volatile sarin (**GB**) as it is one of the forbidden CWAs used by terrorists. But due to its too toxic nature and difficult availability, an associated substance, diethyl chlorophosphate (**DCP**), has been used as a nerve-gas-mimicking agent for experiments because it has a similar chemical structure and comparable reactivity but very low toxicity.

In recent years, many research groups have already introduced a variety of noteworthy tools for detecting nerve-agent-mimicking substances, including colorimetry,[22–24] fluorometry,[25–27] electro-chemistry,[28–30] mass spectrometry,[31–33] interferometry,[34] enzyme-based biosensors,[35–38] surface acoustic wave (SAW) devices,[39,40] enzymatic assays,[41] photoacoustic spectroscopy,[42] PET based probes,[43] ion mobility spectroscopy,[44] cyclization reactions,[45] photonic crystals,[46] nucleophilic substitution reactions,[47,48] lanthanide luminescence,[49] complex

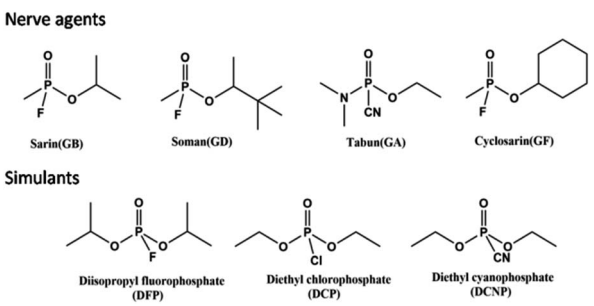


Scheme 1 The structures of chemical warfare agents (CWAs) and their less toxic simulants.

*Department of Chemistry, Jadavpur University, Kolkata-700 032, India. E-mail: tapank.mondal@jadavpuruniversity.in*

† Electronic supplementary information (ESI) available. See DOI: https://doi.org/10.1039/d3ay01296d

Analyst

PAPER

View Article Online
View Journal | View Issue



Cite this: *Analyst*, 2024, **149**, 1557

# Efficient solid- and solution-state emissive reusable solvatochromic fluorophores for colorimetric and fluorometric detection of $CN^-$†

Atanu Maji, Krishnendu Aich, Amitav Biswas, Saswati Gharami, Biswajit Bera and Tapan K. Mondal *

In this work, a novel organic receptor, CPI [(*E*)-3-(4-(9*H*-carbazol-9-yl)phenyl)-2-(1*H*-benzo[*d*]imidazol-2-yl)acrylonitrile], was rationally designed and successfully fabricated for selective and sole recognition of $CN^-$ ions over other competitive anions through an obvious chromogenic and ratiometric emission change in DMSO. The distinct and prominent color change upon the addition of $CN^-$ can be attributed to the typical ICT process, which is induced by the deprotonation of acidic NH protons in the imidazole moiety. The sensor displayed strong solvatochromic effects in commonly used organic solvents such as *n*-hexane, toluene, diethyl ether, DCM, THF, DMF and DMSO. The chemical structure of the sensor was characterized by single-crystal X-ray diffraction, $^1$HNMR, $^{13}$CNMR, IR and mass spectroscopy. Significantly, the probe can function as a fluorescence-based sensor for the efficient detection of low-level water in organic solvents. The solid-state emission properties of CPI were successfully applied to recognise cyanide in a solid-state platform with naked eye-visualized distinct color change. The probe can be made reusable by adding TFA into the $CN^-$ treated probe solution. The detection limit of CPI towards $CN^-$ was determined to be $4.48 \times 10^{-8}$ M. More importantly, the sensor is capable of detecting $CN^-$ in food samples and has been employed for wastewater treatment. Besides, easy-to-prepare CPI-coated test strips provide a simple, reusable and easy-to-handle protocol for the qualitative identification of $CN^-$ conveniently. Finally, density functional theory and time-dependent density functional theory were performed to verify the experimental outcomes theoretically.

Received 5th October 2023,
Accepted 13th January 2024

DOI: 10.1039/d3an01697h

rsc.li/analyst



## Introduction

Many researchers have recently paid attention to the development of anionic chemosensors due to their broad application in many fields including chemical, biological, medical and technological processes.[1–6] Among various anions, cyanide ion is one of the deadliest poisonous anions towards human beings. Even trace amounts of $CN^-$ ions can affect human health in many ways, and it may lead to several health risks because of their excellent binding affinity towards $Fe^{3+}$ ions in cytochrome c oxidase, eventually leading to the incapability to produce ATP in cells, which subsequently results in respiratory arrest and ultimately death.[7–10] Some insects and food samples such as sprouting potatoes, bitter almonds, apple seeds as well as cassava contain cyanide, and it reaches to the environment through the hydrolysis process of cyanogenic glycosides.[11–14] Despite its toxicity, cyanide has been extensively used in many industrial production such as petrochemicals, electroplating, steel production, photography, metallurgy, gold mining, and synthesis of resins and fibres due to its critical role in multi-functional reactions.[15] Therefore, water pollution and food safety issues by toxic cyanide pose a serious threat to human health and environment nowadays.[16–18] The maximum intake of $CN^-$ ions as per the guidelines approved by WHO and USEPA is 1.9 μM (200 μg $L^{-1}$).[19] In view of its vital role in industries and toxicity, the development of a new method to monitor trace amounts of $CN^-$ ions in biological and environmental samples is one of the most sensitive hotspots among researchers. In the past few decades, numerous types of chemosensors based on co-ordination,[20–22] the Sonogashira cross-coupling,[23–25] nucleophilic addition reaction,[26,27] hydrogen-bonding interactions[28,29] and many other mechanisms have been reported for the sole detection of poisonous cyanide. However, these methods have many limitations such as complicated synthetic steps, poor sensitivity and selectivity, use of sophisti-

*Department of Chemistry, Jadavpur University, Kolkata- 700032, India.*
*E-mail: tapank.mondal@jadavpuruniversity.in*

†Electronic supplementary information (ESI) available: NMR and MS of all new compounds, limit of detection determination, quantum yield calculation. See DOI: https://doi.org/10.1039/d3an01697h

CRYSTAL GROWTH & DESIGN

pubs.acs.org/crystal

Article

# Adaptable Biomolecule-Interactive Dual Colorimetric Chemosensor for $Cu^{2+}$ and $Pd^{2+}$: Insight from Crystal Structure, Photophysical Investigations, Real-Time Sampling, and Molecular Logic Circuits

Subrata Mandal, Akash Das, Amitav Biswas, Arpan Halder, Dibyendu Mondal, and Tapan K. Mondal*

Cite This: *Cryst. Growth Des.* 2024, 24, 1051−1067

Read Online

ACCESS | Metrics & More | Article Recommendations | Supporting Information

**ABSTRACT:** Considering the crisis of single probes for the simultaneous colorimetric detection of both $Cu^{2+}$ and $Pd^{2+}$ metal ions, which are toxic to living organisms even in trace amounts, in this communication, we report the facile synthesis and characterization, including single-crystal X-ray diffraction (SCXRD), of a single molecular probe (E)-3-((2-(methylthio)phenyl)diazenyl)-[1,1′-biphenyl]-4-ol (**TABH**). **TABH** is bioactive and avidly interacts with biomolecules such as BSA protein and CT DNA, as evidenced by spectrofluorometric and photometric tests. The probe is also proficient in the selective and swift colorimetric sensing of $Cu^{2+}$ and $Pd^{2+}$ ions in ACN/$H_2O$ (4/1 v/v, pH = 7.2) medium over other metal ions. The sensor's ability to selectively bind the analytes is demonstrated by a noticeable color shift from yellow to reddish brown for $Cu^{2+}$ and violet for $Pd^{2+}$, which is clearly visible to the human eye. A detailed investigation of the recognition mechanism using Job's plot, $^1H$ nuclear magnetic resonance (NMR), infrared (IR) analysis, electrospray ionization (ESI) mass analysis, and density functional theory (DFT) calculations confirmed a 1:1 binding stoichiometry for both ions. Furthermore, the chemosensor exhibits a strong association affinity ($7.61 \times 10^4$ and $1.42 \times 10^5$ $M^{-1}$ for $Cu^{2+}$ and $Pd^{2+}$, respectively) and a low detection limit (54.8 and 5.32 nM for $Cu^{2+}$ and $Pd^{2+}$, respectively). Binding data and absorption studies revealed that $Pd^{2+}$ had a higher affinity for the probe than $Cu^{2+}$. This makes it simple for $Pd^{2+}$ to replace $Cu^{2+}$ in the [**TAB-Cu**$^{2+}$] complex, increasing $Pd^{2+}$'s differential selectivity over $Cu^{2+}$. $Cu^{2+}$ sensing is reversible with the addition of both ethylenediaminetetraacetic acid (EDTA) and triphenylphosphine ($PPh_3$), whereas $Pd^{2+}$ sensing is exclusively reversible with the presence of $PPh_3$ only. The sensing activities were also investigated with molecular logic operations of AND, OR, and NOT gates. In addition, the chemoprobe proved to be effective in identifying $Cu^{2+}$ and $Pd^{2+}$ in actual water samples. It was then converted into test strips, creating a portable device for on-site analysis and testing.

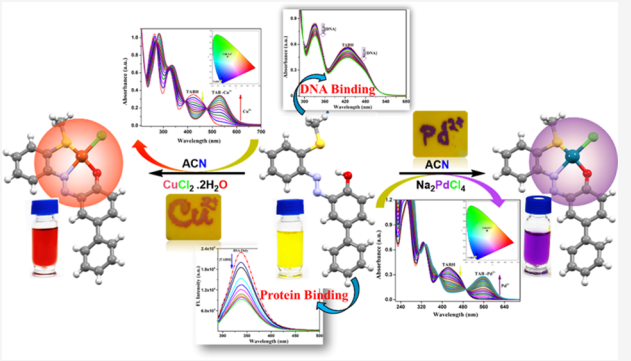




## INTRODUCTION

The industrial boom of the 21st century, particularly the extensive expansion of chemical businesses and mining projects around the world, has harmed Mother Earth, endangering a variety of living things.[1,2] Although heavy metals play an important part in human metabolic activities, excessive consumption can lead to serious health concerns.[3−5] As a result, recognizing and sensitively detecting heavy metals as well as transition metal ions such as cadmium, mercury, lead, copper, and palladium are of great contemporary excitement and have garnered a lot of attention recently in chemistry, biology, and environmental research.[6−8] The $Cu^{2+}$ ion is the third (after iron and zinc) prevalent necessary trace element in living beings.[9,10] A large number of fundamental physiological and pathological processes, including the maintenance of nerves and blood vessels, the production of red blood cells, the formation of bone and connective tissues, iron absorption, signal transduction, free radical detoxification, and dioxygen transport, depend on $Cu^{2+}$. Tyrosinase, cytochrome c oxidase, and superoxide dismutase all use it as an important cofactor.[11−13] Additionally, copper is widely utilized in a variety of industrial applications, including wiring, etching, electroplating, and metal polishing; thus, it is no surprise that industrial effluent contains higher quantities of copper.[14] Though beneficial, the copper ion at an excessive concentration is very toxic for living organisms. Excess intake of it can trigger severe neurodegenerative diseases such as Alzheimer's, Menke's, Parkinson's, and Wilson's diseases as well as gastrointestinal issues like vomiting, headaches, weakness, and diarrhea.[15−18] In contrast, the precious platinum group metal (PGM) palladium is utilized extensively in a variety of

**Received:** September 10, 2023
**Revised:** January 10, 2024
**Accepted:** January 11, 2024
**Published:** January 27, 2024

Sensors & Diagnostics

PAPER

View Article Online
View Journal | View Issue



Cite this: *Sens. Diagn.*, 2024, **3**, 1866

# Modulation of the binding sites for an adaptable DNA interactive probe: efficient chromo-fluorogenic recognition of $Al^{3+}$ and live cell bioimaging†

Atanu Maji, Debarpan Mitra, Amitav Biswas, Moumita Ghosh, Rahul Naskar, Saswati Gharami Nabendu Murmu and Tapan K. Mondal *

Herein, a chromone-based simple reversible fluorescent "turn-on" probe, HMCP [6-(hydroxymethyl)-*N*′-((6-methyl-4-oxo-4*H*-chromen-3-yl)methylene)picolinohydrazide], was successfully utilized to detect $Al^{3+}$ over a group of other coexisting metal cations in MeOH/$H_2O$ (9 : 1, v/v) (HEPES buffer, pH = 7.2). The "turn on" emission response along with the effective enhancement of the fluorescence intensity upon addition of $Al^{3+}$ can be attributed to the inhibition of photo-induced electron transfer (PET) and C=N isomerization, as well as the initiation of chelation-enhanced-fluorescence (CHEF). The HMCP sensor binds $Al^{3+}$ in a 1 : 1 stoichiometry with an excellent binding constant and good detection limit on the orders of $10^3$ $M^{-1}$ and $10^{-7}$ M, respectively. The mode of binding interaction between HMCP with $Al^{3+}$ was evidenced by $^1H$ NMR titration, HRMS, and Job's plot analyses. Theoretical calculations and molecular logic gate applications were also used to demonstrate the binding mode. A DNA binding study was also executed to elucidate the possible bioactivity of the probe and found that HMCP interacts with DNA more effectively than the other analogues studied. Furthermore, the applicability of the probe in a live cell imaging study indicated that HMCP is highly efficient for the detection of exogenous $Al^{3+}$ in living cells. In addition, real water sample analysis and a dip-stick experiment demonstrate that the probe can be used in a wide range of practical and convenient applications.

Received 30th June 2024,
Accepted 10th September 2024

DOI: 10.1039/d4sd00242c

rsc.li/sensors



## Introduction

Materials comprising of multiple applications are important and an emerging field in modern science. A Schiff base is one such kind of material. The low cost, user-friendliness and speed of use of Schiff bases has led to attempts to use them for sustainable development in pharmacy, medicine, molecular memory storage, chemical synthesis and analysis, photochromic materials and in colorimetric and fluorometric chemosensors.[1–6] Several analytical scientific techniques have been developed for the recognition of metal ions including spectrometry, chromatography, spectrophotometry, titrimetry and electrochemical strategies.[7,8] The above mentioned methods are complicated, lengthy and costly. Of the various techniques utilized for metal ion recognition, fluorescence signaling is one of the first preferences as it is reliable, simple, rapid as well as profoundly sensitive for the recognition of environmentally and biologically important metal ions.[9,10]

Aluminum is the third most abundant metal of all elements (after oxygen and silicon) and the most plentiful (8.3% by weight) metallic element in the Earth's crust. The extensive use of aluminum in our daily life appears in diverse areas, for example, in cosmetics, food packaging, medicine, water purification systems, food additives and electronic devices. Thus, the probability of human exposure to aluminum has increased, leading to a serious concern in recent years.[11] In addition, the concentration of $Al^{3+}$ in soil and water resources has dramatically increased due to acid rain and thus inhibits the growth of plant and aquatic ecosystems.[12–20] As directed by the WHO (World Health Organization), the weekly permissible intake limit of $Al^{3+}$ by human beings is around 7 mg $kg^{-1}$ of body weight.[21] On the other hand, long-term intake of excess $Al^{3+}$ could cause major diseases, for example, Alzheimer's, Parkinson's, kidney stones, osteoporosis, cardiac arrest, anemia, headaches, rickets, dementia and many more.[22–27] Doctors refers to $Al^{3+}$

*Department of Chemistry, Jadavpur University, Kolkata-700032, India.*
*E-mail: tapank.mondal@jadavpuruniversity.in*

† Electronic supplementary information (ESI) available: NMR and MS spectra of all new compounds, limit of detection determination, quantum yield calculations, CCDC no. 1535847 & 1535849 *etc.* See DOI: **https://doi.org/10.1039/d4sd00242c**